

PL-TR-97-2027

IONOSPHERIC STRUCTURE SPECIFICATION AND SYSTEMS EFFECTS

**M. Patricia Hagan
Cesar E. Valladares**

**Boston College
Institute for Scientific Research
Chestnut Hill MA 02167**

15 January 1997

DTIC QUALITY INSPECTED 4

**Final Report
28 November 1989 - 27 November 1996**

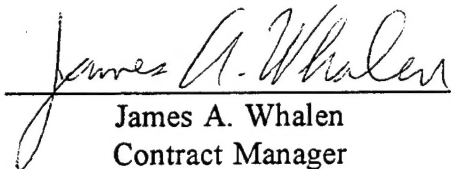
Approved for public release; distribution unlimited

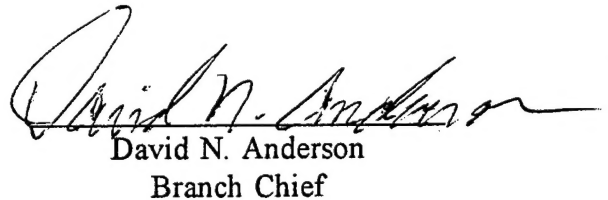


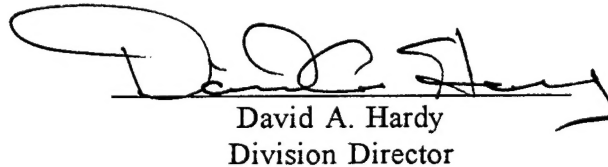
**PHILLIPS LABORATORY
Directorate of Geophysics
AIR FORCE MATERIEL COMMAND
HANSCOM AIR FORCE BASE, MA 01731-3010**

19970508 072

"This technical report has been reviewed and is approved for publication"


James A. Whalen
Contract Manager


David N. Anderson
Branch Chief


David A. Hardy
Division Director

This report has been reviewed by the ESC Public Affairs Office (PA) and is releasable to the National Technical Information Service (NTIS).

Qualified requestors may obtain additional copies from the Defense Technical Information Center (DTIC). All others should apply to the National Technical Information Service (NTIS).

If your address has changed, if you wish to be removed from the mailing list, or if the addressee is no longer employed by your organization, please notify PL/IM, 23 Randolph Road, Hanscom AFB, MA 01731-3010. This will assist us in maintaining a current mailing list.

Do not return copies of this report unless contractual obligations or notices on a specific document require that it be returned.

REPORT DOCUMENTATION PAGE			Form Approved OMB No. 0704-0188	
<small>Public reporting burden for this collection of information is estimated to average 1 hour per response, including the time for reviewing instructions, searching existing data sources, gathering and maintaining the data needed, and completing and reviewing the collection of information. Send comments regarding this burden estimate or any other aspect of this collection of information, including suggestions for reducing this burden, to Washington Headquarters Services, Directorate for Information Operations and Reports, 1215 Jefferson Davis Highway, Suite 1204, Arlington, VA 22202-4302, and to the Office of Management and Budget, Paperwork Reduction Project (0704-0188), Washington, DC 20503.</small>				
1. AGENCY USE ONLY (Leave blank)	2. REPORT DATE 15 January 1997	3. REPORT TYPE AND DATES COVERED Final (28 Nov 89 - 27 Nov 96)		
4. TITLE AND SUBTITLE IONOSPHERIC STRUCTURE SPECIFICATION AND SYSTEMS EFFECTS		5. FUNDING NUMBERS PE 62101F PR 2310 TA G9 WU AM		
6. AUTHOR(S) M. Patricia Hagan Cesar E. Valladares		Contract: F19628-90-K-0007		
7. PERFORMING ORGANIZATION NAME(S) AND ADDRESS(ES) Boston College Institute for Scientific Research 140 Commonwealth Avenue Chestnut Hill MA 02167-3862		8. PERFORMING ORGANIZATION REPORT NUMBER		
9. SPONSORING/MONITORING AGENCY NAME(S) AND ADDRESS(ES) Phillips Laboratory 29 Randolph Road Hanscom AFB MA 01731-3010 Contract Manager: James Whalen/GPIA		10. SPONSORING/MONITORING AGENCY REPORT NUMBER PL-TR-97-2027		
11. SUPPLEMENTARY NOTES				
12a. DISTRIBUTION/AVAILABILITY STATEMENT Approved for public release; distribution unlimited.		12b. DISTRIBUTION CODE		
13. ABSTRACT (Maximum 200 words) This is a comprehensive study of the sources of scintillation that disrupts world-wide Air Force systems dependent on trans-ionospheric radiowave propagation. Measurement of the complete electrodynamics of sun-aligned polar cap arcs has determined that the electromagnetic energy can be larger than the particle energy and can be an important contributor to the polar cap energy budget. An analysis of 1400 images from Qaanaaq, Greenland implies that the motion of polar cap arcs is controlled by the entry of open field lines into the polar cap. Based on a few substorm cases, polar cap arcs can persist for up to 90 min after B _z becomes southward. Experimental evidence and numerical simulation (GTIM) have shown that a patch formation event was associated with a large plasma jet. The level of plasma lines associated with auroral arcs can increase due to the action of bump-on-tail instability. We have deployed 6 RACAL and 2 GPS receivers at the equatorial station at Ancon, developed software to perform on-line and off-line processing of the received scintillation signals, and determined for the first time the climatology of the zonal drifts of the irregularities that produce equatorial scintillation.				
14. SUBJECT TERMS scintillation, ionospheric irregularities, gradient-drift instability, irregularity anisotropy, sun-aligned arc electrodynamics, dayside merging, substorm-related currents, theta aurora, polar cap patch formation, large plasma jet, IMF reversals, plasma wave temperature, upper hybrid waves, neutral-ion coupling, drift climatology.		15. NUMBER OF PAGES 292		
		16. PRICE CODE --		
17. SECURITY CLASSIFICATION OF REPORT UNCLASSIFIED	18. SECURITY CLASSIFICATION OF THIS PAGE UNCLASSIFIED	19. SECURITY CLASSIFICATION OF ABSTRACT UNCLASSIFIED	20. LIMITATION OF ABSTRACT SAR	

TABLE OF CONTENTS

1. INTRODUCTION	1
2. POLAR CAP PLASMA IRREGULARITIES	1
2.1 Plasma Structuring in the Polar Cap	1
2.2 IMF Control of Drifts and Anisotropy of High Latitude Irregularities	1
3. HIGH LATITUDE PLASMA STRUCTURES DURING NORTHWARD IMF	1
3.1 Electrodynamics of Sun-Aligned Polar Cap Arcs	2
3.2 IMF Dependency of Stable Sun-Aligned Polar Cap Arcs	2
3.3 Antisunward Decay of Polar Cap Arcs	2
3.4 Model-Observation Comparison Study of Multiple Polar Cap Arcs	3
3.5 Motion of Transpolar Arcs and Their Relation to the Motion of Auroral Boundaries	3
4. HIGH LATITUDE PLASMA STRUCTURES DURING SOUTHWARD IMF	3
4.1 Experimental Evidence for the Formation and Entry of Patches	3
4.2 Modeling the Formation of Polar Cap Patches Using Large Plasma Flows	4
4.3 Formation of Polar Cap Patches Associated with North-to-South Transitions of the IMF	4
5. REMOTE SENSING OF E-REGION PLASMA STRUCTURES BY RADIO, RADAR AND UV TECHNIQUES	6
6. STUDY OF PLASMA LINES	6
6.1 Statistical Analysis and Modeling of Plasma Line Measurements from Sondrestrom During 1985-87	6
6.2 Measurement of Plasma Lines with the EISCAT IS Radar	10
7. EQUATORIAL PLASMA STRUCTURES	10
7.1 Zonal Irregularity Drifts and Neutral Winds Measured Near the Magnetic Equator	13
7.2 Climatology of Zonal Irregularity Drifts	13
8. REFERENCES	13
9. JOURNAL ARTICLES	14

10. REPRINTS OF SELECTED JOURNAL ARTICLES	16
Plasma Structuring in the Polar Cap	17
Interplanetary Magnetic Field Control of Drifts and Anisotropy of High-Latitude Irregularities	31
The Electrodynamic, Thermal, and Energetic Character of Stable Sun-aligned Arcs in the Polar Cap	56
Interplanetary Magnetic Field Dependency of Stable Sun-aligned Polar Cap Arcs	78
Model-Observation Comparison Study of Multiple Polar Cap Arcs	104
Antisunward Decay of Polar Cap Arcs	115
Experimental Evidence for the Formation and Entry of Patches into the Polar Cap	171
Modeling the Formation of Polar Cap Patches Using Large Plasma Flows	199
Formation of Polar Cap Patches Associated with North-to-South Transitions of the Interplanetary Magnetic Field	220
Remote Sensing of Auroral E Region Plasma Structures by Radio, Radar, and UV Techniques at Solar Minimum	250
Zonal Irregularity Drifts and Neutral Winds Measured Near the Magnetic Equator in Peru	264
The Multi-Instrumented Studies of Equatorial Thermosphere Aeronomy Scintillation System: Climatology of Zonal Drifts	276

IONOSPHERIC STRUCTURE SPECIFICATIONS AND SYSTEMS EFFECTS

1. INTRODUCTION

The objective of this investigation is to study the impact of the scintillation caused by the irregular ionosphere on trans-ionospheric radio wave propagation employed by Air Force Systems. We have achieved an understanding of several structuring processes and started to develop realistic models of the evolution of plasma structures. The principal areas where significant progress has been obtained are: 1) Polar cap plasma irregularities, 2) Polar cap patch formation, 3) Sun-aligned polar cap arcs, 4) Remote sensing using UV techniques, 5) Study of plasma lines, and 6) Equatorial plasma structures.

2. POLAR CAP PLASMA IRREGULARITIES

The studies of polar cap plasma irregularities conducted during tenure of this contract have advanced our knowledge of how plasma structuring develops at polar latitudes and how plasma irregularities grow when embedded in the meso-scale structures typically found at these latitudes. The most important findings are described in the following subsections.

2.1. Plasma Structuring in the Polar Cap

Analysis of scintillation and TEC data obtained in conjunction with arcs and patches observed at Thule, Greenland during the high sunspot period of December 1988 were used to indicate the importance of the ExB gradient drift and the Kelvin-Helmholtz instabilities for the generation of irregularities. A description of this work is contained in the paper "Plasma structuring in the polar cap" by Su. Basu, S. Basu, E. J. Weber, and G. J. Bishop. A copy of this paper is included in this report (Appendix 1).

2.2. IMF control of drifts and anisotropy of high latitude irregularities

A comprehensive study with spaced receiver drifts demonstrated that the patch-related irregularities at Thule have very large anisotropy. In such cases, only the apparent drift of the diffraction pattern can be derived. For the case of sun-aligned arcs, however, the true drift can be derived, and distinct examples of sheared flows were obtained. Extending the measurements to Sondrestrom provided evidence that E-region ionization tends to reduce the anisotropy of the patch-related irregularities. Under these circumstances, the true drift of the diffraction pattern can be measured even in the presence of patch-related irregularities. It was found that the true drift agreed well with the simultaneously measured plasma drift by the incoherent scatter radar at Sondrestrom. A description of this work is contained in the paper entitled: "IMF control of drifts and anisotropy of high latitude irregularities" by Su. Basu, S. Basu, E. Costa, C. Bryant, C. E. Valladares, and R.C. Livingston. A copy of this paper is included in this report (Appendix 1).

3. HIGH LATITUDE PLASMA STRUCTURES DURING NORTHWARD IMF

Significant progress has been achieved to understand the formation, lifetime and decay of the E- and F-region polar cap arcs. One of the most important issues in polar cap arc research deals with determining the region of the magnetosphere to which the polar cap arcs map. Several studies have been undertaken to achieve this goal. They are described in the following subsections.

3.1. Electrodynamics of Sun-Aligned Polar Cap Arcs

The complete analysis of data collected by the Sondrestrom incoherent scatter radar (ISR) during a polar cap arc campaign on February-March 1987 prompted a calculation of the Joule heating rate, the field-aligned currents, and the Poynting flux associated with single and multiple sun-aligned arcs. It was found that enhanced ionization signatures of the arc are produced by incoming energetic electrons carrying the outgoing field-aligned current. Electron temperature enhancements of magnitude larger than 2000 K were found within the sheets of the ionizing particle precipitation. Dawn to dusk decreases in the antisunward plasma flow on the order of 1 km s^{-1} , across the arc of order 100 km width, corresponded to upward currents of order $1 \mu\text{A m}^{-2}$. It was also determined that the high-velocity antisunward flow on the dawnside of the arc marked the location of strong persistent Joule heating driven by downward Poynting flux. It was found that a channel of strongly enhanced ion temperature, well above the electron temperature, located along the high-velocity edge of the arc, was quantitatively accounted for by ion frictional heating. It was also concluded that the deposition rate into the ionosphere of the net electromagnetic energy well exceeded the net particle energy deposited by the energetic electron flux. A description of this work is contained in the paper "The electrodynamics, thermal, and energetic character of stable sun-aligned arcs in the polar cap" by C.E. Valladares and H.C. Carlson, Jr. A copy of this paper is included in this report (Section 10).

3.2. IMF Dependency of Stable Sun-Aligned Polar Cap Arcs

This research effort was the first study in which almost 1400 images were analyzed to correlate the presence, orientation, and motion of stable polar cap arcs with the three components of the IMF. It was determined that the probability of observing arcs within the polar cap varied sharply as a function of the arc location; arcs were observed 40% of the time on the dawnside and only 10% on the duskside. Polar cap arcs were mainly detected during northward orientations of IMF B_z . However, 20% of the arcs were observed during "southward IMF conditions". After close inspection, it was found that they were formed under northward IMF conditions. The polar cap arcs were found to be sun-aligned to a first approximation, but presented deviations from this orientation depending upon the location of the arc in the polar cap. The arcs located in the morning and afternoon sectors were found to point toward the cusp. The B_y dependency of the arc alignment is consistent with a cusp displacement in local time according to the sign of B_y . It was found that the arc motion in the dawn-dusk direction depended both on B_y and the arc location within the polar cap. For a given value of B_y , two regions of common flow exist. Between each region the arcs move in the same direction toward the boundary between the regions. Arcs located in the duskside move downward, and vice versa. In this scenario the size of each region is controlled by the magnitude of B_y . The persistent motion of the polar cap arcs was interpreted in terms of newly open flux tubes entering the polar cap and exerting a displacement of the convective cells and the polar cap arcs which are embedded within them. A description of this work is contained in the paper "Interplanetary magnetic field dependency of stable sun-aligned polar cap arcs" by C.E. Valladares, H.C. Carlson, Jr., and K. Fukui. A copy of this paper is included in this report (Section 10).

3.3. Antisunward Decay of Polar Cap Arcs

This study investigated eight cases of polar cap arcs decaying antisunward following an IMF southward turning. The arcs analyzed in this study presented arcs disappearing first in the part of the arc closest to the sun; the effect seemed to propagate toward the midnight part arc in an antisunward fashion. The lags from the IMF reversal to the arc decay were found to vary between 19 and 32 min for 6 of the cases and 60-70 min for the remaining two cases. Data from the J4 sensor on-board the DMSP satellites was also used to characterize the mapping of the polar cap arcs to open or closed field lines. Both open and closed field line arcs were seen in association

with the short lag arcs, while the two arcs associated with 60-70 min lags are on closed field lines. Antisunward decay of polar cap arcs 20 min after B_z turns positive is consistent with convection of new open flux tubes from the cusp due to dayside merging. The long delays can be understood by the development of a substorm-related DP-1 current pattern. A description of this work is contained in the paper "Antisunward decay of polar cap arcs" by J.V. Rodriguez, C.E. Valladares, K. Fukui, and H.A. Gallagher, Jr. A copy of this paper is included in this report (Section 10).

3.4. Model-Observation Comparison Study of Multiple Polar Cap Arcs

This study was designed to prove that the structure of polar cap arcs, say their multiplicity, is mainly determined by the magnetosphere-ionosphere coupling processes and that the spacing of multiple polar cap arcs is related to the hardness of the magnetospheric precipitation. This work is described in the paper entitled "Model-observation comparison study of multiple polar cap arcs" by L. Zhu, C.E. Valladares, J.J. Sojka, R.W. Schunk, and D.J. Crain. A copy of this paper is included in this report (Section 10).

3.5. Motion of Transpolar Arcs and Their Relation to the Motion of Auroral Boundaries

We have completed the first phase of the analysis of images obtained by the DE-1 satellite during passes over the northern hemisphere. It is known that the imager on-board the DE satellite is able to provide simultaneously the location of the transpolar arcs and the location of the auroral oval. Figure 1 presents 12 images obtained on November 08, 1981 with a 12-minute time interval. Values of the IMF were gathered by the ISEE-3 satellite located at 196 earth radius. B_z was positive until 1455 UT when it switched to a southward orientation (-6 nT). The theta aurora disappeared at 1613 UT (not shown in the Figure), this is in good agreement with a delay of ~1.2 hr for the solar wind to reach the magnetopause. It was postulated by Meng (1981) that during B_z northward conditions the polar cap continuously reduces in size. We have calculated in Figure 1 that the equivalent radius of the polar cap (seen as white lines) decreases during the first 7 images, but it increases after 1436 UT and the event ends at 1600 UT with an area larger than the initial size of the polar cap at 1311 UT. The increase and the decrease in the area of the polar cap is proportional to the difference between dayside merging and magnetotail reconnection. Figure 1 also outlines the location of the theta aurora in each of the 12 images. Reiff and Burch [1985] have explained how recently merged field lines move, depending on the 3 components of the IMF and how reconnection proceeds in the nightside to form reclosure cells. The transpolar arc of Figure 1 shows that the area between the arc and the auroral oval grows in size in qualitative agreement with the predictions of Reiff and Burch [1985].

4. HIGH LATITUDE PLASMA STRUCTURES DURING SOUTHWARD IMF

Three different studies have been conducted which have provided observational and numerical verification that polar cap patches can be produced from sub-auroral or auroral plasma that gets fragmented when entering the polar cap. Two mechanisms of meso-scale plasma structuring have been suggested: 1) large plasma flows and 2) north-to-south transitions of the IMF.

4.1. Experimental Evidence for the Formation and Entry of Patches

Based on data collected by the Sondrestrom incoherent scatter radar, Greenland magnetometers and digisondes at Sondrestrom and Qaanaaq, we have shown that a fast plasma jet containing velocity in excess of 2 km s^{-1} can erode a section of the tongue-of-ionization, dividing it into regions of low and high densities. The regions of high density constitute the polar cap patches. This work is described in the paper entitled "Experimental evidence for the formation and entry of patches into

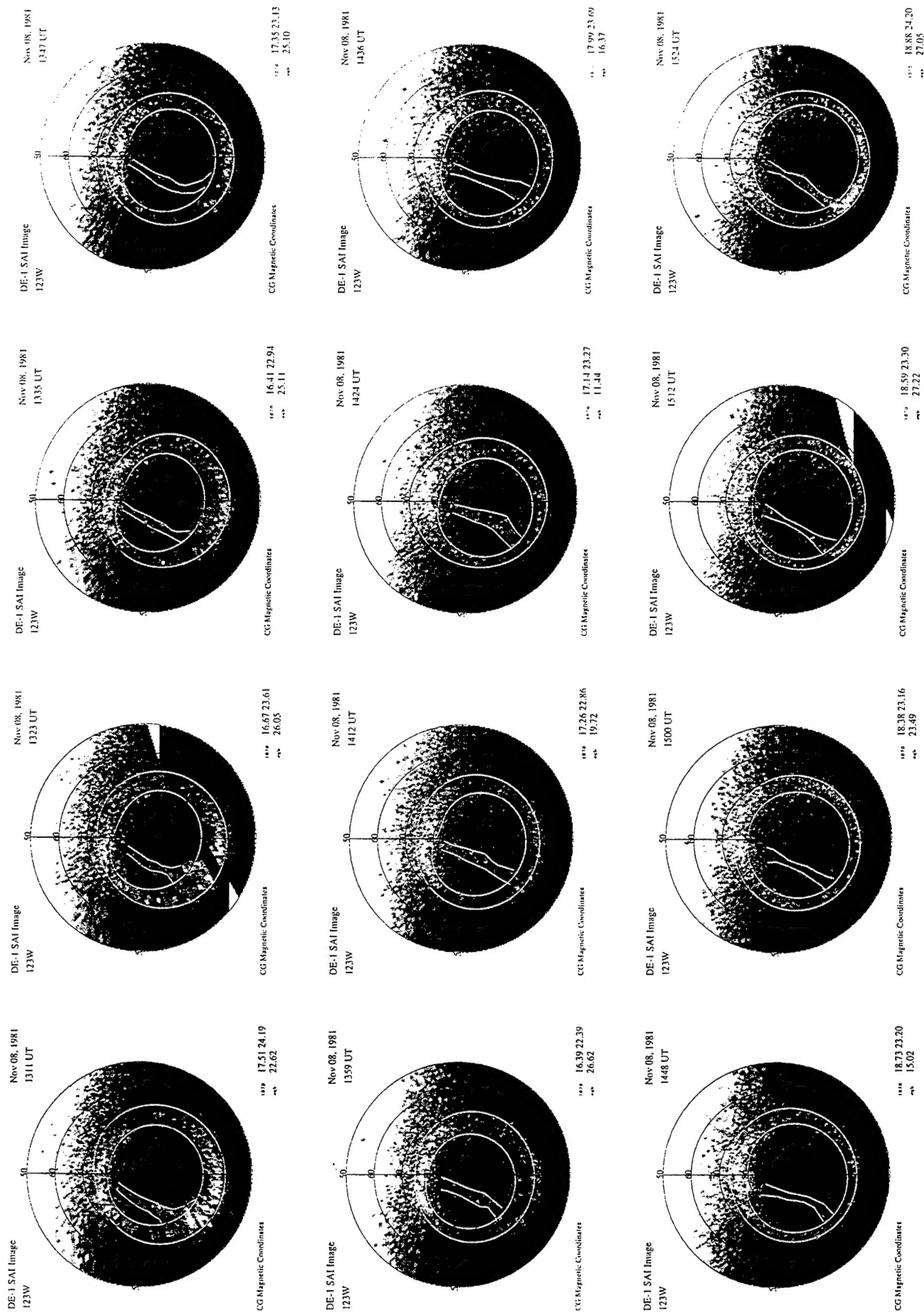


FIGURE 1. Sequence of images measured by the imager on-board DE-1. Ellipsoidal geometrical forms have been fitted to the boundaries of the polar cap and the auroral oval. The transpolar aurora is also highlighted.

the polar cap" by C.E. Valladares, Su. Basu, J. Buchau, and E. Friis-Christensen. A copy of this paper is included in this report (Section 10).

4.2. Modeling the Formation of Polar Cap Patches Using Large Plasma Flows

This study investigated the role of plasma jets on patch formation, determined the temporal evolution of the density structure, and assessed the importance of O^+ loss rate and transport mechanisms. We used a time-dependent model of the high latitude F region ionosphere and model inputs guided by experimental data collected by radar and ground-based magnetometers. Several different scenarios of patch formation were studied. The first attempt employed a Heelis-type pattern to represent the global convection and two stationary vortices to characterize the localized velocity structure. No discrete isolated patches were evident in this simulation. The second modeling study allowed the vortices to travel according to the background convection. Discrete density patches were seen in the polar cap for this case. The third case involved the use of a Heppner and Maynard pattern of polar cap potential. Like the second case, patches were seen only when traveling vortices were used in the simulation. When the Joule frictional heating term was "artificially" removed, it was found that transport of low density plasma from earlier local times can contribute to 60% of the depletion. It was also determined that patches can be created only when the vortices are located in a narrow local time sector, between 1000 and 1200 LT. This work is described in the paper entitled "Modeling the formation of polar cap patches using large plasma flows" by C.E. Valladares, D.T. Decker, R. Sheehan, and D.N. Anderson. A copy of this paper is included in this report (Section 10).

4.3. Formation of Polar Cap Patches Associated with North-to-South Transitions of the IMF

Based on experimental measurements and computer modeling, we have demonstrated that patches can be generated when sun-produced plasma, augmented by particle precipitation, enter the polar cap due to the development of antisunward flows acting in response to a new, even if short lived, B_z south-type global pattern. The data clearly indicated that structured density enhancements can be present near midday during a prolonged period (>1 hour) of steady northward IMF conditions. The nature of the ionospheric flows near the auroral poleward boundary, during B_z northward conditions, prevented the high density plasma from transiting across the polar cap. The experimental evidence was provided by the Sondrestrom incoherent scatter radar, an all-sky imaging photometer located at Qaanaaq, two digisondes located at high latitudes, and a magnetometer placed on-board the IMP-8 satellite. In summary, the data reinforced the view that patches only exist inside the polar cap shortly after negative excursions of the IMF B_z occur. Indeed, the Sondrestrom data gave conclusive evidence for the existence of a quasi-stationary structure of high densities detached from a uniform high density plasma. Convergent electric fields and slightly elevated T_e signatures were seen accompanying the F-region N_e feature. This fact supported the conclusion that soft precipitation was probably responsible for slightly augmenting the density and elevating the electron temperature. Several minutes after B_z changed from north to south, a poleward motion of the density structure was detected by the radar, together with the appearance of a large flow jet equatorward of the original location of the N_e structure. Nearly 34 minutes after the N_e structure departed from the Sondrestrom field-of-view, the Qaanaaq digisonde measured a factor of 2 increase in the f_oF_2 values. We also explored the possibility of sudden north-to-south-to-north transitions as a likely generation mechanism of polar cap patches. The results of the modeling work are in quantitative agreement with the time that the patch appears and the density values measured by the Qaanaaq digisonde. The modeling work also predicted the existence of stationary structures residing near the boundary of the auroral oval and the polar cap during B_z northward conditions. This work is described in the paper entitled "Formation of polar cap patches associated with north-to-south transitions of the IMF" by C.E. Valladares, R. Sheehan, D.T. Decker, D.N. Anderson, T. Bullett, and B.W. Reinisch. A copy of this paper is included in this report (Section 10).

5. REMOTE SENSING OF E-REGION PLASMA STRUCTURES BY RADIO, RADAR AND UV TECHNIQUES

A very comprehensive study was conducted that employed the unique capability of the Polar Bear satellite to simultaneously image auroral luminosities at multiple ultraviolet (UV) wavelengths and to remotely sense large-scale and small scale plasma density structures with its multifrequency beacon package. Coordinated observations between Polar Bear overflights and Sondrestrom incoherent scatter measurements were presented for two nights during January-February 1987. It was confirmed that the energetic particle precipitation responsible for the UV emissions causes the electron density increases in the E region. Large magnitudes of phase and amplitude scintillations were measured at 137 and 413 Mhz in the regions of E-region enhancements. Steep phase spectral slopes with spectral index of 4 were found in these regions. Strength of turbulence computations utilizing the ISR density profiles and observed characteristics of phase and amplitude scintillations suggested an irregularity amplitude varying between 10 and 20% at several km outer scale size in the E region and extending 50 km in altitude. An estimate of the linear growth rate of the gradient-drift instability in the E region showed that these plasma density irregularities could have been generated by this process. This work is described in the paper entitled "Remote sensing of auroral E region plasma structures by radio, radar, and UV techniques at solar minimum" by Su. Basu, S. Basu, R.E. Hoffman, R.E. Daniell, P.K. Chaturvedi, C.E. Valladares, and R.C. Livingston. A copy of this paper is included in this report (Section 10).

6. STUDY OF PLASMA LINES

We have performed two studies of plasma lines to investigate the importance of wave-particle interaction in the amplitude of the plasma lines. The first study deals with an statistical study of many experiments conducted at Sondrestrom and the second study used observations with the EISCAT UHF system.

6.1. Statistical Analysis and Modeling of Plasma Line Measurements from Sondrestrom During 1985-87

We have completed the analysis of several plasma line observations at Sondrestrom, which were conducted between the years 1985 and 1987. The main purposes of these experiments were to make precise observations of the plasma line intensity associated with auroral arc events and to use this experimental data for comparison with a computer model of plasma line intensity. Our model of the plasma line intensity included the eigenvalue solution of the electron transport equation and the Perkins relation of the plasma line intensity.

The first task of this project was to determine the distribution of the primary electron (P_0). This was achieved by performing iterative fittings to the measured electron density and temperature until the error between the measured and predicted parameters was less than 10%. A schematic of this method is depicted in Figure 2. Figures 3 and 4 show the plasma line intensity expressed in terms of Plasma Wave Temperature (PWT). PWT corresponding to phase energies (E_f) less than 1.35 eV is plotted in Figure 3 and that for E_f larger than 1.75 is displayed in Figure 4. We also included the theoretical PWT profiles (continuous line) for: a) E_f equal to 1.35 eV (Figure 3) and b) $E_f = 1.90$ eV (Figure 4). Good agreement was found between the theoretical and experimental PWT for phase energies below 1.35 eV. However, the model predicts almost an order of magnitude smaller plasma line intensities for values of E_f larger than 1.75 eV. The disagreement may be reconciled if production of upper hybrid waves is considered and a subsequent flattening of the distribution of secondaries in the energy range between 1.75 and 5 eV has occurred. A similar flattening of the velocity distribution has been observed to occur at mid-latitudes [Basu et al., 1982]. Based on these characteristics of the auroral plasma line, we inferred that upper hybrid waves produced a

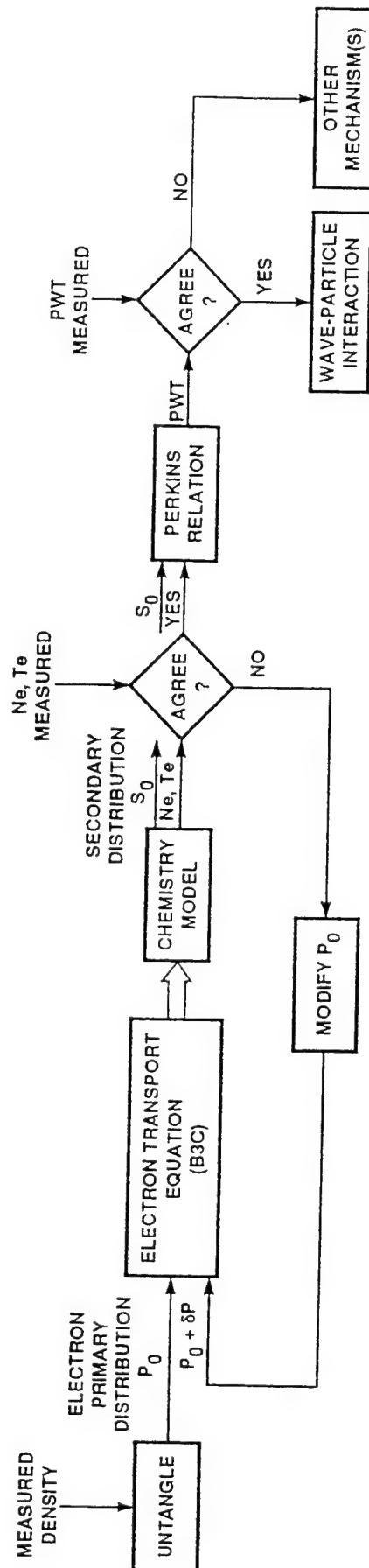


FIGURE 2

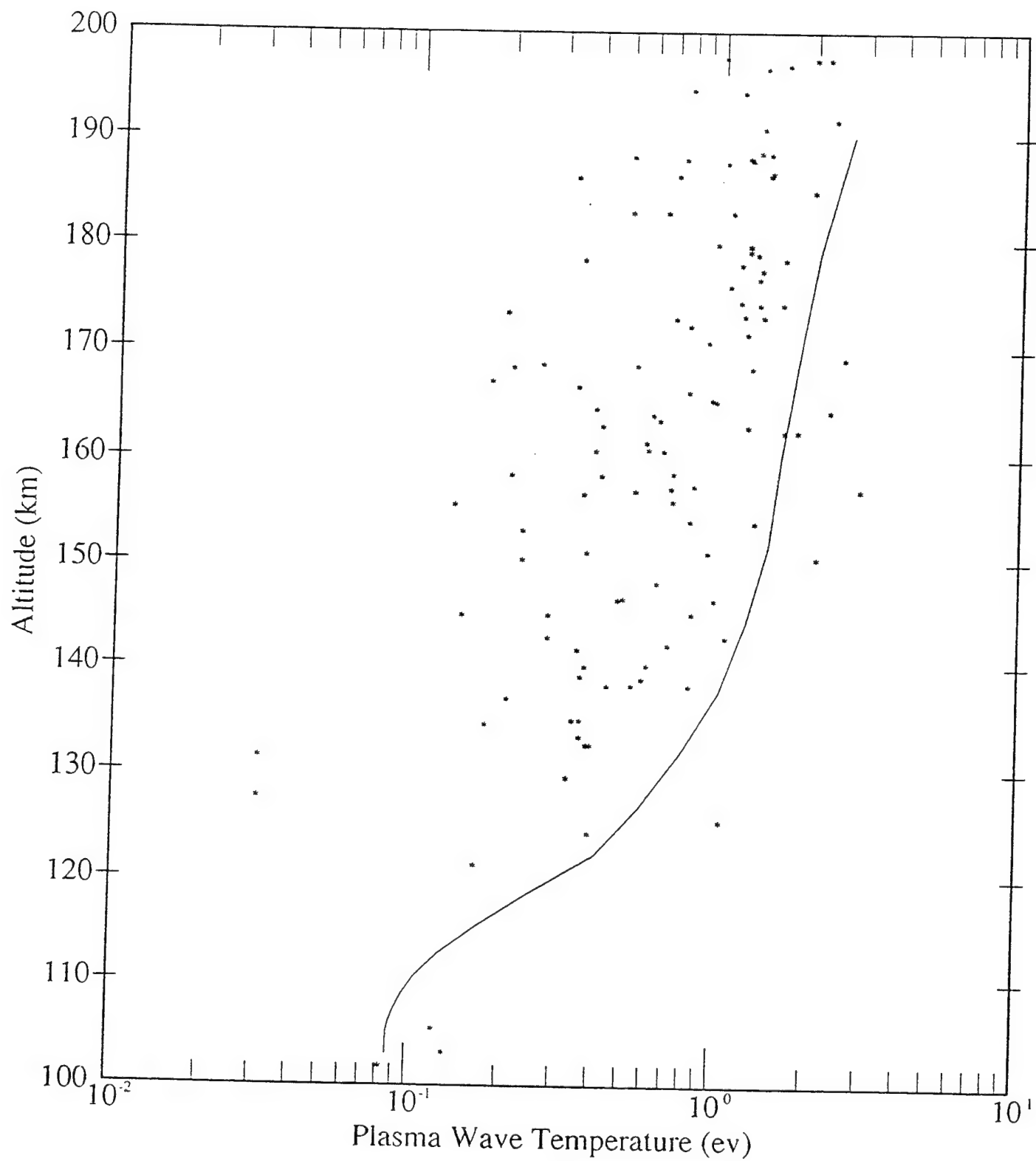


FIGURE 3

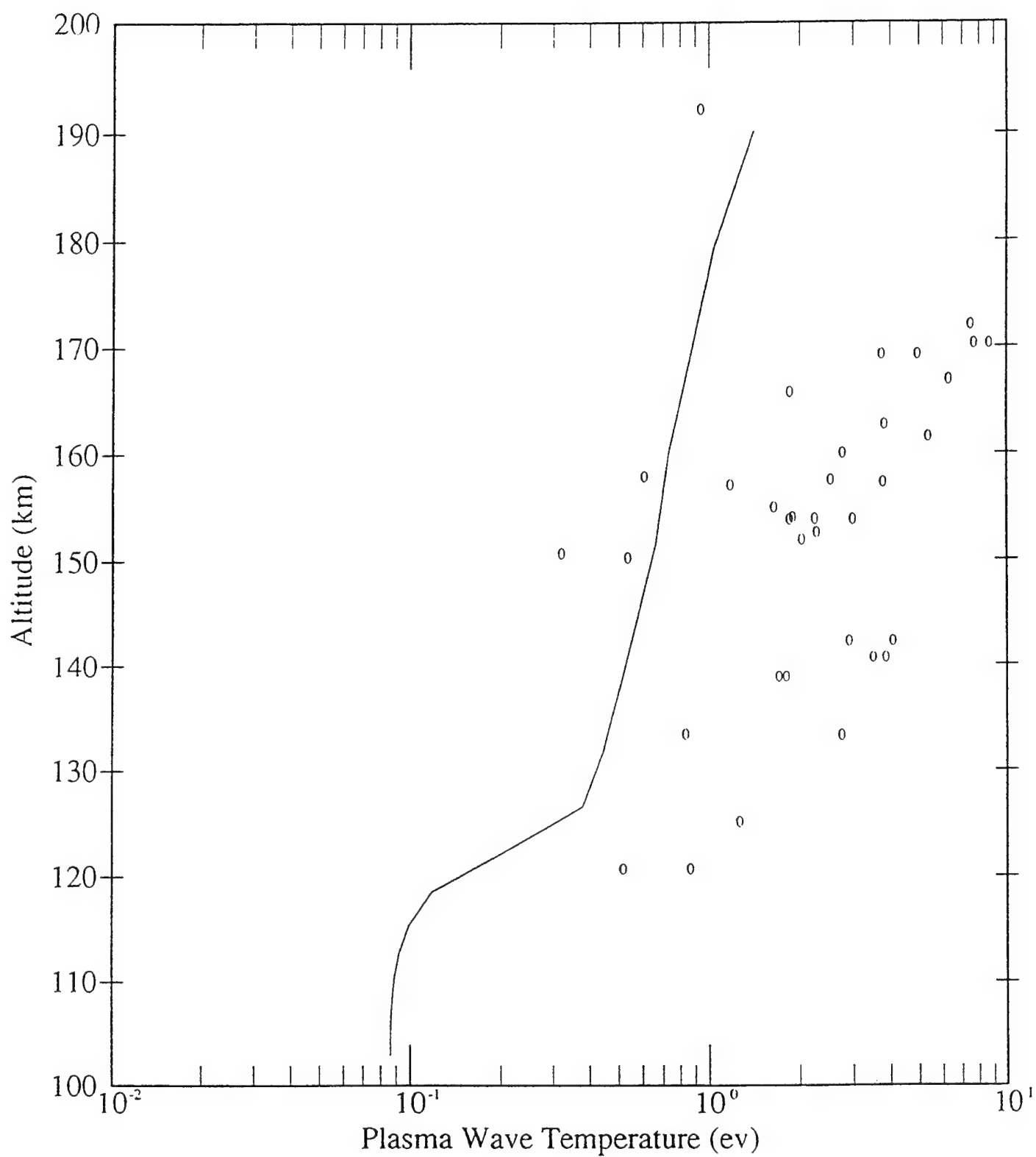


FIGURE 4

flattening of the distribution of the secondaries ($E_f > 1.75$ eV), consequently decreasing the Landau damping of the plasma waves and greatly increasing the amplitude of the plasma lines.

6.2. Measurement of Plasma Lines with the EISCAT IS Radar

Plasma line data measured by the EISCAT UHF radar, during auroral arc events on February 28, 1992, was analyzed and compared to the results of a computer model of the plasma line intensity. The model consisted of the eigenvalue solution of the electron transport equation and the Perkins relation of the plasma line intensity.

The prominent feature of the plasma line data is the altitude at which the plasma line echoes were produced, 435 km. These observations constitute the first time that plasma lines associated with auroral precipitation were seen at F-region altitudes. Moreover, the plasma line enhancements reached values well over 100 times their thermal level. This is the same magnitude or larger than the level of E-region plasma line enhancements that have been measured previously with the Sondrestrom incoherent scatter radar. During the experiments the EISCAT UHF radar was operated in a monostatic mode, with the radar beam directed along the magnetic field. Pulses were transmitted at two frequencies, first a 350-ms pulse at 929 MHz and then followed by a 160-ms pulse at 928 MHz. Integration time was only 10 seconds. The long pulse was used to measure the ion line auto-correlation functions (ACFs) and the short pulse for observing the ion line and the plasma line power profiles. A 128-ms pulse was also transmitted for plasma line spectra.

Four receivers were used to measure plasma line signals and were tuned to detect only the down-shifted plasma line. The four receivers were set at offset frequencies between 5 and 8 MHz and were spaced every 1 MHz. Plasma line echoes originating from each of the two transmitted pulses were recorded, and in some cases all 4 plasma line channels made clear detections. The lower panels of Figure 5 show the power profiles measured by the four plasma line receivers, and the left upper panel displays the density profile obtained by the ion line receiver at 2227:10 UT. A large plasma line echo is seen centered at 435 km in the 8 MHz channel; another plasma line detection was also performed with the 7 MHz channel. These signals correspond to a plasma wave temperature above 10 eV, as can be seen in the right upper panel of Figure 5. The spectra of the down-shifted plasma line signal are displayed in the upper panels of Figure 6. The five traces in the upper panel correspond to the plasma line spectra at -8.5 MHz for 5 different altitudes, starting at 435 km altitude and separated by 5 km. The middle panel shows the spectra of the plasma line down-shifted by 8 MHz. The narrowness of the spectra indicates that the plasma line signal originated near the peak of the F-region.

The intermittent nature of the enhanced plasma lines and the large value of the down-shifted line served to rule out the possibility that a photoelectron flux from the conjugate hemisphere was responsible for the plasma line echoes. The results of the modeling effort suggested that secondary electrons created locally or transported from below were not able to generate plasma lines at the level that was observed. Then, another mechanism or plasma instability must be in effect to produce the level of plasma lines that were detected with the EISCAT radar at F region altitudes.

7. EQUATORIAL PLASMA STRUCTURES

We have performed two studies aimed at understanding the ion-neutral coupling during the development of the equatorial spread-F (ESF) phenomena and determining the climatology of the zonal irregularity drifts. These two research efforts are described in the following two subsections.

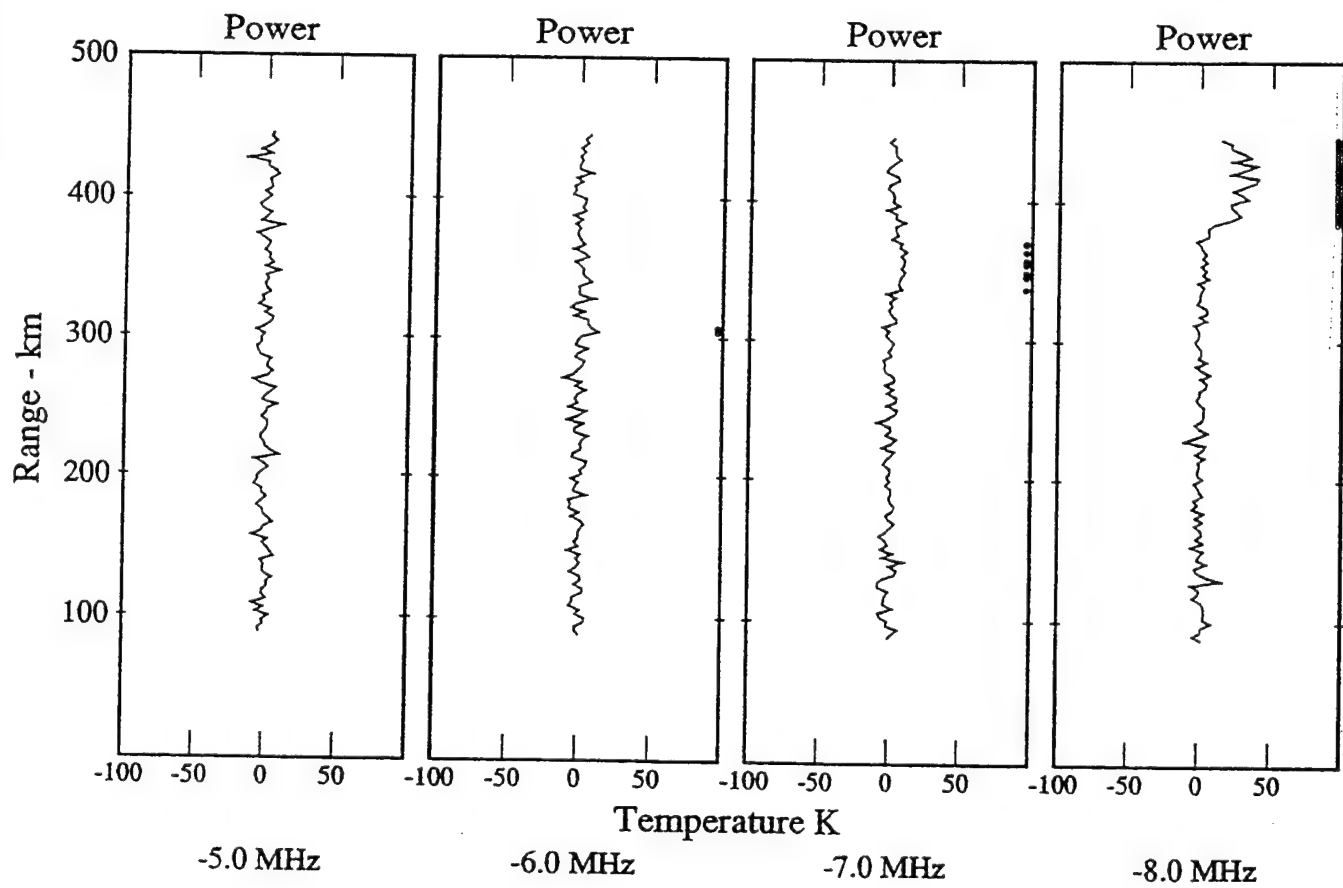
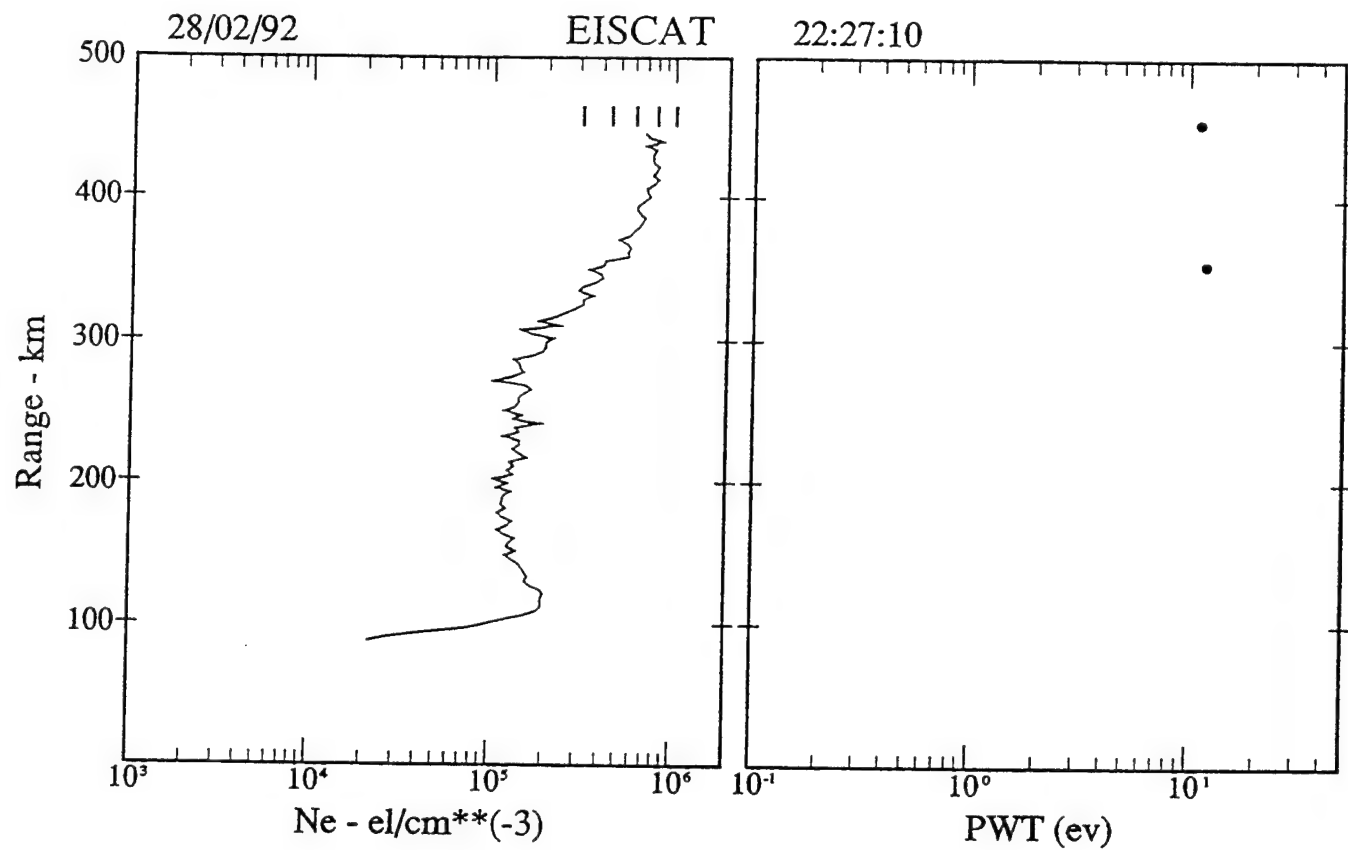


FIGURE 5

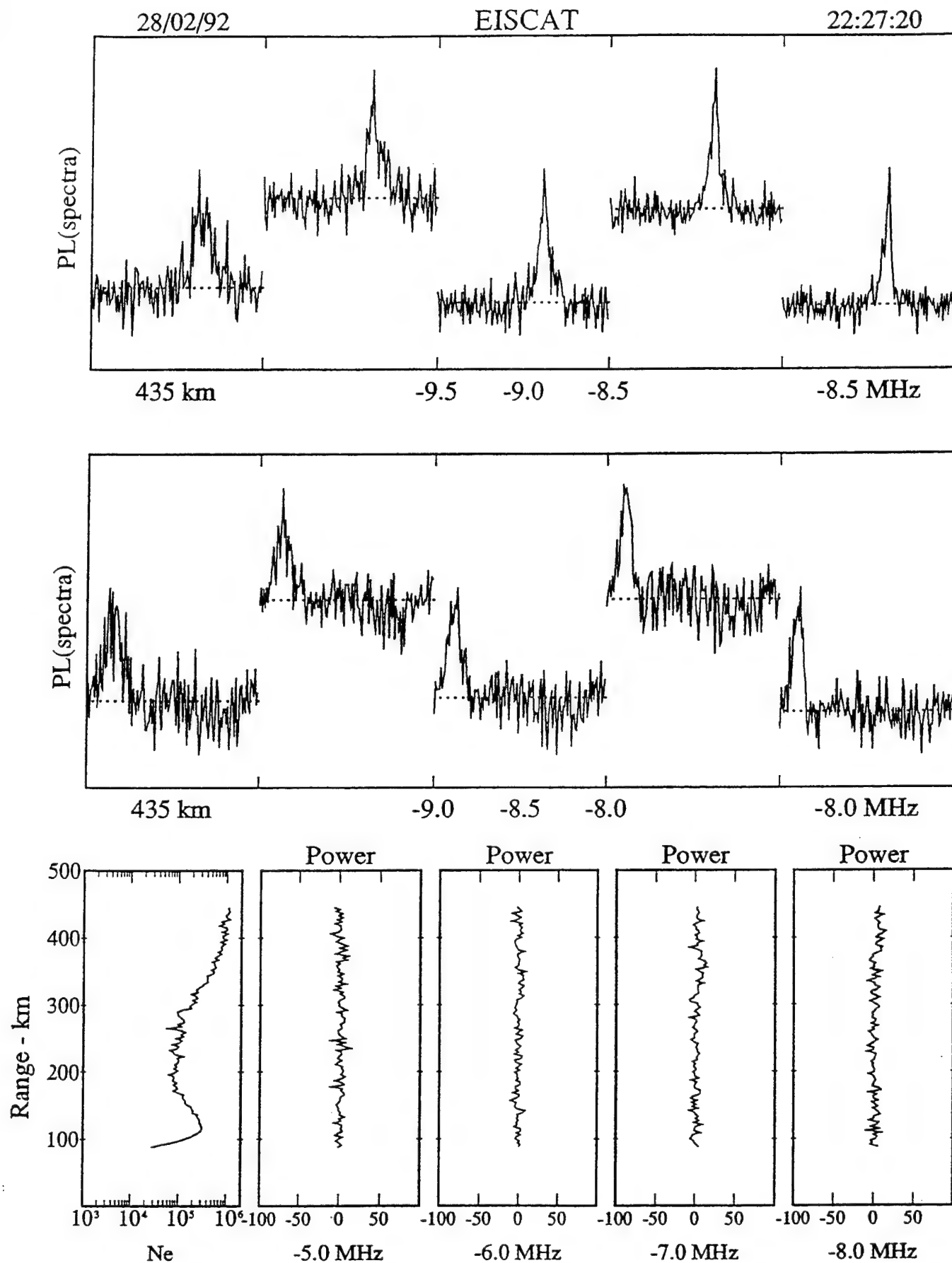


FIGURE 6

7.1. Zonal Irregularity Drifts and Neutral Winds Measured Near the Magnetic Equator

This study consists of the first detailed examination of zonal irregularity drifts made by spaced receiver scintillation and radar interferometer techniques and zonal neutral winds measured simultaneously with a Fabry-Perot Interferometer. These concurrent measurements were performed during evening hours in the presence of equatorial spread-F. The drift of km-scale irregularities obtained by the scintillation technique agreed with the drift of 3-m irregularities. The neutral winds, however, were sometimes a factor of two higher. This result was understood as a partial reduction of the vertical polarization electric field in the F-region caused by the effect of integrated Pedersen conductivity in the off-equatorial nighttime E-region coupled to the F-region at high altitudes above the magnetic equator. This work is described in the paper entitled "Zonal irregularity drifts and neutral winds measured near the magnetic equator in Peru" by S. Basu, Su. Basu, E. Kudeki, H.P. Zengingonul, M.A. Biondi, and J.W. Meriwether. A copy of this paper is included in this report (Section 10).

7.2. Climatology of Zonal Irregularity Drifts

A spaced-antenna scintillation system was deployed at the equatorial station of Ancon (11.09°S, dip latitude 1.4°N). The system initially consisted of three UHF antennas aligned in the magnetic east-west direction, and a 10-m dish used for L-band scintillation. The system was later augmented by two more receivers forming another baseline. At the present time 2 GPS receivers (Novatel and Ashtech) complete the system and provide measurements of L-band scintillations from the GPS constellation of satellites.

We have established the climatology of the zonal drifts of the irregularities and compared these values to the climatology of zonal neutral wind which is the driver of the equatorial electrodynamics. The statistics of the first year's drift and scintillations have been presented as a function of local time, season and magnetic activity and compared with the statistics of ion drift based on the incoherent scatter technique. We found the scintillation drifts to be in good agreement with the Jicamarca radar observations except for the fact the scintillation drifts exhibit a value 20 - 30 ms⁻¹ higher. This discrepancy was attributed to lower ion drag experienced in the presence of ESF due to a sustained uplifting of the ionosphere. This work is described in the paper entitled "The multi-instrumented studies of equatorial thermosphere aeronomy scintillation system: Climatology of zonal drifts" by C.E. Valladares, R. Sheehan, S. Basu, H. Kuenzler, and R.C. Livingston. A copy of this paper is included in this report (Section 10).

8. REFERENCES

Basu, B., T. Chang, and J.R. Jasperse, Electrostatic plasma instabilities in the daytime lower ionosphere, *Geophys. Res. Lett.*, 9, 68, 1982.

Reiff, P.H., and J.L. Burch, IMF B_y-dependent dayside plasma flow and Birkeland currents in the dayside magnetosphere, 2. A global model for northward and southward IMF, *J. Geophys. Res.*, 90, 1595, 1985.

9. JOURNAL ARTICLES

- (1) Basu, Su., S. Basu, E.J. Weber, and G.J. Bishop, Plasma structuring in the polar cap, *J. Geomag. Geoelectr.*, 42, 763-776, 1990.
- (2) Valladares, C.E. and H.C. Carlson, Jr., The electrodynamic, thermal, and energetic character of stable sun-aligned arcs in the polar cap, *J. Geophys. Res.*, 96, 1379, 1991.
- (3) Basu, S., Su. Basu, E. Kudeki, H.P. Zengingonul, M.A. Biondi, and J.W. Meriwether, Zonal irregularity drifts and neutral winds measured near the magnetic equator in Peru, *J. Atm. Terr. Phys.*, 53, 743-755, 1991.
- (4) Basu, Su., S. Basu, E. Costa, C. Bryant, C.E. Valladares, and R.C. Livingston, Interplanetary magnetic field control of drifts and anisotropy of high-latitude irregularities, *Radio Sci.*, 26, 1079-1103, 1991.
- (5) Basu, Su., S. Basu, R. Estes, R.E. Huffman, R.E. Daniell, P.K. Chaturvedi, C.E. Valladares, and R.C. Livingston, Remote sensing of auroral E region plasma structures by radio, radar, and UV techniques at solar minimum, *J. Geophys. Res.*, 98, 1589-1602, 1993.
- (6) Sojka, J.J., M.D. Bowline, R.W. Schunk, D.T. Decker, C.E. Valladares, R. Sheehan, D.N. Anderson, and R.A. Heelis, Modeling polar cap F-region patches using time varying convection, *Geophys. Res. Lett.*, 20, 1783-1786, 1993.
- (7) Valladares, C.E., Su. Basu, J. Buchau, and E. Friis-Christensen, Experimental evidence for the formation and entry of patches into the polar cap, *Radio Sci.*, 29, 167-194, 1994.
- (8) Basu, S., Su. Basu, P.K. Chaturvedi, and C.M. Bryant, Jr., Irregularity structures in the cusp/cleft and polar cap regions, *Radio Sci.*, 29, 195-207, 1994.
- (9) Fukui, K., J. Buchau, and C.E. Valladares, Convection of polar cap patches observed at Qaanaaq, Greenland during the winter of 1989-1990, *Radio Sci.*, 29, 231-248, 1994.
- (10) Decker, D.T., C.E. Valladares, R. Sheehan, D.N. Anderson, and R.A. Heelis, Modeling daytime F layer patches over Sondrestrom, *Radio Sci.*, 29, 249-268, 1994.
- (11) Valladares, C.E., H.C. Carlson, and K. Fukui, Interplanetary magnetic field dependency of stable sun-aligned polar cap arcs, *J. Geophys. Res.*, 99, 6247-6272, 1994.
- (12) Basu, S., Su. Basu, J.J. Sojka, R.W. Schunk, and E. MacKenzie, Macroscale modeling and mesoscale observations of plasma density structures in the polar cap, *Geophys. Res. Lett.*, 22, 881-884, 1995.
- (13) Valladares, C.E., D.T. Decker, R. Sheehan, and D.N. Anderson, Modeling the formation of polar cap patches using large plasma flows, *Radio Sci.*, 31, 573-593, 1996.
- (14) Zhu, L., C.E. Valladares, J.J. Sojka, R.W. Schunk, and D.J. Crain, Model-observation comparison study of multiple polar cap arcs, *J. Geophys. Res.*, 101, 323, 1996.
- (15) Anderson, D.N., D.T. Decker, and C.E. Valladares, Modeling boundary blobs using time varying convection, *Geophys. Res. Lett.*, 23, 579, 1996.

- (16) Obara, T., T. Mukai, H. Hayakawa, A. Matsuoka, K. Tsuruda, K. Fukui, J.V. Rodriguez, and C.E. Valladares, Simultaneous satellite and ground based observations of polar cap phenomena, *J. Geomag. Geoelectr.*, **48**, 935-946, 1996.
- (17) Basu, S., E. Kudeki, Su. Basu, C.E. Valladares, E.J. Weber, H.P. Zengingonul, S. Bhattacharyya, R. Sheehan, J.W. Meriwether, M.A. Biondi, H. Kuenzler, and J. Espinoza, Scintillation, plasma drifts, and neutral winds in the equatorial ionosphere after sunset, *J. Geophys. Res.*, **101**, 26795-26809, 1996.
- (18) Weber, E.J., S. Basu, T.W. Bullett, C.E. Valladares, G. Bishop, K. Groves, H. Kuenzler, P. Ning, P.J. Sultan, R.E. Sheehan, and J. Araya, Equatorial plasma depletion precursor signatures and onset observed at 11° south of the magnetic equator, *J. Geophys. Res.*, **101**, 26829-26838, 1996.
- (19) Valladares, C.E., S. Basu, R. Sheehan, H. Kuenzler, and J. Espinoza, The multi-instrumented studies of equatorial thermosphere aeronomy scintillation system: Climatology of zonal drifts, *J. Geophys. Res.*, **101**, 26839-26850, 1996.
- (20) Valladares, C.E., R. Sheehan, D.T. Decker, D.N. Anderson, T. Bullett, and B.W. Reinisch, Formation of polar cap patches associated with north-to-south transitions of the interplanetary magnetic field, submitted to *J. Geophys. Res.*, 1996.
- (21) Rodriguez, J.V., C.E. Valladares, K. Fukui, and H.A. Gallagher, Jr., Antisunward decay of polar cap arcs, submitted to *J. Geophys. Res.*, 1997.

10. REPRINTS OF SELECTED JOURNAL ARTICLES

The reprints in this section refer to the following article numbers in the Journal Article list of Section 9.

<u>Article No.</u>	<u>Page</u>
1	17
4	31
2	56
11	78
14	104
21	115
7	171
13	199
20	220
5	250
3	264
19	276

Plasma Structuring in the Polar Cap

Sunanda BASU¹, Santimay BASU², E. J. WEBER², and G. J. BISHOP²

¹*Institute for Space Research, Boston College, Newton Center, MA 02159, U.S.A.*

²*Geophysical Laboratory (LIS), Hanscom AFB, MA 01731, U.S.A.*

(Received February 19, 1990; Accepted March 8, 1990)

Propagation experiments providing scintillation, total electron content and drift data in the field of view of an all-sky imager near the magnetic pole in Greenland are utilized to investigate the manner in which ionospheric plasma becomes structured within the polar cap. It is found that under IMF B_z southward conditions, large scale ionization patches which are convected through the dayside cusp into the polar cap get continually structured. The structuring occurs through the $E \times B$ gradient drift instability process which operates through an interaction between the antisunward plasma convection in the neutral rest frame and large scale plasma density gradients that exist at the edges of the ionization patches. It is shown that with the increase of solar activity the strength of the irregularities integrated through the ionosphere is greatly increased. Under the IMF B_z northward conditions, the plasma structuring occurs around the polar cap arcs in the presence of inhomogeneous electric field or disordered plasma convection. In that case, the irregularity generation is caused by the competing processes of non-linear Kelvin-Helmholtz instability driven by sheared plasma flows and the gradient drift instability process which operates in the presence of dawn-dusk motion of arc structures. The integrated strength of this class of irregularities also exhibits marked increase with increasing solar activity presumably because the ambient plasma density over the polar cap is enhanced.

1. Introduction

Plasma subject to stress can structure if the stress-driven instability growth-rates exceed the rates of structure dissipation over a sufficiently large number of instability growth-times. At ionospheric E -region altitudes relatively short chemical time constants (photo-chemical lifetimes of minutes) tend to tie structures to irregularity sources. F -region irregularities are quite complex because their lifetimes could be several hours depending on their scale size (VICKREY and KELLEY, 1982). Over hours polar F -region plasma can move thousands of kilometers. Thus its instantaneous structure represents the cumulative consequence of competing variable growth and dissipative processes encountered over the history of its transpolar and/or return flow trajectory. It is thus not surprising that we are at present a long way from confidence in our ability to physically model or even specify the dominant processes controlling high latitude ionospheric plasma structuring.

It is for this reason that a working group has been set-up under the U.S. National Science Foundation's "Coupling, Energetics and Dynamics of Atmospheric Regions (CEDAR)" initiative to study high latitude plasma structures (HLPS). HLPS is an ambitious program to address the goal of understanding the processes controlling source,

evolution and decay of ionospheric structures using a transpolar array of instrumentation defining key physical parameters. The work of the HLPS group has been primarily organized around the finding that the large scale structuring (\sim hundreds of km) in the very high latitude ionosphere-magnetosphere (I-M) system is controlled by the north-south component, namely, B_z of the IMF. Using sensitive all-sky imaging photometers (ASIPs) located deep within the dark winter polar cap, it has been shown that when IMF B_z is negative, large (~ 1000 km) regions of convecting density enhancement known as patches are observed, whereas, when IMF B_z is positive, sun-aligned arcs are found to populate the polar cap (WEBER *et al.*, 1984; BUCHAU *et al.*, 1985). That both patches and arcs are associated with small-scale density and electric field turbulence (\sim kms to m) has been determined by a variety of in situ and remote sensing techniques (CARLSON *et al.*, 1988a).

The first multi-technique HLPS campaign of February 1988 offered a unique opportunity to further investigate the structuring of patches and arcs. Coordinated measurements carried out with the Sondrestrom incoherent scatter radar, all-sky imaging photometers (ASIPs), orbiting and quasi-stationary satellites and ionosondes allowed us to present a study of these two distinct classes of large scale plasma structures and associated turbulence in the polar cap. These results obtained under low sunspot conditions (SSN=40) have already been published (BASU *et al.*, 1989). A similar data base was utilized to investigate plasma structuring over the polar cap during the second HLPS campaign in December 1988 when the sunspot number was as high as 180. During this campaign, spaced receiver scintillation measurements could be performed to obtain drift and anisotropy of the plasma density irregularities. In this paper the nature of irregularity structures in polar cap arcs and patches observed during the second HLPS campaign under high sunspot conditions will be discussed and contrasted with the results of the first HLPS campaign which as previously mentioned was performed under low sunspot conditions.

2. Results

A polar cap patch and an arc event are studied in detail here and contrasted with the February events published by BASU *et al.* (1989). The patch event was observed on December 6, 1988, while the arc event was observed on December 12, 1988.

2.1 Polar cap patch

The patches were identified on the imager located at Qaanaaq, Greenland between 00–02 UT on December 6, 1988. This period corresponded to extremely low magnetic activity with $\Sigma Kp=7^+$ and 6^+ for December 5 and 6, respectively. In fact, the period December 5–7 constituted the three quietest days of the month. Yet polar cap patches were observed contrary to generally held opinion that patches are observed under moderately high and variable Kp conditions (ANDERSON *et al.*, 1988). No IMF data was available at this time but B_z was predominantly southward (-2 to -3 nT) between 21–23 UT of December 5, 1988 and between 02:30–05:30 UT on December 6 and B_y was positive for 22 hours before and 18 hours after the data gap. Given the experimental evidence for the existence of patches during the IMF data gap, it seems fairly reasonable to assume that B_z remained southward throughout the period.

Figure 1 shows the geometry of the observations. At Qaanaaq (QA), an all-sky

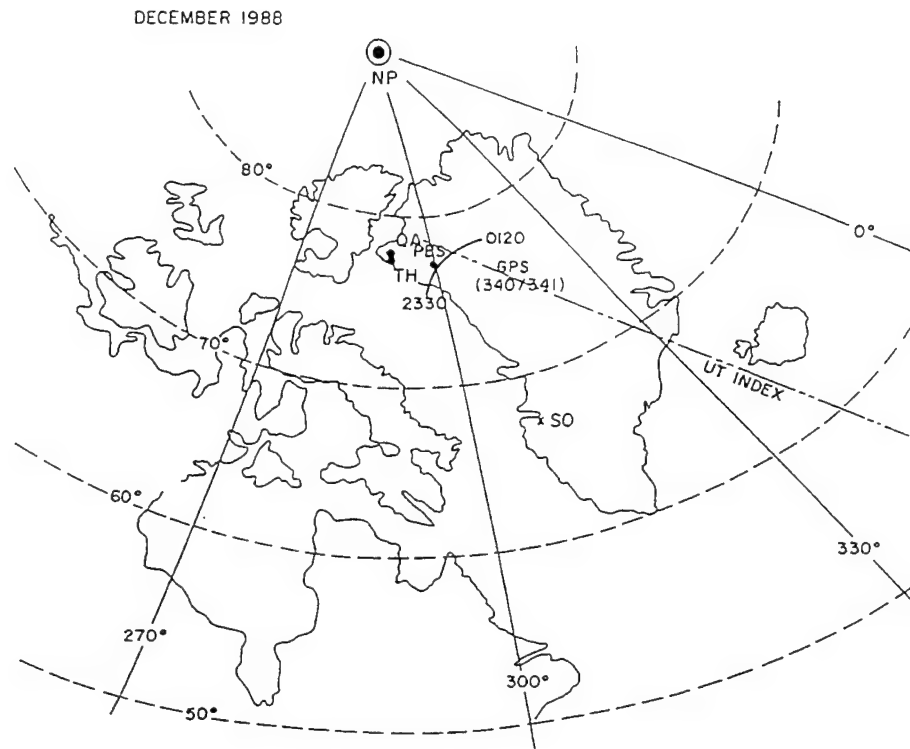


Fig. 1. The geometry of the scintillation and TEC observations in Greenland on December 6, 1988.

imager was operated, while at Thule (TH), polar beacon satellite signals at 244 MHz were acquired by a spaced receiver system which provided amplitude and phase scintillations, as well as, irregularity drift velocity. The intersection of the propagation path with an ionospheric height of 350 km is indicated by a dot (\cdot) and identified by PBS. The phase coherent signals at 1.2 and 1.6 GHz transmitted by the Global Positioning Satellite (GPS) were also monitored at Thule to obtain the total electron content (TEC) of the ionosphere. The locus of the 350 km ionosphere intersection with the ray path for this satellite between 23:30 and 01:20 UT is indicated on the diagram and identified by GPS.

Figure 2 shows the results of the relative TEC obtained from the differential phase measurements with the GPS satellite. The series of increases and decreases of TEC indicates successive encounters of the propagation path with the drifting polar cap patches of ionization. The average enhancement of TEC in these patches above the neighboring minimum amount to $10 \times 10^{16} \text{ m}^{-2}$. Correcting for the slant orientation of the propagation path, the equivalent vertical TEC of the ionization patches above the background is obtained as $7 \times 10^{16} \text{ m}^{-2}$. This contrast of TEC between the patch and the neighboring background may be considered to be equivalent to a variation of $f_o F_2$ from 7 MHz with a slab thickness of 200 km within the patch to $f_o F_2$ of 5 MHz in the background with a slab thickness of 150 km.

The time history of irregularities of several km to several tens of m as observed by 250 MHz phase and amplitude scintillation at the ionospheric intersection point PBS in

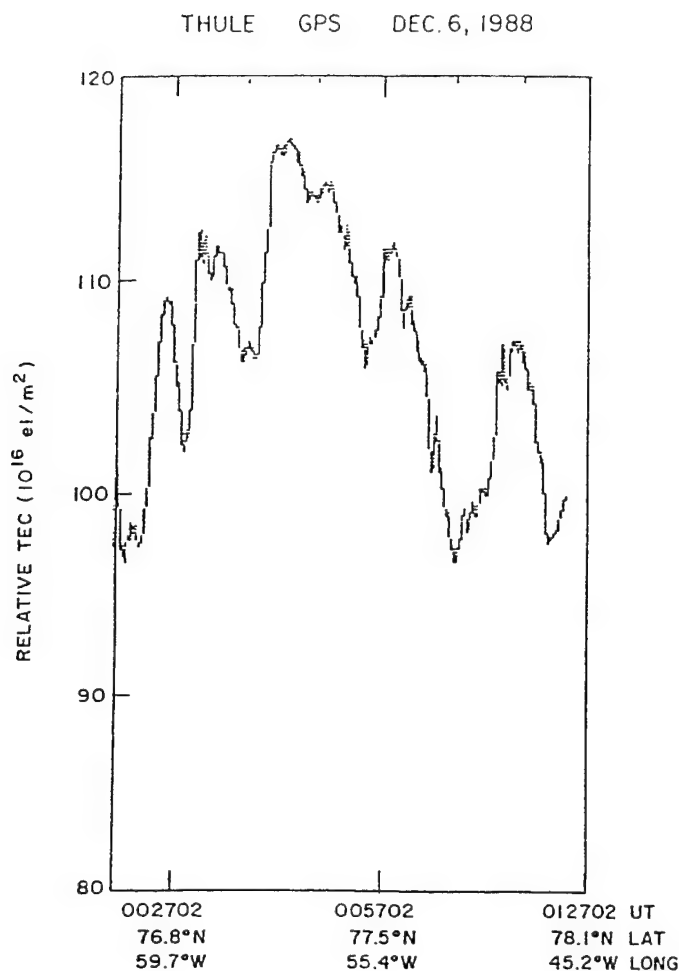


Fig. 2. TEC observations using a GPS satellite from Thule during a polar cap patch event on December 6, 1988.

Fig. 1 which occur in association with the larger scale TEC enhancements is shown in Fig. 3. Large peaks with $S_4=0.8$ are observed in conjunction with phase scintillations exceeding 10 radians (for 82-sec detrend intervals). The other interesting feature of the data is that the decorrelation interval (for 50 percent decorrelation) is fairly constant with time varying at most by a factor of 2 from 0.2 to 0.4 sec.

The scintillation data were being taken with three spaced antennas defining approximately an isosceles right-triangle with smaller sides of approximately 170 m, and using a slightly modified version of the FEDOR (1967) technique as discussed at length by COSTA *et al.* (1988) in their Subsection 4.1, we obtain the direction and magnitude of the vector drift as given in Fig. 4. The magnitude of the drift generally varies between 0.4–0.8 km s^{-1} . The direction of the drift varies between 90–140° with this range of directions indicating drifts varying between magnetic eastward to southeastward (i.e., approximately

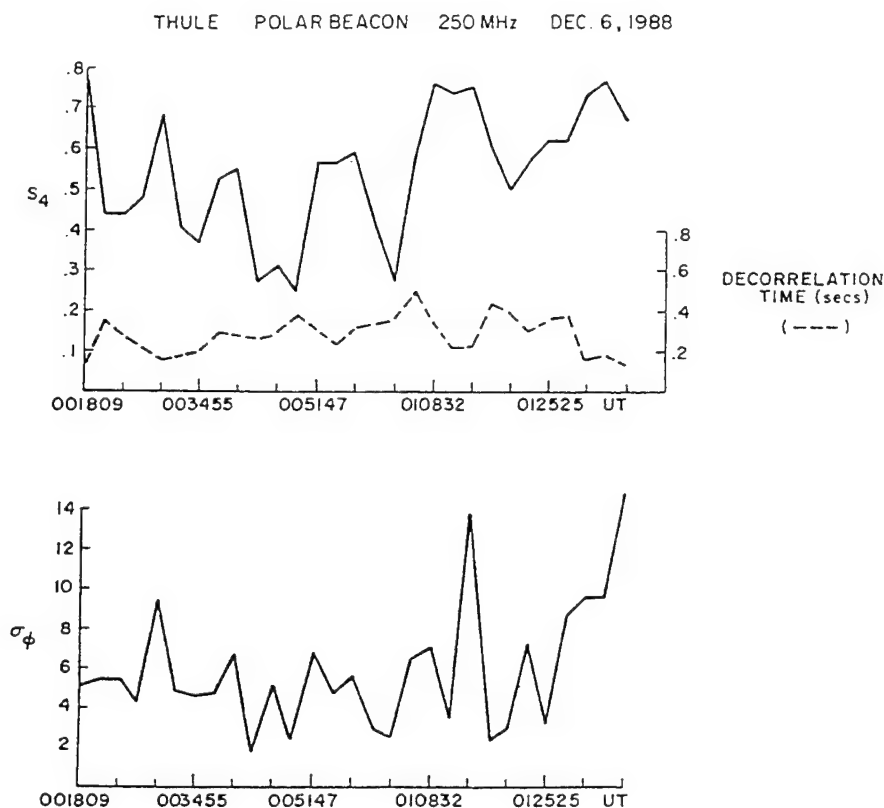


Fig. 3. The same as Fig. 2 for phase and intensity scintillations and decorrelation time at 250 MHz. The phase scintillation is measured in radians, while the intensity scintillation is expressed in terms of the S_4 index, i.e., the second central moment of the intensity.

antisunward), as shown on the corrected geomagnetic latitude (CGL) and time (CGLT) polar plot in Fig. 5.

Neutral wind measurements were available from Thule where the University of Michigan personnel were operating their Fabry-Perot interferometer. Between 00–02 UT the average antisunward drift was 300 ms^{-1} (J. P. Thayer, private communication). It is possible to estimate the time required by the trailing edges of convecting patches to develop small-scale structures as they drift antisunward in the rest frame of the neutrals. The zero-order growth time is given by $L_N/(V_d - U_N)$ where L_N is the density gradient scale length and V_d and U_N are the plasma drift and neutral wind velocities, respectively. Now L_N may be estimated by converting the temporal variations of vertical TEC at the trailing edges of patches to spatial gradients by utilizing the plasma drift velocity. Using this method one gets L_N values as small as 40 km. This when combined with the average plasma drift of approximately 600 ms^{-1} and the neutral wind of 300 ms^{-1} provides growth times on the order of 2 mins which is very short indeed. Thus we can expect the density gradients at the edges of patches to become quickly unstable and generate scintillation producing irregularities. This finding is consistent with earlier studies of patches (WEBER

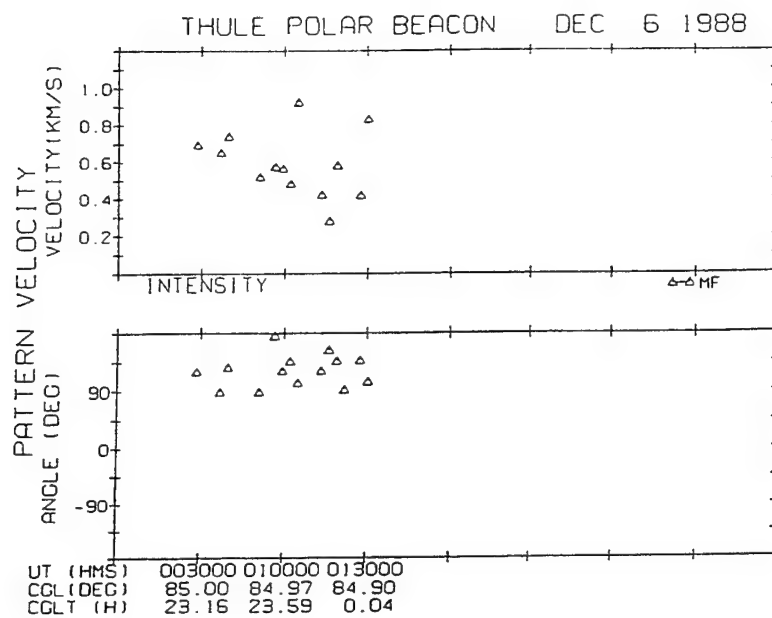


Fig. 4. The pattern drift velocity and its direction obtained for the data shown in Fig. 3 by using spaced antennas.

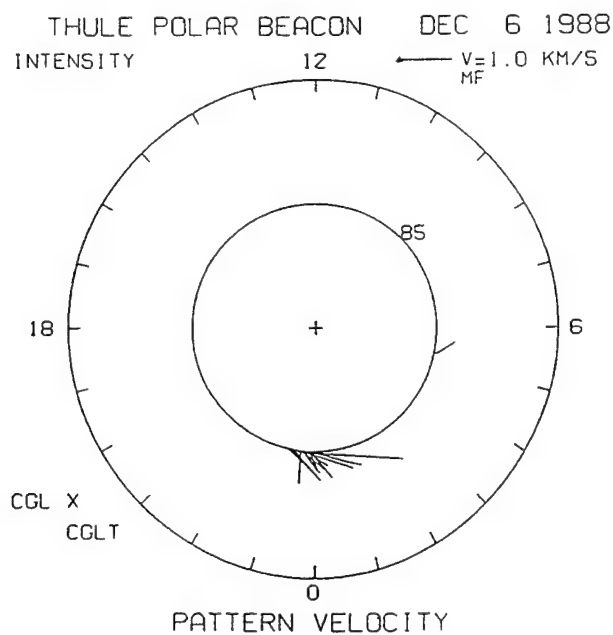


Fig. 5. The drift velocity vector for the December 6, 1988 patch event shown on a polar plot of corrected magnetic latitude and local time.

et al., 1984, 1986; BUCHAU *et al.*, 1985). What remains rather enigmatic is the process whereby a succession of patches can enter the polar cap under extended quiet magnetic conditions. As already mentioned, this is contrary to modeling studies performed earlier (ANDERSON *et al.*, 1988). The cross polar cap potential which can be estimated from the DMSP drift measurements (HAIRSTON and HEELIS, 1989) during this event will be utilized in future to provide further insight into the problem.

2.2 Polar cap arc

The geometry of supporting measurements during the appearance of the sun-aligned arc on December 12, 1988 between 10:30–11:30 UT is shown in Fig. 6 with the symbols having the same meaning as in Fig. 1. Two images of the sun-aligned arc using the Qaanaaq ASIP at 630 and 427.8 nm are shown in Fig. 7. The original all-sky lens (180° field of view) images have been transformed to geographic projections, and the polar cap is displayed as if viewed from above. In order to perform these transformations, an altitude of 250 km was assumed for the 630 nm and 110 km for the 427.8 nm emission height, respectively. Geographic latitudes from 70° to 85° N are shown at 5° intervals, and geographic longitudes from 0° to 135° W are shown at 15° intervals. The “p” and the “g” on the images are the 250 (110) km intersections of the ray paths for the 630 (427.8) nm emissions from Thule to the polar beacon and to the GPS satellites. The scintillation and spaced-receiver drift measurements obtained from the polar beacon (p) and the TEC

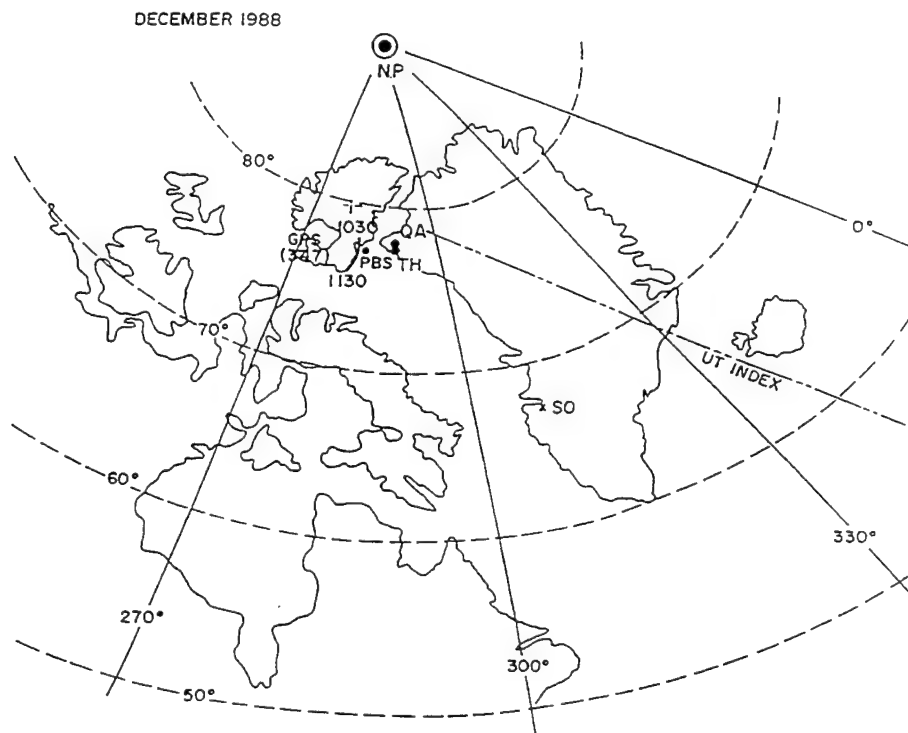


Fig. 6. The geometry of the scintillation and TEC observations in Greenland on December 12, 1988.

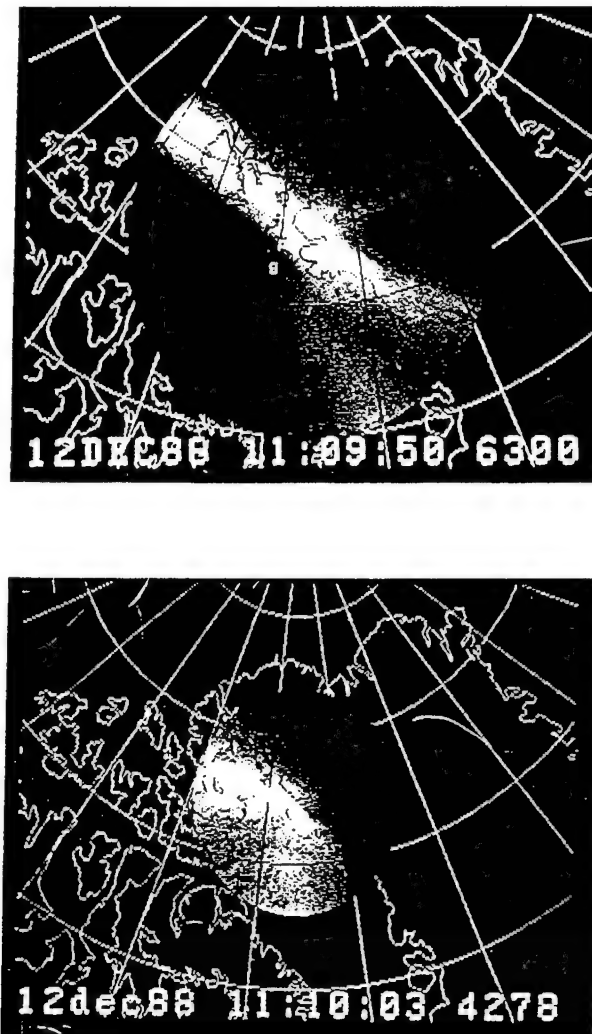


Fig. 7. Two ASIP images of the polar cap sun-aligned arc from Qaanaaq obtained on December 12, 1988 at 630 and 427.8 nm. The images are projected to 250 (110) km for the 630 (427.8) nm images. The points p and g represent the 250 (110) km intersections of the ray path from Thule to the polar beacon and GPS satellites.

from the GPS (g) will thus provide information regarding the large and small-scale structuring of this polar cap arc. The arc is observed at Qaanaaq in the local morning hours such that its equatorward side is toward dawn and consequently its poleward side is towards dusk. The fact that both emissions are present indicates that the particle precipitation responsible for this sun-aligned arc is energetic enough to create ionization in the *E*-region in addition to the *F*-region ionization which produces the 630-nm emission.

The TEC from GPS associated with the arc is shown in Fig. 8. The differential

THULE GPS DEC.12, 1988

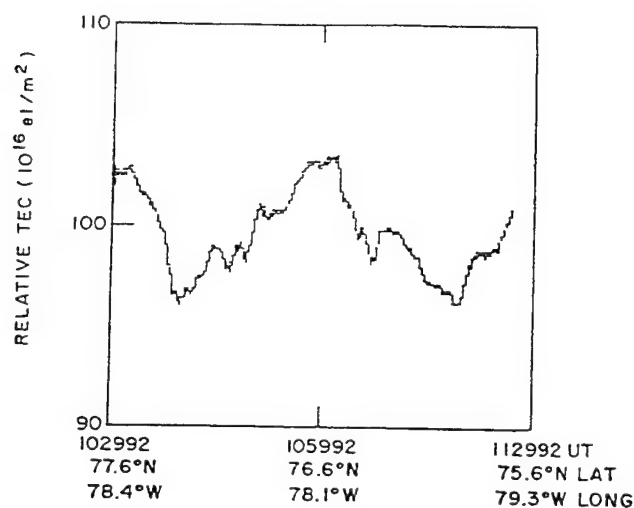


Fig. 8. TEC observations using a GPS satellite from Thule during the sun-aligned polar cap arc event on December 12, 1988.

content increase of $7 \times 10^{16} \text{ el m}^{-2}$ along the slant path, equivalent to a vertical TEC increase of $5 \times 10^{16} \text{ el m}^{-2}$, is less than that seen in patches but the more important difference is the rather gradual rate of increase and decrease for the central structure. This could be due to the generally smaller magnitude of the velocities perpendicular to the length of the arc as obtained from the spaced-receiver technique to be presented below. However, the TEC behavior for this sunspot maximum arc does provide a fairly dramatic contrast when compared with the sunspot minimum arc (BASU *et al.*, 1989).

The phase and amplitude scintillations associated with the arc shown in Fig. 9 is much lower than that observed in the case of patches. There is a peak in the scintillation magnitude at approximately 11:15 UT. Of considerable interest is the variability of the decorrelation time and larger magnitude observed which (since all the scintillations are in the weak-scatter regime) indicates slower drift velocities and variation in their magnitude. The drift variability can also be gauged from the intensity scintillation spectrum obtained at 11:12:08 UT when compared with that obtained at 11:17:45 UT. Whereas the Fresnel filter frequency ($=u/\sqrt{2\lambda z}$, where u is the drift velocity perpendicular to the ray path, λ is the radio wavelength and z the distance between the screen and the receiver) is at 0.2 Hz in Fig. 10(a), it is pushed out to 1.5 Hz in Fig. 10(b). This indicates a factor of seven variation in the drift velocity.

The spaced receiver drift measurements shown in Figs. 11 and 12 provide direct measurements of the magnitude and azimuth of the drift velocity vector in cartesian and polar coordinates as already described in Figs. 4 and 5 for the case of patches. From Fig. 11 we find that just after 11:15 UT the pattern velocity direction changes from -90° azimuth to $+90^\circ$ and at the same time the magnitude of the velocity increases by a factor of seven from 100 to 700 ms^{-1} in agreement with the information obtained from the

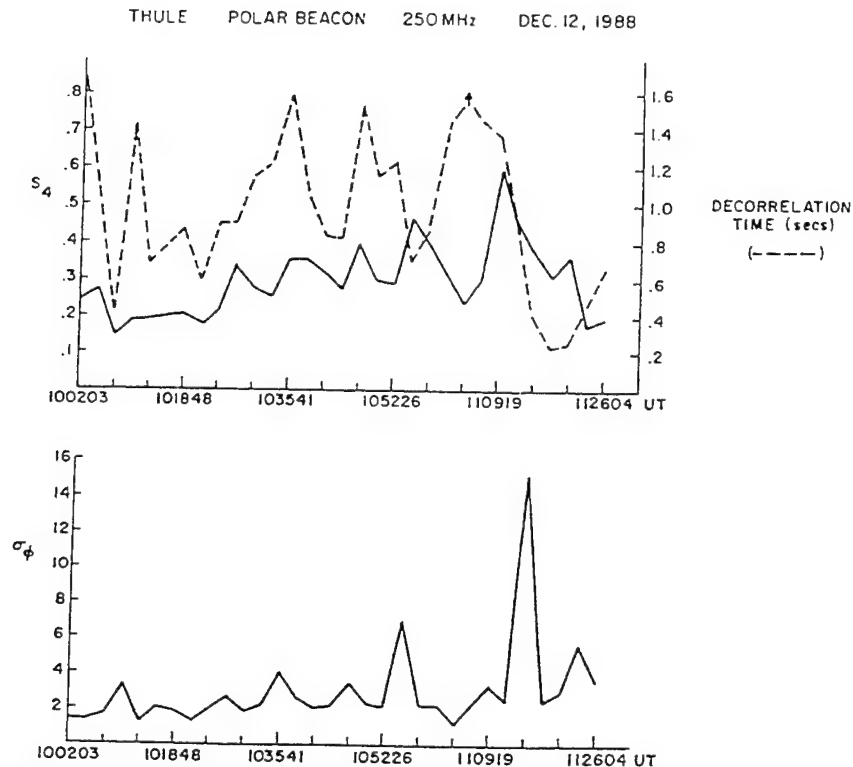


Fig. 9. Same as in Fig. 3 except for the sun-aligned polar cap arc event on December 12, 1988.

spectral comparison. It was mentioned earlier that the peak in the scintillations was at approximately 11:15 UT. From Fig. 11, we note that the scintillation peak is co-located with this velocity shear. From the polar plot in the CGL-CGMLT coordinate system in Fig. 12 we note that the shear is in a direction such that an antisunward drift seen at earlier local time reverses to a sunward drift at a later time. If the time history of the images of the type presented in Fig. 7 shows that initially the point p was equatorward of the arc and at a later time it was encompassed by the arc, then this finding will be consistent with the view that sun-aligned polar cap arcs are found in a region of convergent electric fields (CARLSON *et al.*, 1988b; VALLADARES and CARLSON, 1990). A careful comparison will be made between the position of the point p and the arc boundaries in order to establish the location of the sheared flow.

3. Comparison with Earlier Observations

A comparison between patches obtained at various phases of the sunspot cycle provide evidence for considerable variability for TEC within patches. The first TEC measurements with GPS at Thule in February 1984 with monthly mean sunspot number of 85 provided patches with TEC varying between 10×10^{16} el m⁻² to 15×10^{16} el m⁻² (WEBER *et al.*, 1986). The patches observed during the low sunspot conditions of

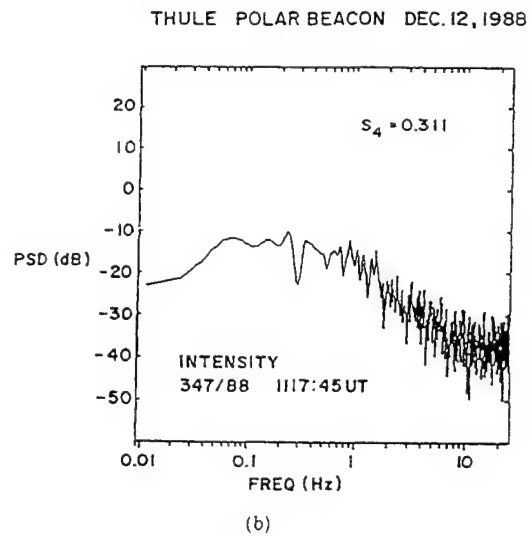
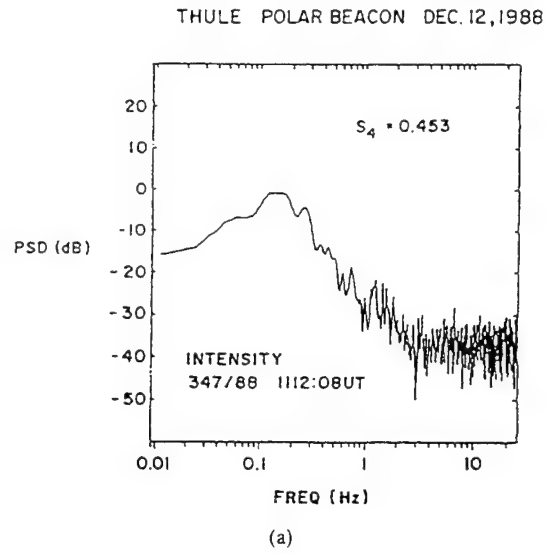


Fig. 10. (a) Intensity scintillation spectrum at 11:12:08 UT on December 12, 1988. (b) The same at 11:17:45 UT on December 12, 1988 during a large sheared flow event.

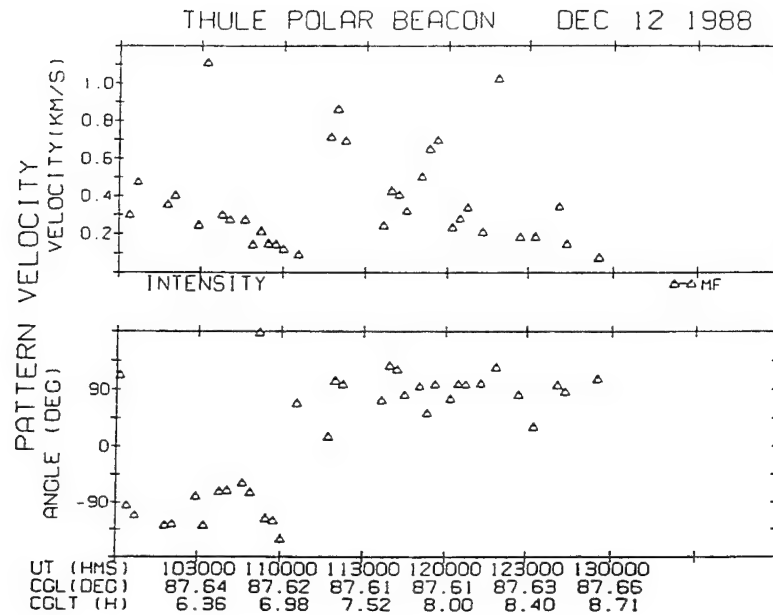


Fig. 11. Same as in Fig. 4 but for the data shown in Fig. 9. Note the velocity shear at 11:15 UT.

February 1988 (sunspot number 40) provided evidence for TEC in patches varying between 5 and $10 \times 10^{16} \text{ el m}^{-2}$ (BASU *et al.*, 1989) which were not unlike those found in the present case. It should be remembered though that these patches seen during this high sunspot period were observed during a time of very little magnetic activity. The mechanism whereby a succession of patches can enter the polar cap during such an extended period of magnetic quiet merits much further investigation.

The structuring of these patches by the $E \times B$ instability is fairly well understood (TSUNODA, 1988). However, as with the TEC structures observed in December 1988 the leading edge occasionally seems steeper than the trailing edge. In prior studies, similar situations were observed in in situ data (TSUNODA, 1988; BASU *et al.*, 1990).

The comparison of TEC associated with polar cap arcs as a function of sunspot cycle and their structuring still remains an intriguing problem. The TEC increase was approximately 3 times larger in the high sunspot case ($5 \times 10^{16} \text{ el m}^{-2}$) as compared to the February 1988 arc (about $2 \times 10^{16} \text{ el m}^{-2}$). Indeed many other arcs observed during the Polar Arcs Campaign of February 1987 provided similarly low values of TEC. Since we are measuring the relative TEC increase, this seems to indicate that particle precipitation during high sunspot conditions creates a much higher level of ionization. It is necessary to verify this hypothesis with modeling studies. Further, the increased scintillation coinciding with the sheared plasma flow gives further credibility to the velocity shear-driven Kelvin-Helmholtz instability as a plausible mechanism for structuring associated with polar cap arcs (BASU *et al.*, 1988; KESKINEN *et al.*, 1988). The weaker irregularities could be generated at the TEC gradients by the background drifts through the $E \times B$ process (WEBER *et al.*, 1989).

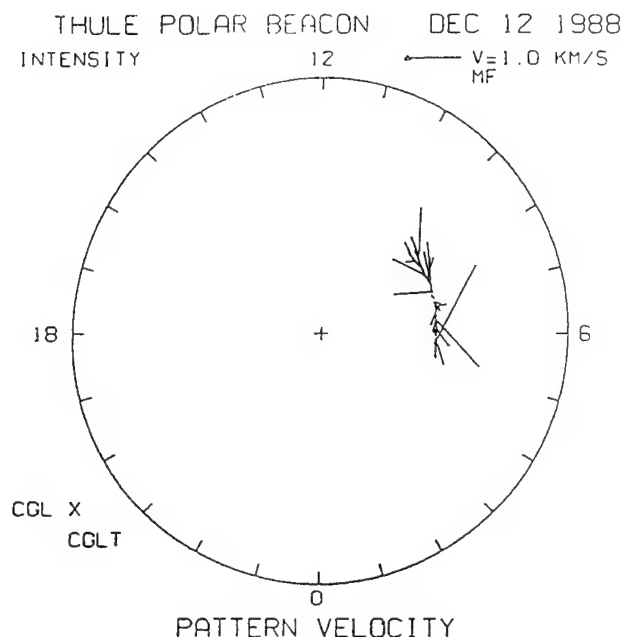


Fig. 12. Same as in Fig. 5 but for the polar cap sun-aligned arc event of December 12, 1988.

The work at Boston College was partially supported by NSF Grant ATM-8715445 and by GL Contract F19628-90-K-0007. We thank the Danish Commission for Scientific Research in Greenland for permission to conduct ground and aircraft experiments for Thule AB under Projects 28-88 and 30-88.

REFERENCES

- ANDERSON, D. N., J. BUCHAU, and R. A. HEELIS, Origin of density enhancements in the winter polar cap ionosphere, *Radio Sci.*, **23**, 513, 1988.
- BASU, S., S. BASU, E. MACKENZIE, P. F. FOUGERE, W. R. COLEY, N. C. MAYNARD, J. D. WINNINGHAM, M. SUGIURA, W. B. HANSON, and W. R. HOEGY, Simultaneous density and electric field fluctuation spectra associated with velocity shears in the auroral oval, *J. Geophys. Res.*, **93**, 115, 1988.
- BASU, S., S. BASU, C. E. VALLADARES, E. J. WEBER, J. BUCHAU, G. J. BISHOP, and B. W. REINISCH, Coordinated observations of high latitude ionospheric turbulence, *SPI Conference Proceedings and Reprint Series*, **8**, 137, 1989.
- BASU, S., S. BASU, E. MACKENZIE, W. R. COLEY, J. R. SHARBER, and W. R. HOEGY, Plasma structuring by the gradient-drift instability at high latitudes and comparison with velocity-shear driven processes, *J. Geophys. Res.*, **95**, 1990 (in press).
- BUCHAU, J., E. J. WEBER, D. N. ANDERSON, H. C. CARLSON, JR., J. G. MOORE, B. W. REINISCH, and R. C. LIVINGSTON, Ionospheric structures in the polar cap: Their origin and relation to 250-MHz scintillation, *Radio Sci.*, **20**, 325-338, 1985.
- CARLSON, H. C., JR., E. J. WEBER, L. P. BLOCK, and S. BASU, Satellite, airborne, and radar observations of auroral arcs, *Proc. Symp. Multipoint Measurements of Magnetospheric Processes, COSPAR*, **8**, 9(49), 1988a.
- CARLSON, H. C., JR., R. A. HEELIS, E. J. WEBER, and J. R. SHARBER, Coherent mesoscale convection patterns during northward interplanetary magnetic field, *J. Geophys. Res.*, **93**, 14501, 1988b.

- COSTA, E., P. F. FOUGERE, and S. BASU, Cross-correlation analysis and interpretation of spaced-receiver measurements, *Radio Sci.*, **23**, 141, 1988.
- FEDOR, L. S., A statistical approach to the determination of three-dimensional ionospheric drifts, *J. Geophys. Res.*, **72**, 5401, 1967.
- HAIRSTON, M. R. and R. A. HEELIS, Determination of the ionospheric convection pattern from DMSP data, *SPI Conference Proceedings and Reprint Series*, **8**, 391, 1989.
- KESKINEN, M. J., H. G. MITCHELL, J. A. FEDDER, P. SATYANARAYANA, S. T. ZALESAK, and J. D. HUBA, Nonlinear evolution of the Kelvin-Helmholtz instability in the high-latitude ionosphere, *J. Geophys. Res.*, **93**, 137, 1988.
- TSUNODA, R. T., High-latitude *F*-region irregularities: A review and synthesis, *Rev. Geophys.*, **26**, 719-760, 1988.
- VALLADARES, C. E. and H. C. CARLSON, Jr., The electrodynamic, thermal, and energetic character of intense stable sun-aligned arcs in the polar cap, submitted to *J. Geophys. Res.*, 1990.
- VICKREY, J. F. and M. C. KELLEY, The effects of a conducting *E* layer on a classical *F* region cross-field plasma diffusion, *J. Geophys. Res.*, **87**, 4461, 1982.
- WEBER, E. J., J. BUCHAU, J. G. MOORE, J. R. SHARBER, R. C. LIVINGSTON, J. D. WINNINGHAM, and B. W. REINISCH, *F* layer ionization patches in the polar cap, *J. Geophys. Res.*, **89**, 1683-1694, 1984.
- WEBER, E. J., J. A. KLOBUCHAR, J. BUCHAU, H. C. CARLSON, Jr., R. C. LIVINGSTON, O. DE LA BEAUJARDIERE, M. MCCREADY, J. G. MOORE, and G. J. BISHOP, Polar cap *F* layer patches: Structure and Dynamics, *J. Geophys. Res.*, **91**, 12121-12129, 1986.
- WEBER, E. J., M. C. KELLEY, J. O. BALLENTIN, S. BASU, H. C. CARLSON, J. R. FLEISCHMAN, D. A. HARDY, N. C. MAYNARD, R. F. PFAFF, P. RODRIGUEZ, R. E. SHEEHAN, and M. SMIDDY, Rocket measurements within a polar cap arc: Plasma, particle, and electric circuit parameters, *J. Geophys. Res.*, **94**, 6692, 1989.

Interplanetary magnetic field control of drifts and anisotropy of high-latitude irregularities

Sunanda Basu,¹ S. Basu,² Emanuel Costa,³ C. Bryant,¹ C. E. Valladares,¹ and R. C. Livingston⁴

(Received October 29, 1990; revised January 22, 1991; accepted January 22, 1991.)

Recently, much attention has been focused on the control exerted by the north-south component of the interplanetary magnetic field (IMF) on the nature of large-scale plasma structures in the polar cap ionosphere. In this paper we investigate whether the above IMF control also extends to the small-scale irregularities of plasma density associated with the large-scale structures. For this purpose, we have performed spaced-receiver scintillation measurements at Thule and Sondrestrom, Greenland, using the 250-MHz transmissions from quasi-geostationary polar beacon satellites. Under IMF B_z northward conditions, moderate levels of amplitude ($S_4 < 0.6$) and phase scintillations are observed with highly variable decorrelation times. Spaced-receiver drifts under this situation show dramatic reversals of the true drift of the diffraction pattern from antisunward to sunward with moderate values of the axial ratio ranging between 4 and 12. For southward B_z we detect, in the central polar cap, a series of large magnitude scintillation ($S_4 \sim 1$) structures drifting at speeds of the order of 500 m s^{-1} in the antisunward direction indicating the passage of large-scale ionization structures in the F region. In these cases the apparent drift speed of the diffraction pattern can only be determined as the pattern on ground is highly anisotropic (axial ratios 15 to 40) which makes it difficult to determine the true drift velocity. However, with suitable orientation of our antenna baseline we find that the apparent drift gives a fair estimate of the actual velocity. We also demonstrate that when these irregularities associated with the ionization patches in the F region transit across the polar cap and are observed at Sondrestrom, in conjunction with underlying E region ionization caused by auroral particle precipitation (as sensed by simultaneous incoherent scatter radar measurements of densities and temperatures), the irregularity anisotropy is much reduced. This reduction of anisotropy is possibly a result of increased cross-field diffusion due to coupling with the E region having enhanced density. The true drift of the diffraction pattern measured at Sondrestrom on one evening agrees remarkably well with the simultaneous incoherent scatter radar measurements of F region plasma drifts, both sets of drifts showing equatorward and eastward motion varying between 0.5 and 1 km s^{-1} .

1. INTRODUCTION

The current solar maximum has given us a unique opportunity to study plasma structure and dynamics deep within the dark polar cap by utilizing coordinated optical and radio techniques. The ongoing NSF initiative in the geosciences known as CEDAR, an acronym for coupling, energetics, and dynamics of atmospheric regions, has provided an incentive for several research groups to make simultaneous measurements to determine different

sources of high-latitude plasma structure (HLPS) during designated "campaigns." Hitherto, four such HLPS campaigns have been conducted between February 1988 and February 1990. The first campaign was conducted when the sunspot cycle was low (monthly mean sunspot number 40), while for the other campaigns the sunspot numbers were high varying between 130 and 180. Careful analysis of the multitechnique data has just begun [Basu *et al.*, 1989, 1990a; Doolittle *et al.*, 1990]. However, what has become very evident is the extent to which plasma structuring is controlled by the north-south component B_z of the interplanetary magnetic field (IMF). For instance, it is well established that when B_z is negative, large (~ 100 – 1000 km) regions of convecting density enhancement known as patches are observed, whereas, when IMF B_z is positive, Sun-aligned arcs are found to populate the polar cap [Weber *et al.*, 1984; Buchau *et al.*, 1985; Lassen and Danielsen, 1978; Gussenhoven, 1982]. That both patches and arcs are associated with

¹ Institute for Space Research, Boston College, Newton, Massachusetts.

² Phillips Laboratory (AFSC)/GP, Ionospheric Physics Division, Hanscom Air Force Base, Massachusetts.

³ Centro de Estudos em Telecomunicacoes, Pontifica Universidade Catolica do Rio de Janeiro, Brazil.

⁴ SRI International, Menlo Park, California.

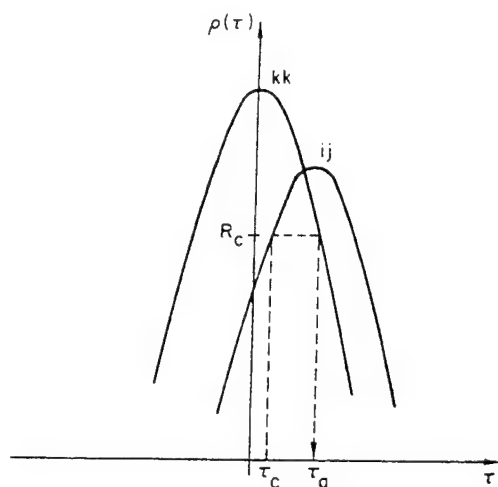


Fig. 1. Illustrates autocorrelation and cross-correlation functions of spaced-receiver signals and their identity at time delays τ_a and τ_c .

small-scale density and electric field turbulence (approximate kilometers to meters) has been determined by a variety of in situ and remote sensing techniques [cf. Basu *et al.*, 1988, 1990a, b]. Further, using spaced-receiver scintillation measurements during the high sunspot conditions prevailing during the second and third campaigns, we shall show in this paper that the drift of the in situ irregularities, the anisotropy of the ground diffraction pattern, and the intensity of the several kilometers to hundreds of meters irregularities are also indirectly controlled by B_z .

The IMF control comes through its effects on the magnetospheric convection pattern and, possibly, also through the specific instability mechanisms which create the plasma structuring for each orientation of B_z . It is important to note that there is very little published material on spaced-receiver drifts from within the polar cap. Most of the earlier measurements at auroral latitudes have come from orbiting satellites which are more suitable for providing information regarding the anisotropy of irregularities [Livingston *et al.*, 1982]. Costa *et al.* [1988] discussed two consecutive evening's observations made at Goose Bay, and Rino *et al.* [1983] presented one evening's observations from Poker Flat. Both these latter observations used quasi-geostationary satellites with the receiving stations being in the auroral oval. One day's observations of irregularity drifts at Thule using similar satellites in con-

junction with optical observations under southward B_z conditions have been published [Weber *et al.*, 1984]. Basu *et al.* [1990a] published preliminary observations of one patch and one arc event from Thule, Greenland. In the current paper we present more detailed analysis of four such events recorded at Thule and one evening's observations from Sondrestrom when simultaneous incoherent scatter radar (ISR) observations of plasma densities and convection were also available. The Sondrestrom radar velocity measurements provide an important source for the calibration of the spaced-receiver drift measurements, and, to our knowledge, this is the first report of a comparison between these two sets of measurements made simultaneously.

2. CORRELATION ANALYSIS OF SPACED-RECEIVER DATA

The correlation analysis of spaced-receiver data has been developed from the original idea that signals which interact with a moving medium and are detected by closely spaced probes display similar structures displaced in time (cf. paper by Costa *et al.* [1988, and references therein]). Application of this idea to transionospheric satellite signals detected by a small number (generally three) of non-aligned and relatively inexpensive receivers, combined with some modeling and substantial data processing, provides an estimate of the true drift velocity and the anisotropy of the diffraction pattern defined by the moving medium on the ground. In the following paragraphs we will present an overview of the method used for our data analysis.

It is assumed that the correlation functions $\rho_{ij}(\tau)$ calculated for all possible combinations of the received signals $s_i(\tau)$ and $s_j(\tau)$; $i, j = 1, \dots, N$, are special cases of a single function of three variables. Two of these represent the rectangular coordinates (x, y) of the vector spacings between the receivers, $x_{ij} = x_j - x_i$, while the other measures the time delay between different observations. These variables are combined into a single argument, as follows:

$$\begin{aligned} \rho_{ij}(\tau) &= R\{[a(x_{ij} - V_x\tau)^2 + 2h(x_{ij} - V_x\tau)(y_{ij} - V_y\tau) \\ &\quad + b(y_{ij} - V_y\tau)^2] + k\tau^2\} \\ &= R\{ax_{ij}^2 + 2hx_{ij}y_{ij} + by_{ij}^2 \\ &\quad + 2fx_{ij}\tau + 2gy_{ij}\tau + c\tau^2\} \end{aligned} \quad (1)$$

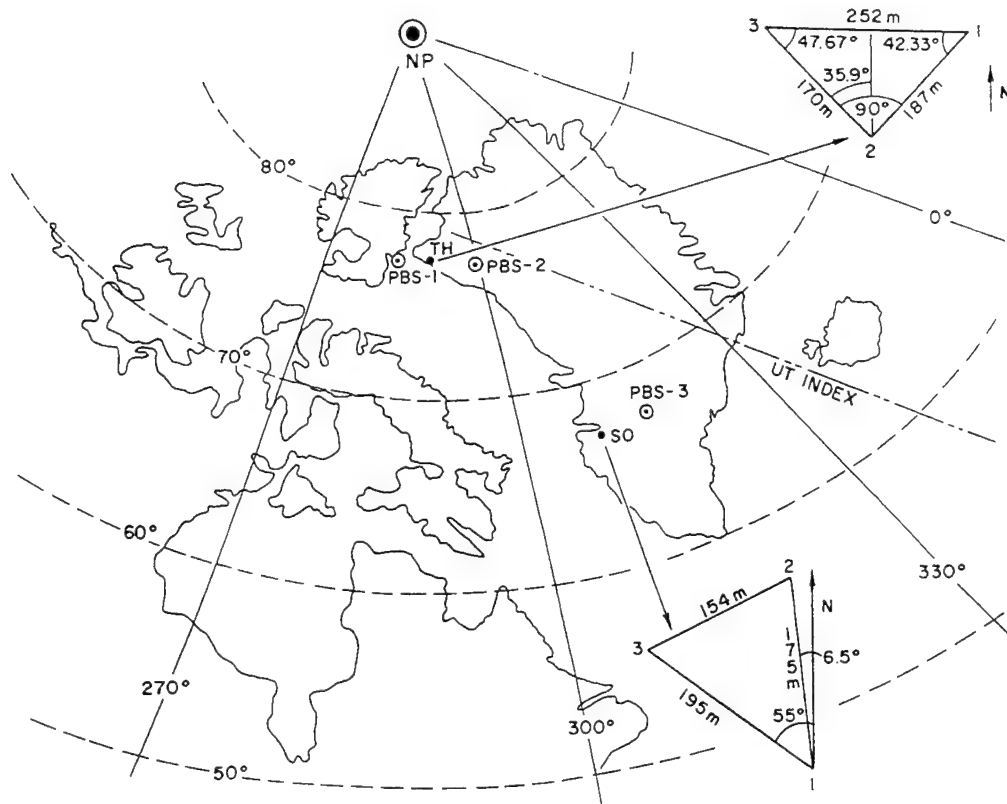


Fig. 2. Location of satellite intersection points for Thule (PBS-1) and (PBS-2) and Sondrestrom (PBS-3) and the geometry of spaced receivers at both these stations.

where R is a decreasing function, normalized in such a way that $R(0) = 1$; the parameters a , h , b , f , g , and c are constants to be estimated from the analysis; and V_x and V_y are the two components of the true drift velocity of the ground diffraction pattern, calculated from the previous parameters.

The original justifications for the equivalent representations of the "space-time" correlation function in (1) can be found in the work by Briggs *et al.* [1950]. Better agreements between the model and actual correlation functions are obtained for small values of τ . Consequently, the analysis, in general, only uses high-value samples within the main lobes of the correlation functions. The above model also results from calculations combining a thin phase-screen scintillation model with an analogous characterization for the random electron density fluctuation in the ionosphere [Costa *et al.*, 1988]. As discussed by Briggs [1968], the term within square brackets in (1) represents the "frozen-in" motion contribution to decorrelation between two received

signals. The remaining term represents the turbulent motion contribution to decorrelation. Equation (1) thus assumes that the two motions additively contribute to the correlation functions through the same (quadratic) form. It is also assumed that surfaces of constant correlation level characterize concentric and equishaped ellipsoids in three-dimensional space (x , y , τ). It can be shown from (1) that the necessary and sufficient conditions for these assumptions are $a, b > 0$, $ab - h^2 > 0$, and $k > 0$ (that is, the equivalent arguments within curly brackets should represent positive-definite quadratic forms). These conditions are not generally imposed during the analysis. Instead, results not conforming to them are simply rejected.

Several algorithms have been proposed to estimate the values of the parameters in (1). A slightly modified version of that suggested by Fedor [1967] has been used in the present work and will be briefly reviewed.

Let R_i be the value of $\rho_{ij}(\tau_c)$ at the time delay τ_c .

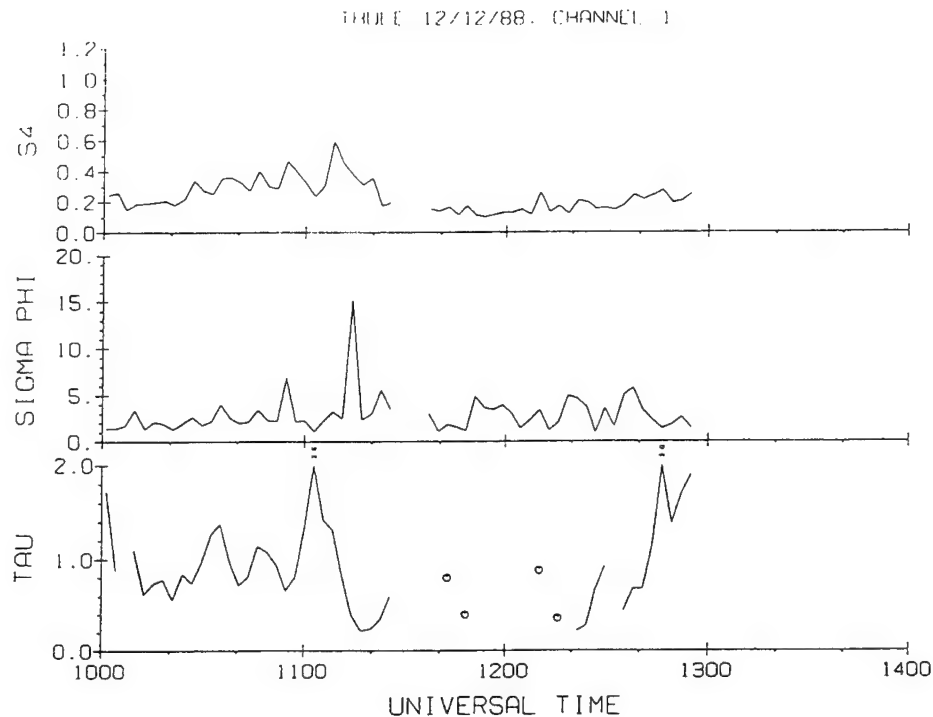


Fig. 3. Amplitude and phase scintillations at 250 MHz and decorrelation time observed at Thule in conjunction with Sun-aligned arcs on December 12, 1988.

The value of τ_a such that $R_c = \rho_{kk}(\tau_a)$ can then be calculated, as indicated in Figure 1. From the equality $\rho_{ij}(\tau_c) = \rho_{kk}(\tau_a)$ and the assumption that R is a decreasing function, one gets

$$(ax_{ij}^2 + 2hx_{ij}y_{ij} + by_{ij}^2 + 2fx_{ij}\tau_c + 2gy_{ij}\tau_c)/c = (\tau_a^2 - \tau_c^2) \quad (2)$$

This expression can be used as a building block for a $N \times 5$ system of linear equations $\mathbf{D} \cdot \mathbf{X} = \mathbf{T}$, where $\mathbf{X} = (a, h, b, f, g)/c$. The N rows of this system are obtained by selecting different combinations of cross-correlation, autocorrelation functions, and time delays τ_c in (2), from which the elements of the matrices \mathbf{D} ($N \times 5$) and \mathbf{T} ($N \times 1$) are easily inferred. The obtained system is generally over-determined and should be solved by the least squares method. That is, $\mathbf{X} = (\mathbf{D}^T \cdot \mathbf{D})^{-1} \cdot \mathbf{D}^T \cdot \mathbf{T}$, where \mathbf{D}^T indicates the transpose of \mathbf{D} .

Once the parameters of the ellipsoids are determined, those characterizing the anisotropy and the true drift velocity of the ground diffraction pattern can be calculated. It should be noted that this anisotropy ellipse of the diffraction pattern is the geometrical projection along the ray path on the

ground of the ellipsoid defining the anisotropy of the in situ irregularities. The surfaces of the constant correlation levels of the in situ irregularities are ellipsoids with axes in the ratio $1:B:A$, with A being aligned with the magnetic field, B being in the magnetic E-W direction and the other axis being along the magnetic N-S direction. The spaced-receiver technique provides a measure of the anisotropy of the diffraction pattern and not of the in situ irregularities per se.

The anisotropy of the diffraction pattern is characterized by the common axial ratio AR and orientation Ψ_a of the major axes of the concentric and equishaped ellipses along which the ellipsoids in (1) intersect the plane $\tau = 0$. It can be shown that

$$AR = \{[1 + (1 - \alpha^2)^{1/2}]/[1 - (1 - \alpha^2)^{1/2}]\}^{1/2};$$

$$\alpha = 2(ab - h^2)^{1/2}/(a + b) \quad (3)$$

where $0 \leq \alpha \leq 1$, and

$$\Psi_a = \frac{1}{2} \arctan \psi; \quad \psi = 2h/(a - b) \quad (4)$$

The orthogonal components V_x and V_y of the true drift velocity can be written as functions of the

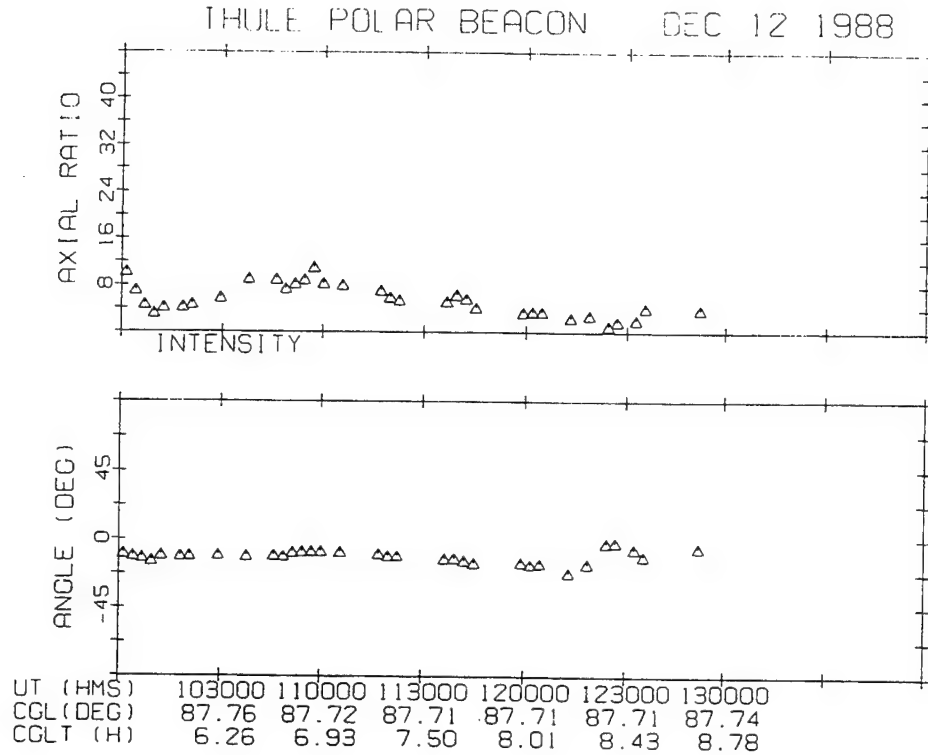


Fig. 4. Axial ratios and orientation angles of the anisotropy ellipses of the diffraction pattern for the spaced receiver intensity data corresponding to the time interval indicated in Figure 3.

parameters of the ellipsoids by comparing the coefficients of identical terms in (1). It follows that the amplitude V and direction Ψ_v of the true drift velocity can be expressed as

$$V = [(gh - fb)^2 + (fh - ga)^2]^{1/2} / (ab - h^2) \quad (5)$$

$$\Psi_v = \arctan [(fh - ga) / (gh - fb)] \quad (6)$$

A discussion of the errors involved in the correlation analysis of spaced-receiver data is important for a better understanding of the limitations of the technique. A full error analysis will probably be extremely involved and difficult to apply on a routine basis. One example of such a calculation can be found in the work by *Banerji* [1960], who applied his results to a very limited number of cases, finding a large standard deviation (27 m s^{-1}) for measurements of the true drift velocity (typically 63 m s^{-1}). Recently, *May* [1988] has discussed statistical errors in the determination of wind velocities by the spaced-antenna technique.

Rather than following the above routes, the present discussion of the limitations of the spaced-

receiver technique will be centered on expressions (3) to (6), in the important case of elongated diffraction patterns (AR very large or, equivalently, α very small). It can then be written that

$$AR \approx 2/\alpha \rightarrow \Delta(AR) \approx -\frac{2}{\alpha^2} \Delta\alpha \quad (7)$$

$$\Delta\Psi_a = \frac{1}{2} \frac{1}{1 + \psi^2} \Delta\psi \quad (8)$$

Expression (7) shows that, for elongated patterns, errors in α , caused by those in the estimation of the correlation functions (which are then transmitted to the parameters of the ellipsoids), lead to large errors in the axial ratio. That is, this parameter is very sensitive to errors. On the other hand, expression (8) shows that the opposite is true with regard to the orientation of the major axes of the anisotropy ellipses.

It is more instructive to perform an error analysis of the procedure used in the estimation of the true drift velocity by using its components V_M and V_m

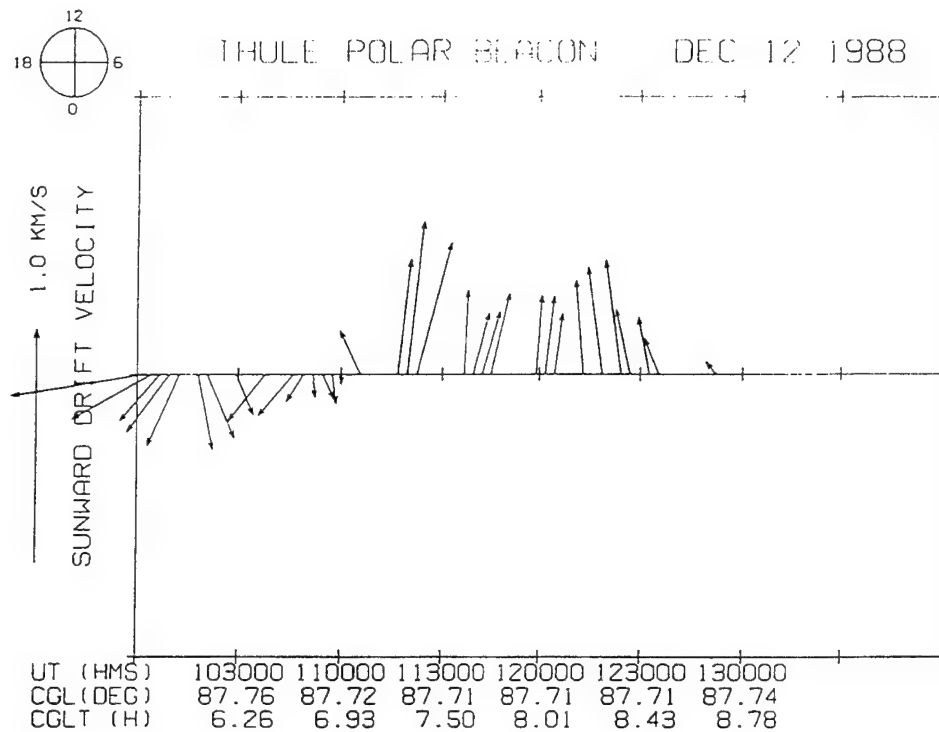


Fig. 5. Magnitudes and directions of the true drift velocity of the diffraction pattern corresponding to the time interval shown in Figure 3. The direction toward the Sun at magnetic noon is indicated. Clear reversals of the drift velocity may be noted.

along the major (M) and minor (m) axes of the anisotropy ellipses, respectively. After some manipulation it can be shown that, for elongated patterns

$$V_m \cong -\frac{(fh + gb)}{2b(a + b)^2} \quad (9)$$

$$V_M \cong -(AR)^2 \frac{(fh - ga)}{2a(a + b)^2} \quad (10)$$

Being independent of the axial ratio, the component V_m along the minor axes is relatively insensitive to errors in the limit of interest. The opposite behavior has been obtained for the component V_M along the major axes. That is, the sensitivity to errors exhibited by AR is transmitted to V_M . Further, the estimated value for this component of the true drift velocity increases fast for elongated patterns, regardless of its actual value. Indeed, two closely spaced receivers defining a baseline aligned with the major axes of the anisotropy ellipses of very elongated irregularities would almost simultaneously detect the same structure. This observation would

be interpreted as being caused by a very large velocity component along this direction, completely masking the actual situation.

In general, the spaced-receiver technique has been utilized to derive drift and anisotropy parameters in the relatively benign mid-latitude ionosphere [Moorcroft and Arima, 1972] or it has been used at the magnetic equator where the drift velocities are determined to be in the magnetic E-W direction, perpendicular to the plane of anisotropy of the irregularities [Kent and Koster, 1966]. The polar cap and auroral environment, on the other hand, can provide extreme conditions such as order kilometer per second antisunward drifts, abrupt reversals to sunward drifts, a total absence of the E region in the dark polar cap or an E region with densities higher than the F region caused by particle precipitation generally, in the auroral region. As a matter of fact, we encounter all the above conditions in the case studies to be presented. We will attempt to point out how such background conditions either help or hinder the application of this technique for the derivation of the true drift of the

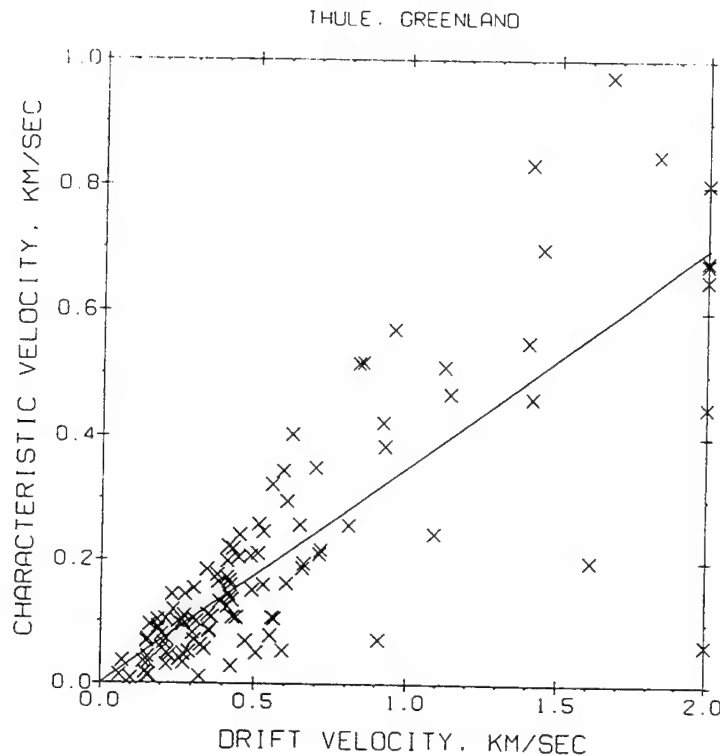


Fig. 6. Scatter diagram illustrates the dependence of characteristic velocity V_c , on the true drift velocity of diffraction pattern for the two Sun-aligned arc events shown in Figures 3 and 7.

diffraction pattern. For instance, our analysis of polar cap spaced-receiver data at Thule has shown that convecting polar cap patches detected on the nightside yield large axial ratios varying generally between 10 and 40 for the receiver layout shown on the upper right-hand corner of Figure 2. (The rest of the diagram will be described in section 3.) In such cases, as the above analysis shows, the true velocity is very difficult to determine accurately. It is, however, fortuitous that the geometry of the three spaced receivers at Thule is such that the direction along the baseline connecting receivers 2 and 3 points approximately in the direction of magnetic north which thus happens to be close to the antisunward direction for time periods around magnetic midnight. It is further important to note that the orientation angle of the major axis of the diffraction pattern, which depends on the viewing geometry of the satellites, is along the magnetic E-W direction, i.e., approximately along the baseline connecting receivers 1 and 2. Under these circumstances V_m , as defined above, and evaluated in the direction 3-2 of the receivers, is approximately equal to the

apparent drift of the diffraction pattern as computed from (7) and (8) given by *Brown and Chapman* [1972]. It should be noted that the apparent velocity, so determined, is not the resultant of the three component velocities, but is weighted toward the direction of the minor axis of the diffraction ellipse. In general, for an anisotropic pattern the true drift velocity magnitude is smaller than the apparent drift and its direction may be somewhat different also. However, we believe the apparent drift magnitude and direction are able to provide a significant amount of information regarding the background plasma convection field as will become evident in later sections. Underlying *E* region conductivity has a positive role to play in the application of this technique as we shall show for polar cap Sun-aligned arc and auroral precipitation events.

There is one further correction necessary to the drift measurements made at these polar latitudes. We note that any instrumentation that is ground-based provides experimental data in geographic coordinates and the reference frame of these measurements will be corotating with the earth. How-

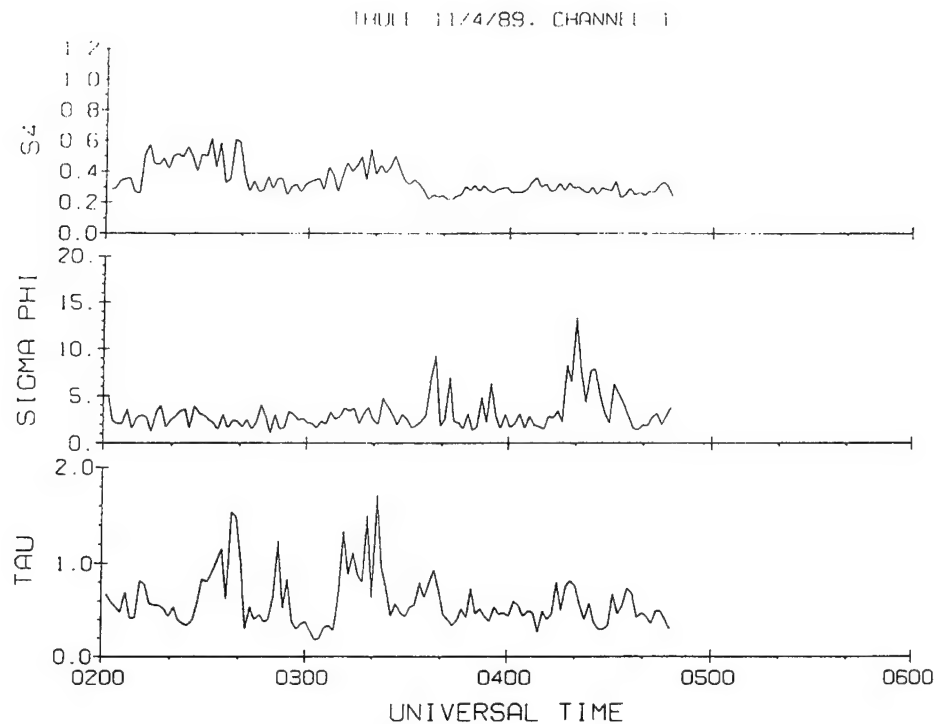


Fig. 7. Same as in Figure 3 except data are obtained on November 4, 1989.

ever, particularly in the polar cap, it is preferable to present the measured velocities in an inertial frame moving with the auroral oval with one of its axis oriented in the Sun-Earth direction. It is important to note that the oval as viewed from the sun will exhibit a wobbling motion due to the corotation of the magnetic poles as reviewed by *Killeen and Roble* [1988]. Thus in this study we have corrected for corotation by introducing a coordinate translation from the geographic frame to the oval frame which includes two terms following the method outlined by *Sojka et al.* [1979]. One term is due to the corotation of the location where the measurements have been made (namely, Thule and Sondrestrom), and the other is due to the corotation of the north magnetic pole.

3. RESULTS AND DISCUSSION

Spaced-receiver scintillation measurements have been conducted at Thule, Greenland, using quasi-geostationary satellite transmissions at 250 MHz for several years. The satellites were generally viewed either to the west or east of the station as shown by their 350-km intersection points denoted by PBS-1

and PBS-2 in Figure 2. The zenith angle of the observations reported here were high varying between 30° and 35° . The received signals were sampled at 50 Hz. The satellite frequency was updated every 168 s, thus creating a loss of lock during a fraction of this time, in the beginning. As a result, and also due to some preprocessing of the received information, data blocks of 72-s length (corresponding to 3600 observations of the signal intensity per channel) approximately centered at the middle of each cycle were used in the correlation analysis. A more detailed description of the receiving system and preprocessing of the data was presented by *Basu et al.* [1985].

We will present spaced-receiver drifts obtained during two Sun-aligned arc events at Thule, to be followed by drift measurements during two patch events there. Finally, we shall present drift measurements at Sondrestrom when the patches observed at Thule convect to Sondrestrom and are detected there in the presence of underlying *E* region ionization caused by particle precipitation. The satellite viewing direction from Sondrestrom is indicated by PBS-3 in Figure 2. These measurements are also made at a zenith angle of 30° . The

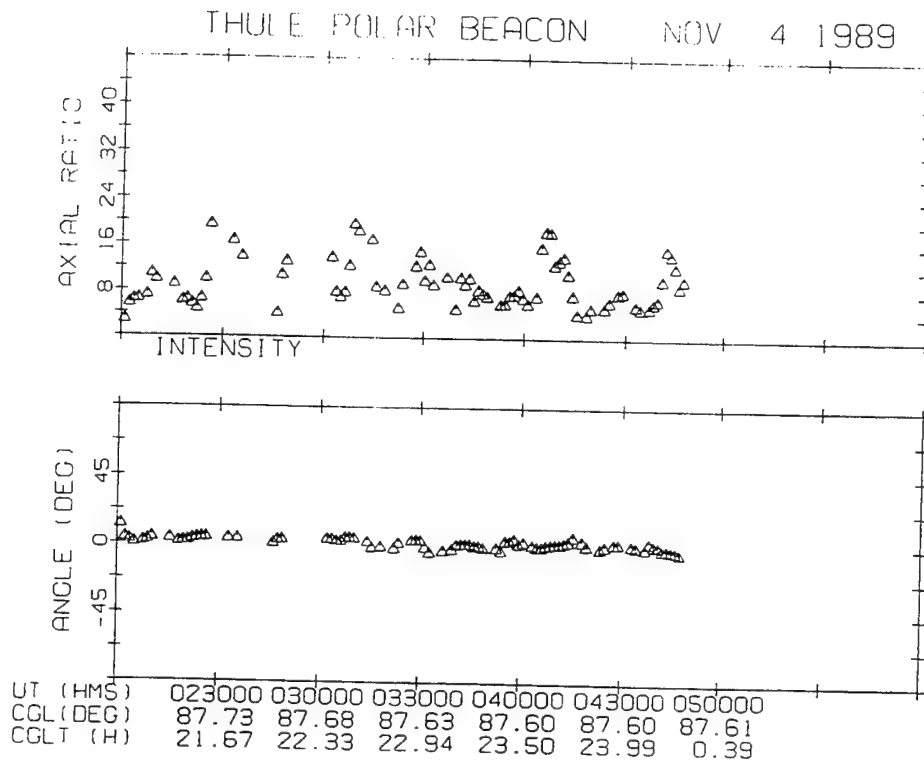


Fig. 8. Same as in Figure 4 except data are obtained on November 4, 1989.

spaced-receiver drifts at Sondrestrom, using the layout at the bottom right-hand corner of the figure are also compared with the simultaneously measured plasma convection measurements by the collocated ISR.

3.1. Sun-aligned arc events at Thule

A well-documented Sun-aligned polar cap arc event was observed at Thule between 1000 and 1300 UT on December 12, 1988 [Basu *et al.*, 1990a; Trudell *et al.*, 1990]. The geometry for these observations and of all the others to be discussed in this paper are shown in Figure 2. It is important to note that several quasi-geostationary polar beacon satellites are viewed in different directions from Thule and Sondrestrom as a function of universal time. The satellite is viewed due west of Thule on December 12 for the Sun-aligned arc event.

The phase and amplitude scintillations associated with the arc event are shown in Figure 3. The scintillations are much lower than that observed in the case of patches to be presented later. There is a peak in the scintillation magnitude at approximately

1115 UT. Of considerable interest is the observed variability of the decorrelation time (defined as the time for which the autocorrelation falls to 0.5 of its maximum value). The large magnitude of the decorrelation time indicates small drift velocities and vice versa (since all the scintillations are in the weak-scatter regime). Some of the gaps in the decorrelation time panel are caused by low values of the S_4 index ($S_4 \leq 0.15$ is the cutoff for computation of τ). The drift variability will become apparent when the spaced-receiver drifts are presented. The axial ratios and orientation angles of the major axis of the diffraction pattern computed from the spaced-receiver amplitude data using (3) and (4) given in section 2 are shown in Figure 4. The axial ratios are generally smaller than 10 and the orientation angle is approximately 10° west of magnetic north. The intersection point to the satellite is almost at 88° CGL (i.e., very close to the magnetic pole) and the arcs were observed in the dawn sector between approximately 0600–0900 CGLT, where the coordinate system used is corrected geomagnetic latitude and time [Whalen, 1970].

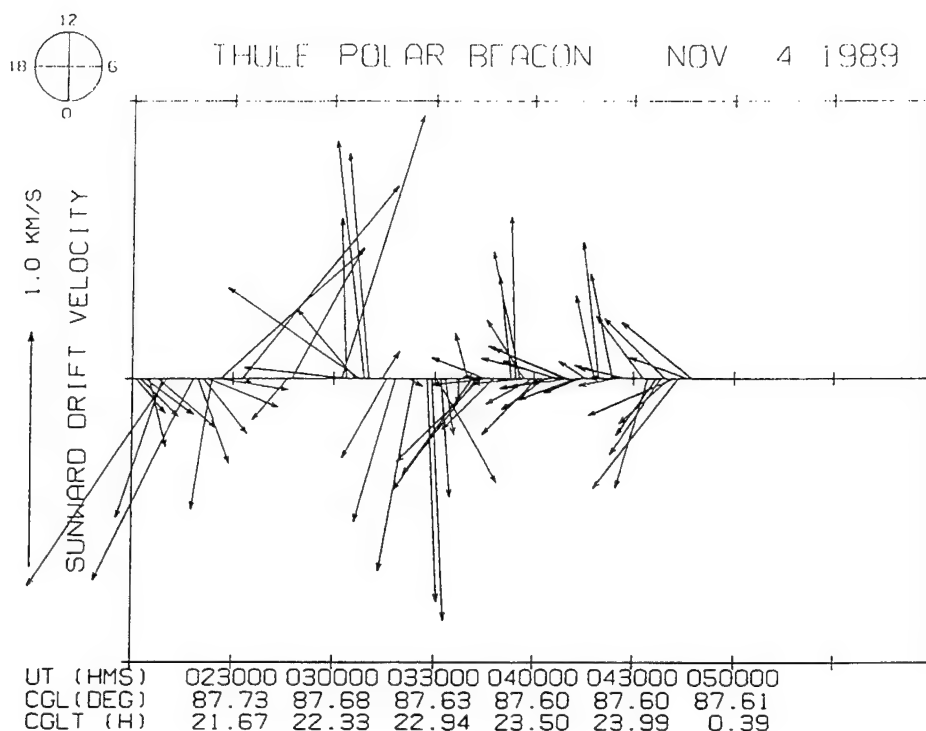


Fig. 9. Same as in Figure 5 except data are obtained on November 4, 1989.

As discussed by *Costa et al.* [1988], it is not possible to use the results on the axial ratio of the diffraction pattern to derive unique solutions for the anisotropy of F region irregularities in the present case of satellite observations with fixed viewing angle. As a result, the present study cannot unfortunately provide irregularity anisotropy information needed by global scintillation model, WBMOD [Fremouw and Secan, 1984]. Similar studies with orbiting satellites can provide information on irregularity anisotropy but, on the other hand, fail to yield information on irregularity drift velocity.

The magnitude and direction of the true velocities of the diffraction pattern computed using (5) and (6) are shown in Figure 5 after the corotation correction has been performed as discussed in section 2. The velocity vectors are plotted on a cartesian system with the direction to the Sun (i.e., 12 CGLT) being indicated. A running mean of three consecutive vector velocities is taken to reduce the random variability that is introduced by noise contamination of the correlation functions. From Figure 5 it is evident that initially the velocities are antisunward with a westward component (i.e., toward dusk), changing occasionally to an eastward or dawnward

component. At approximately 1100 UT, the anti-sunward drift reverses to a sunward drift with the sunward drift being observed until 1230 UT. This drift reversal is associated with the large value of the decorrelation time observed at 1100 UT in the bottom panel of Figure 3. Sunward plasma velocities in the polar cap have been measured by in situ [Burke et al., 1979; Carlson et al., 1988] and radar techniques [Valladares and Carlson, 1991], but to our knowledge this is the first such measurement using spaced receivers. The digisonde at Qaanaaq (87° CGL) has also provided evidence for shears in the plasma flow and sunward drifts under IMF B_z northward conditions [Buchau et al., 1988].

It is interesting to note that the large increase in phase scintillation at 1115 UT is accompanied by a large increase of velocity in the sunward direction. The change in shape of the amplitude spectra before and after the velocity increase has been presented by Basu et al. [1990a]. A comparison with the type of all-sky imaging photometer (ASIP) images shown by Basu et al. [1990a] indicates, in general, that the antisunward flows are observed on the equatorward side (or dawnside) of the arc, while the sunward flows are observed within and on the duskside of

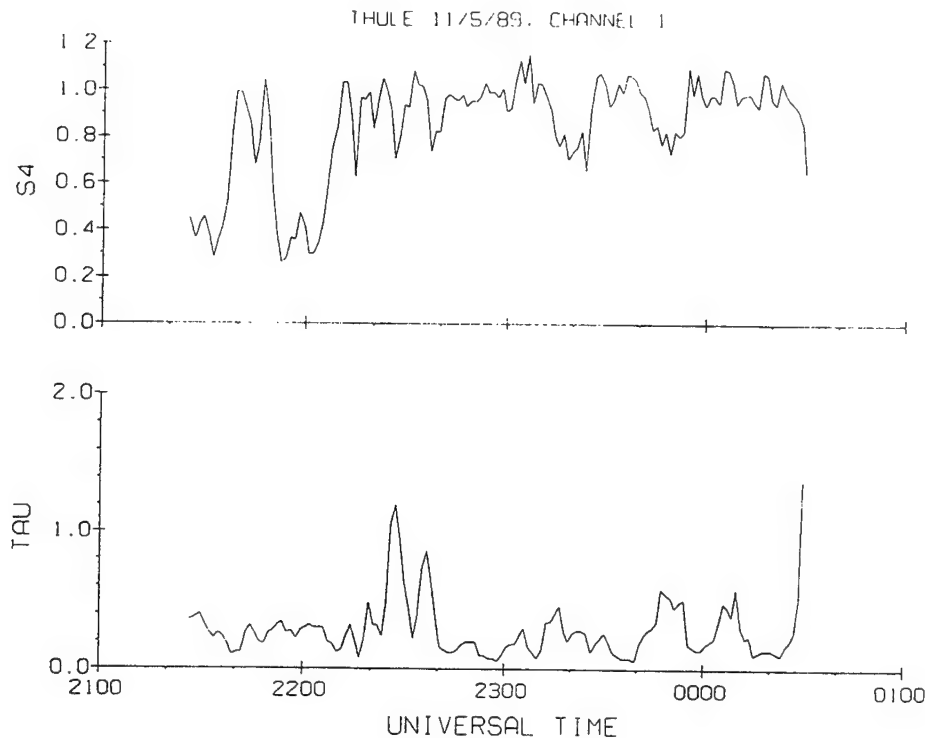


Fig. 10. Intense amplitude scintillations at 250 MHz and decorrelation time observed at Thule in conjunction with polar cap patches on November 5, 1989.

the arc. However, the arc structures were far from static, developing hooks and other protrusions, so that it is difficult to make a definitive statement. A reversal in the direction of the drift such as shown in Figure 5 is expected to be accompanied by an increase in V_c , the characteristic velocity, which is a measure of the random component of the drift [Bhattacharya *et al.*, 1989]. However, as shown in Figure 6, V_c is always less than half of the true velocity in magnitude. The points plotted are those for the true velocity of the diffraction pattern and characteristic velocity observed during the Sun-aligned arc event discussed above, as well as, those observed during the second such event whose description follows below. The straight line on the graph is a linear least squares fit to the points. The fact that the characteristic velocity does not exceed half the true velocity provides more confidence in the results obtained from the spaced-receiver technique in the case of arcs exhibiting sheared flows. It is important to note that the apparent velocity measurements also show a concomitant reversal in the direction of the drifts, with the directions being

rotated anticlockwise from those of the true drift. (This figure is not shown to minimize the number of diagrams.) Such shears in the plasma flow were also measured by the ion-drift meter on board the DMSP F-8 satellite between 1112 and 1114 UT at a location to the west of the Qaanaaq ASIP image of the arc of December 12, 1988. However, detailed discussion of the satellite data is beyond the scope of this paper.

The scintillations observed during another Sun-aligned arc event at Thule are shown in Figure 7. This event was observed during the third HLPS campaign on November 4, 1989. Again, the amplitude and phase scintillations are moderate as compared to the cases of polar cap patches to be presented in the next section. The decorrelation interval also shows large variability. The axial ratio and orientation angles are shown in Figure 8. There are some values of the axial ratio that are larger than in the previous case, but the majority of them are under 12 and the orientation angle is aligned approximately along magnetic north, a situation which is not too different from the previous case. This is not surprising since the subionospheric

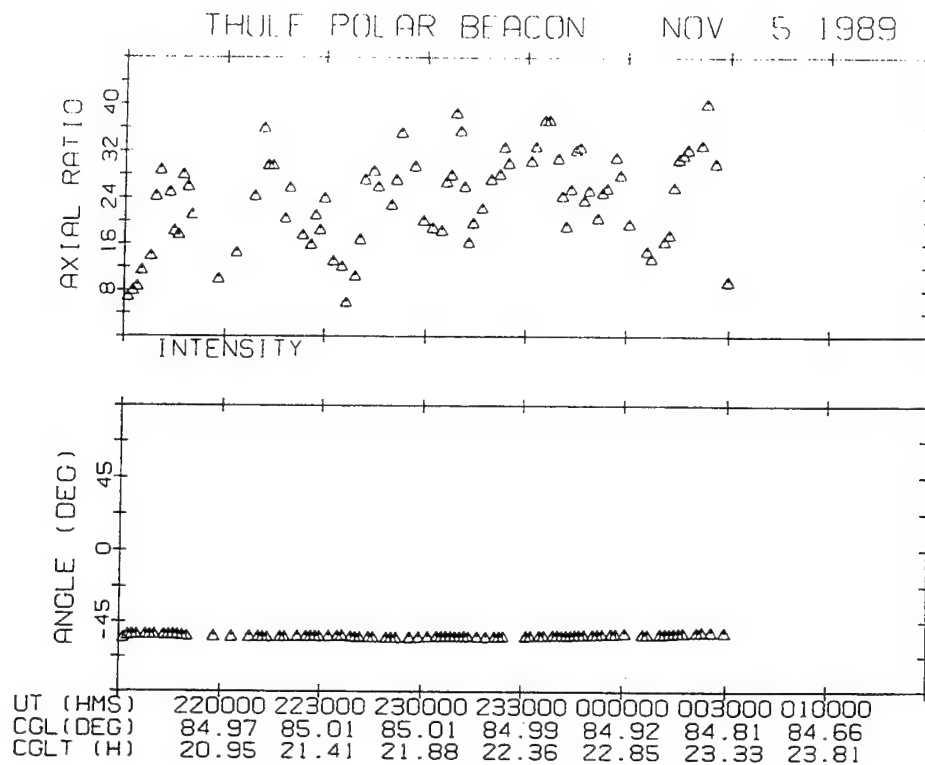


Fig. 11. Same as in Figure 4 except data are obtained on November 5, 1989. Large axial ratios are observed for patch associated irregularities.

intersection to the satellite is also given by PBS-1, even though the CGLT of the observations are quite different being in the premidnight rather than in the dawn sector.

The vector velocities representing the true drift of the diffraction pattern are shown in Figure 9 in the same format and subject to the corotation correction and averaging discussed in conjunction with Figure 5. Several reversals in the drift direction are observed together with a large variability in the magnitude of the drift giving rise to the large variability in the decorrelation time. The DMSP F-8 satellite orbits during this time show multiple arc structures and drift reversals consistent with the drifts measured by the spaced-receiver technique. The apparent drifts show reversals at the same time as the true drifts with the directions rotated anticlockwise from those of the true drifts. The characteristic velocity which is a measure of the random component of the drift has already been shown in Figure 6 and found not to exceed half the true velocity in magnitude. Thus it seems that the spaced-receiver technique is a viable one to sense

the complex convection pattern when IMF B_z is northward.

3.2. Patch events at Thule

It has already been mentioned that patches, i.e., convected plasma density enhancements, are observed in the central polar cap for southward B_z conditions. The object of this section will be to describe the scintillation patterns, anisotropy, and drifts when patches are seen at Thule.

The first patch event to be discussed here was observed on November 5, 1989 as part of the HLPS-3 campaign. Unfortunately, the phase scintillation was unavailable for this period. The time history of the amplitude scintillations at 250 MHz and the decorrelation time at the ionospheric intersection point PBS-2 (in Figure 2) are shown in Figure 10. The intensity scintillation is saturated for most of the time and the decorrelation time shows less variability when compared to the arc cases. The axial ratios and orientation angles of the diffraction pattern are shown in Figure 11. The axial

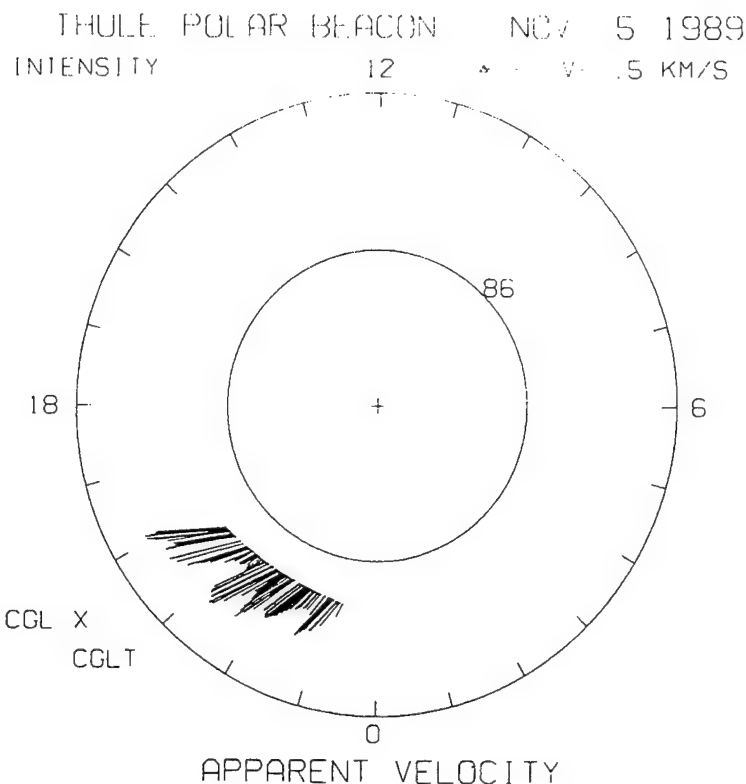


Fig. 12. Apparent drift of the diffraction pattern plotted in corrected geomagnetic latitude and time corresponding to the data shown in Figure 10.

ratios for the receiver layout shown in Figure 2 are quite large with many values between 20 and 30. The orientation angle is approximately -55° , i.e., for eastward azimuths of the satellite relative to the station the major axis of the elliptical diffraction patterns is at a large angle to magnetic north. The CGL of the intersection point is 85° for this case.

We determined that it was not possible to obtain the true drift of the diffraction pattern with our current receiver separation when the axial ratios are so large. For this reason we show in Figure 12 the apparent drifts computed using (7) and (8) by *Brown and Chapman* [1972] on a CGL-CGLT coordinate system. It should be noted that for this time period near midnight the expected antisunward drifts are approximately perpendicular to the orientation angle of the major axis of the ellipse. The largest apparent drifts measured were about 600 m s^{-1} and the smallest were about 100 m s^{-1} , but all of them are ordered in their approximately equatorward flow direction somewhat west of antisunward. This behavior is very different from the drift reversals

seen in both the apparent and true drifts for the case of Sun-aligned arcs. Reversals of the apparent drift were seen in the auroral oval by *MacDougall et al.* [1990].

The second patch case was observed on December 6, 1988, the scintillation behavior of which was presented by *Basu et al.* [1990a]. Both phase and amplitude scintillations in Figure 13 are found to be high, and the decorrelation time in this case shows little variability. The ionospheric intersection point is also given by PBS-2 (in Figure 2) corresponding to 85° CGL. The axial ratios shown in Figure 14 are mostly between 15 and 20 and the orientation angle is -80° , i.e., almost perpendicular to magnetic north. Again, the large axial ratios preclude the determination of the true velocity of the diffraction pattern. We thus show the apparent drifts in Figure 15 where indeed there is virtually no drift variation over the hour's observation, consistent with the behavior of the decorrelation time, the apparent drift magnitude being approximately 500 m s^{-1} equatorward and antisunward. It should be noted

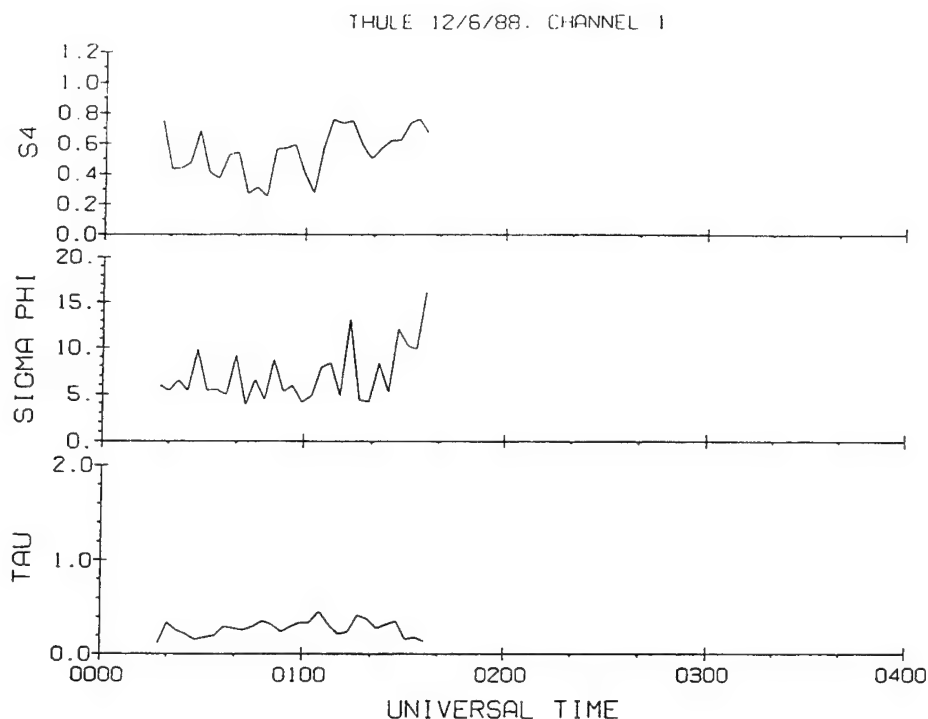


Fig. 13. Large amplitude and phase scintillations at 250 MHz and decorrelation time observed at Thule in conjunction with polar cap patches on December 6, 1988.

that this was a period of very quiet magnetic activity with December 5 and 6 having a ΣKp of 7^+ and 6^+ , respectively. The primary reason for discussing this particular patch event is the availability of simultaneous data at Sondrestrom where the ISR provides a means for calibrating the spaced-receiver drift measurements.

3.3. Nighttime drift measurements at Sondrestrom

The Sondrestrom station in the evening hours can be either an auroral or polar cap station depending on auroral oval dynamics. On the night of December 5–6, 1988, scintillations started abruptly at about 2335 UT at the PBS-3 location at 75° CGL as shown in Figure 16. In particular, phase scintillations in excess of 15 rad were found to accompany a moderate level of amplitude scintillations, the S_4 level being about 0.5. We shall presently show that the very large phase scintillations is due to the effect of E region irregularities, in addition to F region irregularities, and a good way of identifying such cases is through the phase scintillation spectra. We shall also show, using the radar density measurements,

that the two peaks of large decorrelation time (τ) at 2345 and 0145 are caused by a quick buildup of E region ionization giving a sharp edge-type diffraction pattern on the signal amplitude which creates problems for velocity determination with the spaced-receiver technique.

The 630.0-nm ASIP observations at Qaanaaq showed the existence of polar cap patches between 0000–0200 UT [Basu *et al.* 1990a]. The edge of the ASIP field of view at 250-km altitude (where most of the 630.0-nm airglow emission is assumed to take place) comes close to the latitude of Sondrestrom. From a succession of such ASIP measurements it was apparent that the patches seen at Qaanaaq drifted in an antisunward direction towards Sondrestrom during this time (the ASIP data at Sondrestrom are not available because of overcast conditions). By considering the character of scintillations and the axial ratios of the diffraction pattern shown in Figures 16 and 17, we surmise that the patches observed earlier at Thule arrived at Sondrestrom approximately around 0030 UT. This is consistent with an antisunward drift velocity of approximately 500 m s^{-1} measured at Thule and the distance

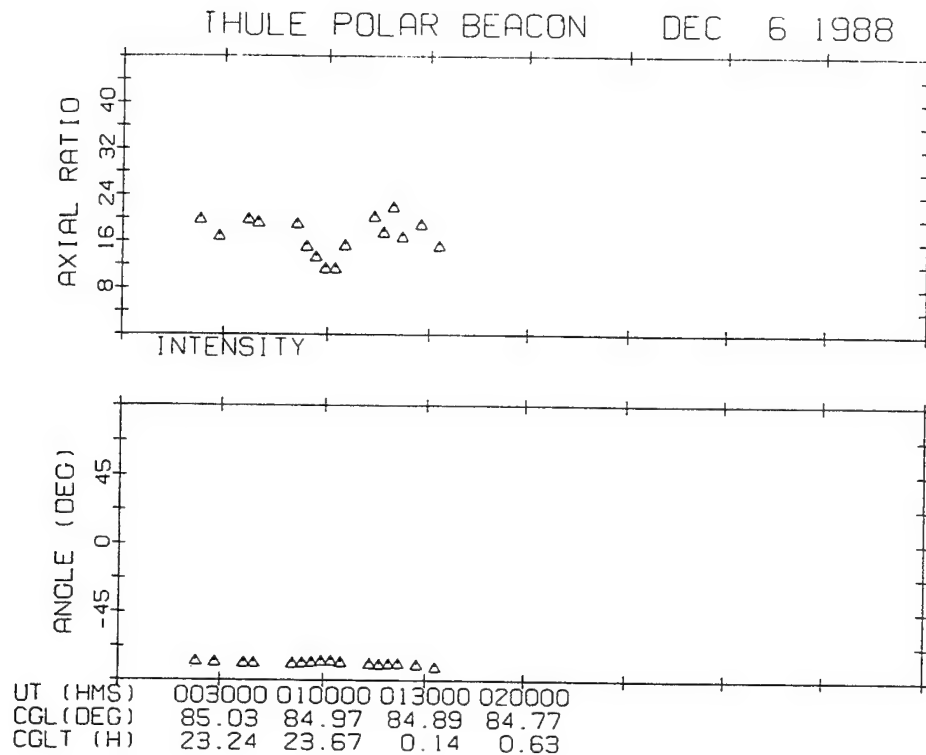


Fig. 14. Same as in Figure 4 except data are obtained on December 6, 1988.

between the two stations. Using radar and optical measurements, *Weber et al.* [1986] provided evidence for the transit of large-scale ionization patches from Thule to Sondrestrom.

The important point to note in Figure 17 is that the anisotropy of the diffraction pattern is quite small, namely around 5, up to 0000 UT and increases after that. What is very interesting, is the fact that the *E* region ionization seems to reduce the anisotropy of the diffraction pattern caused by the patch-associated irregularities. For instance, if one determines the average anisotropy of the patch related irregularities at Thule between 0030 and 0130 UT on December 6 (Figure 13) and compares that with the anisotropy at Sondrestrom (Figure 16) for the same period, then one finds a 45% reduction in the average value of the parameter.

We wish to digress for a moment to discuss the physical implications of the above result. Several authors have shown that when the *F* region is coupled to a conducting *E* region, the ambipolar electric field that keeps ions from freely diffusing across geomagnetic field lines is decreased thereby enhancing the cross-field diffusion [*Völk and Haer-*

endel, 1971; *Vickrey and Kelley*, 1982] (also cf. review by *Tsunoda* [1988 and references therein]). Now, the anisotropy of the irregularities (for simplicity considered to be cylindrical in shape with its longer dimension aligned along the magnetic field) can be considered to be proportional to $(D_{\parallel}/D_{\perp})^{1/2}$, where D_{\parallel} is the ambipolar diffusion coefficient for electrons and D_{\perp} is the cross-field ion diffusion [*Rozhanskiy and Tsendin*, 1984]. It has been mentioned above that D_{\perp} is increased when a conducting *E* region is present. Thus one may postulate a reduction in irregularity anisotropy in the presence of a conducting *E* region. It is worth mentioning that the above ratio of diffusion coefficients may be identified with the ratio of $(\sigma_{\parallel}/\sigma_{\perp})^{1/2}$, which controls the mapping of transverse perturbations along the magnetic field where σ_{\parallel} and σ_{\perp} are, respectively, the direct and Pedersen conductivities [*Völk and Haerendel*, 1971]. The above discussion relating anisotropy to the ratio of diffusion coefficients holds only in the absence of large background convection [*Gurevich and Tsedilina*, 1966] and a careful study of the anisotropy behavior of *F* region because of the highly anisotropic nature of the

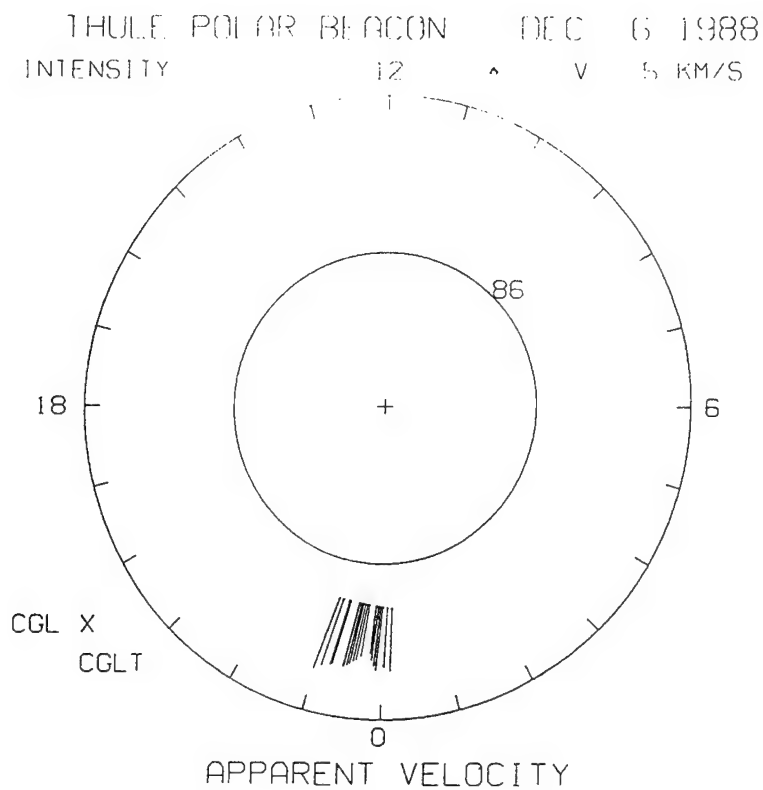


Fig. 15. Same as in Figure 12 except data are obtained on December 6, 1988.

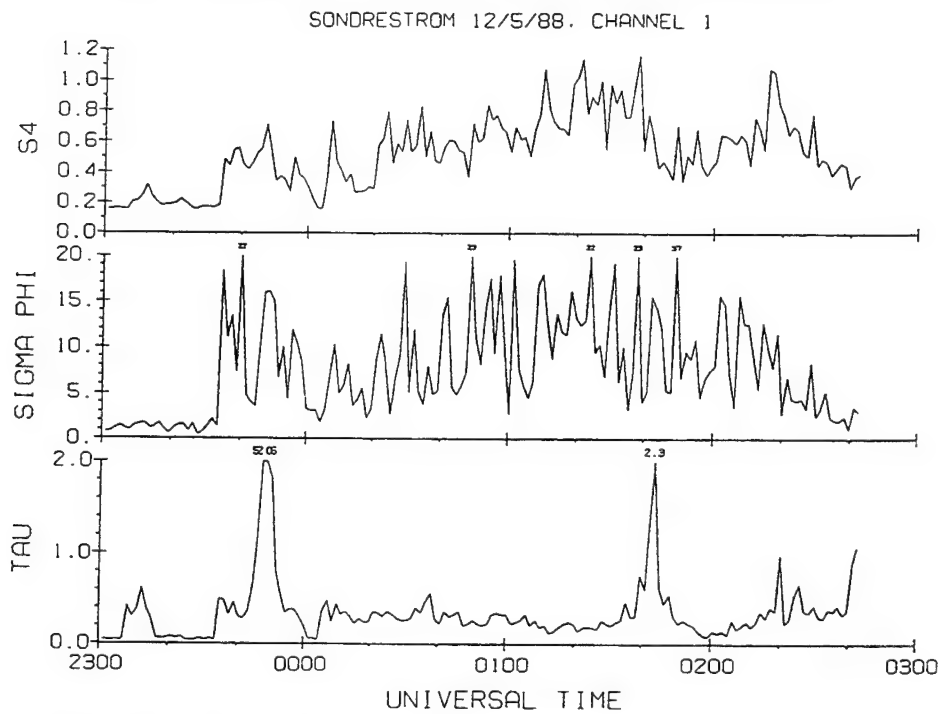


Fig. 16. Amplitude and phase scintillations at 250 MHz and decorrelation time observed at Sondrestrom on December 5-6, 1988.

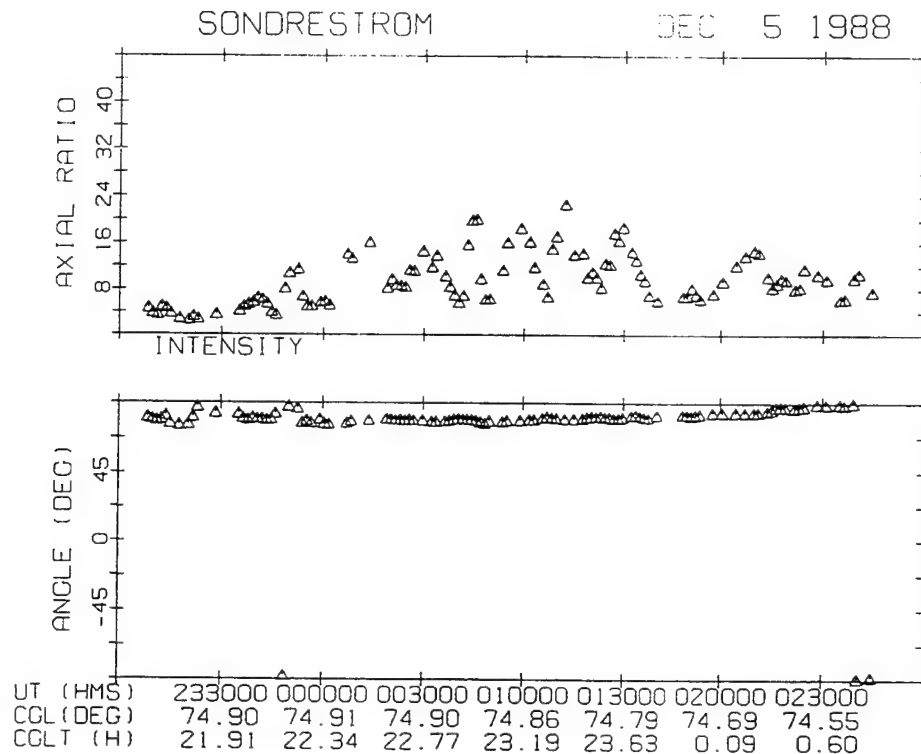


Fig. 17. Same as in Figure 4 except the data were taken in Sondrestrom on December 5–6, 1988.

diffraction pattern. However, at Sondrestrom we were able to determine the true drift velocities of the diffraction pattern which are shown in the bottom panel of Figure 18. The drifts generally varied in magnitude between 0.5 and 1 km s^{-1} with the direction of the drifts being mostly equatorward and eastward.

The Sondrestrom ISR was being run simultaneously in support of two CEDAR campaigns: the Lower Thermosphere Coupling Study (LTCS) and HLPS. The ISR mode was optimized to get accurate densities and velocities in the E region for LTCS objectives. This required 5-min integration time at each of the three azimuths (21° , 141° , and -99°) at 70° elevation angle used for this mode of operation. The vector velocities obtained with this technique are shown on the top panel of Figure 18. Actually the two panels on Figure 18 had to be displaced by 1° to prevent the superimposition of both sets of measurements, thereby making it difficult to compare the data sets. The comparisons were thus made at overlapping latitudes with the azimuth of the spaced-receiver measurements being a little to the east of the ISR. With the caveat that

the ISR measurements are averages over 5 min while the spaced-receiver measurements are made every 72 s (with a running mean over three consecutive points), the agreement is quite good in both magnitude and direction, the latter being primarily equatorward and eastward on both sets of measurements. Thus it is presumed that the irregularities in the F region, in general, drift with the background convection velocity. Since the drifts are either equatorward or in an eastward direction, it seems that Sondrestrom, possibly because of the limited radar latitude coverage, was not able to observe the Harang discontinuity on this magnetically quiet evening. *Rino et al.* [1983] had earlier hypothesized the reduction in irregularity anisotropy near the Harang discontinuity. We find that even in the absence of the Harang discontinuity E region ionization is able to reduce the anisotropy as we shall show with the radar density profiles discussed below.

As mentioned earlier, we found at least two time periods when the spaced-receiver technique either did not provide drift estimates in agreement with the ISR drifts or could not provide any reliable

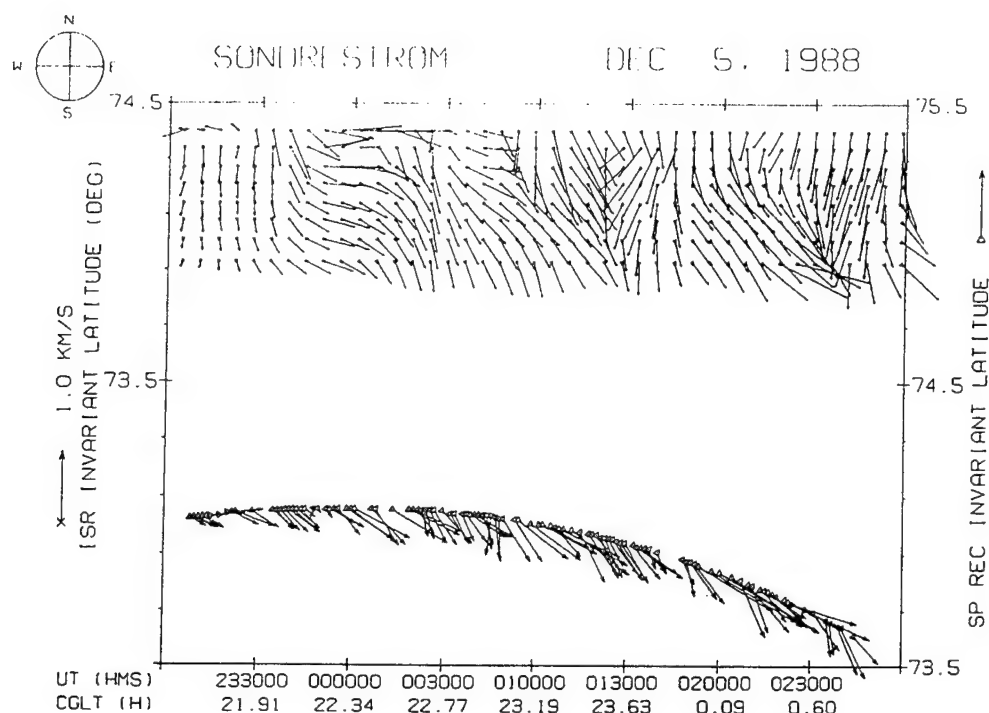


Fig. 18. Comparison of the magnitudes and directions of the true drifts of the diffraction pattern corresponding to the time interval shown in Figure 16 with the simultaneously measured incoherent scatter radar plasma drifts in the F region. Note the displacement of the latitude scales for clarity. A good agreement is observed between the velocities measured by the two techniques.

solutions for the correlation analyses which form the basis of these drift measurements. The first of these periods is around 2345 UT when very small spaced-receiver drifts (less than 100 m s^{-1}) were measured while the ISR measured about five times the velocity much more in keeping with the general convection speed. When one looks at one sample of signal amplitude and phase during this period shown in Figure 19a, the amplitude shows many of the "ringing" characteristics evident in sharp-edge diffraction patterns while the phase shows an abrupt lenslike increase. Such signatures in the signal amplitude provide either very large cross-correlation delays or no meaningful solutions at all. Figure 19b provides an example of a situation occurring 1 hour later that same evening where no solutions were obtained for the correlation analysis. We wish to point out with the help of Figures 19a and 19b that the spaced-receiver analysis cannot handle such nonstationary signal amplitude structure, a pattern that may occur relatively frequently in the auroral oval due to particle precipitation as we shall presently show with the ISR density profiles.

In general, in the absence of such non-stationarity in signal amplitude, we have been able to determine two classes of phase spectra at Sondrestrom depending on the relative contribution of E region structure vis-a-vis F region structure. When E region peak densities are comparable to F region densities (even though the F region electron content is obviously much higher than the E region content), we find a two-slope phase spectrum and single-slope amplitude spectrum as shown on the right-hand panel in Figure 20a, with the signal amplitude and phase shown on the left-hand panel. The two-phase slopes are fitted at frequencies smaller than, and larger than 0.2 Hz respectively. When the E region effect on signal structure is evident the low-frequency slope (p_1) is very steep such as in the case shown where $p_1 = -5.1$. The high-frequency slope, p_2 , is much shallower and usually similar in magnitude to the intensity spectral slope, p . In this case $p_2 = -2.3$, while $p = -2.5$. These situations, in which E region structure is clearly discernible, provides examples of high-phase scintillations for relatively moderate levels of

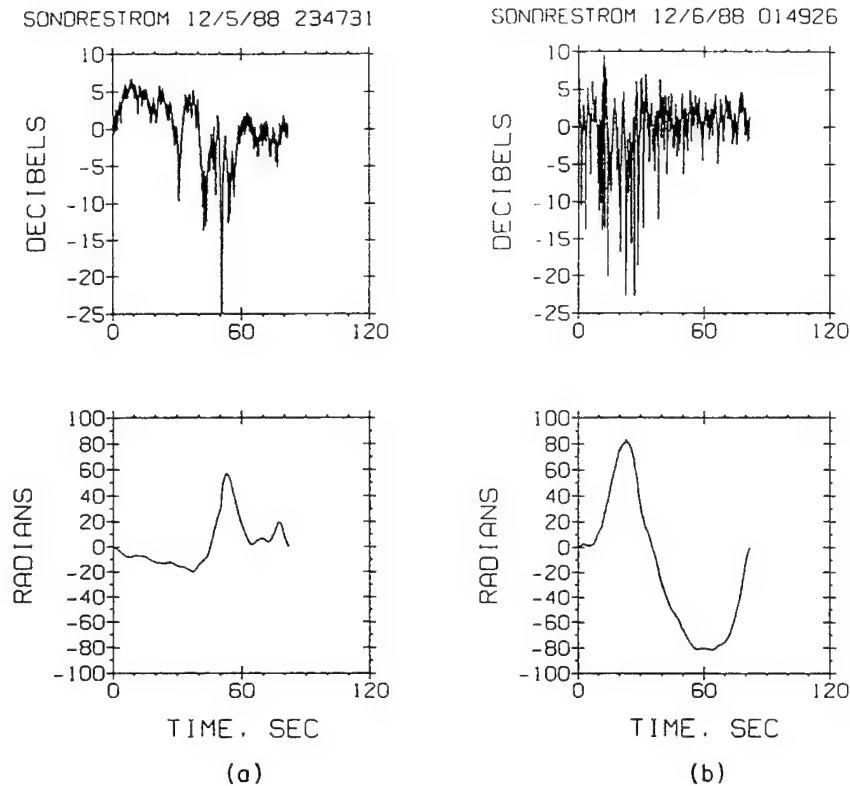


Fig. 19. Samples of signal intensity and phase at (a) 2347:31 UT on December 5 and (b) 0149:26 UT on December 6, 1988, at Sondrestrom.

amplitude scintillation and are generally observed at auroral locations. On the other hand, if the E region density and structure provide an insignificant contribution to the total perturbations imposed on the radio signal, one tends to see a uniform phase spectral slope at low and high frequencies. Such an example is given in the right-hand panel of Figure 20b where phase spectral slopes p_1 and p_2 are respectively -2.9 and -2.4 . The intensity scintillations are usually largest in such cases and a significant amount of small-scale structure is also evident in signal phase as can be seen from the lower left-hand panel of Figure 20b. Since the amplitude scintillation index S_4 exceeds unity, one sees a steepening, possibly a result of refractive scattering [Booker and MajidiAhi, 1978], in the slope of the amplitude scintillation spectrum which is -3.2 in this case. We have frequently encountered these situations at Thule during the current sunspot maximum cycle where structure in the high-density F region convecting plasma in the absence of E region is the norm.

The great advantage of making scintillation observations at Sondrestrom is that the ISR can provide the information on background large-scale E and F region behavior in which the small-scale structuring is taking place. The four ISR density profiles shown in Figures 21a–21d provide a wealth of information regarding the various signal structure categories exhibited in Figures 19a and 19b and 20a and 20b. For instance a comparison of Figures 21a and 21b provides a dramatic example of density buildup in the E region. It should be noted that since the integration time itself was 5 min, no finer temporal resolution is available. An order of magnitude increase in the E region density is seen when comparing the 2342–2347 UT profile with the 2348–2353 UT profile. The corresponding electron temperature T_e , derived from the ISR measurements, increased from 1000° to 3000°K . Undoubtedly, intense particle precipitation must have occurred which probably created a localized wall of ionization which intercepted the satellite ray path at approximately 2348:30 UT as evident, in particular,

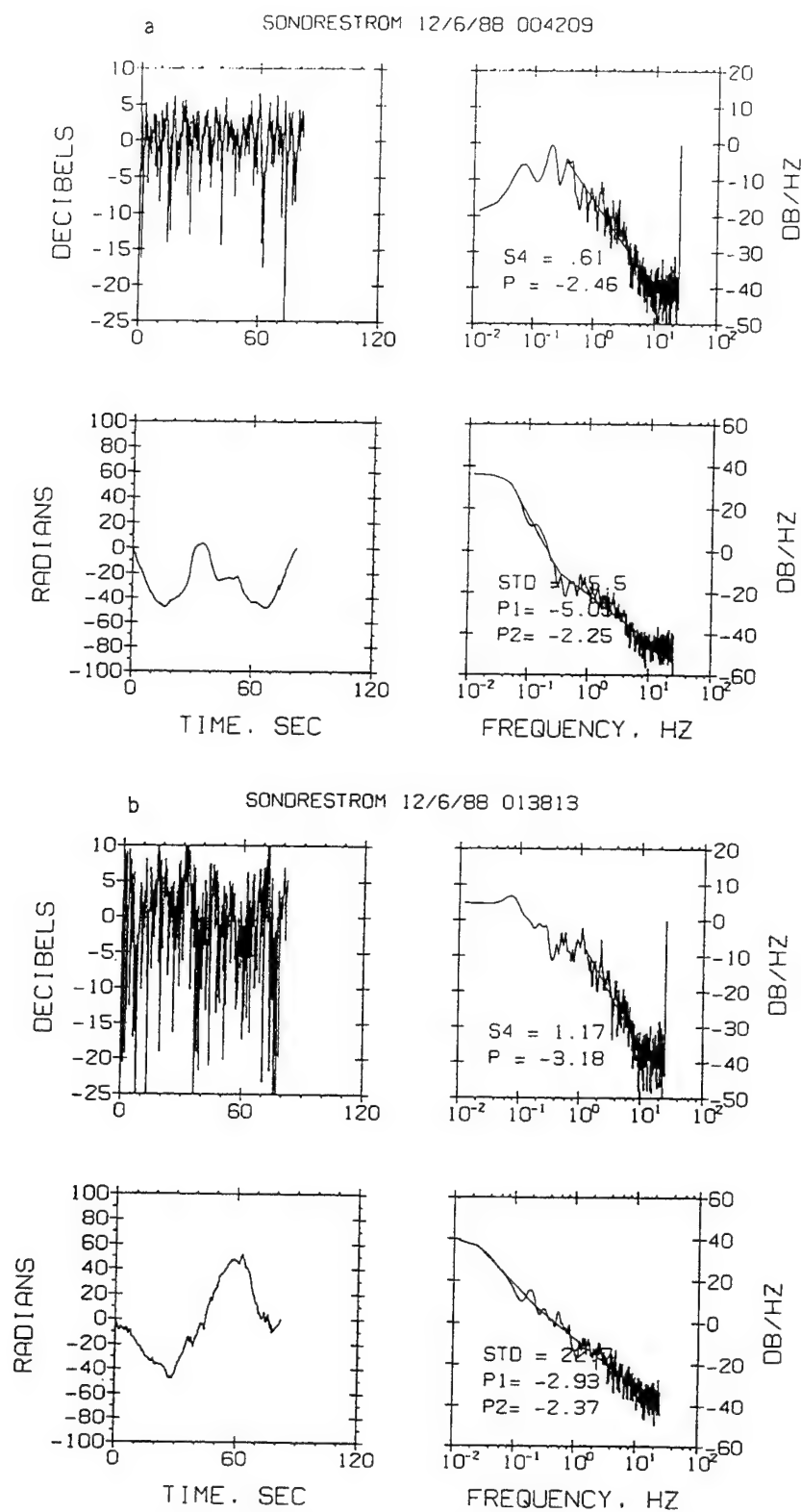


Fig. 20. Samples of signal intensity and phase and their corresponding spectra at (a) 0042:09 UT and (b) 0138:13 UT on December 6, 1988 obtained at Sondrestrom. Note two-slope phase spectrum in Figure 20a and a single-slope phase spectrum in Figure 20b.

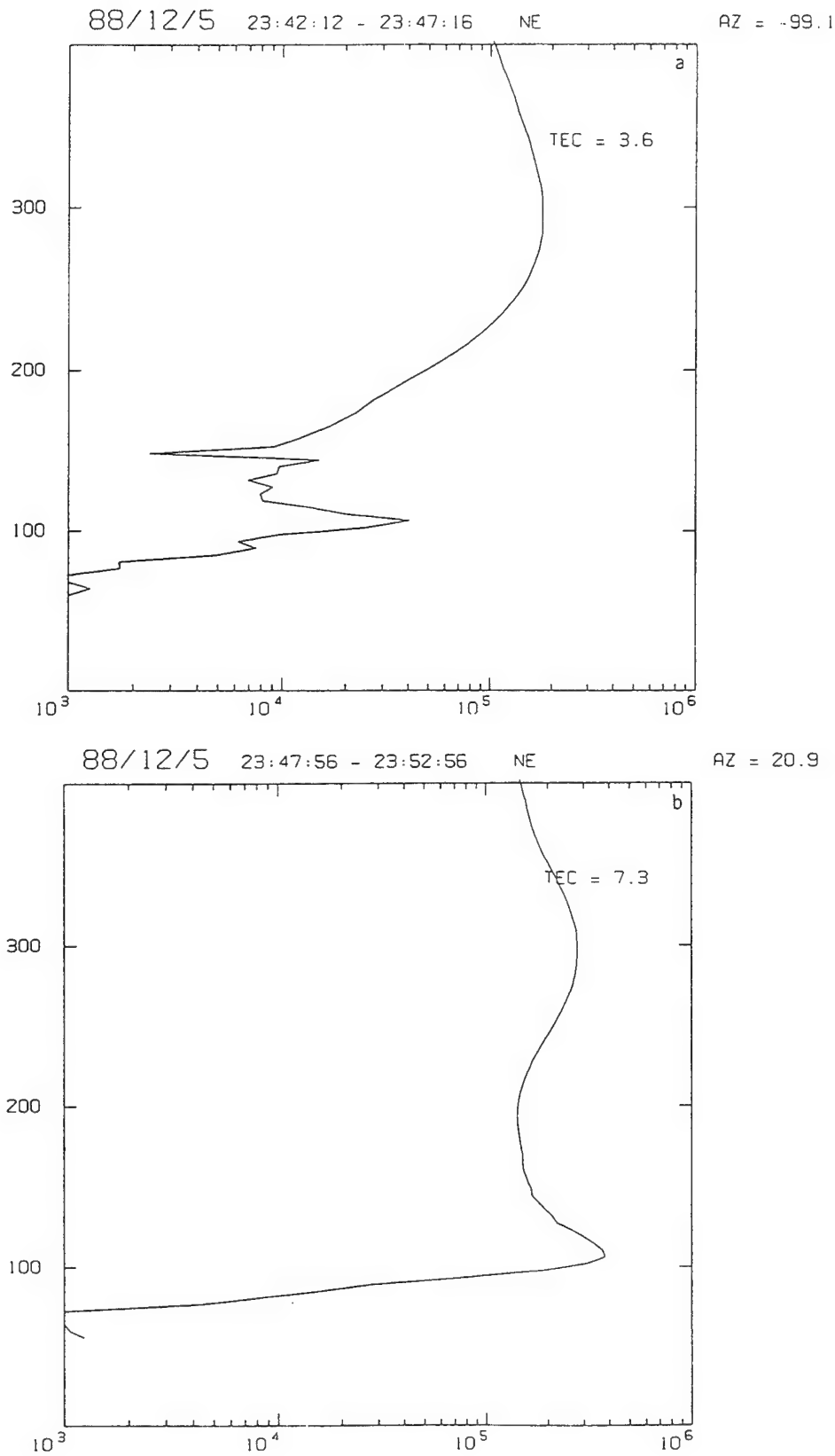


Fig. 21. Four samples of Sondrestrom incoherent scatter radar density profiles: (a) 2342:12 UT and (b) 2347:56 UT on December 5, 1988; (c) 0136:19 UT, and (d) 0142:03 on December 6, 1988.

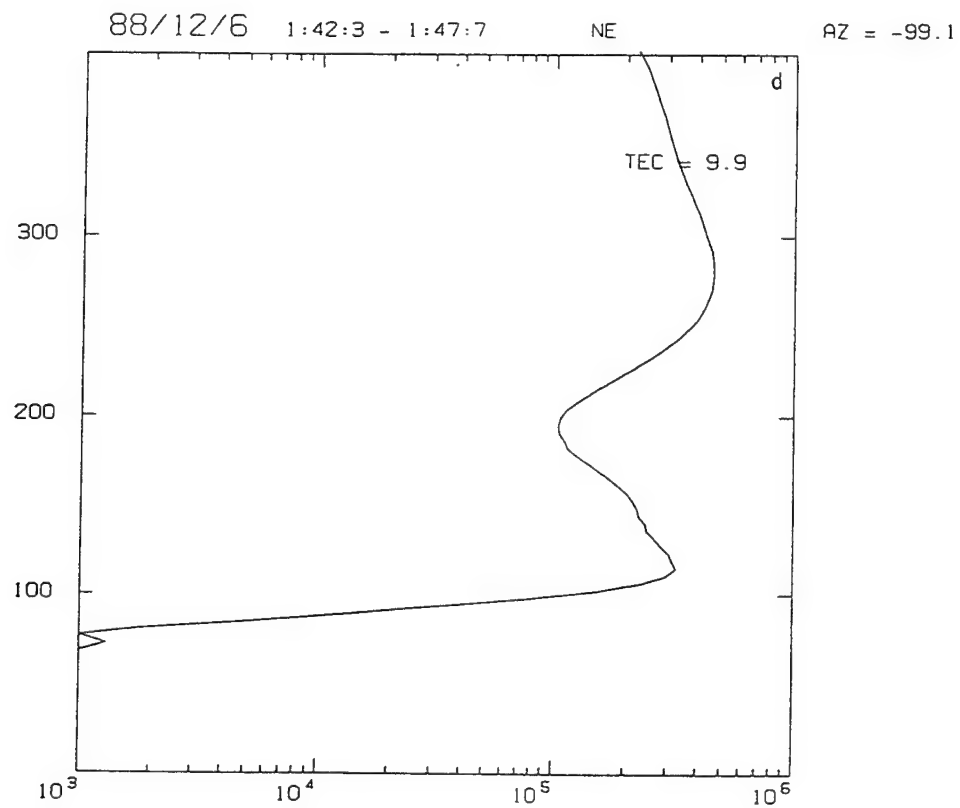
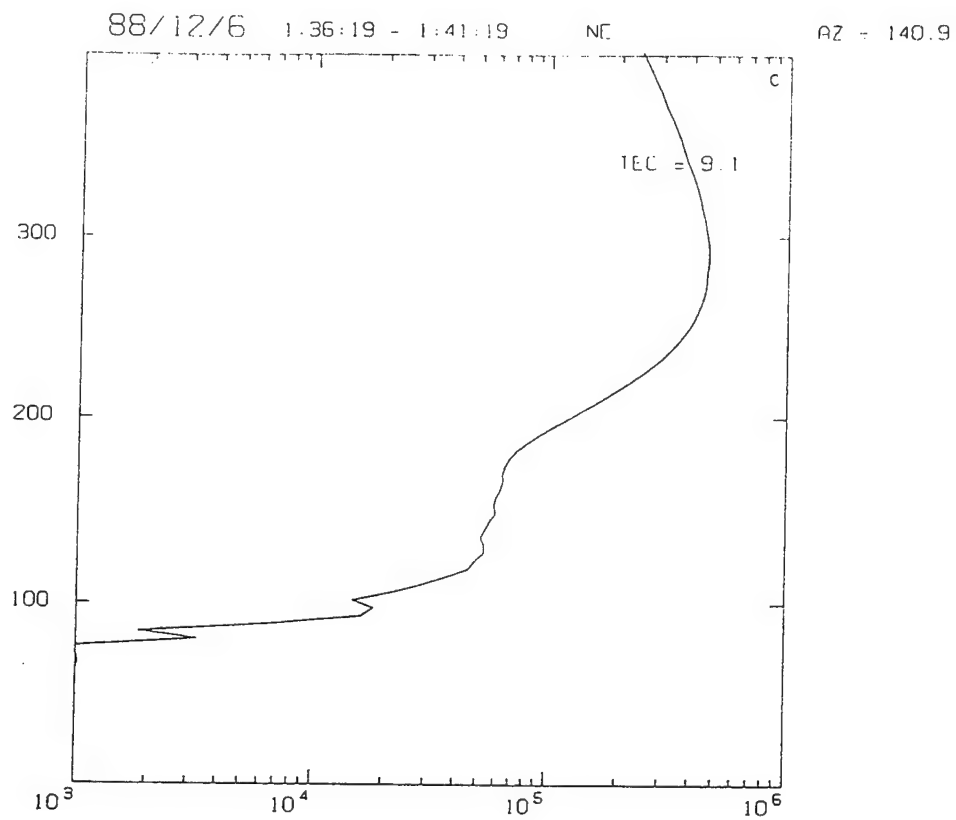


Fig. 21. (continued)

from the signal amplitude structure in the top panel of Figure 19a. We have already pointed out that in such cases the spaced-receiver technique does not give us a correct picture of the *F* region drift velocities. It is important to note that the *F* region densities do not vary greatly from Figure 21a and 21b so that the *E* region content in Figure 21b is a significant fraction of the total electron content which increases from 3.6×10^{16} to 7.3×10^{16} electrons m^{-2} when the integration on the density profiles are made up to a height of 480 km. Profiles such as that observed in Figure 21b usually give rise to the two-slope phase spectrum with a moderate amount of amplitude scintillation accompanying large phase scintillations such as shown in Figure 20a.

A comparison of Figures 21c with 21d, on the other hand, shows a similar change in the *E* region densities but by now the *F* region densities are about three times higher than those observed earlier in Figures 21a and 21b. The high *F* region densities are, in all probability, associated with the polar cap patches which have made their way from the central polar cap at Thule to the edge of the oval near Sondrestrom. The situation portrayed in Figure 21c is exactly time coordinated with the signal structure and spectra shown in Figure 20b. The amplitude fades are saturated, the amplitude spectrum shows steepening, while the signal phase shows the development of significant small-scale structure and a one-slope phase spectrum. Even though we sample saturated amplitude scintillations at Sondrestrom which are in all probability patch-related, we are yet able to determine the true drift of the diffraction pattern because of the reduced anisotropy caused by the seemingly omnipresent *E* region ionization which even in its reduced state is much higher than that available in the dark central polar cap. Thus this coordinated ISR and spaced-receiver amplitude and phase scintillation data set has provided much new information on high-latitude *E* and *F* region irregularity behavior.

4. SUMMARY

The results presented above clearly demonstrate that the *F* region irregularity strength, their anisotropy and drifts within the polar cap are sensitively controlled by the IMF.

For IMF B_z northward conditions, scintillation magnitudes are moderate at 250 MHz, decorrelation times are highly variable, axial ratios are small and

the spaced-receiver drifts show clear evidence of shears in the irregularity flow patterns. Such irregularity drift reversals are consistent with in situ and ISR velocity measurements in the vicinity of Sun-aligned polar cap arcs.

For IMF B_z southward conditions, saturated amplitude and large phase scintillations are seen at 250 MHz, decorrelation times are small and much less variable, axial ratios are large. The large axial ratios preclude measurements of the true drift velocity of the irregularities which cause the intense scintillations. With suitable orientation of the antenna baselines, it is still, however, possible to obtain a semiquantitative estimate of the background drifts which are found to be ordered in the antisunward direction. Earlier airglow and ionosonde measurements had provided evidence for convecting *F* region plasma density enhancements which traveled from the central polar cap in an antisunward direction toward the auroral oval.

Spaced-receiver observations made at Sondrestrom provided an opportunity of studying polar cap patches as they convect into a region of intense particle precipitation. We show here by means of coordinated ISR and spaced-receiver scintillation measurements, that the underlying *E* region ionization caused by the particle precipitation leads to an enhancement of the cross-field diffusion of the kilometer-scale irregularities, thereby causing a reduction in anisotropy of the *F* region irregularities. This reduction in the anisotropy allows the determination of the true drift velocity which shows remarkably good agreement with the simultaneously measured ISR drift velocities. The presence of significant density in the *E* region manifests itself in a two-slope phase spectrum and occasionally in its fast development stage can give rise to edge diffraction effects.

Future extensions of this work should encompass spaced-receiver drift measurements with multiple baselines oriented in different directions to be able to handle the effect of large anisotropy on drift measurements. The entire question of the effects of underlying *E* region ionization and background convection on anisotropy of *F* region irregularities also needs to be put on a more quantitative footing by numerical simulation studies of field-aligned coupling effects [Heelis *et al.*, 1985; Heelis and Vickrey, 1990] using the simultaneously measured ISR parameters.

Acknowledgments. We thank K. Bounar for help with data processing. The work at Boston College was partially supported by GL contract F19628-90-K-0007 and NSF grant ATM-8715445. The work at GL was funded by AFOSR Task 2310G9. We thank the Danish Commission for Scientific Research in Greenland for permission to conduct ground experiments at Thule and Sondrestrom.

REFERENCES

- Banerji, R. B., Radio measurements of ionospheric drift as a problem in parameter estimation, in *Statistical Methods in Radio Wave Propagation*, edited by W. C. Hoffman, Pergamon, New York, 1960.
- Basu, S., Su, Basu, C. E., Valladares, E. J., Weber, J., Buchau, G. J., Bishop, and B. W. Reinisch, Coordinated observations of high latitude ionospheric turbulence, *SPI Conf. Proc. Reprint Ser.*, 8, 137, 1989.
- Basu, Su., S. Basu, E. MacKenzie, and H. E. Whitney, Morphology of phase and intensity scintillations in the auroral oval and polar cap, *Radio Sci.*, 20, 347, 1985.
- Basu, Su., et al., Simultaneous density and electric field fluctuation spectra associated with velocity shears in the auroral oval, *J. Geophys. Res.*, 93, 115, 1988.
- Basu, Su., S. Basu, E. J. Weber, and G. J. Bishop, Plasma structuring in the polar cap, *J. Geomagn. Geoelectr.*, 42, 763, 1990a.
- Basu, Su., S. Basu, E. MacKenzie, W. R. Coley, J. R. Sharber, and W. R. Hoegy, Plasma structuring by the gradient drift instability at high latitudes and comparison with velocity shear driven processes, *J. Geophys. Res.*, 95, 7799, 1990b.
- Bhattacharyya, A., S. J. Franke, and K. C. Yeh, Characteristic velocity of equatorial *F* region irregularities determined from spaced receiver scintillation data, *J. Geophys. Res.*, 94, 11,959, 1989.
- Booker, H. G. and G. MajidiAhi, Theory of refractive scattering in scintillation phenomena, *J. Atmos. Terr. Phys.*, 43, 1199, 1981.
- Briggs, B. H., On the analysis of moving pattern in geophysics, 1, Correlation analysis, *J. Atmos. Terr. Phys.*, 30, 1777, 1968.
- Briggs, B. H., G. J. Phillips, and D. H. Shinn, The analysis of observations on spaced receivers of the fading of radio signals, *Proc. Phys. Soc. London, Ser. B*, 63, 106, 1950.
- Brown, G. M., and J. W. Chapman, Full correlation ionospheric drift analysis for a general observing triangle, *Ann. Geophys.*, 28, 349, 1972.
- Buchau, J., E. J. Weber, D. N. Anderson, H. C. Carlson, Jr., J. G. Moore, B. W. Reinisch, and R. C. Livingston, Ionospheric structures in the polar cap: Their origin and relation to 250-MHz scintillation, *Radio Sci.*, 20, 325, 1985.
- Buchau, J., B. W. Reinisch, D. N. Anderson, E. J. Weber, and C. Dozois, Polar cap plasma convection measurements and their relevance to the modeling of the high-latitude ionosphere, *Radio Sci.*, 23, 521, 1988.
- Burke, W. J., M. C. Kelley, R. C. Sagalyn, M. Smiddy, and S. T. Lai, Polar cap electric field structures with a northward interplanetary magnetic field, *Geophys. Res. Lett.*, 6, 21, 1979.
- Carlson, H. C., Jr., R. A. Heelis, E. J. Weber, and J. R. Sharber, Coherent mesoscale convection patterns during northward interplanetary magnetic field, *J. Geophys. Res.*, 93, 14,501, 1988.
- Costa, E., P. F. Fougere, and S. Basu, Cross-correlation analysis and interpretation of spaced-receiver measurements, *Radio Sci.*, 23, 141, 1988.
- Doolittle, J. H., S. B. Mende, R. M. Robinson, G. R. Swenson, and C. E. Valladares, An observation of ionospheric convection and auroral arc motion, *J. Geophys. Res.*, 95, 123, 1990.
- Fedor, L. S., A statistical approach to the determination of three-dimensional ionospheric drifts, *J. Geophys. Res.*, 72, 5401, 1967.
- Fremouw, E. J., and J. A. Secan, Modeling and scientific application of scintillation results, *Radio Sci.*, 19, 687, 1984.
- Gurevich, A. V., and Ye. Ye. Tsedilina, Spreading and shape of inhomogeneities in a plasma, *Geomagn. Aeron.*, 6, 200, 1966.
- Gussenhoven, M. S., Extremely high latitude auroras, *J. Geophys. Res.*, 87, 2401, 1982.
- Heelis, R. A., and J. F. Vickrey, Magnetic field-aligned coupling effects on ionospheric plasma structure, *J. Geophys. Res.*, 95, 7995, 1990.
- Heelis, R. A., J. F. Vickrey, and N. B. Walker, Electrical coupling effects on the temporal evolution of *F* layer plasma structure, *J. Geophys. Res.*, 90, 437, 1985.
- Kent, G. S., and J. R. Koster, Some studies of nighttime *F*-layer irregularities at the equator using very high frequency signals radiated from Earth satellite, *Ann. Geophys.*, 22, 405, 1966.
- Killeen, T. L., and R. G. Roble, Thermosphere dynamics: Contributions from the first 5 years of the Dynamics Explorer Program, *Rev. Geophys.*, 26, 329, 1988.
- Lassen, K., and C. Danielsen, Quiet time pattern of auroral arcs for different directions of the interplanetary magnetic field in the *Y-Z* plane, *J. Geophys. Res.*, 83, 5277, 1978.
- Livingston, R. C., C. L. Rino, J. Owen, and R. T. Tsunoda, The anisotropy of high-latitude nighttime *F* region irregularities, *J. Geophys. Res.*, 87, 10,519, 1982.
- MacDougall, J. W., G. E. Hall, and D. R. Moorcroft, Bistatic auroral radar system and three-receiver-ionospheric-motions velocities: A comparison, *J. Geophys. Res.*, 95, 15,219, 1990.
- May, P. T., Statistical errors in the determination of wind velocities by the spaced antenna technique, *J. Atmos. Terr. Phys.*, 50, 21, 1988.
- Moorcroft, D. R., and K. S. Arima, The shape of the *F* region irregularities which produce satellite scintillations: Evidence for axial symmetry, *J. Atmos. Terr. Phys.*, 34, 437, 1972.
- Rino, C. L., R. C. Livingston, R. T. Tsunoda, R. M. Robinson, J. F. Vickrey, C. Senior, M. D. Cousins, J. Owen, and J. A. Klobuchar, Recent studies of the structure and morphology of auroral zone *F* region irregularities, *Radio Sci.*, 18, 1167, 1983.
- Rozhanskiy, V. A., and L. D. Tsendin, Evolution of strong inhomogeneities of the ionospheric plasma, 1, *Geomagn. Aeron.*, 24, 345, 1984.
- Sojka, J. J., W. J. Raitt, and R. W. Schunk, Effect of displaced geomagnetic and geographic poles on high-latitude plasma convection and ionospheric depletions, *J. Geophys. Res.*, 84, 5943, 1979.
- Trudell, E. S., T. L. Killeen, R. J. Niciejewski, Su. Basu, and B. W. Reinisch, An investigation of a polar cap arc sequence using ground-based measurements at Thule, Greenland, *EOS Trans. AGU*, 71, 581, 1990.
- Tsunoda, R. T., High-latitude *F* region irregularities: A review and synthesis, *Rev. Geophys.*, 26, 719, 1988.
- Valladares, C. E., and H. C. Carlson, Jr., The electrodynamic, thermal, and energetic character of intense Sun-aligned arcs in the polar cap, *J. Geophys. Res.*, 96, 1379, 1991.

- Vickrey, J. F., and M. C. Kelley, The effects of a conducting E layer on classical F region cross-field plasma diffusion, *J. Geophys. Res.*, **87**, 4461, 1982.
- Völk, H. J. and G. Haerendel, Striations in ionospheric ion clouds, I, *J. Geophys. Res.*, **76**, 4541, 1971.
- Weber, E. J., J. Buchau, J. G. Moore, J. R. Sharber, R. C. Livingston, J. D. Winningham, and B. W. Reinisch, F layer ionization patches in the polar cap, *J. Geophys. Res.*, **89**, 1683, 1984.
- Weber, E. J., J. A. Klobuchar, J. Buchau, H. C. Carlson, Jr., R. C. Livingston, O. de la Beaujardiere, M. McCready, J. G. Moore, and G. J. Bishop, Polar cap F patches: Structure and dynamics, *J. Geophys. Res.*, **91**, 12,121, 1986.
- Whalen, J. A. Auroral oval plotter and nomograph for determining corrected geomagnetic local time, latitude, and longitude for high latitudes in the northern hemisphere, *Rep. AFCRL-70-0422*, Air Force Cambridge Res. Lab., Bedford, Mass., July 1970.
- S. Basu, Phillips Laboratory (AFSC)/GP, Ionospheric Physics Division, Hanscom AFB, MA 01731.
- Su. Basu, C. Bryant, and C. E. Valladares, Boston College, Institute for Space Research, Newton, MA 02159.
- E. Costa, Centro de Estudos em Telecomunicacoes, Pontificia Universidade Catolica do Rio de Janeiro, Brazil.
- R. C. Livingston, SRI International, Menlo Park, CA 94025.

The U.S. Government is authorized to reproduce and sell this report.
Permission for further reproduction by others must be obtained from
the copyright owner.

The Electrodynamic, Thermal, and Energetic Character of Intense Sun-Aligned Arcs in the Polar Cap

C. E. VALLADARES

Institute for Space Research, Boston College, Newton Center, Massachusetts

H. C. CARLSON, JR.

Geophysics Laboratory, Hanscom Air Force Base, Massachusetts

The electrodynamic, thermal, and energetic character of stable Sun-aligned arcs in the polar cap can be meaningfully diagnosed by an incoherent scatter radar, provided a suitable observing scheme is selected. We report here such measurements of two intense Sun-aligned arcs. The two arcs were diagnosed on two different nights (February 26 and March 1, 1987) using the Sondre Stromsfjord radar as a stand-alone diagnostic. Repeatable patterns are found in mesoscale area (order 10^3 km by 10^3 km) maps of altitude profiles for observed electron and ion gas number densities, temperatures, and line-of-sight velocities, and projected mesoscale area maps of derived electric fields, Pedersen and Hall conductivities (N_e , T_e , T_i , V , E , Σ_P , Σ_H), horizontal and field-aligned currents, joule heating rate, and Poynting flux. We confirm, for the first time with continuous mesoscale area maps, that the arcs have the anticipated simple arc electrodynamics. That is, the visual and enhanced ionization signatures of the arc are produced by incoming energetic electrons carrying the outgoing current from the electric field convergence in the arc. Strong electron temperature enhancements (>2000 K) are found as expected within the sheets of ionizing particle precipitation. Dawn to dusk decreases in the antisunward plasma flow of order 1 km s^{-1} , across order 100 km, correspond to peak electron densities of order 10^5 cm^{-3} down to altitudes as low as 120 km, and upward currents of order 1 μA m^{-2} . These data also lead to important implications for the physics of polar cap arcs. The high-velocity (antisunward flow on the dawnside) edge of the arc marks the location of strong persistent Joule heating driven by downward Poynting flux. There is a channel of strongly enhanced ion temperature (well above the electron temperature) along the high-velocity edge of the arc, quantitatively accounted for by ion frictional heating as the strong electric field drags the ions through the neutral gas. The deposition rate into the atmosphere of the net electromagnetic energy well exceeds the net particle energy deposited by the ionizing energetic electron flux. This heating is a substantial source of heat into the polar thermosphere. As estimated by heat into the ions, heat lost by the ions to the neutrals, or energy available from the Poynting and energetic particle flux, several ergs cm^{-2} s^{-1} are deposited in channels of order 100 km for good fractions of an hour in these arcs; this contributes to resolving the problem of the missing polar thermosphere heat source. Finally, a reasonably simple yet self-consistent, accurate, and comprehensive representation of stable intense Sun-aligned arcs is presented, including the electrodynamic, thermal, and energetic character.

1. INTRODUCTION

Morphological studies of intense polar cap aurora began during the International Geophysical Year (IGY). Measurements performed during this year at Antarctica [Weill, 1958; Denholm and Bond, 1961] and at Resolute Bay, Canada [Davis, 1960] found intense polar cap arcs oriented in the Sun-Earth direction. Later, a scanning photometer on board ISIS 2 [Berkey et al., 1976; Ismail et al., 1977] and all-sky cameras in Greenland [Lassen and Danielsen, 1978] revealed that the occurrence of intense polar arcs throughout the polar cap correlates well with northward interplanetary magnetic field (IMF).

New initiatives to observe the intense Sun-Earth aligned arcs involved airborne observatories [Romick and Brown, 1971; Eather and Akasofu, 1969] and also particle and optical emission detectors on Defense Meteorological Satellite Program (DMSP) satellites [Meng and Akasofu, 1976; Akasofu, 1976]. The new instrumentation served to indicate that the

polar arcs are usually produced by soft (<1 keV) electrons and to characterize the different types, locations and shapes of intense polar cap auroras.

Statistical and case studies of auroras and particle precipitation in the polar cap indicated that intense polar cap auroras preferentially occur in the morning sector [Gussenhoven, 1982]. The average energy of intense electron precipitation in the polar cap was found to be between 50 and 300 eV [Hardy, 1984]. Burke et al. [1982] inferred that intense polar cap arcs are the optical signature of upward Birkeland currents associated with corresponding velocity gradients.

The DE 1 spacecraft provided images of intense Sun-aligned arcs extending across the polar cap. The transpolar auroras together with the auroral oval resembled the Greek letter theta [Frank et al., 1982, 1986]. The salient features of this striking auroral pattern are the presence of precipitating ions accompanying the energetic electrons (>1 keV), its location in a region of sunward convection, and the possible existence of four cells of plasma convection. Burke et al. [1979] have also presented data suggesting four convecting cells. A valuable description of the convection for different values of the three components of the IMF has been presented by Reiff and Burch [1985]. Their analysis implies a

Copyright 1991 by the American Geophysical Union.

Paper number 90JA01765.
0148-0227/91/90JA-01765\$05.00

four-cell convection pattern for strong northward IMF and a three-cell convection for smaller positive values of B_z .

There is a general consensus that some of the intense polar cap Sun-aligned (S-A) arcs are formed in a region of closed field lines [Akasofu *et al.*, 1984; Frank *et al.*, 1986] with precipitating electrons having the characteristics of plasma sheet or plasma sheet boundary layer electrons [Peterson and Shelley, 1984; Obara *et al.*, 1988]. Kan and Burke [1985] have argued that the less intense polar arcs possibly occur on open field lines. Other high-latitude arcs may well correspond to a poleward widened auroral oval [Meng, 1981; Murphree *et al.*, 1982]. Data presented by Huang *et al.* [1987] collected by ISEE 1 during excursions in the magnetotail suggest filaments of plasma sheet plasma extend into the lobes. Even though the filaments have been observed for any orientation of B_z , their presence reflects the discrete nature of the plasma source and suggests a causal link between the IMF and the formation of the polar cap arcs.

With the advent of intensified imaging photometers, much more common weak stable Sun-aligned arcs were found in the polar cap [Weber and Buchau, 1981]. The Sondrestrom incoherent scatter radar was also used to study the morphology of these weak S-A arcs. Carlson *et al.* [1984] determined sheared (antisunward to sunward reversal) flow which was coincident with bottomside F region density enhancements and with optical emissions, both produced by the precipitating particles. The plasma velocity gradients coincided with a simple arc electrodynamics interpretation. Robinson *et al.* [1987] obtained the field-aligned currents for a Sun-aligned arc observed near local midnight and merging into the auroral oval. Their measurements implied an upward current on the western edge of the arc and a downward current on the eastern side. Mende *et al.* [1988] have also presented measurements from Sondrestrom. Their observations of multiple polar cap arcs showed a preferential antisunward flow within the arcs.

Carlson *et al.* [1988] have presented convection patterns representing northward B_z conditions which were obtained by combining the optical emissions associated with S-A arcs and the one-dimensional velocity measurements of DE 2. These quantitatively confirm electron impact production of the arc, and local simple electrodynamics for the arc. Weber *et al.* [1989] used data from a rocket that traversed a polar cap arc to model the circuit parameters of the arc. They also showed enhanced electron temperature variation across the arc.

The purpose of this paper is to examine more comprehensive diagnostics and analysis of the electrodynamics, the energy, and the thermal properties of a few Sun-aligned arcs which were located in the polar cap. The data are more comprehensive by virtue of time continuous measurement, over a wide spatial area, of a significantly more complete set of geophysical parameters. The arcs to be described in this work were probed with the Sondrestrom radar on the evenings of February 26 and March 1, 1987. The common signature of these arcs consists in that they were produced by electrons with energies larger than 1 keV, as deduced from the altitude of significant E region ionization. Although we diagnosed over 30 stable Sun-aligned arcs, using all-sky imaging photometers (ASIPs) and/or the incoherent scatter radar (ISR) during this campaign, here we will concentrate on only two of these arcs. The arcs we concentrate on are the two most intense, for optimum signal to noise ratio or

measurement statistics on derived parameters. The arc of February 26 was transpolar as observed by the DMSP/F6 satellite [Niedjowski *et al.*, 1989]. This stable arc had an electron density above 10^5 cm^{-3} in the E region. On March 1, 1987 we observed three polar cap arcs. Two of them were Sun-aligned and the other hook-shaped. The two Sun-aligned arcs were initially separated by 80 km with peak densities located at substantially different altitudes. They subsequently merged into a single broad arc. We discuss the properties of Sun-aligned arcs for these two nights to demonstrate repeatability of some basic characteristics.

In section 2 we identify a data-taking mode designed for such studies, and present Sun-aligned arc parameters directly observable by this technique. In section 3 we extend analysis of the ISR data to present important derived parameters. In section 4 we discuss the implications of these measurements, develop their interpretation, and identify their significance to understanding of the electrodynamics, thermal character, and energetics of the arcs. Finally, in section 5 we summarize the main conclusions from this study.

2. DATA-OBSERVING MODE AND DIRECT OBSERVABLES

The Sondre Stromfjord incoherent scatter radar (66.987°N, 50.949°W, 74° Invariant Latitude), is situated 100 miles (160 km) inland from the west coast of Greenland. Its location at a very high magnetic latitude makes this station capable of probing the nighttime polar cap and examining the dynamics of polar Sun-aligned arcs [Carlson *et al.*, 1984; Robinson *et al.*, 1987; Mende *et al.*, 1988].

While it is difficult, if not impossible, to recognize Sun-aligned arcs with conventional ISR observing modes in the absence of coincident optical imaging data, it is possible to design a radar mode that can unambiguously recognize them. We describe the design here, illustrated in Figure 1. The design is based on what we know of their morphology from optical imagery. The essence of the design is simple. One wants to map the electron density profile and velocity field over an area, with the area large compared to the arc, and with time resolution short compared to the time for the arc to pass through the ISR field of view. Signal to noise considerations determine look elevation and area of coverage, and limit azimuth scan rates and cycle time resolution.

Variability in the motion and lifetime of S-A arcs [Weber *et al.*, 1989] also imposes some restrictions. For this reason we implemented the azimuthal sweeps (AZ) at two different speeds. One AZ scan was performed at a rapid scanning velocity, with the purpose of obtaining a snapshot of the electron density inside fast moving arcs. Two slow AZ scans swept 90° in 2 min, probing slower moving arcs and providing the line of sight (LOS) velocity and the number density with smaller error bars. Good horizontal transarc spatial resolution was also achieved (15 km at 150 km of altitude when pointed across the arc, and ultimately limited to the 2.5-km radar beam width smeared over the integration time when pointed along the arc). These measurements were complemented with an elevation (EL) scan (perpendicular to the anticipated arc direction) that gives the dependence of the geophysical parameters on altitude and distance across the arc. The scan sequence (shown in the bottom panel of Figure 1) was slow AZ-fast AZ-slow AZ-EL. For the data

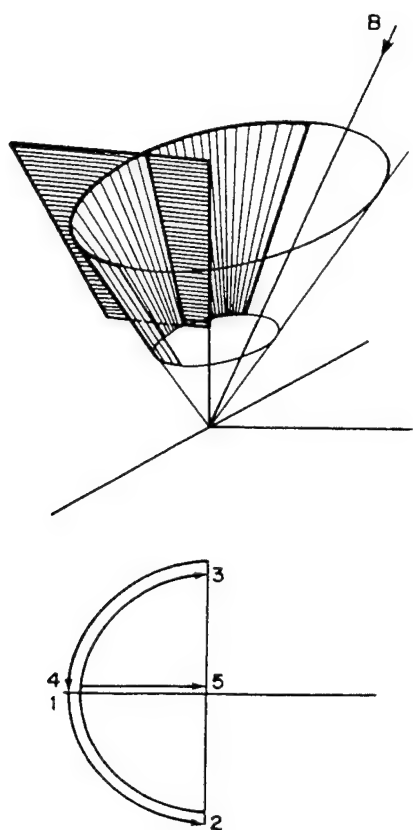


Fig. 1. Schematic representation of the volume scanned by the Sondrestrom radar during the EL and AZ sweeps of February 26, 1987. The bottom panel shows the sequence followed by the antenna. The initial azimuth was selected in order to align node 3 with the Sun-Earth direction.

presented here, one complete cycle was performed in 8 min and 40 s. Figures 2a–2h present the data corresponding to two consecutive cycles of this antenna pattern.

We will also show data from two other observing modes. One, tailored to a specific need, looked directly up the magnetic field line so as to give true instantaneous altitude profiles within a Sun-aligned arc. Such time continuous observations during the full passage of an overhead arc thus allow detailed diagnosis of the properties of a transverse section of an arc. These observations are presented in Plates 1a and 1b.

The third data set presented here, Figures 4a–4c, for March 1, 1987, again shows electron number density and LOS velocity. The antenna pattern consisted of a full 360° AZ scan and two 120° EL scans embedded at planes perpendicular to each other. By chance, a Sun-aligned arc is clearly apparent 150 to 200 km duskward (and westward) of the ISR on the Figure 4a scan, although the 20-min time resolution of this standard Sondrestrom observing mode is too slow to track or in general unambiguously recognize an arc. The Sondrestrom ISR is able to make a proper identification of polar cap arcs based upon (1) the ability of the radar to measure the number density and the LOS velocity while doing rapid scans, and (2) the well-known distribution of density gradients and velocity shears within the arcs [Carlson *et al.*, 1984]. Moreover, *E* region polar cap arcs exhibit enhanced densities below 200 km. Recall that chemical lifetimes are so short below 200 km that strong N_p enhance-

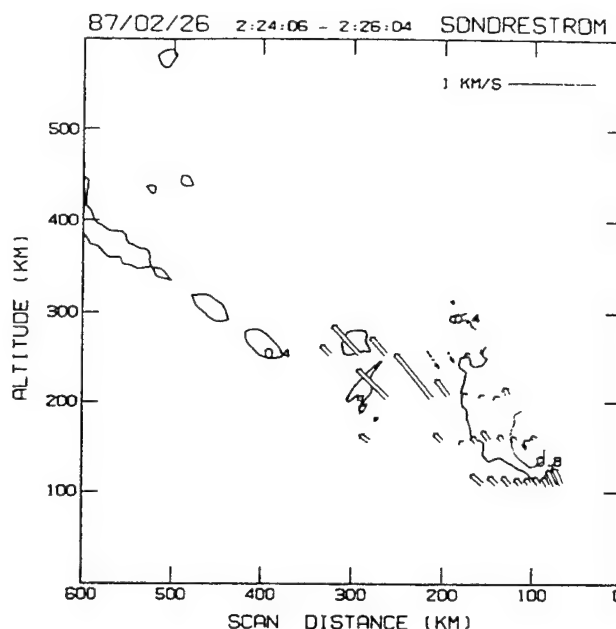


Fig. 2a. Number density contours and line of sight (LOS) velocity measured by the Sondrestrom radar on February 26, 1987 and during the time interval from 0224 to 0226. The azimuth was kept fixed at 231° and the elevation varied from 25° to 60°. The initial density contour corresponds to $0.4 \times 10^5 \text{ cm}^{-3}$, and consecutive contours increase linearly in steps of $0.4 \times 10^5 \text{ cm}^{-3}$. The LOS velocity was scaled in order to represent a velocity equal to 1 km s^{-1} as a segment 100 km long. The dashed line vectors indicate LOS velocities directed toward the radar, and the double line vectors characterize plasma motion away from the radar.

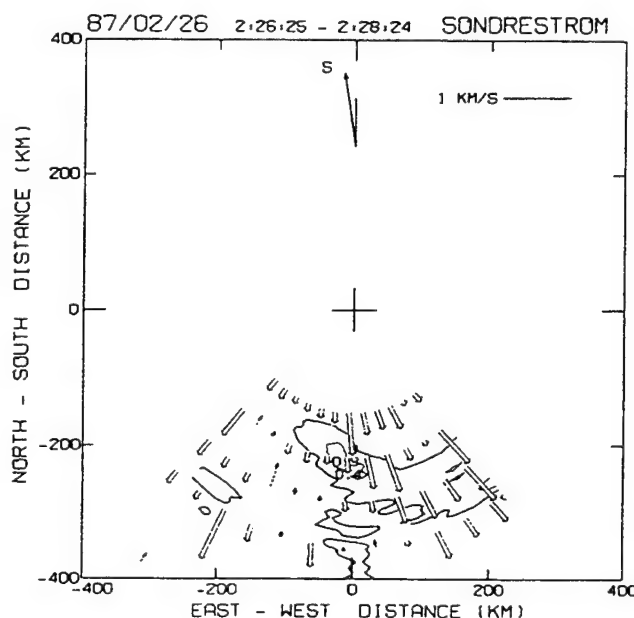


Fig. 2b. Plasma parameters corresponding to the AZ scan of 0226–0228. The constant elevation was 35° and the azimuth changed from 231° to 141°. The measured velocity and density have been projected to a horizontal plane using the same scaling factors employed in Figure 2a. Geographic north is at the top and west is on the left side of the plot. The arrow at the top central part indicates that during the experiment the direction of the Sun was 7° west of geographic north.

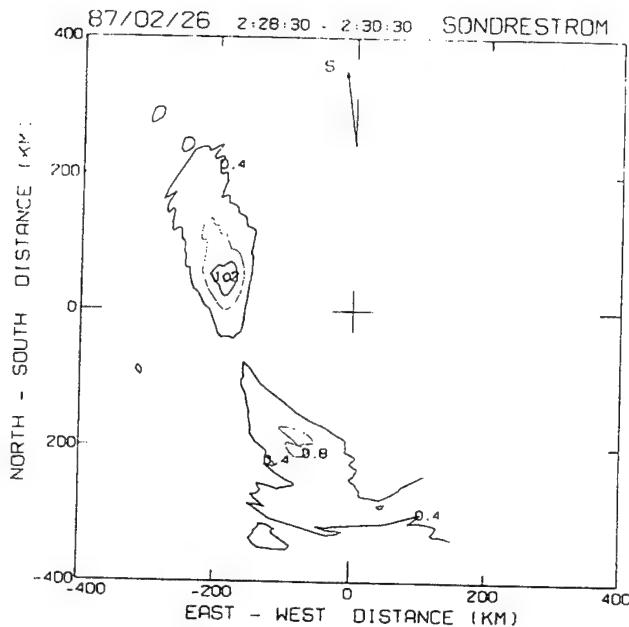


Fig. 2c. Plasma density for February 26, 1987 and time interval between 0228 and 0230. The antenna scanned 180° in 2 min using a fixed elevation of 35° . The scan started at an azimuth of 141° and ended at 321° . The measured LOS velocity is not shown in this plot.

ments identify local production of ionization. We have used the density and LOS velocity mapping capabilities provided by the AZ scans to properly determine the occurrence of arcs.

The densities plotted in Figures 2-4 and Plate 1 are on a linear scale. The initial value and the interval between consecutive levels are both equal to $0.4 \times 10^5 \text{ cm}^{-3}$. The arrows superimposed to the N_e contours represent the LOS

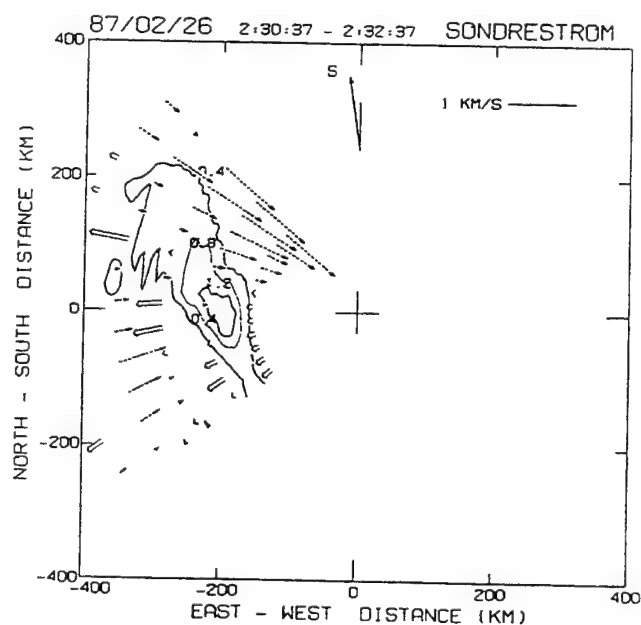


Fig. 2d. Top view of the density and the LOS velocity, both projected to a horizontal plane. The scan time is from 0230 up to 0232. This plot corresponds to the northern quadrant. The elevation is 35° and the scan starts at 321° of azimuth and continues until 231° . The scaling factor is the same as in previous figures.

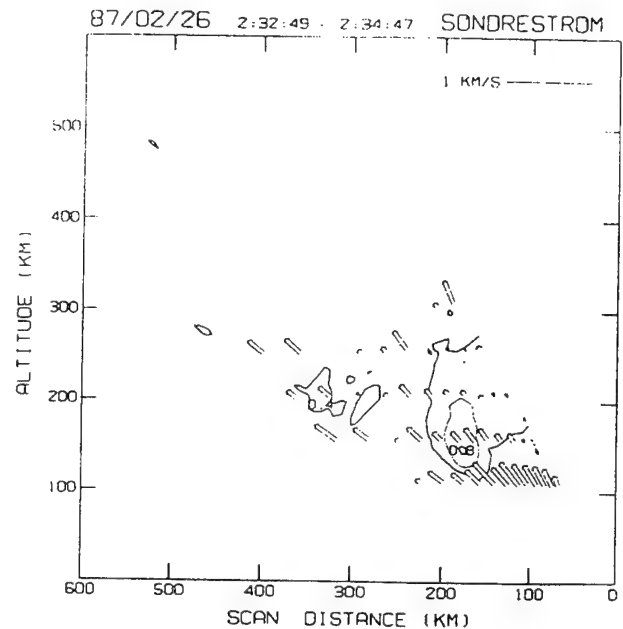


Fig. 2e. Similar to Figure 2a, but for the time interval 0232-0234.

velocities; they have different patterns and lengths according to the sign and magnitude of the LOS velocity. At 150 km of altitude the density and velocity statistical uncertainties were about 5% and $<100 \text{ m s}^{-1}$ respectively.

2.1. February 26, 1987 Scans

Data from this day show a stable Sun-aligned polar arc that stayed in the radar field of view for 40 min. This arc penetrated to the E layer (N_e was enhanced at altitudes as low as 120 km), and was detected near local midnight. Its southernmost region was observed to be merged to the poleward edge of the auroral oval during the early part of the

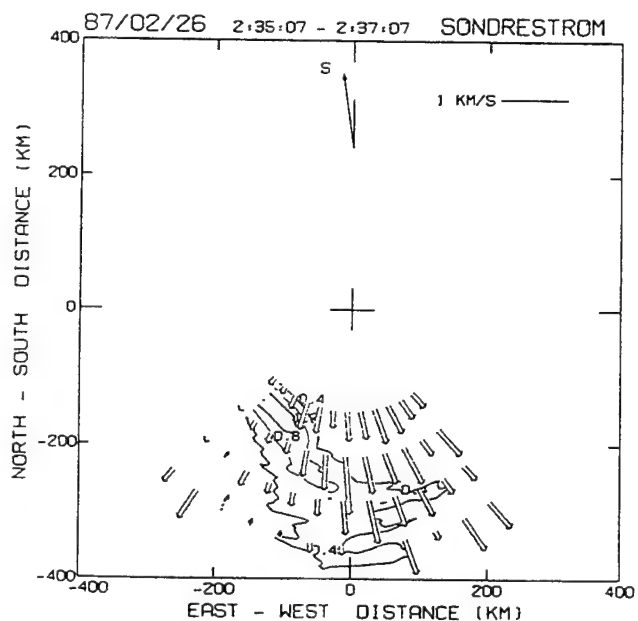


Fig. 2f. Similar to Figure 2b, but corresponding to the time between 0235 and 0237.

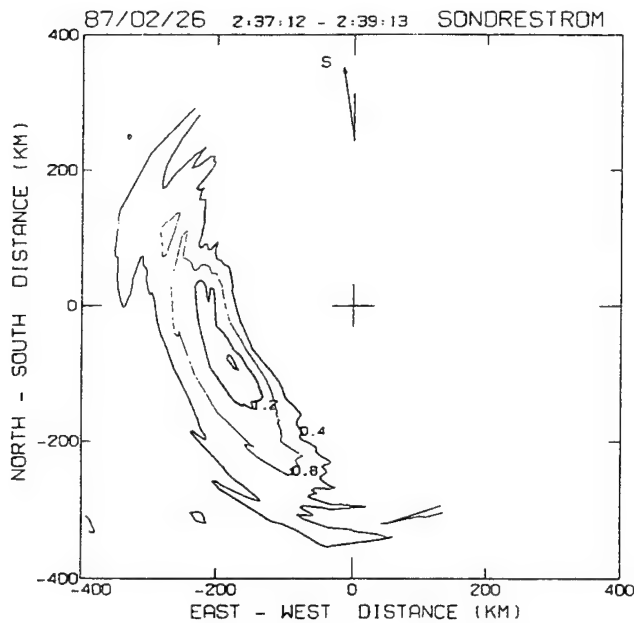


Fig. 2g. Similar to Figure 2c, but for time 0237.

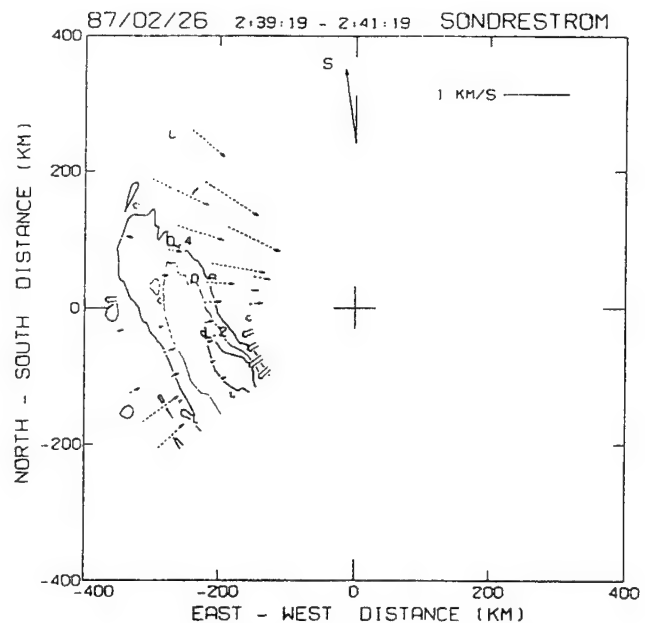


Fig. 2h. Similar to Figure 2d, but for time 0239.

arc transit. At the time of the experiment the background density in the polar cap F region was $0.2 \times 10^5 \text{ cm}^{-3}$, a value well below the lowest density contour level of Figure 2. The Pedersen conductivity peak values corresponding to each scan are presented in Table 1, which also includes the altitude, distance along the dawn-dusk meridian, and displacement velocity of both maxima. The geomagnetic K_p index was 1+ and the solar flux (S_a) 73.9.

The data of Figure 2a were obtained between 0224 and 0226 UT when the S-A arc, as defined by scans of Figures 2b–2d, was located to the west of the radar station. The beam scanned through most of the arc, and also probed a duskward region beyond the arc (left side). In this region beyond the duskward and equatorward edge of the arc the LOS velocity was directed away from the Sun and radar (the small electron density in this region precludes measurement of a precise magnitude of the velocity). Within the arc, at F region altitudes (see range gates 2 and 3 placed at 160 and 210 km of altitude), the LOS velocities (looking transverse to the arc) were less than 100 m s^{-1} . That the density contours trace to lower altitudes in the dawn (right) side of the arc suggests harder precipitation there.

Figure 2b presents the data gathered with the slow AZ scan of 0226. Here, the Sun-aligned arc is identified by the high N_e structure seen in the lower south to southwest part of the plot, with an orientation much more clearly seen in Figures 2d, 2f, 2g, and 2h. The southern extreme of the arc shows (in Figures 2b, 2c, and perhaps 2f) a dawnside (eastward) extension with an electron density (about $>0.5 \times 10^5 \text{ cm}^{-3}$) larger than the background N_e at altitudes about 200 km. This segment, not Sun-aligned, but more auroral oval-aligned, is probably associated with the connection of the Sun-aligned arc to the poleward edge of the auroral oval. The northern extreme of the Sun-aligned arc N_e contours mapped here in Figure 2b, all clearly pointing sunward, is determined by the simple geometry of the arc intersect with the conical radar scan.

Still in Figure 2b, gates 2 and 3, set at the same heights of

the previous EL scan, indicate a general antisunward motion and a shear inside the arc. Outside in the duskside there is a small sunward flow; conversely the dawnside region has a large antisunward flow. We will come back to this point in section 3, where we include the Earth corotation velocity and compute the direction of the plasma flow in the Earth-Sun frame of reference.

Figure 2c shows the same S-A arc during the fast AZ, 180° scan of 0228. The two quasi-ellipsoids that are observed represent the intersection of the arc and the cone generated by the azimuthal motion of the antenna (see Figure 1). The north and south cross sections of the arc have a maximum density of 1.6 and $0.8 \times 10^5 \text{ cm}^{-3}$ respectively. The angle between geographic north and the arc alignment was equal to -23.5° . The LOS velocity, in spite of being measured, is not presented here because of its poor statistical accuracy and its coarse spatial resolution following from the rapid radar scan.

Figure 2d shows the slow AZ scan that starts at 0230. The LOS velocity measured in the F region (second range gate) shows smaller values as the counterclockwise AZ scan progresses. At -90° azimuth it changes from a toward orientation to a direction away from the radar. The LOS velocity corresponding to the E region (first gate) shows a similar characteristic, with the reversal occurring earlier in the scan. The statistical error of the LOS velocity measurement is 20 m s^{-1} for gate 1 and about 50 m s^{-1} for gate 2. In spite of the latter being a sizable error when the magnitude of the velocity is small, the velocity reversal can be visualized following the trend of the velocity values. At the end of the scan (southwest), gates 1 and 2 exhibit LOS velocities oriented away from the radar and with a value of order 100 m s^{-1} . The density contours indicated that the arc was oriented -30° away from the north.

The second partial EL scan, in Figure 2e, measured the complete cross section of the arc, and also probed the dawnside region outside the arc (right side). The region of maximum density was found displaced 84 km toward mag-

TABLE 1. Motion of the S-A Arc Along the Dawn-Dusk Meridian

Type of Scan	Maximum Pedersen Conductivity, $\times 10^4$ mho/m	Time, UT	Altitude, km	Dawn-Dusk Displacement, km	Time, Difference,* s	Distance Difference,* km	Velocity, Dawn to Dusk,† m s ⁻¹
EL	1.96	0225:26	129.9	107.6			
AZ	1.86	0226:45	125.3	152.6	79	45.0	569 (469)
AZ	2.43	0229:50	120.7	151.1	185	-1.5	-8 (-108)
AZ	1.95	0231:37	131.1	171.9	107	20.8	194 (94)
EL	2.20	0233:19	121.2	170.2	102	-1.7	-16 (-116)
AZ	3.60	0235:07	125.2	175.3	108	5.1	47 (-53)
AZ	2.89	0238:12	128.5	187.3	185	12.0	65 (-35)
AZ	2.84	0240:59	128.5	188.6	167	1.3	8 (-92)

*Differences are relative to the preceding scan.

†Left-hand number Earth corotating frame, right-hand number Earth-Sun frame.

netic west from its previous location 9 min earlier (a dawn to dusk virtual velocity by the N_e contours of about 150 m s^{-1}). The LOS plasma velocity within (and nominally transverse to) the arc was about 150 m s^{-1} in the F region and 300 m s^{-1} for the E region, a factor of 3 increase with respect to the velocities of Figure 2a. The F region LOS velocities in the dawnside of the Sun-aligned arc (right side of the plot) are the reverse of on the duskside, with a value equal to 100 m s^{-1} .

For altitudes below 150 km in the (production-recombination) chemical equilibrium region of the N_e profile (examination of the slope of, for example, the $0.4\text{--}0.8 \times 10^5 \text{ cm}^{-3}$ N_e contours of Figures 2a and 2e and Plate 1) we find the duskside slope entering the arc shallower than the dawnside slope leaving the arc. This suggests a gradual hardening of the precipitating electron flux across the arc from the leading edge to the trailing dawnside, where the greatest depth of penetration occurs. There is a relatively sharp cutoff of ionizing electron flux on the (trailing) dawnside of the arc. We cannot claim here a statistically significant sample (three out of the three cases of 0224, 0233, 0210 on February 26, 1987, and consistency for the fourth case of Figure 4c at 0340, March 1, 1987).

The difference in character (bifurcated versus continuous) between the N_e contours of Figures 2c and 2g is due to the geometry of the ISR conical scan intersecting the slab of arc ionization. This may be appreciated by visualizing a vertically elevated slab or small horizontal cylinder, either piercing the (55° vertex angle) vertical conical surface and passing through near its axis, or grazing (and encompassing a portion of) the conical surface to one side. Thus the intersection of a conical scan with Sun-aligned cylindrical forms will depend on the distance of the axis of the horizontal cylinder from the vertical axis of the cone, and will look very much like Figures 2d, 2f, 2g, and 2h. The intersection of a conical scan with a horizontally stratified ionosphere is a set of concentric circle N_e contours. Figures 2b and 2c show Sun-aligned arc contours merging to the southwest with some horizontally stratified ionospheric plasma. The core ionization in Figure 2 ($\approx 0.8 \times 10^5 \text{ cm}^{-3}$) is continuous, Sun-aligned, and quite stable in density, size, and height (e.g., Figures 2a and 2e), and separates F region plasma flowing away from the Sun on its dawnside from plasma flowing much more slowly and toward the Sun on its duskside (the plasma is predominantly antisunward within this arc).

Several characteristics of the measured LOS velocity and the number density associated with the arc of February 26

can also be explained by changes in the relative location of the arc with respect to the radar. The small LOS velocity of Figure 2d at -90° azimuth is interpreted as a near perpendicularity between the flow and the sight direction. The differences in the peak density observed on consecutive AZ scans or during two sectional cuts of the same arc (Figure 2c) are due to variations in the distance between the radar and the S-A arc. E region velocities collected during the AZ scans can be used to reassure that the null LOS velocity is due to a near perpendicularity of the flow and the sight direction. The velocity in the E layer, being smaller and rotated clockwise with respect to the F region flow, will give a null LOS velocity at a different look angle, as in Figure 2d.

Figure 3 shows the density contours of Figures 2d and 2f superimposed to the OI (6300 Å) emissions (hatched region) recorded simultaneously by the GL all-sky imaging photometer. Both radar and optical data sets have been transformed and scaled to a common coordinate system that depicts geographic latitude and longitude. The red line optical aurora was assumed to originate at 200 km of altitude. The emission produced by impact excitation shows a bright, discrete, and isolated feature located westward of the radar station. The number density contours measured by the ISR mostly overlap the hatched region, except for a small part to the south. This region may correspond to the oval F layer. Figure 3 confirms genuinely and unambiguously that the radar, in fact, diagnosed an arc which was Sun-aligned and locally produced.

2.2. February 26, 1987 Dwells

Plates 1a and 1b show observations of the same stable and energetic arc as in Figure 2, obtained between 0204 and 0222 as the arc passed overhead the antenna parked in the direction up B, the magnetic field. An integration time of 1 min was selected in order to provide temperature error bars smaller than 10% at a 200-km altitude. The arc motion across the radar beam cannot be assumed constant. However from Figures 2a–2h (see Table 1) we know that the Sun-aligned arc moved westward (toward dusk) at order of 100 m s^{-1} in the Earth corotating frame. As a result of this motion, the duskside of the arc appears earlier (lefthand side) in Plates 1a and 1b. Color-coded vertical profiles of T_i and T_e/T_i are superimposed on the density contours in Plates 1a and 1b, respectively. In the center of the arc the ion temperature is 500 K in the E layer and about 700 K at F region heights. T_i

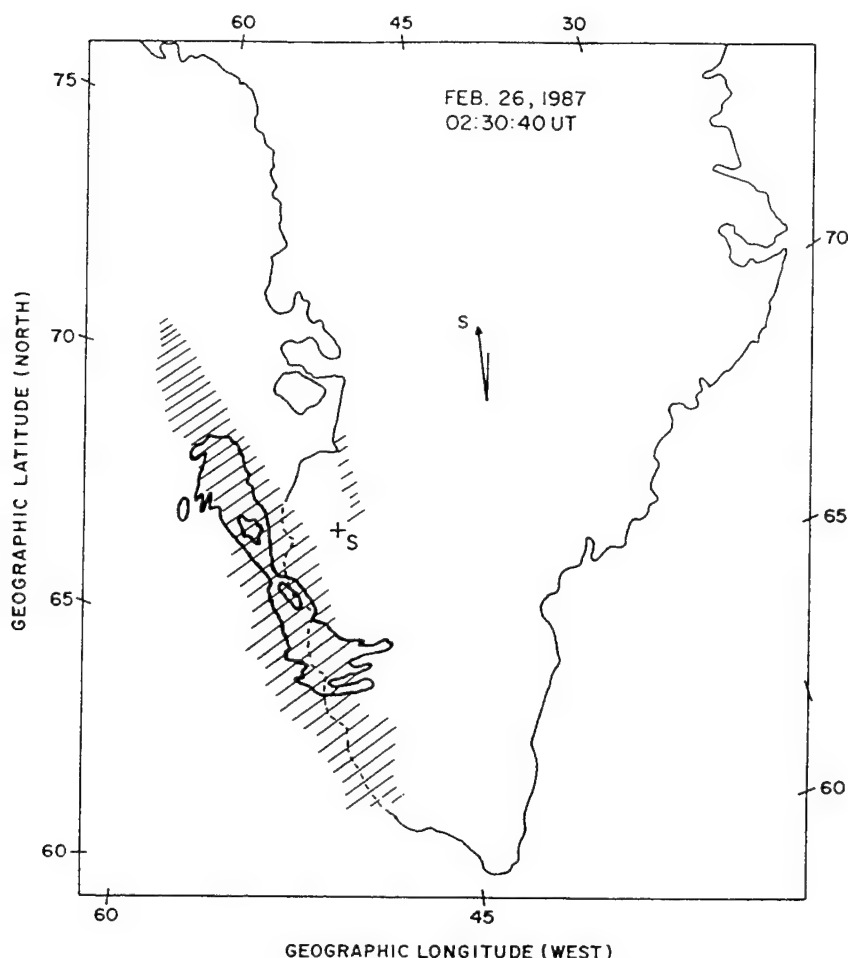


Fig. 3. Schematic representation of the auroral luminosity observed by the GL/ASIP on February 26, 1987. The number density measured by the Sondrestrom ISR is superimposed as a thick line contour. The two contour levels correspond to 0.4 and $1.2 \times 10^5 \text{ cm}^{-3}$. Both 6300 \AA intensities and radar N_e have been transformed to geographic coordinates. They are both colocated and aligned in the same direction (about 24° west of north).

sharply increases in the dawnside of the arc reaching 1300 K and exceeding T_e at both E and F layers. The electron temperature has a different pattern, with T_e enhancements of 500 K colocated with regions of higher bottomside electron densities (more intense precipitation). This behavior is reflected in Plate 1b, where the T_e/T_i ratio is observed to decrease from >1.5 to 0.8 near the dawn edge boundary. The S-A arc, defined by the 0.8×10^5 contour, drifted across the radar beam in 10 min. If we take the average westward speed to be of order 100 m s^{-1} in the Earth frame, which implies a width of about 60 km for the S-A arc, we get reasonable agreement with the 0.8×10^5 contours of Figure 2. The maximum density was $1.9 \times 10^5 \text{ cm}^{-3}$ at 130 km of altitude. The width of the arc and the number density are both consistent with the view that the arc properties are rather stable over the time period covered by Figure 2 and Plate 1 (over half an hour).

2.3. March 1, 1987

To demonstrate that the conclusions to be reached from the February 26 data do not represent a unique circumstance, we present data for another Sun-aligned arc of comparable intensity, observed three nights later. On this night a system formed by two Sun-aligned arcs traversed the

Sondrestrom field of view while the radar performed a 20-min sequence of AZ-EL-EL scans. (At this time the K_p and the solar flux indices were $2+$ and 72.8 respectively).

Figure 4a shows the number density and the LOS velocity measured with the full circular AZ scan of 0324 with the antenna at a fixed elevation of 45° . Most of the patchy features to the east and south of the station are radar intersections of the polar cap F region. The elongated trace located 135 km westward of the radar is the clear signature of a S-A arc. We have already noted that any significant ionization enhancement near 150 km is due to ongoing ionization, and will have attendant impact-excited optical emissions. Thus we must say something about the oval electron density enhancements approximately 80 km east of the northern and southern extremes of this elongated trace. These have electron density, electron temperature, and electrodynamics consistent with Sun-aligned arc signatures (piercing rather than grazing the conical radar scan). However, the ISR alone cannot unambiguously identify that they are connected by continuous Sun-aligned enhanced electron density contours, and thus they will not be discussed further in this paper.

A pair of EL scans (Figures 4b and 4c) cut this arc system, respectively in its northwest and southwest regions, 8 and 14

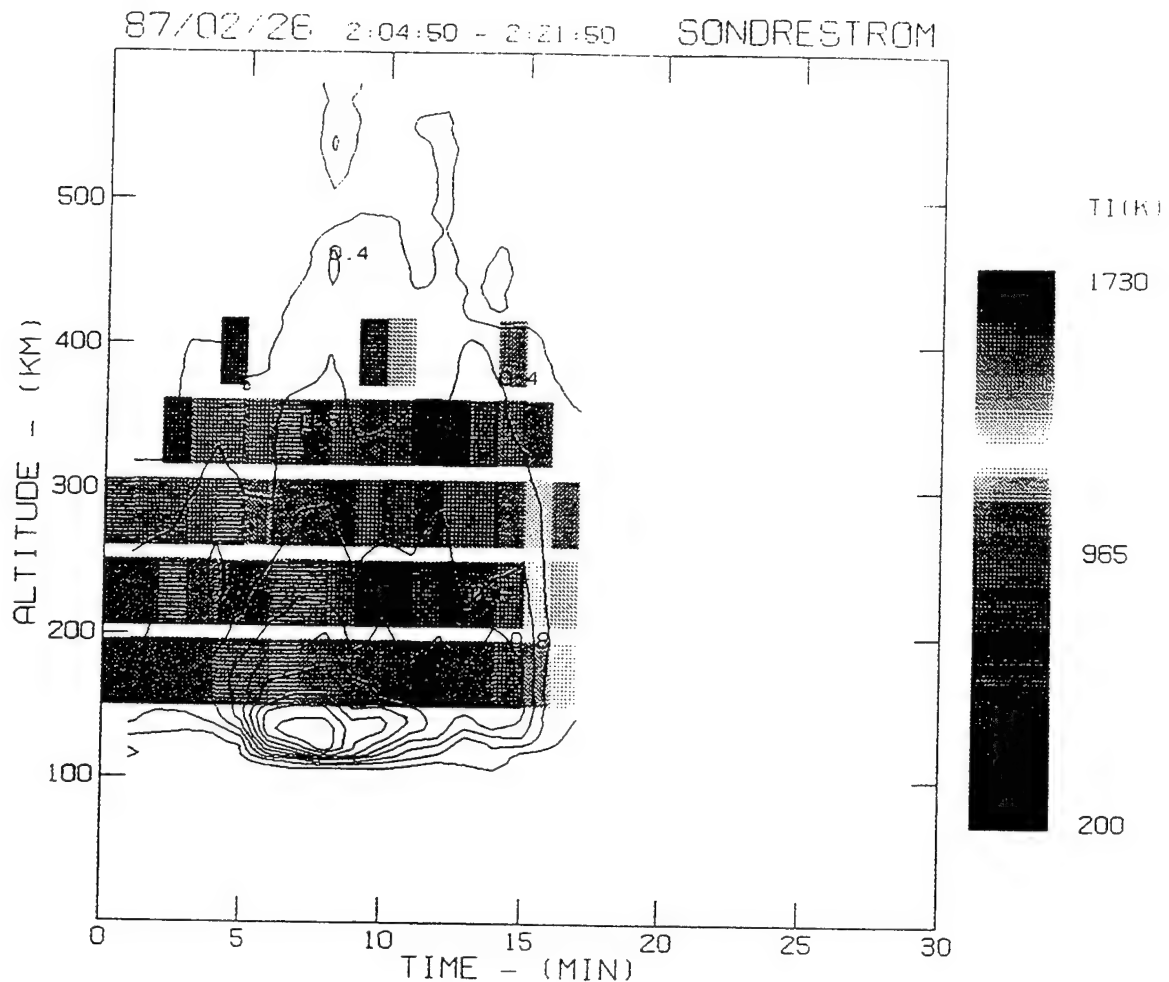


Plate 1a. Color-coded representation of the ion temperature as a function of altitude and time for February 26, 1987, time interval from 0204 to 0221. The N_e contours, measured simultaneously, are superimposed. The antenna was pointing parallel to the local B lines ($EL = 80^\circ$, $AZ = 141^\circ$). Each individual profile is the result of 1-min integration time. Density contours start at $0.2 \times 10^5 \text{ cm}^{-3}$.

min after it was mapped by the AZ scan. An ionization feature to the northeast is seen at 0343 on the EL scan at 51° azimuth. This (soft ionizing flux) feature is not a stable Sun-aligned arc, as it does not extend into the southeast radar scan. This will be discussed later.

The right side of Figure 4b (southern distances) shows the LOS velocity at 160 km of altitude (gate 2) varying as expected if the velocity is constant and the variation is produced only by changes in the radar look angles. A different behavior is observed in the northern part (left side) of the plot, where the LOS velocities increase abruptly and then start decreasing at ~ 100 km of distance. The region of larger LOS velocity coincides with the downward edge of the arc.

3. DATA ANALYSIS

This section presents the analysis of the data corresponding to February 26 and March 1, 1987. Here, we describe the method that was used to calculate the velocity vector, the Hall and Pedersen conductivities, the electric field, the horizontal and the field-aligned currents, the vertical component of the Poynting flux and the ion-neutral differential temperature. The data acquired during the EL and AZ scans

have been processed independently using different algorithms (sections 3.1 and 3.2) which were tailored respectively for each of these two types of scans. The results of these independent calculations provide mutually consistent values of the geophysical parameters, lending further confidence to the analysis procedures and results.

3.1. Analysis of Elevation Scans

At F altitudes the plasma drifts in the $\mathbf{E} \times \mathbf{B}$ direction. In the E layer the large ion-neutral collision frequency prevents the ions from moving perpendicular to \mathbf{E} . Brekke *et al.* [1973, 1974] used the relation between winds, drifts and electric fields to obtain the E region neutral winds. They employed ion velocity vectors measured at two different altitudes but connected by the same field line.

A different approach was exercised by Doupnik *et al.* [1977] and de la Beaujardiere *et al.* [1977] in which simultaneous LOS velocities measured from the E and F layers and the radar-deduced wind velocity were used to determine two components of the velocity vector; the third component (parallel to \mathbf{B}) was assumed to be null.

Nevertheless, the ion motion along \mathbf{B} is seldom zero. Mechanisms such as adiabatic expansions, parallel electric

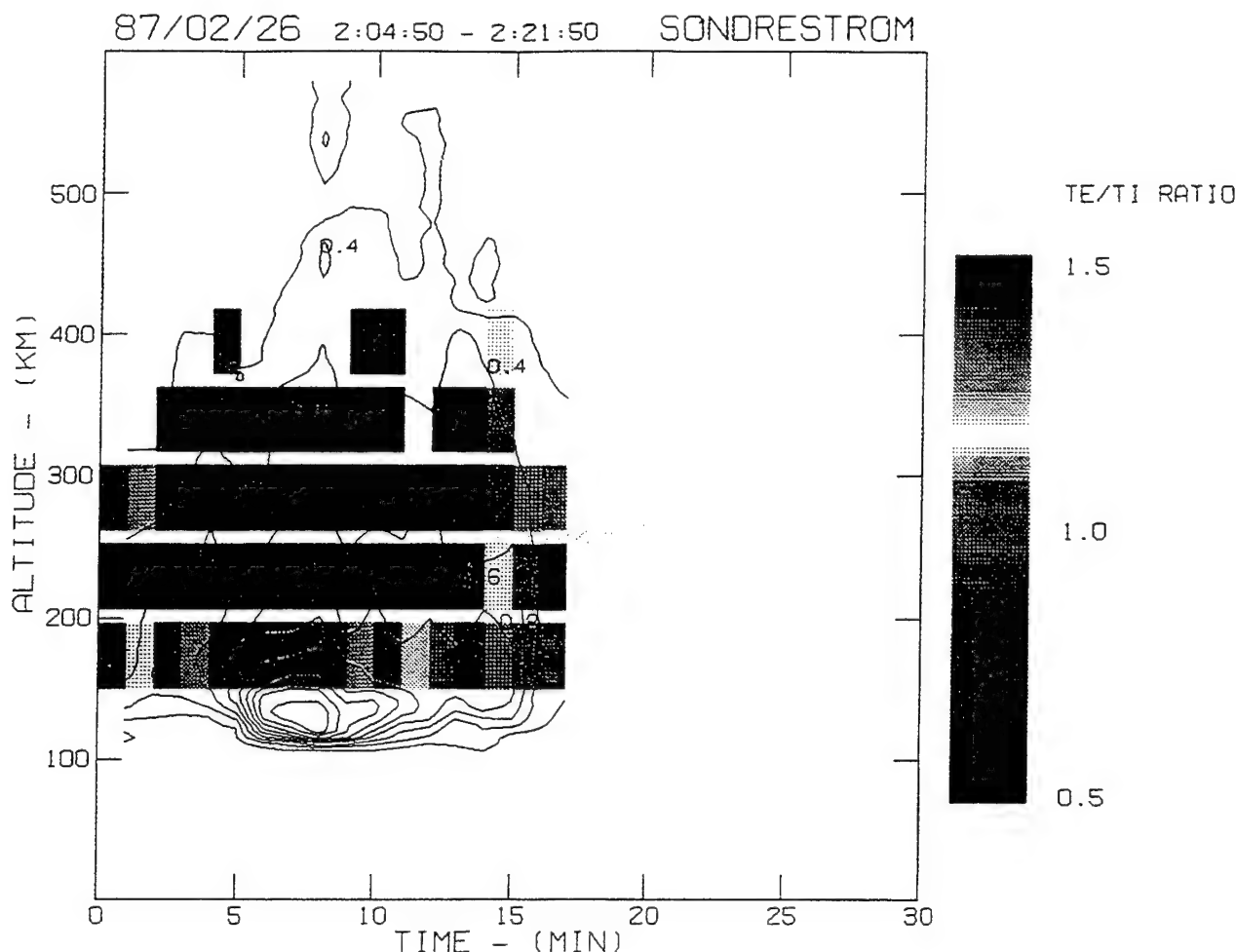


Plate 1b. Similar to Plate 1a, but the color-coded diagram represents the temperature ratio (T_e/T_i). The time is the same as in the previous figure.

fields or the small component of the neutral wind along B , all drive ion motions along magnetic lines. *Spencer et al.* [1976] detected vertical neutral winds in the auroral zone, less than or of the order of 80 m s^{-1} . *Petekerych et al.* [1985] observed values of 15 m s^{-1} associated with auroral arcs. Here we measure the magnitude of the ionic motion in the direction parallel to B by pointing the antenna along B on February 26, 1987 between 0204 and 0222, before the sequence of EL and AZ scans and during the overhead transit of the arc. V_{\parallel} was found equal to $25 \pm 7 \text{ m s}^{-1}$. In general a nonzero V_{\parallel} will introduce an error equal to $V_{\parallel} \times \tan(\text{EL})$. Consequently the null V_{\parallel} assumption fails when the radar is directed near the up B position.

The velocity vectors were derived using the algorithm described in Appendix A. This method has some of the characteristics of the one employed by *Doupnik et al.* [1977], with the main difference that the input data were collected by EL scans instead of dwells. Appendix A also includes a description of the pulse configuration that was used, and a list of the different constraints which curtail the capability of the radar to measure the ionospheric parameters.

Concurrently with the radar, a Fabry-Perot interferometer recorded the intensity and the Doppler velocity of OI (6300 Å) emissions at the zenith and four cardinal points (J. Meriwether, personal communication, 1988). The neutral wind pattern measured on February 26, 1987 has been

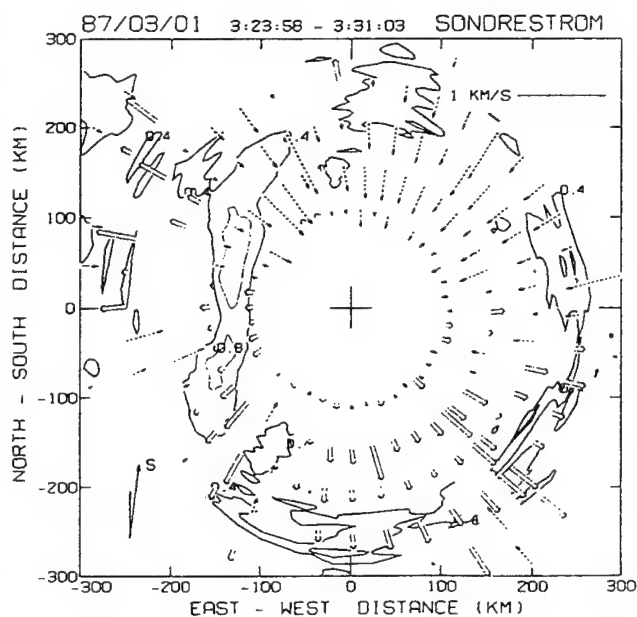


Fig. 4a. Number density and LOS velocity corresponding to March 1, 1987. The time interval is between 0323 and 0331. The antenna scanned 360° in about 7 min; the elevation was maintained fixed at 45° . The Sun direction is indicated in the lower left corner of the plot.

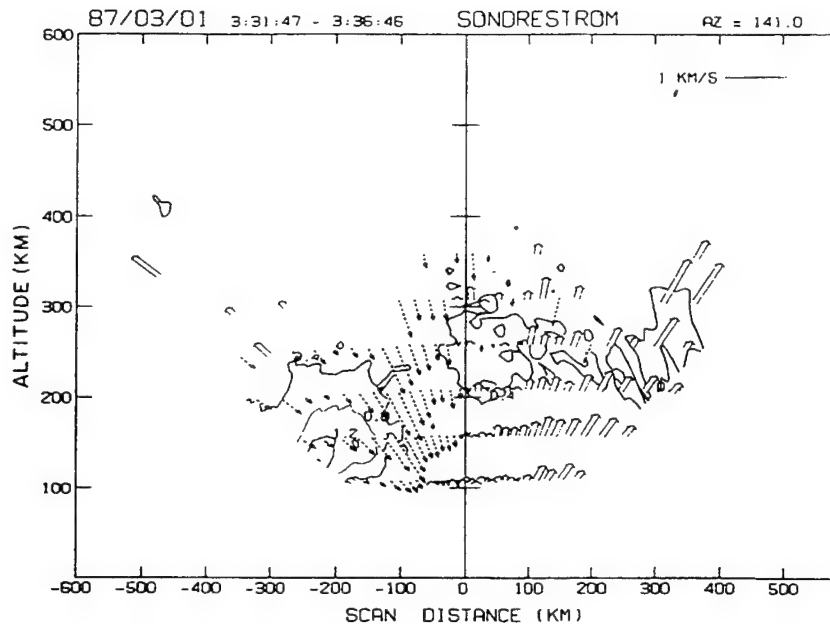


Fig. 4b. Elevation scan performed in the plane of the magnetic meridian between 0331 and 0336. Magnetic north is at the left side of the plot. Only arc A was probed by the radar during this scan.

described by *Niciejewski et al.* [1989]. They showed that the direction of the wind was southerly during the zenithal transit of the arc.

For all the data presented here, we have performed a complete velocity vector analysis, including actual measured neutral winds, and a three-dimensional magnetic field model. The results of the velocity analysis for the two EL scans of Figure 2 are displayed in Figures 5c and 6c. Here we present the resolved vectors and their error bars (dashed line). Geographic north is at the top of the panel and the arrow in the upper part points toward the Sun location. The top panels of these figures show the height-integrated Pedersen

and Hall conductivities plotted as a function of westward distance from the radar. Both Hall and Pedersen conductivities were calculated using the radar-measured number density, the *Schunk and Walker* [1970] expression of the ion-neutral collision frequency, and the *Banks and Kockarts* [1973] expression of the electron-neutral collision frequency. The neutral densities are from the MSIS-86 model [*Hedin*, 1987].

Figure 5 corresponds to the EL scan of 0224. During this time the Pedersen conductivity peaked at a horizontal distance of 105 km away from the radar, the Hall conductivity at 95 km. The three vectors farthest to the west have very

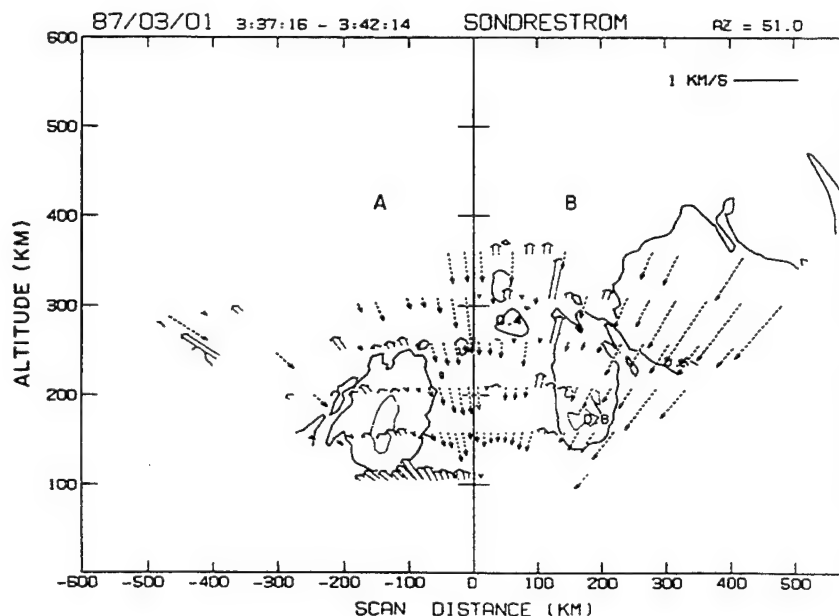


Fig. 4c. Same as Figure 4b, but for the elevation scan in a plane perpendicular to the magnetic meridian. The cross sections of both arcs are displayed at -180 and 150 km. The polar cap F region is on the right side of the plot at altitude of 300 km.

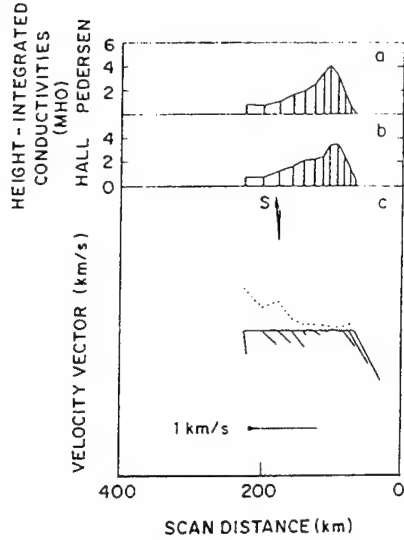


Fig. 5. Plasma parameters deduced from the data corresponding to the EL scan of 0224 on February 26, 1987 (Figure 2a): (a) Height-integrated Pedersen conductivity; (b) height-integrated Hall conductivity; (c) the velocity vectors calculated from the LOS velocity measured at *E* and *F* region altitudes as described in the text. The arrow at the middle of Figure 5c points, in geographic coordinates, to the direction of the Sun.

large uncertainties and are given least statistical weighting. On the contrary, the velocities closer to the arc have small error bars because of the higher N_e . These vectors show a very consistent antisunward flow. The magnitude of the velocity varies from less than 100 m s^{-1} at the center of the arc up to 900 m s^{-1} in the limits of the EL scan. The region of large conductivities coincides with the small ($<100 \text{ m s}^{-1}$) velocities. The sharp decline of the conductivities in the dawnside (right side) of the arc is partially due to our limited EL scan, which did not probe the *F* region at distances close to the radar.

Figure 6 shows the velocity vectors from the analysis of Figure 2e (0232). At this time the region of maximum

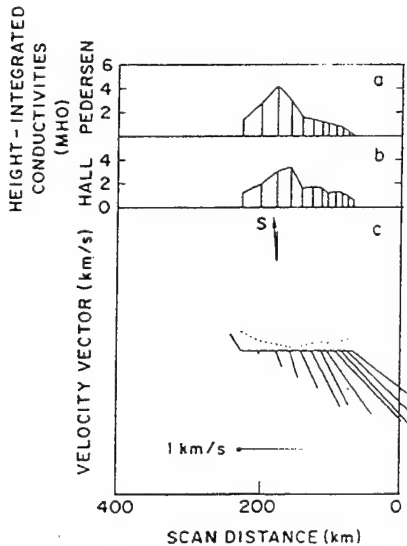


Fig. 6. Same as in Figure 5, but for the EL scan of 0232 (Figure 2e).

Pedersen conductivity was located at 175 km ground range from the station and the Hall conductivity peak at a horizontal distance of 155 km. Similar to Figure 5, the velocity shows a steady antisunward flow. Besides, the region of velocity gradients is extended in the dawnside of the arc reaching a value of 1484 m s^{-1} and then, slightly decreasing when the Pedersen conductivity returns to its background level of 0.2 mhos. Our results agree with those of Robinson *et al.* [1987] and Mende *et al.* [1988].

The unchanging characteristic of both Pedersen and Hall conductivities during two EL scans separated by 8 min argues in favor of this S-A arc being very stable with no appreciable variation of its source and dynamics. Based on the steadiness of this arc, we proceeded to merge the data of Figures 5 and 6 and form the three upper panels of Figure 7. This new set of velocity vectors and conductivities was used to compute the height-integrated and field-aligned currents following the expressions given by Brekke *et al.* [1974] and de la Beaujardiere *et al.* [1977].

$$\mathbf{J}_\perp = \Sigma_P \mathbf{E}_\perp + \Sigma_H \mathbf{E}_\perp \times \mathbf{B}/B + \Sigma_P \mathbf{U}_\perp \times \mathbf{B}$$

$$+ \Sigma_H (\mathbf{U}_\perp \times \mathbf{B}) \times \mathbf{B}/B \quad (1)$$

$$j_\parallel = \nabla \cdot \mathbf{J}_\perp \quad (2)$$

where \mathbf{J}_\perp and j_\parallel are the current perpendicular and parallel to \mathbf{B} . Σ_P and Σ_H are the height-integrated Pedersen and Hall conductivities.

The geophysical parameters and their error bars shown in Figures 7d–7g were all calculated in a coordinate system for which the $+X$ axis is perpendicular to the arc alignment and directed toward dawn. The $+Y$ axis is parallel to the arc and points sunward (poleward). The orientation of the arc was determined from the AZ scans displayed in Figures 2b–2h. It was found that the angle between the arc alignment and geographic north is equal to -24 ± 5 . The direction of the sun is 7° west of north.

Figure 7d shows the component of the electric field perpendicular to the arc E_x (component of the velocity along the arc). E_x is less than 12 mV m^{-1} in the duskward edge of the arc. It reaches its minimum value of 5.4 mV m^{-1} in the region of maximum conductivity. Then, it gradually increases in the dawnside until it presents a peak value of 72 mV m^{-1} at 94 km eastward from the center of the arc. E_y , plotted in Figure 7e, has a different behavior. It remains constant and below 6 mV m^{-1} except for a region (distant 73 km from the center) in the extreme dawnward end of the arc, where E_y increases to 28 mV m^{-1} .

Both components of the height-integrated horizontal currents are plotted in Figures 7f and 7g. J_x (transverse component) is proportional to E_x , it is directed toward dusk and has a maximum value of 0.096 A m^{-1} . J_y , the component along the alignment, presents two different regions. Dawnward from the center of the arc the average current is 0.058 A m^{-1} . Duskward, J_y is below the uncertainty level of 0.008 A m^{-1} .

Considering that the \mathbf{E} field and the conductivities do not vary along the arc alignment, j_\parallel is given by

$$j_\parallel = E_x \frac{\partial \Sigma_P}{\partial x} + E_y \frac{\partial \Sigma_H}{\partial x} + \Sigma_P \frac{\partial E_x}{\partial x} + \Sigma_H \frac{\partial E_y}{\partial x} \quad (3)$$

The parallel current associated with the arc of February 26, 1987 was calculated following (3). The numerical deriv-

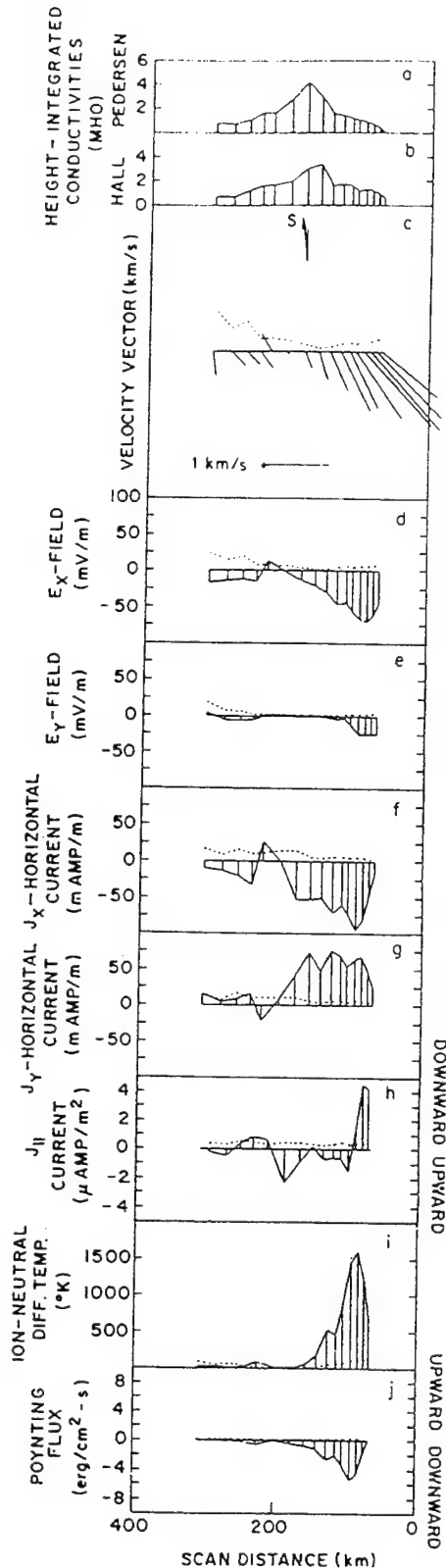


Fig. 7. Geophysical parameters which were derived using the conductivities and velocity vectors of both EL scans of February 26, 1987 (Figures 2a and 2e): (a) Pedersen conductivity; (b) Hall conductivity; (c) velocity vectors; (d) x component of the E field and the statistical error inherent to the measurement; (e) same as Figure 7d for y component; (f) x component of the height-integrated horizontal current; (g) y component of the height-integrated horizontal current; (h) field-aligned current density; (i) ion-neutral differential temperature computed from the measured ion and neutral velocity; and (j) vertical component of the Poynting flux.

atives were obtained by fitting a second-order polynomial to four consecutive values of E_x and E_y . In Figure 7h, downward currents are plotted as positive numbers. The second and fourth terms of the right side of (3) produce very small contributions to $j_{||}$ and can be neglected. In the duskside, the parallel current is less than $1 \mu A m^{-2}$. In the region of maximum conductivity, $j_{||}$ is directed upward with an average value equal to $1 \mu A m^{-2}$. Between 156 and 140 km $j_{||}$ decreases to a level near zero. This decrease is due to a large ($+2 \mu A m^{-2}$) current originated by a negative gradient of the Pedersen conductivity, first term in the right-hand side of (3).

The temperature enhancements of the ion gas observed on the dawnside of the arc are colocated with regions of large plasma flow. This fact led us to calculate the frictional heating due to the ions being dragged through the neutral gas by an electric field. Fedder and Banks [1972] have indicated that ion temperature effects can be described by the ion energy equation. In the steady state T_i depends on the vector difference between ion and neutral velocities [Baron and Wand, 1983]. Hence, if ions transfer momentum to the neutrals sufficiently rapidly that the neutral particles approach the ion velocity, only modest T_i enhancements will occur. Following the derivation of Baron and Wand [1983] for momentum transfer, we found that for the number density of the S-A arcs analyzed here the time constant is several hours, so for large ion velocities, large T_i enhancements and heating rates should occur. We have used the radar ion velocity of Figure 7c and the neutral velocity from the FPI to calculate the ion-neutral differential temperature shown in Figure 7i. Our calculations show that between the dusk and the center part of the arc the differential temperature is less than 100 K. Substantial T_i enhancements occur on the dawn edge, up to 1600 K here. This is simply because this is where the largest ion velocities occur, while the neutral particles do not have time to experience significant acceleration.

Poynting's theorem states that the rate of energy flow per unit area is equal to $E \times \delta H$. Here, we present the calculation of the vertical component of the Poynting flux (P_z) which was computed using the electric field and the horizontal current obtained solely from radar measurements. Following Ampere's law and the current continuity equation (2) and assuming that (1) only the field-aligned current sheets contribute to δH , and (2) the magnitude of the total downward $j_{||}$ current is equal to the magnitude of the upward $j_{||}$ (they are considered to be closed by horizontal Pedersen currents), the P_z is nonzero within the arc and given by

$$P_z = -E_x(J_x - \langle J_x \rangle) \quad (4)$$

where $\langle J_x \rangle$ is the average value of the horizontal current measured at the dawn and dusk boundaries of the S-A arc. Figure 7j displays the values of P_z calculated according to this simple algebraic relation. Negative values refer to a downward energy flux. The region of more intense precipitation has a small Poynting flux, $< 1 \text{ erg cm}^{-2} \text{ s}^{-1}$. However, P_z is maximum, about $5 \text{ erg cm}^{-2} \text{ s}^{-1}$ further east of the arc, on the dawnside and coincident with the region of maximum E_x field. Consistency with these findings can also be claimed from less direct calculations (E. J. Weber, private communication, 1989) which lead to similar findings of a downward Poynting flux on the dawnside of a Sun-aligned arc diagnosed by a rocket flight [Weber et al., 1989]. The time span for that segment of rocket data, however, was short com-

pared to an Alfvén bounce period, so temporal variation cannot be excluded from those data, whereas the ISR data here show steady conditions.

The arc cross sections of Figure 2 were also used to determine the motion of the S-A arc. The enhanced electron density profiles measured by the radar were transformed to Pedersen conductivity profiles. The maximum σ_p value corresponding to each scan is tabulated in Table 1. The numbers in parentheses in the last column refer to the arc motion along a dawn-dusk meridian in a frame fixed with the Sun-Earth frame of reference (positive numbers represent duskward velocities). The arc velocities show some scatter. However, the general trend is a duskward motion of 460 m s^{-1} before 0227 UT followed by a dawnward drift of 60 m s^{-1} .

Figure 8 presents the derived geophysical parameters for the EL scans of March 1, 1987. This figure has the same format of Figures 5, 6, and 7. However, when the statistical uncertainty of the velocity was large or the antenna was pointing close to the up B position the parameters were deleted from the plot.

Figure 8 shows the derived parameters for the EL scan that was performed along the magnetic east-west. Both Pedersen and Hall conductivities present two peaks corresponding to both arcs of Figure 4c. The background conductivity was 0.3 mhos . Both arcs were located at regions of large velocity gradients where $\nabla \cdot \mathbf{E} < 0$. However, one of them (arc B, see Figure 4c) had a sunward flow and the other had an antisunward convection. Figure 8, as well as Figure 7, shows the anticorrelation between the magnitude of \mathbf{E} and the conductivities. This means that a near-zero \mathbf{E} field occurs when the densities are the largest. The Y component of \mathbf{E} is only -4 mV m^{-1} in the center and dawnside of arc A. The E_x component varies from a peak value of -90 mV m^{-1} in the dawn edge of arc A to $+120 \text{ mV m}^{-1}$ in the dusk boundary of B. J_x is proportional to E_x with a maximum value near 0.1 A m^{-1} . J_y reaches values up to 0.075 A m^{-1} . The field-aligned current is upward ($2 \text{ } \mu\text{A m}^{-2}$) in the region of arc A; j_{\parallel} is downward in the duskside of arc B, reversing to the highest upward value of this plot ($4 \text{ } \mu\text{A m}^{-2}$) at the center of arc B. The ion-neutral differential temperature of Figure 8i and the Poynting flux of Figure 8j show enhanced values at the boundaries of arcs A and B.

3.2. Analysis of Azimuthal Scans

Figure 9 presents the velocities which were obtained following the method outlined in Appendix B. We used data from the four partial AZ scans of Figures 2b, 2d, 2f, and 2h. This figure is in geographic coordinates, where the light traces refer to antisunward convection and the heavy traces indicate sunward flow. The vectors corresponding to each scan were shifted along the dawn-dusk meridian in order to compensate for any displacement of the S-A arc which occurred between the scans. We also averaged the velocity vectors when two or more vectors were located within $\pm 20 \text{ km}$ from each other.

The vector velocities of Figure 9 reproduce (verify) many of the characteristics that were obtained from the analysis of the EL scan data. Furthermore, they present additional features which were not resolved by the limited coverage of the EL scan. The common features are as follows: (1) There is the large antisunward velocity in the dawnside of the arc

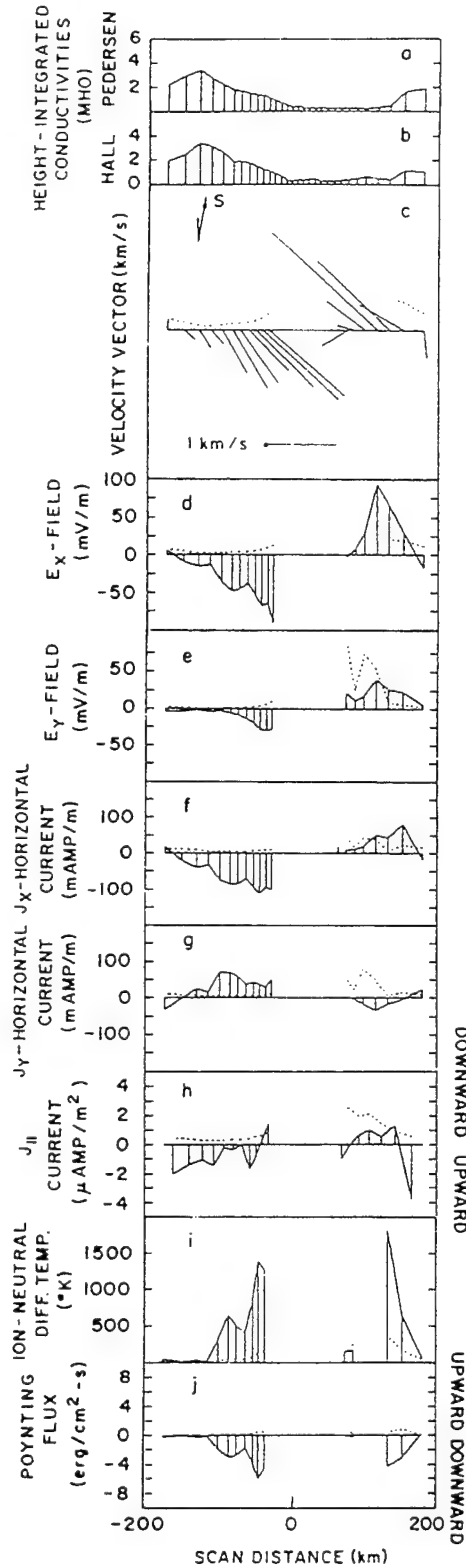


Fig. 8. Same as Figure 7, except that it corresponds to time 0337 of March 1, 1987.

with a peak value near 1200 m s^{-1} . (2) The region of velocity gradients with negative divergence has a width of about 175 km measured along the dawn-dusk meridian. (3) Antisunward velocity decreases beyond the dawn edge of the arc. (4) There is a high degree of consistency during consecutive

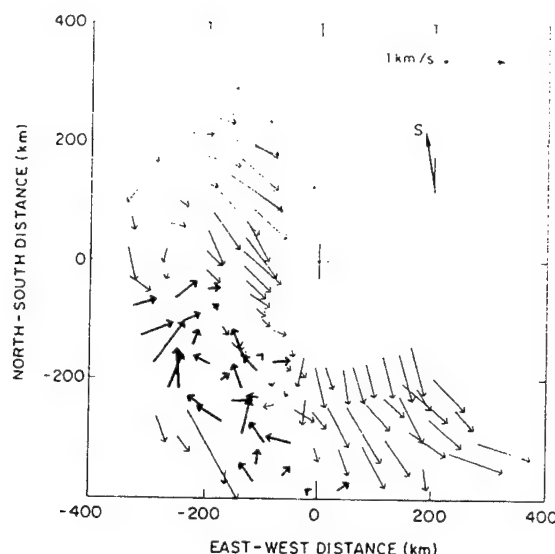


Fig. 9. Velocity vectors obtained from the four slow AZ scans of February 26, 1987. A 1 km s^{-1} vector is represented as a segment 100 km in length. The inclination of the vector indicates the direction of the flow.

antenna cycles. The new signatures are as follows: (1) The duskside of the arc presents a strong sunward flow, with a peak value of 500 m s^{-1} . (2) The region of sheared flow follows the arc alignment in the area covered by the scan (about 700 km). (3) The antisunward flow in the dawnside shows that beyond the first-order constancy of plasma flow parallel to the arc, there is a gentle second-order variation along the alignment of the arc. The magnitude of the vectors decreases from 1200 m s^{-1} in the poleward part of the scan to 900 m s^{-1} in the equatorward region. (4) The northern part shows only a gradient but not a reversal. (5) Near the center of the plot the sunward flow shows a rotational reversal which suggests the limit of the sunward motion. (6) Further duskward from the region of sunward convection, the flow is again antisunward. There is a sharp shear with positive divergence. (7) The width of the sunward flowing region is of order 100 km.

3.3. Analysis of Data Collected With the Antenna Directed Up B

Derived parameters of the data collected during the dwells of February 26, 1987 are shown in Figure 10, together with the Poynting flux and Joule heating rate from the EL scans. Figures 10a, 10b, 10c, and 10e correspond respectively to the Pedersen conductivity calculated from the number density obtained from the overhead transient of the arc, the energy deposition from precipitating electrons, Q_p , which was computed following the method outlined by Wickwar *et al.* [1975], the electron temperature measured at 250 km and the ion temperature from 110 km of altitude. Figure 10d, reproduced from Figure 7j, displays the Poynting flux. The horizontal scale was changed using a constant arc motion of 180 m s^{-1} . Figure 10f shows the Joule heating rate, which was calculated according to the relation: $JH = \Sigma_p(E + U \times B)^2$. Figure 10g presents the height-integrated ion cooling rate due to collisions with the neutrals. Banks and Kockarts [1973] showed that the energy transfer rate

from ions to neutrals can be approximated as $dU_i/dt = -n_i N_n \beta_{in} (T_i - T_n)$, where $N_n(N_i)$ and $T_n(T_i)$ are the neutral (ion) density and temperature, and β_{in} is the ion energy loss rate. N_n and T_n were calculated using the MSIS-86 thermospheric model and an exospheric temperature equal to 850 K. The upper and lower traces correspond to the energy transferred to N_2 particles (the major neutral constituent at E region altitudes) from N_2^+ and O_2^+ ions.

Figures 10a–10c show a prominent maximum occurring at 0211 UT. The coincidence of elevated temperature and enhanced Σ_p indicates the intrinsic relationship between these parameters. The second peak in T_e may be produced by the decrease in the electron cooling rate due to smaller values of N_e . Figures 10d–10g present a well-defined peak at 0220. In spite of the fact that some of these curves are not completely independent (the circulation of some of them includes common input parameters), the similarity in their shapes and location of their maxima suggests a direct relation.

A more quantitative view of the T_e and T_i enhancements associated with the center and dawnside of the February 26 arc is presented in Figure 11. The four profiles, labeled E or I, were obtained during the overhead transit of the arc, when the antenna was pointing antiparallel to B. The dashed lines

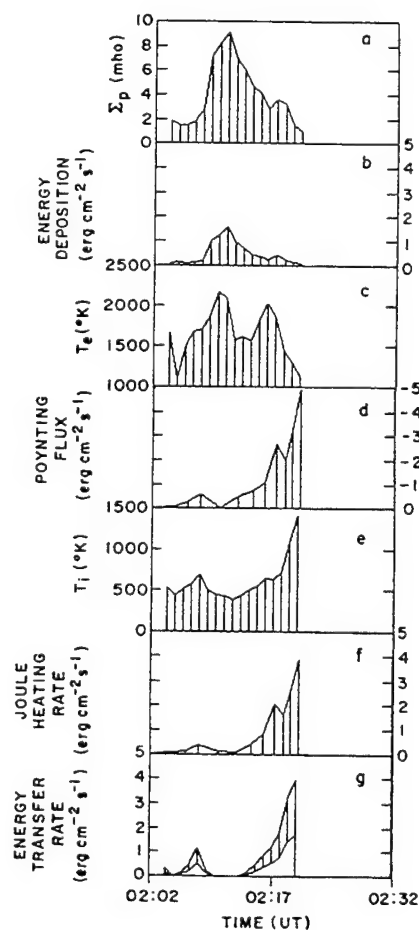


Fig. 10. Directly measured and derived parameters of the Sun-aligned arc of February 26, 1987: (a) height-integrated Pedersen conductivity; (b) energy deposition from precipitating electrons; (c) T_e at 250 km altitude, (d) Poynting flux, (e) T_i at 110 km, (f) Joule heating rate, and (g) energy transferred from ions to neutrals.

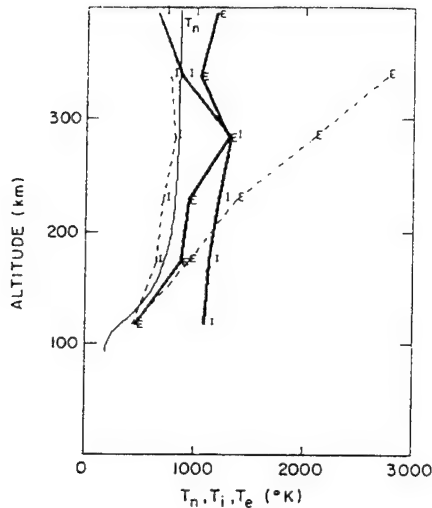


Fig. 11. Electron and ion temperatures measured during the up *B* position. Dashed lines correspond to 0211 UT and the thick solid line to measurements at 0220 UT. The thin trace represents the neutral temperature calculated using the MSIS-86 model.

are the electron (E) and ion (I) temperature profiles measured between 0211 and 0212 and when the region of higher density was being probed. The thick continuous traces are the T_e and T_i profiles measured at 0220 and near the dawnward edge of the arc. The T_e curve corresponding to the center of the Sun-aligned arc shows an enhancement of >1000 K in the *F* region. Notice that this profile increases linearly at altitudes above 150 km. The T_i curve measured in the duskside was enhanced by 700 K in the *E* and lower *F* regions.

3.4. Thermal Analysis of the March 1, 1987 Elevation Scan

The isodensity contours on Figure 4c are reproduced in Plate 2. Superimposed on the N_e traces are two color-coded contours corresponding to the ion (blue) and electron (red) temperatures. The electron isothermal contour of 1000 K penetrates to lower altitudes near the regions of enhanced number density. The ion temperature is enhanced in the dawnside of the arc labeled A, reaching a value of 2000 K at 150 km. The duskside of arc B is also a region of high T_i values. This plot agrees and extends the observations shown in Figures 10 and 11. T_e and T_i are both enhanced but in different regions which do not necessarily collocate. T_i is enhanced at the dawn or dusk (or both) sides of the Sun-aligned arc.

Figure 12 has the same format as Figure 10. The curves shown in the seven panels were calculated based on the EL scan data of March 1, 1987. They correspond to arc A of Figure 4c. In spite of the large variability in the parameters displayed in this figure, the trend is the same: Regions of enhanced T_e are located near the center of the arc, and T_i enhancements are situated at the arc boundaries.

4. DISCUSSION

We have extensively analyzed two Sun-aligned arcs diagnosed by the incoherent scatter radar. Excepting unusual circumstances, this requires an ISR observing mode tailored

to nominal temporal and geometric properties of Sun-aligned arcs.

The two arcs studied here are relatively intense Sun-aligned arcs. This optimizes the statistical error bars on the parameters derived from the ISR data. One of the two arcs has been reported elsewhere [Niciejewski *et al.*, 1989], with detailed analysis of its optical, ion production-loss rates, and ionizing flux properties. Observed in the UV by Polar Bear, and the visible from DMSP and ground-based imagers with time continuity, this is a well-documented example of a strong Sun-aligned arc. We show in Figure 3 that the position of its optical signature is colocated with the ISR signature. A second Sun-aligned arc is presented primarily to demonstrate that the key findings here are repeatable.

The observations reported here apply directly to Sun-aligned arcs bright enough to be readily seen by conventional all-sky cameras or visible and UV satellite images. The findings thus apply to stable Sun-aligned arcs as reported prior to the 1980s, which are found in the polar cap of the order of 5% of the time. The physical processes that we demonstrate are important in these arcs are, however, candidates for applying to a much broader class of arcs. The degree to which they represent the character of the much more common weaker Sun-aligned arcs [Weber and Buchau, 1981; Carlson *et al.*, 1988], found a third to a half of the time in the polar cap, is the subject of a separate study now in progress.

4.1. ISR Observing Mode

We have presented and illustrated an ISR mode which, we maintain, can in general identify and diagnose Sun-aligned arcs in the polar cap. Based on nominal properties of Sun-aligned arcs found with image-intensified all-sky photometers, the mode maps mesoscale (order $10^3 \times 10^3$ km) areas with adequate time resolution to track the passage of arcs.

Arc identification is based on a two-step rationale. The ISR signature of the Sun-aligned arc is a Sun-aligned sheet or cylinder of persistent enhanced ionization below 200 km (at "*F*₁ region" or "photochemical" altitudes). For ionization to persist much below 200 km, it must represent the presence of ongoing ionization, because its chemical lifetime is so short. However, a region of stable or persistent production of Sun-aligned ionization must by the same token also be a region of stable or persistent Sun-aligned production of (electron impact excited) optical emissions. Thus when looking at contours of greater than 10^5 electrons cm^{-3} near 150 km, with chemical lifetime of order of a minute, and with persistence over 10 min, one cannot help but also expect to see enhanced airglow within the field-aligned projection of these contours. One example of this is shown in Figure 3.

4.2. Directly Observed Parameters

The directly observed parameters are electron density, electron and ion temperature, and plasma line-of-sight velocities. The electron densities show persistent Sun-aligned ridges of enhancements. Contours of constant electron density are Sun-aligned over mesoscale distances of 500–1000 km for altitudes between 100 and 200 km. Electron temperatures are enhanced along magnetic field lines above these enhanced ridges of ionization, consistent with the expecta-

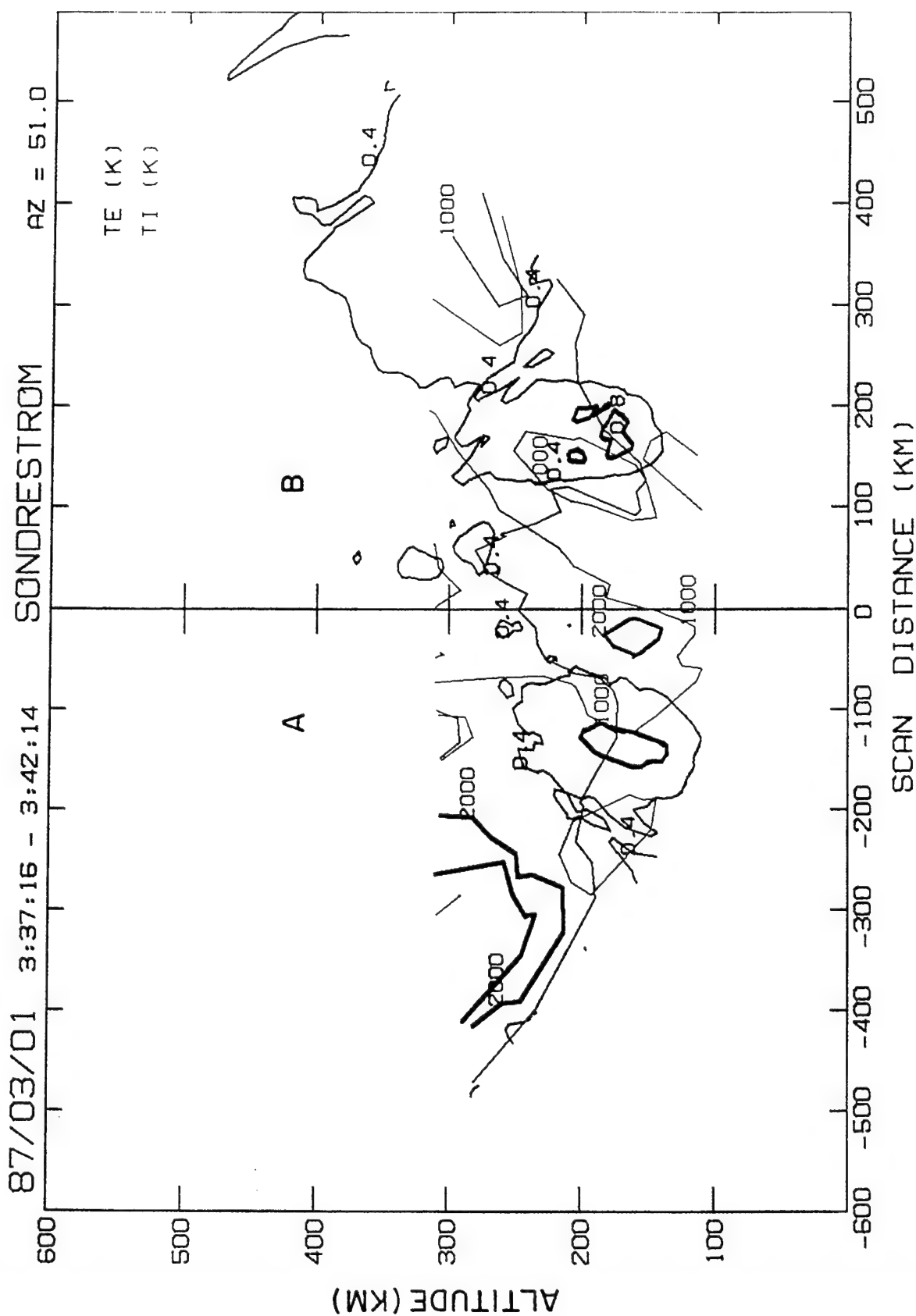


Plate 2. Superposition of the contours corresponding to three different parameters measured by the ISR: electron density (black), T_e (red) and T_i (blue). The data were taken on March 1, 1987 at 0337:16 UT.

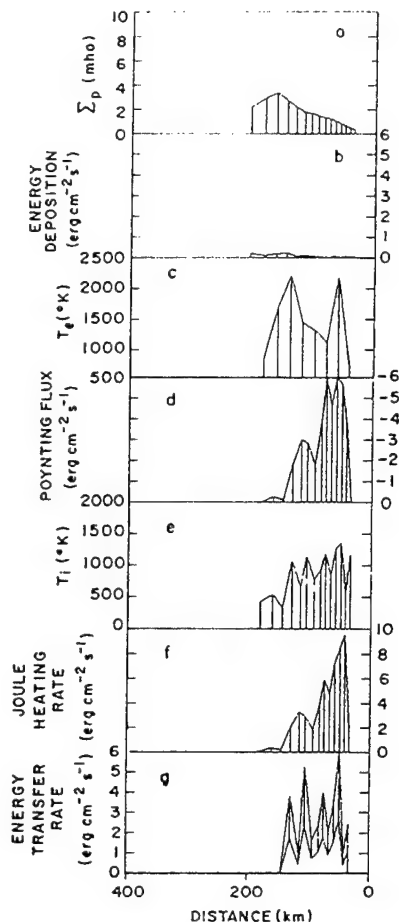


Fig. 12. Parameters derived from the left-hand half of the EL scan of 0337 UT on March 1, 1987. Figures 12a–12g display the same geophysical quantities as in Figure 10. The statistical uncertainties of T_e and T_i are 250 K and 500 K respectively.

tion of heating by a (sheet) flux of incident energetic electrons.

On the dawnside of the Sun-aligned arc, there is a channel of high ion temperature, exceeding that of the electron gas. This channel of ion heating is where the antisunward plasma flow is still near its maximum value. As one moves, dawn to dusk, into the arc, the ion temperature falls to equilibrium with the neutral particle gas, and only the electron gas has significantly enhanced temperature. These data confirm, refine, and extend the ion temperature enhancement finding and semiquantitative interpretation by Carlson *et al.* [1984]. Antisunward velocity gradients are both coaligned with the Sun-aligned contours of enhanced (below 200 km altitude) electron density. That is, where the antisunward plasma flow velocity decreases in going from dawn toward dusk, ionization is enhanced; when the dawn-to-dusk plasma velocity gradient has the opposite sense (increases dawn to dusk) or is constant, there is no enhanced ionization below 200 km. These confirm a simple arc electrodynamics interpretation (convergent electric fields produce converging Pedersen currents whose continuity is maintained across the arc by incident energetic electrons).

4.3. Derived Parameters

The derived parameters are horizontal and Birkeland currents, E field, and Poynting and particle flux. We esti-

mated the steady state currents within the arc from the plasma density and velocity data. The Birkeland currents were calculated by two independent means. First the electron density contours of a cross section of the arc (found to match the density contours several hundred kilometers upstream and downstream and on earlier and later measurements) were used to estimate the steady state production rate of the arc, and hence the upward current above the arc carried by the estimated incident energetic electron flux. In the second method the horizontal electric field gradient across the arc was derived from the plasma velocity gradient across the arc. This electric field, applied to the ionospheric conductivity (derived from observed electron density profiles and a standard model atmosphere), led to derived Pedersen and Hall currents. Based on arc symmetry upstream and downstream, transarc gradients in calculated Pedersen currents were then used to derive (from the horizontal divergence of currents across the arc) the variation of Birkeland currents across the arc. The upward Birkeland currents derived from these two different approaches were comparable, and both peaked near the center of the arc at about $1 \mu\text{A m}^{-2}$. Because downward Birkeland currents (presumably carried by upgoing thermal electrons) can be derived only where electron densities are large enough to give a useful ISR signal, complete current mapping cannot be done. However, this approach gave a rather comprehensive estimate of the ionospheric current system in and near the stable Sun-aligned arcs observed, an estimate that should extrapolate well to such arcs in general. This is summarized in Figure 14.

We have performed three independent calculations of the energy into the Sun-aligned arc by nonparticle heating. While this nonparticle energy input is distributed across the full arc, it is strongest into the dawn edge. The three calculations are motivated by recognition that energy external to the ionosphere (ultimately mechanical energy in the solar wind) is carried down into the ionosphere along magnetic field lines as electromagnetic energy or Poynting flux. This is dissipated as frictional heating of the ions dragged through the neutral atmosphere, or Joule heating. Heat, initially deposited mostly in the ion gas, is rapidly passed onto the neutral gas.

The first calculation follows the rationale of a $\delta E \times \delta B$ Poynting flux calculation. We note that the Sun-aligned arc changes much more slowly along than across its axis, and is very stable over times large compared to an Alfvén bounce period. Neglecting the spatial and time derivatives then, we take a cross section transverse to the arc, and slice it into a series of adjacent differential elements. We look at the electric field differential (dawn to dusk reduction) and Pedersen current differential across each element (the electric field is in this measured neutral wind rest frame). The current is then crossed against the electric field strength to derive the first estimate of energy, plotted in Figures 7j, 10d, and 12d, and labeled Poynting flux. Relative to an idealized measurement of Poynting flux this calculation has its shortcomings. Yet we feel it is useful, partly to underscore the real energy source, and partly because of the good quantitative agreement between the $\text{ergs cm}^{-2} \text{s}^{-1}$ found from this calculation and from the following two.

The second calculation is based on the additional measurement of the ion gas temperature. Given the measured value of the plasma velocity and the neutral atmospheric velocity,

we can calculate the rate at which heat should be going into the ion gas, due to the relative motion of the ions through the neutral gas. This leads to the second estimate of energy flow, and is verified by the good agreement between the calculated and the actually observed ion temperature.

The third calculation deals with the heat loss from the ion gas, to the neutrals. It is based on the measured ion gas temperature and the neutral gas temperature. Because of the cooling rate cross section dependence on ion composition, which we do not measure, we show two values for the extremes of 100% NO^+ versus 100% O_2^+ . Within this relatively large uncertainty, this third energy estimate agrees with the first two (with better agreement for the more likely dominant ion).

We then applied an approximate energy balance calculation to these data. It was reasoned not only that was it logical to expect a magnetospheric energy source to drive the high-speed ionospheric plasma flow through thermospheric frictional-drag "loading," but that this energy dissipation should ultimately end up mostly in the neutral atmosphere below the enhanced ionospheric densities in the arc. It was possible to estimate this latter quantity in two ways: (1) from the steady state rate of heat going into the ion gas; and (2) from the steady state rate of heat lost from the ion gas. The former is derived from the conversion of ordered ion gas energy due to coherent motion under the action of the driving electric field, to disordered energy (heat) as the ions suffer randomizing collisions with neutral particles. This is proportional to the square of the difference between the ion and the neutral gas bulk velocity [Stubbe and Chandra, 1971]. The latter is derived from the observed difference between the neutral atmospheric and ion gas temperatures. Uncertainty in the ion composition leads to greater uncertainty in this latter estimate than in the former. However, both of these methods give a value for the energy deposition rate into the neutral atmosphere of a few $\text{ergs cm}^{-2} \text{ s}^{-1}$, comparable to the Poynting flux into this region. These three independent calculations thus lead to a simple but reassuringly self-consistent interpretation of the data.

It is important to note a critical step in the above argument before proceeding. We note that T_i can be derived in two complementary independent ways, one (theoretically) from measured ion and neutral particle velocities, the other directly from the radar-observed spectra. Our calculations of the differential temperature based on the ion and neutral velocities show good agreement with the observed T_i enhancements (see Plate 1a and Figure 7i). The Fabry-Perot also measured enhanced neutral temperatures, possibly collocated with the region of larger ion temperatures (R. Niciejewski, personal communication, 1989). The observed ion heating can be explained solely on the basis of a quantitative analysis of the large observed plasma flow V relative to the observed neutral atmospheric rest frame U . Since all three of these parameters are observed, not modeled, we are thus able to determine, not merely assume, that these ion temperatures are explained solely on the basis of this heating mechanism (within small statistical uncertainty). It is this use of the directly observed T_i , V , and U that allows us to justify calculating the rate of heat flowing into the thermosphere on the basis of a steady state ion thermal balance argument.

We then point out that the magnitude of this heating rate is also of significance. The Poynting flux and energetic particle

flux deposit energy to the neutral atmosphere near and above 120 km of several $\text{ergs cm}^{-2} \text{ s}^{-1}$ over the Sun-aligned arc of width of order 100 km. This compares to about $0.5 \text{ erg cm}^{-2} \text{ s}^{-1}$ for a global mean thermospheric EUV heating rate. Parts of the arc experienced 10 times this reference average, and the average across the arc was three or four times this reference. Given that the arc is of order 100 km wide and persists for a few hours, it is a significant local heat source. It is not a negligible heat source even when averaged over its motion across the dark polar cap (of order 10% to tens of percent of the global mean EUV and thus comparable to a presently missing polar thermospheric heating component [e.g., Carlson and Crowley, 1989].) While the February 26 arc discussed is unusually intense, the polar cap under northward IMF conditions typically has several stable Sun-aligned arcs of a tenth or more of this visual (particle precipitation) intensity over a 2000 km or less polar cap width, with temporal persistence of order an hour or more. Estimates based on measured particle precipitation energy flux alone under these conditions may underestimate the thermospheric heating rate due to stable Sun-aligned arcs by a factor of 3 or more.

Note that for the March 1 Sun-aligned arc the particle precipitation energy (Figure 12) is about a sixth that for the February 26 case (Figure 10) although both arcs have comparable incident Poynting flux.

Here we have stressed taking advantage of the stability of the arc, in time and in space along its axial (Earth-Sun) dimension, to optimally diagnose its character. Ultimately, temporal and spatial variations must occur and become large enough to be of interest during one series of arc observations. During the 40 min observation of the February 26, 1987 arc, it drifted from overhead (0212 UT) to 100 km west (0225) to 180 km west (0234). A composite image of the arc was constructed from the many conical and planar cross sections of the arc to estimate departures from idealized constancy along its axial length. This analysis indicates a velocity gradient along the arc axis, with penetration of sunward drifting plasma only part way into the polar cap. The two-dimensional cross section (Figure 9) suggests flow from where the arc connects to the auroral oval, partial entry into the polar cap, and then clockwise rotational flow back to antisunward, exiting again from the polar cap. Farther into the polar cap there is slowing of antisunward plasma flow, but not a reversal to sunward. This is sketched schematically in Figure 13. (This is very reminiscent of the interpretation of some DE data by Hoffman *et al.* [1985] under similar conditions.)

It is clear from Figure 13 that the net velocity difference from the dawnside to the duskside of the arc is greater in the velocity reversal region than the merely velocity reduction region. Thus it is apparent from examination of this figure that the Pedersen current divergence, and balancing Birkeland currents, lead to extra energetic particle input within the tongue of sunward moving plasma, relative to that in the region of simply a velocity gradient deeper in the polar cap. Furthermore, while Hall currents along the dawn edge of an arc of constant properties along its axial length simply continue into the polar cap, those in the region of partial penetration of sunward flow penetrate only partially into the polar cap and then must rotate westward near their region of maximum poleward penetration. These effects can combine to produce the "bright spot" or extra particle precipitation

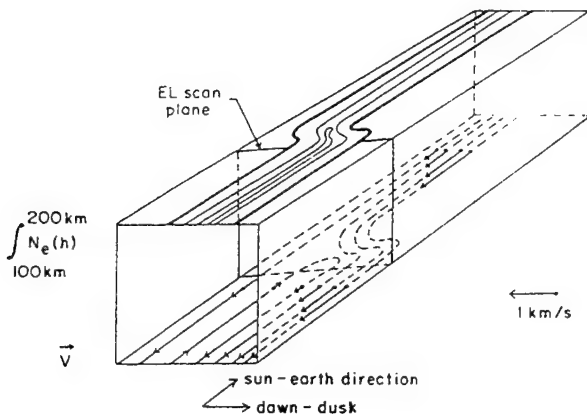


Fig. 13. Schematic representation of the height-integrated density (upper side) and the plasma flow pattern (lower surface). This figure is based on the EL and AZ scans of February 26, 1987.

often seen near where the Sun-aligned arc connects to the nightside auroral oval.

Finally, we condense the essential character we have found as characteristic of the electrodynamic, thermal, and energetic properties of these Sun-aligned arcs into the illustration of Figure 14. The character of these two sample arcs (February 26 near midnight MLT and March 1 post-midnight MLT, 1987), understood within the context of Figure 14, extends and extrapolates to at least the broad class of strong Sun-aligned arcs. We are now combining ISR and ASIP data for a large number of stable Sun-aligned arcs, to establish the extent to which these findings characterize typical polar cap conditions for northward IMF conditions [Carlson *et al.*, 1988].

The qualitative features of this "cartoon" must apply to

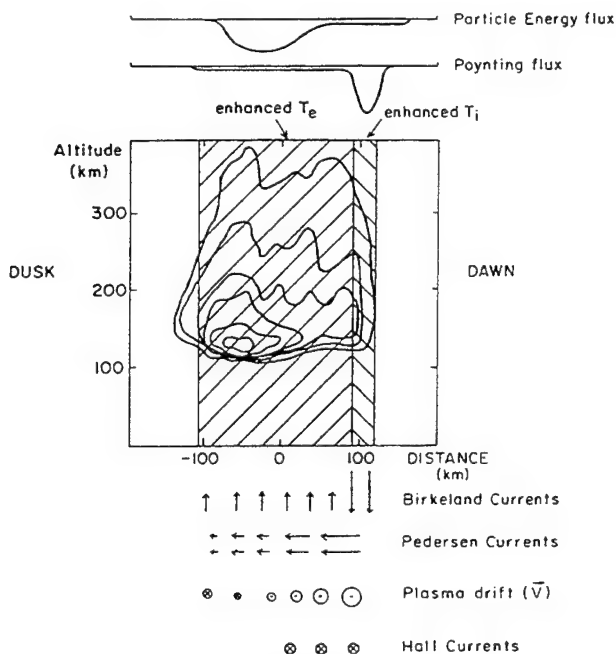


Fig. 14. Cross-sectional view of the Sun-aligned arc of February 26, 1987. Electrical parameters of the arc and energy going into the ionosphere are also indicated. This representation is in a semiquantitative fashion.

Sun-aligned arcs in general. Within the center of the arc, where N_e is enhanced below 200 km, T_e must be enhanced by the incoming flux of impact ionizing electrons. These must also carry an incoming particle energy flux, and an outgoing Birkeland current, to one side, while there must be a return (incoming) current on the other side. The Pedersen currents must decrease from dawn to dusk, as the antisunward plasma drifts must decrease from dawn to dusk. The plasma drifts may simply decrease, or reverse as in this illustration. The ion temperature will be enhanced where the difference between the plasma and neutral atmospheric velocities is sufficiently great. This depends on the thermospheric winds across the polar cap, and the extent to which plasma drifts may have strong sunward flow on the duskside of the arc. T_i will generally be enhanced on the dawnside, and occasionally on the duskside. Likewise, the Poynting flux typically peaks on the dawnside, but peaks on the duskside if there are strong sunward flows on the duskside. The magnitude of the Poynting flux is many $\text{ergs cm}^{-2} \text{s}^{-1}$ for relatively intense Sun-aligned arcs, exceeding the particle energy, and smaller by a factor to be statistically defined for more common weaker arcs.

5. CONCLUSIONS

This study has led to the following:

1. The first direct measurement over full mesoscale horizontal areas (of order $10^3 \times 10^3 \text{ km}$) of persistent plasma velocity gradient across long-lived ($\geq 10^3$ seconds) stable Sun-aligned arcs has been made. The sign of these gradients confirms simple arc electrodynamics. This is true for single and double Sun-aligned arcs observed.

2. New experimental diagnostic techniques have been developed, including illustration of an ISR observing mode capable of diagnosing polar electrodynamic features with temporal stability of at least several minutes and spatial coherence of at least 100 to a few hundred kilometers; extension of a potential fitting procedure to map polar plasma flow from ISR data; and illustration of a plasma rotational feature near where a Sun-aligned arc merges with the midnight auroral oval.

3. The cross sectional area map of the plasma density and thermal character across stable Sun-aligned arcs has been measured. The electron gas temperature is enhanced over the arc, supporting the expectation that the arc is produced by a sheet of incoming energetic electrons.

4. It has been determined that along the high-velocity dawnside of the incoming energetic electron sheet (producing the arc) there is a channel of enhanced ion temperature within which the ion temperature exceeds that of the electron gas. This Sun-aligned channel within which heat flows from the ion gas to the electron gas coincides with the high antisunward velocity channel along the dawn edge of the Sun-aligned region of enhanced electron density. In addition, if there is also return sunward flow at sufficiently high speed, ion heating is also found on the duskside of the arc. The ion gas heating can be explained solely on the basis of ion frictional drag of high plasma velocity in the thermosphere rest frame.

5. Persistent strong Joule heating driven by Poynting flux down into a Sun-aligned arc has been calculated and found to be at a rate well exceeding the particle energy flux. This rate is estimated by three independent calculations based on a

horizontal current differential, a velocity differential, and a temperature differential. Furthermore, the magnitude of this newly measured heat flux is several $\text{ergs cm}^{-2} \text{s}^{-1}$ and as such is of significance to the polar thermospheric energy budget, and contributed to solution of the missing polar thermospheric heat source.

6. Present knowledge of the basic character of stable Sun-aligned arcs in the polar cap ionosphere has been extended to a relatively complete yet simple description, consistent with theoretical interpretation.

APPENDIX A

We show in this appendix that the LOS ion velocity measured by an ISR during elevation scans can be used to derive the full velocity vector (\mathbf{V}). The only conditions for the determination of \mathbf{V} are that the LOS velocity from both E and F layers needs to be measured almost simultaneously, and the probed volumes need to be connected by the same magnetic line.

In the F region the ion motion is controlled by

$$\mathbf{V} = \mathbf{E} \times \mathbf{B}/B^2 \quad (\text{A1})$$

and for the E region

$$\mathbf{V} = (1 - k_2)\mathbf{U}_\perp + k_1\mathbf{U}_\perp \times \mathbf{B}/B + k_1\mathbf{E}/B + k_2\mathbf{E} \times \mathbf{B}/B^2 \quad (\text{A2})$$

where \mathbf{E} , \mathbf{V} , and \mathbf{U}_\perp are the electric field, the ion velocity and the neutral wind in a plane perpendicular to \mathbf{B} . With

$$k_1 = \frac{\nu_i \Omega_i}{\nu_i^2 + \Omega_i^2} \quad (\text{A3})$$

$$k_2 = \frac{\Omega_i^2}{\nu_i^2 + \Omega_i^2} \quad (\text{A4})$$

ν_i is the ion-neutral collision frequency and Ω_i the ion gyrofrequency. The line of sight velocity (V_{LOS}) depends on the velocity vector according to

$$V_{\text{LOS}} = \mathbf{V} \cdot \mathbf{A} \quad (\text{A5})$$

where \mathbf{A} is the unit vector in the antenna pointing direction expressed in magnetic coordinates.

The transmitted pulse pattern consisted of two pulses, a narrow pulse, $30 \mu\text{s}$ (4.5 km) long, and a long pulse, $320 \mu\text{s}$ (48 km) in length. Data sampling time was set equal to $8 \mu\text{s}$ and a 32-lag autocorrelator was used to provide the ac function of the incoherent scatter signal. This setup allows the spectra to accept contributions from a range of 82 km. The volume probed by the single long pulse during one integration period is equal to the product of 82 km, the arc segment scanned during the integration time and the radar beam width. In the E region, the number density, the ion velocity and the neutral wind vary with altitude very rapidly; in this sense the long pulse measurements are not able to resolve narrow layers and only provide a weighted average over the entire E region. This weighting factor depends on the local number density the inverse of the range squared and a triangular function to compensate for the fact that all the lag products have different spatial resolution which linearly decrease for the longer delays. Expressions (A1) and (A2) were weighted following the procedure described before, then multiplied by the \mathbf{A} vectors to form dot products

for the E and F layers [Brekke *et al.*, 1973] and made equal to the measured LOS velocities.

Radar observations are subject to several types of constraints which need to be considered in any calculation of the velocity vectors. One of them is related to the drift of the S-A arcs. These arcs move along the dawn-dusk meridian, and the Earth rotational motion will modulate the measured velocities resulting in the following distortions. (1) The Doppler velocity is reduced by the term $\mathbf{V}_c \cdot \mathbf{A}$, where \mathbf{V}_c is the corotation velocity. At Sondrestrom \mathbf{V}_c is equal to 180 m s^{-1} . (2) There is also a small spatial displacement between contiguous integration periods, equal to $(\mathbf{V}_c + \mathbf{V}_{\text{arc}}) \times T$, where \mathbf{V}_{arc} is the velocity of the arc with respect to a fixed frame, and T is the time interval between E and F region measurements (about 30 s). Although this effect is small (6 km), it could generate significant errors when the E region measurements are mapped to the F region. The large range resolution (82 km) hinders also the ability to resolve the vector. In particular, low-elevation measurements can include a large contribution of the horizontal variations of the ion flow (i.e., plasma boundaries).

In a strict sense the E to F region mapping algorithm can be employed only for data that have been collected in a plane coincident with the \mathbf{B} field; for Sondrestrom, this corresponds to -39° azimuth. During our experiments the EL scans were performed at -129° and 51° azimuth; consequently, the E region projections of the F region measurements are located slightly north and west of the measured E layer values. However, for the data presented here, the arcs were aligned -24° and -25° with respect to geographic north, and the equipotential contours (aligned with the arc) deviate 14° or 15° from the magnetic meridian. The E region intersections were between 1 or 2 km away from equipotential lines that crossed the E region measurements.

In order to gain some confidence in the analysis of data from EL scans, we performed a zero order calculation of the velocity vector using the LOS velocities measured at 110 and 160 km of altitude and 105 km of distance (see arrow in Figure 2e). For simplicity \mathbf{U}_\perp is considered to be zero and \mathbf{B} to be pointing downward. After subtracting the corotation term the radar LOS velocities are $V_{\text{LOS}}(E) = 173 \text{ m s}^{-1}$, $V_{\text{LOS}}(F) = -101 \text{ m s}^{-1}$. Equations (A1) and (A5) indicate that the velocity component along the scan is -168 m s^{-1} . Then, using (2), $k_1 = 0.292$ and $k_2 = 0.298$; the other component (perpendicular to the scan) is -968 m s^{-1} . After a rotation to geographic coordinates, we obtain $V_{\text{east}} = 739 \text{ m s}^{-1}$ and $V_{\text{south}} = 647 \text{ m s}^{-1}$. Instead, when we use all the terms of (A2), the IGRF-85 model of \mathbf{B} , a second V_{LOS} measurement in the F region and the neutral wind from the Fabry-Perot, the result is $V_{\text{east}} = 647$, $V_{\text{south}} = 900 \text{ m s}^{-1}$. This is a velocity that points closer to the antisunward direction. All the derived velocities (\mathbf{V}) presented in Figures 4-8 were obtained using the more precise and complete algorithm that considered all the terms of (A1)-(A5). The zero approximation shown above can be employed when a computer is not available.

APPENDIX B

The LOS velocity measured during radar azimuthal scans can also be used to derive the ionospheric electric field \mathbf{E} , on the velocity vector, using the property of \mathbf{E} of being irrotational. The electric field is derivable from a scalar potential following

$$\mathbf{E} = -\nabla V \quad (\text{B1})$$

where V is the electrostatic potential that varies as a function of latitude and longitude. Now, if the scan is performed at a low elevation, then V can be represented by $V(r, a)$, where r is range and a the azimuth.

An incoherent backscatter radar measures the radial component of the ion velocity at several distances along the line of sight. At high latitudes this radial drift is closely related to the azimuthal component of \mathbf{E} . Consequently, V could be determined by integrating the azimuthal component of (B1) and using a known initial value of the potential, $V(r, a_0)$. At the Millstone Hill radar, the boundary potential can be assumed to be null at the southernmost part of the scan [Holt *et al.*, 1984]. However, no similar statement can be used to reduce data from Sondrestrom.

Another method that has been used to resolve the magnitude and the direction of the ion flow is the beam swinging technique. Here, the LOS velocity from several adjacent azimuthal sectors are least squared fitted to extract the three components of the velocity [Hagfors and Behnke, 1974]. This method has been employed at Arecibo, where the more uniform ionosphere of this mid-latitude station grants confidence for the application of this type of analysis.

Although $V(r, a_0)$ could be calculated from the velocity vectors of section 3.1, we instead computed the boundary potential using the data from the same azimuthal scan. We employed the LOS velocity of three adjacent integration periods and the condition of negligible ion motion along B (less than or of order 25 m s^{-1} as measured) to obtain space-averaged velocity vectors. Then, the initial boundary potential was calculated for every integration period and served as the initial condition for the more precise value of V which was obtained by integrating (B1). The boundary potential as calculated in this way smooths rapid spatial variations of the velocity but will be less affected by statistical errors. This scheme was adopted to avoid cumulative errors produced by random fluctuations in V_{LOS} which sometimes are of the same order of magnitude as the measured velocity.

Acknowledgments. We would like to acknowledge S. Basu and Su. Basu for critical readings of the manuscript, R. Niciejewski and J. Meriwether for useful conversations concerning the FPI data, E. Weber for providing the ASIP image data, and J. Kelly for making the radar data available for this study. This research was supported in part by Air Force Office of Scientific Research under task 2310G9. The work at Boston College was supported by Geophysics Laboratory F19628-90-K-0007. We thank the Danish Commission for Scientific Research in Greenland for permission to conduct these experiments.

The Editor thanks two referees for their assistance on this paper.

REFERENCES

- Akasofu, S.-I., Recent progress in studies of DMSP auroral photographs, *Space Sci. Rev.*, **19**, 169, 1976.
- Akasofu, S.-I., R. Williams, and M. Roederer, Effects of the passage of an IMF discontinuity on the polar cap geometry and the formation of a polar cap arc, *Planet. Space Sci.*, **32**, 119, 1984.
- Banks, P. M., and G. Kockarts, *Aeronomy: Part B*, Academic, San Diego, Calif., 1973.
- Baron, M. J., and R. H. Wand, F region ion temperature enhancements resulting from Joule heating, *J. Geophys. Res.*, **88**, 4114, 1983.
- Berkey, T., L. L. Cogger, S. Ismail, and Y. Kamide, Evidence for a correlation between Sun-aligned arcs and the interplanetary magnetic field direction, *Geophys. Res. Lett.*, **3**, 145, 1976.
- Brekke, A., J. R. Doupnik, and P. M. Banks, A preliminary study of the neutral wind in the auroral E region, *J. Geophys. Res.*, **78**, 8235, 1973.
- Brekke, A., J. R. Doupnik, and P. M. Banks, Incoherent scatter measurements of E region conductivities and currents in the auroral zone, *J. Geophys. Res.*, **79**, 3773, 1974.
- Burke, W. J., M. C. Kelley, R. C. Sagalyn, and M. Smiddy, and S. T. Lai, Polar cap electric field structures with a northward interplanetary magnetic field, *Geophys. Res. Lett.*, **6**, 21, 1979.
- Burke, W. J., M. S. Gussenhoven, M. C. Kelley, D. A. Hardy, and F. J. Rich, Electric and magnetic field characteristics of discrete arcs in the polar cap, *J. Geophys. Res.*, **87**, 2431, 1982.
- Carlson, H. C., Jr., and G. Crowley, The equinox transition study: An overview, *J. Geophys. Res.*, **94**, 16,861, 1989.
- Carlson, H. C., V. B. Wickwar, E. J. Weber, J. Buchau, J. G. Moore, and W. Whiting, Plasma characteristics of polar cap F -layer arcs, *Geophys. Res. Lett.*, **11**, 895, 1984.
- Carlson, H. C., R. A. Heelis, E. J. Weber, and J. R. Sharber, Coherent mesoscale convection patterns during northward interplanetary magnetic field, *J. Geophys. Res.*, **93**, 14,501, 1988.
- Davis, T. N., The morphology of the polar aurora, *J. Geophys. Res.*, **65**, 3497, 1960.
- de la Beaujardiere, O., R. R. Vondrak, and M. J. Baron, Radar observations of electric fields and currents associated with auroral arcs, *J. Geophys. Res.*, **82**, 5051, 1977.
- Denholm, J. V., and F. R. Bond, Orientation of polar auroras, *Aust. J. Phys.*, **14**, 193, 1961.
- Doupnik, J. R., A. Brekke, and P. M. Banks, Incoherent scatter radar observations during three sudden commencements and a Pc 5 event on August 4, 1972, *J. Geophys. Res.*, **82**, 499, 1977.
- Eather, R. H., and S.-I. Akasofu, Characteristics of polar cap auroras, *J. Geophys. Res.*, **74**, 4794, 1969.
- Fedder, J. A., and P. M. Banks, Convection electric fields and polar thermospheric winds, *J. Geophys. Res.*, **77**, 2328, 1972.
- Frank, L. A., J. D. Craven, J. L. Burch, and J. D. Winningham, Polar views of the Earth's aurora with Dynamic Explorer, *Geophys. Res. Lett.*, **9**, 1001, 1982.
- Frank, L. A., et al., The theta aurora, *J. Geophys. Res.*, **91**, 3177, 1986.
- Gussenhoven, M. S., Extremely high latitude auroras, *J. Geophys. Res.*, **87**, 2401, 1982.
- Hagfors, T., and R. A. Behnke, Measurement of the three-dimensional plasma velocities at the Arecibo Observatory, *Radio Sci.*, **9**, 89, 1974.
- Hardy, D. A., Intense fluxes of low-energy electrons at geomagnetic latitudes above 85° , *J. Geophys. Res.*, **89**, 3883, 1984.
- Hedin, A. E., MSIS-86 thermospheric model, *J. Geophys. Res.*, **92**, 4649, 1987.
- Hoffman, R. A., R. A. Heelis, and J. S. Prasad, A Sun-aligned arc observed by DMSP and AE-C, *J. Geophys. Res.*, **90**, 9697, 1985.
- Holt, J. M., R. H. Wand, and J. V. Evans, Millstone Hill measurements on 26 February 1979 during the solar eclipse and formation of a midday F -region trough, *J. Atmos. Terr. Phys.*, **46**, 251, 1984.
- Huang, C. Y., L. A. Frank, W. K. Peterson, D. J. Williams, W. Lennartsson, D. G. Mitchell, R. C. Elphic, and C. T. Russell, Filamentary structures in the magnetotail lobes, *J. Geophys. Res.*, **92**, 2349, 1987.
- Ismail, S., D. D. Wallis, and L. L. Cogger, Characteristics of polar cap Sun-aligned arcs, *J. Geophys. Res.*, **82**, 4741, 1977.
- Kan, J. R., and W. J. Burke, A theoretical model of polar cap auroral arcs, *J. Geophys. Res.*, **90**, 4171, 1985.
- Lassen, K., and C. Danielsen, Quiet time pattern of auroral arcs for different directions of the interplanetary magnetic field in the Y - Z plane, *J. Geophys. Res.*, **83**, 5277, 1978.
- Mende, S. B., J. H. Doolittle, R. M. Robinson, R. R. Vondrak, and F. J. Rich, Plasma drifts associated with a system of Sun-aligned arcs in the polar cap, *J. Geophys. Res.*, **93**, 256, 1988.
- Meng, C.-I., The auroral electron precipitation during extremely quiet geomagnetic conditions, *J. Geophys. Res.*, **86**, 4607, 1981.
- Meng, C.-I., and S.-I. Akasofu, The relation between the polar cap auroral arc and the auroral oval arc, *J. Geophys. Res.*, **81**, 4004, 1976.
- Murphree, J. S., C. D. Anger, and L. L. Cogger, The instantaneous relationship between polar cap and oval auroras at times of

- (Received October 27, 1989;
revised August 6, 1990;
accepted August 6, 1990.)

The U.S. Government is authorized to reproduce and sell this report.
Permission for further reproduction by others must be obtained from
the copyright owner.

Interplanetary magnetic field dependency of stable Sun-aligned polar cap arcs

C. E. Valladares

Institute for Space Research, Boston College, Newton, Massachusetts

H. C. Carlson Jr. and K. Fukui

Phillips Laboratory, Geophysical Directorate, Hanscom Air Force Base, Massachusetts

Abstract. This is the first analysis, using a statistically significant data set, of the morphological dependence of the presence, orientation, and motion of stable sun-aligned polar cap arcs upon the vector interplanetary magnetic field (IMF). For the one winter season analyzed we had 1392 all-sky 630.0-nm images of 2-min resolution containing a total of 150 polar cap arcs, all with corresponding values of the IMF as measured by IMP 8 or ISEE 2. After demonstrating an unbiased data set with smooth normal distributions of events versus the dimensions of time, space, and IMF component, we examine IMF dependencies of the properties of the optical arcs. A well-defined dependence for B_z is found for the presence/absence of stable Sun-aligned polar cap arcs. Consistent with previous statistical studies, the probability of observing polar cap aurora steadily increases for larger positive values of B_z , and linearly decreases when B_z becomes more negative. The probability of observing Sun-aligned arcs within the polar cap is determined to vary sharply as a function of the arc location; arcs were observed 40% of the time on the dawnside and only 10% on the duskside. This implies an overall probability of at least 40% for the whole polar cap. 20% of the arcs were observed during "southward IMF conditions," but in fact under closer inspection were found to have been formed under northward IMF conditions; these "residual" positive B_z arcs had a delayed residence time in the polar cap of about what would be expected after a north to south transition of B_z . A firm dependence on B_y is also found for both the orientation and the dawn-dusk direction of motion of the arcs. All the arcs are Sun-aligned to a first approximation, but present deviations from this orientation, depending primarily upon the location of the arc in corrected geomagnetic (CG) coordinates. The arcs populating the 06–12 and the 12–18 quadrants of the CG coordinate system point toward the cusp. The B_y dependency of the arc alignment is consistent with a cusp displacement in local time according to the sign of B_y . We found that the arc direction of motion depended both on B_y and the arc location within the polar cap. For a given value of B_y , two well-defined regions (or cells) exist. Within each cell the arcs move in the same direction toward the boundary between the cells. The arcs located in the duskside move downward; those in the dawnside move duskward. The relative size of these dusk and dawn regions (or cells) are controlled by the magnitude of B_y . This persistent dusk-dawn motion of the polar cap arcs is interpreted in terms of newly open flux tubes entering the polar cap and exerting a displacement of the convective cells and the polar cap arcs that are embedded within them.

1. Introduction

The study of polar cap aurora started at the beginning of this century with the pioneering work of D. Mawson. Mawson [1916, 1925], based on visual observations of auroral luminosities assembled during the Australian Antarctic expedition of 1907–09, was the first scientist to report the occurrence of aurora at very high latitudes. Important breakthroughs of his polar aurora research were (1) the determination that the aurora was nearly aligned with the Sun-Earth direction and (2) a measurement of the "body" auroral

motion, as it was termed then, to be of the order of 100 ms^{-1} . During the International Geophysical Year (IGY) it was realized that this type of aurora only developed at latitudes poleward of the auroral oval [Weill, 1958; Denholm and Bond, 1961; Davis, 1960]. A few years later it was discovered that the Sun-aligned arcs preferentially developed when the interplanetary magnetic field (IMF) pointed northward [Berkey *et al.*, 1976], and during periods of quiet magnetic conditions [Davis, 1963; Lassen, 1972; Ismail *et al.*, 1977]. More precise measurements of the morphology of the polar cap aurora indicated that these arcs were Sun-aligned only in a first approximation. Arcs located on each side of the noon-midnight meridian were observed to be directed toward noon [Lassen, 1972]. Similarly, more refined

Copyright 1994 by the American Geophysical Union

Paper number 93JA03255.
0148-0227/94/93JA-03255\$05.00

determinations of the arc velocity revealed that this motion could reach values as large as 700 ms^{-1} [Danielsen, 1969; Akasofu, 1972]. All these observational facts suggested that the appearance of arcs in the polar cap was intrinsically associated with a different topology of the magnetosphere which prevails when the IMF is directed northward.

A new era in the research on polar cap aurora was initiated by means of satellite-borne instrumentation. The particle sensor on-board the Defense Meteorological Satellite Program (DMSP) satellites revealed that the polar cap aurora was collocated with low-energy ($<500 \text{ eV}$) electron precipitation. The spectra of this soft precipitation was found to contain characteristics similar to the electrons injected at the poleward boundary of the auroral oval [Meng, 1981a, b]. Almost at the same time, optical images collected by the ISIS 2 satellite indicated the existence of a diffuse type of aurora filling in between the classical oval and the polar cap arcs. It was also pointed out that during extended periods of B_z northward conditions, the polar cap was observed to be contracted into a teardrop shape [Murphree et al., 1982]. These facts suggested that polar cap arcs were actually an extension of the system of discrete oval arcs [Murphree et al., 1982] and that the poleward flanks of the oval expand and occupy much of the otherwise polar cap region [Meng, 1981a]. The expanded auroral oval model implicitly suggests that the polar cap arcs are located in regions of closed field lines mapping to the boundary layers of the magnetosphere. Consequently, the aurora should exhibit a high degree of symmetry between conjugate hemispheres. Within the context of the oval expansion model the polar cap arcs map to and are driven by processes taking place at the low-latitude boundary layer (LLBL) or at the plasma sheet boundary layer (PSBL) [Lundin et al., 1991]. Satellite excursions in the magnetosphere, such as the ISEE 1, satellite have determined that the LLBL widens during positive B_z values [Mitchell et al., 1987], giving further credit to the oval expansion model.

A different view in the study of polar cap auroras was brought up by the high-altitude imaging capability of the DE 1 satellite. The imager on-board DE 1 provided a global view of the auroral oval and revealed the existence of the transpolar auroras extending between the midnight oval and the midday auroral zone. This auroral configuration was called the theta aurora [Frank et al., 1982, 1986]. The precipitating particles in the central "bar" of the theta aurora were observed to clearly resemble a population of plasma sheet particles, the density, the temperature and the differential fluxes, all showed trends similar to the plasma sheet particles. This fact led Menietti and Burch [1987] to suggest that the theta aurora was also on closed field lines, but contrary to the oval expansion model, the transpolar aurora delineated the ionospheric footprints of field lines connected to a bifurcated magnetotail [Frank et al., 1986]. Conjugate measurements on both hemispheres have indicated that the theta aurora, in fact occurs simultaneously at both poles [Mizera et al., 1987; Obara et al., 1988; Craven et al., 1991]. ISEE 2 excursions downtail discovered the presence of filaments of plasma sheet plasma intruding into the tail lobes [Huang et al., 1987, 1989], suggesting a topological connection between transpolar arcs and the filamentary structures.

Ground-based intensified photometers have observed a type of subvisual, Sun-aligned arcs which are present in the polar cap more often than it is implied by satellite imager

data [Weber and Buchau, 1981]. These weak polar cap arcs are associated with gradients in the velocity pattern and with low-energy ($<500 \text{ eV}$) precipitating electrons. Because most of this particle energy is deposited at altitudes above 240 km, they have been named *F* region arcs. An instrumented rocket launched into a polar cap *F* region arc [Weber et al., 1989] measured sunward flow within the polar arc and a particle spectral shape with characteristics of boundary plasma sheet and magnetosheath populations. This fact suggested that some of the polar cap arcs could map to regions of open field lines [Kan and Burke, 1985]. Another rocket flight, this time over a system of Sun-aligned *F* layer polar cap arcs (L. A. Weiss et al., Convection and electrodynamic signatures in the vicinity of a Sun-aligned arc: Results from the polar acceleration regions and convection study (Polar ARCS), submitted to *Journal of Geophysical Research*, 1994) provided precise observations of the electrodynamics in the arc vicinity. The measurements were consistent with a model in which the arc is formed on open field lines on the duskside of a bifurcated polar cap or alternatively on closed field lines threading an expanded low-latitude boundary layer. Hardy [1984] observed that intense fluxes above polar rain levels were embedded in the polar rain suggesting that the polar cap arcs were not attached to the auroral oval and consequently were on a region of open field lines. More recently, Gussenhoven and Mullen [1989] have reported observations of relativistic electrons concurrent with precipitating electron and ions associated with a polar cap aurora. Their measurement argues in favor of the formation of polar cap arcs to occur on open field lines. The fact that polar cap arcs are on open or closed field lines has important implications not only for topological considerations but also for energetic implications and to determine whether particle energy can be stored or directly precipitated into polar cap arcs [Hardy et al., 1982].

The strong observational evidence in favor of both closed field line models and similarly for the open field line model of polar cap arcs can be understood if each model correspond to a specific class of polar cap arcs (e.g., Sun-aligned arcs, theta aurora) [Meng and Mauk, 1991]. It is also possible that the development of several models was propitiated by the large number of different sensors all with distinct sensitivity thresholds which have been used to measure characteristics of polar cap arcs.

The electrodynamics of the polar cap aurora has also been the topic of intense investigation. Burke et al. [1982] based on observations performed by the DMSP satellite found a correspondence between the optical aurora and upward Birkeland currents. Carlson et al. [1984] used the Sondrestrom incoherent scatter radar to indicate that the polar cap arcs were embedded in regions of intense gradients in the plasma flow, satisfying the $\nabla \cdot \mathbf{E} < 0$ condition for the presence of an upward field-aligned current. Mende et al. [1988] found several Sun-aligned arcs that presented strong reversals from a predominant antisunward direction in the dawnside of the arc to a more sunward oriented flow outside and in the duskside. More recently, Valladares and Carlson [1991] have presented data gathered on two energetic Sun-aligned arcs that drifted across the Sondrestrom field of view. These authors concluded that the Sun-aligned polar cap arcs also delineate regions where the downward component of the Poynting flux and the flow of electrons that constitute the field-aligned currents have elevated values.

These downward flows of electromagnetic and kinetic energy were found to lead to ionospheric regions where enhanced values of the ion and electron temperatures were clearly identified. *Carlson et al.* [1988] combined electric field measurements of DE 2 and ground-based camera displays of Sun-aligned auroras to construct convection pattern configurations containing multiple cells. *Jankowska et al.* [1990] used the property of the polar cap aurora to delineate regions where the field-aligned currents are directed upward to determine that the global convection patterns can be formed by three or four cells. Other researches have also employed concurrent measurements to imply the global pattern. *Marklund et al.* [1991] found a transpolar arc embedded in a distorted two-cell pattern and *Nielsen et al.* [1990] presented the temporal evolution of the convection associated with a transpolar arc.

The number of convective cells and the plasma circulation within them during B_z northward conditions has been presented by several authors. *Reiff and Burch* [1985] applied the antiparallel merging theory of *Crooker* [1979] to investigate the consequences of merging of northward IMF field lines with closed field lines at the dayside polar cap boundary and subsequent reconnection on the nightside. They postulated the existence of a region of closed field lines flowing sunward at the center of the polar cap. Convection patterns for northward IMF inferred from experimental data also show the existence of a region of the polar cap containing sunward flow [*Potemra et al.*, 1984; *Heppner and Maynard*, 1987]. *Burch et al.* [1992] have used DE 1 images and in situ measurements to further develop a suggested conceptual model for the quiet time polar cap, IMF dependencies included. The polar cap auroras they dealt with, and refer to as Sun-aligned arcs, theta aurora, and horse collar aurora, are of necessity sufficiently intense to be seen by the DE 1 imager. The database we deal with here, using ground-based all-sky image-intensified photometers (ASIPs) have over 10 times the sensitivity, and see Sun-aligned polar cap aurora more like half the time, rather than the few percent of the time for which they can be seen by satellite based observations.

This present study extends previous work not only on the correlation of the occurrence of polar cap arcs with the IMF but also the dependencies of other arc properties upon IMF. Here we relate (1) the presence/absence of polar cap arcs, (2) their alignment, and (3) the arc motion in the dusk-dawn direction to the IMF as measured by IMP 8 and ISEE 2. Most of the arcs examined here exhibit red line emission intensities of the order of 100 R, similar to the intensity of the weak polar cap F region arcs studied by *Weber and Buchau* [1981]. The arc velocity as measured here, corresponds to the spatial displacement of the red line emissions, which may not be necessarily equal to the drift of the thermal plasma. Since we have used images, with a time sequence that samples rapidly relative to the lifetime of the visual feature, we can make certain assurances about the data. We excluded hooks, loops, spots, and branches. We are dealing with optical features that are relatively extended (unkinked or primarily linear or quadratic), their extent filling much if not all of the nominal 1000 km circular field of view of the ASIP. All extended optical features meeting this criteria have been retained in the data set. It is emphasized that extra attention was dedicated to exclude oval and substorm related aurora.

The paper outline follows. Section 2 presents the methodology that was employed to compute the geophysical parameters of interest. Section 3 describes the statistical analysis and the correlative study of the three parameters of the arc with the three components of the IMF. In section 4 we formulate the implications of our results within the context of the current theories of the formation of polar cap arcs during northward orientations of the IMF.

2. Data Presentation

Figure 1 shows the location and the field of view of the all-sky imaging photometers (ASIP) that have been deployed in the arctic region and are currently operated by the Phillips Laboratory (formerly AFGL). The ASIPs are located at Qaanaaq (77.5°N, 69.2°W), Nord (81.67°N, 16.67°W), and Ny Alesund (78.9°N, 11.95°E). While, restricted to nighttime clear skies, they can provide simultaneous measurements of the airglow and aurora in the polar cap and auroral oval regions. The circles around the stations show the limits of the ASIPs field of view for an assumed emission height equal to 250 km. The ASIPs are intensified posses wide-angle lenses and have a sensitivity dynamic range from 50 R to several kilorayleighs [*Weber and Buchau*, 1981; *Weber et al.*, 1984]. All three cameras operate continuously for periods during the winter months when the Moon is below the horizon. The combined field of views of the three ASIPs covers more than half of the polar cap at any universal time almost independently of the size of the polar cap. Here the polar cap is understood as the region located poleward of the auroral oval [*Hones et al.*, 1989]. This paper presents the analysis of data gathered only at one station, Qaanaaq, and during one winter season, the winter of 1986–1987.

The proximity of Qaanaaq to the magnetic north pole gives an uncommon capability to this station; the entire field of view (155°) of the ASIP is inside the polar cap region at almost any local time. This imager alternatively diagnoses both 630.0 nm (O I) and 427.8 nm (N_2^+) emissions, completing a two-line cycle every 2 min. The red and the blue lines are respectively more characteristic of lower (hundreds of eV) and higher (≥ 1 keV) energy electron precipitation. The results presented here are based on data collected by the red filter. Figures 2 and 3 show two sequences of images containing polar cap arcs with typical morphological characteristics. These figures show selected images from the full set sampled once every two minutes. Other auroral forms, such as hooks, loops, and branching were observed occasionally during the winter of 1986–1987 but are not presented here. Two geographic cardinal directions are also indicated in every image using a dark L-shaped mark placed near the upper border of each image. The vertical and horizontal bars of the L-shaped mark point to geographic north and east, respectively.

2.1. December 5, 1986, ASIP Frame

The sequence of images of Figure 2 were obtained during a prolonged period of northward B_z . The 630.0-nm data shows elongated bright emissions, aligned with the Sun-Earth direction. These are the typical properties of polar cap arcs, as has been described by *Weber and Buchau* [1981], *Buchau et al.* [1983], and *Carlson et al.* [1984]. Other characteristics of polar cap aurora, such as the appearance of new arcs, the continuous variation of the aurora intensity

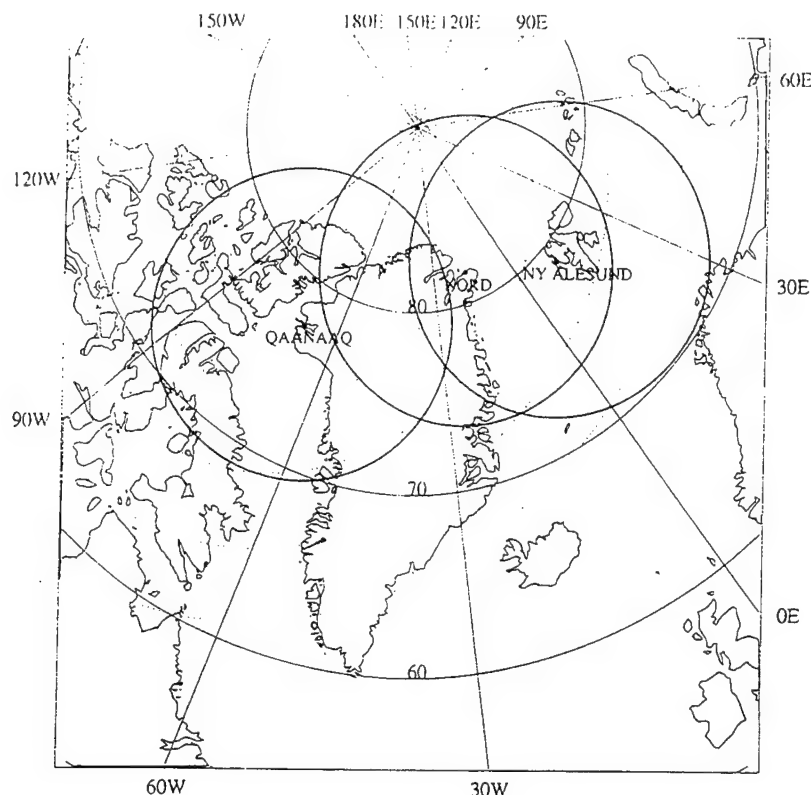


Figure 1. Site locations and field of view (10° elevation) of the three all-sky imaging photometers (ASIP) operated by the Phillips Laboratory. The regions of the high-latitude ionosphere which are imaged by the three ASIPs are (1) the camera located at Qaanaaq (77°N , 69°W geographic) mostly observes the polar cap; (2) the Nord's ASIP (81°N , 17°W) can image both the polar cap and the poleward part of the oval; and (3) the all-sky camera deployed at Ny Alesund (79°N , 12°E) mainly probes the auroral oval and the equatorward side of the polar cap.

and the arc bifurcation are also clearly displayed on these images. The full set of images, from which these are selected, allows unambiguous continuous tracking of the stable reference arcs. The image of 0953 UT shows two arcs that are nearly parallel to the Sun-alignment direction, both arcs contain different intensity levels. The image collected 4 min later shows that the arc that was seen overhead at 0953 UT has dimmed and drifted southward. In later images this arc continues dimming, drifting southward, and even bifurcating at 1005 UT. The appearance of a new arc in a region of no previous aurora is illustrated by the most northward arc in the image of 0957 UT and also by the thin arc located overhead at 1005 UT.

2.2. February 19, 1987, ASIP Frame

The four images of Figure 3 exemplify common characteristics of a system of several typical polar cap arcs: arcs that occur simultaneously seem to move in the same direction and almost always at the same speed. The polar cap arcs of February 19, 1987, are seen drifting rapidly (about 200 m s^{-1}) in the ASIP frame. The swift movement of the arcs can be visualized if we compare the relative location of the arcs and the dark spot depicted in the lower left quadrant of each image. The dark mark is stationary. As time progresses, the southernmost arc is seen moving northward (downward) then drifting across the dark mark (2253 UT) and then moving north of it (2301 UT). After 2259 UT, the two other arcs located further north show a separation gradually

diminishing with time until they merge at 2303 UT. Another example of an arc pair that merged was published by Valladares and Carlson [1991, Figures 4a, 4b, and 4c]. A new arc is seen entering the southern end of the field of view at 2257 UT.

The ASIP records the images in a microfilm media. To extract precise information about the arc dawn-dusk displacements and the deviations from the Sun-Earth direction, it was required to convert the images to a digital format. To accomplish this, the bright traces of the 630.0-nm images were projected onto specially scaled draft sheets. Then a graphics tablet was used to read the coordinates of selected points along the center of the sketch of the arcs. As most of the arcs were relatively narrow, no information about the arc width was entered into the computer.

2.3. December 5, 1986, Frame Transformations

Figure 4 shows the three arcs which were seen by the Qaanaaq imager at 1005 UT on December 5, 1986 (Figure 2 lower right panel). The arcs are represented in three different coordinate systems (Figures 4a–4c). In addition, Figure 4d shows the arc motion, in the dusk-dawn direction, of selected points along the arcs. Figure 4a presents all three arcs as they were detected by the all-sky camera, it obviously resembles Figure 2d. Geographic north is to the top and west to the left of the plot (270°). Figure 4b shows the location of the arc after each point in the arc has been transformed to a geographic coordinate system. Here we have assumed that

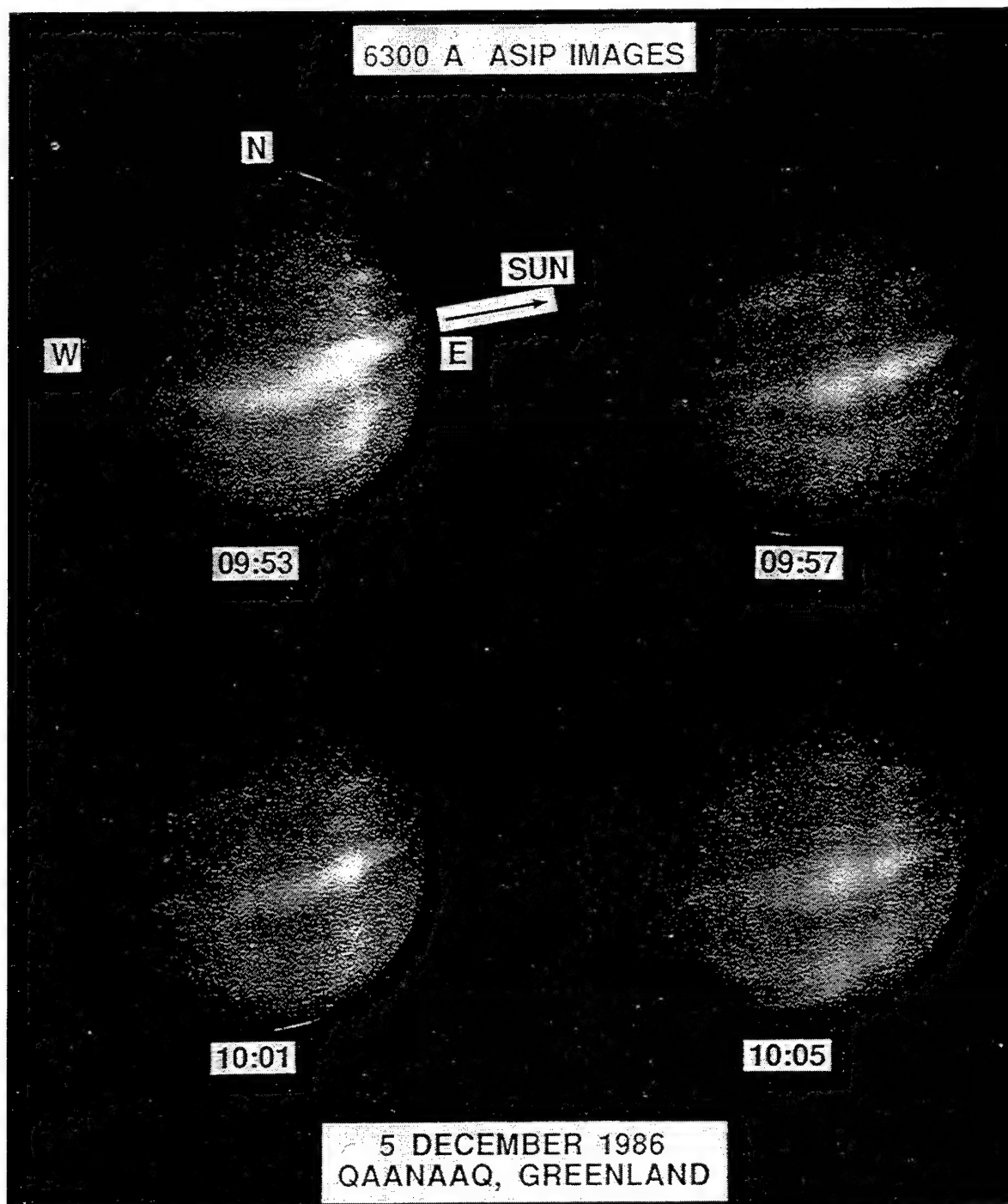


Figure 2. Sequence of 630.0-nm images depicting a system of Sun-aligned arcs. The polar cap arcs were measured at Qaanaaq on December 5, 1986. Geographic north is at the top of each image, and geographic west is to the left. The direction toward the Sun is also indicated by the arrow in the top left frame.

the emissions originate at 250 km altitude. Figure 4c depicts the arcs in a corrected geomagnetic (CG) coordinate system (based on the IGRF 1980 model). In this system the arcs approximate straight lines almost parallel to the noon-midnight meridian; all three arcs have a small offset angle. A careful examination of the arcs indicates that there are small undulations along the arc alignment. These structures resemble the twists and folds which have been observed on auroral arcs, such as Hallinan and Davis [1970] suggested, they were associated with Kelvin-Helmholtz instabilities. Figure

4d shows the dusk-to-dawn velocities which were obtained by comparing two consecutive frames. Here the length of the arrow is proportional to the dusk-to-dawn velocity of the arc. The arc motion was determined in the following fashion: for each individual point along the arc a line was traced in the dawn-dusk direction (almost perpendicular to the arc alignment) until it intersected the location of the arc in the next 2-min frame. This displacement measured in geographic coordinates was then divided by the time interval between the frames. The result is the velocity along the dawn-dusk

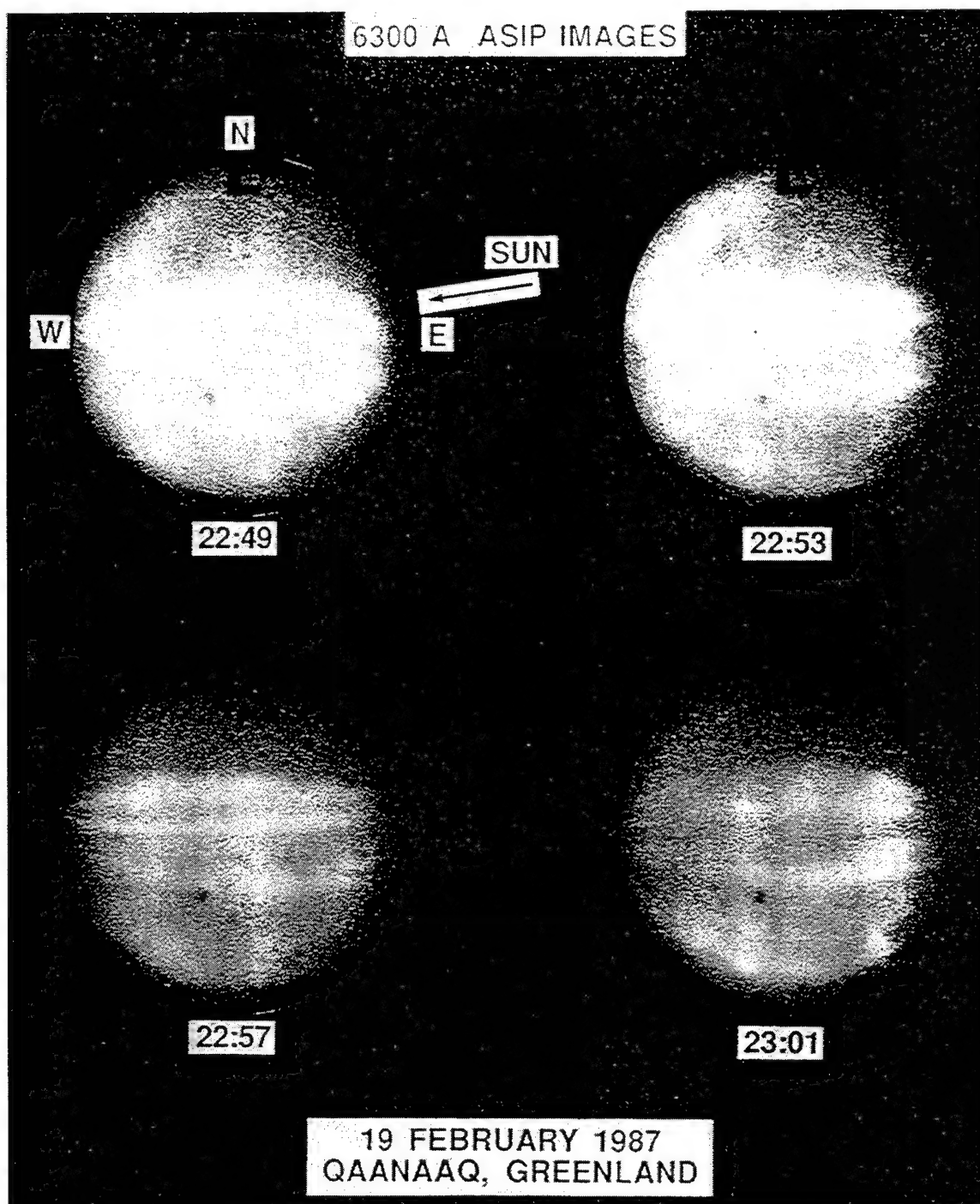
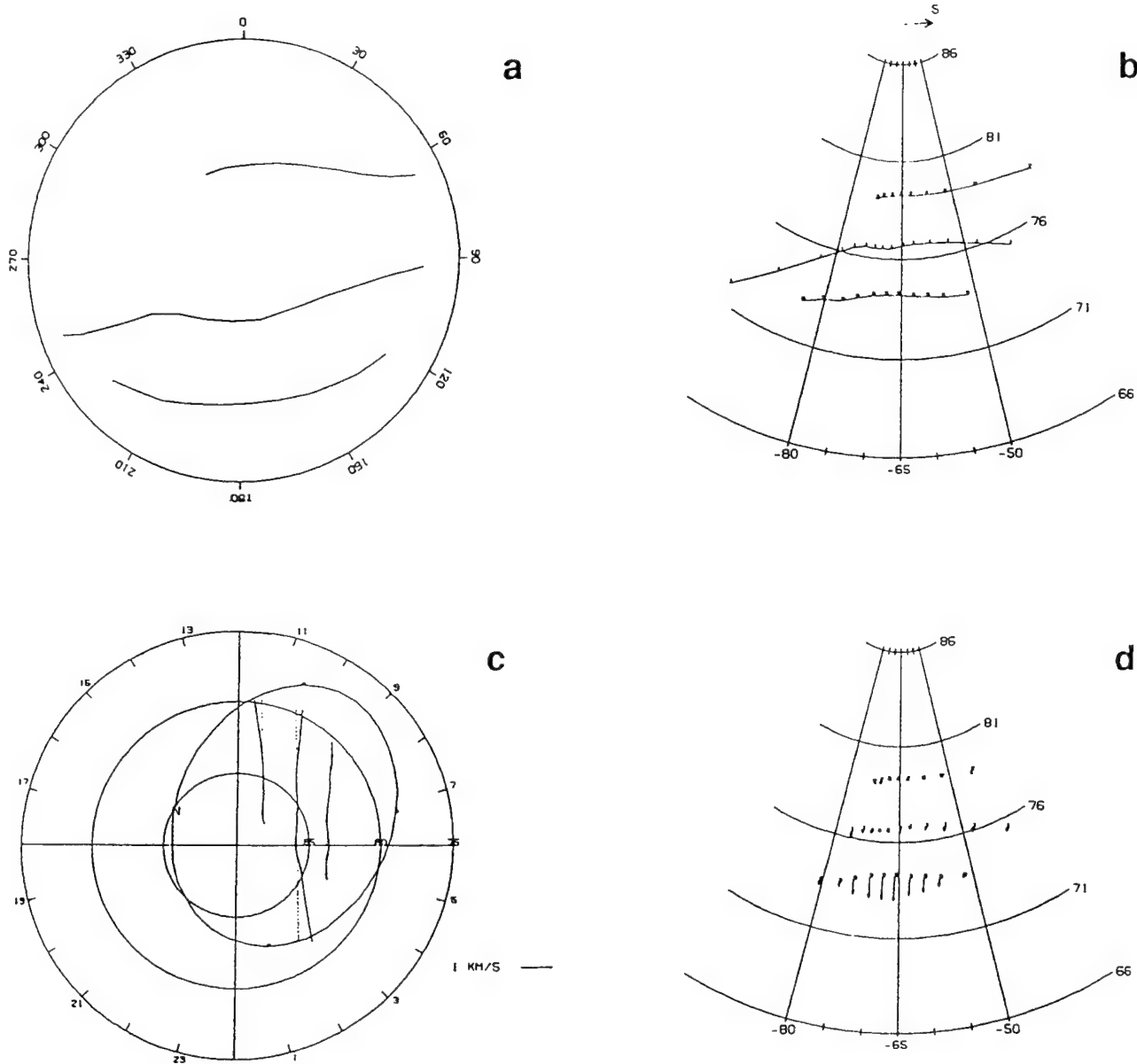


Figure 3. Same as Figure 2 but for a system of polar cap arcs observed on February 19, 1987. This figure shows typical polar cap arcs. These arcs appear as long, thin, and bright stripes of luminosity moving northward.

direction. This velocity was subsequently corrected to take into account the Earth's corotation both at Qaanaaq and at the magnetic north pole [Sojka *et al.*, 1979]. This method is subjected to few types of error due to our assumption of a fix altitude of the emissions and a thin emitting layer and our decision to use the arc center to represent the arc location. The error is never severe; it has been calculated that the maximum error is always less than 22% of the magnitude of the arc displacement.

Figure 4d shows that the two most poleward arcs have constant velocities, suggesting that these arcs move uniformly with little change in shape or direction of alignment. The most equatorward arc shows a different behavior. The center of the arc moves with a downward velocity near 600 m s^{-1} while at both ends of the arc, the velocity is less than 100 m s^{-1} . Such nonuniform arc motion has been found to be present in a large number of the polar cap arcs. The variable arc motion (motion of the optical emission feature nominally

6300 Å ASIP IMAGE
10:05 UT



5 DECEMBER 1986
QAANAAQ, GREENLAND

Figure 4. The 630.0-nm image obtained on December 5, 1986, at 1005 UT (Figure 2d). The polar aurora is presented in three different coordinate systems: (a) ASIP frame, (b) geographic coordinate, and (c) polar plot of corrected geomagnetic (CG) local time versus CG latitude. (d) The arc motion in the dusk-dawn direction of selected points along the arc. The arc displacements are calculated based on the arc location on this frame and on the succeeding image.

transverse to its length) is caused by the undulations which provide additional displacement to certain parts of the arc. Consequently, if the dusk-dawn velocity is computed taking a simple average of all the displacements calculated along the arc, then the resultant velocity will be contaminated by the undulations. A different approach to obtain the arc motion is presented in subsection 2.5.

2.4. February 19, 1987, CG Frame

Figure 5 shows the four images of Figure 3 converted into a CG latitude versus CG local time coordinate system. This representation permits a much finer inspection of the arc displacement and angle with respect to the noon-midnight meridian. All three arcs at 2249 and 2253 UT have nearly the same downward (clockwise) tilt angle with respect to the noon-midnight meridian. The three arcs located further downward change orientation of their tilt angles. A fourth arc enters Qaanaaq's field of view at 2257 UT. This arc moves faster than the other arcs between the time interval of 2257 and 2301 UT.

2.5. February 19, 1987, Dusk-Dawn Motion Calculation

The dawn-dusk motion of each arc was calculated making a least squares fit to the displacements corresponding to all the points along the arc in seven consecutive images. The effect of the wavy features being quasi-stationary will cancel out leaving a good estimate of the more uniform background dusk-to-dawn velocity of the arc.

Figure 6 shows the dusk-dawn velocity that was calculated following the least squares fitting method. The motion of four polar cap arcs is presented in Figures 6a–6d. Figures 6e and 6f show the B_y and B_z components of the IMF in geocentric solar magnetospheric (GSM) coordinate system, measured by IMP 8. The IMF B_z remains constant and equal to +10 nT for almost 2 hours. B_y presents a reversal from negative to positive at 2330 UT; 15 min later the velocity of arcs 1 and 3 are seen to reverse sign to a duskward orientation. While these two quantities (B_y and the arc velocity) seem to be related for the arcs of February 19, 1987, no well-sustained conclusion can be implied from a single-case study. It is then, the purpose of this paper to validate (or negate) in a statistical sense several hypotheses of the relation between the IMF and the morphological parameters of polar cap arcs.

2.6. Qaanaaq 1986–1987 Database

During the winter of 1986–1987 the Qaanaaq ASIP operated between the months of October and February. A total of 850 hours of film were recorded. Owing to cloudy sky conditions or to the lack of IMF information, this number of hours was reduced to 223 hours. If we further exclude events that show airglow associated with polar cap patches or times when no aurora was present, then we end with only 46.4 hours of red line emissions collected on 20 different days. The intensity of the polar cap arcs observed during this winter, varied between 50 R and 1 kR. A complete list of the days and times when the Qaanaaq imager detected polar cap arcs and the IMF was measured by either IMP 8 or ISEE 2 is listed on Table 1. Blue line measurements were even more scarce, only 16.8 hours, which represents only 36% of the time that red line emissions were observed. We also counted the number of polar cap arcs that were seen transiting Qaanaaq's field of view, such as the arcs of Figures 2 and 3.

The total number was 143. Because a polar cap arc can change its orientation or velocity in a time as short as 2 min, the statistics reported in this paper are based on every 2-min sight of a bright emission in the red line. On other occasions the arc characteristics change at a slower pace and our 2-min sampling rate will introduce multiple counts. The only consequence of this oversampling is to introduce a grouping of counts at certain values in the unnormalized histograms of Figures 12–17. This effect can be easily identified. The total number of arc frames used in this study is 2722. Henceforth, they will be referred to simply as arcs.

3. Statistical Analysis

This section describes the statistical analysis of three different polar cap arc morphological parameters that have been studied in this paper: (1) the presence of at least one arc in the ASIP field of view, (2) the deviation of the arc orientation (offset angle) from the Sun-Earth direction, and (3) the dusk-dawn "body" motion of the arc.

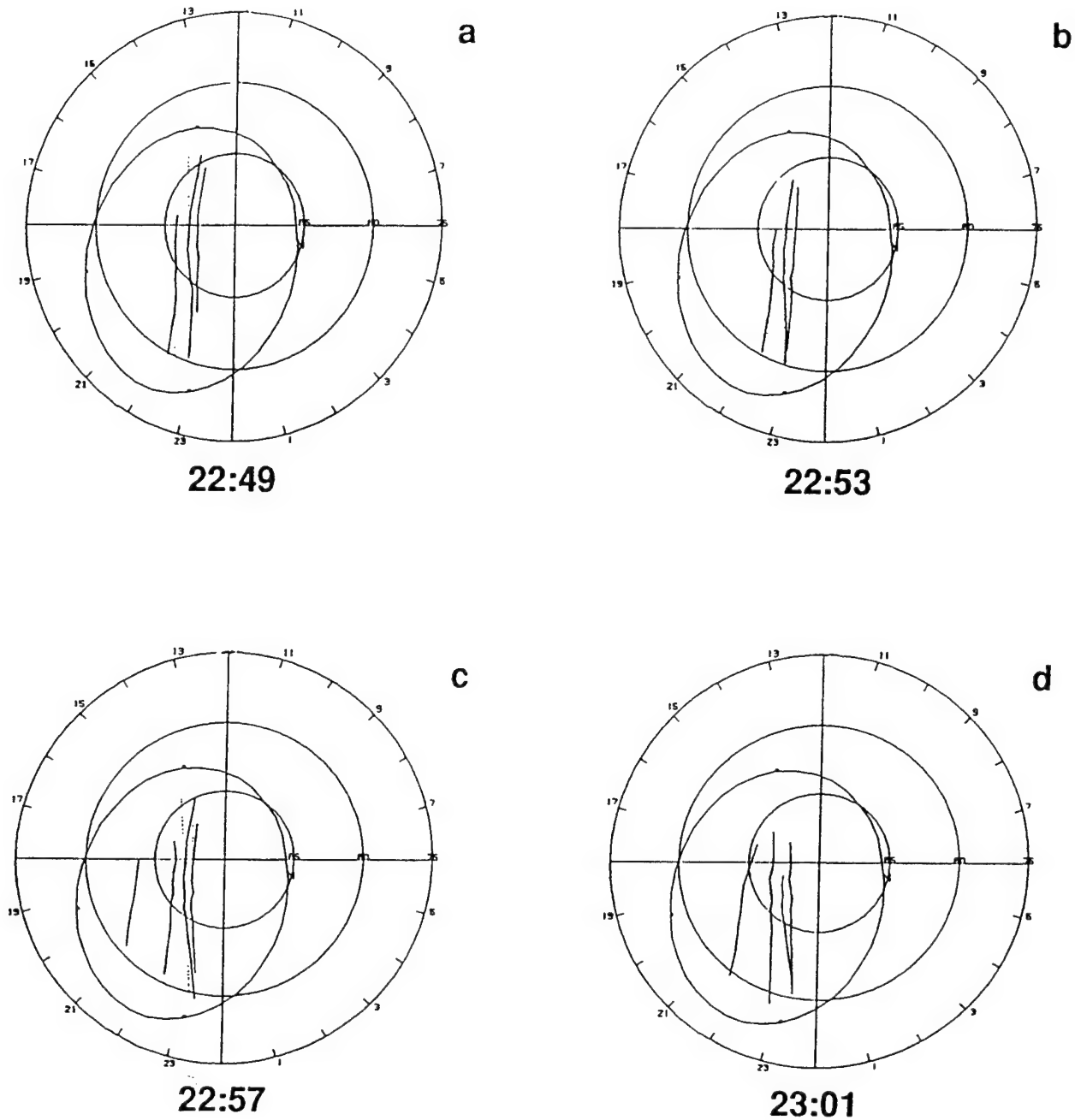
Figure 7 shows the distribution of the number of arcs as a function of the arc orientation, (labeled offset angle in Figure 7a) and as a function of the dusk-dawn arc motion (Figure 7b). The center of gravity of each histogram is indicated by the arrows and the initials CG. A positive offset angle means a downward (clockwise) rotation of the arc border closest to the Sun. The distribution of Figure 7a has a shape that approaches a Gaussian curve. The mean value is equal to -5° , and the standard deviation = 14.4° . The largest offset values are -45° and 40° for counterclockwise and clockwise rotations, respectively.

The arc velocity is defined positive for downward displacements and negative for duskward translations. The velocity distribution of Figure 7b has a center of gravity equal to -21 m s^{-1} and a standard deviation = 108 m s^{-1} . However, a significant number of arcs possess duskward velocities exceeding 240 m s^{-1} . This tail in the velocity distribution displaces the center of gravity toward more negative values.

3.1. Presence of Polar Cap Arcs

Figures 8–11 present the number of minutes and the probability of detecting one or more arcs. Our statistics of the ASIP data has been binned according to the values of each of the three components of the IMF. The histograms of Figure 8 show the distribution of the number of minutes that the Qaanaaq imager was on operation during the winter of 1986–1987 and besides the sky condition was optimum for a clear detection of weak arcs. The purpose of presenting these histograms is to show the degree of biasing that may be introduced in our data set by a nonuniform sampling of the IMF. The distribution of B_x shows two peaks one at 3 nT and the other at -3 nT , and a valley in between. The B_x histogram is quite symmetric, with only a slight bias toward positive values of B_x . The B_y distribution is asymmetric, skewed to -2 nT and containing a rapid fall off at its negative side. The number of minutes of negative B_y outnumber the total number of minutes of positive B_y . The B_z histogram shows stronger asymmetries and a more uneven sampling in the $\pm 6 \text{ nT}$ interval. There are clearly more minutes during which B_z was positive than negative. The B_z distribution peaks at $+2 \text{ nT}$, with a total of 2008 min when it was between

6300 Å ASIP IMAGES
CORRECTED GEOMAGNETIC COORDINATE SYSTEM



19 FEBRUARY 1987
QAANAAQ, GREENLAND

Figure 5. Arcs corresponding to February 19, 1987 (Figure 3) presented in a polar display of CG latitude versus CG local time coordinates. (a)–(d) Polar cap arcs extending almost parallel to the noon-midnight meridian.

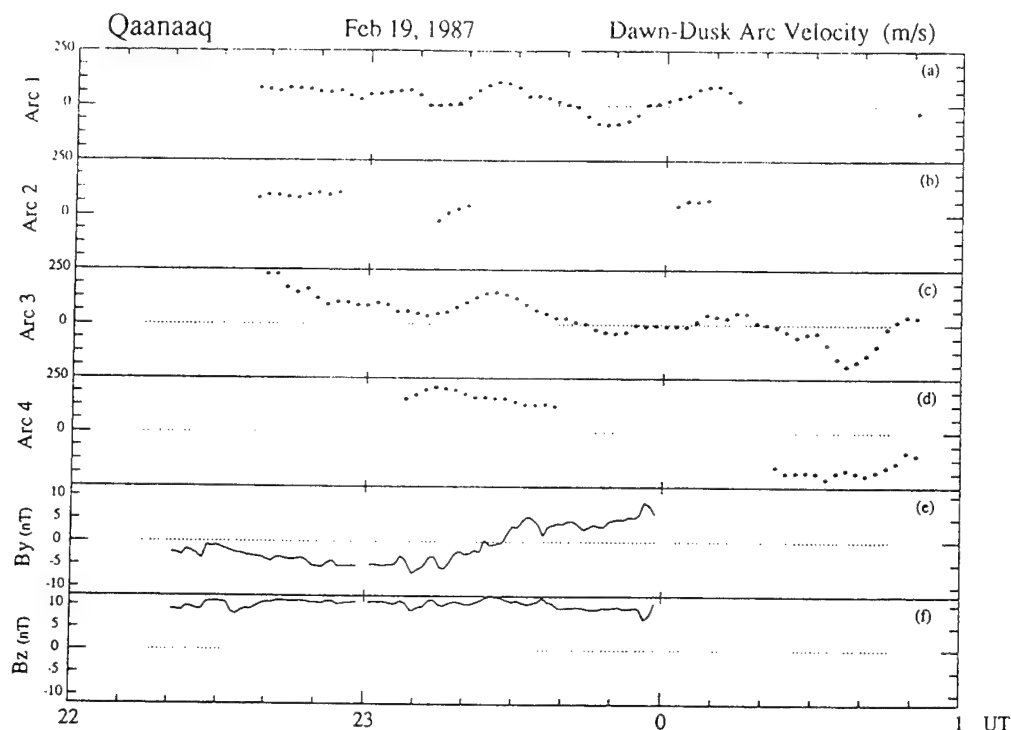


Figure 6. Arc motion in the dusk-dawn direction for the four polar cap arcs observed at Qaanaaq on February 19, 1987. (a)–(d) The arc velocities in meters per second corresponding to arcs 1–4. (e) and (f) show the B_y and B_z components of the IMF in GSM coordinates. The dawn-dusk velocity of arc 1 approximately follows the same trend of the arc 3 velocity.

+1 and +2 nT. There are two smaller secondary peaks at +10 and –10 nT.

The histograms of Figure 9 were obtained by dividing the total number of minutes that the ASIP detected one or more polar cap arcs by the number of minutes that the imager was operating (Figure 8). We do not claim that this distribution is equal to the probability of occurrence of polar cap arcs in the whole polar cap but only to the probability of having at least one arc in the area covered by the ASIP. In this sense the statistics that we are presenting here will give a value smaller than the true probability of occurrence of arcs in the polar cap. Similar to Figure 9, we present here the distributions for each of the three components of the IMF. The number of minutes that the arcs were observed at Qaanaaq are printed on top of the bars. Because the number of events is largely reduced for amplitudes >5 nT, it is conceivable that if any of the three components of the IMF has a large magnitude and this value remains large for several minutes, then the statistics at those values would be drastically controlled by one single event. This has occurred at values of B_x less than –6 nT (top panel) and of $B_z > +8$ nT (bottom panel).

The B_x distribution of Figure 9 is very well uniform and maintains an amplitude equal to 20% between –6 and +6 nT. However, at values smaller than –6 nT, the probability increases to 80%. This high percentage is entirely due to the arcs observed on February 2, 1987, when B_x fluctuated between –6 and –8 nT during a 100-min time interval. Thus the B_x distribution for values of $B_x < -6$ nT is not statistically significant. The B_y distribution shows a quasi-uniform shape with the amplitude of the histogram varying between 15 and 25%. We conclude that the probability of observing at least one polar cap arc at the Qaanaaq station is

Table 1. Simultaneous Observations of Polar Cap Aurora At Qaanaaq and Solar Wind Parameters During the Winter of 1986–1987

Date	Time, UT	Satellite
October 4, 1986	0700–0731	IMP 8
October 16, 1986	0659–0920	IMP 8
November 2, 1986	2027–2107	IMP 8
November 2, 1986	2258–2334	IMP 8
November 3, 1986	0211–0352	IMP 8
November 8, 1986	2102–2325	ISEE 2
November 12, 1986	0644–1016	IMP 8
November 12, 1986	1132–1154	IMP 8
November 12, 1986	2056–2106	IMP 8
November 12, 1986	2143–2157	IMP 8
November 13, 1986	0541–0815	IMP 8
November 13, 1986	1011–1132	IMP 8
November 14, 1986	0800–0935	IMP 8
November 22, 1986	1856–1931	ISEE 2
November 28, 1986	0053–0200	IMP 8
December 5, 1986	0650–1230	IMP 8
December 5, 1986	2339–0021	ISEE 2
December 6, 1986	0244–0321	IMP 8
December 6, 1986	0608–1002	IMP 8
December 9, 1986	1226–1518	IMP 8
December 21, 1986	1819–1849	IMP 8
January 25, 1987	0559–0611	IMP 8
February 2, 1987	2125–0045	ISEE 2
February 6, 1987	0621–0947	IMP 8
February 19, 1987	0727–1105	IMP 8
February 19, 1987	2231–2400	IMP 8
February 20, 1987	0000–0058	IMP 8
February 25, 1987	0359–0528	IMP 8

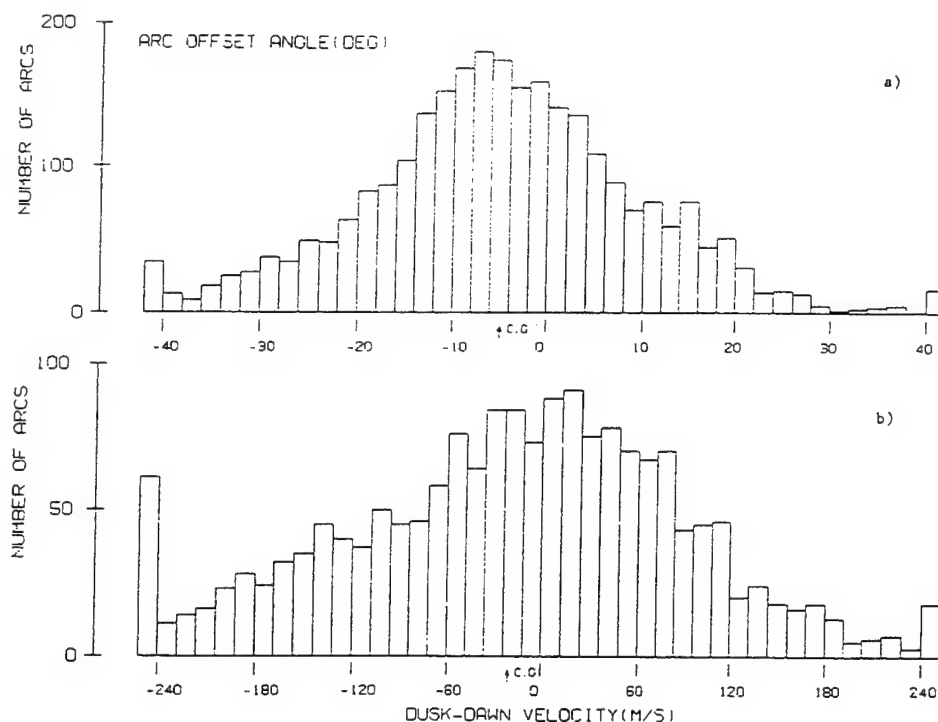


Figure 7. Histograms of the number of arcs versus (a) the arc offset angle in degrees. (b) Dusk-dawn motion of the arcs in meters per second. The distribution of the number of arcs as a function of offset angle closely resembles a Gaussian curve.

about 20% and seems to be independent of the magnitude and sign of B_x and B_y .

As expected, B_z shows very different statistics. The probability of observing an arc is larger than 20% when B_z is positive. This result agrees with the findings of *Berkey et al.* [1976] and *Lassen and Danielsen* [1978]. They found good correlation between B_z northward conditions and the occurrence of polar cap arcs. However, here Figure 9 provides some extra information: polar cap arcs are sometimes seen during B_z southward conditions, but the probability of occurrence decreases linearly as B_z becomes more negative. All the polar cap arcs observed during B_z south conditions originated before the IMF turned south and remained detectable, in some cases, for tens of minutes after B_z changed sign. These arc events followed prolonged periods of northward B_z or during short (<15 min) negative excursions of B_z . The probability of observing an arc becomes practically zero when $B_z < -5$ nT. The distribution of the B_z shows a plateau of 20% probability between 0 and +5 nT and a rapid increase reaching 100% at $B_z > +9$ nT. However, the statistical significance for $B_z \geq 7$ nT is very limited. The distribution of arc occurrence for B_z negative has some similarities to the histogram presented by *Hardy* [1984, Figure 6] of the occurrence of intense electron fluxes at latitudes above 85° . As the arcs are closely related to the existence of intense enhanced precipitating electron fluxes in the polar cap, the agreement of these two distributions endorses the view that as mentioned above, polar cap arcs can be seen when the B_z component of the IMF is negative. In the discussion section we comment about the time that is needed for polar cap arcs, formed under extended $B_z > 0$ conditions, to flush out of the polar cap after a B_z southward turning.

The probability of observing polar cap arcs at the dawn and dusk hemispheres is displayed in Figures 10 and 11. The B_x and B_y distributions in these figures are quasi-uniform. They are basically similar in shape to the histograms of Figure 9. The prominent feature of these figures is the difference between hemispheres in the average value of the arc occurrence probability. It is about 40% for arcs located in the dawnside and only 10% for the duskside. This factor of 4 difference may be due to a distinct intensity of the aurora between hemispheres. If the duskside arcs are fainter than the dawnside arcs, then they could more easily fall below the ASIP sensitivity threshold and the statistics would be greatly diminished. In this scenario the statistics for the duskside would be scaled down with respect to its dawnside counterpart. The B_z histogram of Figure 10 shows a trend different to the B_x and B_y histograms. For values larger than -5 nT the dawnside distribution increases linearly reaching values close to 50% at $+7$ nT. No values of B_z larger than 8 nT were measured when Qaanaaq was located on the dawnside of the polar cap. The B_z distribution of arcs located on the duskside presents a shape different from the histogram corresponding to the dawnside; it increases between -5 and 0 nT, then decreases in the interval from 0 and $+5$ nT. For values larger than 7 nT the limited number of polar cap arcs greatly reduce the statistical significance of any statement that could be made. The 40% probability of a Sun-aligned arc within the dawn sector field of view of Qaanaaq, which is $1/4$ the diameter of the entire polar cap, puts a floor but not a ceiling in the percentage of time Sun-aligned arcs exist in the polar cap for B_z north conditions.

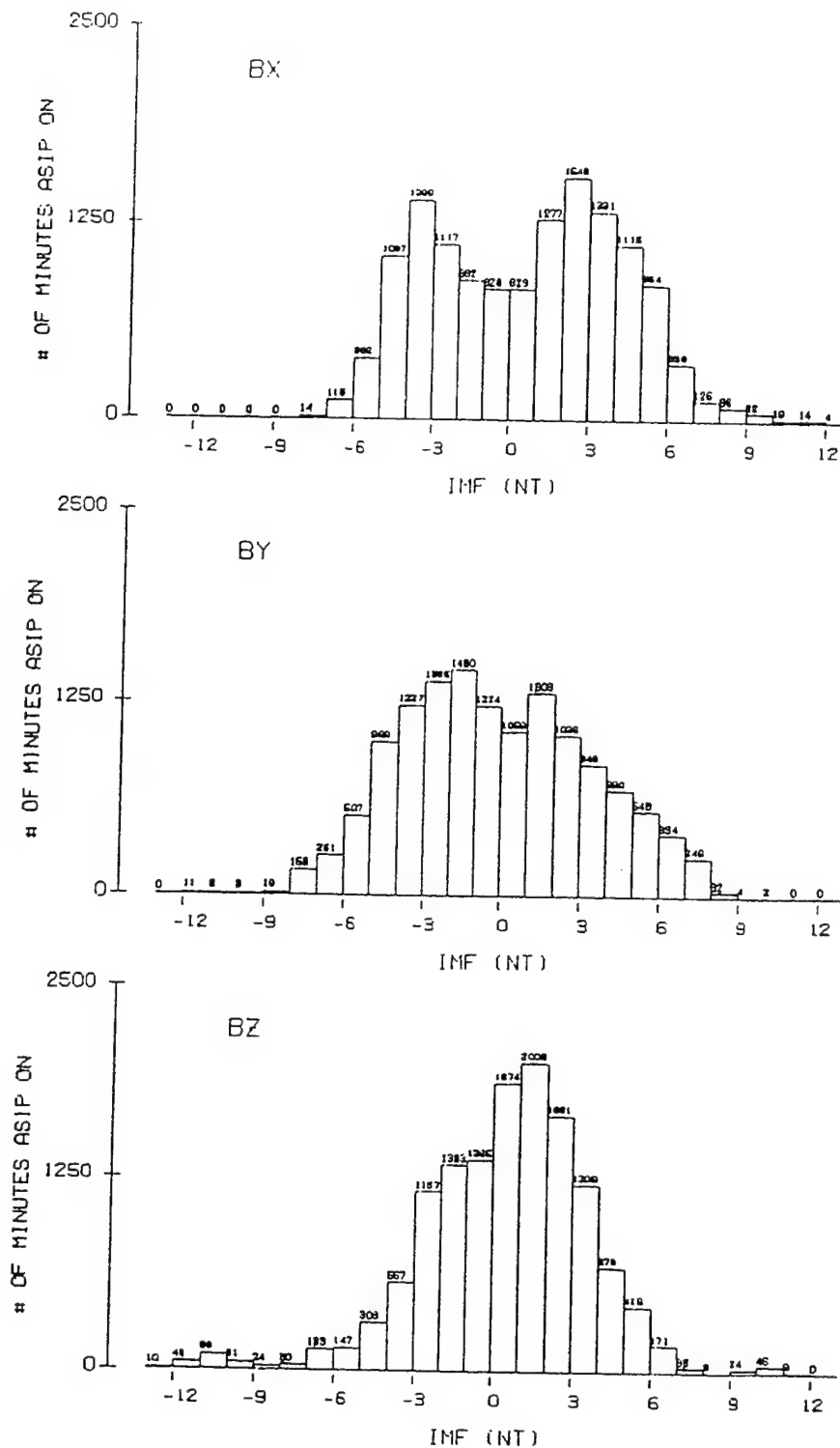


Figure 8. Histograms of the total number of minutes that the Qaanaaq imager operated during the winter of 1986–1987 and the observing conditions were unhampered by meteorological effects. The histograms are plotted as a function of the value of the three components of the IMF: B_x , B_y , and B_z . The numbers at the top of the bars indicate the amount of minutes for each IMF bin.

3.2. Arc Orientation

To measure the arc offset angle or arc orientation, the digitized images were transformed to a CG coordinate system. In this frame a line was fitted to the arc and the angle between this line and the noon-midnight meridian was cal-

culated and included in our statistics when the arc was 30° or more above the horizon and the fitting procedure indicated a small deviation error. Plate 1 shows the location of the polar cap arcs that were observed during the winter of 1986–1987 portrayed in a CG latitude versus CG local time polar frame.

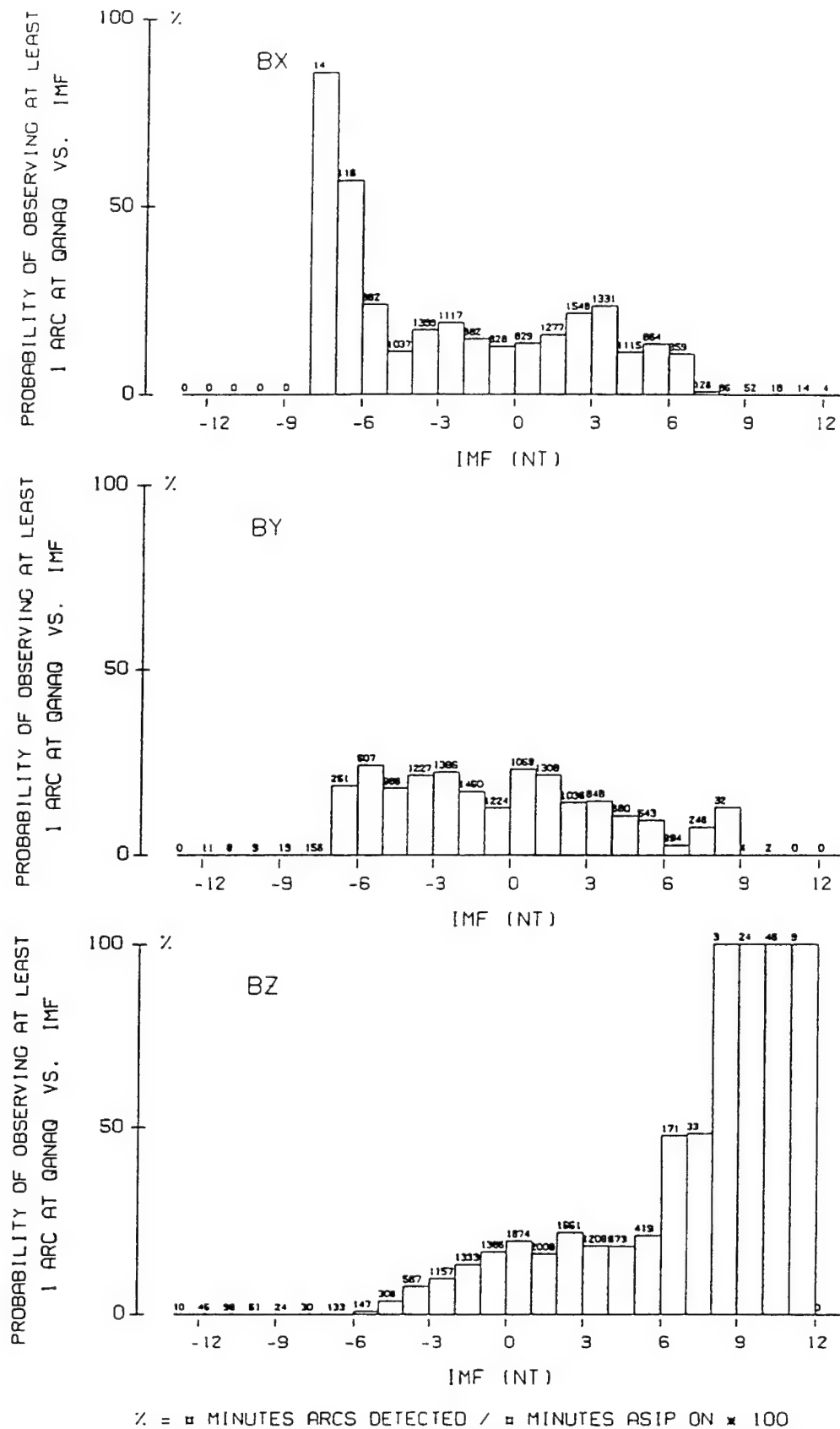


Figure 9. Probability of observing at least 1 arc inside the Qaanaaq's field of view versus each of the three components of the IMF. The probability is expressed in units of percentage. The numbers at the top of the bars are repeated from Figure 8. The B_z distribution (bottom panel) shows the probability of arc occurrence increasing for larger positive values and decreasing for negative values of B_z .

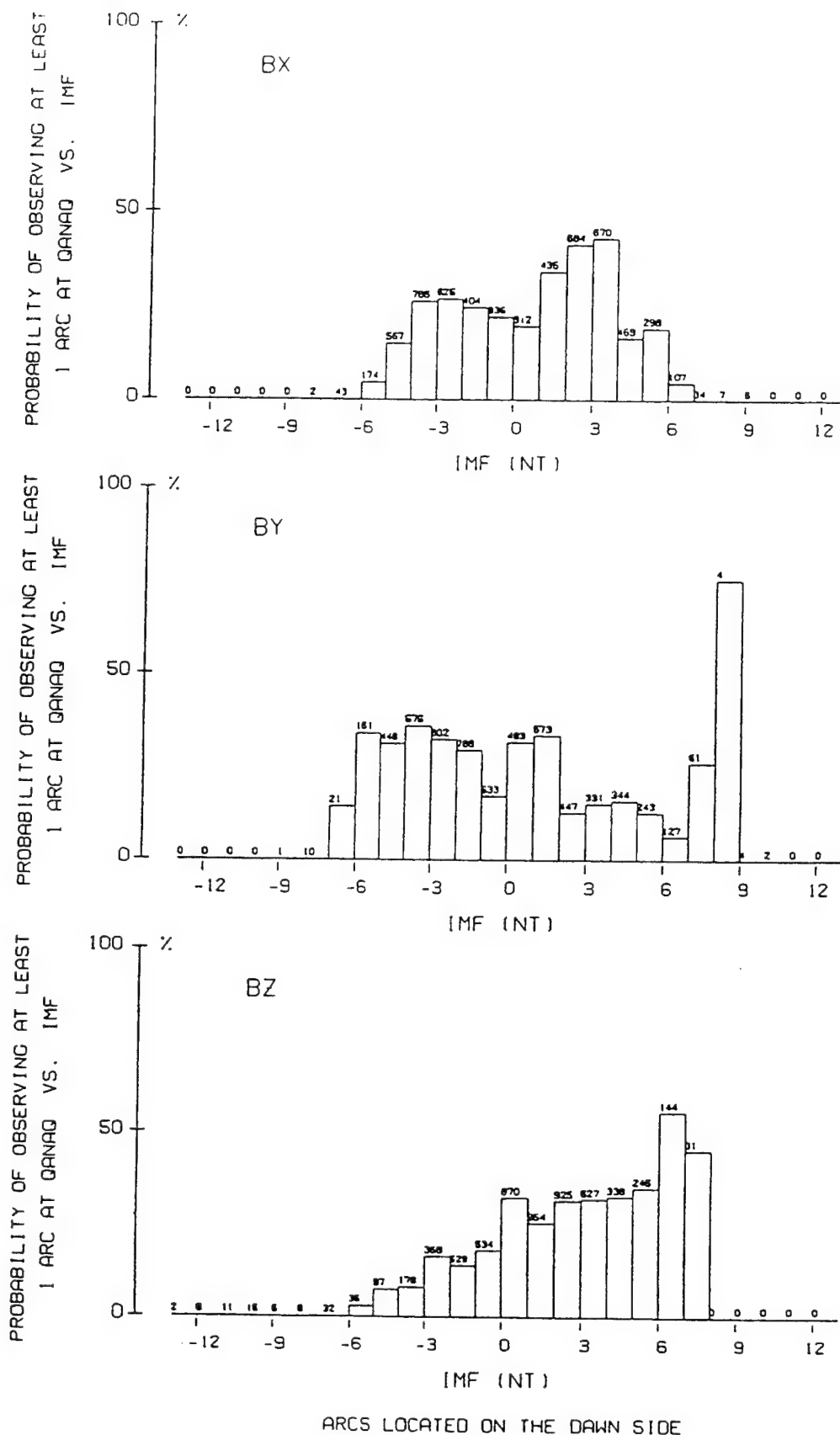


Figure 10. Same as Figure 9, but restricted to polar cap arcs observed on the dawnside. (i.e., located in the 0000–0600 and 0600–1200 CG local time sectors). The quantities at the top of the bars indicate the total number of minutes that the Qaanaq station was in the dawn sector.

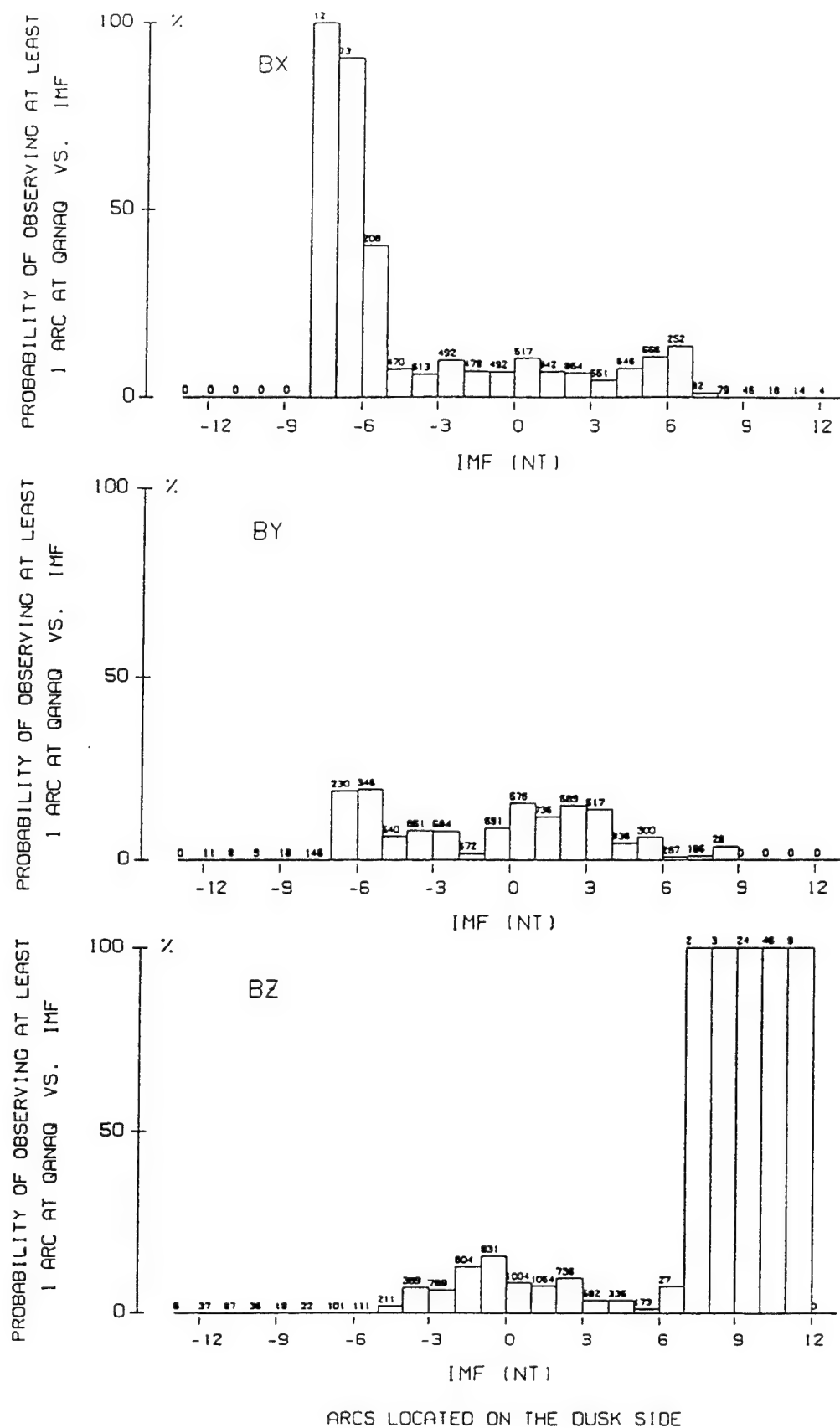


Figure 11. Same as Figure 9, but for arcs located on the duskside of the polar cap (i.e., 1200–1800 and 1800–2400 CGLT sectors).

ARC OFFSET ANGLE

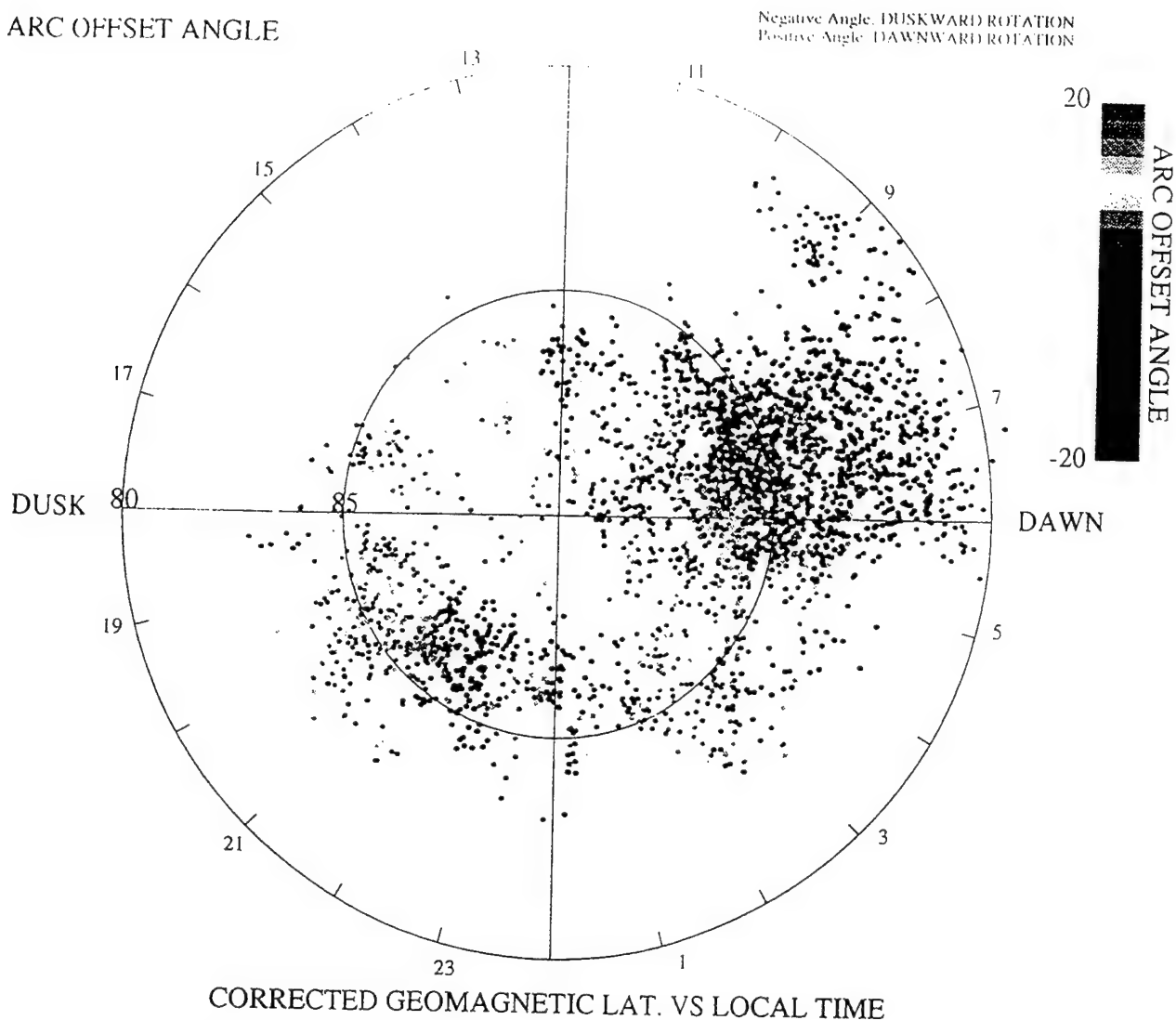


Plate 1. Polar plot of the location of all the polar cap arcs observed during the winter of 1986–1987 and their offset angle with respect to the noon-midnight meridian. Each arc is represented by a small circle that is color coded according to the value of the arc offset angle. A red dot denotes downward rotation equal to 20° or more, and a dark blue dot represents a duskward rotation of at least 20° . All the arcs in the 1200–1800 CGLT quadrant have dawnward rotations and most of the arcs in the 0600–1200 quadrant possess duskward rotations.

Since the arc extension varies from less than 100 km up to few thousand kilometers (typical of transpolar arcs), it usually spans more than one hour of CGLT. We selected the center of the arc to indicate the location where the arc occurs. The information about the arc orientation is color coded according to positive (dawnward or clockwise) rotations of 20° or more are in red and negative (duskward or counterclockwise) angles equal to -20° or less are in blue. Angles in between follow the color scale displayed in the upper right corner. It is evident that a larger number of arcs were observed in the 0000–0600 and 0600–1200 CGLT quadrants and that a minimum in the arc population was detected in the 1200–1800 quadrant. This effect is partially due to the uneven local time sampling through the winter months, but also to the lesser probability for arcs to be seen in the duskside as it is shown in Figure 11. The imager operated less hours in the 1200–1800 quadrant than in any of the other 6-hour sectors. Plate 1 shows that most of the arcs of the

0600–1200 quadrant have a negative offset angle (they are seen in blue or light blue), contrary to the arcs of the 1200–1800 quadrant, which are mostly depicted in red, orange, and yellow. The other two quadrants, 1800–2400 and 0000–0600 CGLT possess almost equal numbers of positive and negative rotations. There is a large number of arcs in the 0600–1200 quadrant between 80° and 85° CG latitude.

A more quantitative view of the arc orientation is presented in Figure 12. Here we plot 4 histograms each one corresponding to a CGLT quadrant. These histograms show the number of arcs binned according to the arc offset angle in steps of 2° . The histogram of 0600–1200 CGLT indicates that the arc offset angles cluster at the negative values, around a maximum of -8° . The center of gravity of this histogram is near -10° . The number of arcs in the 1200–1800 CGLT histogram is much less than in the 0600–1200 quadrant; nevertheless, it is possible to distinguish that the histogram bars group at the positive angles and near 16° . The center of

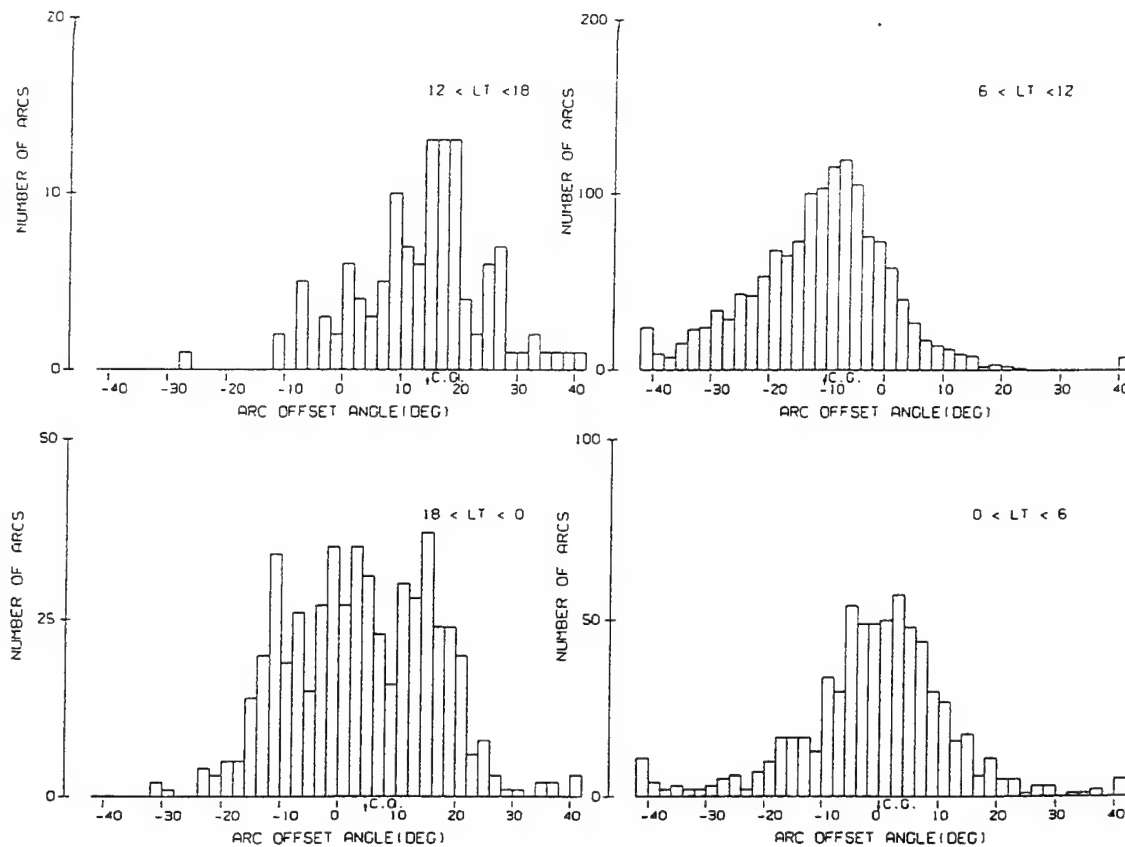


Figure 12. Histograms for the number of arcs plotted as a function of the arc offset angle. Each histogram corresponds to one CG local time quadrant. Notice the different scale that was used for each histogram. The histogram of 0600–1200 CGLT is displaced toward negative (duskward) rotations. The histogram of 1200–1800 CGLT presents mostly positive (dawnward) rotations.

gravity of this histogram is $+14^\circ$. The histograms of 1800–2400 and 0000–0600 CGLT have a center of gravity equal to $+4^\circ$ and $\sim 0^\circ$ respectively, they are symmetric with respect to an axis set near the center of gravity.

To determine the effect of the B_y component of the IMF on the distribution of the arc offset angle, the four histograms of Figure 12 were recalculated taking into consideration the sign of B_y . Figure 13 shows the number of arcs observed for B_y positive, Figure 14 for B_y negative. A careful comparison of the histograms corresponding to 1800–0000 and 0000–0600 CGLT of Figures 12, 13, and 14 suggests that the center of gravities remain almost unchanged irrespective of the sign of B_y . Nevertheless, the histograms for the other two quadrants (0600–1200 and 1200–1800 CGLT) show a small variation in their center of gravity. This feature is more easily seen in the histogram of 0600–1200 CGLT, which has a higher number of arcs and a better statistical significance. The B_y negative histogram shows a peak in the distribution displaced few degrees toward more positive values as compared to the peak of the histogram for B_y positive. The histograms for the 1200–1800 quadrant show also a displacement similar to the histogram corresponding to the 0600–1200 quadrant. We also generated histograms considering the sign of the other two components of the IMF. No significant differences were observed for either the shape or the center of gravity of the offset angle distributions.

3.3. Dusk-Dawn Arc Velocity

Figure 15 shows the distribution of the number of arcs versus the dusk-dawn velocity divided for each CGLT quadrant. The center of gravity corresponding to the four distributions vary between $\pm 40 \text{ m s}^{-1}$. The dawnside histograms show an average negative (duskward) velocity, and the dawnside histograms show a general positive (dawnward) arc motion. Being the dawnside arcs more numerous than the arcs in the other hemisphere, Figure 15 implies that an observer in space will more commonly observe arcs moving down to dusk than in the opposite direction.

In order to determine the control exerted by the B_y component of the IMF, the histograms of Figure 15 were splitted according to the sign of this component. Figures 16 and 17 present the distributions of the number of arcs for positive and negative values of B_y . In spite of the fact that the statistical significance is reduced for the 1200–1800 CGLT quadrant, the other three segments strongly suggest a B_y dependency of the dusk-dawn arc motion. The B_y control can be described as follows: the dawnside histograms (0000–0600 and 0600–1200 CGLT) of Figure 16 (B_y positive) show an average dusk-dawn motion equal to -120 m s^{-1} . In fact, most of the arc velocities have negative values, which indicates duskward motions. Contrary to this view, the histogram of 1800–2400 CGLT presents almost the same

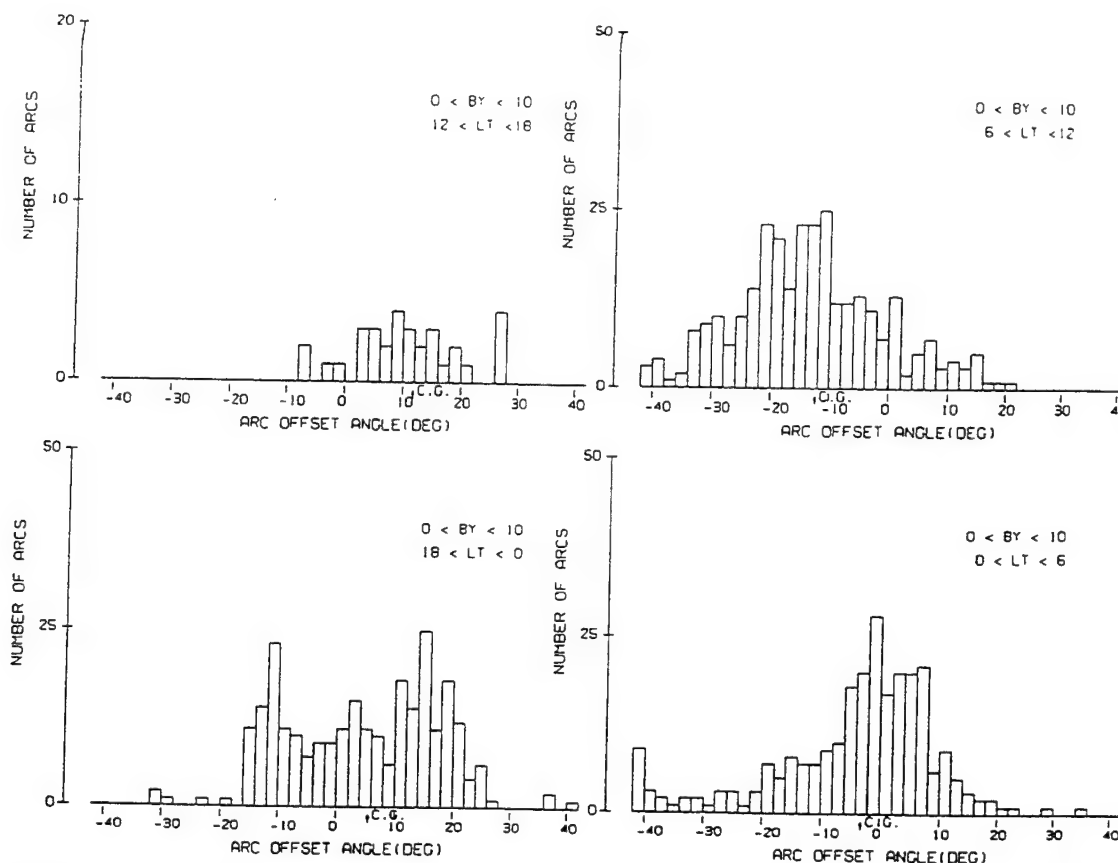


Figure 13. Same as Figure 12, but here only the arcs which occurred when B_y was larger than zero have been considered. The histograms corresponding to 0600–1200 CGLT show the same general characteristics of arc tilt angle that was observed in Figure 12.

number of arcs drifting toward dusk than toward dawn and a center of gravity near zero. The histograms of Figure 17 show a remarkably different behavior, they look like the mirror image of Figure 16. The dawnside histograms possess a center of gravity close to 0 m s^{-1} and the 1800–2400 CGLT histogram (up to some extent the 1200–1800 CGLT histogram) show a mean value equal to about 100 m s^{-1} . In summary, Figures 16 and 17 clearly point out that the polarity of B_y reverses the hemisphere, in which rapidly moving arcs are found, and the direction of motion of the polar cap arcs. A more refined analysis of the B_y dependency of the arc motion is presented in the next subsection.

3.4. Arc Motion-Location Versus IMF

Plate 2 shows the variability of both the arc velocity and the arc location versus the value of B_y in steps of 1 or 2 nT. We present the arcs that have downward velocities in red and the duskward moving arcs as blue arrows. The length of the arrows in these two figures follow the magnitude of the dusk-dawn velocity. Starting with the plot corresponding to $-6 < B_y < -4 \text{ nT}$ (upper left corner): the arcs moving downward (red) are seen to be located in the dusk hemisphere and covering a large part of the dawn hemisphere. They extend up to 82° of latitude in the dawn hemisphere. The magnitude of the velocity of the dawnward moving arcs shows a large variability, it changes as a function of the location of the arc in the polar cap. It is maximum and about 200 m s^{-1} in the far left side of the subframe, then diminishes near the pole and becomes approximately equal to 0 m s^{-1} at

the extreme dawn side of the plot. This behavior of the arc velocity suggests that the arcs slow down when they reach a boundary where the motion of the arcs changes from a dawnward to a duskward orientation. Examining the blue arrows in this frame indicates that most of the duskward moving arcs are located at the dawnside and equatorward of 84° in a region where almost no dawnward moving arcs are observed. Similar to the red arrows, the magnitude of the velocities are small near the boundary and larger further away from this line. We interpret that there is a velocity boundary that sets a demarcation line between the dawnward moving arcs (located to the left) and the duskward transiting arcs (situated to the right). The other subframes of panel 2 (left to right and top to bottom) show that as B_y becomes more positive the population of dawnward moving arcs results greatly reduced in the dawn hemisphere, it is replaced by duskward moving arcs. Concurrently with this, the velocity boundary seems to be shifted in the direction of B_y positive. For B_y positive values the location of duskward moving arcs covers not only the dawn hemisphere but also extends into the dusk hemisphere.

3.5. Miscellaneous Statistics

On the basis of the examination of 800 hours of data, we analyzed 1392 images of 2 min time resolution, measured with the 630.0-nm filter. In addition, an equal amount of 427.8-nm images were also tabulated. The average number of arcs per image that was observed by the Qaanaaq's ASIP during the winter of 1986–1987 was 2. The average lifetime of

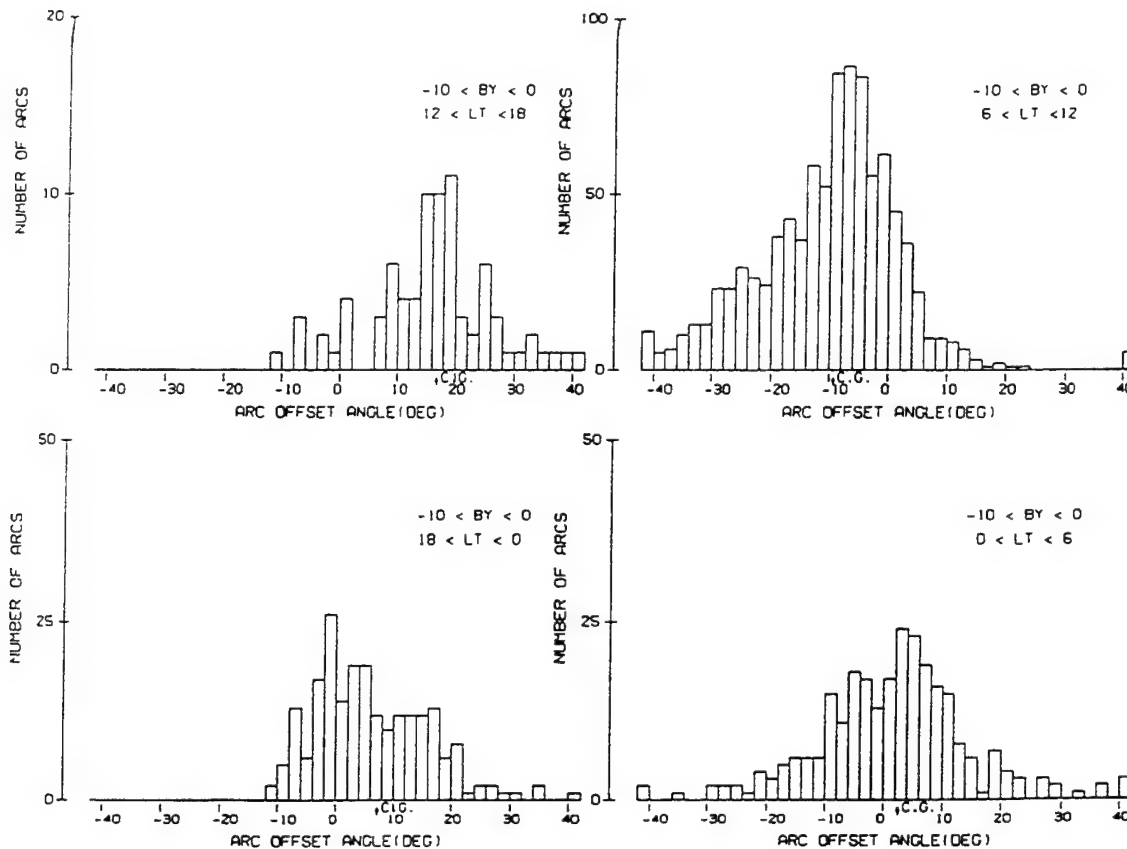


Figure 14. Same as Figure 12, but corresponding to negative values of B_z . The histograms of 0600–1200 and 1200–1800 CGLT show almost the same trend of Figure 12.

the polar cap arcs was 38 min, and the longest lasting arc was detected on December 5, 1986. This polar cap arc was inside the field of view for 3 hours and 46 min.

4. Discussion

4.1. Presence of Polar Cap Arcs

Previous studies of the morphology of polar cap aurora have consistently concluded that a northward oriented IMF favors the development of arcs inside the polar cap [Berkey *et al.*, 1976; Ismail *et al.*, 1977; Lassen and Danielsen, 1978] and a southward pointing IMF restrains the appearance of this type of arcs. The histograms presented here indicated that about 20% of the polar cap arcs were observed during times when the IMF was directed southward (allowing for solar wind propagation time from actual IMF sensing satellite to dayside magnetopause at 350 km s^{-1} , zero to less than 15 min). This apparent discrepancy can be reconciled if a proper consideration is taken of the time delay that the magnetosphere employs to fully reorganize from a northward IMF driven topology to a more southward IMF configuration.

To demonstrate that the “ B_z south” polar cap arcs are steady structures in a transitional state of the magnetospheric topology, we carefully selected all the arc events that were observed during B_z south conditions and tabulated the characteristics of B_z at these times. We found a total of 14 cases which had time intervals ranging in duration between 5 and 30 min. Close analysis of these events indicated that all the “ B_z south” arcs were preceded by unambiguous detec-

tions of polar cap arcs by the Qaanaaq’s ASIP, except for one occasion when the ASIP was not operating immediately before the IMF changed to a B_z negative value and there is no proof that polar cap arcs were absent prior to that reversal. Moreover, all of the “ B_z south” polar cap arcs, which we have analyzed occurred after prolonged periods of steady northward IMF.

Figure 18 shows two types of B_z transitions that were commonly observed during the winter of 1986–1987. One type of B_z transition, seen on five events, consists of a short negative excursion of the IMF B_z component. This is depicted in Figure 18a. The duration of these excursions was between 10 and 15 min and the behavior of the polar cap arcs at the time of B_z south was quite variable. The auroral emissions sometimes faded, in other instances they intensified, in one special case when the three components of the IMF changed sign simultaneously, the polar cap arcs evolved into semiclosed loops and finally in another case an arc fragmentation was observed. The other nine events showed a single transition from positive to negative as displayed in Figure 18b. The common characteristic of all of these events is the particular manner with which the arc fading progresses. The extreme of the arc closest to noon vanishes first and then the fading proceeds toward the midnight sector. A system of two or more polar cap arcs were seen on two of these nine events; in both cases the arc located further duskward died out first.

Thus the unexpected presence of polar cap arcs during southward orientations of the IMF can be understood in terms of the gradual evolution from one magnetospheric

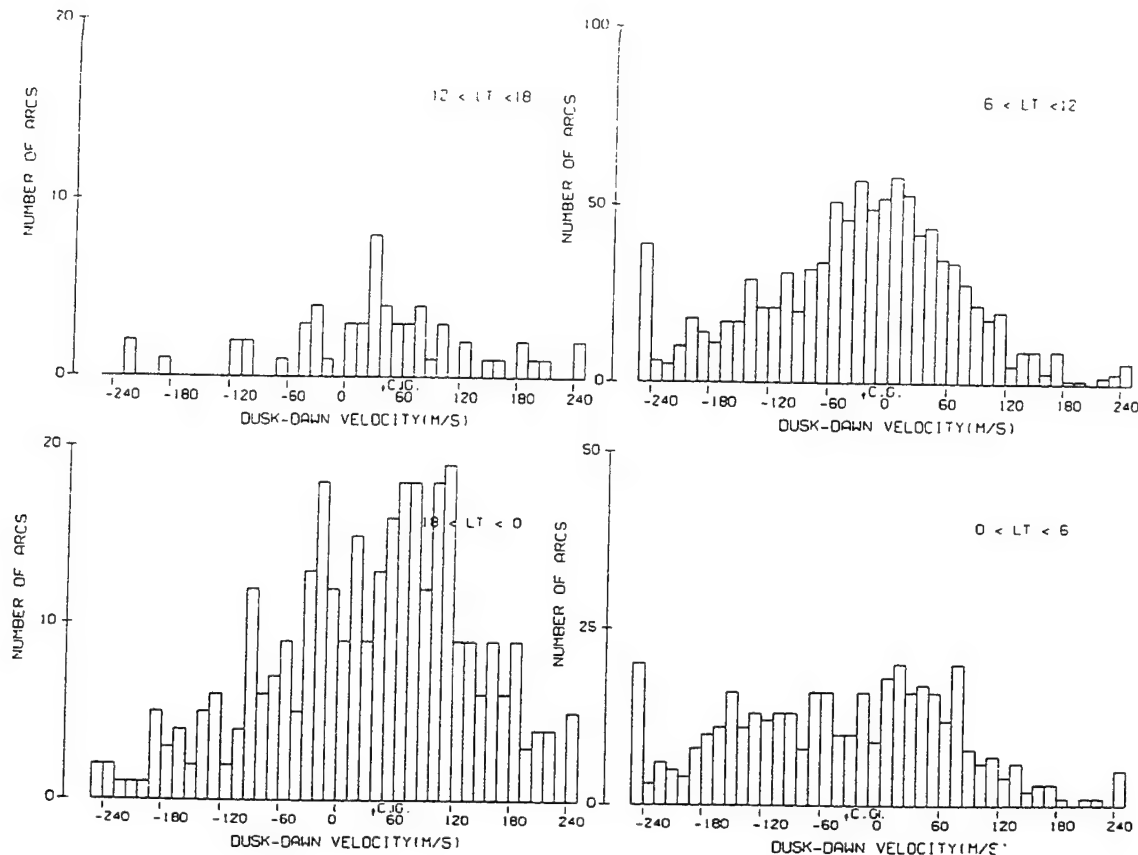


Figure 15. Same as Figure 12, but the histograms show the arc distribution as a function of the dusk-dawn velocity.

configuration into another, caused by the reversal of B_z . Knowing that it takes about 30 min for a solar wind disturbance to travel from the nose of the magnetopause up to the far regions of the magnetotail (for typical values of the solar wind velocity, say 300 km s^{-1}). Consequently, the information of a B_z reversal would not be expected to be communicated across the polar cap faster than the solar wind can carry this information. Thus we conclude that the maximum 30-min delay time between the negative B_z reversal and the complete disappearance of the polar cap arcs is due to the time that the IMF disturbance needs to propagate from the dayside magnetopause to the near-midnight part of the polar cap. This tailward region of the polar cap may still thread field lines connected to the old magnetic configuration that favor the flow of downgoing electrons, while other sunward regions of the polar cap may map to the new magnetic topology.

Another striking characteristic of polar cap arcs is the difference between the occurrence probability of the arcs located on the duskside versus the occurrence probability of the dawnside arcs. In this study we found a 40% (10%) probability of observing a polar cap arc in the dawn (dusk) hemisphere. This result is not in agreement with previous findings of Gussenhoven [1982] based on 1600 DMSP polar images. Gussenhoven found Sun-aligned arcs only a few percent of the time. We attribute this to the relatively weak DMSP sensitivity, allowing it to see only the most intense arcs, while our sensitivity threshold lets us detect a significantly larger representative sample. We thus look at the subset of DMSP passes for which arcs were detected.

Gussenhoven reported that 51% of the ~ 300 DMSP passes that detected high-latitude aurora contained arcs in the morning sector (her P2 category), but only 9% of the polar cap arcs were located on the evening sector (P3). Similarly, Rairden and Mende [1989], based on all-sky camera observations from the South Pole Station also measured that the dawnside Sun-aligned polar cap arcs outnumbered the dusk-side arcs by a ratio of 2:1. Lassen and Danielsen [1978] also found a strong preference for the polar cap arcs to be observed on the dawnside. The property of Sun-aligned polar cap arcs of being collocated with regions of intense velocity shears possessing convergent electric fields [Carlson et al., 1984; Hoffman et al., 1985; Mende et al., 1988; Weber et al., 1989; Valladares and Carlson, 1991] and upward flowing currents [Reiff et al., 1978] can be used to investigate whether or not the different convection patterns, reported in the literature also support a larger number of polar cap arcs in the dawnside. Zanetti et al. [1990] reported observations of a transpolar arc that was embedded on the dawn, clockwise rotating cell and collocated with a region of upward northward B_z (NBZ) Birkeland currents. The convection patterns presented by Potemra et al. [1984] and Reiff and Burch [1985] contained a region of convergent electric fields on the dawnside for both positive and negative values of B_y . Potemra et al. [1984] places a region of upward currents in the dawnside of the polar cap and the return downward currents on the duskside. The dusk cell of the Reiff and Burch model also contains a region of $\nabla \cdot \mathbf{E} < 0$, but only when $B_y > 0$. The convection patterns of Potemra et al. [1984] do not favor convergent E fields in the dusk cell for

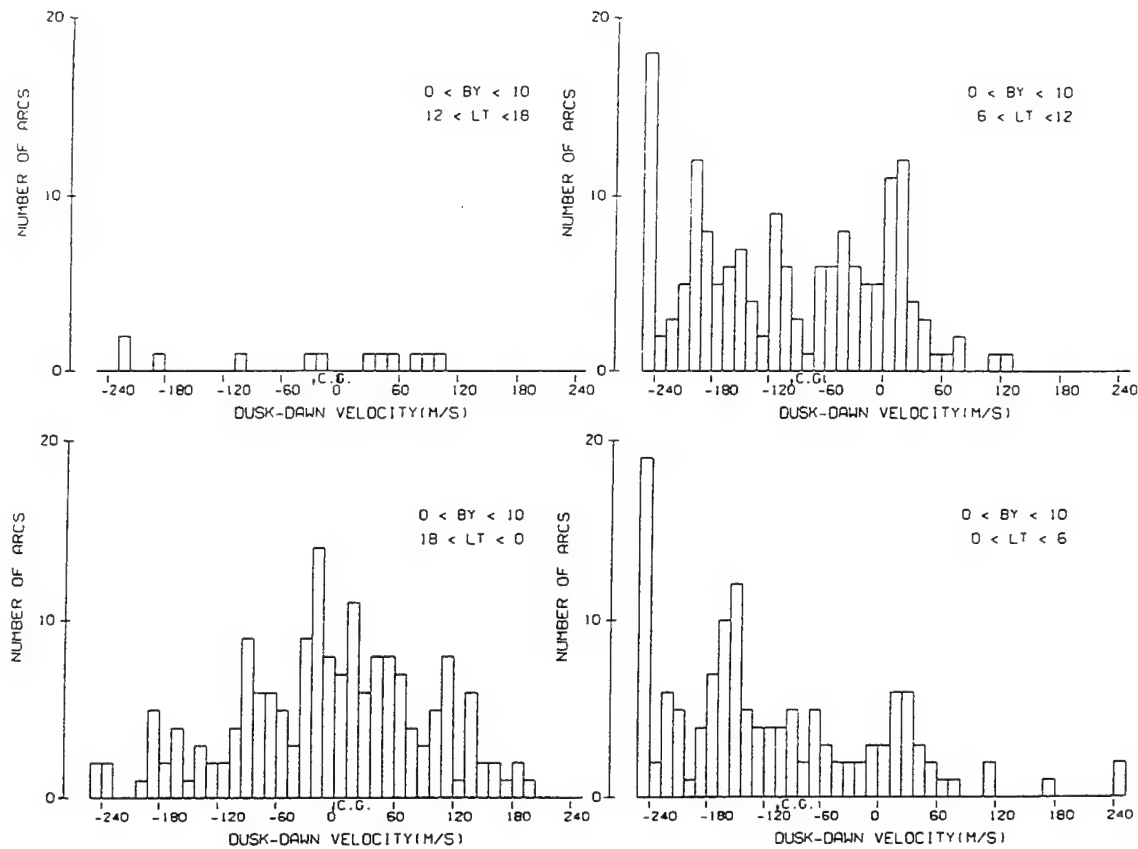


Figure 16. Same as Figure 12, but for dusk-dawn velocity distributions of polar cap arcs observed during $B_y > 0$ IMF conditions. Most of the arcs in the 0000–0600 and 0600–1200 CGLT quadrants display negative (duskward) velocities. The 1800–2400 CGLT quadrants histogram has a center of gravity near zero.

any value of B_y . In conclusion, both models favor a higher rate of arc occurrence on the dawn cell of the polar cap.

The 40% probability of observing one or more arcs in the dawnside of the polar cap well implies that the overall probability of having at least one arc within the polar cap is no less than 40%. The existence of a sensitivity threshold (tens of rayleighs) of the Qaanaaq's ASIP precludes stating conclusively that the dusk sector polar cap arcs were less numerous than their dawnside counterpart. It is possible that the dawn cell arcs are only brighter than the dusk cell polar cap arcs, and the duskside arcs are simply more difficult to detect. Remember that B_z is positive 50% of the time, while we have found that the overall arc occurrence probability is only 40%; this leaves a 10% deficit that could well be filled by less intense arcs that were not detected by the present sensitivity of the Qaanaaq's ASIP. Nonetheless, in contrast to previous studies that detected Sun-aligned arcs only a few percent of the time, this study is based on images collected by ASIPs with a low-sensitivity threshold (50 R).

Leaving statistical sampling uncertainties aside, we did not find a clear B_x , B_y , or B_z dependency on the side of the polar cap where the arcs were located. Previous studies of polar cap arcs using satellites have reported that B_y controls the side of the polar cap where arcs reside. During B_y positive conditions, high-latitude aurora are seen on the dusk sector [Murphree et al., 1982; Elphinstone et al., 1990]. While these studies concentrated on energetic transpolar arcs, our observations pertain more to weak polar cap F

region arcs, which are certainly more numerous than the transpolar arcs.

4.2. Orientation of Polar Cap Arcs

The near alignment of the polar cap arcs with respect to the Sun-Earth direction, their long extension spanning hundreds of kilometers and together with the well-accepted characteristic of Sun-aligned polar cap arcs to delineate regions of intense velocity shears [Carlson et al., 1988] can be used to infer properties of the convection cells in which the polar cap arcs are embedded.

The histograms of Figure 7a indicated that 99% of the polar cap arcs had a deviation less than 40° with respect to the Sun-Earth direction, and 87% of the total number of arcs presented orientations that were no more than 20° from the Sun-alignment direction. This fact puts some constraints on the shape and the alignment of the cells. The polar cap arcs could well be placed within the lobe cells presented by Reiff and Burch [1985] or in the dawn lobe cell of Potemra et al. [1984], subjected to small deformations in the noon-midnight alignment of the cells. However, the Heppner and Maynard [1987] patterns for B_z northward conditions, containing two largely distorted cells would predict the occurrence of arcs with much larger offset angles. Polar cap arcs located in the near noon region of the Heppner and Maynard convection pattern could easily reach offset angles near 90° . The polar cap arcs observed at Qaanaaq never presented such large offset angles.

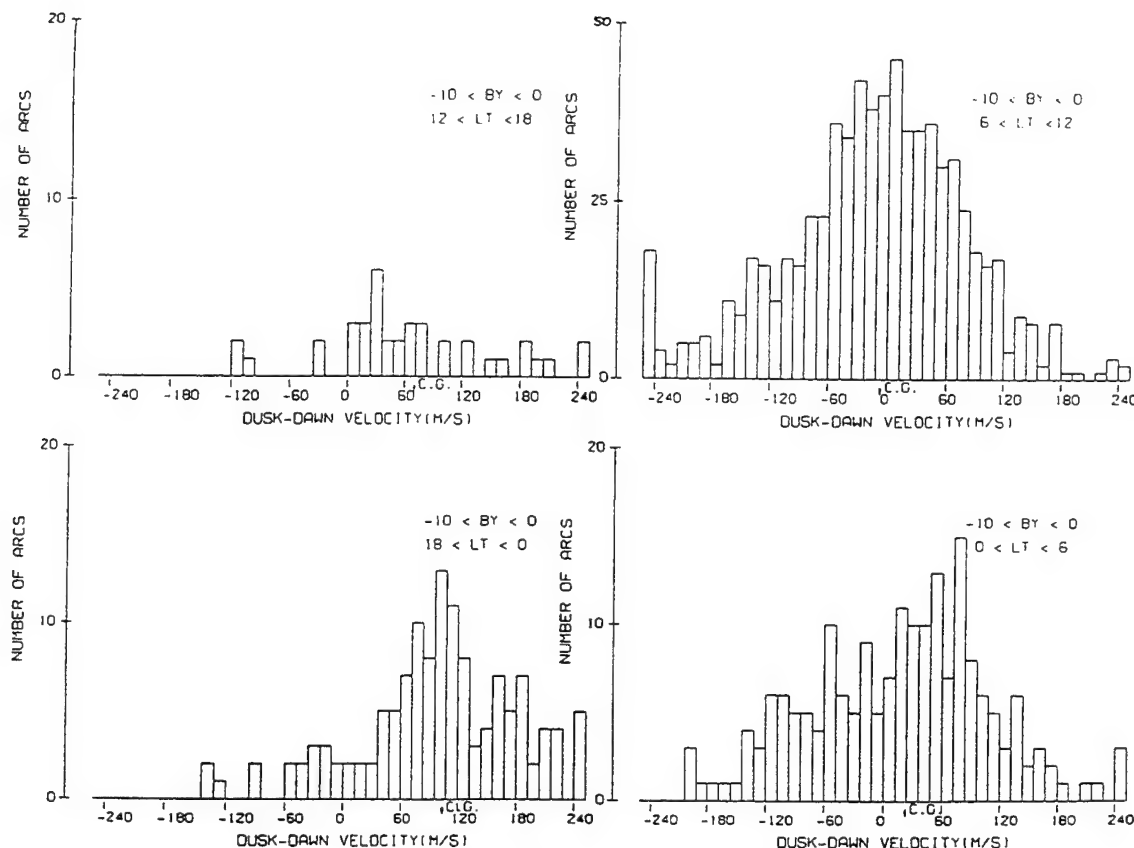


Figure 17. Same as Figure 12, but for B_y negative values. The histograms of the 0000–0600 and 0600–1200 CGLT quadrants have a center of gravity near zero. The other two sectors present arcs mainly moving downward.

The histograms of Figures 12 and also Figures 13 and 14 indicated that the arcs that were located at the 0600–1200 and 1200–1800 CGLT quadrants point toward noon and the arcs that populate the other two CGLT quadrants had an orientation that was randomly distributed around the Sun-alignment direction. When the arc orientation was binned according to the sign of B_y , we obtained that the histograms corresponding to the 0600–1200 CGLT quadrant were slightly skewed depending on the direction of B_y . The angle with respect to the Sun-alignment became larger for values of $B_y > 0$ and smaller for $B_y < 0$. This behavior can be understood if the polar cap arcs are pointing toward the cusp and the cusp displaces from noon according to the direction of B_y , as shown by Newell *et al.* [1989].

The polar cap arcs observed in the 1800–2400 and 0000–0600 CGLT sectors presented offset angle histograms with center of gravity near zero. These arcs do not seem to point toward a center location as the arcs located in the other two quadrants, which are directed toward the cusp.

4.3. Dusk-Dawn Motion of Polar Cap Arcs

Previous studies of the motion of the polar cap aurora have universally concluded that the motion of this type of arcs is in a direction perpendicular to the Sun–Earth line. Craven and Frank [1991] based on a few case studies of the theta aurora in the northern hemisphere noted that the central “bar” drifted in the dawn direction for a negative IMF B_y [Frank *et al.*, 1985] and in the dusk direction for a positive B_y value [Huang *et al.*, 1989]. Simultaneous optical

observations of transpolar arcs in both polar caps also indicated that the motion of the transpolar arc in the southern hemisphere was in opposite direction to the motion of the arcs in the northern polar cap [Craven *et al.*, 1991]. Rairden and Mende [1989] based on a statistical study of few polar cap arcs observed at the South Pole Station also presented a B_y dependency contrary to the north pole’s and in agreement with the observations of Craven *et al.* [1991]. Our statistical analysis of the dusk-dawn motion of the polar cap arcs have revealed that the arc motion depends on the sign and magnitude of the IMF B_y component and the location of the arc within the polar cap. Figure 19 clearly illustrates this arc motion for three distinct values of B_y .

The downward motion of the duskside polar cap arcs (and vice versa) has already been discussed in the literature, in the context of cell motions, by Reiff and Burch [1985]. These authors predicted the same sense of motion versus the sign of B_y , as experimentally observed. They also predicted that the motion of the southern hemisphere cells would be in the opposite direction. It was suggested by Reiff and Burch [1985] that for $B_y < 0$ open field lines will enter the polar cap in the duskside and equatorward of a channel of return sunward flow of closed field lines. Consequently, the closed field line region will move downward as the dusk cell size expands. For the $B_y > 0$ case the mirror image will occur. Our large database experimentally confirms this near the central polar cap, lending further validation to describing polar flow by this Reiff and Burch model.

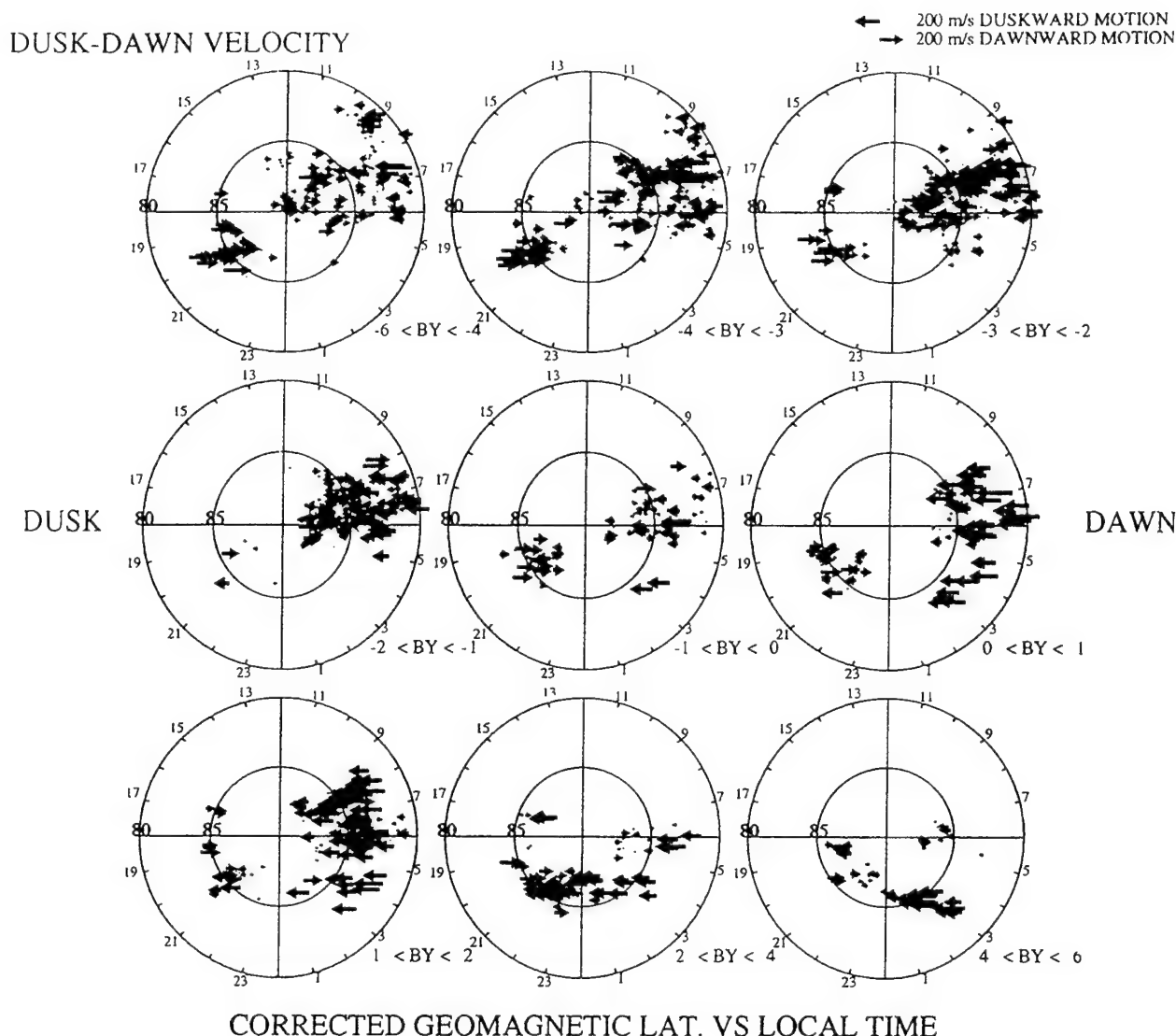


Plate 2. A series of polar plots showing the location within the polar cap of arcs moving toward dawn (red) and toward dusk (blue). The size of each arrow is proportional to the magnitude of the dusk-dawn velocity. The polar cap arcs moving downward (in red) populate most of the polar cap for large and negative values of B_y . As B_y becomes more positive, the location of arcs containing large downward velocities becomes more restricted to the dusk side. The location of the duskward moving arcs is opposite to the arcs moving toward dawn. In the upper left panel the arcs in blue, populate only the far dawnside but are detected in any place of the polar cap for large positive B_y values.

However, in this study we found that the motion depends also on the location of the arc within the polar cap. For a given value of IMF B_y the polar cap arcs can move duskward or dawnward depending upon whether the arcs are located in the dawn or dusk regions. Had prior studies looked simultaneously in opposite cells and away from the center of the polar cap, they would have seen arcs moving in opposite directions. Our findings are interpreted in the context of field lines being reconnected near midnight, producing an increase in the size of the auroral oval and a decrease of the polar cap. This is to say, for $B_y < 0$ then, field lines being closed near the midnight region will move sunward along the dawnside and will force open field lines located poleward to move duskward, in general the dawn cell and the arcs embedded within will be displaced toward dusk.

Our model also makes several predictions for the appearance of global auroral configurations such as the theta aurora [Frank *et al.*, 1982] and the horse collar aurora [Hones *et al.*, 1989]. For example, if B_y is near zero and steady for tens of minutes, two systems of polar cap arcs could move toward the central polar cap. One from the dawnside and the other from the duskside of the oval and start drifting toward the center. When the polar cap arcs are well apart from the oval they will form the two bars of the horse collar aurora configuration. When B_y is large in magnitude, either positive or negative only one arc system will move away from the oval and will be able to reach the center of the polar cap. This auroral configuration will resemble the theta auroral pattern. The model proposed here also predicts a shrinkage of the polar cap for any value of B_y and a consequent

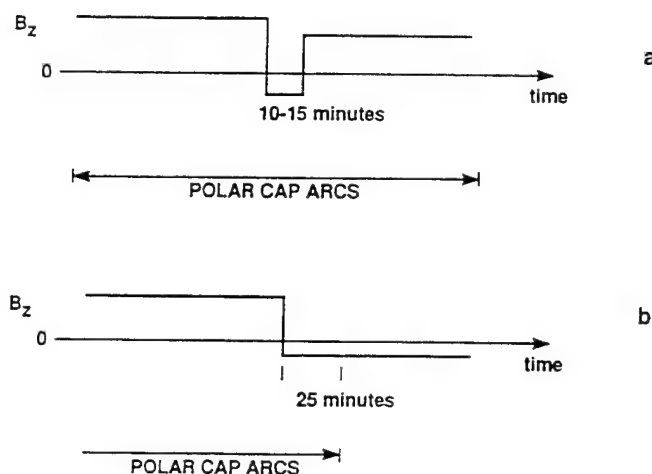
COMMON B_z TRANSITIONS DURING OCCURRENCE OF POLAR CAP ARCS

Figure 18. Schematic representation of common transitions of the Z component of the IMF and the occurrence of arcs in the polar cap.

expansion of the auroral oval. This is in accord with the oval expansion model.

4.4. Existence of Two or More Cells in the Polar Cap

Several characteristics of the polar cap arcs reported here seem to suggest that each of the arcs in a system of several arcs may be associated with an independent cell of plasma convection. The dusk-dawn velocities of Figure 6 for arcs 1 and 3 are not exactly equal but instead, it seems that there is a constant bias between the velocities plotted in Figures 6a and 6c. When two or more polar cap arcs were fading after a B_z reversal, they did not disappear simultaneously, one arc vanished completely before the other arc started fading.

At the present time we feel that more questions may have emerged and only few answers have been proposed here. We hope that the analysis of the vast database that has been accumulated between the years 1987 and 1992 for all three

high-latitude stations and correlative studies with other sensors, such as the instrumentation on-board the DMSP satellites or ground-based digisondes will help us to understand the physics of the polar cap arcs.

5. Conclusions

This study has led to the following:

1. In agreement with findings reported by other researchers, more polar cap arcs were seen, above the sensitivity threshold of the images (several tens of rayleighs), on the dawnside (40% probability) than on the duskside (10%). This large difference in the observed occurrence of polar cap arcs may follow from the convergent/divergent nature of the electric fields that are usually encountered in the polar cap during B_z north values of the IMF. The dawn cell has been generally described as a region of convergent \mathbf{E} fields, that

DUSK-DAWN MOTION OF POLAR CAP ARCS

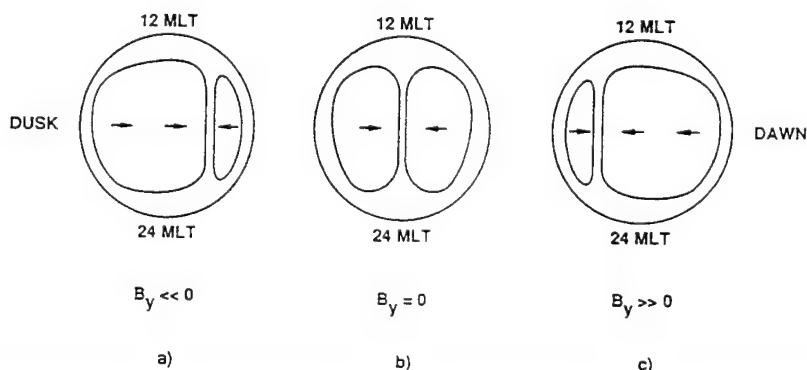


Figure 19. Schematic representation of the relative location of the arcs within the polar cap and their corresponding dusk-dawn motion for three different values of B_y . (a) $B_y \ll 0$, (b) $B_y = 0$, and (c) $B_y \gg 0$.

contain upward Birkeland currents. This fact facilitates the flow of more intense electron fluxes, thereby generating brighter auroral emissions. Contrary to this, the dusk cell has been classified as a region of downward currents which are not conducive to intense precipitation. The overall probability of observing an arc in the polar cap was found to be at least 40% (for a threshold of several tens of rayleigh in 630 nm).

2. As expected, the probability of detecting a polar cap arc was found to depend strongly on the value of B_z . This probability becomes large when B_z is positive, and increases for larger B_z . It sharply diminishes during negative values of B_z . Unexpectedly, we found that about 20% of the total number of the polar cap arcs observed during the winter of 1986–1987 occurred under B_z south conditions. However, inspection showed that these arcs developed after prolonged periods of northward B_z , and followed steady displays of B_z north generated Sun-aligned polar cap aurora. We interpret the 30-min delay between the B_z reversal and the disappearance of the polar cap arcs, as the time needed for the magnetosphere to complete reconfiguration into a B_z south topology, that is, the time for the IMF change to propagate from the dayside magnetopause to the near midnight region.

3. When we looked at all arcs visible to our imagers, we found a very weak dependence of the location of the arcs within the polar cap, on either the B_x or the B_y components of the IMF. However, there is a significant B_y dependence of the dawn-dusk direction of motion of the arc. Therefore it must follow that if B_y maintains a fixed sign for an extended period of time (order an hour), the arc must shift to a favored hemisphere (e.g., duskside for $B_y > 0$). It is in such cases that the arcs become sufficiently intense ($> kR$) that they are visible from space or conventional all-sky cameras. Because satellites only see the few brightest arcs, they would get the impression of a stronger B_y dependence.

4. The polar cap arcs which were observed in the 0600–1200 and 1200–1800 CGLT quadrants presented a small offset angle with respect to the Sun-Earth line. The offset angles are such that the arcs in both quadrants tilt toward the cusp. In addition, there is a small, but detectable variation of the arcs orientation with B_y . We interpret this latter modest rotation as a displacement of the cusp region in magnetic local time coordinates.

5. Polar cap arcs observed in the 0000–0600 and 1800–2400 CGLT were Sun-aligned, with no detectable dependence on B_y .

6. Polar cap arcs located at the dawnside “cell” were observed to move duskward and the arcs situated at the duskside cell moved toward dawn. However, the size of the cells was found to depend on the magnitude and sign of B_y . Temporal variations in the X or Y components of the IMF, ($\partial B_x / \partial t$ and $\partial B_y / \partial t$), do not seem to affect the arc motion. It is suggested here that the arc motion is the result of the entrance of open flux tubes into the polar cap ionosphere/magnetosphere, producing a general displacement of the cells and consequently of the arcs which are embedded within the convection cells.

7. Following the line of reasoning of Reiff and Burch [1985], but guided by the additional data base of our time continuous polar photometric images, we postulate polar plasma circulation for northward IMF that leads to a persistent forcing of open and closed field lines poleward from both the dawn and dusk regions. For $B_y < 0$ field lines open

into a dusk cell forcing a dawnward motion of shear lines in a growing dusk cell, concurrently field lines close near midnight forcing a duskward displacement of shear lines in a residual dawn cell. For $B_y > 0$ the mirror image situation will occur. This simple model can provide the behavior of the 150 Sun-aligned stable polar cap arcs we have used as the basis of this statistical study, as well as “theta” aurora [Frank et al., 1986] and the teardrop-shaped aurora [Meng, 1981a; Murphree et al., 1982], also called a horse collar aurora [Hones et al., 1989].

Acknowledgments. We thank R. Lepping for making the IMF data available for this study and C. Russell and the National Space Science Data Center for supplying the ISEE 2 fluxgate magnetometer data. One of the authors (C.E.V.) wishes to acknowledge helpful discussions with Pat Reiff. The work at Boston College was supported by Phillips Laboratory contract F19628-90-K-0007, NSF grant ATM-9016465, and NASA grant NAG5-1544. We thank the Danish Commission for Scientific Research in Greenland for permission to conduct ground experiments at Qaanaaq under continuing project A16-91.

The Editor thanks R. A. Hoffman and another referee for their assistance in evaluating this paper.

References

- Akasofu, S.-I., Midday auroras and polar cap auroras, *Geophys. Publ.*, 29, 73, 1972.
- Berkey, T., L. L. Cogger, S. Ismail, and Y. Kamide, Evidence for a correlation between Sun-aligned arcs and the interplanetary magnetic field direction, *Geophys. Res. Lett.*, 3, 145, 1976.
- Buchau, J., B. W. Reinisch, E. J. Weber, and J. G. Moore, Structure and dynamics of the winter polar cap F region, *Radio Sci.*, 6, 995, 1983.
- Burch, J. L., N. A. Saflekos, D. A. Gurnett, J. D. Craven, and L. A. Frank, The quiet time polar cap: DE 1 observations and conceptual model, *J. Geophys. Res.*, 97, 19,403, 1992.
- Burke, W. J., M. S. Gussenhoven, M. C. Kelley, D. A. Hardy, and F. J. Rich, Electric and magnetic field characteristics of discrete arcs in the polar cap, *J. Geophys. Res.*, 87, 2431, 1982.
- Carlson, H. C., V. B. Wickwar, E. J. Weber, J. Buchau, J. G. Moore, and W. Whiting, Plasma characteristics of polar cap F -layer arcs, *Geophys. Res. Lett.*, 11, 895, 1984.
- Carlson, H. C., R. A. Heelis, E. J. Weber, and J. R. Sharber, Coherent mesoscale convection patterns during northward interplanetary magnetic field, *J. Geophys. Res.*, 93, 14,501, 1988.
- Craven, J. D., and L. A. Frank, Diagnosis of auroral dynamics using global auroral imaging with emphasis on large-scale evolution, in *Auroral Physics*, p. 273, edited by C.-I. Meng, M. J. Rycroft, and L. A. Frank, Cambridge University Press, New York, 1991.
- Craven, J. D., J. S. Murphree, L. A. Frank, and L. L. Cogger, Simultaneous optical observations of transpolar arcs in the two polar caps, *Geophys. Res. Lett.*, 18, 2297, 1991.
- Crooker, N. U., Dayside merging and cusp geometry, *J. Geophys. Res.*, 84, 951, 1979.
- Danielsen, C., Auroral observations at Thule 1961–65, *Geophys. Pap. R-9*, Dan. Meteorol. Inst., Charlottenlund, Denmark, 1969.
- Davis, T. N., The morphology of the polar aurora, *J. Geophys. Res.*, 65, 3497, 1960.
- Davis, T. N., Negative correlation between polar-cap visual aurora and magnetic activity, *J. Geophys. Res.*, 68, 4447, 1963.
- Denholm, J. V., and F. R. Bond, Orientation of polar auroras, *Aust. J. Phys.*, 14, 193, 1961.
- Elphinstone, R. D., K. Jankowska, J. S. Murphree, and L. L. Cogger, The configuration of the auroral distribution for interplanetary magnetic field B_z northward, 1. IMF B_x and B_y dependencies as observed by the Viking satellite, *J. Geophys. Res.*, 95, 5791, 1990.
- Frank, L. A., J. D. Craven, J. L. Burch, and J. D. Winningham, Polar views of the Earth's aurora with Dynamic Explorer, *Geophys. Res. Lett.*, 9, 1001, 1982.
- Frank, L. A., J. D. Craven, and R. L. Rairden, Images of the

- Earth's aurora and geocorona from the Dynamics Explorer mission, *Adv. Space Res.*, 5, 53, 1985.
- Frank, L. A., et al., The theta aurora, *J. Geophys. Res.*, 91, 3177, 1986.
- Gussenhoven, M. S., Extremely high latitude auroras, *J. Geophys. Res.*, 87, 2401, 1982.
- Gussenhoven, M. S., and E. G. Mullen, Simultaneous relativistic electron and auroral particle access to the polar caps during interplanetary magnetic field B_z northward: A scenario for an open field-line source of auroral particles, *J. Geophys. Res.*, 94, 17,121, 1989.
- Hallinan, T. J., and T. N. Davies, Small scale auroral arc distortions, *Planet. Space Sci.*, 18, 1735, 1970.
- Hardy, D. A., Intense fluxes of low-energy electrons at geomagnetic latitudes above 85° , *J. Geophys. Res.*, 89, 3883, 1984.
- Hardy, D. A., W. J. Burke, and M. S. Gussenhoven, DMSP optical and electron measurements in the vicinity of polar cap arcs, *J. Geophys. Res.*, 87, 2413, 1982.
- Heppner, J. P., and N. C. Maynard, Empirical high-latitude electric field models, *J. Geophys. Res.*, 92, 4467, 1987.
- Hoffman, R. A., R. A. Heelis, and J. S. Prasad, A sun-aligned arc observed by DMSP and AE-C, *J. Geophys. Res.*, 90, 9697, 1985.
- Hones, E. W., Jr., J. D. Craven, L. A. Frank, D. S. Evans, and P. T. Newell, The horse-collar aurora: A frequent pattern of the aurora in quiet times, *Geophys. Res. Lett.*, 16, 37, 1989.
- Huang, C. Y., L. A. Frank, W. K. Peterson, D. J. Williams, W. Lennartsson, D. G. Mitchell, R. C. Elphic, and C. T. Russell, Filamentary structures in the magnetotail lobes, *J. Geophys. Res.*, 92, 2349, 1987.
- Huang, C. Y., J. D. Craven, and L. A. Frank, Simultaneous observations of a theta aurora and associated magnetotail plasmas, *J. Geophys. Res.*, 94, 10,137, 1989.
- Ismail, S., D. D. Wallis, and L. L. Cogger, Characteristics of polar cap Sun-aligned arcs, *J. Geophys. Res.*, 82, 4741, 1977.
- Jankowska, K., R. D. Elphinstone, J. S. Murphree, L. L. Cogger, D. Hearn, and G. Marklund, The configuration of the auroral distribution for interplanetary magnetic field B_z northward, 2, Ionospheric convection consistent with Viking observations, *J. Geophys. Res.*, 95, 5805, 1990.
- Kan, J. R., and W. J. Burke, A theoretical model of polar cap auroral arcs, *J. Geophys. Res.*, 90, 4171, 1985.
- Lassen, K., On the classification of high-latitude auroras, *Geophys. Publ.*, 29, 87, 1972.
- Lassen, K., and C. Danielsen, Quiet time pattern of auroral arcs for different directions of the interplanetary magnetic field in the Y-Z plane, *J. Geophys. Res.*, 83, 5277, 1978.
- Lundin, R., L. Eliasson, and J. S. Murphree, The quiet-time aurora and the magnetospheric configuration, in *Auroral Physics*, edited by C.-I. Meng, M. J. Rycroft, and L. A. Frank, p. 159, Cambridge University Press, New York, 1991.
- Marklund, G. T., et al., On the electrodynamic state of the auroral ionosphere during northward interplanetary magnetic field: A transpolar arc case study, *J. Geophys. Res.*, 96, 9567, 1991.
- Mawson, D., Auroral observations at the Cape Royds Station, Antarctica, *Trans. Proc. R. Soc. S. Aust.*, XL, 151, 1916.
- Mawson, D., Australasian Antarctic expedition 1911-1914, *Sci. Rep., Ser. B*, vol. II, part I, records of the Aurora Polaris, Sydney, Australia, 1925.
- Mende, S. B., J. H. Doolittle, R. M. Robinson, R. R. Vondrak, and F. J. Rich, Plasma drifts associated with a system of Sun-aligned arcs in the polar cap, *J. Geophys. Res.*, 93, 256, 1988.
- Meng, C.-I., Polar cap arcs and the plasma sheet, *Geophys. Res. Lett.*, 8, 273, 1981a.
- Meng, C.-I., The auroral electron precipitation during extremely quiet geomagnetic conditions, *J. Geophys. Res.*, 86, 4607, 1981b.
- Meng, C.-I., and B. H. Mauk, Global auroral morphology, *U.S. Natl. Rep. Int. Union Geod. Geophys. 1987-1990, Rev. Geophys.*, 29, 1028, 1991.
- Menietti, J. D., and J. L. Burch, DE-1 observations of theta aurora plasma source regions and Birkeland current charge carriers, *J. Geophys. Res.*, 92, 7503, 1987.
- Mitchell, D. G., F. Kutchko, D. J. Williams, T. E. Eastman, L. A. Frank, and C. T. Russell, An extended study of the low-latitude boundary layer of the dawn and dusk flanks of the magnetosphere, *J. Geophys. Res.*, 92, 7395, 1987.
- Mizera, P. F., D. J. Gorney, and D. S. Evans, On the conjugacy of the aurora: High and low latitudes, *Geophys. Res. Lett.*, 14, 190, 1987.
- Murphree, J. S., C. D. Anger, and L. L. Cogger, The instantaneous relationship between polar cap and oval auroras at times of northward interplanetary magnetic field, *Can. J. Phys.*, 60, 349, 1982.
- Newell, P. T., C.-I. Meng, D. G. Sibeck, and R. Lepping, Some low-altitude cusp dependencies on the interplanetary magnetic field, *J. Geophys. Res.*, 94, 8921, 1989.
- Nielsen, E., J. D. Craven, L. A. Frank, and R. A. Heelis, Ionospheric flows associated with a transpolar arc, *J. Geophys. Res.*, 95, 21,169, 1990.
- Obara, T., M. Kitayama, T. Mukai, N. Kaya, J. S. Murphree, and L. L. Cogger, Simultaneous observations of Sun-aligned polar cap arcs in both hemispheres by EXOS-C and Viking, *Geophys. Res. Lett.*, 15, 713, 1988.
- Potemra, T. A., L. J. Zanetti, P. F. Bythrow, A. T. Y. Lui, and T. Iijima, B_y -dependent convection patterns during northward interplanetary magnetic field, *J. Geophys. Res.*, 89, 9753, 1984.
- Rairden, R. L., and S. B. Mende, Properties of 6300-Å auroral emissions at the south pole, *J. Geophys. Res.*, 94, 1402, 1989.
- Reiff, P. H., and J. L. Burch, IMF B_y -dependent dayside plasma flow and Birkeland currents in the dayside magnetosphere, 2, A global model from northward and southward IMF, *J. Geophys. Res.*, 90, 1595, 1985.
- Reiff, P. H., J. L. Burch, and R. A. Heelis, Dayside auroral arcs and convection, *Geophys. Res. Lett.*, 5, 391, 1978.
- Sojka, J. J., W. J. Raitt, and R. W. Schunk, Effect of displaced geomagnetic and geographic poles on high-latitude plasma convection and ionospheric depletions, *J. Geophys. Res.*, 84, 5943, 1979.
- Valladares, C. E., and H. C. Carlson, Jr., The electrodynamic, thermal, and energetic character of intense Sun-aligned arcs in the polar cap, *J. Geophys. Res.*, 96, 1379, 1991.
- Weber, E. J., and J. Buchau, Polar cap F-layer auroras, *Geophys. Res. Lett.*, 8, 125, 1981.
- Weber, E. J., J. Buchau, J. G. Moore, J. R. Sharber, R. C. Livingston, J. D. Winningham, and B. W. Reinisch, F layer ionization patches in the polar cap, *J. Geophys. Res.*, 89, 1683, 1984.
- Weber, E. J., et al., Rocket measurements within a polar cap arc: Plasma, particle, and electric circuit parameters, *J. Geophys. Res.*, 94, 6692, 1989.
- Weill, G., Aspects de l'aurore observée à la base Dumont-d'Urville en Terre Adélie, *C. R. Acad. Sci.*, 246, 2925, 1958.
- Zanetti, L. J., T. A. Potemra, R. E. Erlandson, P. F. Bythrow, B. J. Anderson, J. S. Murphree, and G. T. Marklund, Polar region Birkeland current, convection, and aurora for northward interplanetary magnetic field, *J. Geophys. Res.*, 95, 5825, 1990.

H. C. Carlson Jr. and K. Fukui, Phillips Laboratory, Geophysical Directorate, Hanscom Air Force Base, MA 01731. (e-mail: SPAN.afgl::carlsonh; SPAN.afgl::fukui)
C. E. Valladares, Institute for Space Research, Boston College, Newton, MA 02159. (e-mail: SPAN.afgl::cesar)

(Received March 24, 1993; revised September 29, 1993; accepted November 10, 1993.)

The U.S. Government is authorized to reproduce and sell this report.
Permission for further reproduction by others must be obtained from
the copyright owner.

Model-observation comparison study of multiple polar cap arcs

L. Zhu, C. E. Valladares,¹ J. J. Sojka, R. W. Schunk, and D. J. Crain

Center for Atmospheric and Space Science, Utah State University, Logan

Abstract. A quantitative model-observation comparison of multiple polar cap arcs has been conducted by using a time-dependent theoretical model of polar cap arcs. In particular, the electrodynamic features of multiple polar cap arcs with various spacings are simulated and the results are compared with the images obtained from the All-Sky Intensified Photometer at Qaanaaq. The results show that the observed and simulated arcs are quite similar, both spatially and temporally. The results support the theory proposed by Zhu *et al.* [1993a, 1994b] that the structure of polar cap arcs is mainly determined by the magnetosphere-ionosphere (M-I) coupling processes and that the spacing of multiple polar cap arcs is closely related to the hardness of the primary magnetospheric precipitation. It is found that for the multiple polar cap arcs with both narrow and wide spacings, the associated field-aligned currents are mainly closed by Pedersen currents. It is also found that a hard precipitation can lead to a highly structured secondary arc because of the nonlinear M-I coupling processes.

1. Introduction

Polar cap arcs are the auroral arcs seen at very high geomagnetic latitudes ($> 80^\circ$) that extend from 100 km up to the size of the whole polar cap and that are aligned parallel to the Sun-Earth direction [Davis, 1960; Nielson *et al.*, 1990]. The arcs are mainly observed during northward interplanetary magnetic field (IMF) and quiet magnetic conditions. Some of the arcs are very bright and luminous and cross the entire polar cap from the dayside to the nightside of the auroral oval to form a pattern that resembles the Greek letter "theta" [Frank *et al.*, 1986; Nielsen *et al.*, 1990]. Other arcs are confined to the polar cap and are relatively weak, and these tend to be either in the evening or morning sectors of the polar cap [Weber and Buchau, 1981; Carlson *et al.*, 1984; Rich *et al.*, 1990]. Some observations suggest that the Sun-aligned arcs at high latitudes are in regions of open field lines because polar rain electrons are sometime observed adjacent to and outside of the arcs [Hardy *et al.*, 1982]. However, in other observations, the precipitating electrons have the characteristics of the plasma sheet or plasma sheet boundary layer, suggesting that the arcs are on closed field lines [Peterson and Shelley, 1984; Obara *et al.*, 1988]. It has been confirmed by many observations that the arcs are associated with upward field-aligned currents carried by energetic precipitating electrons, with the energy range extending from a few hundred eV to a few keV [Hardy *et al.*, 1982; Valladares and Carlson, 1991].

More recently, a series of campaigns conducted under the auspices of the CEDAR High Latitude Plasma Structure (HLPS) Working Group have accumulated a wealth of new information on polar cap arcs and have extended our observations from the

large-scale, steady state features to the more dynamical, mesoscale features of polar cap arcs. The new observations have provided information on, for example, the dawn-dusk motion and the multiple fine structure of polar cap arcs [Valladares *et al.*, 1994], the sudden rotation of the adjacent convection prior to the breakup of polar cap arcs [Berg, 1992], and the field-aligned depletions of *F* region plasma [Doe *et al.*, 1992].

Compared to the observations, theoretical studies of polar cap arcs, especially quantitative studies, are still in an early stage. On the basis of S3-2 data, Burke *et al.* [1982] proposed a model for polar cap arcs that occur on open field lines. By introducing the concept of a multiple bifurcation of magnetic field lines, Kan and Burke [1985] constructed a model of polar cap arcs and proposed that theta aurora can occur on closed field lines and that the less intense polar cap arcs can occur either on closed or open field lines. More recently, Chiu [1989] formulated a model in which polar cap arcs are assumed to be on open field lines, and he showed that the formation of polar cap arcs is due to the current response to a mesoscale velocity shear structure in the ionosphere. Because these theoretical models are either qualitative, semiquantitative, or steady state models, they cannot be used to study the dynamical features associated with both the temporal evolution and the fine spatial structure of polar cap arcs. Also, these models cannot be used in a detailed quantitative comparison with observations, which is essential for furthering our understanding of the dynamics of polar cap arcs.

Recently, we have conducted a series of polar cap arc studies using a time-dependent magnetosphere-ionosphere (M-I) coupling model [Zhu *et al.*, 1993a, b; Sojka *et al.*, 1994; Zhu *et al.*, 1994a, b]. These studies have provided satisfactory "theoretical" explanations for a number of important issues concerning polar cap arcs, which include the active role of the ionosphere for the formation of the arcs, the appearance of multiple arcs, and the physical parameters determining the spacing of multiple arcs.

In this paper, we present the results obtained in a detailed quantitative comparison of the M-I coupling model with

¹Institute for Space Research, Boston College, Newton, Massachusetts.

were taken and about 30% of them have polar cap arcs. Among the images having polar cap arcs, at least 80% of them show the multiple arc structures. The development of multiple polar cap arcs is quite dynamical. In about 85% cases of multiple polar cap arcs, the arcs with a multiple structure did not appear simultaneously. It is quite common that new arcs develop near the arc that appear in a early time to form multiple structures. The locations of individual arcs are not spatially stable, and they typically move in a dawn-dusk direction with a speed that ranges from tens of meters per second to several hundred meters per second. The typical spacing of the structured arcs can range from tens of kilometers to a few hundred kilometers. This paper is not to touch the details of the above statistical features of multiple polar cap arcs. Instead, we choose two typical cases of multiple arcs based on the above statistical results and perform model-observation comparison study to test the model predictions and reveal more dynamical features of the arcs.

Figure 1 shows an image taken by the all-sky camera at Qaanaaq at 0826 UT, November 12, 1990. Clearly, the polar cap arcs are structured and the edge-to-edge spacing (the width of the dark region between two arcs) is found to be about 40 km. These polar cap arcs are not the transpolar arcs, instead, they are localized and confined to the morning sector of the polar cap.

3. Theoretical Model

The modeling of multiple polar cap arcs was conducted by using the time-dependent M-I coupling model developed by Zhu *et al.* [1993a]. The mathematical formulation of the model will not be discussed in this paper and the interested readers are referred to the Zhu *et al.* [1993a] paper. A key feature of this M-I coupling model of polar cap arcs is that the arcs are not treated as phenomena merely controlled by the magnetosphere, with the ionosphere only acting as a passive load. Instead, the polar cap arcs are treated as the processes that are coherently determined by the dynamics in both the ionosphere and magnetosphere.

Initially, a magnetospheric shear flow carried by Alfvén waves propagates towards the ionosphere. The significance of the assumed initial magnetospheric shear flow in the model has been discussed by Zhu *et al.* [1993a] and is not repeated here. The downward propagating Alfvén waves are partially reflected from the ionosphere and then bounce back and forth between the ionosphere and magnetosphere. The nature of the wave reflections depends on both the conditions in the ionosphere and magnetosphere. The propagating Alfvén waves carry both upward and downward field-aligned currents. The precipitating electrons associated with upward field-aligned currents enhance the conductivity in the ionosphere. The modified ionospheric conductivity launches secondary Alfvén waves towards the magnetosphere. The upward propagating Alfvén waves, which consist of the reflected waves and the secondary Alfvén waves launched by the temporal change of the ionospheric conductivity, carry the ionospheric information back to the magnetosphere, thus reflecting the active ionospheric role in the dynamics of the M-I coupling process. The whole process is transient, during which all physical quantities in the ionosphere change self-consistently in time, and subsequently, polar cap arcs develop. Because of the finite conductivity in the ionosphere, the temporal variation of the Alfvén waves in the coupled M-I

system diminishes with time, and the M-I system, as well as the development of polar cap arcs, approach an asymptotic steady state after several bounce periods.

One important issue that need to be addressed here is the treatment of the relationship between the Alfvén waves and the conductivity enhancement caused by precipitations. Due to the great variation of the Alfvén speed along the magnetic field lines, the resonance between the precipitating particles and the Alfvén waves may not be able to sustain all the time. To avoid the complicated wave-particle interaction component in the model, we use the following simplified approach to tackle the issue. On the basis of MHD theory, enhanced E field associated with Alfvén waves leads to an enhanced field-aligned current. By assuming a linear relationship [Fridman and Lemair, 1980], we connect the upward field-aligned current and the field-aligned potential drop. The increasing potential drop along magnetic field lines causes the energization of the current carriers (we assume mainly electrons). By using continuity equation, we treat the conductivity enhancement caused by the energized precipitating electrons. In the reality, the picture for the connection between the Alfvén waves and the resulted conductivity enhancement could be much more complicated.

The ionosphere is treated as a two-dimensional slab with an integrated conductivity. The X axis measures the noon-midnight dimension and points to the dayside, and the Y axis measures the dawn-dusk dimension and points to the duskside. The magnetosphere is a two-dimensional pseudoplane that is used as a boundary for the reflection of Alfvén waves. The magnetosphere and ionosphere are connected by magnetic field lines which are assumed to be perpendicular to the ionosphere. The communication between the magnetosphere and ionosphere is characterized by the bouncing of Alfvén waves between the two regions, and both the upward and downward field-aligned currents are associated with the propagating Alfvén waves. Initially, the large-scale ionospheric convection and conductivity are specified. These large-scale patterns are consistent with the overall solar, geomagnetic, and IMF conditions.

Interesting theoretical results concerning the electrodynamics of multiple polar cap arcs have recently been obtained with the M-I coupling model. With this model, Zhu *et al.* [1993a] showed that multiple polar cap arcs might not be due to multiple structures in the magnetospheric source region. Instead, they can be internally generated in the M-I system as a result of the self-consistent coupling of the magnetosphere and ionosphere. Sojka *et al.* [1994] found that the appearance of multiple polar cap arcs has a strong dependence on the magnitude of the large-scale ionospheric background convection (E). With the same initial magnetospheric driver, they found that the number of the arcs increased with an increase in the strength of the background convection, while the spacing between the arcs remained constant. This dependence is "not" a linear effect in which the polar cap arcs simply scale with the magnitude of the background convection. The degree of striation, or multiple character, of the arcs increases rapidly from a single arc at $E < 20$ mV/m to 5 arcs at 30 mV/m. These results further indicate that the ionosphere plays an active role in the formation of multiple polar cap arcs and that the ionosphere dynamically responds to the magnetospheric driver. Expanding on the Sojka *et al.* [1994] results, Zhu *et al.* [1994b] reached a qualitative theoretical conclusion about the appearance and spacing of multiple polar cap arcs. They predicted that

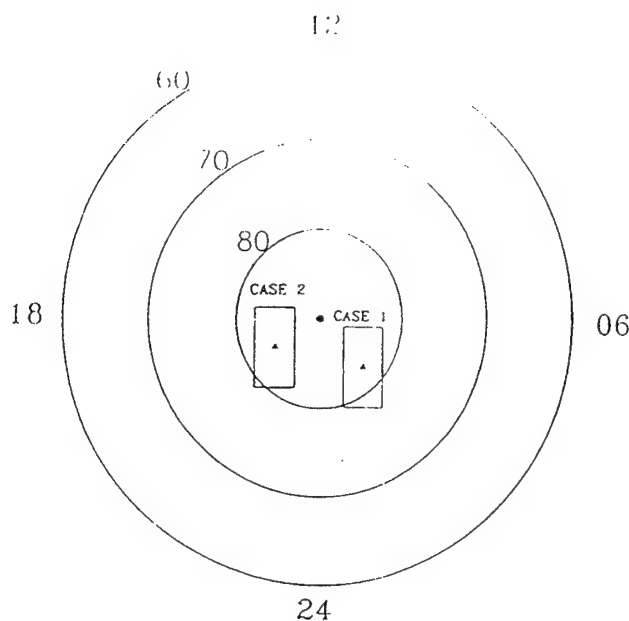


Figure 2. A schematic diagram showing the location of the ionospheric simulation domain in the polar cap. A magnetic latitude-magnetic local time (MLT) coordinate is used.

multiple polar cap arcs are more likely to occur when the large-scale ionospheric convection field is larger than 20 mV/m and the background ionospheric Hall conductance is in the range of from 0.5 to 2 mho. When the large-scale convection is weak and the ionospheric conductance is high, a single arc is more likely to be seen in the polar cap. With a variable conductance ratio, it was found by Zhu *et al.* [1994b] that the spacing of multiple polar cap arcs is mainly determined by the hardness of the primary magnetospheric precipitation. A harder precipitation causes a wider spacing between individual arcs and vice versa. The edge-to-edge spacing between arcs varies from about 20 km to about 60 km when the ratio of the enhanced Hall and Pedersen conductances changes from 1 to 2.

The above quantitative theoretical predictions concerning multiple polar cap arcs can be tested with the Qaanaq data. By using model inputs that are consistent with the conditions when the observed multiple polar cap arcs occurred, we can compare the time-dependent electrodynamical features of both the simulated and observed arcs. If the corresponding spatial and temporal scales are largely consistent, that would confirm the theoretical predictions made by the M-I coupling model to zero-order. Also, the modeling results would provide a much more detailed picture of the electrodynamics of multiple polar cap arcs than the observations. The model yields information about the conductivity enhancement, the Joule heating, the connection between field-aligned currents and horizontal currents, the cross-flow associated with multiple polar cap

arcs, etc. Such information would improve our understandings of the underlying physics of multiple polar cap arcs.

4. Model-Observation Studies

Case 1: November 12, 1990

The polar cap arcs observed on November 12, 1990, occurred in the morning sector of the dark polar cap. The time period we are interested in is from 0822 to 0828 UT, during which the arcs went through the stages from breaking up to a quasi-steady state. During this time period, the IMF B_z was positive (~ 1.5 nT) and B_y was negative (~ -1.5 nT). Before this period, the IMF B_z component had been positive for almost 24 hours, and after the period under study the IMF B_z remained positive for another 24 hours. The Kp index was 1- for almost 9 hours. This is a typical condition for the occurrence of polar cap arcs.

The location of the ionospheric simulation domain in the polar cap for case 1 is shown in Figure 2. The simulation domain is 1500 km long in the X (midnight-noon) direction and 1000 km wide in the Y (dawn-dusk) direction. The grid size is 30 km in the X direction, and 10 km in the Y direction. It should be noted that Figure 2 is just a schematic diagram and is not precisely scaled. With the M-I coupling model, we need to specify some initial conditions, which include the large-scale background convection and background conductance patterns before the breakup of the polar cap arcs and the small-scale shear flow associated with the arcs. Unfortunately, for both observational periods in this study, there were either no DMSP data or the pass of DMSP was far away from the field of view of the all-sky camera. Therefore the DMSP satellite was not able to provide information on either the large-scale convection pattern or the small-scale shear flow associated with the arcs for the modelings. Hence we had to use

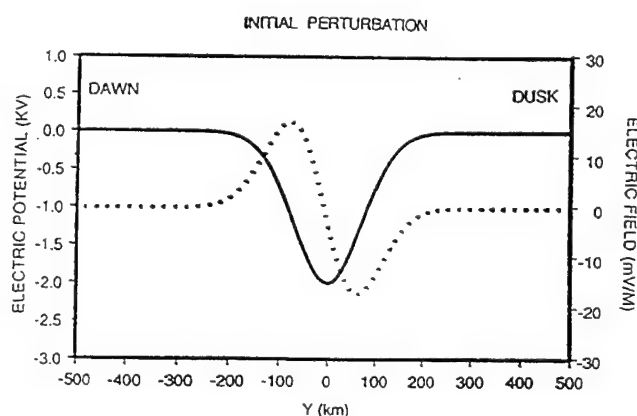
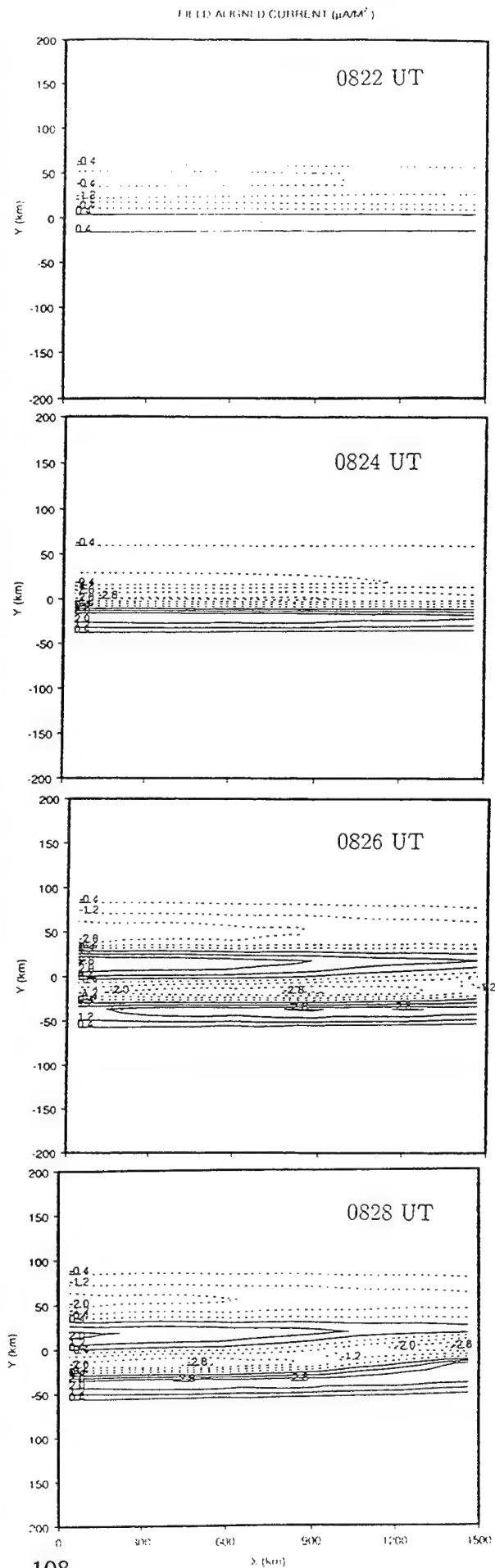
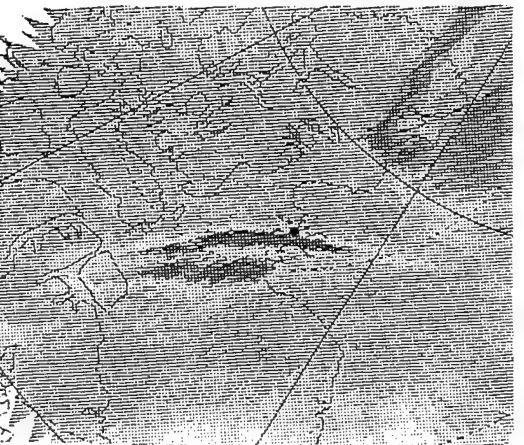
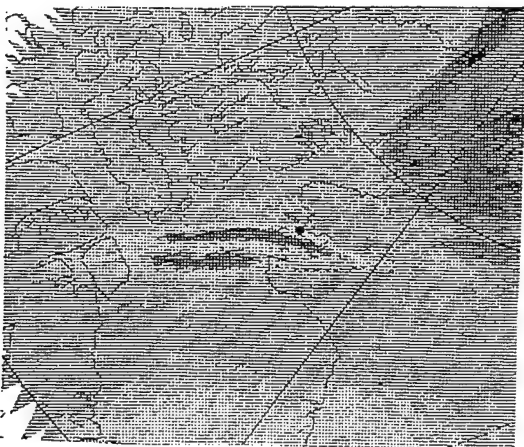


Figure 3. Potential distribution in the dawn-dusk cross section associated with the initial magnetospheric shear flow (solid) and the corresponding electric field distribution (dashed).

Figure 4. (left) A sequence of the images showing polar cap arcs starting at 0822 UT, November 12, 1990, with a 2-min interval and (right) the snapshots of the evolution of the field-aligned current distribution from the modeling. The dashed lines indicate upward field-aligned currents. The ionospheric dimension of the images in the left column is about 1430 km in noon-midnight (X) direction and about 1165 km in dawn-dusk (Y) direction.



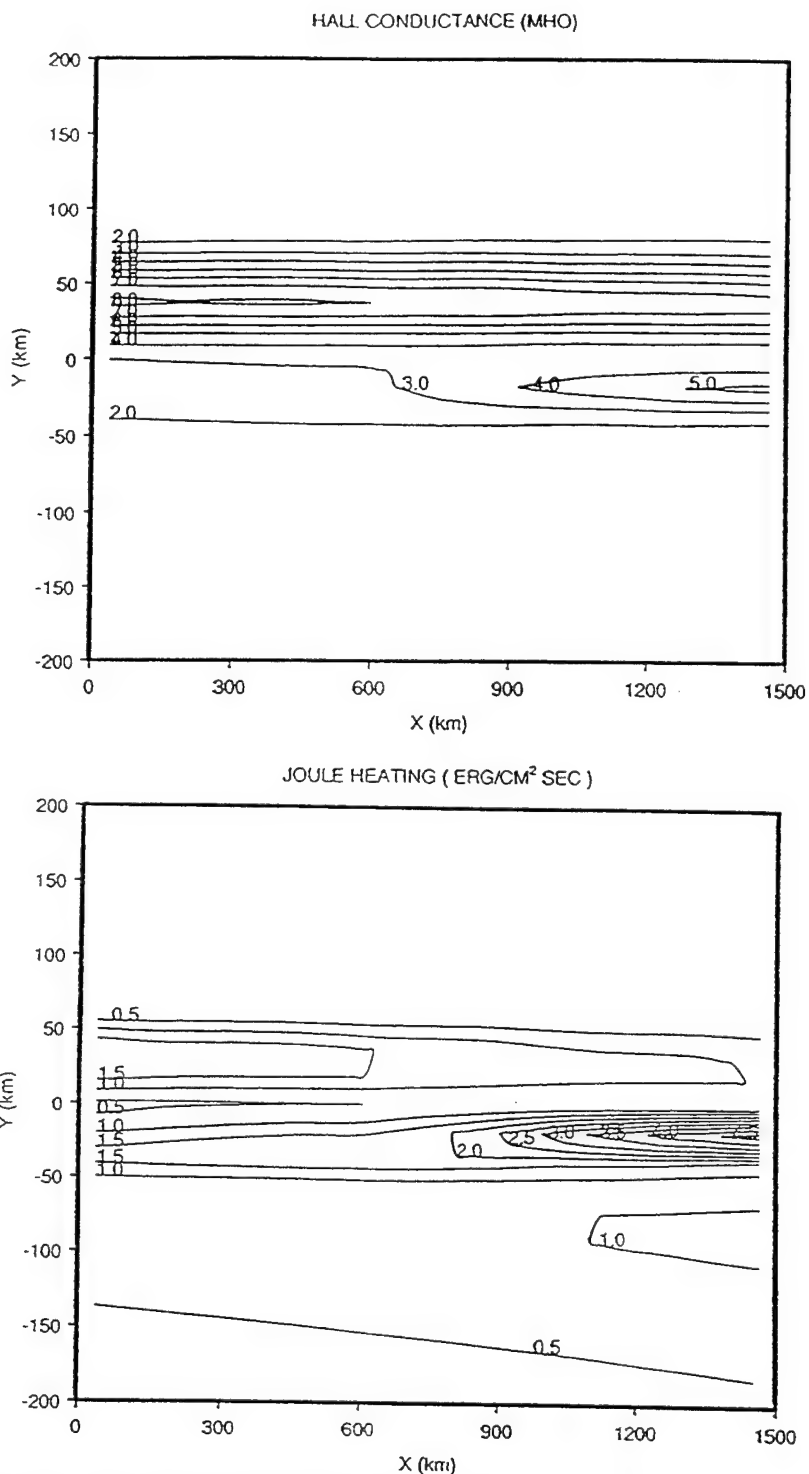


Figure 5. The distributions of the (top) enhanced Hall conductance and (bottom) Joule heating rate near the asymptotic steady state (0826 UT). No neutral wind effect is included in the calculation of the Joule heating rate.

statistical large-scale convection patterns for the IMF and geomagnetic conditions similar to those when the polar cap arcs occurred. On the basis of the *Heppner and Maynard* [1987] convection model, the large-scale background convection in the region where the arcs occurred for case 1 is basically uniform and antisunward. The background ionospheric conductance for the modelings was obtained from the conductivity model developed by *Rasmussen et al.* [1988]

using the appropriate geomagnetic, solar, and seasonal conditions.

The M-I coupling model also needs the initial small-scale shear flow originated in the magnetosphere. Since *Zhu et al.* [1994b] found that the appearance and spacing of "multiple" polar cap arcs are not determined by the spatial scale of the initial magnetospheric shear flow and they are determined by the M-I coupling processes, we used the same shear flow

profiles for both of the cases we studied. The initial small-scale shear flow was assumed to be carried by a downward propagating Alfvén wave. It extended uniformly along the Sun-aligned direction (X direction) and had a "single" precipitation channel. The cross-section profiles of the electric field associated with the assumed initial small-scale shear flow (dashed line) and the corresponding electric potential (solid line) are shown in Figure 3.

It should be noted again that a guideline for our simulations is the theoretical results of Zhu *et al.* [1994b]. They found that the observed multiple polar cap arcs may not be due to multiple structures in the magnetosphere, but instead may primarily be determined by the coupled magnetosphere-ionosphere system in which the ionosphere plays an active role. The spacing of multiple polar cap arcs is mainly determined by the hardness of the primary magnetospheric precipitation. A harder precipitation causes a wider spacing between individual arcs and vice versa. Accordingly, for case 1, in which the arcs have a narrow spacing, we assumed that the ratio between Hall and Pedersen conductances is 1.4, which reflects a relatively soft precipitation.

The simulation for case 1 started at 0818 UT, which is the time when the assumed downward propagating Alfvén wave hit the ionosphere. Figure 4 shows snapshots of the evolution of the field-aligned current distribution from the modeling (right column) and the corresponding time sequence of polar cap arc images (left column). From the images, starting at 0822 UT with a 2-min interval, we can see that the polar cap arcs started to appear at 0822 UT and took about 6 min to reach a steady state. The arcs were structured with an edge-to-edge spacing

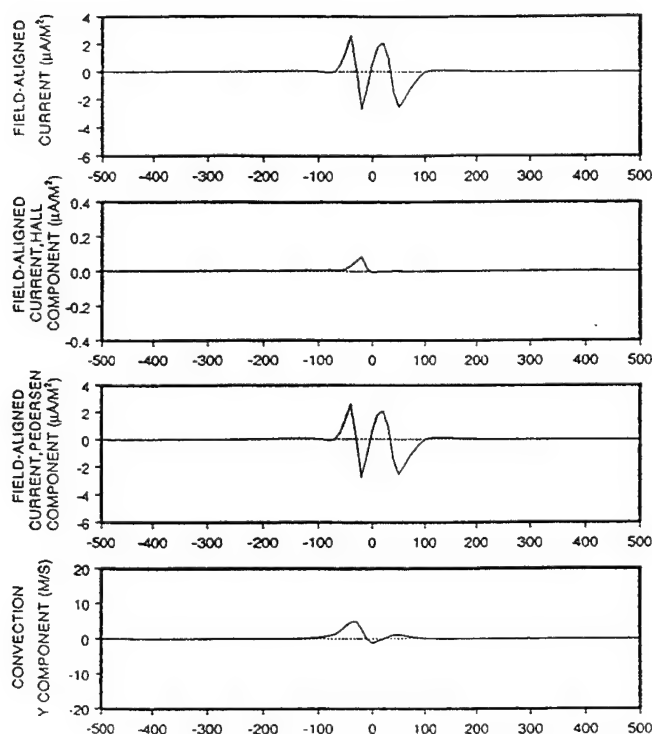


Figure 6. The cross-section profiles of the total field-aligned current, the Hall and Pedersen components of the field-aligned currents, and the cross flow associated with the polar cap arcs at 0826 UT from the modelings. The negative values of field-aligned current mean the upward field-aligned currents.

(dark region between two arcs) of about 40 km. The arcs were aligned mainly in the noon-midnight direction. The first plot of the modeled field-aligned currents is for 0822 UT, which is 4 min after the initial magnetospheric shear flow reaches the ionosphere. The successive plots are also at 2-min intervals. The dashed lines represent the upward field-aligned currents. Comparing the left and right columns, it is apparent that both the spatial and temporal features of the model predictions and measurements are quite similar except the intensity of the poleward arc at 0824 UT. These similarities indicate that our adopted initial conditions for the modeling are largely reasonable and that the M-I coupling model describes the appropriate physics associated with multiple polar cap arcs.

Figure 5 shows the distributions of the enhanced Hall conductance (top panel) and the Joule heating rate (bottom panel) at the asymptotic steady state (0826 UT). It can be seen that the Hall conductance is enhanced from about 0.5 mho (background conductance) to a peak conductance of 8 mho and that the enhanced conductance is structured. The Joule heating rate is also substantially increased and structured. It should be noted that there is no neutral wind effect in the calculation of Joule heating rate.

Figure 6 shows the cross-section profiles of the modeled total field-aligned current, the Hall and Pedersen components of the field-aligned currents, and the cross-flow associated with the polar cap arcs at 0826 UT, as obtained from the modelings. A negative value in the field-aligned current plots means upward current. These cross-section profiles clearly show the multiple structure of the polar cap arcs. Comparing the first three plots in Figure 5, we can see that the field-aligned currents associated with multiple polar cap arcs are mainly closed by the Pedersen currents, and only a small part of the field-aligned currents is closed by the Hall currents. The Hall current contribution to the field-aligned currents is due to the small-scale conductivity gradient caused by the arc precipitation. It should be noted that if the ionosphere is in a steady state and the conductivity is uniform, there is no Hall current component of field-aligned currents. However, if the ionospheric system is temporally varying or the conductivity is nonuniform, the Hall current can make contribution to the field-aligned current. In principle, the closure of the ionosphere-originated field-aligned currents, which could include both Pedersen and Hall components, at the magnetosphere is achieved through the adjustment of magnetic field configuration in the magnetosphere. However, the detailed picture is still not clear and the mechanism for the current closure at the magnetosphere has not been self-consistently treated in our model. The bottom panel shows that a cross flow exists in association with the multiple polar cap arcs, but the magnitude of the cross flow is small. It should be noted that this cross-flow results from the M-I coupling processes associated with the multiple arcs, since the initial magnetospheric shear flow is symmetric and does not contain a cross flow.

Case 2: December 11, 1990

The polar cap arcs observed on December 11, 1990, occurred in the evening sector of the dark polar cap. The time period we are interested in is from 2112 to 2118 UT. The IMF turned northward at about 1800 UT and remained northward until 0030 UT of the next day. During the period we are interested in, the B_z was ~ 5 nT and B_y was ~ -1.5 nT, and Kp

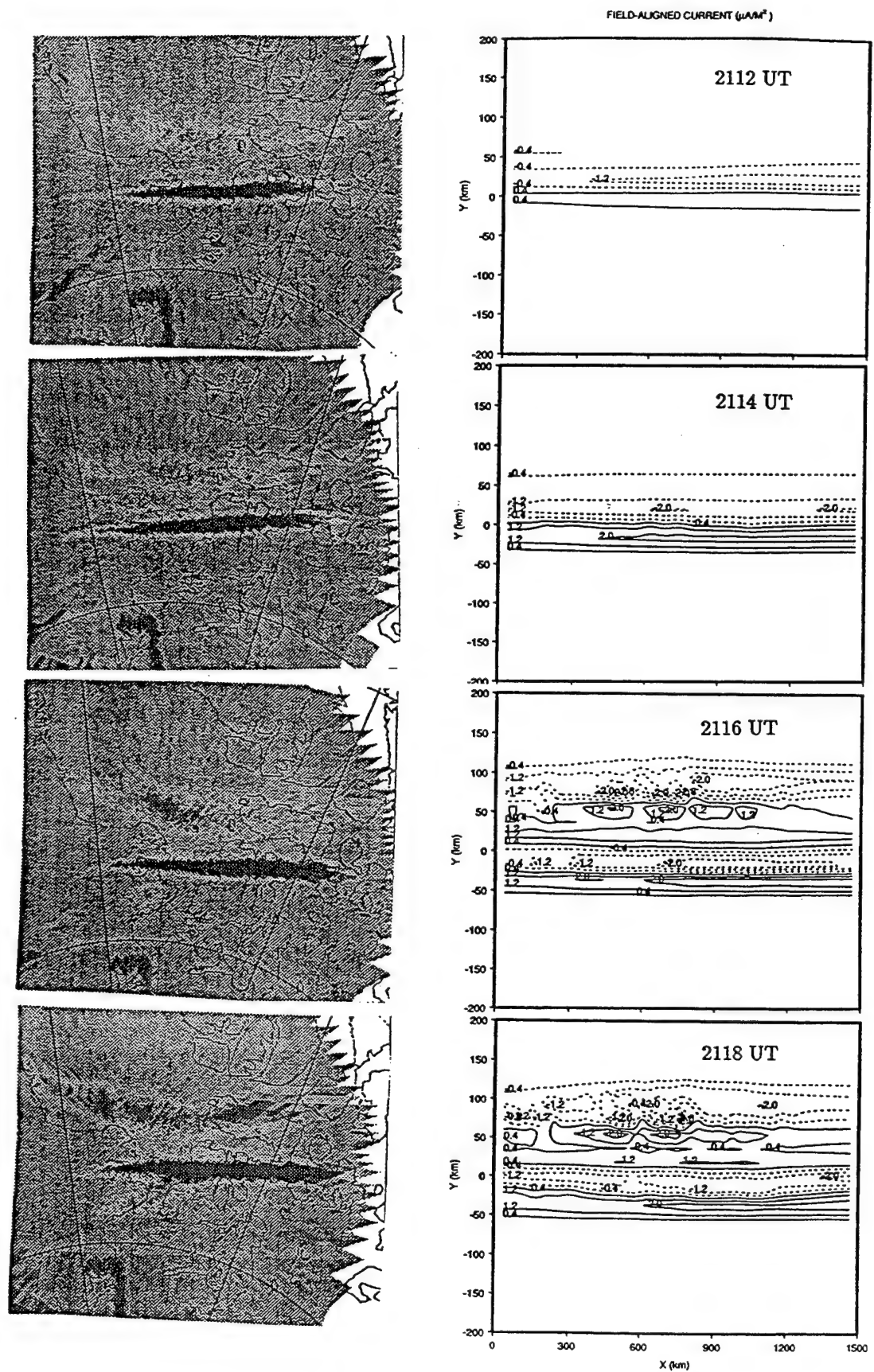


Figure 7. (left) A sequence of images showing polar cap arcs starting at 2112 UT, December 11, 1990, with a 2-min interval and (right) the snapshots of the evolution of the field-aligned current distribution from the modeling.

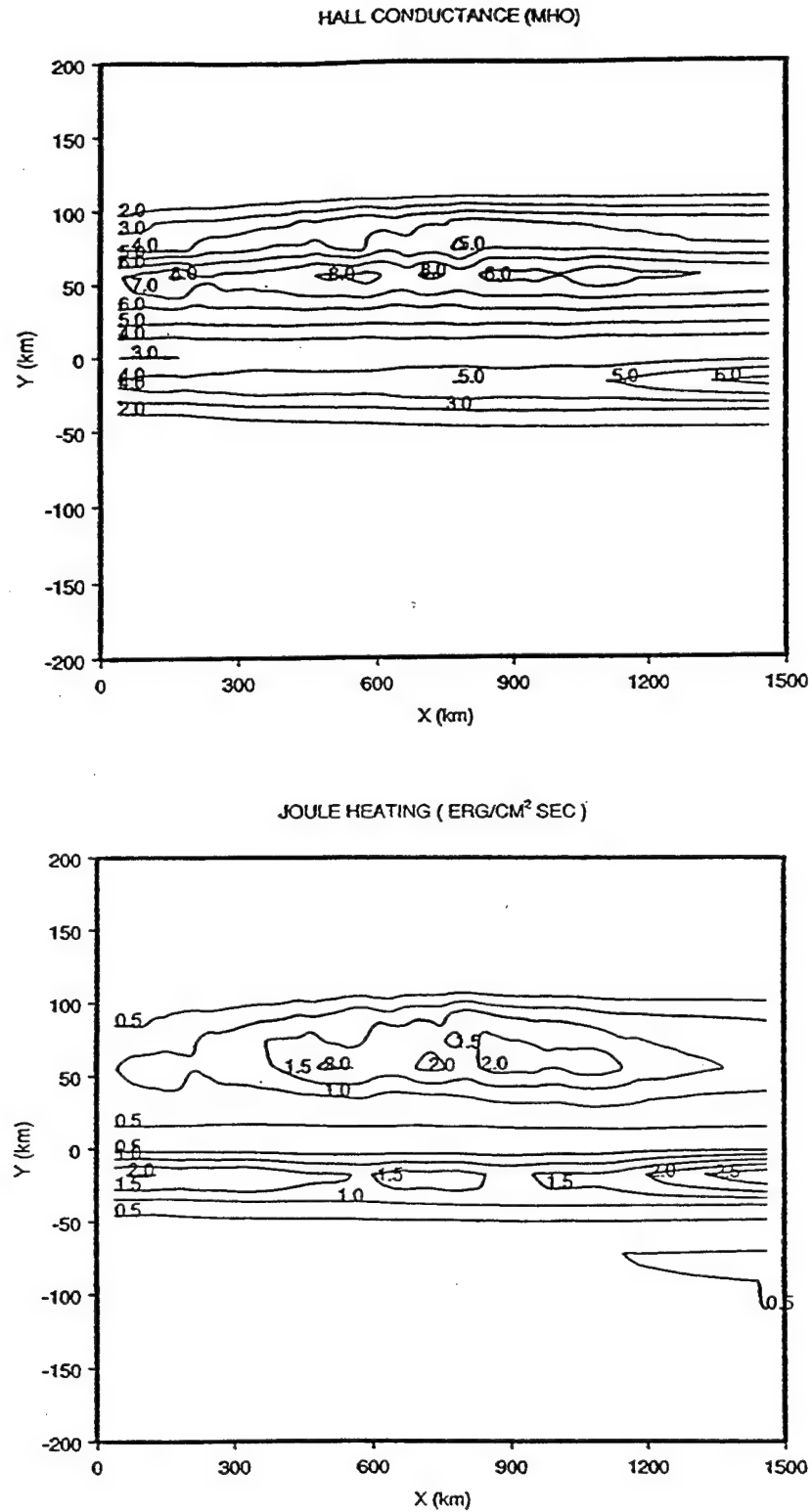


Figure 8. The distributions of the (top) enhanced Hall conductance and (bottom) Joule heating rate near the asymptotic steady state (2118 UT). No neutral wind effect is included in the calculation of the Joule heating rate.

was 1. This is also a typical condition for the occurrence of polar cap arcs. The location of the ionospheric simulation domain in the polar cap for case 2 is schematically shown in Figure 1.

For this case, the DMSP-F8 pass was about 1000 km away from the edge of the field of view of the all-sky camera. Therefore we again had to depend on statistical convection models for information about the large-scale background convection pattern. The *Heppner and Maynard* [1987] convection model shows that under the above specific IMF and geomagnetic conditions, the convection in the region where the multiple arcs in case 2 occurred is also basically uniform and antisunward. Then, by using the same magnetospheric shear flow and background ionospheric conductance as for case 1, we conducted the modeling for case 2. The ratio of the Hall and Pedersen conductances for case 2 is 1.9, which is different from that in case 1 and reflects a relatively harder precipitation.

The simulation for case 2 started at 2108 UT, which is the time when the assumed downward propagating Alfvén wave hit the ionosphere. Figure 7 shows snapshots of the evolution of the field-aligned current distribution from the modeling (right column) and the sequence of polar cap arc images (left column). The images start at 2112 UT with a 2-min interval. The arc pattern consists of two arcs with an edge-to-edge spacing of about 90 km, which is much wider than that in case 1. The arcs are again aligned mainly in the noon-midnight direction. It may be noticed that there is a significant bending associated with the equatorward arc at 2118 UT. This bending is due to the instrument effect which occurs when the altitude of the arc varies significantly along the arc and the arc is far away from the center of the field of view. The first plot of the modeled field-aligned currents is for 2112 UT, which is 4 min after the initial magnetospheric shear flow reaches the ionosphere. The successive plots are also at 2-min intervals. Again, a comparison of the left and right columns indicates that the two are quite similar, both spatially and temporally.

Special attention needs to be paid to the second arc. *Zhu et al.* [1993a] suggested that the nature of the primary and secondary arcs could be quite different. The primary arc is directly related to the magnetospheric driver. The appearance of the secondary arc and the spacing between the primary and secondary arcs are largely determined by the M-I coupling processes. Here, as a nonlinear response to a harder magnetospheric precipitation from the coupled M-I system, there is a wider spacing between the primary and secondary arcs. Also, the secondary arc shows fine structure feature. The feature of fine structure in the secondary arc from the simulation for the situation of hard precipitation is quite similar to that of the secondary arc in the images. This correspondence is a surprising finding. Further theoretical and modeling are needed to explore the underlying physics of this new feature.

Figure 8 shows the distributions of the enhanced Hall conductance (top panel) and the Joule heating rate (bottom panel) near the asymptotic steady state (2118 UT). It can be seen that the Joule heating associated with the secondary arc is distributed. Figure 9 shows the cross-section profiles of the total field-aligned current, the Hall and Pedersen components of the field-aligned currents, and the cross-flow of the polar cap arcs at 2118 UT, as predicted by the modelings. From Figure 6, we can see that in the case of the arcs with a wide spacing, the field-aligned currents associated are also mainly

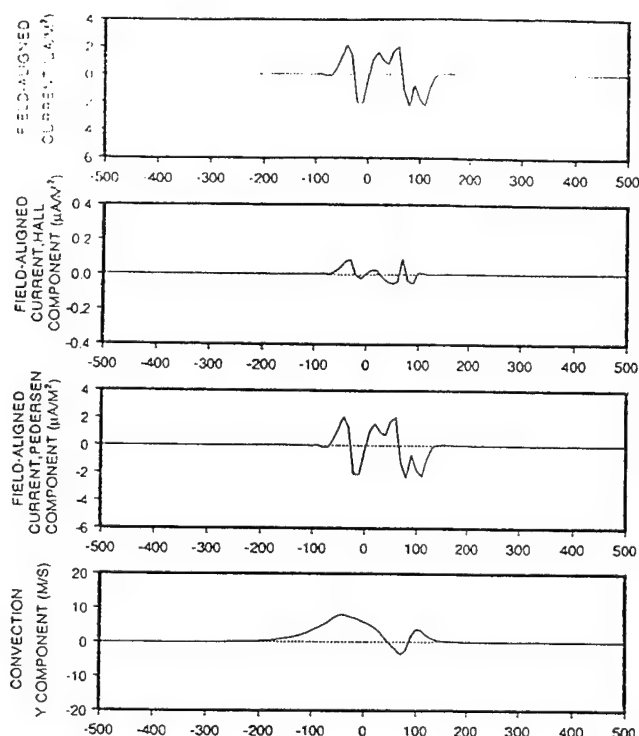


Figure 9. The cross-section profiles of the total field-aligned current, the Hall and Pedersen components of the field-aligned currents, and the cross flow associated with the polar cap arcs at 2118 UT from the modelings. The negative values of field-aligned current mean the upward field-aligned currents.

closed by Pedersen currents. In addition to the two distinct arcs, fine structure is clearly evident in the secondary arc. The bottom panel shows that there also exists a cross flow for the multiple polar cap arcs with a wide spacing, but the cross flow is considerably more distributed than that for the arcs with a narrow spacing, case 1.

5. Discussion and Conclusion

For a first time, a quantitative model-observation comparison of multiple polar cap arcs has been conducted by using a time-dependent theoretical model of polar cap arcs and the initial results are encouraging. The arcs observed with the all-sky camera at Qaanaaq and the simulated ones are quite similar, both spatially and temporally. This direct comparison study of both temporal and spatial features of polar cap arcs is beyond the capability of previous theoretical models. The key difference between the two cases we considered was the arc spacing. *Zhu et al.* [1994b] predicted that the spacing of multiple polar cap arcs is mainly determined by the hardness of the primary magnetospheric precipitation. A harder precipitation causes a wider spacing between individual arcs and vice versa. Our model-observation study confirms this prediction. However, the prediction can be further tested in a study by combining precipitation data from DMSP satellites with ground-based image data. The precipitation observation would define the spectral hardness that has been used as an assumed input parameter in this study.

The initial magnetospheric shear flow for both cases under

study was a simple symmetric convection shear with a single precipitation channel, but we successfully produced arcs that had multiple structures which were very similar to the observed ones. This further indicates that the observed multiple polar cap arcs may not be due to multiple structures in the magnetosphere but instead may primarily be determined by the coupled magnetosphere-ionosphere system in which the ionosphere plays an active role.

Our results show that for the multiple polar cap arcs with both narrow and wide spacings, the associated field-aligned current are mainly closed by Pedersen currents, and the Hall currents only make a small contribution. A cross flow occurs for both type of multiple arcs, but the cross flow for the arcs with a wide spacing is more spread.

In the observed arcs of case 2, the secondary arc is highly structured. To our surprise, the model developed a secondary arc with a similar fine structure. The fine structure in secondary arc for the multiple arcs with wide spacing (or hard precipitation) is a new finding. We believe this is due to the nonlinear M-I coupling process, but more theoretical analyses and modelings are needed to understand the detailed underlying physics.

This work is just one of the coordinated endeavors of the HLPS campaigns to understand the plasma structures observed in the high-latitude regions. In past years, CEDAR-HLPS campaigns have led to a very extensive observational database of polar cap arcs and many new features have been discovered. This makes quantitative model-observation studies very feasible, and they are essential for improving our understanding of polar cap arcs.

Acknowledgment. The work at Utah State University was supported by NASA grant NAG5-1484 and by NSF grants ATM-93-08163 and ATM-93-02165. The work at Boston College was supported by Phillips Laboratory contract F19628-90-K-007 and by NSF grant ATM-9404088. We thank the Danish Commission for Scientific Research in Greenland for permission to conduct ground experiments at Qaanaaq under continuing project A16-91. We thank Katsura Fukui and Hugh Gallagher for helping to digitize the images presented here. We thank two referees for their very constructive comments and suggestions.

The Editor thanks F. J. Rich and another referee for their assistance in evaluating this paper.

References

- Berg, G. A., In-situ and ground-based observations of Sun-aligned arcs, paper presented at the Joint Workshop for CEDAR HLPS/STEP GAPS, NSF, Peaceful Valley, Colo., June 1992.
- Burke, W. J., M. S. Gussenhoven, M. C. Kelley, D. A. Hardy, and F. J. Rich, Electric and magnetic characteristics of discrete arcs in the polar cap, *J. Geophys. Res.*, **87**, 2431, 1982.
- Carlson, H. C., Jr., V. B. Wickwar, E. J. Weber, J. Buchau, J. G. Moore, and W. Whiting, Plasma characteristics of polar cap F-layer arcs, *Geophys. Res. Lett.*, **1**, 895, 1984.
- Chiu, Y. T., Formation of polar cap arcs, *Geophys. Res. Lett.*, **16**, 743, 1989.
- Davis, T. N., The morphology of the polar aurora, *J. Geophys. Res.*, **65**, 3497, 1960.
- Doc, R., M. Mendillo, J. Vickrey, M. Ruohoniemi, and R. Greenwald, Coordinated convection measurements in the vicinity of auroral cavities and arcs, paper presented at the Joint Workshop for CEDAR HLPS/STEP GAPS, NSF, Peaceful Valley, Colo., June 1992.
- Frank, L. A., et al., The theta aurora, *J. Geophys. Res.*, **91**, 3177, 1986.
- Fridman, M., and J. Lemaire, Relationship between auroral electron fluxes and field-aligned electric potential difference, *J. Geophys. Res.*, **85**, 664, 1980.
- Hardy, D. A., W. J. Burke, and M. S. Gussenhoven, DMSP optical and electron measurements in the vicinity of polar cap arcs, *J. Geophys. Res.*, **87**, 2413, 1982.
- Heppner, J. P., and N. C. Maynard, Empirical high-latitude electric field models, *J. Geophys. Res.*, **92**, 4467, 1987.
- Kan, J. R., and W. J. Burke, A theoretical model of polar cap auroral arcs, *J. Geophys. Res.*, **90**, 4171, 1985.
- Nielsen, E., J. D. Craven, L. A. Frank, and R. A. Heelis, Ionospheric flows associated with a transpolar arc, *J. Geophys. Res.*, **95**, 21169, 1990.
- Obara, T., M. Kitayama, T. Mukai, N. Kaya, J. S. Murphree, and L. L. Cogger, Simultaneous observations of Sun-aligned polar cap arcs in both hemispheres by EXOS-C and Viking, *Geophys. Res. Lett.*, **15**, 713, 1988.
- Peterson, W. K., and E. G. Shelley, Origin of the plasma in a cross-polar cap auroral feature (theta aurora), *J. Geophys. Res.*, **89**, 6729, 1984.
- Rasmussen, C. E., R. W. Schunk, and V. B. Wickwar, A photochemical equilibrium model for ionospheric conductivity, *J. Geophys. Res.*, **93**, 9831, 1988.
- Rich, F. J., D. A. Hardy, R. H. Redus, and M. S. Gussenhoven, Northward IMF and patterns of high-latitude precipitation and field-aligned currents: The February 1986 storm, *J. Geophys. Res.*, **95**, 7893, 1990.
- Sojka, J. J., L. Zhu, D. J. Crain, and R. W. Schunk, Effect of high latitude ionospheric convection on Sun-aligned polar cap arcs, *J. Geophys. Res.*, **99**, 8851, 1994.
- Valladares, C. E., and H. C. Carlson, The electrodynamic, thermal, and energetic character of intense sun-aligned arcs in the polar cap, *J. Geophys. Res.*, **96**, 1379, 1991.
- Valladares, C. E., H. C. Carlson, and K. Fukui, Interplanetary magnetic field dependency of stable Sun-aligned polar cap arcs, *J. Geophys. Res.*, **99**, 6247, 1994.
- Weber, E. J., and J. Buchau, Polar cap F-layer auroras, *Geophys. Res. Lett.*, **8**, 125, 1981.
- Zhu, L., J. J. Sojka, R. W. Schunk, and D. J. Crain, A time-dependent model of polar cap arcs, *J. Geophys. Res.*, **98**, 6139, 1993a.
- Zhu, L., J. J. Sojka, R. W. Schunk, and D. J. Crain, Influence of horizontal inhomogeneity in the ionosphere on the reflection of Alfvén waves, *Geophys. Res. Lett.*, **20**, 313, 1993b.
- Zhu, L., J. J. Sojka, R. W. Schunk, and D. J. Crain, Theoretical study of polar cap arcs: Time-dependent model and its applications, *Radio Sci.*, **29**, 283, 1994a.
- Zhu, L., J. J. Sojka, R. W. Schunk, and D. J. Crain, Model study of multiple polar cap arcs: Occurrence and Spacing, *Geophys. Res. Lett.*, **21**, 649, 1994b.
- D. J. Crain, R. W. Schunk, J. J. Sojka, and L. Zhu, Center for Atmospheric and Space Sciences, Utah State University, Logan, UT 84322-4405. (zhu@theory.cass.usu.edu)
- C. E. Valladares, Institute for Space Research, Boston College, Newton, MA 02159.

(Received September 28, 1994; revised September 1, 1995; accepted September 1, 1995.)

Antisunward Decay of Polar Cap Arcs

J. V. Rodriguez¹

Phillips Laboratory, Geophysics Directorate (PL/GPIA), Hanscom AFB, MA 01731

C. E. Valladares and K. Fukui

Institute for Scientific Research, Boston College, Newton, MA 02159

H. A. Gallagher, Jr.

Department of Physics, Boston College, Chestnut Hill, MA 02167

Received _____; accepted _____

submitted to *Journal of Geophysical Research*, January 6, 1997

Short title: DECAYING POLAR CAP ARCS

¹Now at Ball Aerospace & Technologies Corp., Boulder, Colorado.

Data from an all-sky imaging photometer (427.8 and 630.0 nm) in the central polar cap, the IMP 8 and ISEE 2 satellites in the solar wind, and the DMSP F6, F7, and F8 satellites in the topside ionosphere have been used to investigate eight cases of polar cap arcs decaying antisunward following an IMF southward turning that results in $B_z < 0$ lasting at least 20 min. The lags from the IMF reversal to the arc decay are corrected for the solar wind travel time from IMP 8 or ISEE 2 to the subsolar magnetopause. For six of the arcs, the lags range from 19 to 32 min, consistent with previous observations of changes in polar cap convection following IMF reversals. In the remaining two cases, the arcs first appear in the central polar cap 30–40 min after the southward turning, then decay antisunward during the expansion phase of a small substorm, 60–70 min after B_z turned negative. In all cases, the direction of dawn-dusk drift is in the direction of B_y , and in the cases in which B_y also reversed, the corrected lags to a change in dawn-dusk drift are < 10 min (in two cases) or ~ 20 min (in two other cases). In the five cases in which a DMSP satellite traverses the Qaanaaq field-of-view or its conjugate while the arc was present, the precipitation data indicate an origin on open (closed) field lines in two (three) cases. Both open and closed field line arcs are characterized by $\sim 20 - 30$ min B_z lags, while the two arcs associated with 60–70 min lags are on closed field lines. Antisunward decay of polar cap arcs $\sim 20 - 30$ min after B_z turns negative is consistent with the B_y -dependent convection of new open flux tubes from the cusp to the center of the polar cap due to dayside merging. The behavior of the other two arcs suggests an evolution in polar cap convection driven at first by dayside merging or viscous processes, then by the development of a substorm-related DP 1 current pattern. If polar cap arcs map to the distant tail flanks, they may be associated with instabilities due to velocity shears between the plasmashet and the LLBL. The dawn-dusk drift and antisunward decay of polar cap arcs may represent the stirring of the tail flanks by dayside driven merging.

Introduction

The alignment toward the Sun of auroral arcs in the polar cap was first determined from visual observations by the British Antarctic Expedition during the austral winter of 1908 [Mawson, 1916]. This alignment was confirmed by using networks of all-sky cameras to make auroral observations during the International Geophysical Year (IGY) of 1957–58 [e.g., Weill, 1958; Davis, 1962; Feldstein, 1963]. Analysis of IGY all-sky images also revealed that the existence of Sun-aligned arcs in the polar cap was anticorrelated with geomagnetic activity [Davis, 1963; Feldstein *et al.*, 1967, and references therein]. These results and the finding by Fairfield and Cahill [1966] that polar geomagnetic disturbances were associated with southward interplanetary magnetic field (IMF) were the first indications that the magnetosphere has a different topology under northward IMF ($B_z > 0$).

Studies of satellite imagery confirmed that the presence of Sun-aligned arcs in the polar cap is strongly correlated with northward IMF [Berkey *et al.*, 1976] and generally associated with low levels of geomagnetic activity [Ismail *et al.*, 1977]. Lassen and Danielsen [1978] used all-sky images from Greenland to show that visible discrete arcs developing within the polar cap under northward IMF conditions are Sun-aligned. Starkov and Feldstein [1971] noted that Sun-aligned arcs in the polar cap disappear 10–30 min before the onset of an auroral substorm. Sun-aligned arcs near the dusk oval have been observed to intensify briefly, then fade 20–30 min following a southward turning and 30–60 min prior to a poleward or westward auroral surge [Wu *et al.*, 1991]. In a study of five years of Vostok all-sky camera and IMF data from IMP 8, Troshichev *et al.* [1988] showed that, on average, Sun-aligned arcs disappear 20 min after a southward turning of the IMF and appear 55 min after a northward turning. Similarly, the response of polar cap convection to B_z reversals lags southward turnings by 17–25 min and northward turnings by 28–44 min, as observed from four simultaneously operational Defense Meteorological Satellite Program (DMSP) satellites [Hairston and

Heelis, 1995]. The close association of polar cap arcs with upward Birkeland currents and gradients or shears in the convection electric field such that $\nabla \cdot E < 0$ [e.g., Burke *et al.*, 1982; Frank *et al.*, 1986; Carlson *et al.*, 1988; Weber *et al.*, 1989] suggests that their response to B_z reversals is related to that of the ionospheric convection pattern.

In a study of one winter of northern hemisphere all-sky images, Valladares *et al.* [1994] showed that the presence of polar cap arcs under $B_z < 0$ implied that the polarity of B_z had reversed from positive to negative within 30 min prior to the observation. When the reversal resulted in $B_z < 0$ lasting about 30 min or greater, the arcs invariably disappeared, sometimes in a characteristic fashion whereby the fading started at the end of the arc closest to noon, then proceeded along the arc in the antisunward direction. Valladares *et al.* [1994] interpreted these observations as evidence of the minimum time required for the full evolution of a southward IMF convection pattern, 30 min being roughly the amount of time required for a solar wind-induced disturbance to convect from the dayside magnetopause to the midnight sector of the polar cap. Such antisunward decay is distinct from the characteristic dawn-dusk drift of polar cap arcs and has been reported only rarely [Starkov and Feldstein, 1971; Burke, 1988; Murphree *et al.*, 1989].

We have analyzed eight cases of antisunward-decaying polar cap arcs in the northern hemisphere for which IMF data are available. These cases are characterized by clear optical (630.0 nm) signatures in ground-based intensified all-sky images and a well-defined IMF southward turning and, sometimes, an accompanying reversal in the B_x or B_y components. Postulating that IMF reversals lead to arc decay, we determine the lag from the arrival of the reversal at the subsolar magnetopause to the arc decay. Four cases in which a DMSP satellite traversed the all-sky imager field-of-view around the time of the arc decay are analyzed in detail. The precipitating particle and ion drift data from the satellite are used to determine the state of the polar cap before and after the reversal and the origin of the arcs on open or closed field lines. The results of

this analysis are applied to the questions of whether the lags from the IMF southward turning can be used to distinguish the open or closed field line origin of polar cap arcs, and whether the arc response is driven by changes in dayside merging of solar wind and magnetospheric field lines, or by changes in nightside processes such as field line reconnection or viscous interactions in the distant tail flanks.

Sources of Data

Since 1983, a Phillips Laboratory intensified all-sky imaging photometer (ASIP) has been operating at the Danish Meteorological Institute Geophysical Observatory in Qaanaaq, Greenland (77.47°N, 69.23°W), during the northern hemisphere autumn and winter when the sun is 10° or more below the horizon and the moon is at or below the horizon. At 86° N corrected geomagnetic (CG) latitude [Gustafsson *et al.*, 1992], the Qaanaaq ASIP has a field-of-view that, projected to 250 km altitude, includes the CG pole and lies poleward of the statistical auroral oval for all levels of geomagnetic activity [Whalen, 1970]. (In its original sense, and the sense used in the present paper, the term "polar cap" refers to the region poleward of the auroral oval [e.g., Eather and Akasofu, 1969], a definition based on the occurrence frequency of aurora observed with ~ 1 kR-sensitivity white-light all-sky cameras during the IGY [Feldstein, 1963; Eather, 1973].) On February 12, 1988, the 155° fish-eye lens was replaced with a 180° lens.

As with the original monochromatic all-sky imagers [Mende and Eather, 1976], the Qaanaaq ASIP images the night sky at wavelengths characteristic of aeronomical processes associated with auroral precipitation (630.0 and 427.8 nm). Images at 427.8 nm and 630.0 nm are recorded on 35-mm black-and-white film once every two minutes, with exposure times of 8 s for the 630.0 nm filter, and 16 and 32 s for the 427.8 nm filter before and after March 1989, respectively. With an original sensitivity of 50 R s at 630.0 nm, the Qaanaaq ASIP can detect subvisual Sun-aligned arcs consisting of 630.0 nm emissions caused by precipitation of < 0.5 keV electrons to *F* region altitudes

[Weber and Buchau, 1981]. The appearance of the 427.8 nm emission indicates an increase in the differential number flux of keV electrons [Eather and Mende, 1972].

Data sets from several satellite-based instruments are used to relate the observed polar cap arcs to conditions in the solar wind and the high-latitude ionosphere. IMF data were recorded by the magnetometers on the Interplanetary Monitoring Platform (IMP) 8 and International Sun-Earth Explorer 2 (ISEE 2) satellites. Precipitating ion and electron data from the polar-orbiting (~ 840 km altitude) DMSP F6, F7, and F8 satellites [Hardy *et al.*, 1984] and ion drift data from F8 [Rich and Hairston, 1994] are used to characterize the high-latitude ionosphere before and after the decay of an arc.

Following the scheme of Shinohara and Kokubun [1996], the DMSP precipitation signatures of the decaying arcs are classified as “type A” (electron and ion) or “type B” (electron only) polar showers, which are distinguished from other kinds of precipitation by their integral electron number fluxes ($\Phi_{n,e} > 10^7 \text{ cm}^{-2} \text{ s}^{-1} \text{ sr}^{-1}$), and from each other by their integral ion number fluxes ($\Phi_{n,i} > 10^5 \text{ cm}^{-2} \text{ s}^{-1} \text{ sr}^{-1}$, type A; $\Phi_{n,i} < 10^5 \text{ cm}^{-2} \text{ s}^{-1} \text{ sr}^{-1}$, type B). Type B polar showers have IMF- and seasonally-dependent statistical properties similar to those of polar rain, while type A showers have ion fluxes characteristic of the low-altitude “boundary plasma sheet” (BPS) populations [e.g., Newell *et al.*, 1991]. Consequently, in the present paper, type A and type B polar showers are considered to be on closed and open field lines, respectively.

Only cross-track drift data are available for the F8 orbits presented here. The cross-cap potential distribution, which quantitatively determines convection cell boundaries, is calculated by integrating the dawn-dusk polar cap electric field distribution, derived from the F8 ion drift data and the IGRF internal field model ($\mathbf{E} = -\mathbf{v} \times \mathbf{B}$) [Rich and Hairston, 1994].

Selection of Cases and Their Relationship to IMF Reversals

We searched film records from the winters of 1986–87, 1988–89, 1989–90, and 1990–91 for Sun-aligned arcs whose luminosity decayed lengthwise within the field-of-view. (Films from the winter of 1987–88 were omitted from this study owing to damage from electrostatic discharges.) The number of cases in which lengthwise decay was clear was fundamentally limited by the sampling period of 2 min, which precludes the identification of decay lasting less than 4 min. Only cases with simultaneous satellite magnetometer data from the solar wind or magnetosheath were included in this study. In all of these cases the decay was antisunward.

The study was limited further to cases in which a reversal in at least one component of the IMF, followed by > 20 min of the new polarity, occurred within 2 h prior to the decay of the arc. This restriction led to the elimination of two cases from the study. (In both cases the IMF polarity was generally $B_x > 0$, $B_y < 0$, and $B_z > 0$, but there were multiple departures from this polarity, particularly in B_z , each lasting no more than 10 min.) The resulting number of cases is three from 1986–87, two from 1988–89, three from 1989–90, and none from 1990–91. If all forms of arc disappearance following a well-defined IMF reversal were considered, we would have about five times as many cases to consider.

The period between an IMF reversal and the Qaanaaq all-sky image in which the sunward tip of the decaying arc approached the geomagnetic latitude of the imager most closely is defined as the observed lag (t_{obs}). This lag is corrected for the solar wind travel time from the observing spacecraft to the subsolar magnetopause (t_{sm}). The corrected lags (t_{obs}^*) can be considered as the response time of the polar cap relative to when the IMF reversal reaches the nose of the magnetosphere. The details of this correction, involving a minimum variance analysis of the IMF reversals [Sonnerup and Cahill, 1968], are given in the Appendix. IMF reversal times and corrected lags are summarized in Table 1. Also noted are the UT of the image in which the sunward tip

of the decaying arc approached 86°N CG most closely, and the corresponding corrected geomagnetic local time (MLT) of the tip of the arc.

In all eight cases, the IMF reversal involved B_z turning negative. The corrected lags $t_{obs,z}^*$ between the IMF southward turnings and the antisunward decay of the arcs fall into two groups, with six of the cases between 18 and 32 min, and the other two between 60 and 70 min (Table 1). Additionally, in four cases B_y nearly simultaneously reversed polarity, while only in one case did B_x also reverse polarity. (All of these cases belong to the group with shorter B_z -lags.) The corrected lags $t_{obs,y}^*$ from the B_y reversals to the changes in the direction of arc dawn-dusk drift are given in Table 2, using the t_{sm} from the associated southward turning.

Polar Cap Arc Decay Occuring $\sim 20 - 30$ Minutes After the IMF Turns Southward

In this section we discuss the six arcs that decayed $\sim 20 - 30$ min after the IMF turned southward. The range of lags is similar to that observed by *Troshichev et al.* [1988] in the general disappearance of polar cap arcs, as well as to that observed by *Hairston and Heelis* [1995] in the development of a new convection pattern. In all six cases, after the arc decays, no arc-like emission remains in the field-of-view. The two cases in which the DMSP F8 satellite passed through the field-of-view just prior to the decay of the arc are analyzed in detail, then discussed in the context of the remaining four cases.

January 6, 1989

Arcs at 630.0 and 427.8 nm were observed between the zenith and the dawnside edge of the Qaanaaq field-of-view from the first image on this day (0247 UT) through the 0409 UT image. At 0411 an arc appeared near the duskside edge of the field-of-view, where previously no arc had been observed, and drifted dawnward, reaching the zenith

by 0423 and fading completely by 0429 (Figure 1). Meanwhile, another arc drifting dawnward behind this arc brightened, then started to decay antisunward by 0431, disappearing by 0441 (Figure 1). After this no arcs were observed until 0635. Both the first and second arcs emitted at 427.8 nm (not shown), the first at 0422, the second between 0428 and 0438.

Based on the observed doubling of the total IMF magnitude (from ~ 20 to ~ 40 nT), IMP 8 was probably within the magnetosheath from 0030 at least through the period of interest here. Its orbit during this period is consistent with a location just inside the magnetosheath [Fairfield, 1971]. B_z was large (~ 20 nT) and positive from 0030 to 0354, when a reversal occurred (Figure 2). Using simultaneous measurements on two spacecraft, *Freeman and Southwood* [1988] showed that magnetosheath B_y and B_z behave similarly to the corresponding components in the solar wind. Indeed, the dawnward arc drift first evident at 0411 is consistent with $B_y < 0$, as discussed below. Because of the location of IMP 8 in the magnetosheath, we assumed a purely north-south IMF reversal and a gardenhose orientation in order to calculate $t_{sm} \simeq 10$ min. The resulting corrected lag $t_{obs,z}^*$ between the B_z reversal at 0354 and the antisunward decay of the second arc is 26 min (Table 1).

A series of DMSP F8 passes shows an evolution between conditions characteristic of northward and southward IMF, consistent with the B_z reversal at 0354 UT. The 0322–0336 southern hemisphere pass revealed highly structured weak flow, including sunward flow in the central polar cap, and structured electron precipitation throughout the cap (Figure 3a). This precipitation pattern characteristic of $B_z > 0$ was similar to that observed in the preceding northern hemisphere pass (not shown). In contrast, the subsequent northern hemisphere pass (0413–0427 UT) revealed an asymmetry in the intensity of ion and electron precipitation in the polar cap (Figure 3b), with more intense fluxes on the dawnside, some on closed field lines. The driftmeter observed flows consistent with an overall two-cell convection pattern. Two smaller cells with the same

sense of rotation embedded in the dawn cell correspond to small regions of sunward flow in the dawn cell observed between 0416 and 0418. Strong antisunward polar cap flow ($> 1 \text{ km s}^{-1}$) is observed in the dusk cell. The asymmetry in the precipitation and flows may indicate a polar cap in transition from northward to southward IMF conditions, ~ 10 min before the arc decayed. The subsequent (0502–0516) southern hemisphere pass revealed regular antisunward flow and unstructured polar rain in the polar cap, consistent with $B_z < 0$ (Figure 3c).

As best as can be determined, the inverted V crossed by F8 at 0419:12 at the duskward edge of the region of closed field lines (Figure 3b, "1") is just dawnward of the arc near zenith in the images at 0419:58 (Figure 4), which is the same as that near zenith at 0423:58 (Figure 1). The arc that decayed antisunward later probably was caused by one of the electron precipitation enhancements observed between 0420 and 0421 by F8. The most intense of these, at 0420:04 (Figure 3b, "2"), is a type B polar shower, probably on open field lines and suggestive of intensified polar rain [Hardy *et al.*, 1982; Shinohara and Kokubun, 1996]. The appearance and brightening of the 427.8 nm emission in this arc after 0428 UT indicates a hardening of the electron fluxes [Eather and Mende, 1972], suggesting the development of an acceleration region along this open field line that is associated with the arc decay. Both arcs were located amid antisunward flow, well duskward of the sunward flow observed within the dawn cell (Figure 3b). The dawnward drift of the two arcs observed after 0411 is consistent with the initiation of duskward flow following an IMF southward turning when B_y is negative [Newell and Meng, 1995]. For $B_z < 0$ and $B_y < 0$, flows at the throat are expected to be directed toward the duskside in the northern hemisphere [Heelis, 1984], consistent with the large flows observed there (Figure 3b). The corrected lag from the southward turning at 0354 to the first evidence of dawnward drift is no more than 5 min. The antisunward decay of the second arc after 0431 may be due to the polar cap flow turning more directly antisunward as B_y decreased in magnitude after 0410, implying a corrected lag

$t_{obs,y}^* \simeq 9$ min. These short delays are consistent with the expectation that the effects of a new flow direction at the throat caused by changes in B_y (or changes in B_z while B_y remains constant) are propagated across the polar cap by a magnetohydrodynamic wave before the "new" flux tubes can convect the equivalent distance [Cowley and Lockwood, 1992].

October 30, 1989

Using an ASIP at Søndre Strømfjord, Greenland, a polar cap arc was observed forming near zenith at 0440 UT, possibly connected to the oval near 3 MLT [Gallagher *et al.*, 1995]. Subsequently, this arc drifted duskward, appearing at the dawn edge of the Qaanaaq field-of-view by 0456 and continuing to drift duskward until 0542. Soon thereafter (c. 0556 UT), it started to decay antisunward, disappearing nearly entirely by 0610 (Figure 5). B_z was positive throughout this period (Figure 6). Between 0420 and 0530, B_y pointed primarily duskward. A sharp north-to-south IMF reversal at 0532 followed 10 min of $B_z \simeq 7$ nT preceded by ~ 1 hr of weakly northward IMF with some short-lived southward excursions. The corrected lag $t_{obs,z}^*$ between this reversal and the arc decay is 19 min (Table 1).

Three consecutive DMSP F8 passes reveal the response of polar cap convection and precipitation to IMF changes during the lifetime of this polar cap arc. During the 0419–0433 southern hemisphere pass and the 0510–0524 northern hemisphere pass, the most intense and energetic precipitation was in the center of the cap (Figure 7a,b). In contrast, during the 0559–0613 southern hemisphere pass, structured ion and electron precipitation was limited to the dawnside of the polar cap (Figure 7c). In all three cases, antisunward flows were stronger on the dawnside, and the potential pattern consisted of two primary cells, with the dusk cell much broader in extent. The relative smoothness of the southern hemisphere flows before and after the B_z reversal may be a polar summer phenomenon.

Using the response times of polar cap convection to B_z reversals determined by *Hairston and Heelis* [1995] (17–25 min following southward turnings, 28–44 min following northward turnings), the IMF conditions corresponding to these three F8 passes were determined to be: (0419–0433, interpolating in a data gap) $B_z > 0$, $B_y < 0$, $B_z \approx 0$; (0510–0524) $B_z > 0$, $B_y > 0$, $B_z \approx 0$; (0559–0613) $B_z > 0$, $B_y < 0$, $B_z < 0$. The dominance of the dusk cell in all three passes, with the strongest antisunward flows on the dawnside, is consistent with the change in the sign of B_y between each pass and with the existence of a merging cell for weakly northward as well as southward IMF [Reiff and Burch, 1985]. The absence of BPS-like fluxes and the presence of polar rain and antisunward flow at the highest geomagnetic latitudes during the 0558–0614 F8 pass suggest that the effect of the B_z southward turning at 0532 has reached the center of the southern polar cap by the time the Sun-aligned arc largely has disappeared from the center of the northern polar cap (Figure 5).

The intense precipitation traversed by F8 at 0516:44 (Figure 7b, “2”; Figure 8) corresponds to the polar cap arc which later decayed antisunward (Figure 5). It is a type A polar shower with a likely origin on closed field lines [Shinohara and Kokubun, 1996]. The optical connection of this arc to the nightside oval observed at Søndre Strømfjord [Gallagher *et al.*, 1995] also suggests a location on closed field lines. Another type A polar shower observed by F8 at 0516:04 (Figure 7b, “1”) corresponds to the emission observed dawnward of the main arc in Figure 8. Both polar showers are associated with a shear in the antisunward flow consistent with $\nabla \cdot E < 0$. Their location on either side of a small region of sunward flow is similar to the configuration of precipitation and flows comprising the transpolar bar of the classic theta aurora of November 8, 1981 [Frank *et al.*, 1986, Plate 17 and Figure 5]. Although the 427.8 nm emission was evident from the appearance of the arc until 0540, it was brightest in the 0514 and 0516 images (Figure 8), then decreased rapidly in intensity. Moreover, the emission associated with the dawnward polar shower disappeared soon after the F8 pass, leaving the single arc which

later decayed antisunward (Figure 5). Since the converging electric fields corresponding to the region of sunward flow were associated with the more dawnward polar shower, it is possible that this sunward flow decreased or reversed as the 427.8 nm emission diminished and the dawnward arc disappeared.

Empirically, duskward drift of northern hemisphere polar cap arcs is expected for $B_y > 0$ and $B_z > 0$ [Valladares *et al.*, 1994]. The IMF duskward turning at 0420 thus may have led to the duskward arc drift observed at Søndre Strømfjord after 0440 [Gallagher *et al.*, 1995], and the dawnward turning at 0530 may have resulted in the cessation of drift by 0542, prior to the onset of antisunward decay. The corrected lag $t_{obs,y}^*$ for this effect was 3 min (Table 2). (If only B_y had reversed c. 0530, the arc might have started to drift dawnward without decaying [Craven *et al.*, 1991; Troshichev and Gusev, 1994].) The short delay suggests that the drift is caused by dayside merging [Cowley and Lockwood, 1992], which is possible for weakly northward IMF [Reiff and Burch, 1985].

Comparison of the Cases with $\sim 20 - 30 B_z$ Reversal Lags

Some of the salient aspects of the two cases analyzed above are discussed here in comparison with the other four cases.

1. In the case of January 26, 1990, when F8 passed through the center of the region conjugate to the Qaanaaq field-of-view (in CG coordinates) while the arc was present, no fluxes consistent with a polar cap arc were observed, indicating that the northern hemisphere polar cap arc was on open field lines. In contrast to the arc on January 6, 1989, this arc was long-lived (68 min), suggesting that the lifetime of the precipitation causing a 630.0 nm polar cap arc is not a good indication of its origin on open or closed field lines. Furthermore, arcs on open (January 6, 1989) and closed (October 30, 1989) field lines can have similar response times to B_z and B_y reversals.

2. Four of the six arcs ceased to drift duskward or dawnward before they started to

decay antisunward. In the case of October 30, 1989, B_y turned dawnward just before B_z turned southward, and the arc ceased to drift duskward, with $t_{obs,y}^* = 3$ min (Table 2). The cases of November 2, 1986, and December 5–6, 1986, are similar to each other in the MLT location of the arc (Table 1), the nature of the IMF reversal (B_y turning duskward and B_z turning southward), and the cessation of the arc's dawnward drift prior to its decay. However, in the former case $t_{obs,y}^*$ was 5–7 min while in the latter case it was 18 min (Table 2), about the same as $t_{obs,z}^*$ (Table 1).

In the case of January 26, 1990, the arc ceased to drift dawnward ~ 30 min before it started to decay antisunward. Since B_y was negative during the lifetime of the arc, the cessation of dawnward drift may be due to the establishment of a new steady state convection pattern ~ 50 min (corrected) after the IMF turned northward during constant B_y [Hairston and Heelis, 1995].

3. In the other two cases, January 6 and December 29, 1989, the arc decayed while it was drifting. The latter case was similar to those of November 2 and December 5–6, 1986, in the duskside location of the arc as well as the nature of the IMF reversal (B_y turning duskward and B_z turning southward). However, its response to the IMF reversal differed. The Sun-aligned arc apparently was stationary at the dawnside edge of the field-of-view prior to the IMF reversal. About 19 min after B_y turned duskward, the arc started to drift rapidly duskward (Table 2), then about 10 min later started to decay antisunward while continuing to drift (Table 1). The ~ 10 nT magnitude of the B_z component after reversal indicates strong antisunward flow that may have caused the rapid arc drift and decay.

In summary, the effect of B_y reversals in these six cases is that, in the northern hemisphere, an arc reverses direction, stops drifting, or starts to drift, with the drift direction being in the direction of B_y . This is consistent with previous observations [e.g., Craven *et al.*, 1991; Troshichev and Gusev, 1994; Valladares *et al.*, 1994]. Although the reason for the two groups of $t_{obs,y}^*$ (< 10 min and ~ 20 min) is not clear, they are well

within the range of B_y -related lags (0–80 min) reported by *Troshichev et al.* [1988]. The shorter group is expected based on the considerations of *Lockwood et al.* [1990] and *Cowley and Lockwood* [1992]. The similarity between the $t_{obs,y}^* \simeq 20$ min and the associated $t_{obs,z}^*$ suggests that, in these two cases, the change in dawn-dusk drift and the antisunward decay both occur when the new open flux tubes reach the center of the polar cap. Finally, the origin of an arc on open or closed field lines does not seem to have a distinguishing effect on its response to B_y or B_z reversals or on the longevity of its 630.0 nm signature.

Polar Cap Arc Decay Occuring $\sim 60 - 70$ Minutes After the IMF Turns Southward

In two of the eight cases, a polar cap arc appeared at the dawnside of the Qaanaaq field-of-view 30–40 min after B_z had turned negative (when arcs normally would be decaying antisunward or would have disappeared) and decayed antisunward ~ 30 min thereafter. Although the detailed arc behavior is unique to each case, both occurred during periods of fairly steady IMF $B_z < 0$ and $B_y > 0$, both occurred near magnetic local midnight, and both decayed antisunward after the onset of the expansion phase of a small substorm in the Greenland sector.

December 6, 1986

When the IMP 8 data started at 0158 UT on December 6, 1986, the IMF was strongly northward but had been so no more than an hour, based on ISEE 2 observations which ceased at 0100. The IMF was mostly in a “gardenhose away” configuration until 0520, although the magnitudes of both B_x and B_y varied substantially. At 0209, B_z reversed polarity sharply and remained negative until 0253 (Figure 9). By 0244, ~ 30 min after this reversal reached the subsolar magnetopause, what seemed to be part of a loop-like polar arc had appeared and brightened within the field-of-view near

the dayside edge (Figure 10). During the following 15 min this arc drifted antisunward, rotating into a more nearly Sun-aligned orientation at the dawnside of the Qaanaaq field-of-view by 0301. In this new configuration, the portion of the arc that had been closest to the dayside was now closest to the nightside. In its new orientation the arc began to drift duskward by 0309 and to decay antisunward by 0315. The 427.8 nm emission (not shown) was observed only briefly, between 0249 and 0253, and again at 0313 and 0315, just as the arc started to decay antisunward. The corrected lag $t_{obs,z}^*$ between the B_z reversal and this decay is 61–63 min (Table 1). The behavior of this arc differs from that of loop-like arcs reported by *Valladares et al.* [1994], which were of shorter duration and evolved from preexisting Sun-aligned arcs during a brief period of $B_z < 0$ following a long period of $B_z > 0$.

The 0238–0253 DMSP F6 pass revealed two isolated regions of electron and ion precipitation inside the polar cap (Figure 11a) that corresponded to two arms of the loop, the dawnside arm being traversed just outside the field-of-view (Figure 12a). The type A polar shower forming the duskside arm of the loop (Figure 11a, “1”) later formed the portion of the Sun-aligned arc closest to the nightside. The 0308–0323 F7 pass skimmed the Qaanaaq field-of-view between 0314 and 0316, after which it traversed ions and inverted-V electrons (Figure 11b, “1”) apparently coincident with the brightest portion of the decaying arc (Figure 12b). Despite the radical evolution in the arc’s orientation, the electron and ion average energies (~ 300 and 2000 eV) and integral energy fluxes ($\sim 10^{11}$ and 4×10^9 eV cm $^{-2}$ s $^{-1}$ sr $^{-1}$) remained nearly constant. These flux levels are consistent with an origin on closed field lines [*Shinohara and Kokubun*, 1996].

November 3, 1988

At 0049 UT on November 3, 1988, B_z turned southward and remained so until 0320 UT, apart from occasional northward impulses lasting ~ 1 min each (Figure.

13). B_z was negative throughout this period, and following ~ 3 hr of dawnward IMF, B_y turned duskward between 2352 and 0000 UT. Thus, during the polar cap arc observations discussed here, the IMF was in a southward and fairly steady "gardenhose away" configuration. At the time of the first all-sky images on this day (0127 UT), just prior to magnetic local midnight at Qaanaaq, scattered patchy emissions at 630.0 nm and at 427.8 nm were observed near zenith. Patchy polar cap aurorae have been reported before [Eather and Akasofu, 1969]. By 0141 UT a bright arc had begun to drift into the field-of-view from the dawnside, ~ 40 min after the southward IMF reached the magnetopause. An approximately Sun-aligned arc evolved out of the patchy emissions by 0147 and drifted duskward in front of the bright arc, disappearing by 0157. The bright arc reached the zenith by 0203, by which time its orientation departed significantly from the Sun-aligned direction (Figure 14).

At 0205, the arc began to break apart near the zenith into two sections, one remaining nearly Sun-aligned and the other rotating into a more latitudinal alignment. Thereafter, the Sun-aligned portion decayed in the antisunward direction, disappearing by 0223, and the rotated portion drifted antisunward behind it, becoming increasingly diffuse. The 427.8 nm emission (not shown) was evident in the bright arc from 0153 until 0221, including the rotated portion (especially after 0209). Using a correction based on the orientation of the well-defined IMF discontinuity at 0030, the lag $t_{obs,z}^*$ between the southward turning at 0049 and the arc decay is 67–68 min (Table 1).

Three consecutive F8 passes before and during the above arc observations reveal evolving polar cap flows and precipitation consistent with duskward and antisunward motion of luminosity originating on the dawnside of the northern polar cap. During the 0034–0052 F8 northern hemisphere pass, the ion drift meter observed highly structured flow in the nightside polar cap consistent either with a four-cell pattern or a distorted two-cell pattern, with a dominant dusk cell (Figure 15a). An isolated region of energetic yet mostly unstructured electron and ion precipitation was colocated with overall

sunward flow and $\nabla \cdot E > 0$ above 81.9° CG latitude on the dawnside, indicating a downward field-aligned current. It lay entirely within a small positive potential cell that may have been an extension of the dawnside oval. Accounting for the 10–11 min solar wind delay between IMP 8 and the magnetopause (Table 1), the region of northward IMF observed between 0030 and 0049 by IMP 8 had just reached the magnetopause when this large region of sunward flow was observed by F8 between 0042 and 0043. Consequently, it must have evolved during the preceding period of weakly southward and northward IMF and $B_y > 0$ (Figure 13).

Localized regions of $\nabla \cdot E < 0$ superposed on a region of downward field-aligned current might be the source of patchy auroral emissions such as observed at Qaanaaq later between 0127 and 0147. In fact, the region observed by F8 between 0042 and 0043 lay at the dawnside edge of the Qaanaaq field-of-view (unfortunately, no images were taken at that time), so if it persisted and remained steady in the Sun-earth frame for another hour it probably was the source of the observed patchy emissions. Indeed, the most intense and energetic electron and ion precipitation observed during the following F8 southern hemisphere pass (0134–0135, Figure 15b) was near the center of the polar cap and conjugate in CG coordinates to the patchy auroral emissions observed simultaneously at Qaanaaq. This pass occurred ~ 30 min after the region of southward IMF reached the magnetopause, and the entire cap was on antisunward flow. However, the enhanced structured polar cap ion and electron precipitation and the relatively weak polar cap potential (~ 30 keV peak) observed during this pass indicate that, in this case, dayside merging for $B_z < 0$ has been unusually slow in changing the state of the southern polar cap. Indeed, these observations and the optical evidence in the north suggest that both polar caps responded sluggishly to the IMF southward turning at 0049 UT, indicating a large degree of connectedness between the two caps, albeit with an asymmetry expected for $B_y > 0$.

During the subsequent (0216–0234) F8 pass, the spacecraft passed through the

Qaanaaq field-of-view sunward of the antisunward decaying arc (Figure 16). The driftmeter observed highly structured but mostly antisunward flow, corresponding to a two-cell potential distribution with the dusk cell predominant (Figure 15c). The presence of flow shears in a region from which the arc had already disappeared indicates that the disappearance of the fluxes sufficiently intense to stimulate detectable 427.8 and 630.0 nm emissions was caused by a change in the electric field configuration, but not a total removal of ionospheric shears.

Relationship of Polar Cap Arc Decay to the Onset of a Substorm Expansion Phase

Despite arc behavior that is as different between these two cases as it is from expected polar cap arc behavior, the two cases are similar in several aspects: a "gardenhose away" IMF configuration, the appearance of new arcs in the center of the polar cap 30–40 min after B_z turned negative, and the decay and disappearance of the arcs after a substorm onset. Data from the magnetometer chain on the west coast of Greenland [Stauning *et al.*, 1994] show poleward-progressing substorm activity starting no later than 0250 UT on December 6, 1986, and 0157 UT on November 3, 1988 (P. Stauning, private communication, 1996). (The start times refer to activity at the Narssarssuaq station, which is part of the AE index chain.)

The westward electrojet associated with such activity may have driven a nightside convection cell (corresponding to the DP 1 current system) with a strong duskward drift component in its poleward portion. The development of such a substorm-driven cell is consistent with the duskward drift of the December 6, 1986, arc starting around 0309 UT after a period of dawnward movement (Figure 10). The segmentation and rotation of the November 3, 1988, arc starting at 0205 UT may represent a rotation in the polar cap flow from nearly antisunward to nearly duskward, with the portion closer to the dayside aligning itself with the new flow direction and the portion closer to the

nightside maintaining its original orientation. This behavior is also consistent with the evolution of a substorm-driven cell.

In the case of December 6, 1986, the substorm onset occurred 34–36 min after southward IMF reached the magnetopause, and the drift identified as the effect of the substorm on the polar cap arc commenced ~ 17 min after the substorm onset, with the arc persisting for at least 12 min thereafter. DMSP F7 particle data from the midnight oval (0319–0322 UT, Figure 11b) and a simultaneous image from the F7 Operational Line Scanner (not shown) reveal the substorm in progress during the polar cap arc decay. In the case of November 3, 1988, the substorm onset occurred 57–58 min after southward IMF reached the magnetopause, and the segmentation and rotation identified as the effect of the substorm on the polar cap arc commenced ~ 6 min after the substorm onset, with the arc persisting for at least 20 min thereafter. While polar cap arcs are generally expected to disappear prior to substorm onset [e.g., *Starkov and Feldstein*, 1971; *Wu et al.*, 1991], the persistence of polar cap arcs 15–30 min after substorm onset has been documented elsewhere by *Henderson et al.* [1996] based on Viking ultraviolet imagery.

Discussion

Ionospheric Convection and the Two Characteristic Lags for Polar Cap Arc Decay

Studies of data from satellite-borne particle detectors, often in combination with ground- or satellite-based auroral imagery, have resulted in seemingly contradictory evidence for the mapping of polar cap arcs to different magnetospheric regions: open field lines linking the mantle and magnetosheath [e.g., *Hardy et al.*, 1982], closed field lines threading an expanded [e.g., *Meng*, 1981] or bifurcated [e.g., *Frank et al.*, 1986] plasma sheet and associated with sunward flow, or closed field lines mapping to the lower

latitude boundary layer (LLBL) and associated with antisunward flow [e.g., *Lundin et al.*, 1991].

In the present study, there is some evidence to support each of these scenarios. The difference in the two time scales ($\sim 20 - 30$ and $\sim 60 - 70$ min) is not attributable to origins on open vs. closed field lines, however. Rather, it seems to be related to the evolution of polar cap convection following an IMF southward turning. Studies of the response of convection and currents in the auroral oval and polar cap to IMF B_z reversals have revealed two characteristic response times. Effects of merging of solar wind and magnetospheric magnetic field lines on dayside convection have been observed to occur with lags of ~ 15 min or less, while the ionospheric signatures of tail reconnection (including substorm processes) exhibit lags of 30–60 min [*Lockwood et al.*, 1990; *Cowley and Lockwood*, 1992].

If polar cap arcs on open field lines are polar rain accelerated by mesoscale velocity shears [*Chiu*, 1989], their decay is probably caused by the introduction of new, possibly unsheared flows into the polar cap following an IMF southward turning. Consequently, the lags (26 and 32 min) associated with the arcs determined to be on open field lines (January 6, 1989, and January 26, 1990) suggest that arc decay lagging an IMF southward turning by $\sim 20 - 30$ min is caused by dayside merging, whether the arc is on open or closed field lines. The rapid duskward drift of the decaying arc on December 29, 1989, also suggests the effect of flows driven by dayside merging. The regular decay of the arcs of November 2 and December 5–6, 1986, and October 30, 1989, may represent the equatorward motion of the oval as open flux tubes are added to the polar cap by dayside merging after the IMF turns southward. Under such conditions, polar cap arcs attached to the nightside oval (as in the case of October 30, 1989) may move equatorward with the oval, and such motion would appear as antisunward decay in an all sky camera. Nonetheless, despite the indications that the sunward flow associated with the October 30, 1989, arc (on closed field lines) disappeared well before the start

of arc decay, a reconfiguration of tail reconnection cannot be ruled out as the cause of arc decay based on the evidence at hand in this study.

In the two cases with long lags (60–70 min) between the IMF southward turning and the arc decay, evidence indicates that the decay is caused by the onset of the expansion phase of a small substorm. The appearance of these arcs in the center of the polar cap 30–40 min after the IMF turned southward (but prior to substorm onset) is harder to understand, however. The duskward drift of the bright arc into the Qaanaaq field-of-view at 0141 on November 3, 1988, may have been caused by open flux tubes convecting antisunward and dawnward after the B_z reversal at 0049 UT, resulting in the detachment of part of the dawnside oval [Newell and Meng, 1995]. In contrast, the arc on December 6, 1986, seemed to appear and brighten while already in the field-of-view, then rotated antisunward and dawnward before drifting duskward. Such behavior is suggestive of turbulence in the polar cap that may map to the distant tail flanks, as discussed next.

Polar Cap Arcs on Closed Field Lines: An Origin at the Plasma Sheet/Lower Latitude Boundary Layer Interface?

The arcs on closed field lines for which there are drift data (November 3, 1988, and October 30, 1989) are at the poleward edge of a dawnside polar cap and oval consisting of mixed antisunward and sunward flow and stagnation (Figure 15a and Figure 7b). This configuration suggests an origin in the lower latitude boundary layer (LLBL) [Mitchell *et al.*, 1987; Newell *et al.*, 1991; Taguchi *et al.*, 1995]. Since the low-altitude precipitation signature of the LLBL has been identified with the dayside cleft [e.g., Newell *et al.*, 1991], an LLBL origin for nightside polar cap arcs has been deemed unlikely [Weiss *et al.*, 1993]. However, field-line tracing using the Tsyganenko [1987] magnetospheric model indicates that regions similar to those equatorward of horse-collar aurora bars [Hones *et al.*, 1989] map to the distant tail flanks (or “distant LLBL”) when

the magnetospheric B_z is positive and enhanced at the tail flanks [Elphinstone *et al.*, 1991; Birn *et al.*, 1991].

In addition to mixed flow directions, such regions may contain precipitation characteristic of a mixture of open and closed field lines (e.g., Figure 7b, Figure 15a). The similarity of the closed field line precipitation to the low-altitude nightside "boundary plasma sheet" (BPS) precipitation signature has led to an identification of such regions as an expanded auroral oval [e.g., Meng, 1981; Newell and Meng, 1995]. Other workers [e.g., Hardy *et al.*, 1982; Rich *et al.*, 1990] have determined that such precipitation may map to magnetospheric boundary layers other than the plasma sheet boundary layer (PSBL), some of which may lie partially or entirely on open field lines (mantle, LLBL, and cusp/cleft). There is also a debate as to whether the BPS originates in the PSBL or the central plasma sheet (see Weiss *et al.* [1993] for a review), and a widely-adopted classification scheme for low-altitude precipitation characterizes the "BPS" label as a "catch-all" for precipitation signatures that may have more than one origin [Newell *et al.*, 1991]. One possible solution to this problem may be that, during quiet times, the PSBL and LLBL are coupled [Lundin *et al.*, 1991]. There is evidence for the intrusion of both plasma sheet and LLBL populations into regions nominally part of the low-density tail lobes, between $x_{GSM} = -12R_e$ and $x_{GSM} = -34R_e$, within $\pm 16R_e$ of the noon-midnight meridian, and at vertical distances of $3 - 12R_e$ from the neutral sheet [Huang *et al.*, 1987, 1989; Zwolakowska and Popielawska, 1992; Popielawska *et al.*, 1993].

As suggested by Elphinstone *et al.* [1994], polar cap arcs may map to surface waves or instabilities on the distant LLBL-magnetosheath boundary. The further downstream the waves lie in the distant LLBL, the closer the arcs lie to the center of the polar cap, and the deeper into the LLBL and adjacent plasma sheet the waves penetrate, the more the arcs extend into the nightside [Birn *et al.*, 1991]. Moreover, the field lines twist such that a roughly circular plasma region lying in the tail equatorial plane between the

plasma sheet and the magnetosheath maps to an elongated feature in the polar cap that stretches from the nightside toward the cusp, much like a polar cap arc [Elphinstone *et al.*, 1994]. Such mapping implies that the duskward or dawnward drift of an arc into the center of the polar cap corresponds to tailward movement of structure in the tail flanks, while antisunward decay corresponds to movement from the flanks toward the center of the plasma sheet.

This concept is illustrated in Figure 17, with specific reference to the cases of December 6, 1986, November 3, 1988, and October 30, 1989. One difference between the discussion of Elphinstone *et al.* [1994] and the present discussion is that we assume that instabilities occur at the boundary between the distant LLBL and the plasma sheet, where flows are likely to be antiparallel, resulting in a velocity shear that favors the Kelvin-Helmholtz instability. Figure 17a illustrates the behavior of arcs such as observed on October 30, 1989, and November 3, 1988, which exhibit dawnward drift followed by antisunward decay. This polar cap arc topology and dynamics are equivalent to a closed field line structure in the tail extending from the plasmasheet to the magnetosheath in the dawnside equatorial plane that drifts antisunward, then decays toward the plasmasheet. The poleward and dawnward flow shown emerging from the throat is driven by dayside merging for $B_y > 0$ [Heelis, 1984] and may be the cause of the duskward drift [Newell and Meng, 1995]. The multiple flow reversals observed on the dawnside may correspond to multiple plasmasheet extensions toward the magnetosheath, possibly surface waves at the plasma sheet/distant LLBL interface [Taguchi *et al.*, 1995]. Possible locations of field aligned currents directed upward from the polar cap to the equatorial plane in the distant tail flanks are indicated by dots in the polar cap and crosses in the equatorial plane. Note that LLBL fluxes may also be accelerated into the polar cap if $\nabla \cdot E < 0$, so alternating LLBL and plasma sheet plasmas may be observed as a DMSP satellite crosses from dawn to dusk.

Figure 17b illustrates one possible explanation for the evolution of the arc on

December 6, 1986 (Figure 10). The persistence of the arc despite the radical change in its alignment suggests that it is at the center of a vortex. This vortex may map to the remnant of a spiral at the plasmasheet/LLBL boundary in the distant tail flank. This would require that the arc was originally connected to the early morning oval. The lack of optical evidence for such a connection may be due either to the Sun-aligned portion of the arc being outside the Qaanaaq field-of-view, or due to the associated precipitation being too weak to stimulate detectable emissions. The latter situation is supported by the observation that the "loop" increased in intensity within the field-of-view rather than drifting in. After the spiral is severed from the main part of the plasma sheet, perhaps by the development of a viscous cell (clockwise in the equatorial plane, counterclockwise in the polar cap) or by the effects of enhanced dawnward convection from the throat in the northern polar cap, the remnant of the spiral rotates inward and sunward in the LLBL, which maps to an antisunward and dawnward rotation in the polar cap. This process energizes the populations in the spiral remnant, which maps to a clockwise vortex in the polar cap. Such a feature in the polar cap was observed on November 3, 1988, when a counterclockwise cell ($\nabla \cdot E > 0$) with diffuse precipitation contained small enhancements associated with $\nabla \cdot E < 0$ (Figure 15a, 0042–0043 UT; note enhancements in integral flux). The final duskward drift and antisunward decay of the arc on December 6, 1986, due perhaps to the substorm onset, corresponds to antisunward drift and inward decay of the spiral remnant in the equatorial plane.

Under this model, if the response of polar cap arcs to a southward turning of the IMF is caused by dayside merging, then recently merged open field lines in the polar cap affect flows and plasma populations in the distant tail flanks. This may represent one means by which a southward turning can affect the tail during the growth phase of a substorm, 20 – 30 min after the IMF turns southward. Conversely, the appearance and motion of polar cap arcs 30 – 40 min after the IMF has turned southward but prior to substorm onset (as in the cases of December 6, 1986, and November 3, 1988) may

represent the mapping to the polar cap of evolving viscous processes in the distant tail flanks.

Summary

An intensified monochromatic all-sky imager at Qaanaaq, Greenland, has been used to observe the lengthwise decay of arcs in the center of the polar cap. Eight such cases have been selected which followed a reversal in at least one component of the IMF within 2 h. These have been analyzed in the context of IMF data (from IMP 8 and ISEE 2) and of DMSP observations of convection and precipitating particles in the topside ionosphere, with the following salient results:

1. In all cases, the arcs decayed antisunward. Moreover, they all drifted dawnward or duskward before or during the arc decay. In four cases, the arc drifted or deformed while decaying. In the remaining cases, it decayed without drifting or deforming. The direction of drift in all cases is in the direction of B_y , consistent with previous observations of northern hemisphere polar cap arcs.
2. All of the IMF reversals involved B_z turning negative. In four cases, B_y also reversed, while B_x reversed in only one case. The lags from the B_z reversals to the decay of the arcs have been measured and corrected for the travel time between the spacecraft and the nose of the magnetosphere. In six cases, the antisunward decay of polar cap arcs was preceded within $\sim 20 - 30$ min by a B_z southward turning.
3. In the other two cases, polar cap arcs appeared on the dawnside near midnight $\sim 30 - 40$ min after B_z reversed under fairly steady "gardenhose away" conditions. They subsequently decayed antisunward following the onset of the expansion phase of a small substorm observed in the Greenland sector, $\sim 60 - 70$ min after the IMF turned southward.
4. In the cases in which B_y also reversed, the lags from the reversal to the change in dawn-dusk drift have also been measured and similarly corrected. In two cases the lag

was < 10 min, while in the other cases the lag was ~ 20 min, similar to the associated B_z lag. The origin of an arc on open or closed field lines does not seem to affect the lag in its response to B_y or B_z reversals or the longevity of the precipitation causing the 630.0 nm emission.

5. Of the five cases in which a DMSP satellite traversed the Qaanaaq field-of-view (or its conjugate region) while the arc was present, two (three) arcs were determined to be on open (closed) field lines based on the precipitating particle data. Both open and closed field line arcs were associated with the $\sim 20 - 30$ min lags, while both of the arcs associated with $\sim 60 - 70$ min lags were on closed field lines.

6. The mechanism which best accounts for the antisunward decay of six arcs $\sim 20 - 30$ min after B_z turns negative is the convection of new open flux tubes from the cusp to the center of the polar cap due to dayside merging, with a pronounced dependence on the sign of B_y . The appearance of the other two arcs in the center of the polar cap $\sim 30 - 40$ min after the IMF turns southward may be related to dayside merging or to viscous processes in the evolving distant LLBL. The behavior of these two arcs just prior to decay suggests a rotation of flow in the early morning polar cap from antisunward to duskward caused by the development of a substorm-driven convection cell.

7. Polar cap arcs on closed field lines may map to waves or instabilities in the distant flanks of the magnetotail, perhaps associated with velocity shears between the plasmashet and the distant LLBL. If so, antisunward arc decay $20 - 30$ min after southward IMF reaches the magnetopause may represent the stirring of the tail flanks by dayside driven merging, while the appearance and motion of polar cap arcs $30 - 40$ min after an IMF southward turning is more likely driven by viscous processes in the distant tail.

Appendix: Correction of Observed Lags for Travel Time in the Solar Wind and Magnetosheath

The observed lag t_{obs} from an IMF reversal to the onset of the decay of a polar cap arc is corrected for the travel time from the observing spacecraft to the magnetopause, which is divided into two segments: from the spacecraft to the subsolar bowshock (t_{sb}), and across the magnetosheath (t_{bm}) [Lockwood *et al.*, 1989]. Additionally, because the 630.0 nm emission has a radiative lifetime of order 100 s, the lag is further corrected by removing this amount ($t_{6300} = 100$ s). The resulting corrected lag is

$$t_{obs}^* = t_{obs} - t_{sb} - t_{bm} - t_{6300}.$$

The lag from the spacecraft to the subsolar bowshock is given by $t_{sb} = (x_{sw} - x_b)/v_{sw}$, where x_{sw} is the point of intersection of the IMF discontinuity with the GSE Sun-earth axis, x_b is the subsolar bowshock radius, and v_{sw} is the bulk solar wind velocity. (The Alfvén velocity of the discontinuity relative to the bulk flow is neglected [Sergeev *et al.*, 1986].) When the observing spacecraft is close to this line (as in the two ISEE 2 observations on December 5 and 10, 1986), the x -coordinate of the spacecraft can be used as x_{sw} with little error. However, when the spacecraft is far from this axis (as in most of the IMP 8 observations shown here), the orientation of the IMF discontinuity must be taken into account. Lacking multiple spacecraft observations in the solar wind, we use a minimum variance analysis [Sonnerup and Cahill, 1968] of the sharp IMF discontinuities to determine this orientation. This technique relies on the fact that the magnetic flux density vector \mathbf{B} component normal to a boundary is continuous across that boundary. The minimum variance method transforms the magnetic field components from the GSE coordinate system to one in which the coordinate axes are directed along the direction of minimum, intermediate, and maximum variance of the magnetic field across the boundary (IMF reversal). The maximum variance direction corresponds to the direction of maximum field reversal (e.g., GSE N-S if only B_z

reverses), and the minimum variance direction is interpreted as the normal direction to the IMF discontinuity, from which its orientation can be determined.

This technique is applied to the IMP 8 data in the following manner. In each case, the calculation is performed on an interval centered on the sharp IMF reversal and varying from ± 15.36 s (the data resolution) to ± 10 min, with the expectation that the calculation should be stable over some range of number of points between the two extremes. The lag t_{sb} is determined over such a range on which the following three criteria (listed in decreasing order of importance) are satisfied:

1. The ratio of the intermediate to the minimum variance axis eigenvalues λ_2/λ_3 is greater than 2 [Lepping and Behannon, 1980].
2. The standard deviation of the average normal component normalized by the value of this component is minimized.
3. The average normal component is minimized.

If the range of valid t_{sb} derived from this calculation is greater than 1 min, this range is reflected in the values of $t_{sm} = t_{sb} + t_{bm}$ and t_{obs}^* given in Table 1.

The travel time across the magnetosheath is given by $t_{bm} = (x_b - x_m)/v_{sh}$, where x_m is the subsolar magnetopause radius and v_{sh} is the bulk velocity in the sheath. For these calculations, it is assumed that $x_b = 1.33x_m$ [Fairfield, 1971] and $v_{sh} = 0.125v_{sw}$ [Spreiter and Stahara, 1980]. The subsolar magnetopause radius in units of Earth radii is given by $x_m = G/(n_{sw}v_{sw}^2)^{1/6}$, where $G = 10750$ (for v_{sw} in m s^{-1} and n_{sw} in m^{-3}) [Holzer and Slavin, 1978]. For the case (January 6, 1989) in which IMP 8 solar wind plasma data are not available, it is assumed that $v_{sw} = 420 \text{ km s}^{-1}$ and $x_m = 11R_E$.

Acknowledgments. We are indebted to Svend Erik Ascanius for his careful and diligent operation of the Qaanaaq all-sky imager, and we thank the Danish Commission for Scientific Research in Greenland for permission to conduct ground experiments at Qaanaaq under continuing project A16-91. We thank E. J. Weber, P. Stauning, F. J. Rich, M. R. Hairston, R. H. Eather, R. W. Eastes, H. C. Carlson, and W. J. Burke for useful discussions; J. James

and K. Martin for assistance in accessing the DMSP data; A. Ridley for making available his code for plotting DMSP data; and P. S. Rodriguez for drafting Figure 17. The IMP 8 magnetometer and electrostatic analyzer data were made available by the NSSDC Data Archive and Distribution Service Automated Retrieval Mail System (NDADS ARMS) by courtesy of R. P. Lepping and J. T. Gosling, respectively. Additionally, the ISEE 2 magnetometer data were provided by NSSDC courtesy of C. T. Russell. O. Rasmussen, Solar-Terrestrial Physics Division, Danish Meteorological Institute, provided data from the Greenland magnetometer chain. The work at Boston College was supported in part by Phillips Laboratory contract F19628-K-0007 and NSF grant ATM-9404088, and in part by the National Aeronautics and Space Administration's Graduate Student Researchers Program. This work was performed while J. V. Rodriguez held a National Research Council-AFOSR Research Associateship at the Phillips Laboratory.

References

- Berkey, F. T., L. L. Cogger, S. Ismail, and Y. Kamide, Evidence for a correlation between Sun-aligned arcs and the interplanetary magnetic field direction, *Geophys. Res. Lett.*, **3**, 145-147, 1976.
- Birn, J., E. W. Hones, Jr., J. D. Craven, L. A. Frank, R. D. Elphinstone, and D. P. Stern, On open and closed field lines regions in Tsyganenko's field model and their possible associations with horse collar auroras, *J. Geophys. Res.*, **96**, 3811-3817, 1991.
- Burke, W. J., The polar cap with northward IMF: what I think I know, in *Physics of Space Plasmas*, SPI Conference Proceedings and Reprint Series, v. 8, ed. by T. Chang, G. B. Crew, and J. R. Jasperse, pp. 154-172, 1988.
- Burke, W. J., M. S. Gussenhoven, M. C. Kelley, D. A. Hardy, and F. J. Rich, Electric and magnetic field characteristics of discrete arcs in the polar cap, *J. Geophys. Res.*, **87**, 2431-2443, 1982.
- Carlson, H. C., Jr., R. A. Heelis, E. J. Weber, and J. R. Sharber, Coherent mesoscale convection patterns during northward interplanetary magnetic field, *J. Geophys. Res.*, **93**, 14,501-14,514, 1988.
- Chiu, Y. T., Formation of polar cap arcs, *Geophys. Res. Lett.*, **16**, 743-746, 1989.
- Cowley, S. W. H., and M. Lockwood, Excitation and decay of solar wind-driven flows in the magnetosphere-ionosphere system, *Ann. Geophys.*, **10**, 103-115, 1992.
- Craven, J. D., J. S. Murphree, L. A. Frank, and L. L. Cogger, Simultaneous optical observations of transpolar arcs in the two polar caps, *Geophys. Res. Lett.*, **18**, 2297-2300, 1991.
- Davis, T. N., The morphology of the auroral displays of 1957-1958, 2. Detail analyses of Alaska data and analyses of high-latitude data, *J. Geophys. Res.*, **67**, 75-110, 1962.
- Davis, T. N., Negative correlation between polar-cap visual aurora and magnetic activity, *J. Geophys. Res.*, **68**, 4447-4453, 1963.
- Eather, R. H., The auroral oval — a reevaluation, *Rev. Geophys.*, **11**, 155-167, 1973.
- Eather, R. H., and S.-I. Akasofu, Characteristics of polar cap aurorae, *J. Geophys. Res.*, **74**, 4794-4798, 1969.

- Eather, R. H., and S. B. Mende, Systematics in auroral energy spectra, *J. Geophys. Res.*, **77**, 660-673, 1972.
- Elphinstone, R. D., D. J. Hearn, J. S. Murphree, and L. L. Cogger, Mapping using the Tsyganenko long magnetospheric model and its relationship to Viking auroral images, *J. Geophys. Res.*, **96**, 1467-1480, 1991.
- Elphinstone, R. D., D. J. Hearn, and J. S. Murphree, Dayside aurora poleward of the main auroral distribution: implications for convection and mapping, in *Physical Signatures of Magnetospheric Boundary Layer Processes*, edited by J. A. Holtet and A. Egeland, pp. 189-200, Kluwer, 1994.
- Fairfield, D. H., Average and unusual locations of the Earth's magnetopause and bow shock, *J. Geophys. Res.*, **76**, 6700-6716, 1971.
- Fairfield, D. H., and L. J. Cahill, Jr., Transition region magnetic field and polar magnetic disturbances, *J. Geophys. Res.*, **71**, 155-169, 1966.
- Feldstein, Ya. I., Some problems concerning the morphology of auroras and magnetic disturbances at high latitudes, *Geomag. Aeron. (Engl. trans.)*, **3**, 183-192, 1963.
- Feldstein, Ya. I., S. I. Isaev, and A. I. Lebedinsky, The phenomenology and morphology of aurorae, *Annals of the IQSY*, **4**, 311-348, 1967.
- Frank, L. A., et al., The theta aurora, *J. Geophys. Res.*, **91**, 3177-3224, 1986.
- Freeman, M. P., and D. J. Southwood, The correlation of variations in the IMF with magnetosheath field variations, *Adv. Space. Res.*, **8**(9), 217-220, 1988.
- Gallagher, H. A., Jr., R. L. Carovillano, E. J. Weber, K. Fukui, and C. E. Valladares, Determination of plasma convection about Sun-aligned polar cap auroral arcs from incoherent scatter radar and all sky imaging photometer observations, *Eos Trans. AGU*, **76**(17), Spring Meet. Suppl., S249, 1995.
- Gustafsson, G., N. E. Papitashvili, and V. O. Papitashvili, A revised corrected geomagnetic coordinate system for epochs 1984 and 1990, *J. Atmos. Terr. Phys.*, **54**, 1609-1631, 1992.
- Hairston, M. R., and R. A. Heelis, Response time of the polar ionospheric convection pattern to changes in the north-south direction of the IMF, *Geophys. Res. Lett.*, **22**, 631-634, 1995.

- Hardy, D. A., W. J. Burke, and M. S. Gussenhoven, DMSP optical and electron measurements in the vicinity of polar cap arcs, *J. Geophys. Res.*, **87**, 2413-2430, 1982.
- Hardy, D. A., L. K. Schmitt, M. S. Gussenhoven, F. J. Marshall, H. C. Yeh, T. L. Schumaker, A. Huber, and J. Pantazis, Precipitating electron and ion detectors (SSJ/4) for the block 5D/flights 6-10 DMSP satellites: calibration and data presentation, *Rep. AFGL-TR-84-0317*, Air Force Geophysics Laboratory, Hanscom AFB, Mass., Nov. 21, 1984. ADA157080
- Heelis, R. A., The effects of interplanetary magnetic field orientation on dayside high latitude convection, *J. Geophys. Res.*, **85**, 2873-2880, 1984.
- Henderson, M. G., J. S. Murphree, and J. M. Weygand, Observations of auroral substorms occurring together with pre-existing "quiet time" auroral patterns, *J. Geophys. Res.*, **101**, 24,621-24,640, 1996.
- Holzer, R. E., and J. A. Slavin, Magnetic flux transfer associated with expansions and contractions of the dayside magnetosphere, *J. Geophys. Res.*, **83**, 3831-3839, 1978.
- Hones, E. W., Jr., J. D. Craven, L. A. Frank, D. S. Evans, and P. T. Newell, The horse-collar aurora: a frequent pattern of the aurora in quiet times, *Geophys. Res. Lett.*, **16**, 37-40, 1989.
- Huang, C. Y., L. A. Frank, W. K. Peterson, D. J. Williams, W. Lennartsson, D. G. Mitchell, R. C. Elphic, and C. T. Russell, Filamentary structures in the magnetotail lobes, *J. Geophys. Res.*, **92**, 2349-2363, 1987.
- Huang, C. Y., J. D. Craven, and L. A. Frank, Simultaneous observations of a theta aurora and associated magnetotail plasmas, *J. Geophys. Res.*, **94**, 10,137-10,143, 1989.
- Ismail, S., D. D. Wallis, and L. L. Cogger, Characteristics of polar cap Sun-aligned arcs, *J. Geophys. Res.*, **82**, 4741-4749, 1977.
- Lassen, K., and C. Danielsen, Quiet time pattern of auroral arcs for different directions of the interplanetary magnetic field in the Y-Z plane, *J. Geophys. Res.*, **83**, 5277-5284, 1978.
- Lepping, R. P., and K. W. Behannon, Magnetic field directional discontinuities, 1. Minimum variance errors, *J. Geophys. Res.*, **85**, 4695-4703, 1980.

- Lockwood, M., P. E. Sandholt, S. W. H. Cowley, and T. Oguti, Interplanetary magnetic field control of dayside auroral activity and the transfer of momentum across the dayside magnetopause, *Planet. Space Sci.*, **37**, 1347–1365, 1989.
- Lockwood, M., S. W. H. Cowley, and M. P. Freeman, The excitation of plasma convection in the high-latitude ionosphere, *J. Geophys. Res.*, **95**, 7961–7972, 1990.
- Lundin, R., L. Eliasson, and J. S. Murphree, The quiet-time aurora and the magnetospheric configuration, in *Auroral Physics*, edited by C.-I. Meng, M. J. Rycroft, and L. A. Frank, pp. 177–193, Cambridge University Press, 1991.
- Mawson, D., Auroral observations at the Cape Royds station, Antarctica, *Trans. Roy. Soc. S. Australia*, **40**, 151–212, 1916.
- Mende, S. B., and R. H. Eather, Monochromatic all-sky observations and auroral precipitation patterns, *J. Geophys. Res.*, **81**, 3771–3780, 1976.
- Meng, C.-I., Polar cap arcs and the plasma sheet, *Geophys. Res. Lett.*, **8**, 273–276, 1981.
- Mitchell, D. G., F. Kutchko, D. J. Williams, T. E. Eastman, L. A. Frank, and C. T. Russell, An extended study of the low-latitude boundary layer on the dawn and dusk flanks of the magnetosphere, *J. Geophys. Res.*, **92**, 7394–7404, 1987.
- Murphree, J. S., R. D. Elphinstone, L. L. Cogger, and D. D. Wallis, Short-term dynamics of the high-latitude auroral distribution, *J. Geophys. Res.*, **94**, 6969–6974, 1989.
- Newell, P. T., and C.-I. Meng, Creation of theta-auroras: the isolation of plasma sheet fragments in the polar cap, *Science*, **270**, 1338–1341, 1995.
- Newell, P. T., W. J. Burke, E. R. Sanchez, C.-I. Meng, M. E. Greenspan, and C. R. Clauer, The low-latitude boundary layer and the boundary plasma sheet at low-altitude: prenoon precipitation regions and convection reversal boundaries, *J. Geophys. Res.*, **96**, 21,013–21,023, 1991.
- Popielawska, B., P. Koperski, D. Zwolakowska, R. Lundin, and A. V. Zakharov, On the low energy electrons in the magnetotail, *Adv. Space Res.*, **13**(4), 53–58, 1993.
- Reiff, P. H., and Burch, J. L., IMF B_y -dependent plasma flow and Birkeland currents in the dayside magnetosphere, 2. A global model for northward and southward IMF, *J. Geophys. Res.*, **90**, 1595–1609, 1985.

- Rich, F. J., and M. Hairston, Large-scale convection patterns observed by DMSP, *J. Geophys. Res.*, **99**, 3827–3844, 1994.
- Rich, F. J., D. A. Hardy, R. H. Redus, and M. S. Gussenhoven, Northward IMF and patterns of high-latitude precipitation and field-aligned currents: the February 1986 storm, *J. Geophys. Res.*, **95**, 7893–7913, 1990.
- Sergeev, V. A., N. P. Dmitrieva, and E. S. Barkova, Triggering of substorm expansion by the IMF directional discontinuities: time delay analysis, *Planet. Space Sci.*, **11**, 1109–1118, 1986.
- Shinohara, I., and S. Kokubun, Statistical properties of particle precipitation in the polar cap during intervals of northward IMF, *J. Geophys. Res.*, **101**, 69–82, 1996.
- Sonnerup, B. U. O., and L. J. Cahill, Jr., Magnetopause structure and attitude from Explorer 12 observations, *J. Geophys. Res.*, **72**, 171–183, 1967.
- Spreiter, J. R., and S. S. Stahara, A new predictive model for determining solar wind-terrestrial planet interactions, *J. Geophys. Res.*, **85**, 6769–6777, 1980.
- Starkov, G. V., and Ya. I. Feldstein, Substorm in auroras, *Geomagn. Aeron. (Engl. transl.)*, **11**, 478–479, 1971.
- Stauning, P., E. Friis-Christensen, O. Rasmussen, and S. Vennerstrøm, Progressing polar convection disturbances: signature of an open magnetosphere, *J. Geophys. Res.*, **99**, 11,303–11,317, 1994.
- Taguchi, S., M. Sugiura, T. Iyemori, J. D. Winningham, and J. A. Slavin, Highly structured ionospheric convection for northward interplanetary magnetic field: A case study with DE 2 observations, *J. Geophys. Res.*, **100**, 14,743–14,753, 1995.
- Troshichev, O. A., and M. G. Gusev, IMF B_x and B_y dependencies of the polar cap auroral distribution for northward IMF orientation inferred from observations at Vostok station, *J. Atmos. Terr. Phys.*, **56**, 237–244, 1994.
- Troshichev, O. A., M. G. Gusev, S. V. Nickolashkin, and V. P. Samsonov, Features of the polar cap aurorae in the southern polar region, *Planet. Space Sci.*, **36**, 429–439, 1988.
- Tsyganenko, N. A., Global quantitative models of the geomagnetic field in the cislunar magnetosphere for different disturbance levels, *Planet. Space Sci.*, **35**, 1347–1358, 1987.

- Valladares, C. E., H. C. Carlson, Jr., and K. Fukui, Interplanetary magnetic field dependency of stable Sun-aligned polar cap arcs, *J. Geophys. Res.*, *99*, 6247–6272, 1994.
- Weber, E. J., and J. Buchau, Polar cap F-layer auroras, *Geophys. Res. Lett.*, *8*, 125–128, 1981.
- Weber, E. J., M. C. Kelley, J. O. Ballenthin, S. Basu, H. C. Carlson, J. R. Fleischman, D. A. Hardy, N. C. Maynard, R. F. Pfaff, P. Rodriguez, R. E. Sheehan, and M. Smiddy, Rocket measurements within a polar cap arc: plasma, particle, and electric circuit parameters, *J. Geophys. Res.*, *94*, 6692–6712, 1989.
- Weill, G., Aspects de l'aurore observée à la base Dumont-d'Urville en Terre Adelie, *C. R. Acad. Sci.*, *246*, 2925–2927, 1958.
- Weiss, L. A., E. J. Weber, P. H. Reiff, J. R. Sharber, J. D. Winningham, F. Primdahl, I. S. Mikkelsen, C. Siefring, and E. M. Wescott, Convection and electrodynamic signatures in the vicinity of a Sun-aligned arc: results from the Polar Acceleration Regions and Convection Study (Polar ARCS), in *Auroral Plasma Dynamics, Geophys. Monogr. Ser.*, v. 80, edited by R. L. Lysak, pp. 69–80, AGU, Washington, D. C., 1993.
- Whalen, J. A., Auroral oval plotter and nomograph for determining corrected geomagnetic local time, latitude, and longitude for high latitudes in northern hemisphere, AFCRL 70-0422, AD713170, 1970.
- Wu, Q., T. J. Rosenberg, F. T. Berkey, and R. H. Eather, Intensification and fading of auroral arcs in the dusk-midnight sector of the polar cap, *J. Geophys. Res.*, *96*, 7709–7719, 1991.
- Zwolakowska, D., and B. Popielawska, Tail plasma domains and the auroral oval — results of mapping based on the Tsyganenko 1989 magnetosphere model, *J. Geomag. Geoelectr.*, *44*, 1145–1158, 1992.

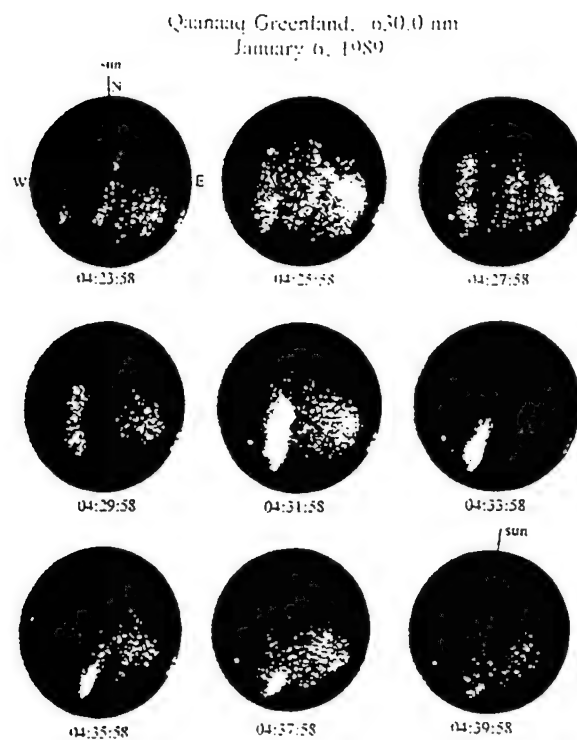


Figure 1. All-sky images at 630.0 nm from Qaanaaq, January 6, 1989, 0423–0439 UT. The vertical and horizontal bars of the L-shaped mark point to geographic north and east, respectively (the images are printed as if viewed from above). The direction of the sun is indicated. The second of two faint arcs drifting downward brightens, then decays antisunward.

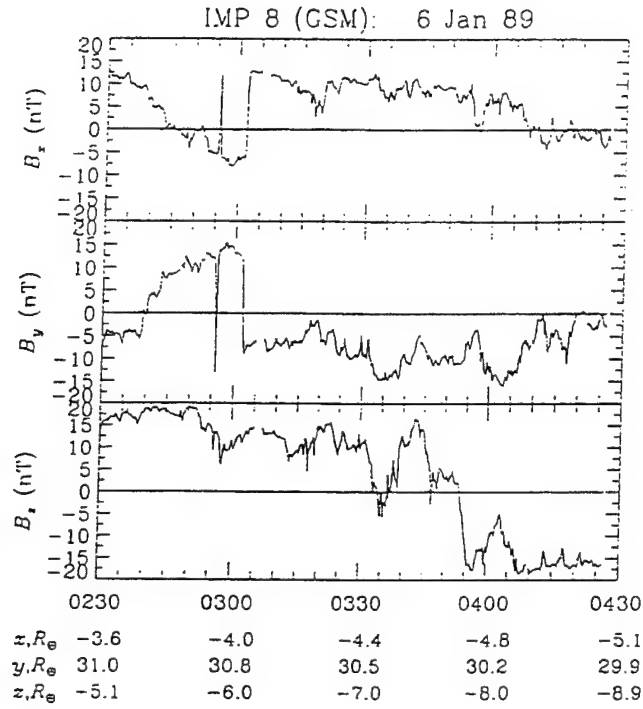


Figure 2. Magnetic field observed by IMP 8 in the duskside magnetosheath, January 6, 1989, 0230–0430 UT. The three components of the IMF are shown, along with the geocentric solar magnetospheric (GSM) coordinates of the spacecraft in Earth radii. The data cease at 0425 UT. The southward turning of B_z at 0354 UT during a period of $B_y < 0$ may have caused the dawnward drift of the two arcs shown in Figure 1, followed by the antisunward decay of the second arc.

revised figures

4

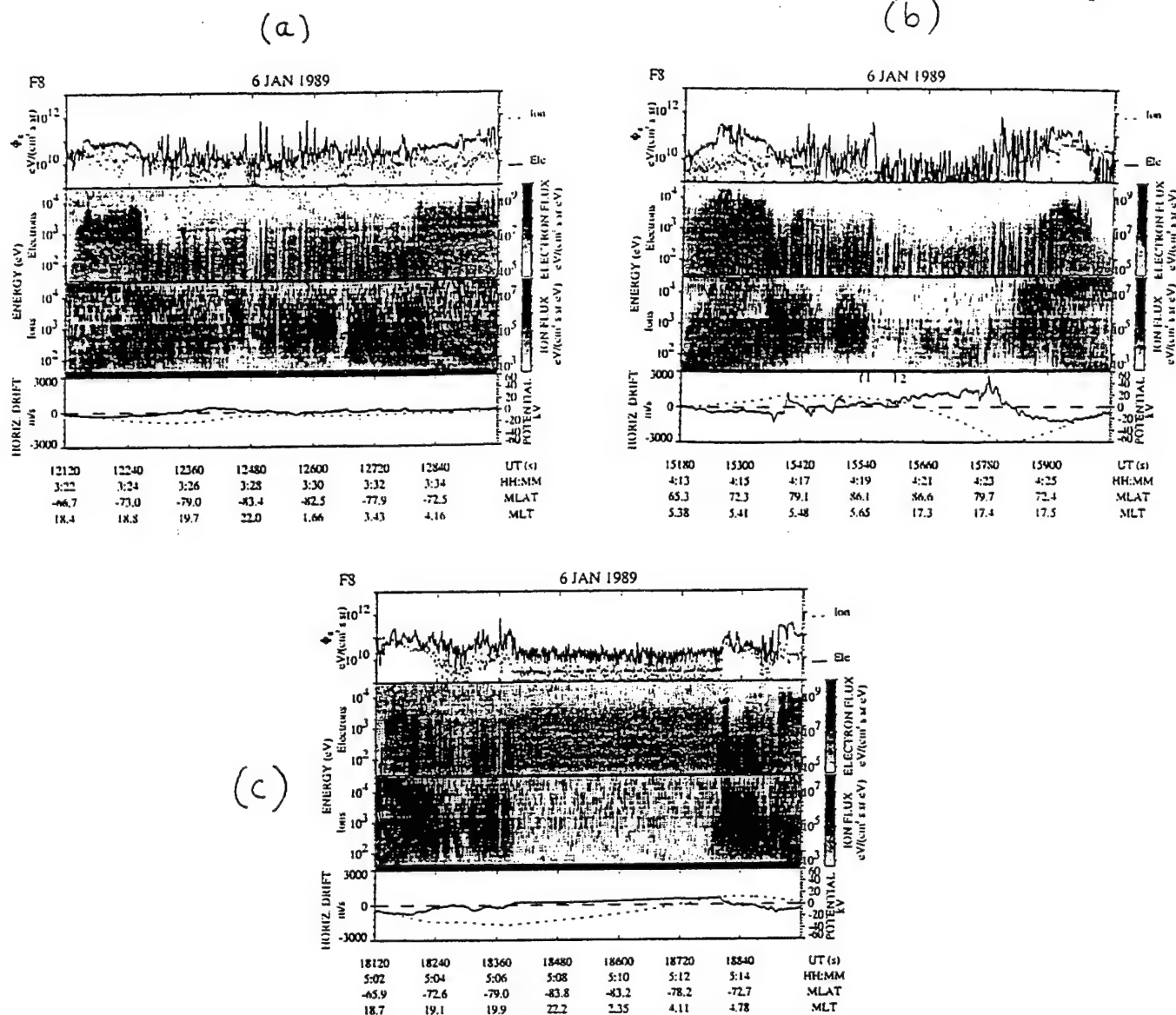
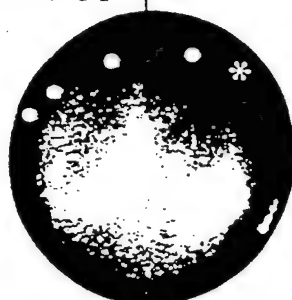


Figure 3. Integral electron and ion energy fluxes (Φ_e , $\text{eV cm}^{-2} \text{s}^{-1} \text{sr}^{-1}$), energy-time ($E-t$) spectrograms of precipitating differential electron and ion energy fluxes ($\text{eV cm}^{-2} \text{s}^{-1} \text{sr}^{-1} \text{eV}^{-1}$), and horizontal cross-track ion drift velocity observed by DMSP F8, January 6, 1989, before and after the arc decay in Figure 1. The resolution of the particle data is 1 s, and the drifts shown here are 1 s block averages of the 6-Hz raw data. Positive drift velocities are antisunward. The derived polar cap potential distribution is represented by a dashed line on the drift velocity plot. (a) 0322–0336 UT (southern hemisphere). (b) 0413–0427 UT (northern hemisphere). The corresponding all-sky image is shown in Figure 4. (c) 0502–0516 UT (southern hemisphere).

Qaanaaq Greenland, 630.0 nm
January 6, 1989
04:19:58 UT | sun



F8, 04:18 - 04:22

Figure 4. DMSP F8 traversal of Qaanaaq field-of-view projected along IGRF magnetic field lines to 250 km altitude, January 6, 1989. Satellite locations at 0418 (asterisk), 0419, 0420, 0421, and 0422 are shown projected onto a 630.0 nm all-sky image at 0419:58 UT. Particle and drift data from this pass are shown in Figure 3b.

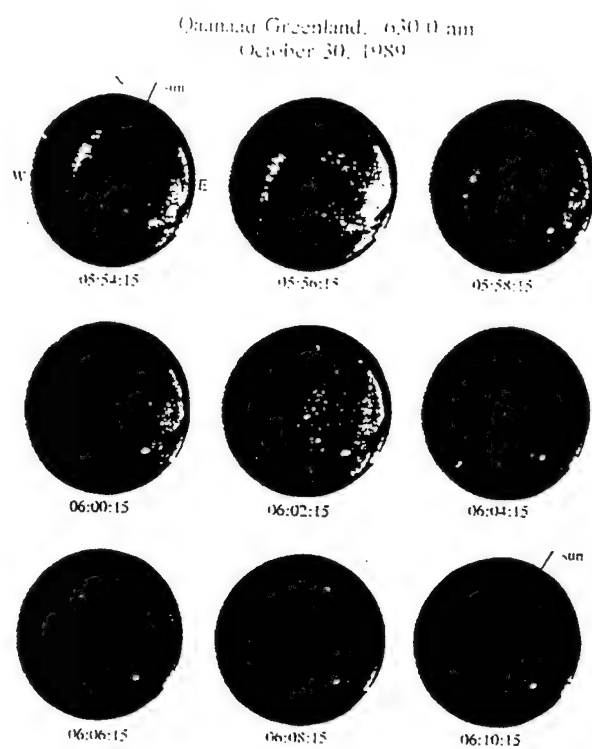


Figure 5. All-sky images at 630.0 nm from Qaanaaq, October 30, 1989, 0554-0610 UT.
The format is similar to that of Figure 1.

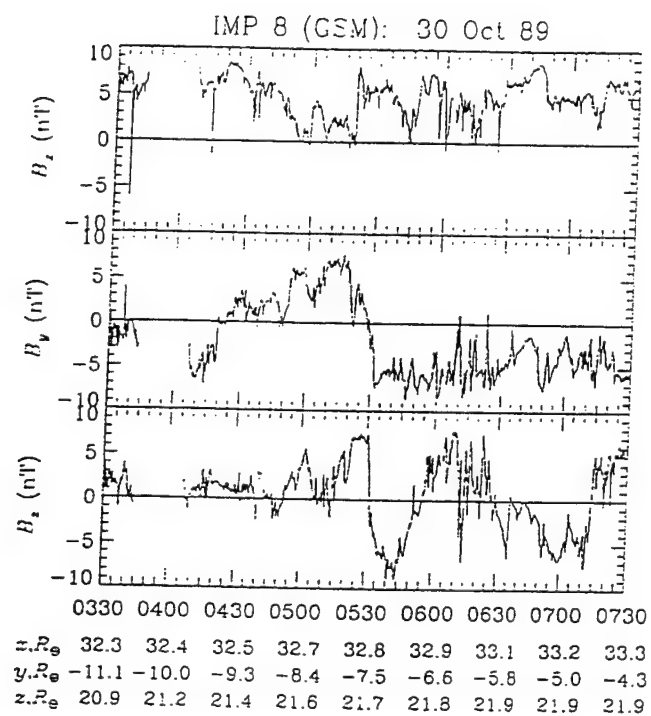


Figure 6. IMF observed by IMP 8, October 30, 1989, 0330–0730 UT. The format is similar to that of Figure 2. B_z turned southward at 0532 UT.

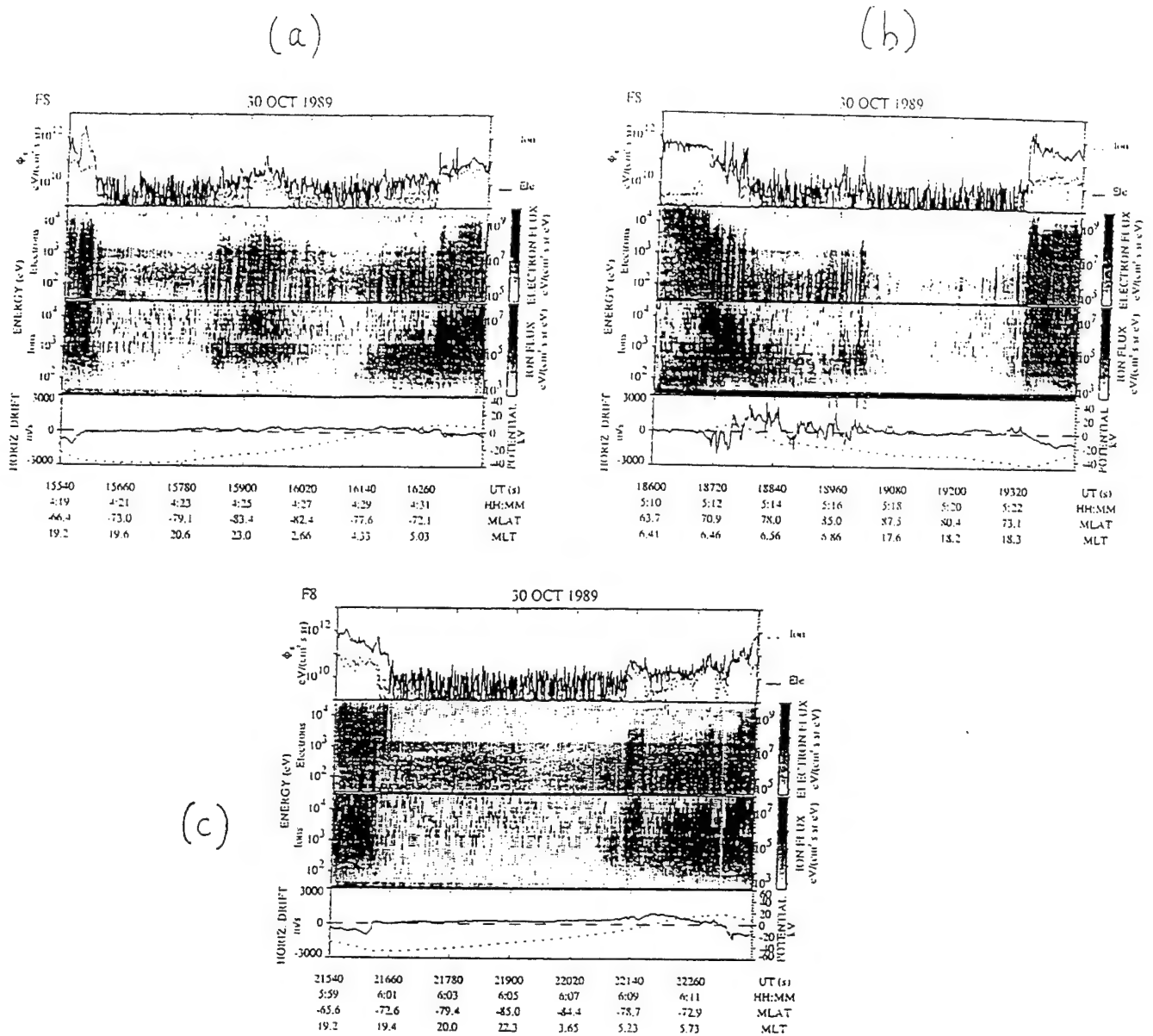


Figure 7. Integral electron and ion fluxes, $E-t$ spectrograms of precipitating electrons and ions, horizontal cross-track ion drift velocity observed by DMSP F8, and derived polar cap potential pattern, October 30, 1989, before and during arc decay. The format is similar to that of Figure 3. (a) 0419–0433 UT (southern hemisphere). (b) 0510–0524 UT (northern hemisphere). The corresponding all-sky image is shown in Figure 8. (c) 0559–0613 UT (southern hemisphere).

Qaanaaq Greenland, 630.0 nm
October 30, 1989
05:16:15 UT / sun



F8, 05:15 - 05:19

Figure 8. DMSP F8 traversal of Qaanaaq field-of-view projected along magnetic field lines to 250 km altitude, October 30, 1989. Satellite locations at 0515 (asterisk), 0516, 0517, 0518, and 0519 are shown projected onto a 630.0 nm all-sky image at 0516:15 UT. Particle and drift data from this pass are shown in Figure 7b.

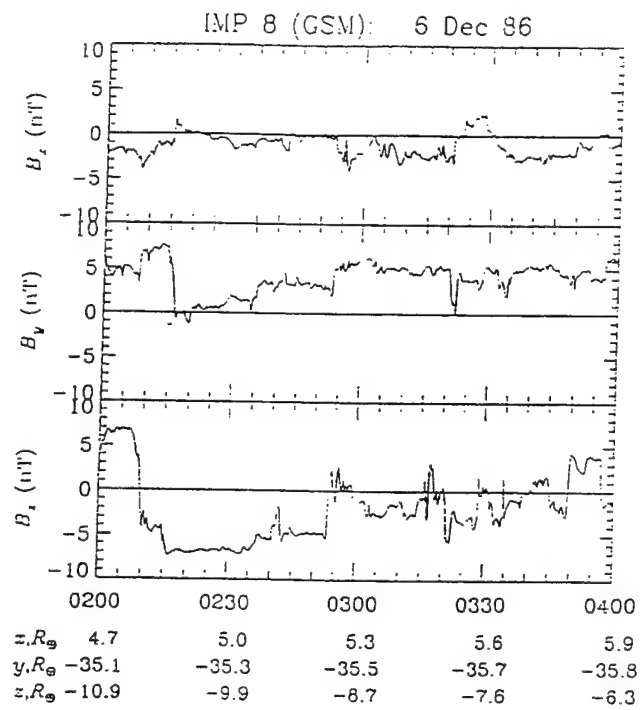


Figure 9. IMF observed by IMP 8, December 6, 1986, 0200-0400 UT. The format is similar to that of Figure 2.

Qaanaaq Greenland, 630.0 nm
December 6, 1986

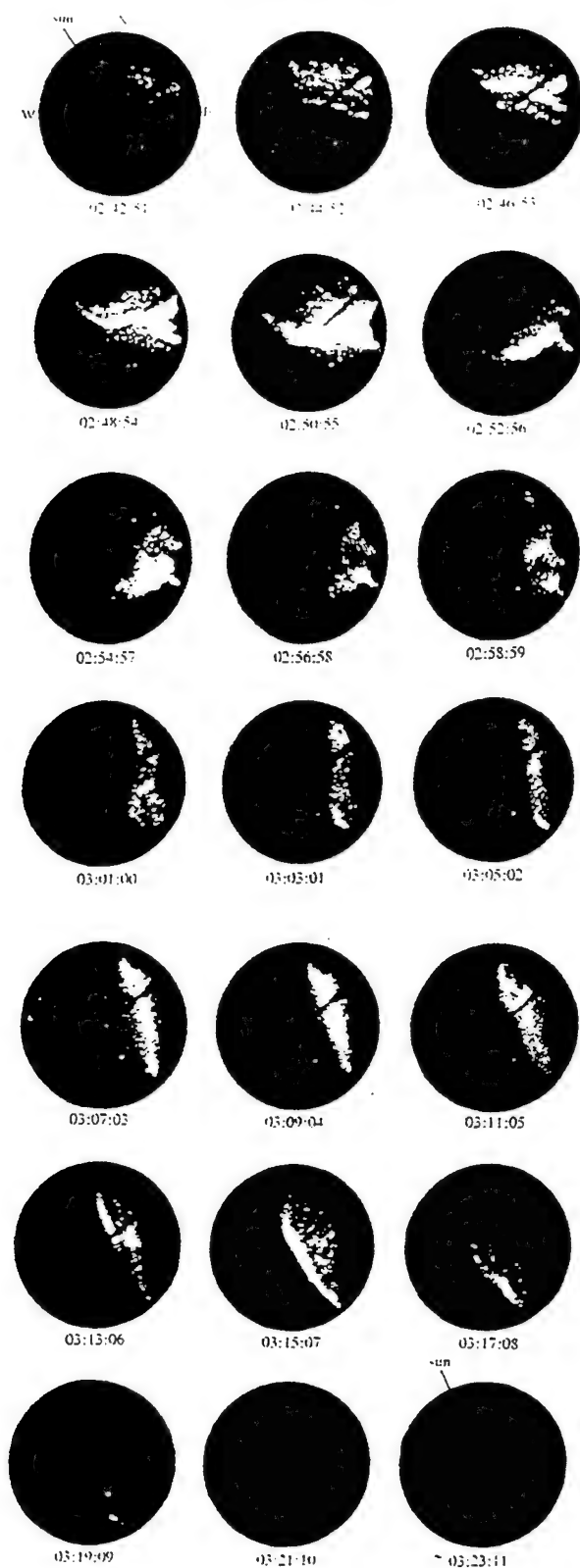


Figure 10. All-sky images at 630.0 nm from Qaanaaq, December 6, 1986, 0242–0323 UT. The format is similar to that of Figure 1.

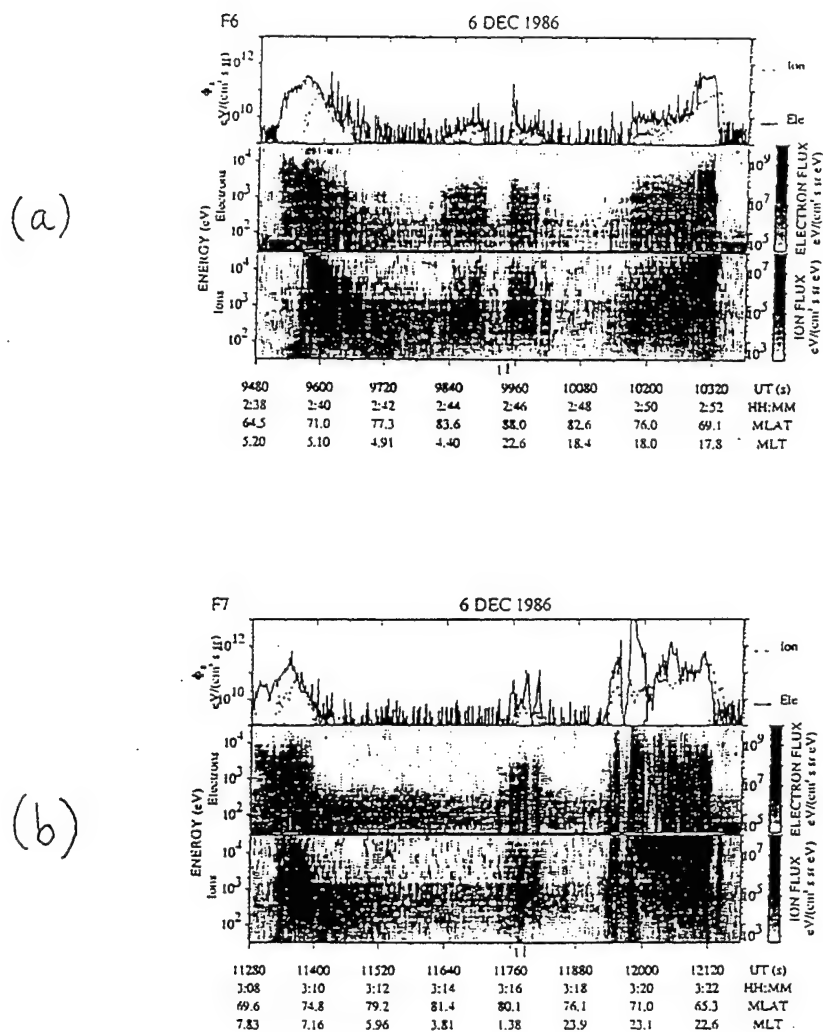


Figure 11. Integral electron and ion fluxes and E - t spectrograms of precipitating electrons and ions observed by DMSP F6 and F7 in the northern hemisphere oval and polar cap, December 6, 1986. (a) F6, 0238–0253. (b) F7, 0308–0323. The corresponding all-sky images for these two passes are shown in Figure 12.

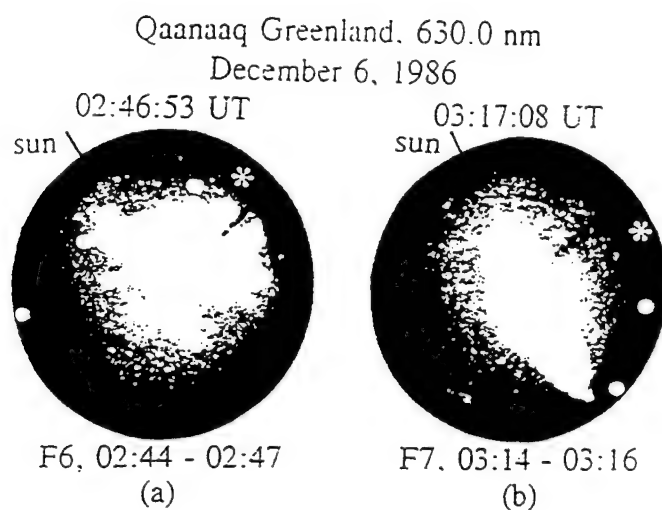


Figure 12. DMSP satellite traversals of Qaanaaq field-of-view projected along magnetic field lines to 250 km altitude, December 6, 1986. (a) Locations of F6 at 0244 (asterisk), 0245, 0246, and 0247 are shown projected onto a 630.0 nm all-sky image at 0246:53 UT. Particle data from this pass are shown in Figure 11a. (b) Locations of F7 at 0314 (asterisk), 0315, and 0316 are shown projected onto a 630.0 nm all-sky image at 0317:08. Particle data from this pass are shown in Figure 11b.

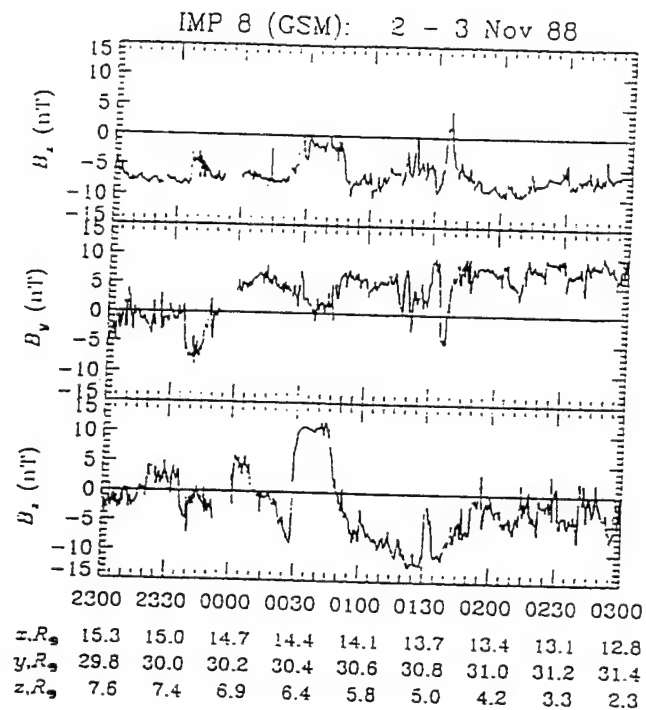


Figure 13. IMF observed by IMP 8, November 2-3, 1988, 2300-0300 UT. The format is similar to that of Figure 2. Apart from a brief period of "gardenhose toward" orientation ($\sim 0135 - 0140$), the IMF was in a "gardenhose away" configuration after 0000 UT, throughout the lifetime of the arc.

Qaanaaq Greenland, 630.0 nm
November 3, 1988

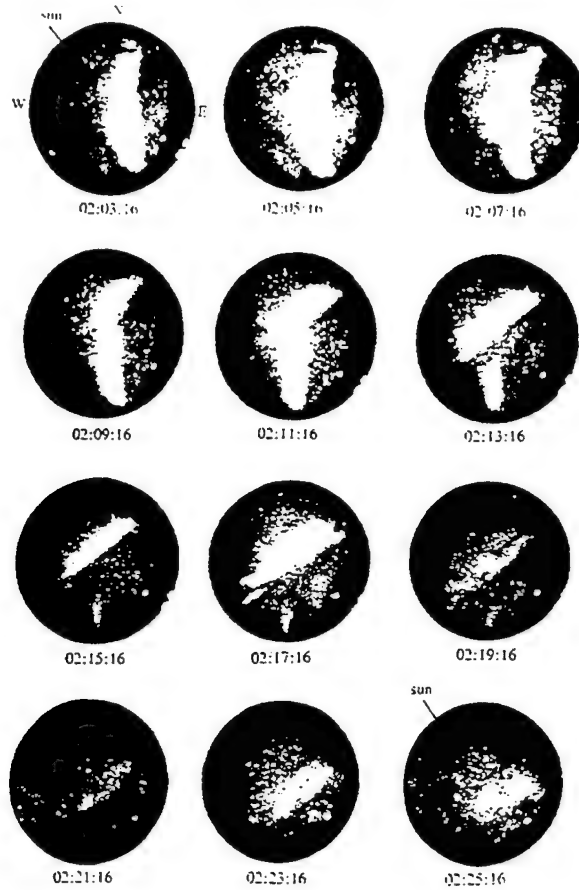


Figure 14. All-sky images at 630.0 nm from Qaanaaq, November 3, 1988, 0203-0225 UT. The format is similar to that of Figure 1.

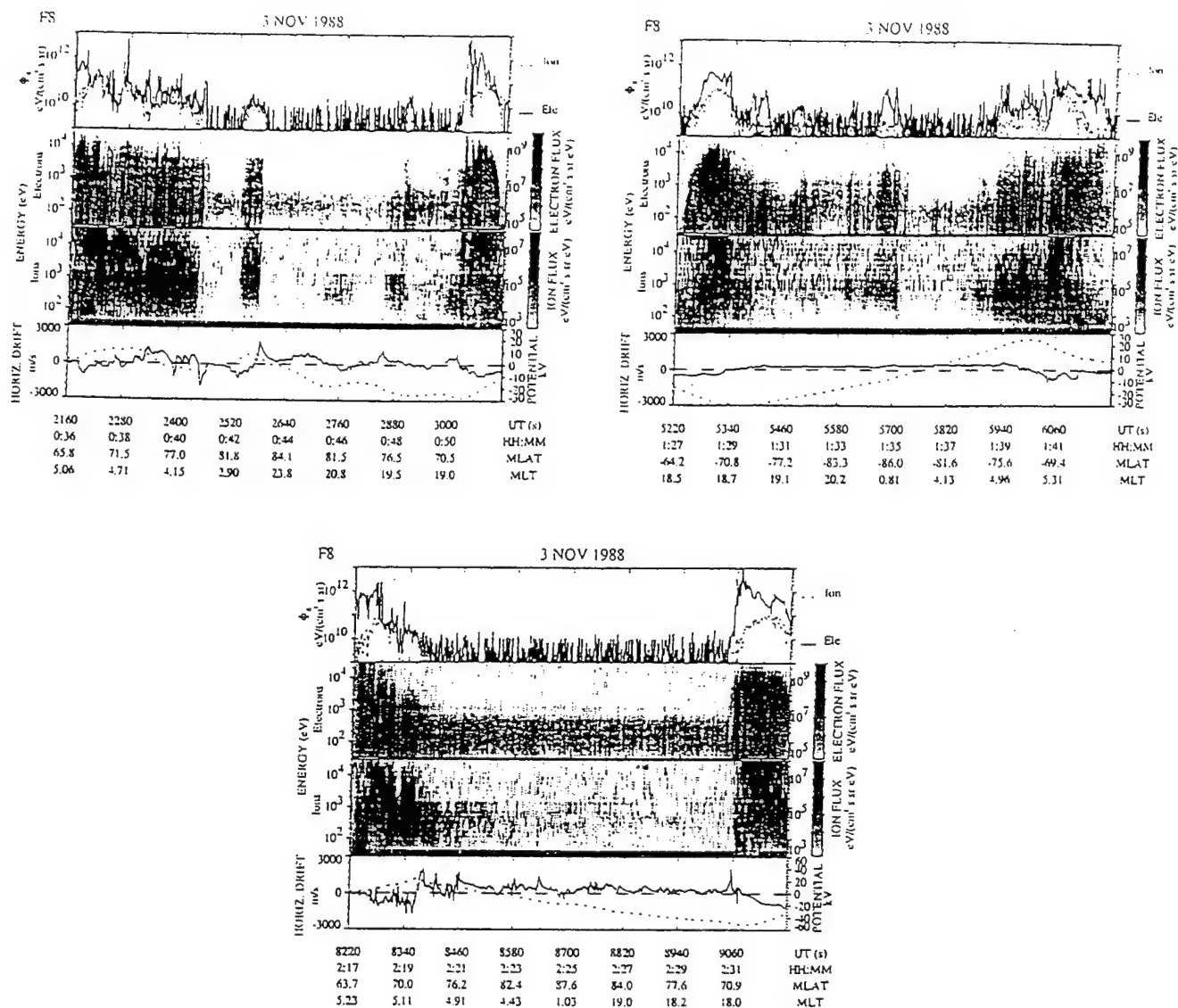
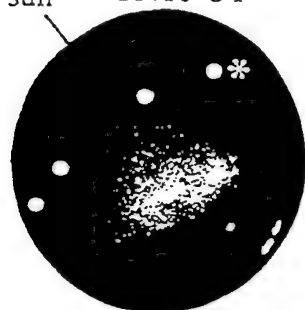


Figure 15. Integral electron and ion fluxes, E - t spectrograms of precipitating electrons and ions, and horizontal cross-track ion drift velocity observed by DMSP F8, November 3, 1988. Derived polar cap potential distribution is shown for the F8 passes. The format is similar to that of Figure 3. (a) F8, 0036-0052 UT (northern hemisphere). (b) F8, 0127-0143 UT (southern hemisphere). (c) F8, 0217-0233 UT (northern hemisphere). The all-sky image corresponding to this pass is shown in Figure 16.

Qaanaaq Greenland, 630.0 nm
November 3, 1988
sun 02:25:16 UT



F8, 02:23 - 02:27

Figure 16. DMSP F8 traversal of Qaanaaq field-of-view projected along magnetic field lines to 250 km altitude, November 3, 1988. Satellite locations at 0223 (asterisk), 0224, 0225, 0226, and 0227 are shown projected onto 630.0 nm image at 0225:16 UT. Particle and drift data from this pass are shown in Figure 15c.

Figure 17. Northern hemisphere polar cap arc motions (left) and possible mapping to motions in the equatorial plane of the distant tail flanks (right), after *Birn et al.* [1991] and *Elphinstone et al.* [1994]. Arrows indicate convection, dots (crosses) indicate upward (downward) field aligned currents, and "BL" and "PS" refer to (low latitude) boundary layer and plasma sheet. Dawnward flow through cusp due to dayside merging for $B_y > 0$ is one possible cause of duskward arc drift [Valladares et al., 1994; Newell and Meng, 1995]. (a) In the case of October 30, 1989 (Figure 5), a polar cap arc attached to the early morning oval (1) drifts duskward (2), then decays antisunward (3) after B_z turns negative. The conjugate behavior in the equatorial plane consists of an extension of the plasma sheet towards the magnetosheath that drifts antisunward, then retracts toward the center of the tail. (b) In the case of December 6, 1986 (Figure 10), a loop-like polar cap arc, possibly detached from the end of a Sun-aligned arc (1), rotates antisunward and dawnward (2), coming to rest as a Sun-aligned arc (3) before drifting duskward (4) and decaying. The conjugate behavior in the equatorial plane is shown in two panels: first, a spiral (due to the Kelvin-Helmholtz instability at a velocity shear near the plasmasheet/LLBL boundary) that maps to the loop-like polar cap arc, and second, the rotation of the remnant of the spiral sunward and inward after being separated from the plasma sheet, followed by its antisunward drift and decay toward the center of the plasma sheet.

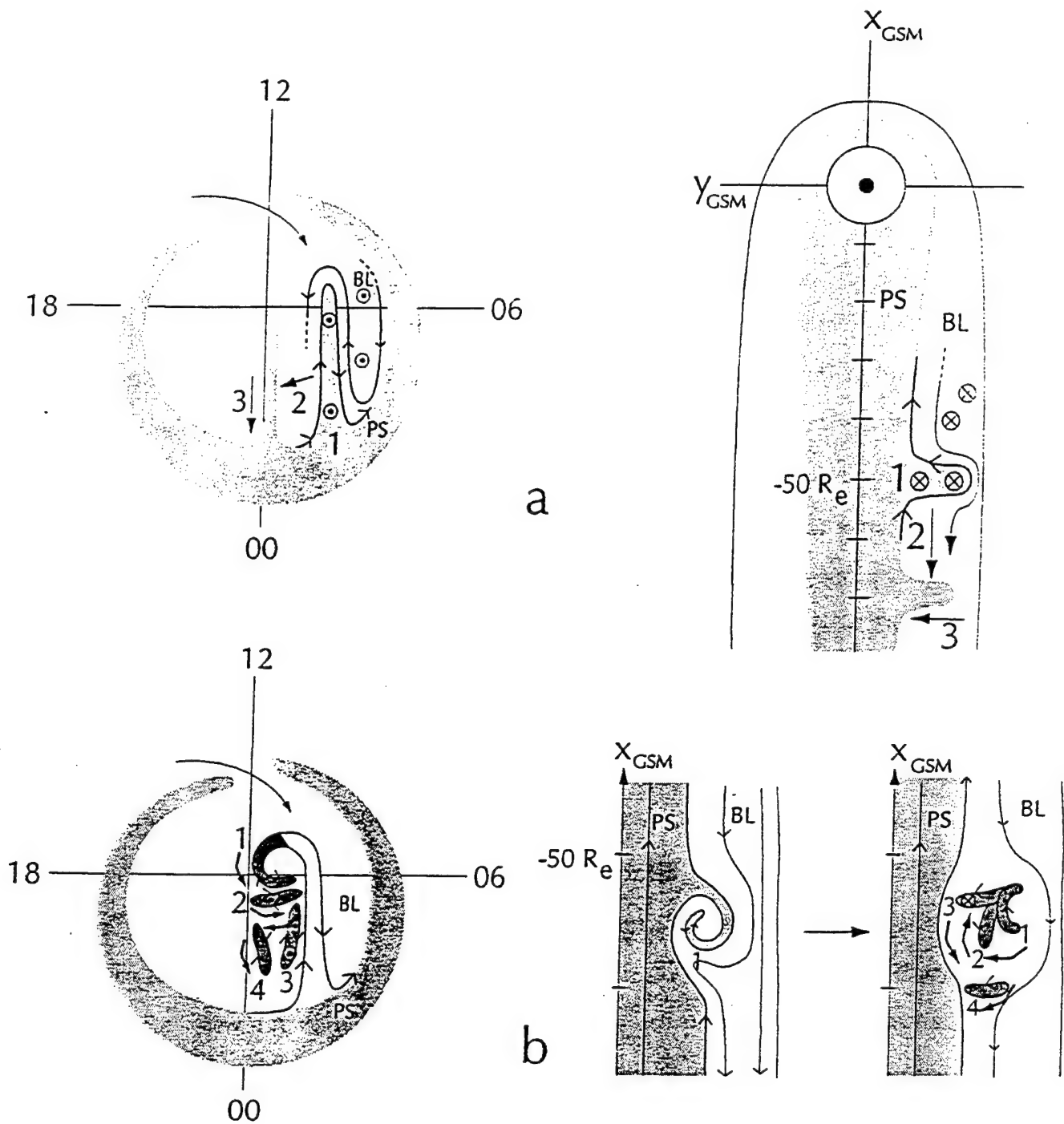


FIGURE 17

Table 1. Lags from IMF Southward Turnings to Polar Cap Arc Decay Observed at Qaanaaq, Greenland ($\Lambda_{CC} = 86^\circ$ N)

Date	B_z Reversal	Tip of Arc at $\Lambda_{CC} = 86^\circ$ N		t_{sm}	$t_{obs.}$
	UT	UT	MLT	(min)	(min)
Nov. 2, 1986	2019	2057	18.4	11-13	23-25
Dec. 5-6, 1986	2343	0013	19.1	8	20
Dec. 6, 1986	0209	0319	23.7	5-7	61-63
Nov. 3, 1988	0049	0209	23.6	10-11	67-68
Jan. 6, 1989	0354	0432	1.2	10	26
Oct. 30, 1989	0532	0600	2.0	7	19
Dec. 29, 1989	1934	1957	17.7	2-3	18-19
Jan. 26, 1990	0137	0223	23.2	12	32

Table 2. Lags from IMF B_y Reversals to Changes in Polar Cap Arc Dawn-Dusk Drift
Observed at Qaanaaq, Greenland ($\Lambda_{CC} = 86^\circ$ N)

Date	B_y Reversal		Dawn-Dusk Drift		t_{sm}	$t_{obs,y}^*$
	Change	UT	Change	UT	(min)	(min)
Nov. 2, 1986	dawnward- duskward	2019	dawnward- duskward	2039	11-13	5-7
Dec. 5-6, 1986	dawnward- duskward	2343	dawnward- stationary	0011	8	18
Oct. 30, 1989	duskward- dawnward	0530	duskward- stationary	0542	7	3
Dec. 29, 1989	dawnward- duskward	1924	stationary- duskward	1948	2-3	19-20

Experimental evidence for the formation and entry of patches into the polar cap

C. E. Valladares and S. Basu¹

Institute for Space Research, Boston College, Newton Center, Massachusetts

J. Buchau²

Phillips Laboratory, Geophysics Directorate, Hanscom Air Force Base, Massachusetts

E. Friis-Christensen

Division of Geophysics, Danish Meteorological Institute, Copenhagen, Denmark

Abstract. A mechanism for the formation of polar cap patches is proposed based on data collected by the Sondrestrom incoherent scatter radar, magnetometers located on the west and east coasts of Greenland and Digisondes, digital ionospheric sounders, operated at Qaanaaq and Sondrestrom. This instrumentation has served to identify the formation of patchlike structures and follow their temporal evolution and entry into the polar cap. Prior to the onset of the event, the background ionospheric plasma was moving in a poleward direction and formed part of a tongue of ionization directed toward and into the polar cap. The event starts with the appearance of a fast plasma jet containing eastward directed velocities in excess of 2 km s^{-1} . This plasma jet consists of a channel extending 300 km in width, where the F region ion temperature reaches values in excess of 4000 K and the E layer T_i is enhanced above 5000 K. The existence of a region containing high electron temperatures associated with soft precipitation (likely the cusp) and located adjacent and equatorward of the fast plasma jet is very suggestive of the jet being the result of a tension force acting upon recently reconnected field lines. This view is supported by the fact that the fast plasma jet was seen in the prenoon sector under IMF B_y negative conditions. The elevated T_i values inside the plasma jet are exactly collocated with depleted F region densities. We suggest that the recombination loss of O^+ is increased by a factor >10 due to the dependence of the $\text{O}^+ + \text{N}_2$ reaction on the ion temperature. The eroding action of the fast plasma jet proceeds until the poleward moving tongue of ionization is divided into regions containing high and low densities. Magnetic field perturbations associated with the fast plasma jet were observed by the different magnetometer stations. The large negative bays recorded at most of the sites have been used to trace the poleward motion of the jet. At the time that the fast plasma jet reaches Qaanaaq, the Digisonde there measured low f_oF_2 values. A few minutes before and after this minimum, high f_oF_2 values were observed. The ratio of the enhanced f_oF_2 values on either side of the minimum, to the minimum f_oF_2 is about 2 (or a density ratio of 4). This is the commonly accepted signature of a polar cap patch. The series of events leading to the formation of the patchlike density structure has been designated a density breakoff event.

¹ Now at the National Science Foundation, Washington, D. C.

² Deceased August 9, 1993.

Copyright 1994 by the American Geophysical Union.

Paper number 93RS01579.

0048-6604/94/93RS-01579\$08.00

1. Introduction

Polar cap F layer ionization "patches" are large regions in the polar cap ionosphere, where the electron density is up to a factor of 10 higher than in its neighboring regions [Buchau *et al.*, 1983; Weber *et al.*, 1984]. Other prominent characteristics of the polar cap patches are the absence of precipitating

fluxes different from polar rain impinging on them [Weber *et al.*, 1986], their dimensions, ranging from 100 to 1000 km, and their typically antisunward motion, which equals in magnitude the background convective flow [Fukui *et al.*, 1993]. Polar cap patches have been observed only when the IMF B_z is directed southward and during magnetically disturbed conditions [Weber *et al.*, 1984].

A great deal of research has been devoted lately to determine the place of origin of the polar cap patches and to identify the process or processes that are responsible for the patchy nature of the plasma enhancements observed at the center of the polar cap. Buchau *et al.* [1985] based on the diurnal distribution of the transport of patches across Thule (near the center of the polar cap), suggested that the patches are formed from subcusp plasma produced by UV solar radiation and carried across the cusp into the polar cap by the high-latitude plasma convection. Incoherent scatter radar measurements have provided evidence that in fact, subauroral plasma is able to enter the polar cap. Measurements performed at Sondrestrom, Greenland [Kelly and Vickrey, 1984], and at Chatanika, Alaska [Foster and Doupnik, 1984], indicated that under active magnetic conditions, a large eastward electric field develops near midday, directing the subauroral plasma northward and forming a tongue of ionization, spanning 2–3 hours in local time. Foster [1984] suggested that the plasma tongue is not a steady feature, developing preferentially during magnetically active conditions, in agreement with the level of activity when polar cap patches are observed.

Tsunoda [1988], clearly summarized these findings when he concluded that "The evidence therefore supports the hypothesis that a patch is indeed solar-produced plasma that has been detached from the dayside subauroral ionosphere." Since then, general interest has been focused on finding the physical mechanism(s) which could produce the plasma detachment. Tsunoda [1988] indicated that sudden changes in the B_y or B_z components of the interplanetary magnetic field (IMF) could be responsible for the formation of the polar cap patches. Foster *et al.* [1980] showed that a southward turning of B_z is usually followed by an expansion of the auroral oval to lower latitudes. This fact facilitates the entry of more dense subauroral plasma. Once subauroral plasma is drawn into the polar cap, the detachment could be produced by a retraction of the global pattern, for example, by a northward

turning of B_z . Tsunoda [1988] also explained how a change in B_y will shift the location of the throat to earlier or later magnetic local times depending on the sign of the transition (see Heppner and Maynard's [1987] convection patterns for B_z south conditions). Thus it is conceivable that consecutive B_y reversals may redirect the entry of subauroral plasma to different locations in the polar cap producing discrete patches from the plasma tongue in this way. The primary objection against the B_y or B_z switching mechanisms is the observational fact that a patch is rarely seen as a single event. It is far more common to observe a succession of many polar cap patches separated by time intervals as short as 10 min. Furthermore, the transit of a series of patches across a polar cap station can last for several hours. This implies sudden reversals of B_y (or B_z) at the same time scale of 10 min, which is not the typical behavior of the IMF.

Several numerical models have been used to study the effect of varying different parameters of the global convection pattern. Anderson *et al.* [1988] performed a numerical simulation of the effect that a time-varying global convection pattern could produce on plasma that is being transported into the polar cap. Their results implied that increasing the cross-polar cap potential and extending the polar cap radius to embrace a larger region of the high-latitude ionosphere, could produce a flow of enhanced density over a polar cap station, such as Thule. The subsequent reduction in polar cap potential cuts off the flow of enhanced density, thus simulating the generation of a patch.

The high degree of structuring that has been observed near the poleward boundary of the midday auroral oval can be better understood if consideration is given to the different processes which occur and deposit energy in the cusp/cleft region. These processes can directly or indirectly produce substantial changes in the longitudinal and latitudinal distribution of the plasma density. Newell and Meng [1988] provided a complete set of rules to distinguish between the cusp and the cleft regions. These authors established that in the cusp the average flux is large and the average energy is low, below 200 eV for precipitating electrons. These soft fluxes have the potential for enhancing the plasma in the flux tubes convecting across the cusp and into the polar cap. The increase in ionization depends on the energy deposited by the soft fluxes, the exact convection geometry and the convection velocity in

the vicinity of the cusp. *Roble and Rees* [1977] determined that a cusp-type precipitation needed at least 15 min to produce a change of the order of 20% in the density of the daytime high-latitude ionosphere. These electron density enhancements are, however, not identical to the order of magnitude increases typically observed at Qaanaaq, especially near solar maximum [*Buchau and Reinisch*, 1991].

Other processes associated with the cusp dynamics are the large flows and the auroral breakup events which have been observed with the EISCAT radar [*Sandholt et al.*, 1990; *Lockwood et al.*, 1990a]. These large flows form channels in the region immediately poleward of the open-closed field line boundary; they are a direct result of the tension force on the newly opened field lines [*Cowley et al.*, 1991]. In the northern hemisphere these flows are predominantly eastward for B_y negative consistent with the Svalgaard-Mansurov effect. More recently, *Lockwood and Carlson* [1992] have proposed that a transient burst of magnetic reconnection and the equatorward motion of the ionospheric projection of the X line could act harmoniously to extract a region of high-density subauroral plasma, divert the subauroral density poleward, and finally "pinch off" the newly formed patch.

This paper presents experimental data that were obtained near midday at auroral and polar cap latitudes. The main thesis of this paper is to provide evidence that the polar cap patches can be formed from the ionization tongue convecting across the cusp just before this tongue enters the polar cap through the action of elevated recombination rates due to very fast plasma jets. Two sets of data have been selected for this study, one was obtained during winter (February 19, 1990) and the other during equinox conditions (September 14, 1991). On both days a variety of different instruments were employed to fully diagnose the evolution of the plasma structuring. Observations were made at Sondrestrom (74°N), monitoring the cusp-related processes and conditions, and Qaanaaq (87°N) which provides central polar cap observations. The different techniques include the Sondrestrom incoherent scatter radar (ISR), two Digisondes (modern digital ionosondes) [*Bibl and Reinisch*, 1978] located at Qaanaaq and Sondrestrom, and the Greenland chain of magnetometers. In this study, we try to combine several ionospheric parameters measured by different instrumentation to reconstruct the sequence of events that led to the formation of

the polar cap patches. This combined view provides evidence for a density break-off event within the region of entry of polar cap patches. The effect of the plasma break-off event is to "slice" the tongue of subauroral ionization convecting poleward through the cusp, into chunks of high-density plasma, the patches, that subsequently convect into the polar cap.

2. Observations

The formation of polar cap patches in the high-latitude region near midday was studied using data from the Sondrestrom incoherent scatter radar (ISR), f_oF_2 values measured by two Digisondes and magnetic field data recorded by the Greenland chain of ground-based magnetometers. Simultaneous observations of the IMF were made by the IMP 8 satellite only during the February 19, 1990, measurements. Figure 1 displays the geographic location of the Sondrestrom incoherent scatter radar, the area scanned by the ISR antenna, the sites of the ground magnetometers, and the location of the terminator at 120 km altitude. The deployment sites of the two Digisondes which operated during the experiment are also included in Figure 1. The Digisondes were located at Qaanaaq (Qa) and Sondrestrom (STF).

2.1. IMP 8 Solar Wind Observations

On February 19, 1990, the IMP 8 satellite was in the solar wind, slightly upstream from the Earth's bow shock and outside the dawn flank of the magnetosphere. At the time of the experiment, the X , Y , and Z coordinates of the IMP 8 spacecraft in the GSM system were 12.5, -35.0 , and 0.1 Earth radii, respectively. Figure 2 shows 1-min averages of the three components of the IMF that were measured in an 8-hour segment centered near the onset time (1251 UT) of the event described in section 2.2. The ground-based sensors first detected the occurrence of this event during a 45-min data gap of the IMF. At 1258 UT, IMP 8 recorded large excursions of both B_y and B_z components. At this time and until 14 UT, the IMF B_z component is negative and large (~ -10 nT). It is well known that there is always a propagation delay for the effect of the IMF transitions measured by a spacecraft upstream from Earth in the solar wind, to reach the radar field of view. We calculated this propagation delay following the work of *Farrugia et al.* [1989] and *Lockwood et al.* [1989]. It was found that for

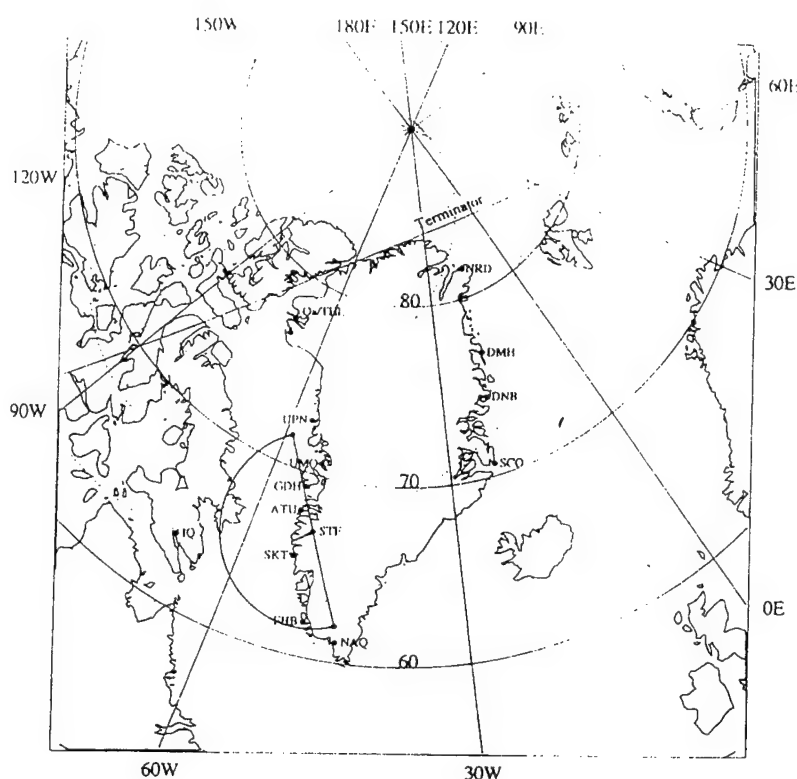


Figure 1. Illustration of the different sites that contain instruments used during the experiments. The digital ionospheric sounders are located at Sondrestrom (STF) and at Qaanaaq (Qa). The other stations correspond to ground-based magnetometers. The antenna scanning configuration of the Sondrestrom radar used on February 19, 1990, is also displayed. The location of the solar terminator line at 120 km altitude can be seen in the upper part of the plot.

the event of February 19, 1990, the ionospheric signatures should lag 109 s behind the IMP 8 observations of the IMF. There are several approximations in this type of calculation, and the computed time delay can be subject to an uncertainty of 2 min. Thus we conclude that the event onset (1251 UT) is not related to the sharp decrease in B_z of 1302 UT. While it is important to establish the cause/effect relationship between the large ion velocities which lead to the patch formation, as observed by the radar, and the type of solar wind-magnetopause interaction that drives this ionospheric signature, this is not the main subject of the present paper. Here we will concentrate basically on studying the effect that this fast plasma jet can produce on the ionospheric plasma that is convecting poleward.

2.2. February 19, 1990, Incoherent Scatter Radar Data

To conduct this study, we designed a radar mode that was able to map electron density variations and

the velocity field over a large area and with a time resolution comparable to the lifetime of daytime transient events. During our first attempt on February 19, 1990, we used the antenna configuration pattern depicted in Figure 1. The antenna scanned in azimuth (AZ) only 180° of the sky, using a relatively low (45°) elevation angle. This scan was followed by two elevation (EL) scans along the magnetic meridian which provided measurements of altitude profiles as a function of latitude.

Figures 3–8 show sequences of ISR data from six consecutive scans recorded between 1247 and 1312 UT. The four basic parameters measured by the Sondrestrom ISR (line-of-sight ion velocity, V_{los} , electron number density, N_e , ion and electron temperature, T_i and T_e) are displayed in the four panels of each of the six scans. These data illustrate the evolution of the density contours as they vary as a function of the magnitude of Joule frictional heat that is being deposited and the flux of soft electron

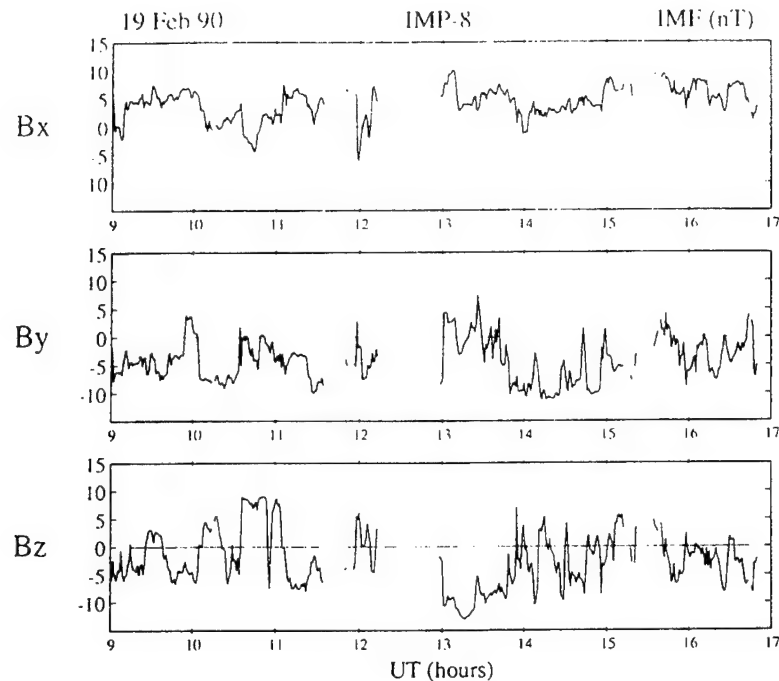


Figure 2. Interplanetary magnetic field data measured by IMP 8. Shown from top to bottom are the three IMF components in GSM coordinates. All three traces are plotted in units of nanoteslas. The event described in the text started at 1251 UT.

precipitation impinging into the ionosphere. While these two parameters are not measured directly, the ISR provides indirect but fairly accurate identification of these processes [Baron and Wand, 1983; Vondrak and Baron, 1977]. The Joule heating manifests itself as enhanced values of T_i , while the signature of local particle precipitation is in the form of elevated values of T_e .

Data from February 19, 1990, show a density break-off event that occurred between 1251 and 1312 UT, approximately 1 hour before local magnetic noon. During the experiment the geomagnetic Kp index was 5- and the solar flux (S_a) was 180. The AZ scan was conducted by sweeping the radar beam along a conical surface and maintaining the elevation constant at an angle of 45° . Figures 3 and 6 show the four basic ionospheric parameters measured by the IS radar. They are displayed after unfolding the conical surfaces and projecting them onto separate 1200×1200 ground maps with the radar at the center. The line-of-sight velocities (Figures 3a and 6a) are displayed using arrows of different patterns and lengths according to the sign and magnitude of the plasma flow. The density contours (Figures 3b and 6b) are on a linear scale

with the initial value and the interval between consecutive levels equal to 1.0 and $0.5 \times 10^5 \text{ cm}^{-3}$, respectively. The T_i (Figures 3c and 6c) and T_e (Figures 3d and 6d) values are depicted in the form of gray-scaled contours varying in discrete steps of 1000 K.

The data of Figure 3 were obtained between 1247 and 1251 UT, a few minutes before the onset of the density break-off event. Because of the nature of the AZ scans, altitude and distance variations of the ionospheric parameters are intermixed. However, it is still possible to distinguish spatial N_e structures if the comparison is performed at a constant range or distance from the radar site. For example, for a horizontally stratified ionosphere, equidensity contours appear as circles, with the peak densities shown at the distance where the conical scan intersects the peak of the F layer. Deviations from the circular pattern indicates the presence of nonuniform densities. The identification of the spatial structures should also be guided by the unambiguous altitude profiles which are measured with the EL scans. Taking this into consideration we have determined that during the scan starting at 1247 UT, the plasma is quasi-uniform. The density contours

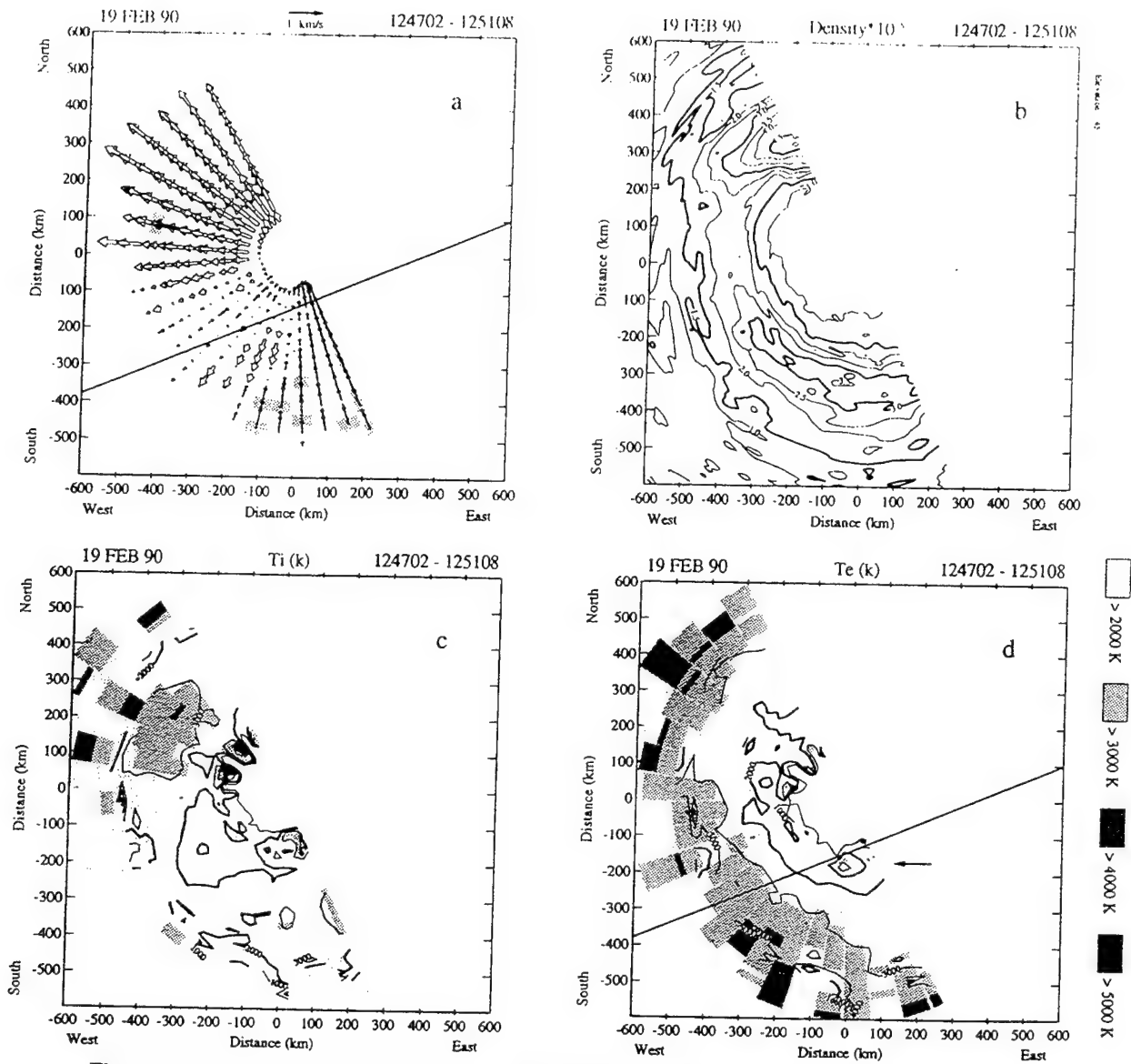


Figure 3. Plasma parameters measured by the Sondrestrom ISR on February 19, 1990, and during the time interval from 1247 and 1251 UT. The constant elevation was 45° and the azimuth changed from magnetic north to magnetic south. Each panel presents one of the four basic parameters measured by the radar. They have been projected to the surface of the Earth. Geographic north is at the top and west is on the left side of the plot. Solid (open) arrows indicate V_{los} directed toward (away from) the radar. The regions where the velocity is directed toward has also been shaded to facilitate their identification. The solid line contours of Figure 3b trace the locations where the plasma density is equal to 1.5 or $3.0 \times 10^5 \text{ cm}^{-3}$. Figures 3c and 3d depict the ion and electron temperatures varying in discrete steps as displayed on the lower right-hand side of the plot.

present two regions containing peak values above $3.0 \times 10^5 \text{ cm}^{-3}$. The first of these two regions is located to the north (300 km north, 250 km west), where the density is $4.5 \times 10^5 \text{ cm}^{-3}$ and the other is located to the south of the station (300 km south,

50 km west), where N_e is $3.5 \times 10^5 \text{ cm}^{-3}$. They are separated in the west by a slab extending ~ 500 km in the N-S direction with the ambient density in this region being $\sim 2 \times 10^5 \text{ cm}^{-3}$. The conical map does not allow us to conclude whether these two en-

hancements to the north and the south of the station are connected by a high-density tongue. The following elevation scan in Figure 4b indeed shows that they are connected by a $3.5 \times 10^5 \text{ cm}^{-3}$ density plasma, while the densities to the west are $\leq 2 \times 10^5 \text{ cm}^{-3}$. The line-of-sight velocities are located primarily away from the radar at latitudes north of the station. These large velocities are coincident with values of T_i above 3000 K. Considering the azimuth scan as a whole, we observe three succeeding velocity reversals at the southern part of the scan which have the appearance of being aligned in the E-W direction. Because the ISR measures only one component of the velocity vector, it is not possible to determine, without further analysis, whether these reversals correspond to a shear or to a rotational velocity discontinuity. The eastern part of the AZ scan presents a region where T_e reaches 3000 K (notice the arrow in Figure 3d). This region of elevated T_e is located slightly south of the reversal line. The elevated T_e , in spite of being localized, supports the hypothesis of the existence of a shear reversal ~ 250 km south of Sondrestrom. The straight lines through the southern part of the scan in Figures 3a and 3d denote the location of this velocity reversal.

Figure 4 presents the data obtained with the magnetic meridian EL scan starting at 1251 UT. In this geometry, both density structures of the previous scan can be seen in a sectional cut along the magnetic meridian. These regions of high density peak at 400 km altitude and they are seen to have drifted to new locations being directly overhead and at 600 km north. Outside these regions, the peak density is only 3 to $3.5 \times 10^5 \text{ cm}^{-3}$. This represents a 30 to 40% variation with respect to the maximum density in the plot. If this latitudinal cross section of the high-latitude ionosphere remains unchanged and continues drifting poleward, and a sounder is properly placed downstream of the plasma convection, the f_oF_2 values measured by the Digisonde should vary between 6.4 and 5 MHz during the passage of this structure. Although this is a significant variation and detectable by any Digisonde, it would hardly qualify as a f_oF_2 variation, commonly associated with polar cap patches [Buchau *et al.*, 1983]. Two regions of elevated T_i values are clearly evident in Figure 4c. In particular, the T_i enhancement observed at 1251:32 UT near 200 km south, marks the initial time when the fast plasma jet event was

observed by the Sondrestrom radar. Notice the large values of V_{los} (Figure 4a) exactly collocated with the T_i structure. T_e was also enhanced above the background level (2000 K is a typical value for daytime winter conditions). The region of elevated T_e extends from at least 300 km south to near 600 km north. It overlaps and extends further poleward of the plasma containing enhanced T_i values. It is important to mention that, when the ion drift is large (as inside the plasma jet) the ion gas becomes anisotropic and the ISR only measures the line-of-sight ion temperature, this is to say, only the component of T_i along the antenna look angle.

The appearance of a region with large ion velocities accompanied by enhancements in T_i becomes more evident after examination of Figures 5a and 5c. This figure displays the early stages of the formation of a deep density depletion. Both regions containing $N_e = 5 \times 10^5 \text{ cm}^{-3}$ have continued drifting poleward. The T_i enhancement seen in Figure 4, 200 km to the south, has moved to an almost overhead location. Between scans, the T_i structure has drifted a distance almost equal to the distance traversed by the N_e structure. In contrast, the T_e enhancement, which was observed in the preceding scan (50 km south), has remained at the same geographic location, although the electron temperature in the *E* region has intensified. The density contours also display prominent differences near the region of the temperature enhancements (~ 100 km south). At altitudes below 200 km, we find densities that seem to have been produced locally. The poleward velocity of the N_e structures is 670 m s^{-1} .

Figure 6 shows the full development of the break-off event and the deepening of the plasma depletion. Because of the discontinuous appearance of the density contours, we have named this process a density break-off event. Three of the parameters measured by the radar (V_{los} , T_i and N_e) display substantial changes in a region extending 200 km in latitude (between 0 and 200 km south) and at least 400 km in longitude, from almost due west to overhead of the ISR. The density depletion region which encompasses this region may stretch well beyond the limits of the AZ scan. Within this region the *F* region density is less than 10^5 cm^{-3} . The Digisonde located at Sondrestrom, as will be shown in section 2.4, only recorded oblique echoes suggesting the near complete loss of the *F* region in the center of the

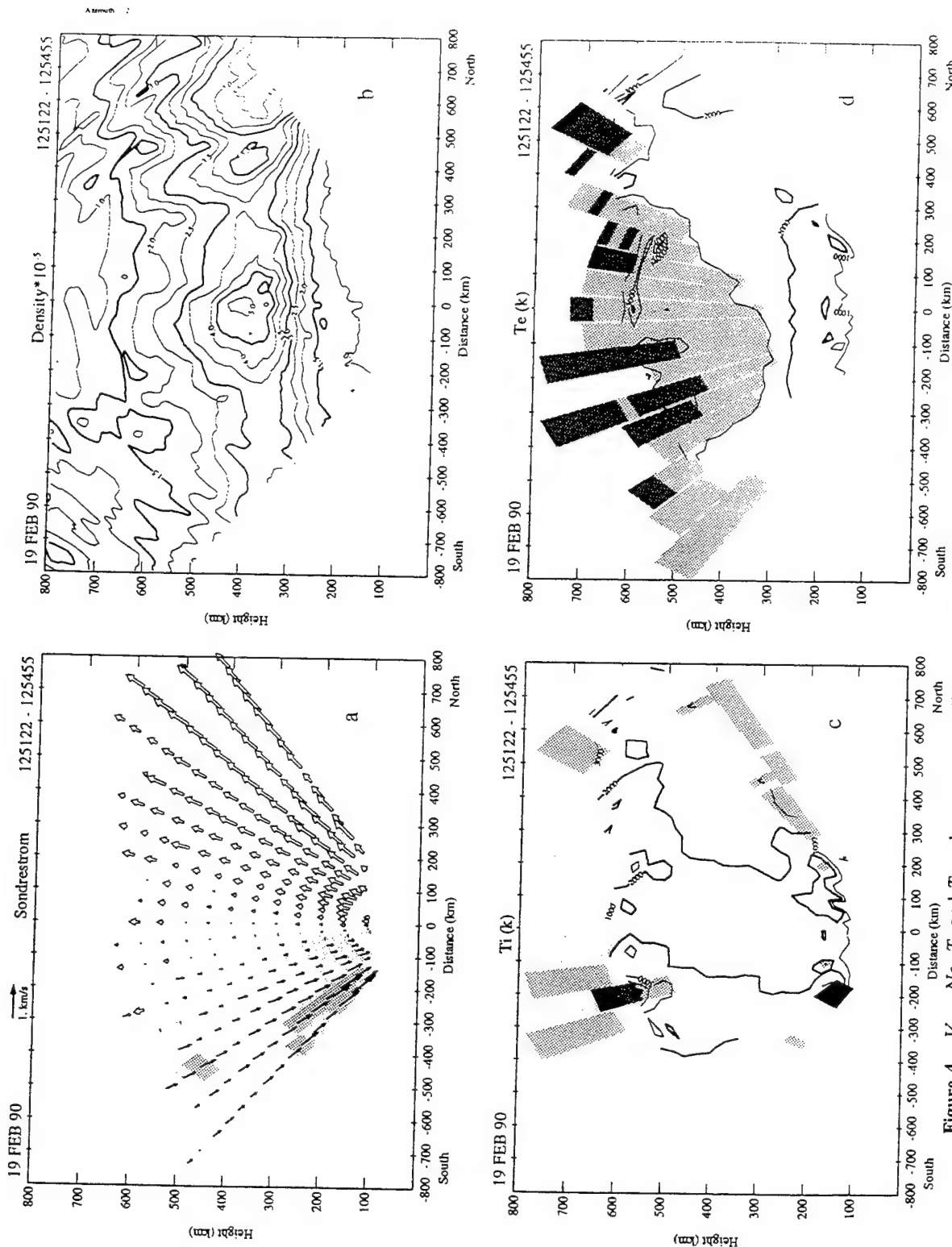


Figure 4. V_{los} , N_e , T_i and T_e values corresponding to the EL scan of 1251–1254 UT on February 19, 1990. The azimuth was kept fixed at -27° , and the elevation varied from 30° south to 30° north. The four directly measured parameters are displayed as a function of height and distance along the magnetic meridian. Contour spacing and gray-scale shading are identical to those used in Figure 3.

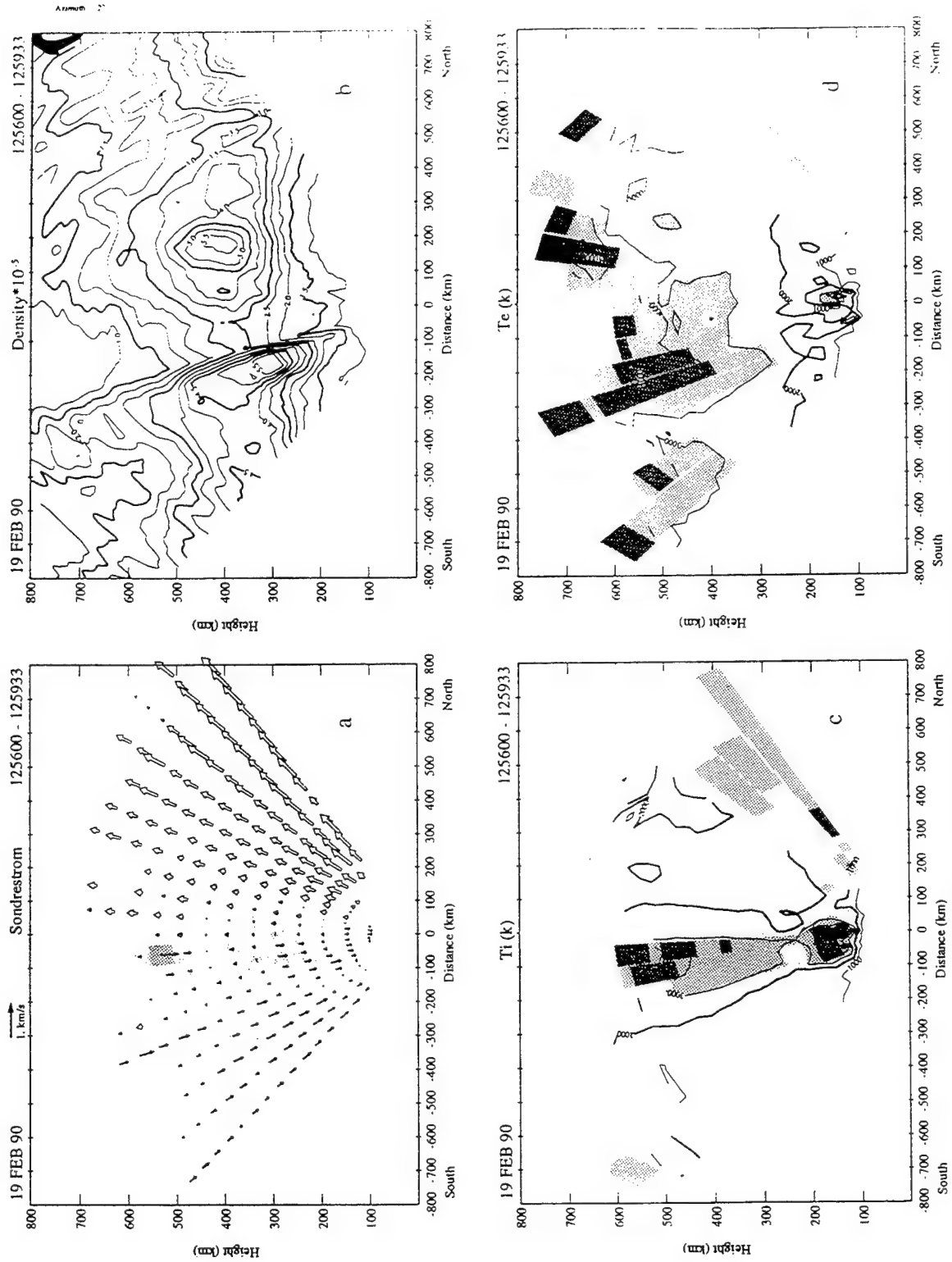


Figure 5. Similar to Figure 4, but for the time interval 1256–1259 UT.

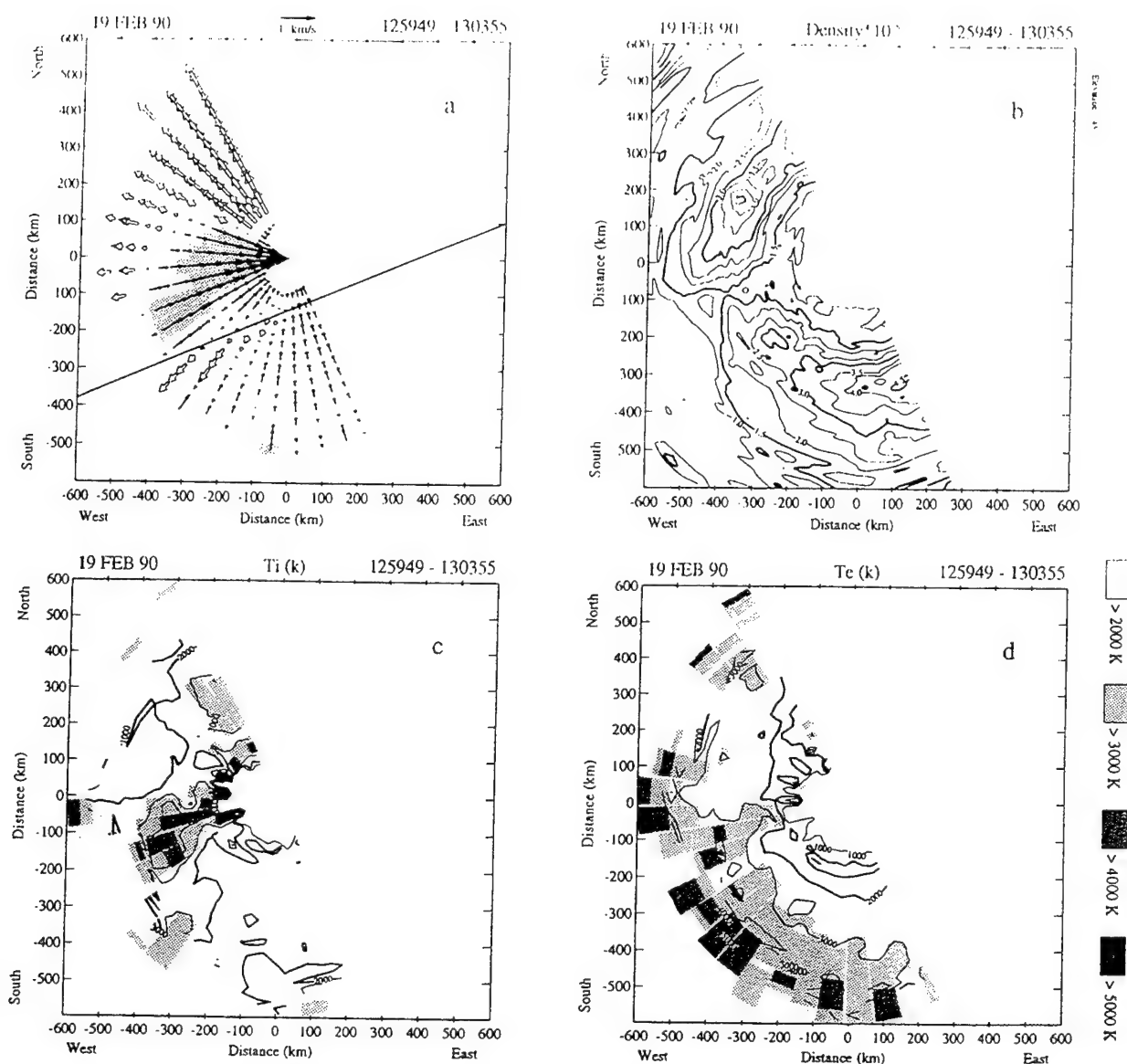


Figure 6. Similar to Figure 3, but corresponding to the time interval between 1259 and 1303 UT.

figure. Figure 6a also depicts the line traced in Figures 3a and 3d; it is drawn here at the same geographic location to indicate that the sheared velocity feature remains stationary in a frame corotating with the Earth. The largest T_i value that we observed during this scan was ~ 5000 K in the E layer and $74^\circ\Lambda$.

Figures 7 and 8 show data obtained during two EL scans in the magnetic meridian. Here the newly formed region of depleted density is seen drifting poleward together with columns of large ion velocities and enhanced values of T_i . By contrast the

region of enhanced T_e containing values above 3000 K (~ 0 km distance) has moved no more than 100 km since the EL scan that started at 1251 UT. The density in the F region has decayed and only a weak F_1 region still persists, probably due to the tenuous solar UV radiation that is present at this latitude during this time of the year. The density profiles within the depleted region peak at 200 km and have a maximum value equal to 10^5 cm^{-3} . Figures 7c and 8c reveal that the enhanced ion temperature is subsiding; T_i has diminished to values near 2000 K, concurrently the ion velocity has also decreased

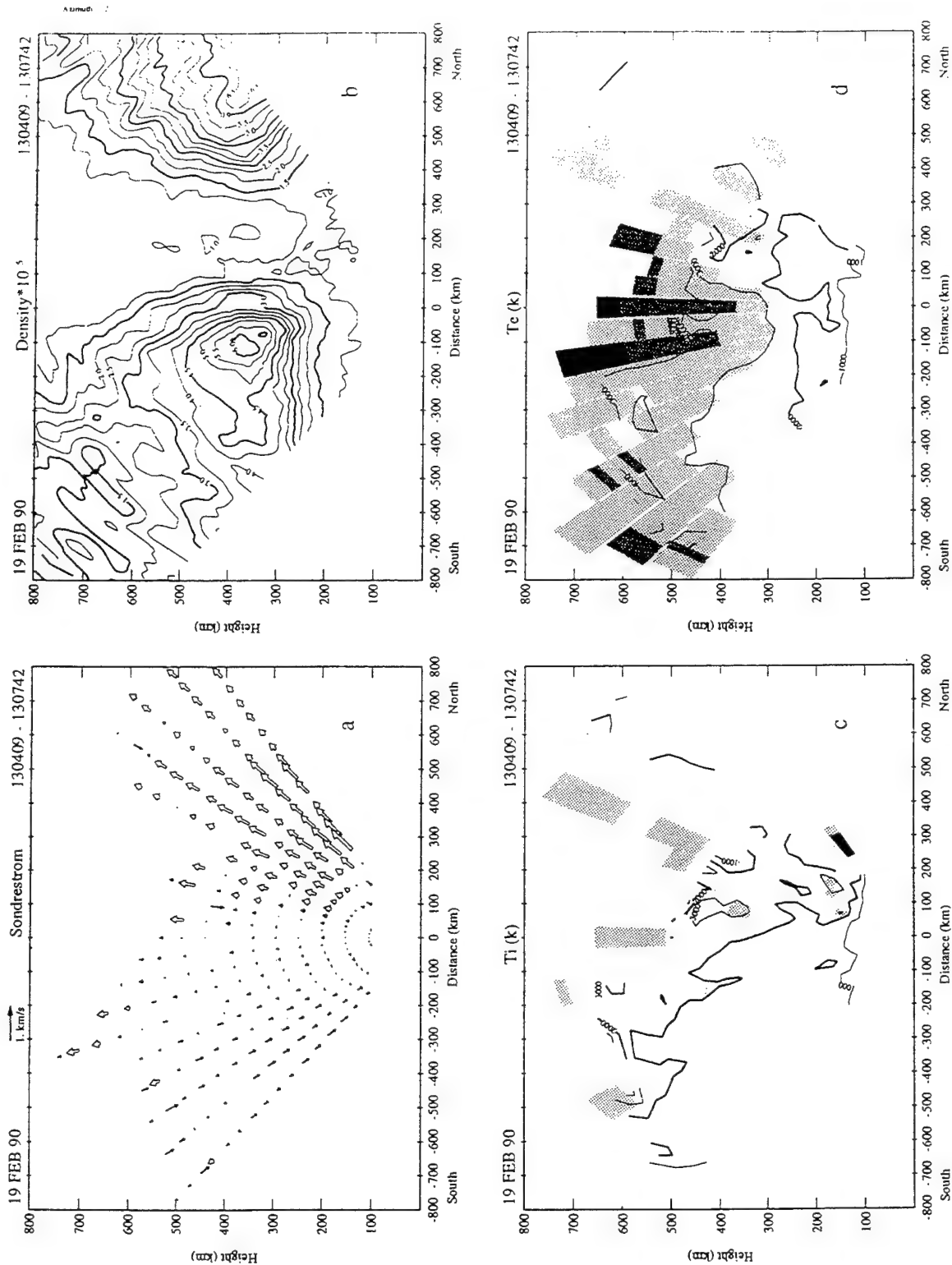


Figure 7. Similar to Figure 4, but for the time interval 1304–1307 UT.

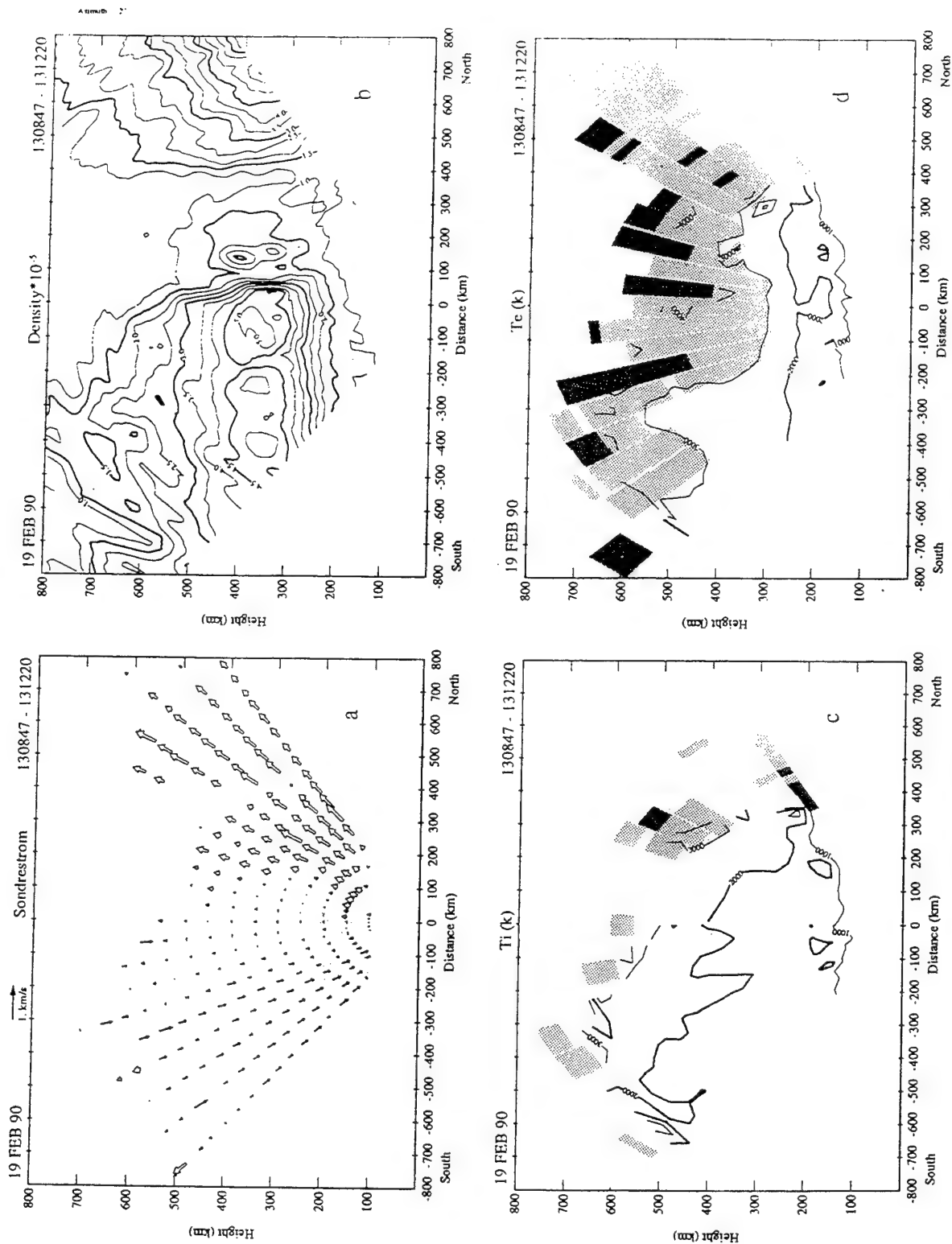


Figure 8. Similar to Figure 4, but for time 1308-1312 UT.

GREENLAND MAGNETOMETER CHAIN

19 FEBRUARY 90

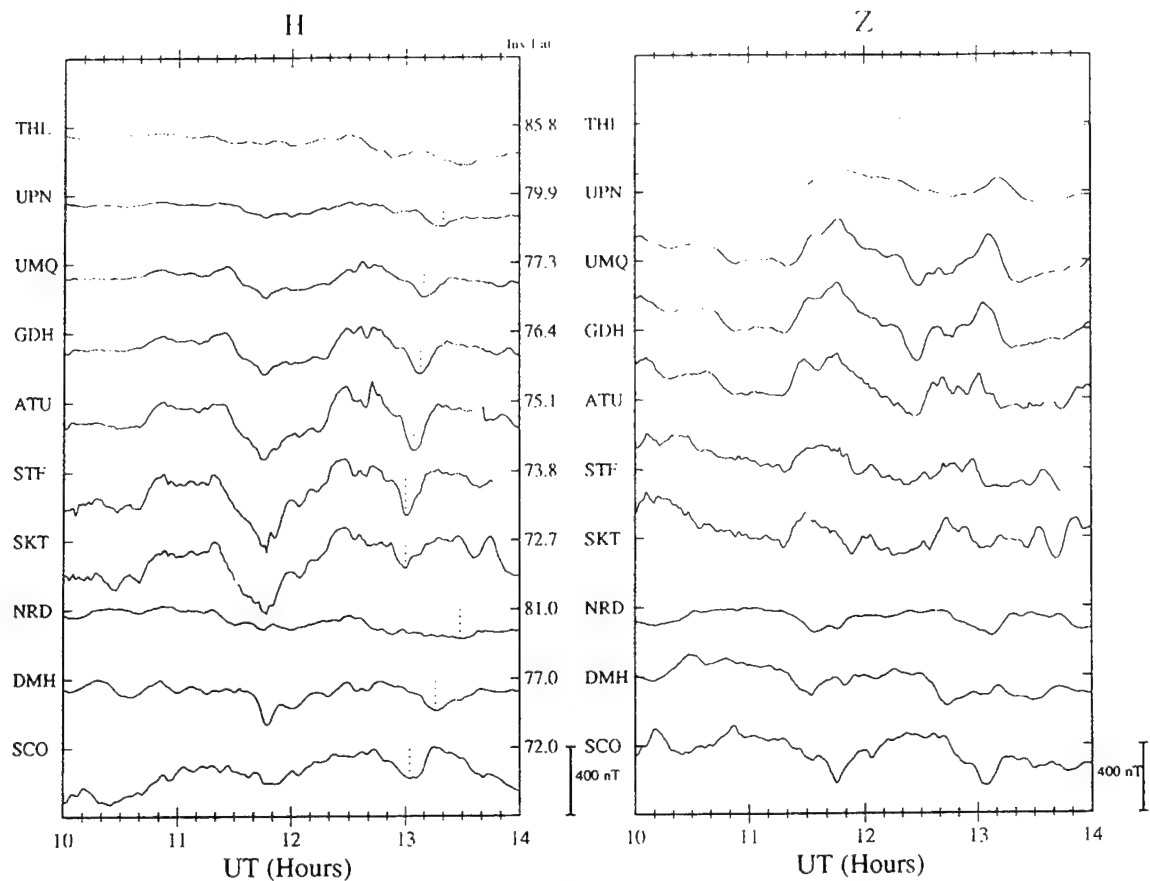


Figure 9. Stacked plot of the (a) H and (b) Z components of the magnetic deviations from the Greenland chain of magnetometers from 1000 to 1400 UT on February 19, 1990. The vertical dotted lines depict the times when each station recorded the largest magnetic fluctuation associated with the fast plasma jet of Figure 6. The locations of the respective stations are shown in Figure 1.

and has become of the order of 1 km s^{-1} . However, the density inside the region of the fast plasma jet will remain at a low level until it is replenished by solar UV radiation. The time needed by solar illumination to rebuild the ionospheric density to a level comparable to the N_e before the density break-off event is of the order of 1 hour. Between 1304 and 1308 UT, the equatorward wall of the N_e structure located further north has drifted at a speed equal to 400 m s^{-1} .

The ISR data show the development of an east-west aligned region of strong eastward plasma flow, the fast plasma jet. This results in enhancement of T_i , and enhanced recombination and the separation of the initially rather uniform plasma tongue into two discrete patch-like structures. We have ob-

served the creation of a "patch" from what was initially a rather uniform plasma tongue.

2.3. February 19, 1990, Magnetometer Data

Figure 9 shows the northward (H) and vertical (Z) components of the magnetic field deviations measured by the Greenland chain of magnetometers. The top seven traces of both panels show data obtained by stations located on the west coast. The other three curves present magnetic field measurements of the magnetometers situated along the east coast of Greenland. The locations of the ground-based magnetometers range from 85°N to 73°N . Close examination of the magnetic deflections measured between 78° and 73°N reveal a high degree of correlation. Large positive and negative bays with

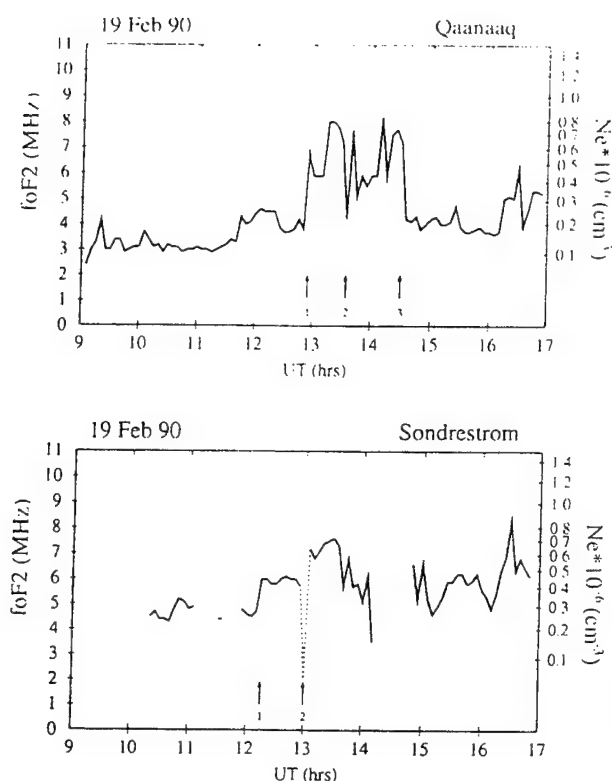


Figure 10. Variations of f_oF_2 as a function of UT on February 19, 1990, recorded at two stations: Sondrestrom (67°N, 51°W) and Qaanaaq (77.5°N, 69.2°W).

amplitudes in excess of 300 nT are seen during this 4-hour segment, typical for midday and active magnetic conditions. Near 1300 UT there is a prominent negative bay in the H component (290 nT at the STF station—Sondrestrom), that lasts 15 min. This magnetic deflection is present in all the west coast stations and displays a phase delay between adjacent stations; the magnetic fluctuations appear at later times at stations located further poleward. The dotted vertical lines highlight the time when the largest negative values occur. Recall that the fast plasma jet was also detected by the ISR during the AZ scan starting at 1259 UT. In section 2.2, we also demonstrated by utilizing two successive EL scans that the fast plasma jet drifted poleward after 1300 UT. The excellent correlation, temporal and spatial, between the large negative bay on the magnetometer and the ISR measurements suggests that the large electric field associated with the fast plasma jet drives large Hall currents which are responsible for the magnetic fluctuations observed on the ground. We also suggest that the deep F

region depletion does not affect substantially the height-integrated Hall conductivity, as this mainly reflects the E layer conductivity. As the plasma jet drifts poleward, it subsides and the amplitude of magnetic field fluctuations, as detected by the different magnetometer stations, sharply decreases. The magnetometer labeled THL and located at Qaanaaq (85°N) detected a weak negative bay at 1329 UT, some 29 min after the one observed at Sondrestrom. This reduction in the flow was confirmed by the T_i and V_{los} measured by the radar during the scans of 1304 and 1308 UT. The vertical component of the magnetic deviations (panel Z) also shows a magnetic disturbance moving poleward.

2.4. February 19, 1990, Digisonde Data

On this day both the Qaanaaq and the Sondrestrom Digisondes recorded digital ionograms at 5-min intervals, each sweep being followed by a series of drift measurements. Figure 10 shows the f_oF_2 time histories for the two stations. The lower panel of Figure 10 shows that patch type f_oF_2 enhancements started at Sondrestrom at 1215 UT (arrow 1), with f_oF_2 rising from a background of 4.5 MHz to initially 6 MHz and after 1300 UT to >7 MHz. At 1300 UT (arrow 2) the enhancement in f_oF_2 is sharply interrupted, the ionogram shows no overhead trace. The only returns observed at this time are identified by the Digisonde as being of clearly oblique origin. At this time the ISR measured an overhead density of less than 10^5 cm^{-3} , and the fast plasma jet was observed. The Sondrestrom magnetometer also measured at this time the previously discussed strong negative bay in the magnetic field H component.

About 40 min later, at 1255 UT the Digisonde observations at Qaanaaq, shown in the top panel, also indicate the onset of an F layer patch event with a sharp increase in f_oF_2 (arrow 1) from a background near 4 MHz to a series of strong 7- to 8-MHz enhancements. These increases are separated into patches by sharp decreases down to between 4.0 and 5.5 MHz. The transit of polar cap patches through the Qaanaaq zenith is abruptly terminated at 1435 UT (arrow 3), approximately 45 min after B_z changed from being strongly negative to a series of short positive and negative reversals. The sharp decrease from 7 down to 4 MHz occurred at 1335 UT (marked by arrow 2). The f_oF_2 behavior described above is typical for patch observations at

Qaanaaq [Buchau *et al.*, 1983; Weber *et al.*, 1984; Buchau and Reinisch, 1991].

The patch events starting at the times marked with arrow 1 in the f_oF_2 time histories of Sondrestrom and Qaanaaq, respectively, are most likely related, with the two Digisondes observing the same F layer patch train at slightly different intersects with respect to the maximum density centers of the respective patches. This may explain the differences in f_oF_2 observed at the two observatories. Throughout the 1200–1500 UT observing period, the Qaanaaq Digisonde observed antisunward convection, with the velocity magnitude at 1200 UT approximately 450 m s^{-1} , increasing to 900 m s^{-1} at 1400 UT, and slowing down to 450 m s^{-1} after 1500 UT. Since 1400 UT is near magnetic local noon for both stations, antisunward drift in this time sector directly connects the two stations. At an average antisunward convection velocity of 600 m s^{-1} , the transit time from Sondrestrom to Qaanaaq (1300 km) is about 36 min, in agreement with the 40-min separation in the observed onset times of the patch events at the two stations (arrows marked 1 in the respective panels). The estimated separation of the times, when the patch trains are ending at the two stations is ≥ 25 min, also in general agreement with the observed average antisunward convection velocity. The overall similarity of the patch observations at the two stations, the supporting evidence provided by the Qaanaaq drift measurements, and the good temporal coincidences of the plasma jet related f_oF_2 depression seen at both stations (marked arrow 2) with the negative bays observed at Sondrestrom and Qaanaaq provide convincing evidence that the ionosonde data at the two stations are actually describing the same F layer patch event. Similar evidence was also provided by scintillation measurements made at Thule and Sondrestrom during the same period of time [Basu *et al.*, this issue].

The inspection of selected ionograms from the two stations (Figure 11) describing the ionosphere on either side and in the center of the plasma jet shows strong similarities and provides further evidence that we are observing the initial plasma break-off event at Sondrestrom, and subsequently the passage of the newly generated patch and the remaining signature of the depletion produced by the plasma jet, at Qaanaaq. The individual frames of two sequences of ionograms shown in Figure 11, on the left side (Figure 11a) are those from Sondre-

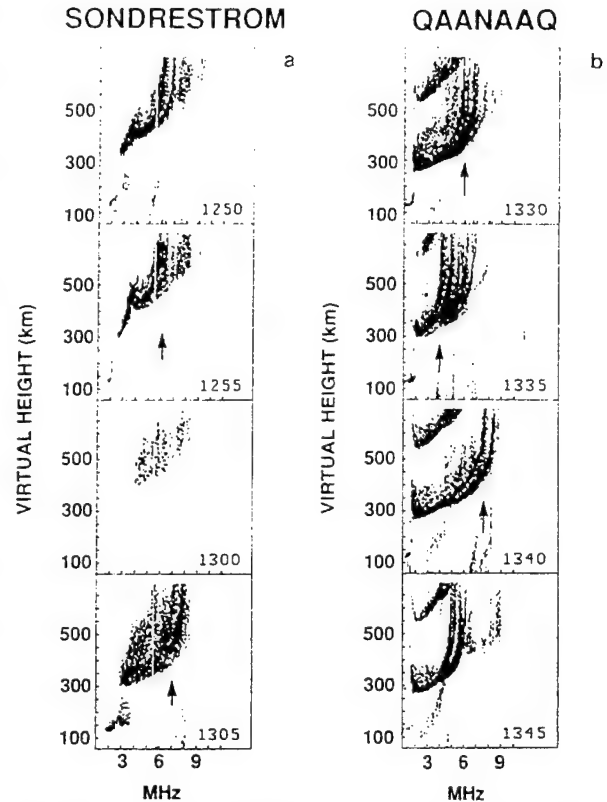


Figure 11. Sequence of selected ionograms taken during the transit of the polar cap patches and the passage of the region of highly depleted plasma on February 19, 1990. The column to the left presents ionograms recorded at Sondrestrom, and the one at the right were obtained at Qaanaaq.

strom, on the right (Figure 11b) those from Qaanaaq, indicate in three different shades the nature of the echoes. Black indicates overhead echoes with o polarization, dark grey represents all x echoes, and light grey oblique (o polarization) returns.

The Sondrestrom ionograms (Figure 11a) at 1250 and 1255 UT show f_oF_2 values near 5.9 MHz, mixed with weak oblique returns. The ionogram at 1300 UT shows complete absence of overhead echoes; only oblique echoes are observed, probably originating from the walls of the two adjacent N_e structures. This unique signature is the result of the low density directly overhead the station, and bounded to the north and to the south by high densities, as seen in Figures 6 and 7. The ionogram at 1305 UT shows the passage of the southern density structure into the zenith, in excellent agreement with the EL scan at 1304 UT (Figure 7). There

are considerable oblique returns; however, the Digisonde is able to measure $f_oF_2 = 7.1$ MHz, in accord with the $6 \times 10^5 \text{ cm}^{-3}$ maximum electron density measured by the radar.

As previously discussed, plasma velocities measured at Qaanaaq, suggested, that the patch structures starting at 1215 UT at Sondrestrom and at 1255 UT at Qaanaaq represented the same ensemble of plasma patches. This was also suggested by the timing of the observation of the negative bay, the magnetic signature of the plasma jet creating the deep break in the plasma tongue, at Sondrestrom and Qaanaaq. On the basis of this conjecture, we proceed to compare the ionograms in Figure 11a with the corresponding Qaanaaq ionograms obtained 30–35 min later (the approximate 36-min travel time inferred from the Qaanaaq drift measurements, and from the 29-min difference in arrival times of the negative bay at the two stations). There is close agreement between the f_oF_2 value measured at Sondrestrom at 1255 UT (5.7 MHz), and the Qaanaaq f_oF_2 value at 1330 UT (5.9 MHz). The Sondrestrom f_oF_2 value at 1305 UT (7.2 MHz) and the Qaanaaq f_oF_2 at 1340 UT (7.7 MHz) are very close in magnitude. The ionograms in between these observations (Sondrestrom at 1300 UT, Qaanaaq at 1335 UT) show a strong reduction in density, which in Sondrestrom had been related to the occurrence of the plasma jet, generating a strong density depletion. While the Sondrestrom ionogram indicated total lack of overhead traces, with the ISR measuring a maximum density of 10^5 cm^{-3} in the depletion, the Qaanaaq ionogram, related to likely that same depletion, indicates a maximum density near $2 \times 10^5 \text{ cm}^{-2}$, a factor of 2 larger than at Sondrestrom. We believe that this discrepancy can be reconciled if we consider that production by solar UV radiation during the transit of the depletion from Sondrestrom to Qaanaaq is replenishing ionospheric plasma in the recently generated depletion. It should be noted that the solar terminator, at the time of the observations, was located north of Qaanaaq.

2.5. September 14, 1991, ISR Data

The scan sequence that was used on September 14, 1991, consisted of a modified scheme of the scan sequence of February 19, 1990. The purpose was to diagnose a larger area of the sky. Consequently, the azimuth scan was extended to cover a full 360° , and the elevation angle was lowered to 30° . This allowed

the radar to map a circular area ~ 1600 km in diameter. The scan rate was also made faster in order to maintain a cycle time comparable to the one used on February 19, 1990.

This section presents another case study of a density break-off event. The data shown were acquired on September 14, 1991. Here again, a section of the ionospheric plasma was “carved” out of a quasi-uniform ionosphere. The prominent feature on this day is the existence of two plasma jets of oppositely directed fast flows, separated by a region of intense precipitation. As will be illustrated in Figures 12–14, a considerable amount of soft precipitation seems to have been deposited between the channels containing large flows, in a region where convergent electric fields exists. In this example, we will see how the F_1 region plasma density (between 200 and 300 km altitude) is augmented. During the experiment the geomagnetic Kp index was 4, and the daily solar flux was 183. At the time of the experiment the IMP 8 satellite did not provide IMF coverage. Equally unfortunate was the loss of the Digisonde receiver at Qaanaaq that prevented us from tracking the patch transit inside the polar cap. Nevertheless, we present this data set to show the ease with which these localized plasma jets produce break-off events. Actually, patches had been observed on this day starting, at least, as early as 1230 UT [Wang *et al.*, this issue].

The line-of-sight velocities of Figure 12a indicate a predominant general poleward convection in almost any direction probed by the radar. It is only in the southwest part of the scan that V_{los} shows a direction and magnitude different to what would be expected from a strictly uniform and steady poleward directed flow. If we assume that the global convection pattern is similar to the statistical pattern presented by Heelis *et al.* [1982] or by Heppner and Maynard [1987] during B_z southward orientation, then we are forced to conclude that the radar was probing the throat region, where the plasma gains direct entry into the polar cap. The equidensity contours of Figures 13a and 13b indicate enhancements of between 5 to $7 \times 10^5 \text{ cm}^{-3}$ to the SE, overhead, and NW, with lower densities ($\leq 4 \times 10^5 \text{ cm}^{-3}$) to the NE and SW. This is most likely the signature of a plasma tongue centered at or slightly to the west of Sondrestrom, convecting approximately along the magnetic meridian. The velocity measurements of Figure 12c show a more structured pattern. One region, situated to the west

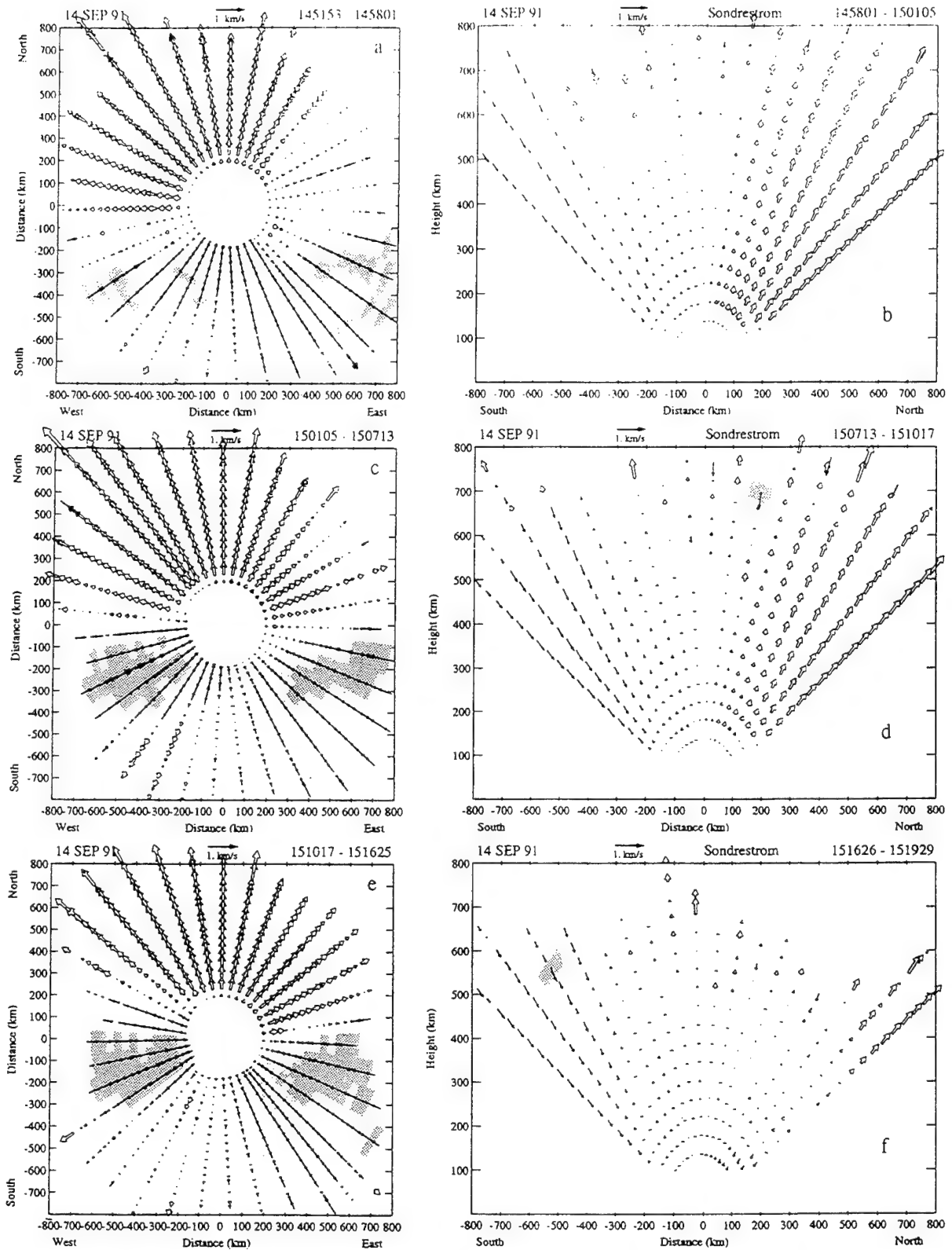


Figure 12. Line-of-sight velocities measured by Sondrestrom ISR during 6 consecutive scans on September 14, 1991. Figures 12a, 12c, and 12e present a top view of the LOS velocity projected to a horizontal plane tangent at the radar site. Figures 12b, 12d, and 12f present LOS velocities in the magnetic meridian plane. Notice the area probed by the radar has been enlarged to cover ± 800 km.

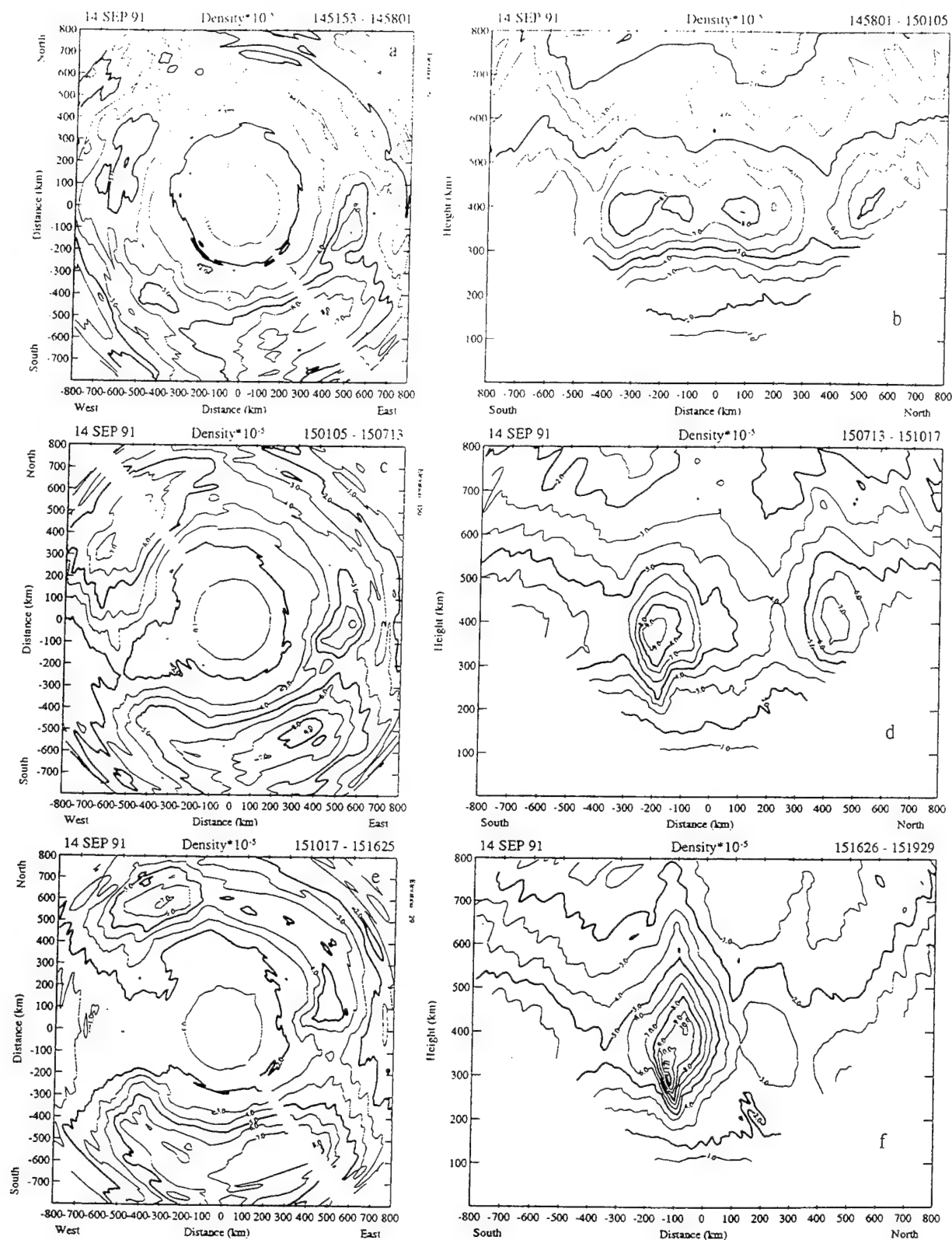


Figure 13. Density contours corresponding to the six scans of Figure 12. The spacing between the contours is 10^5 cm^{-3} . To obtain the densities of Figures 13a and 13e, the antenna beam scanned from 140° (magnetic south) and continued clockwise. In Figure 13c the antenna started at magnetic north and continued counterclockwise.

of the station presents eastward flows and another region located to the east contains large westward velocities. These two large flows bound a region of large convergent electric fields where T_e is observed to exceed 3000 K (see Figure 14b). The LOS velocity of Figure 12e shows that the large flows (plasma jets) move slightly toward the pole. A more structured velocity pattern is observed in the scan of panel f.

Figure 13 shows the density contours corresponding to the six scans of Figure 12. Notice that the contour spacing of Figure 13 has been changed to 10^5 cm^{-3} . The EL scan starting at 1458 UT (Figure 13b) shows that the density profiles are quite uniform in latitude. This scan was performed a few minutes before the plasma jet reached the radar field of view. Figure 13c shows data obtained during the azimuth scan that started at 1501 UT, at the time when the fast plasma jet was first detected inside the ISR field of view. Here the N_e contours reveal the first sign of a density break-off event. In a SW direction from the radar the maximum density intersected is $2 \times 10^5 \text{ cm}^{-3}$, forming a trench which pinches off the plasma tongue at a location, where between 1451–1458 plasma density were $\geq 4 \times 10^5 \text{ cm}^{-3}$. A region containing high T_i values is perfectly collocated with this density depletion. Figure 13d indicates that at 200 km south distance and between 200 and 300 km altitude the density has been augmented. Figure 12c had indicated that near this southward distance, there were large convergent electric fields, suggesting that this region was associated with intense upward field-aligned currents. Even though we do not have information regarding the temporal variation of the particle flux impinging on this region, the presence of an elevated T_e between 200 and 700 km altitude, every time we bisected the southern part of the field of view, is a sure indication of a continuous precipitation of soft electrons. Further, 16 min is a reasonable time interval for soft precipitation to produce a density buildup at 400 km [Roble and Rees, 1977] from near 8×10^5 (1451 UT) to $9 \times 10^5 \text{ cm}^{-3}$ (1507 UT) and at 250 km height from near 4×10^5 (1451 UT) to $5 \times 10^5 \text{ cm}^{-3}$ (1507 UT). The peak densities continue to increase, reaching by 1516 UT 10^6 cm^{-3} (F_2) and $8 \times 10^5 \text{ cm}^{-3}$ (F_1), indicating continued strong soft fluxes. The maximum density increase over the ~ 25 min covered by Figures 13a–13f is 35% (17% in f_oF_2). Thus we are able to conclude, with confidence, that the excess F_2 and

F_1 region densities have been produced locally by soft electrons.

The AZ and EL scans of Figures 13e and 13f show the time evolution of the plasma-eroding process. The density depletion located to the west becomes wider and the fast flow to the east starts eroding the local N_e . The F_1 region enhancement is also seen becoming more pronounced and drifting poleward.

Figure 14a shows a T_e enhancement (>4000 K) to be located 400 km south with its altitude variation aligned parallel to the magnetic field ($\sim 80^\circ$ elevation). Figure 14b shows that the same T_e enhanced region has drifted 200 km to the north, and up to 100 km south of the radar in Figure 14c.

On the basis of the above description, it is possible to reconstruct the disposition of density structure in space instead of along the scan surfaces. The N_e structure should extend approximately 300 km in latitude and at least 1000 km in longitude. The maximum density is $1.1 \times 10^6 \text{ cm}^{-3}$ at ~ 300 km altitude. The density structure has been pinched off from the original tongue by a trench with a maximum density of $3 \times 10^5 \text{ cm}^{-3}$, centered 250 km north of Sondrestrom.

3. Discussion

The data presented here were gathered on two different days each one corresponding to a different season of the year. Nevertheless, the formation of density depletions is readily seen on both days. On February 19, 1990, several different instruments operated simultaneously. The Sondrestrom ISR, the Digisondes at Qaanaaq and Sondrestrom, the Greenland chain of magnetometers and the magnetometer located at Iqaluit, all have provided data to define the extension in longitude and latitude and the time evolution of the patch formation processes. The scan configuration that was adopted by the Sondrestrom radar helped us to obtain a complete view of the dynamics of the fast plasma jet. For the September 14, 1991, case study we are only presenting data obtained by the Sondrestrom radar. The large area mapping of the ionosphere provided by the ISR allow us to observe, every 9 min, an area extending ~ 2 hours of MLT and 12° in latitude.

The common characteristics of the density break-off events which were observed on both days, is the excellent collocation between density depletions, large flows, and elevated ion temperatures. This

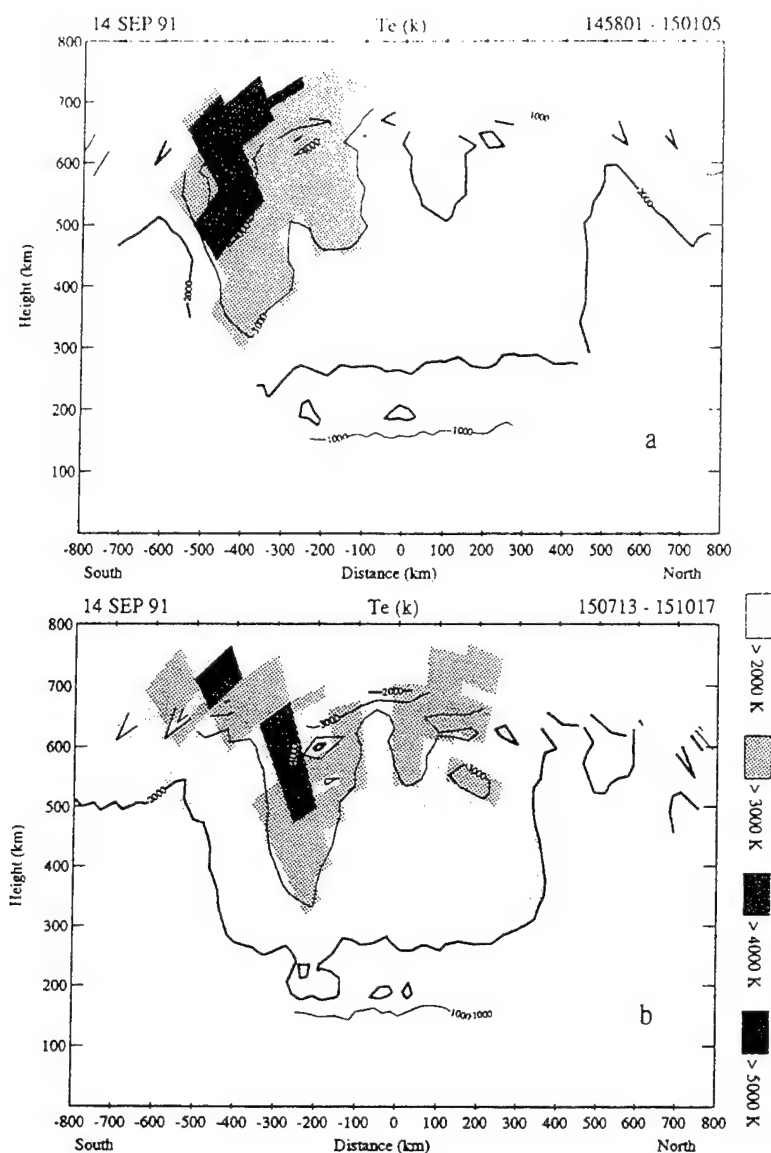


Figure 14. Electron temperature measured by the Sondrestrom ISR during three EL scans on September 14, 1991. The LOS velocities corresponding to these scans were presented in Figures 12b, 12d and 12f.

feature is very suggestive of a T_i -dependent recombination rate which produces a sizeable reduction in the F region density. However, in order to claim that the N_e depletion was in fact produced by enhanced recombination rates, it is necessary to establish that the plasma flowing along the jet had a residence time long enough to produce a significant decay of the F region. This means that the fast plasma jet has to extend a distance of the order of at least 1000 km and have no velocity component

perpendicular to the alignment of the channel, or alternatively, it is necessary to demonstrate that the channel, as a whole, is moving with a speed equal to the component of the background velocity perpendicular to the jet alignment. We will show that the latter case represents fairly well the observations of February 19, 1990.

In section 2, we dedicated special emphasis on the formation of the N_e depletion because the density level that is observed at Sondrestrom mov-

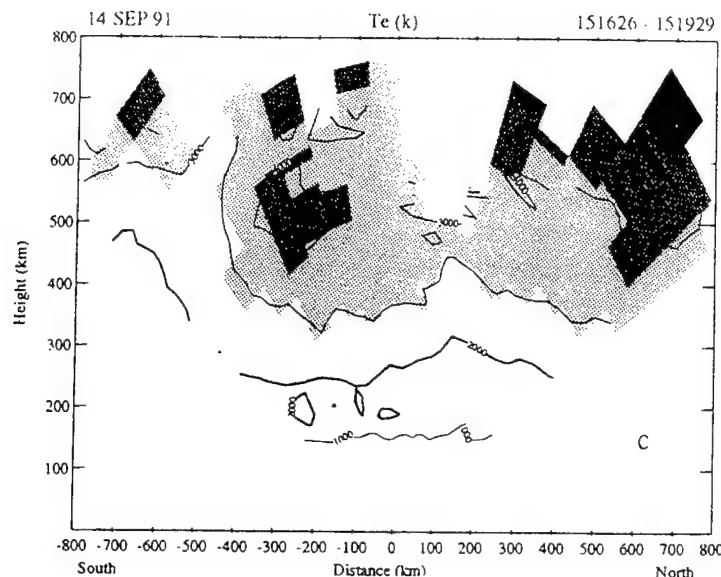


Figure 14. (continued)

ing poleward will be well above the background density level when it reaches Qaanaaq and will automatically qualify as a region of enhanced plasma at the center of the polar cap. Thus we are suggesting in this paper that the patchy structures that are observed in the polar cap can be formed by eroding a part of the ionospheric plasma that is moving toward the polar cap, creating in this way a succession of enhanced and depleted density structures.

3.1. February 19, 1990, Case Study

Figure 15 presents the N-S displacement of three structures that have been identified in the radar and magnetometer data collected on February 19, 1990. These features are (1) the region of enhanced density (N) first seen on the AZ scan starting at 1247 UT and located during this scan at 300 km south, 100 km west of the radar station, (2) the ion temperature enhancement (i), collocated with the region of fast flow and best identified during the AZ scan that started at 1259 UT and situated to the west of the station, and (3) the high electron temperature (e) observed 200 km south of the station at 1256 UT. The lines labeled N , i and e represent the instantaneous location of these three structures along the meridian scan. The dotted line represents the time when different magnetometer stations along the west coast detected peak magnetic deflections. The agreement between the high T_i structures (that

implies large ion velocity) and the dotted line is not a surprise. It points out the fact that the large flow velocities are able to drive large horizontal magnetic deflections. The density structure (labeled N in Figure 15) moves with an average velocity equal to 700 m s^{-1} . The T_i structure follows fairly well the general poleward motion of the density enhancement. The T_e curve shows a swift change at 1257 UT but before and after this time seems to remain quite steady in the radar frame of reference.

Close examination of Figure 15 indicates that there is a 250 m s^{-1} relative velocity between the density and the T_i structures. Knowing that the F region plasma density is subjected to motion according to the magnitude and direction of the imposed $\mathbf{E} \times \mathbf{B}$, we are able to conclude that in the frame of the fast plasma jet, there is a velocity component perpendicular to its alignment. If we take into consideration that the jet is about 300 km wide, then it will take 20 min for the plasma to move across this width.

The longitudinal extension of the plasma jet discussed above can be visualized with the help of Figure 16. Here we plot the equivalent drifts of the magnetic deflections measured by the magnetometers located on the west and east coasts of Greenland and the magnetometer located at Iqaluit (Canada). To obtain the drifts, we have followed the method of Friis-Christensen *et al.* [1988] and Lan-

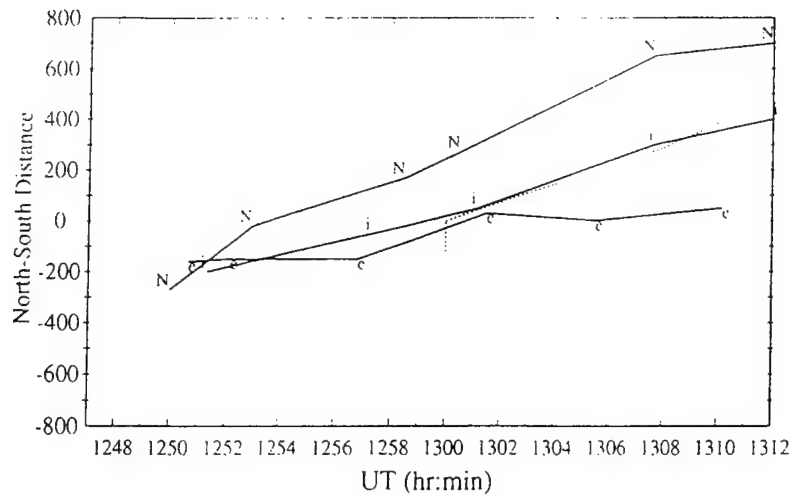


Figure 15. Poleward displacement of the electron density, ion, and electron temperature structures observed during the EL and AZ scans of February 19, 1990. The N-S distance is measured along the meridian. The dotted line depicts the time when the largest negative deflection of the H component was detected by the chain of magnetometers along the west coast of Greenland.

zerotti *et al.* [1987]. Using the same assumptions as were made by these authors, we consider that the main source of the magnetic deflections measured at the ground is the circulation of Hall currents in the E region. Consequently, a 90° counterclockwise rotation was applied to the magnetic horizontal vectors in order to obtain equivalent drift vectors.

Figure 16 shows a series of snapshots obtained every 5 min of the equivalent drifts deduced from nine different magnetometer stations spanning ~ 2000 km in longitude. Figure 16a marks the first time that the fast plasma jet was seen by stations located on the west coast of Greenland. The Iqaluit magnetometer detected an intense eastward flow even before this time. Figure 16b (1300 UT) shows intensification of the plasma jet at the Sondrestrom (STF) station. At later times (Figures 16c and 16d) the intense flow is seen at stations located even further poleward, finally reaching Qaanaq (Qa/THL) at ~ 1330 UT, (see Figure 9). Figure 16 gives an indication of a vortexlike motion at latitudes near 70° . This feature agrees well with the reversal of the line-of-sight velocity detected to the north by the ISR during the AZ scan starting at 1259 UT. The eastward boundary of the fast plasma jet is best illustrated by the vectors measured at the Scoresbysund (SCO) station, located on the east coast of Greenland. The plasma velocity is seen to have rotated to a more poleward direction. Figure 16b delineates the dimensions of the velocity structure

to be about 2000 km in longitude (from the Iqaluit to the Scoresbysund stations) and ~ 600 km in the north-south direction. Figure 17 shows that the amplitude of the resolved velocity in the fast plasma jet is 2 km s^{-1} (requiring an electric field of 100 mV m^{-1}). It will therefore take 16 min for a particle to go along the jet channel. Banks *et al.* [1974] calculated that a time interval of 10 min was required for an electric field of the order of 100 mV m^{-1} to substantially decrease the F region O^+ density under conditions of enhanced recombination using the reaction $\text{O}^+ + \text{N}_2 \rightarrow \text{NO}^+ + \text{N}$. Thus the 16-min time interval is long enough to guarantee substantial loss of the O^+ F region density, corroborating the Sondrestrom ISR and Digisonde measurements. Lockwood *et al.* [1990b] presented evidence suggesting that a recently opened flux tube experiences a magnetic tension force during a time interval between 5 and 10 min. The upper limit is in accord with the time needed for the F region plasma to recombine.

The magnitude and direction of the velocity have been resolved using independently the line-of-sight velocities obtained during the EL and AZ radar scans. These results are plotted in Figure 17. Each of the panels depicts the velocities corresponding to only one scan. To calculate the velocity vectors, we have used the same algorithms employed by Valladares and Carlson [1991]. In essence, this method consists of applying the divergence-free condition of the velocity for data collected during AZ scans

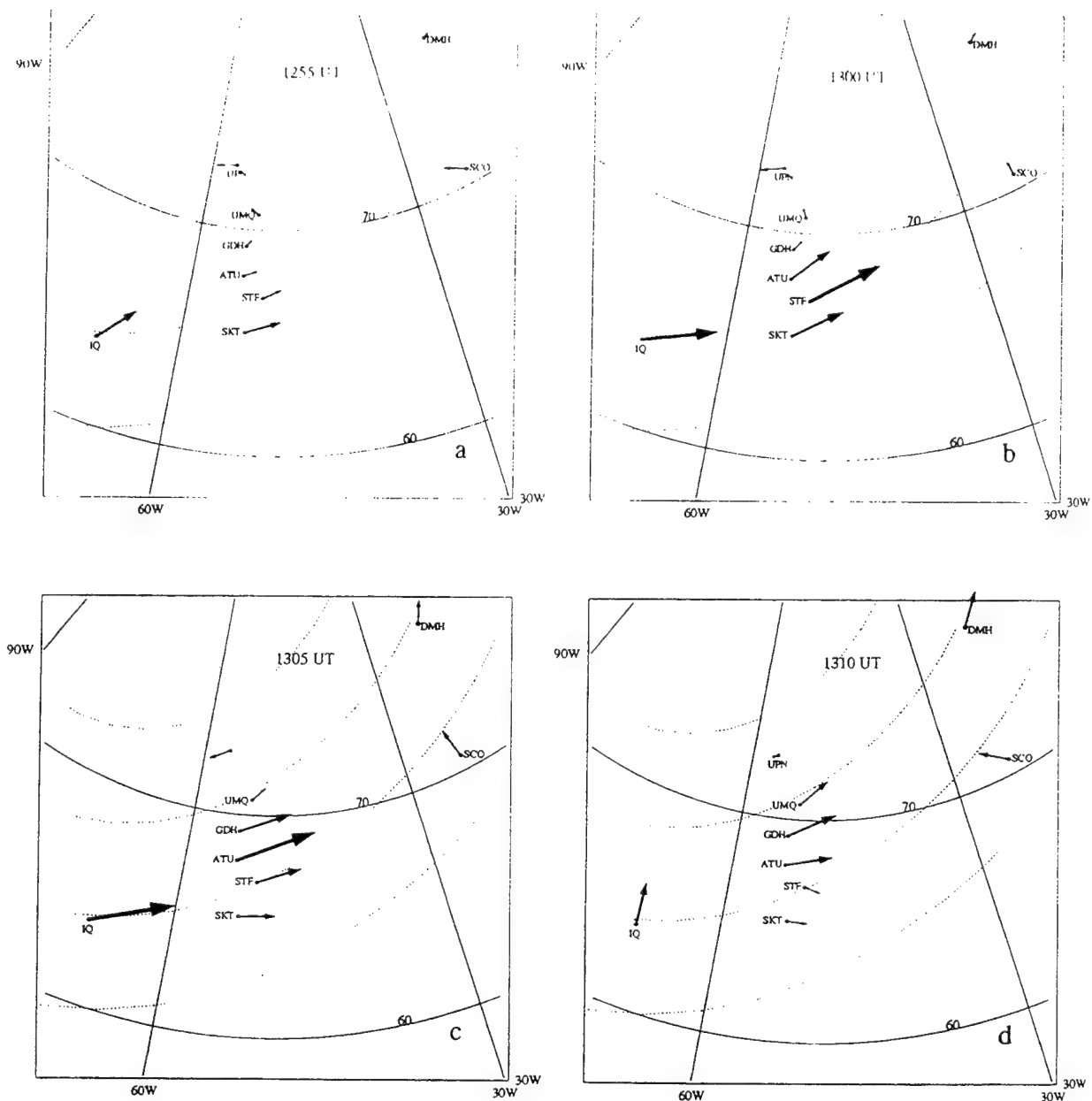


Figure 16. Equivalent drifts calculated from the H and D components of the magnetic fluctuations measured by several stations of the Greenland chain of magnetometers on February 19, 1990. The vector to the left is based on measurements performed by the Iqaluit magnetometer. The dotted lines represent constant L shell starting at 70° invariant latitude and proceeding in steps of 4° .

and the property of the field lines being equipotential for the analysis of the LOS velocities obtained during the EL scans. Figures 17b–17d display the velocity at times when the fast plasma jet event was located inside the field-of-view of the Sondrestrom radar. These three frames show clearly the rotation of the velocity vectors located poleward of the ISR

station. This fact agrees well and confirms the results of the equivalent drifts which were deduced based on the magnetometer recordings alone.

3.2. September 14, 1991, Case Study

The uniform poleward motion of the plasma that was clearly seen during the AZ scan starting at 1451

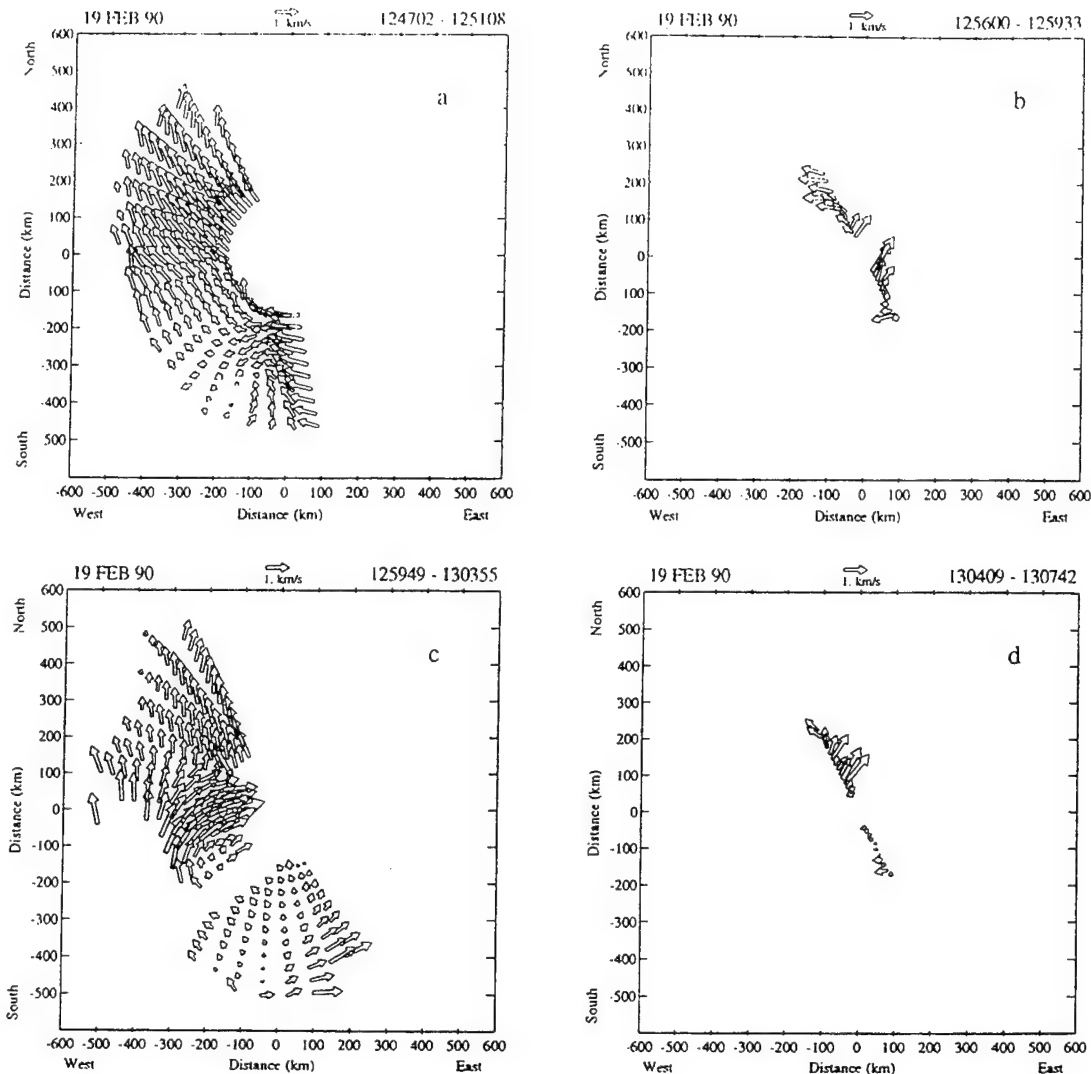


Figure 17. Velocity vectors derived from the LOS velocity corresponding to (a) the azimuth scan of 1247:02 UT (Figure 3), (b) the elevation scan of 1256:00 UT (Figure 5), (c) the azimuth scan of 1259:49 UT (Figure 6), and (d) the elevation scan of 1304:09 UT (Figure 7) on February 19, 1990. The vectors of Figures 17b and 17d were calculated combining the *E* and *F* region LOS velocities measured along the same field line. The vectors of Figures 17a and 17c were computed using the divergence-free property of the velocity ($\nabla \cdot \mathbf{V} = 0$).

UT on September 14, 1991, suggested that the total velocity pattern in the radar field of view can be represented as the addition of two velocity structures. One consists of a uniform horizontal velocity directed poleward, while the other is formed by the residual LOS velocities representing mainly a system of oppositely directed flows.

Figure 18 shows the residual LOS velocities for four AZ scans, three of them were shown in Figure 12. These plots were obtained after subtracting a uniform velocity of $\sim 500 \text{ m s}^{-1}$ pointing almost

magnetic north to the line-of-sight velocities measured during the four AZ scans. The presence of a region containing a sharp velocity reversal located to the south of the station becomes evident from these plots. This sharp velocity shear (indicated in all four panels by a solid line) extends from east to west all across the area probed by the radar. The location of the velocity reversal coincided with the latitude, where enhanced values of T_e were observed in Figure 14 and also with the location of elevated densities at the altitude range of 200 and

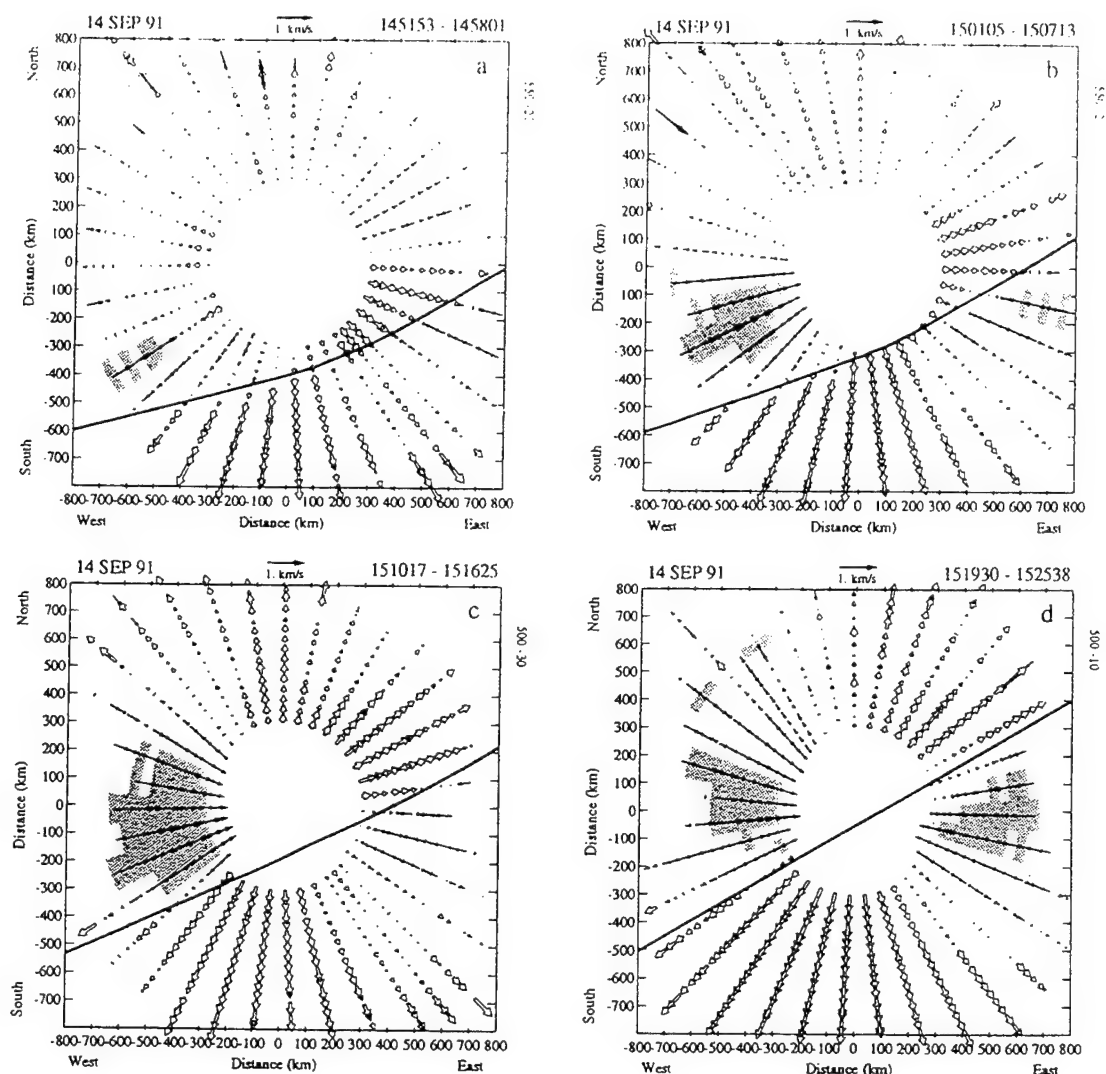


Figure 18. Residual line-of-sight velocity obtained after subtracting a uniform velocity from all the LOS velocities measured by the radar on September 14, 1991. The location of a sharp reversal to the south and propagating poleward becomes more evident in this format.

300 km, as seen in Figure 13. Thus we suggest that this region marks the location of intense upward currents, probably carried by the soft electron population responsible for the tenuous N_e enhancement.

Numerical calculations of the production rate and the density enhancement produced by a downward electron flux containing an average energy of 100 eV have indicated that 15 min is a reasonable time interval to increase the plasma density at 300 km altitude by 30% (R. Sheehan, private communication, 1993) for the ionospheric conditions that prevailed during the observations of September 14, 1991, that is, solar maximum and $N_e \sim 9 \times 10^5 \text{ cm}^{-3}$.

Fast plasma jets accompanied by elevated T_i were also observed during this day exactly collocated with regions of depleted densities. Even though the velocity is only near 1.5 km s^{-1} , the exact collocation of the jets and the density depletions is very suggestive of enhanced recombination being responsible for the almost complete loss of the F region density.

3.3. Model Description

A complete view of the processes leading to the break-off event, therefore, starts to emerge, in which the fast plasma jets are produced by the

TIME SEQUENCE FOR DENSITY BREAK-OFF EVENT

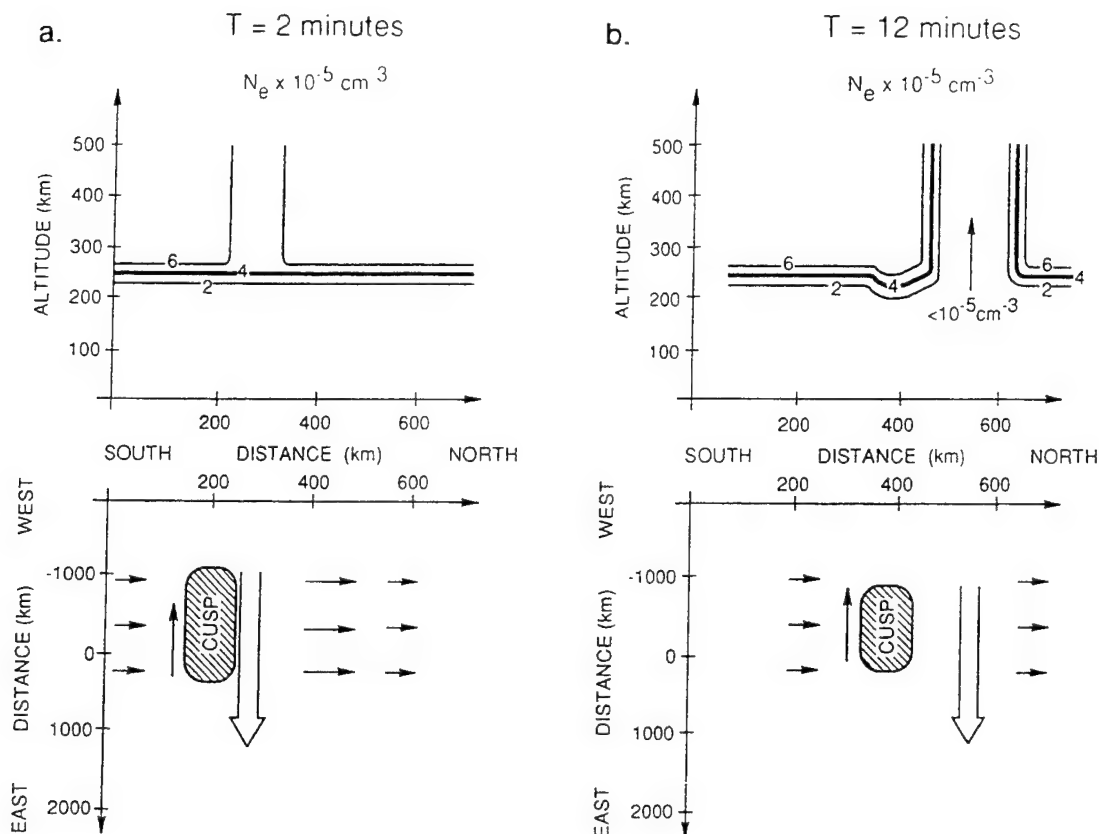


Figure 19. Schematic drawing showing a possible scenario for polar cap patch formation and the evolution of the density break-off event at two different times. (a) At $T = 2$ min, near the beginning of the event and (b) at $T = 12$ min, when the density break-off event was fully developed. The wide arrows in the lower panels depict the location of the region containing large ion velocities. The upper panels show the evolution of the density contours in a latitudinal cross section similar to the radar elevation scans. Note the poleward displacement of the N_e structure along with the fast plasma jet channel.

tension force on recently reconnected field lines. The large velocities are observed in the prenoon sector in accordance with the location of a reconnection impulse when B_y is negative. In the February 19, 1990, data, we observe a region of persistent T_e enhancement located to the south of the jet. This is very suggestive of the cusp region being within the radar field of view. All these features have been included in Figure 19, where we summarize the sequence of events that culminate in a density break-off event. In the diagram we indicate that there is a general poleward ionospheric motion and superimposed on this, we find the fast plasma jet localized in latitude with an eastward velocity. At T

$= 2$ min (Figure 19a), only a tenuous erosion of the F region density has occurred. Later, at $T = 12$ min the density in the F region has decayed to 10^5 cm^{-3} , and both the plasma jet and the density hole have drifted to poleward latitudes.

Thus on the basis of the data presented here and the Cowley *et al.* [1991] model of newly reconnected field lines, we conclude that a density break-off event can occur just poleward of the cusp. In this scenario the formation of a polar cap patch can be understood as the ionospheric response to a time-dependent solar wind-magnetopause interaction. The process described here requires changes in the reconnection rate, to cause a variable flow

pattern containing a fast plasma jet and adjacent regions of smaller velocities. This mechanism is different to the patch production process presented by Lockwood and Carlson [1992]. We claim that the mechanism outlined here is able to form discrete polar cap patches with dimensions of the order of hundreds of kilometers. However, other mechanisms, such as continuous B_y reversals [Sojka *et al.*, 1993] may also help to produce the large variety of patch shapes and sizes that are commonly observed at Qaanaaq.

4. Conclusions

This study leads us to these conclusions:

1. The Sondrestrom ISR and the chain of magnetometers located at Greenland have detected plasma jets containing velocities in excess of 2 km s^{-1} . These large flows were observed to be accompanied by ion temperatures exceeding, in some cases, 5000 K. The extension of the fast plasma jet was determined to be at least 2000 km in longitude and to cover 300 km in the N-S direction.
2. The fact that the fast plasma jet of eastward velocities was observed in the prenoon sector during conditions of negative IMF B_y , and the concurrent radar measurements which indicated the presence of soft precipitation near the equatorward boundary of the plasma jet suggest that the large velocities measured by the radar, and indirectly by the ground-based magnetometers, were intrinsically related to the tension force exerted upon recently reconnected field lines.
3. The fast plasma jet was found to be collocated with regions of low F region density. A factor of 6 decrease in the local density was observed 10 min after the jet was established as a quasi-steady feature. We conclude that an enhanced recombination rate of the $\text{O}^+ + \text{N}_2$ reaction was responsible for eroding a substantial volume of the high-latitude F region.
4. The radar and the Greenland chain of magnetometers have described the temporal evolution of the fast plasma jet. We have observed the jet to move steadily in the poleward direction and with a magnitude close to the speed of the background plasma.
5. It was calculated that any flux tube will reside in the fast plasma jet, at least, for a time as long as 15 min. This time interval is consistent with previous theoretical calculations for the recombination time of the F region density in the presence of large electric fields [Banks *et al.*, 1974].
6. The Digisondes at Sondrestrom, and more importantly at Qaanaaq, detected the passage of three different plasma regions sequentially containing high, low, and high densities. This confirms that on February 19, 1990, the creation of a region of low density at latitudes near Sondrestrom constitute the formation of polar cap patches when they are convected into the polar cap.
7. The September 14, 1991, case study also shows the presence of plasma jets exactly collocated with an F region being eroded by the action of enhanced recombination rates. South of this region we encountered a region where N_e was locally created at altitudes between 200 and 300 km. However, the total increase was not higher than 20% of the background plasma density.

Acknowledgments. We thank R. Lepping for making the IMF data available for this study, L. J. Lanzerotti for supplying the magnetometer data from the Iqaluit station, Maurice Shirley, University of Massachusetts, Lowell for his support of the Digisonde analysis and J. Kelly for providing the Sondrestrom radar data in raw format. We acknowledge the helpful suggestion of H. C. Carlson, Jr., regarding the antenna mode used in this study. The work at Boston College was partially supported by Phillips Laboratory contract F19628-90-K-0007 and by NSF grants ATM-9000273 and ATM-9016465. We thank the Danish Commission for Scientific Research in Greenland for permission to conduct ground experiments at Sondrestrom and Qaanaaq under continuing project A16-91.

References

- Anderson, D. N., J. Buchau, and R. A. Heelis, Origin of density enhancements in the winter polar cap, *Radio Sci.*, 23, 513, 1988.
- Banks, P. M., R. W. Schunk, and W. J. Raitt, NO^+ and O^+ in the high latitude F region, *Geophys. Res. Lett.*, 1, 239, 1974.
- Baron, M. J., and R. H. Wand, F region ion temperature enhancements resulting from Joule heating, *J. Geophys. Res.*, 88, 4114, 1983.
- Basu, S., Su. Basu, P. K. Chaturvedi, and C. M. Bryant, Jr., Irregularities structures in the cusp/cleft and polar cap regions, *Radio Sci.*, this issue.
- Bibl, K., and B. W. Reinisch, The universal ionosonde, *Radio Sci.*, 13, 519, 1978.
- Buchau, J., and B. W. Reinisch, Electron density structures in the polar F region, *Adv. Space Res.*, 11(10), 29, 1991.
- Buchau, J., B. W. Reinisch, E. J. Weber, and J. G. Moore, Structure and dynamics of the winter polar cap F region, *Radio Sci.*, 18, 995, 1983.
- Buchau, J., E. J. Weber, D. N. Anderson, H. C. Carlson,

- Jr., J. G. Moore, B. W. Reinisch, and R. C. Livingston, Ionospheric structures in the polar cap: Their origin and relation to 250-MHz scintillation, *Radio Sci.*, 20, 325, 1985.
- Cowley, S. W. H., J. P. Morelli, and M. Lockwood, Dependence of convection flows and particle precipitation in the high-latitude dayside ionosphere on the X and Y components of the interplanetary magnetic field, *J. Geophys. Res.*, 96, 5557, 1991.
- Farrugia, C. J., M. P. Freeman, S. W. H. Cowley, D. J. Southwood, M. Lockwood, and A. Etemadi, Pressure-driven magnetopause motions and attendant response on the ground, *Planet. Space Sci.*, 37, 589, 1989.
- Foster, J. C., Ionospheric signatures of magnetospheric convection, *J. Geophys. Res.*, 89, 9107, 1984.
- Foster, J. C., and J. R. Doupnik, Plasma convection in the vicinity of the dayside cleft, *J. Geophys. Res.*, 89, 9107, 1984.
- Foster, J. C., G. S. Stiles, and J. R. Doupnik, Radar observations of cleft dynamics, *J. Geophys. Res.*, 85, 3453, 1980.
- Friis-Christensen, E., M. A. McHenry, C. R. Clauer, and S. Vennerstrom, Ionospheric traveling convection vortices observed near the polar cleft: A triggered response to sudden changes in the solar wind, *Geophys. Res. Lett.*, 15, 253, 1988.
- Fukui, K., J. Buchau, and C. E. Valladares, Convection of polar cap patches observed at Qaanaaq, Greenland during the winter of 1989–1990, *Radio Sci.*, this issue.
- Heelis, R. A., J. K. Lowell, and R. W. Spiro, A model of the high-latitude ionospheric convection pattern, *J. Geophys. Res.*, 87, 6339, 1982.
- Heppner, J. P., and N. C. Maynard, Empirical high-latitude electric field models, *J. Geophys. Res.*, 92, 4467, 1987.
- Kelly, J. D., and J. F. Vickrey, F region ionospheric structure associated with antisunward flow near the dayside cusp, *Geophys. Res. Lett.*, 11, 907, 1984.
- Lanzerotti, L. J., R. D. Hunsucker, D. Rice, L. C. Lee, A. Wolfe, C. G. MacLennan, and L. V. Medford, Ionosphere and ground-based response to field-aligned currents near the magnetospheric cusp regions, *J. Geophys. Res.*, 92, 7739, 1987.
- Lockwood, M., and H. C. Carlson, Production of polar cap density patches by transient magnetopause reconnection, *Geophys. Res. Lett.*, 19, 1731, 1992.
- Lockwood, M., P. E. Sandholt, S. W. H. Cowley, and T. Oguti, Interplanetary magnetic field control of dayside auroral activity and the transfer of momentum across the dayside ionosphere, *Planet. Space Sci.*, 11, 1347, 1989.
- Lockwood, M., P. E. Sandholt, A. D. Farmer, S. W. H. Cowley, B. Lybekk, and V. N. Davda, Auroral and plasma flow transients at magnetic noon, *Planet. Space Sci.*, 38, 973, 1990a.
- Lockwood, M., S. W. H. Cowley, and M. P. Freeman, The excitation of plasma convection in the high-latitude ionosphere, *J. Geophys. Res.*, 95, 7961, 1990b.
- Newell, P. T., and C.-I. Meng, The cusp and the cleft/boundary layer: Low-altitude identification and statistical local time variation, *J. Geophys. Res.*, 93, 14,549, 1988.
- Roble, R. G., and M. H. Rees, Time-dependent studies of the aurora: Effects of particle precipitation on the dynamic morphology of ionospheric and atmospheric properties, *Planet. Space Sci.*, 25, 991, 1977.
- Sandholt, P. E., M. Lockwood, T. Oguti, S. W. H. Cowley, K. S. C. Freeman, B. Lybekk, A. Egeland, and D. M. Willis, Midday auroral breakup events and related energy and momentum transfer from the magnetosheath, *J. Geophys. Res.*, 95, 1039, 1990.
- Sojka, J. J., M. D. Bowline, R. W. Schunk, D. T. Decker, C. E. Valladares, R. Sheehan, D. N. Anderson, and R. A. Heelis, Modeling polar cap F layer patches using a time varying convection, *Geophys. Res. Lett.*, 20, 1783–1786, 1993.
- Tsunoda, R. T., High-latitude F region irregularities: A review and synthesis, *Rev. Geophys.*, 26, 719, 1988.
- Valladares, C. E., and H. C. Carlson, Jr., The electrodynamic, thermal, and energetic character of intense sun-aligned arcs in the polar cap, *J. Geophys. Res.*, 96, 1379, 1991.
- Vondrak, R. R., and M. J. Baron, A method of obtaining the energy distribution of auroral electrons from incoherent scatter radar measurements, in *Radar Probing of the Auroral Plasma*, edited by A. Brekke, p. 315, Universitetsforlaget, Oslo, 1977.
- Wang, Z., T. J. Rosenberg, P. Stauning, Su. Basu, and G. Crowley, Calculations of riometer absorption associated with F region plasma structures based on Sondre Stromfjord incoherent scatter radar observations, *Radio Sci.*, this issue.
- Weber, E. J., J. Buchau, J. G. Moore, J. R. Sharber, R. C. Livingston, J. D. Winningham, and B. W. Reinisch, F layer ionization patches in the polar cap, *J. Geophys. Res.*, 89, 1683, 1984.
- Weber, E. J., J. A. Klobuchar, J. Buchau, H. C. Carlson, Jr., R. C. Livingston, O. de la Beaujardiere, M. McCready, J. G. Moore, and G. J. Bishop, Polar cap F layer patches: Structure and dynamics, *J. Geophys. Res.*, 91, 121, 1986.

S. Basu and C. E. Valladares, Institute for Space Research, Boston College, Newton Center, MA 02159.

E. Friis-Christensen, Division of Geophysics, Danish Meteorological Institute, DK-2100, Copenhagen, Denmark.

(Received January 26, 1993; revised May 24, 1993; accepted May 27, 1993.)

Modeling the formation of polar cap patches using large plasma flows

C. E. Valladares, D. T. Decker, and R. Sheehan

Institute for Space Research, Boston College, Newton Center, Massachusetts

D. N. Anderson

Phillips Laboratory, Geophysics Directorate, Hanscom Air Force Base, Massachusetts

Abstract. Recent measurements made with the Sondrestrom incoherent scatter radar have indicated that the formation of polar cap patches can be closely associated with the flow of a large plasma jet. In this paper, we report the results of a numerical study to investigate the role of plasma jets on patch formation, to determine the temporal evolution of the density structure, and to assess the importance of O^+ loss rate and transport mechanisms. We have used a time-dependent model of the high-latitude F region ionosphere and model inputs guided by data collected by radar and ground-based magnetometers. We have studied several different scenarios of patch formation. Rather than mix the effects of a complex of variations that could occur during a transient event, we limit ourselves here to simulations of three types to focus on a few key elements. The first attempt employed a Heelis-type pattern to represent the global convection and two stationary vortices to characterize the localized velocity structure. No discrete isolated patches were evident in this simulation. The second modeling study allowed the vortices to travel according to the background convection. Discrete density patches were seen in the polar cap for this case. The third case involved the use of a Heppner and Maynard pattern of polar cap potential. Like the second case, patches were seen only when traveling vortices were used in the simulation. The shapes of the patches in the two cases of moving vortices were defined by the geometrical aspect of the vortices, i.e. elliptical vortices generated elongated patches. When we “artificially” removed the Joule frictional heating, and hence any enhanced O^+ loss rate, it was found that transport of low density plasma from earlier local times can contribute to ~60% of the depletion. We also found that patches can be created only when the vortices are located in a narrow local time sector, between 1000 and 1200 LT and at latitudes close to the tongue of ionization.

1. Introduction

Large-scale density structures are commonly observed in the polar cap. When the interplanetary magnetic field (IMF) is directed southward mesoscale (100 to 1000 km), density enhancements, named polar cap “patches”, drift across the polar cap in the antisunward direction [Buchau *et al.*, 1983; Weber *et al.*, 1984, 1986; Fukui *et al.*, 1994]. When the IMF is directed northward, elongated streaks of precipitation-enhanced F region

plasma extend aligned to the noon-midnight meridian and move toward dawn or dusk [Buchau *et al.*, 1983; Carlson *et al.*, 1984; Valladares *et al.*, 1994a]. Both types of structures can be associated with intense levels of scintillation [Weber *et al.*, 1984; Buchau *et al.*, 1985; Basu *et al.*, 1985, 1989] and disrupt radio satellite communication systems. In this paper, we investigate theoretically the formation of plasma density enhancements that occur during B_z south conditions. To conduct this study, we have used a three-dimensional time-dependent model of the high-latitude F region ionosphere developed by Anderson *et al.* [1988, 1996] and Decker *et al.* [1994]. Differing from previous attempts, we have incorporated into the model analytical expressions of localized electric field structures and their

Copyright 1996 by the American Geophysical Union.

Paper number 96RS00481.
0048-6604/96/96RS-00481\$11.00

time-dependence. We checked the validity of the model results by conducting a detailed comparison with data gathered from the Sondrestrom incoherent scatter radar (ISR) during patch formation events.

The source of the plasma and the physical processes that form the polar cap patches have been under investigation for over 10 years. *Buchau et al.* [1985] and *de la Beaujardiere et al.* [1985] were the first researchers to address the question of the origin of the density inside the patches. *Buchau et al.* [1985] measured values of f_oF_2 at Thule, Greenland (86° magnetic latitude), showing large fluctuations. The minimum f_oF_2 values were equal to densities produced locally by the sun EUV radiation, but the maximum values were similar to the densities that were produced at locations equatorward of the auroral oval. These observations suggested that the plasma density inside the patches was produced by solar radiation in the sunlit ionosphere, probably at subcusp latitudes, and then carried into and across the polar cap by the global convection pattern. In fact, *Weber et al.* [1984] and *Foster and Doupnik* [1984] confirmed the presence of a large eastward electric field near midday, likely directing the subauroral plasma poleward. *Buchau et al.* [1985] found also that the occurrence of patches displayed a strong diurnal UT control. The patches were seen at Thule almost exclusively between 1200 and 0000 UT. This UT control of the polar cap F layer ionization was interpreted in terms of the displacement of the convection pattern with respect to the geographic pole. It is because of this displacement that the polar convection is able to embrace higher-density plasma only at certain UT hours [*Sojka et al.*, 1993, 1994]. However, the mechanism (or mechanisms) by which the auroral plasma can break up into discrete entities is still a matter of debate.

Tsunoda [1988] summarized the role of different mechanisms conducive for patch generation. He suggested that changes in the B_y and/or B_z components of the IMF could originate temporal variations in the global flow pattern, drastically disturbing the density distribution within the polar cap. In the mid 1980s, several theoretical studies were designed to study the production, lifetime, and decay of large-scale structures inside the polar ionosphere [*Sojka and Schunk*, 1986; *Schunk and Sojka*, 1987]. These authors indicated that hard precipitation could produce plasma enhancements similar to the patches and blobs found in the auroral oval. They argued that in the absence of solar radiation, although the particle-produced E region will rapidly recombine, the longer lifetime enhanced F region ionization could build up and persist for several hours. *Sojka and Schunk*

[1988] theoretically demonstrated that large electric fields could create regions of density depleted by a factor of 4. *Anderson et al.* [1988] presented a model of the high-latitude F region that was used to investigate the effect of sudden changes in the size of the polar cap upon density enhancements transiting the polar cap. While these model studies were able to form structures, most of the success in patch modeling has been attained only after the first High Latitude Plasma Structures meeting was convened at Peaceful Valley, Colorado, in June 1992. *Sojka et al.* [1993] conducted numerical simulations of the effect of temporal changes of the global pattern. The latter two studies were successful in producing density structures at polar cap latitudes. *Decker et al.* [1994] used six different global convection patterns and localized velocity structures to reproduce the digisonde measurements of f_oF_2 values at Sondrestrom. *Lockwood and Carlson* [1992] used the formulation of transient reconnection [*Cowley et al.*, 1991] to suggest that a transient burst of reconnection together with the equatorward motion of the ionospheric projection of the X line could extract a region of the high density subauroral plasma, divert the subauroral density poleward, and finally "pinch off" the newly formed patch. More recently, *Valladares et al.* [1994b] has shown a case study where a fast plasma jet containing eastward directed velocities in excess of 2.5 km s^{-1} was able to increase the O^+ recombination rate and yield an east-west aligned region of reduced densities across a poleward moving tongue of ionization (TOI). *Rodger et al.* [1994] presented data from the Halley Polar Anglo-American Conjugate Experiment radar in Antarctica, suggesting that a region of depleted densities can be carved out by increased O^+ recombination due to large plasma jets.

This paper presents a detailed modeling of the mechanism of patch formation presented by *Valladares et al.* [1994b] and *Roger et al.* [1994]. The mechanism described here operates in conjunction with a background poleward convection to produce mesoscale polar structures from subauroral plasma. This process may also have an essential role in determining the size and the shape of the polar cap patches. The basic elements of this mechanism are (1) a fast plasma jet, observed near the midday auroral oval, (2) enhanced ion temperature due to Joule frictional heating, (3) enhanced recombination rates of O^+ , and, (4) transit of low density plasma from earlier local times.

The paper has been organized in the following manner. Section 2 succinctly describes our model of the high-latitude ionosphere [*Anderson et al.*, 1988; *Decker et al.*, 1994] and the calculations of the localized electric fields

incorporated into the model. Section 3 presents results of a computer model of a patch formation mechanism using convection patterns for typical IMF B_z positive and negative values. An assessment of the ability of enhanced recombination loss to erode parts of the TOI and to disconnect regions from the oval is also discussed in this section. Section 4 presents model calculations for vortices located at several different local times. The paper concludes with the discussion and conclusions section.

2. Model Description

The Global Theoretical Ionospheric Model (GTIM) calculates the density altitude profile of a single ion (O^+) along a flux tube. It solves the coupled continuity and momentum equations for ions and electrons. The solution of the differential equations is simplified by selecting a coordinate system in which one dimension is defined parallel to the local magnetic field. The model attains three-dimensionality by repeating the profile calculations along many (a few thousand) flux tubes. The locations of the flux tubes are selected to cover the range of latitudes and local times desired for the simulation. The mathematical foundation of the GTIM model was introduced by Anderson [1971, 1973]. Although initially used to study the low-latitude ionosphere, it has been extended to include physical processes of the high-latitude ionosphere, such as the effects of large electric fields and particle precipitation [Anderson et al., 1988; Decker et al., 1994]. Recently, Decker et al. [1994] have described how the inputs to the GTIM model can easily accommodate a time-dependent convection pattern and spatially localized regions containing high flows to represent highly variable situations, such as those existing in the cusp region. Other geophysical input parameters, such as the neutral density and wind, along with several initial conditions, such as the plasma density, can be freely defined to simulate different scenarios. In this paper, we have adjusted the global convection pattern and included a local electric field to reproduce the velocities measured on February 19, 1990, by the Sondrestrom ISR.

The radar and magnetometer measurements used to define the model inputs were discussed by Valladares et al. [1994b]. These authors observed a large channel oriented in the east-west direction containing jet-type eastward velocities of order 2 km s^{-1} . In this channel, the ion temperature (T_i) was enhanced and the density (N_e) was depleted. These signatures in the T_i and N_e

values implied a likely increase in the O^+ recombination rate. Successive radar scans indicated that the plasma jet was continuously moving poleward. This motion was also confirmed by the large negative deflection seen at later times by magnetometers located at latitudes poleward of Sondrestrom. The large negative deviation of the H component due to Hall currents appeared at Qaanaaq 29 min after being observed at Sondrestrom. This implied an average poleward displacement of 620 m s^{-1} for the plasma jet. Valladares et al. [1994b] also presented equivalent velocity vectors deduced from the magnetometers located along the east coast of Greenland, implying a flow vorticity. Similar vorticity was seen in the resolved radar velocity vectors. The radar line-of-sight velocity also indicated that adjacent to and both northward and southward of the large plasma jet there existed regions of westward flows. In summary, the radar and magnetometer data suggested the presence of two adjacent vortices of opposite vorticity with the common region in the middle comprising the plasma jet. The GTIM model also requires other geophysical parameters, such as the neutral density, wind and temperature, the ionization, and chemical loss rates, and the diffusion coefficients. These latter atmospheric parameters were selected as described by Decker et al. [1994]. The neutral densities and winds were calculated using the mass spectrometer/incoherent scatter 1986 (MSIS-86) model [Hedin, 1987] and Hedin's wind model [Hedin et al., 1991]. The ion loss rate was computed as a function of an effective temperature. This parameter is derived using the following equation of Schunk et al. [1975]:

$$T_{\text{eff}} = T_n + 0.329E^2$$

where E is the magnetospheric electric field in millivolts per meter.

Plate 1 displays the $N_m F_2$ values of the high latitude ionosphere as a function of magnetic latitude and local time. These values were obtained with the GTIM model after following 7200 flux tubes during 8 hours of simulation time. During this time, the global convection pattern and other relevant ionospheric parameters were kept constant. The purpose here was to obtain the initial ionospheric densities to be used as a convenient starting point for simulating the ionospheric effects of a plasma jet. The actual ionosphere rarely has 8 hours of such steady conditions. However, this allows us to single out individual effects that can be produced by various ionospheric processes. The real ionosphere may be a superposition of several of these plasma jet

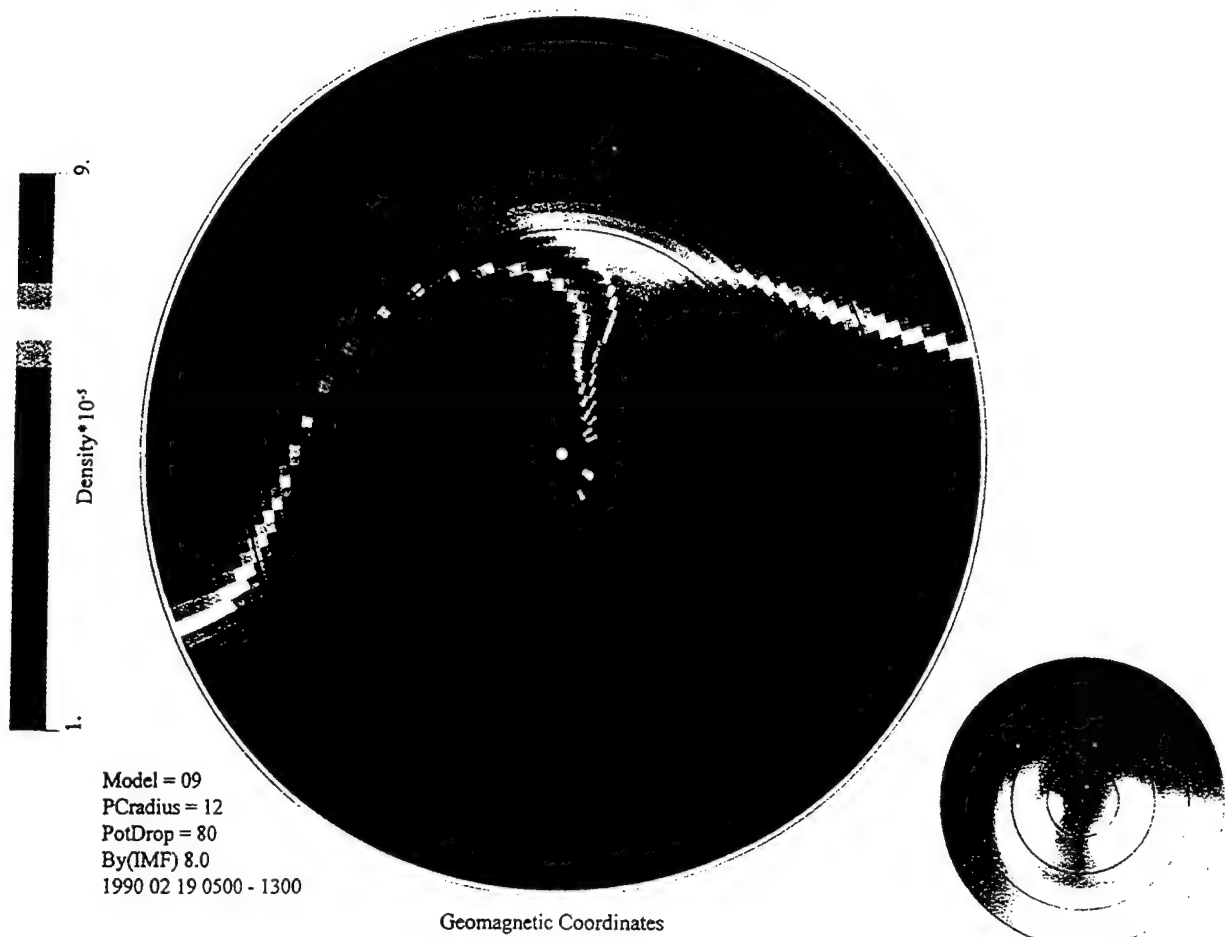


Plate 1. Polar plot of the NmF2 (peak F region density) of the high-latitude ionosphere at 1300 UT. This density plot corresponds to the initial values used in the simulations of sections 3.1, 3.2, 3.4, and 4. The values in this plot were obtained by running the model for 8 hours and using steady state inputs. We include in the lower right corner the black and white version of this plot in a format that will be shown in subsequent plots. The black dots correspond to the locations of the Sondrestrom and Qaanaaq stations, and the white dot indicates the location of the European Incoherent Scatter station. The latitudinal circles are in steps of 10° .

and density break-off events. A prominent feature of Plate 1 is the presence of the TOI. At 1300 UT it extends from longitudes close to European Incoherent Scatter EISCAT (19°E) up to 51°W , where it turns poleward. The TOI is bounded at the equatorward edge by a region of densities reduced by 30% and poleward by densities almost an order of magnitude smaller. The larger densities in the TOI are due mainly to two factors, a small westward flow in the dusk cell and an upward lift of the F region. The longer transit time and the relatively smaller solar zenith angle permit the solar radiation to build up much higher densities in this

confined region. Similar steady structures have been presented by *Crain et al.* [1993] in their total electron content maps of the high-latitude region.

The vorticity suggested by the radar and magnetometer data and other theoretical implications of solar wind - magnetosphere interactions [Newell and Sibeck, 1993] led us to infer that the plasma jet may actually consist of a system of two vortices superimposed on the background convection. With this as a guide, we searched for a system of two ellipsoidal potential vortices added to a global convection pattern. The search was carried out by varying the cross polar

Table 1. Global and Local Velocity Patterns

Global pattern	B_z	Polar Cap Potential, kV	Number of Vortices	Major Axis, deg	Minor axis, deg	Vortex Potential, kV	Latitude of Vortices, deg	Local Time of Vortices, deg
Heelis 12° radius	+	80	2	10, 10	2.4, 1	20, -5	74, 71.5	11, 11
Heppner-Maynard	-	76	2	10, 10	2.4, 1	20, -5	74, 71.5	11, 11

cap potential, the global pattern, the radius of the polar cap and other geometrical parameters of the two-vortex system. The size, peak-to-peak voltage, location, orientation and aspect of the vortices were systematically changed iteratively to obtain the best fit to the radar velocities. We tried over 10 million combinations. Table 1 presents the general parameters of the vortices and the global pattern that provided the best fit to the Sondrestrom velocity data. A Heelis-type pattern gave the smallest error. However, a Heppner and Maynard $B_z < 0$ pattern provided errors almost as small as the Heelis-type pattern. Because the radar azimuthal scan covers a small region of the total pattern, this method is not very sensitive in discriminating the

convection pattern. Figures 1a and 1b show the Heelis-type global convection pattern and the system of the two vortices of Table 1. Figure 1c depicts the result of adding the velocity patterns of Figures 1a and 1b. Figure 1d represents the simulated line-of-sight velocities which would have been measured at Sondrestrom if the pattern in Figure 1c had been in effect. The agreement between Figure 1d and Figure 6a of Valladares *et al.* [1994b], reproduced here as Figure 1e, is very good. Figure 1f shows the total vector velocity that was obtained using the convection pattern of Figure 1c.

Figure 2 shows the plasma density measured by the Sondrestrom ISR on February 19, 1990, during four

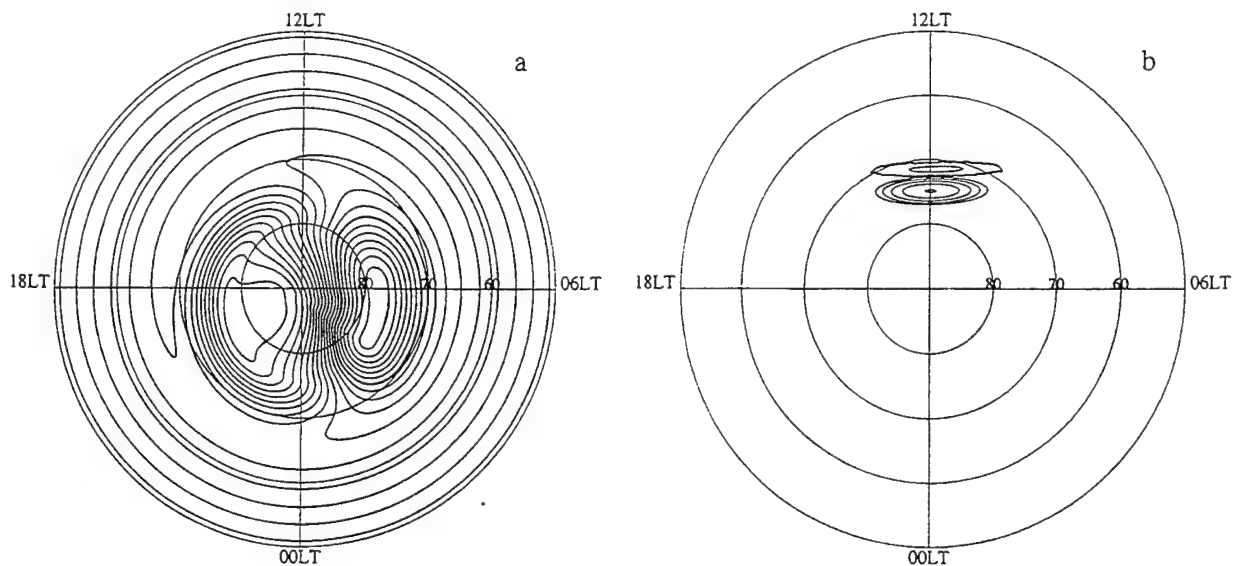


Figure 1. Series of polar plots. (a) High-latitude potential corresponding to a Heelis-type pattern for $B_y = +8$ nT. The cross polar cap potential is 80 kV, and the radius of the polar cap is 12°. (b) the potential of the convective vortices. (c) Addition of the potentials in Figures 1a and 1b. (d) Simulated Sondrestrom line-of-sight velocities considering that the potentials of Figure 1c were in effect. (e) Line-of-sight velocities measured by the Sondrestrom radar on February 19, 1990 [Valladares *et al.*, 1994b, Figure 6a]. (f) Simulated vector velocities using the potential of Figure 1c.

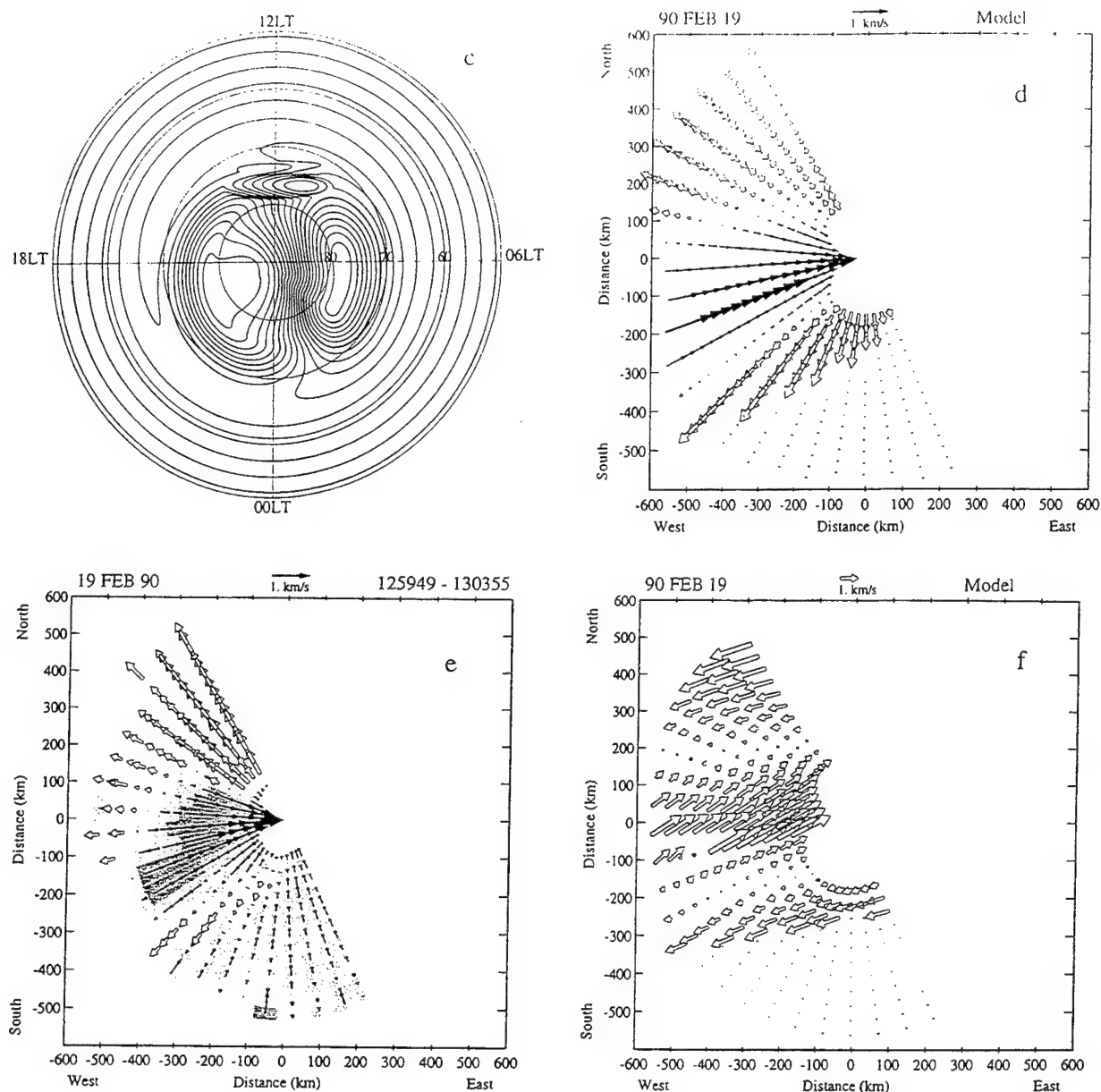


Figure 1. (continued)

consecutive elevation scans. Figure 2a, obtained between 1251 and 1254 UT and before the appearance of the plasma jet, shows a density value above $3 \times 10^5 \text{ cm}^{-3}$ to the south of the radar. Overhead and to the north, the density is structured and peaks at $5.5 \times 10^5 \text{ cm}^{-3}$. These values are in good qualitative agreement with the modeled densities of Plate 1. The maximum modeled peak densities are $5 \times 10^5 \text{ cm}^{-3}$ and $9 \times 10^5 \text{ cm}^{-3}$ for the south and north locations respectively.

3. Patch Modeling Using Mesoscale Velocity Structures

During the last decade, a large array of transient events have been measured in the high-latitude ionosphere. Convective vortices, double vortices, east-west elongated ellipses, and vortices moving poleward, equatorward, downward and duskward have all been observed. While the magnetic response of these events have been studied

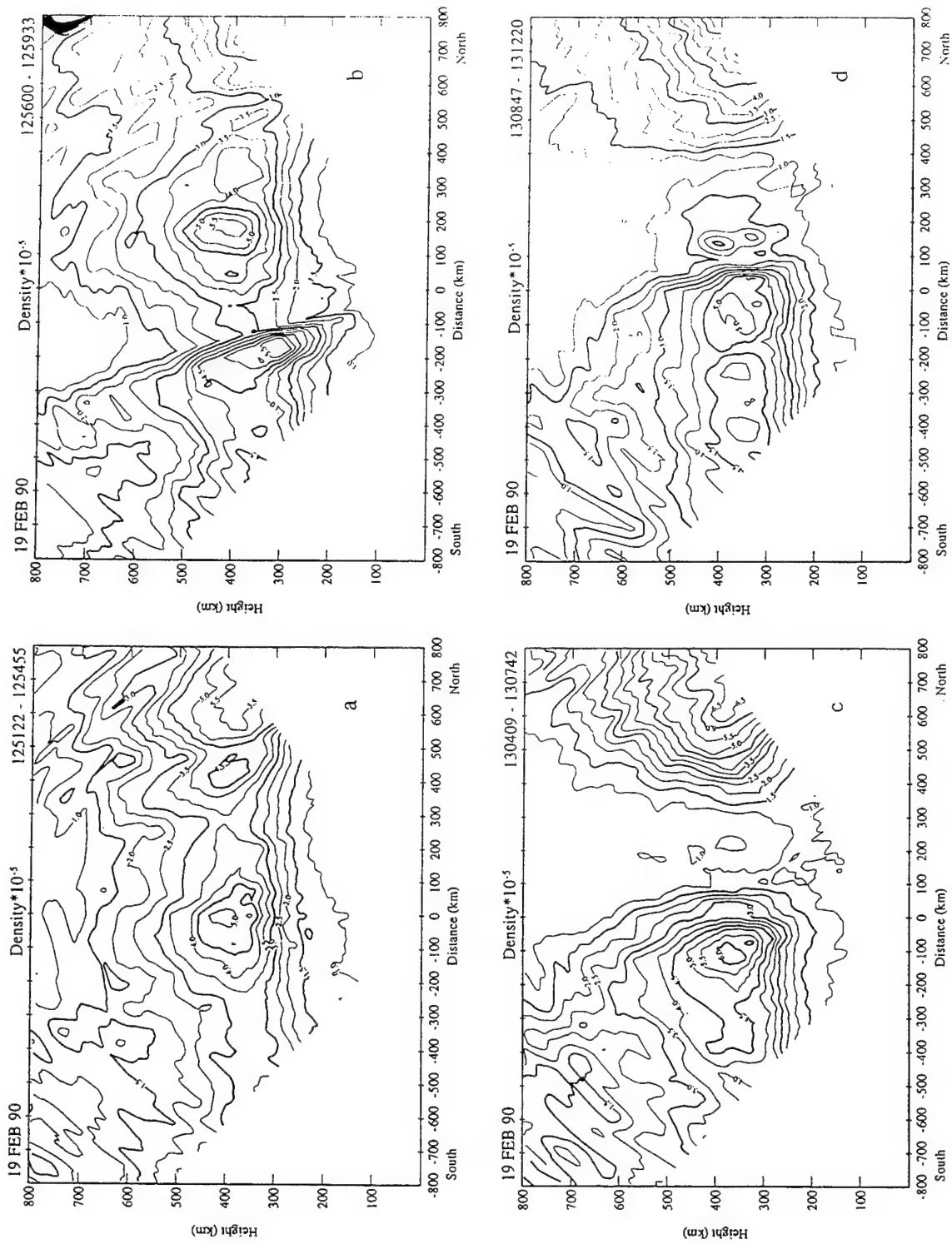


Figure 2. Density contours corresponding to four elevation scans of the Sondrestrom Incoherent Scatter Radar. The spacing between the contours is $.5 \times 10^5$ cm⁻³. The antenna azimuth angle was kept fixed at -27° (magnetic meridian), and the elevation varied from 30° south to 30° north. The number density is displayed as a function of height and distance along the magnetic meridian.

in some detail [Goertz *et al.*, 1985; Heikkilä *et al.*, 1989; Ma *et al.*, 1991], very little is known about their effect upon the ionospheric densities. Furthermore, transient events have been observed to have a fairly complex temporal behavior that is not well understood. As a result, rather than attempting a simulation that tries to include all of the observed behavior of a transient event, we have performed four numerical simulations that focus on just a few key elements of the event. The four scenarios modeled were chosen to help us learn how the density evolves under different conditions of the local and global patterns and to give us some insight as to how sensitive our results are to the various properties of these events. In the next four subsections, we report on the results from these simulations. First, we describe a case study in which a pair of transient vortices are kept fixed in a corrected geomagnetic coordinate system. In the next case, we include the observation that these transient vortices move by allowing the vortices to drift according to the background polar cap flow. We continue with a model case study that uses a Heppner-Maynard-type convection pattern as the global convection. This allows us to assess the sensitivity of our previous results to the global pattern that is chosen. Finally, in the fourth simulation, we establish the importance of the enhancement of the recombination rate in producing regions of depleted density across the TOI.

3.1. Stationary Vortices

The first modeling effort was implemented using two vortices which were maintained stationary in a local time versus latitude frame of reference. The vortices' potential is set equal to the predetermined value at 1300 UT; 15 min later the potential is turned off. Figure 3 and successive figures present a limited region of the northern hemisphere high latitude ionosphere. Here we show a series of snapshots of the $N_m F_2$ corresponding to nine different times during the formation of the density structure. The area covered in each panel is about $3500 \times 3500 \text{ km}^2$. Figures 3a through 3f are 3 min apart. Figures 3g - 3i display the density in steps of 10 min. Figure 3a displays the initial density at the time of the potential vortices onset. This plot corresponds to a view looking down from a satellite that is traveling from the pole toward the equator. Lower latitudes are at the top of the figure, and poleward latitudes are at the bottom. The magnetic pole is at the center of the bottom edge of each panel. The locations of the Sondrestrom and Qaanaq facilities are indicated by white dots.

The TOI is clearly depicted in Figure 3a; it extends nearly aligned with the equipotential lines and turns poleward near Sondrestrom. We remind the reader that the $N_m F_2$ pattern of Figure 3a was calculated for February 19 at 1300 UT using the actual magnetic and solar flux conditions measured on that day and the inferred size of the polar cap, as defined in section 2. A weaker TOI may be obtained for other days of the year, different UT, or even different parameters of the convection pattern. Figure 3b displays the peak density 3 min after the vortex potential has been activated. Even at this time, the TOI is already drastically distorted. A section of the TOI has rotated anticlockwise; simultaneously, three parallel channels containing depleted densities have been created, two equatorward and one poleward of the fragmented TOI segment. All three elongated traces of low density are coincidental with the equatorward, center, and poleward walls of the vortices, which is where the high speed flows and the enhanced temperatures are. Three minutes later at 1306 (Figure 3c), all three low-density channels are further elongated in the east-west direction. A region of low density starts propagating poleward at the poleward edge of the vortex system. The following three panels (Figures 3d to 3f) show further elongation and deeper depletions in all three density channels. Clearly, the presence of the vortices has produced density structures. However, the density structure aligned in the east-west direction (Figure 3f) is still attached to what remains of the TOI. After the localized potential is turned off at 1315 UT, the density structures lose their east-west alignment. Figures 3g to 3i show that the density enhancement acquires instead a more north-south alignment. This additional change in the shape of the density structure is due to a nonuniform velocity near the center of the polar cap of the Heelis-type pattern in Figure 1a. If the flow were uniform, then the equipotential lines should have been parallel lines in the polar plot.

Figure 4 presents simulated radar elevation scans through the modeled ionospheric volume. Each of the panels shows an equivalent elevation scan in the meridian plane that would have been measured at Sondrestrom if the modeled densities were the real densities around the station. This scheme allows us to perform a one-to-one comparison with the data presented by Valladares *et al.* [1994b]. It helps us to better understand the radar data when only elevation scans are conducted during the experiment. Each of the scans of Figure 4 are constructed from the density data displayed in the corresponding panels of Figure 3. The orientation of the scans is shown by the white lines in each panel of Figure 3. The larger

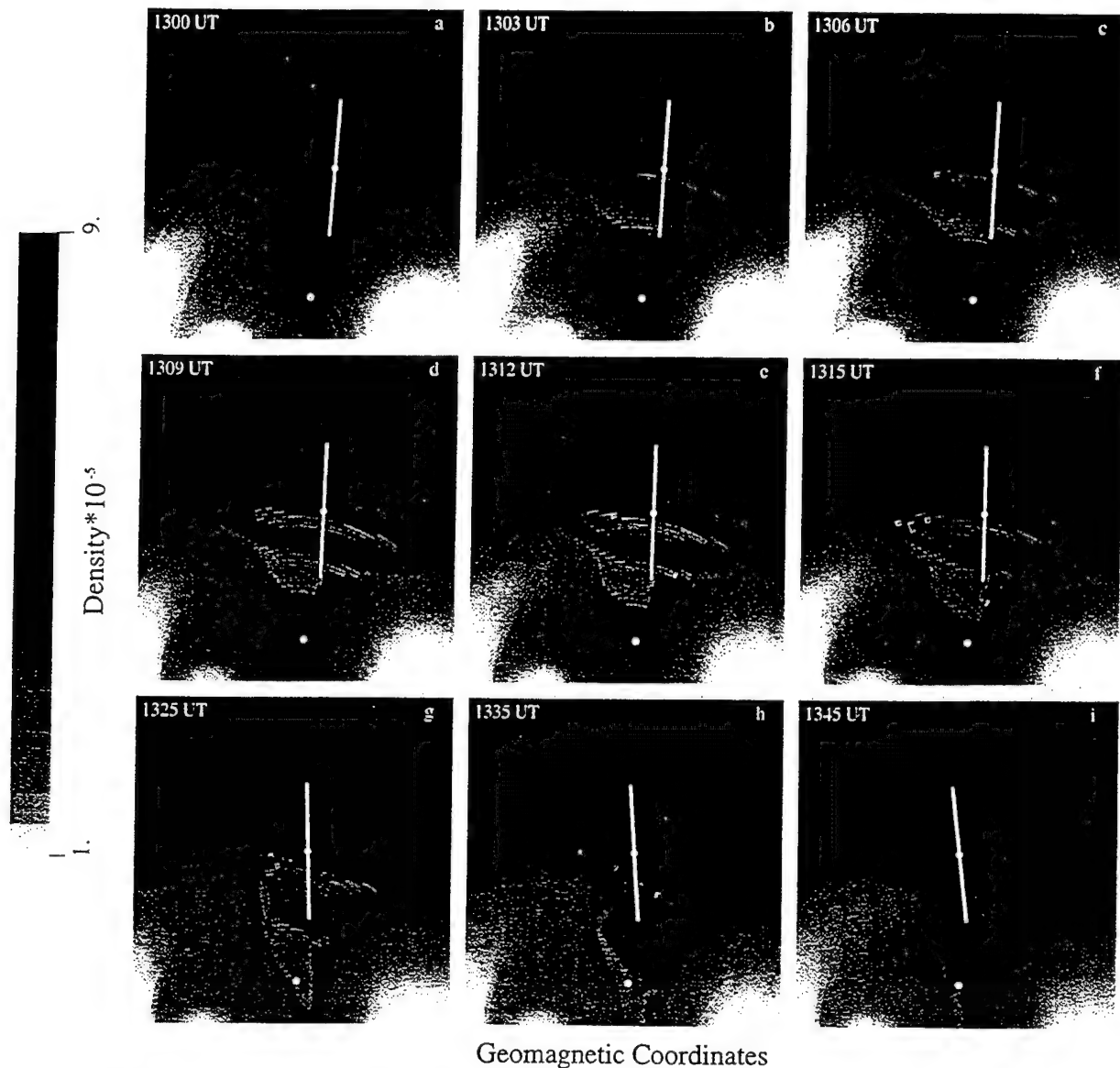


Figure 3. Each panel presents NmF2 values of a section of the high-latitude ionosphere at different times during the modeling that uses stationary vortices as input. See section 3.1 for more details. The white dots correspond to the locations of the Sondrestrom and Qaanaaq stations. The white line that crosses the Sondrestrom site indicates the extension of the elevation scans of Figure 2.

density at the northern part of the scan of Figure 4a is due to the passage of the TOI. Figure 4b, corresponding to 3 min along the simulation, shows mesoscale structuring coincident with the vortices. Two deep depletions are evident, one overhead and the other 500 km north of the station. The density of the northern depletion is $3 \times 10^5 \text{ cm}^{-3}$. The density remains unperturbed at the northern and southern extremes of the scan; no vortices are located

there. At 1309 UT, 9 min after the beginning of the simulation, both depletions reach a minimum value of $2 \times 10^5 \text{ cm}^{-3}$. The N_e depletion located almost overhead coincides with the center of the vortex, where the plasma flow is maximum. Figure 4e presents the modeled densities 12 min after the onset of the potential vortices. These contours can be closely compared with Figure 2c which shows the density measured by the Sondrestrom

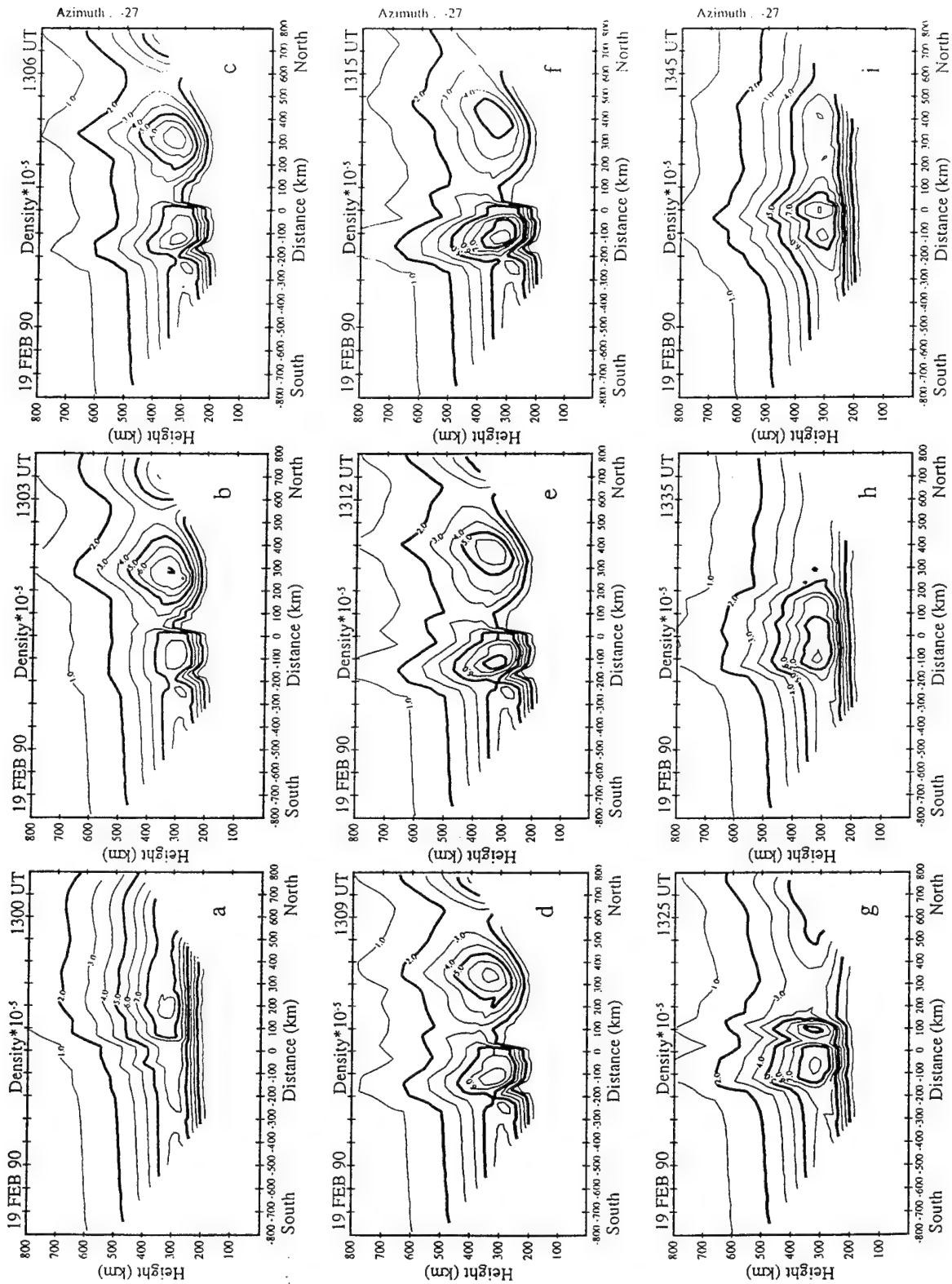


Figure 4. Simulated radar elevation scans through the simulated volume of section 3.1. (a) The large-scale density structure corresponds to the TOI. (b) - (i) The fragmentation of the TOI and formation of smaller-scale structures.

radar ~12 min after the start of the break-off event. Each figure displays two density structures separated by a channel of low density located almost overhead. The peak density in each of the structures shows a good agreement between modeled and measured values. However, the minimum density situated between structures is much more depleted in the experimental data. It is below 10^5 cm^{-3} in the radar data but above $2 \times 10^5 \text{ cm}^{-3}$ in the model. Other differences between the measured and modeled densities are (1) the larger north-south extension of the density depleted region of the measured data, and (2) the noticeable higher bottomside F layer density of the experimental data.

While the stationary vortices scheme increases the amount of density structures transiting within the polar cap, it fails to produce isolated islands of enhanced density structures detached from the auroral oval. A camera located within the polar cap will be able to indicate this effect. Moreover, our definition of polar cap patches postulates that less dense plasma should surround the higher density plasma in all directions in order to qualify as a patch. Thus we conclude that stationary vortices do not reproduce all the characteristics of polar cap patches.

3.2. Traveling Vortices

The second modeling effort was carried out using a set of two traveling vortices moving with the background plasma flow. To generate the motion of the vortices, the two-vortex system was displaced in the antisunward direction as a whole entity. The displacement was set by the velocity of the plasma at the center of the line joining the vortices' centers. Similar to the previous case, the vortices potential was introduced at 1300 UT. The potential was then reduced by half 15 min later. The location of the vortices in the polar cap was updated every 30 s; this interval was equal to the step time of the simulation. Figure 5a repeats the initial density of Plate 1. During the first 9 min of the simulation (Figures 5b - 5d), the TOI is drastically distorted in a fashion similar to the nonconvective case. However, the width of the depletion channel and the depth of the density decrease are larger for the convecting vortices case. The dawn-dusk extension of the density structure is smaller in this convective scenario. We call this structure a region of enhanced density, because N_e is higher inside the structure than in the rest of the polar cap. Figures 5d through 5f show that both density structures develop an east-west or dawn-dusk alignment. They are also well collocated with the corresponding vortices. In contrast to

the nonconvecting vortices case, we see (Figure 5f) that the more northern density structure has no attachment to the oval or subauroral plasma. The last three panels at the bottom of Figure 5 show that as two patches travel antisunward across the polar cap, they suffer little distortion. This feature is also different from the previous case, where only one structure was fully formed. The prominent characteristic continues to be that both structures are individual entities with no attachment to the oval or subauroral plasma. The polar cap patches, as described here, are very similar in shape to the "cigar" patches, elongated in the east-west direction, described by Fukui *et al.* [1994].

A more quantitative view of the formation of the density enhancement and depletion is displayed in Figure 6. Figures 6b and 6c show the cross section in the magnetic meridian plane of two structures that were formed by the convective vortices. The structure located at 100 km south of the station was formed from plasma located at subauroral latitudes (south of the TOI). The N_e structure located at 300 km north is formed from the TOI. The particular location of the vortex causes plasma from the fragmented TOI to intrude into the southern velocity structure and reach values near $9 \times 10^5 \text{ cm}^{-3}$. The minimum density between patches is 10^5 cm^{-3} , as seen at 100 km north in Figure 6e. This depletion is replenished partially by solar radiation and reaches values near $3 \times 10^5 \text{ cm}^{-3}$ in Figure 6h. Comparison of Figures 6e and 2c indicates a good qualitative agreement. The modeled densities of Figure 6e show a slightly higher density value and a narrower width in the region of depleted densities. In this region, the modeled density are $< 10^5 \text{ cm}^{-3}$ at 300 km altitude, similar to the experimental values.

The traveling vortices scenario brought only a qualitative agreement with the density of Figure 2c. However, it was able to produce islands of high density transiting the polar cap. Thus we conclude that the convecting vortices are able to form patches of enhanced densities when they are located near the boundary between the polar cap and the auroral oval.

3.3. Heppner-Maynard-Type B_z Negative Global Pattern

As mentioned in section 2.1, the radar data is not effective at discriminating between different global patterns. Thus it is of interest to see how our results might change if a different global pattern is used with the vortices. For this purpose, we repeated the calculations of the previous section to determine the effect on patch formation using a Heppner-Maynard-type pattern. Figure

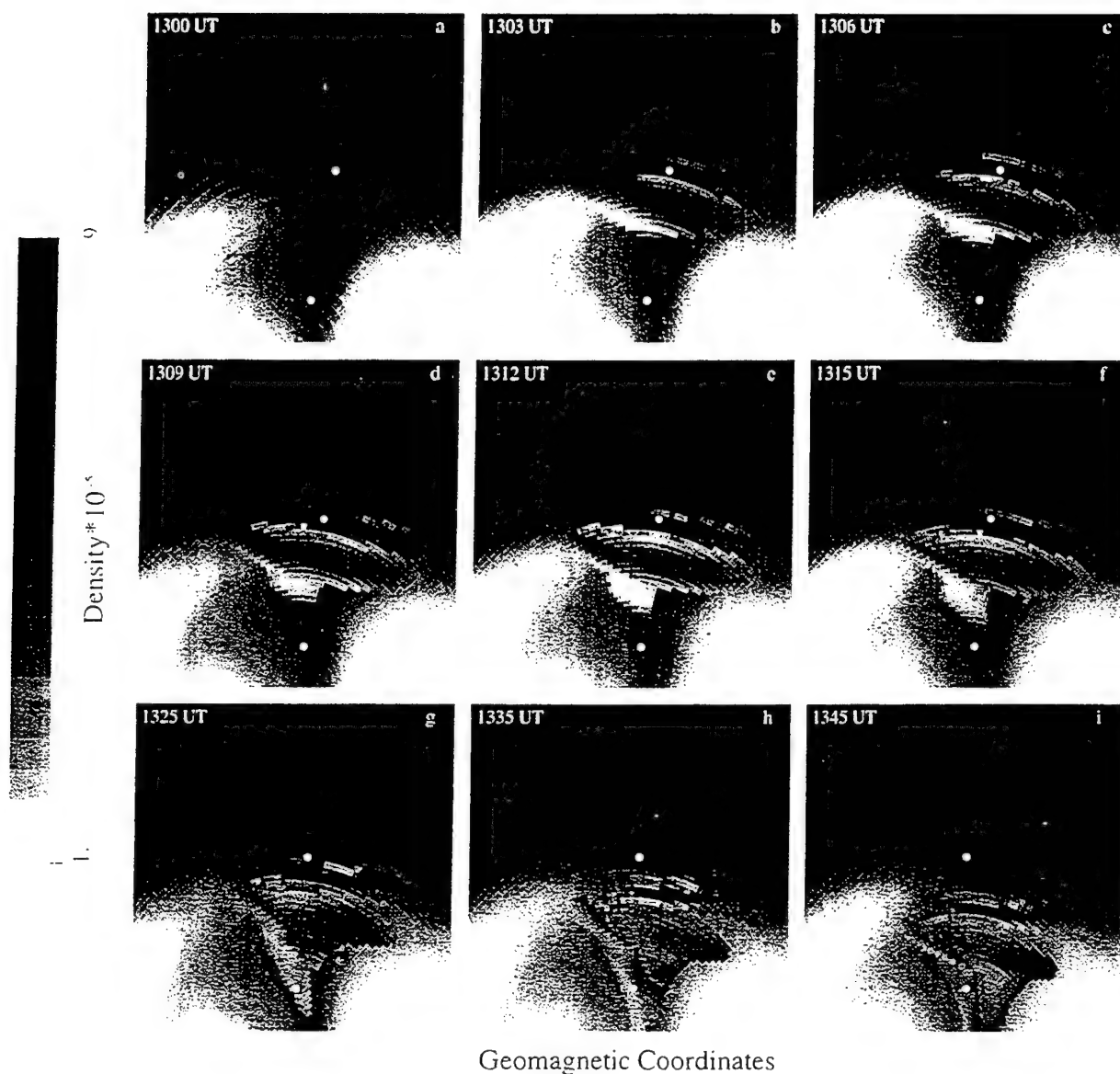


Figure 5. Same as Figure 3 but for the modeling study of traveling convective vortices (section 3.2)

7a displays the initial conditions of the $N_m F_2$ values before the start of the simulation. The TOI shows a few peculiar differences with respect to the Heelis-type convection pattern of section 3.1. The maximum density is slightly higher, and the TOI is a much wider before it turns poleward. These differences are attributed to a slower flow velocity (stagnation region) near the dayside region in the Heppner-Maynard global convection patterns. The initial location of the vortices and the amplitude of each vortex potential are similar to the case described in section 3.2.

Figures 7b and 7c show that the vortices are able to bisect a region of the TOI and orient the major axis of the density structure in the dawn-dusk direction. A second region of depleted densities is seen at the lower latitudes in Figures 7c through 7f; however, this structure is not completely isolated from the TOI. Moreover, it joins the new TOI that is being formed during the last stages of the simulation. The patch located at higher latitudes retains its alignment for several minutes after the potential was reduced by 50% (Figures 7g - 7h). Figure 8 shows that the patch is bounded on the equatorward side by plasma

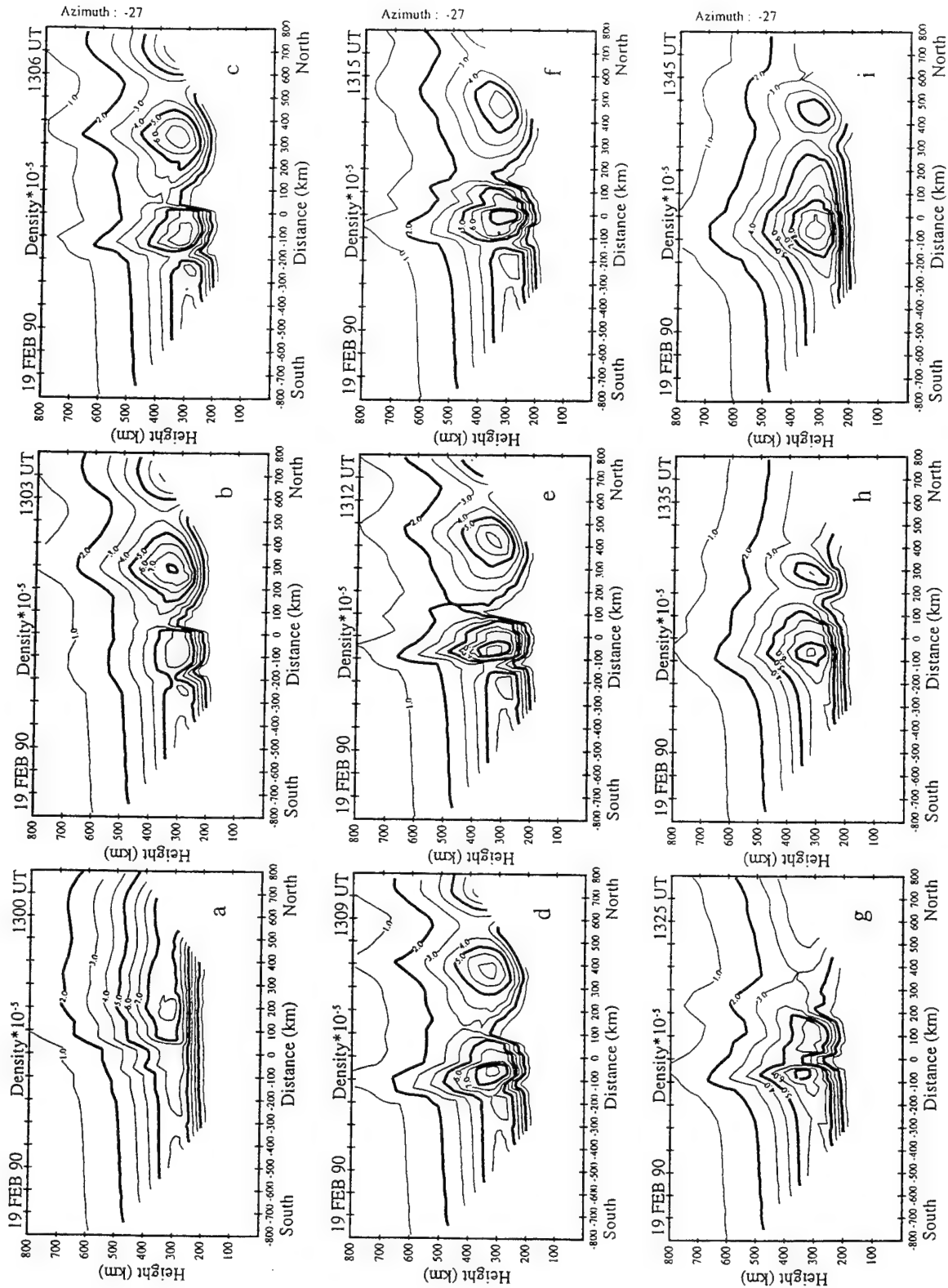


Figure 6. Same as Figure 4 but for the modeling study of traveling convective vortices (section 3.2).

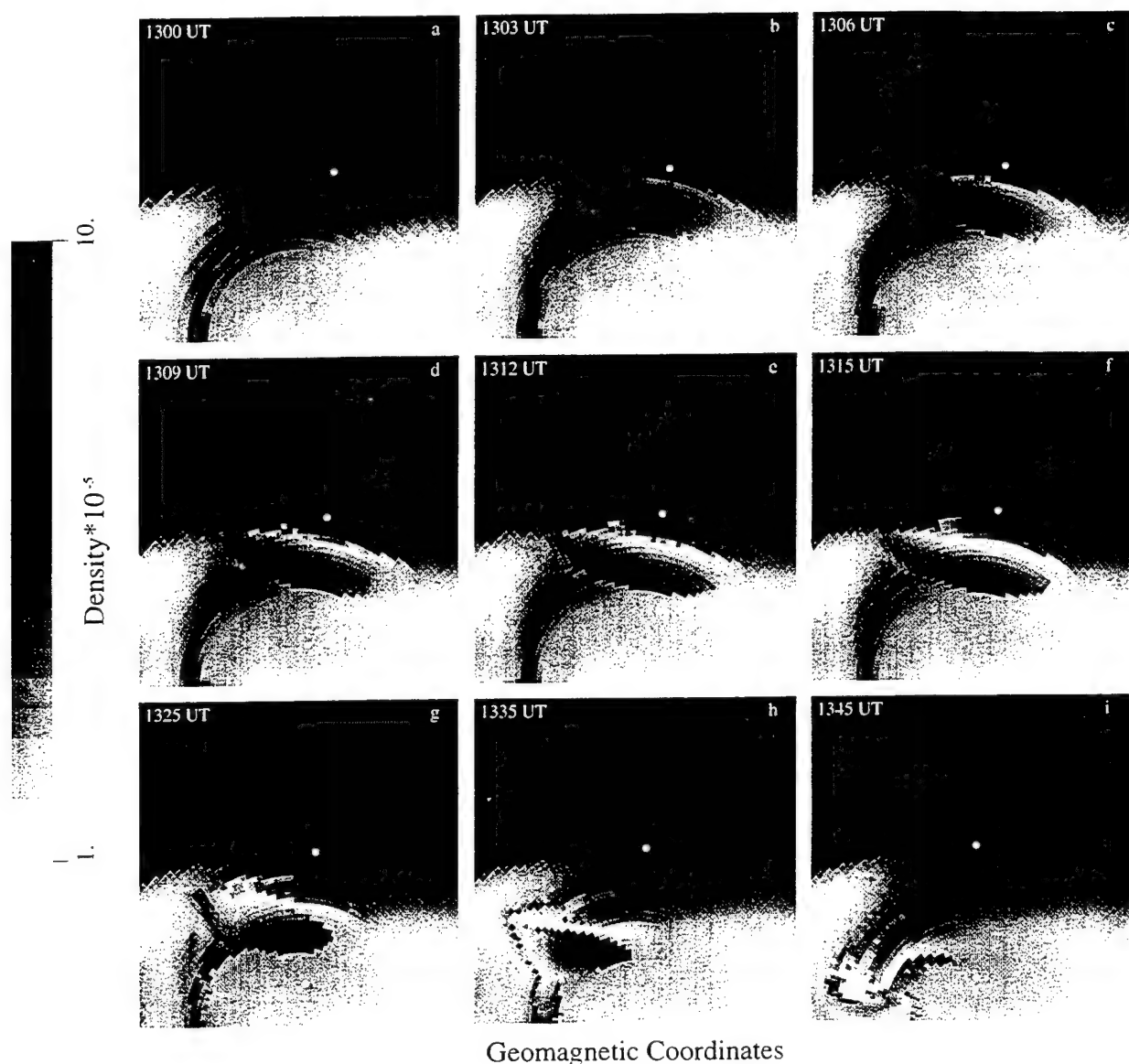


Figure 7. Same as Figure 3 but for the Heppner-Maynard convection pattern (section 3.3).

as low as 10^5 cm^{-3} . It also demonstrates that the patch moves toward the pole and subsequently breaks from the TOI. When the patch is circulating across the polar cap, the peak density inside the patch is $8 \times 10^5 \text{ cm}^{-3}$, a value much higher than the typical $1\text{--}2 \times 10^5 \text{ cm}^{-3}$ seen in the polar cap and outside the TOI. Figures 8e and 8f show a more pronounced depletion between the density structures as compared to the Heelis/traveling vortices scenario. When compared to the experimental values of Figure 2c, we notice that several features are well

reproduced. The altitude extension of both structures are very similar. $N_c = 7 \times 10^5 \text{ cm}^{-3}$ at 700 km is observed in both experimental and modeled data. The region of depleted density is wider than in the previous case. The poleward motion of the structures also resembles more closely the movement of the structures seen in the experimental data. The Heppner-Maynard pattern successfully produced a density structure with all the characteristics of a polar cap patch. In contrast to the Heelis convection pattern, it creates a single structure.

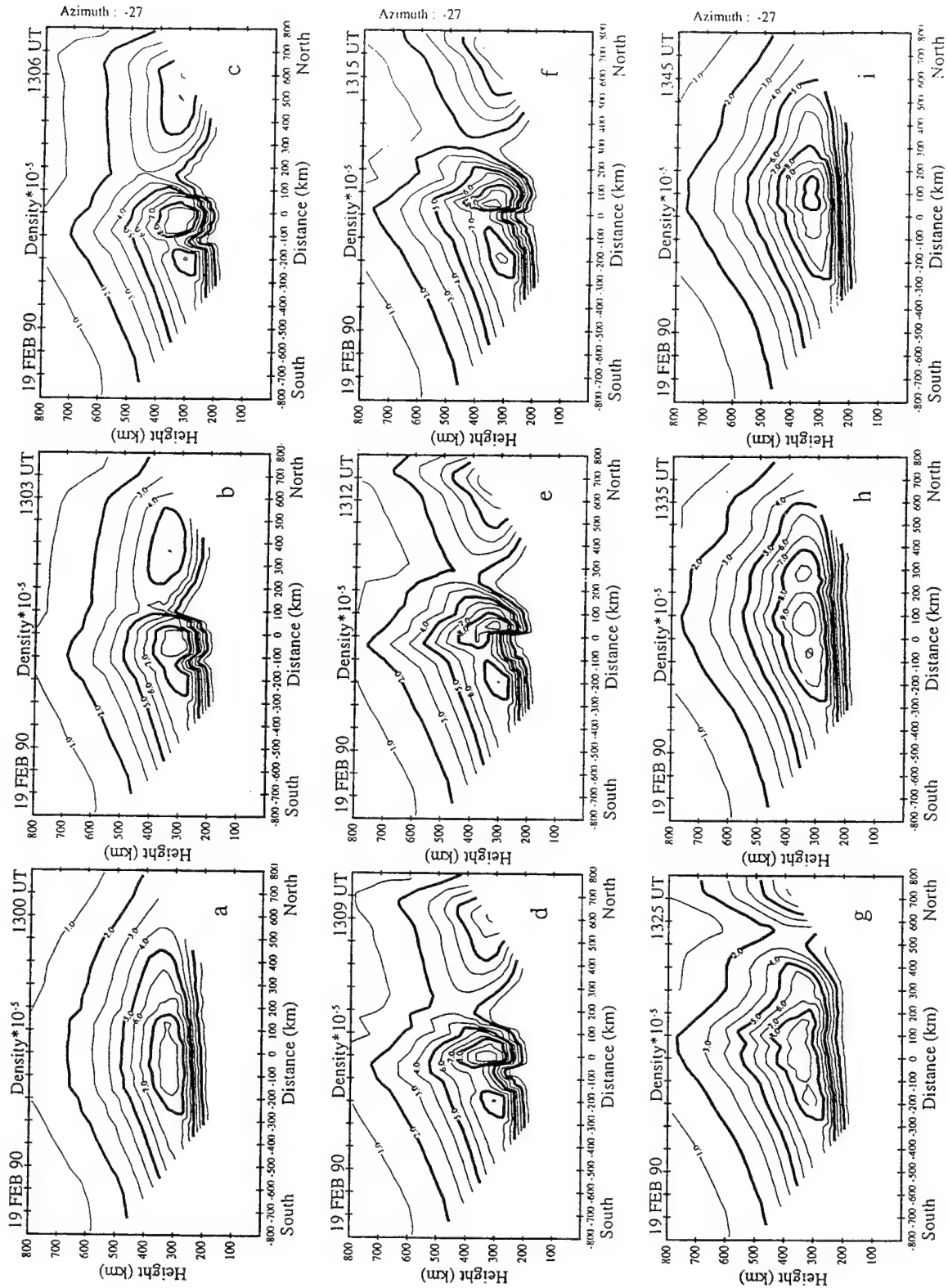


Figure 8. Same as Figure 4 but for the Heppner-Maynard convection pattern (section 3.3).

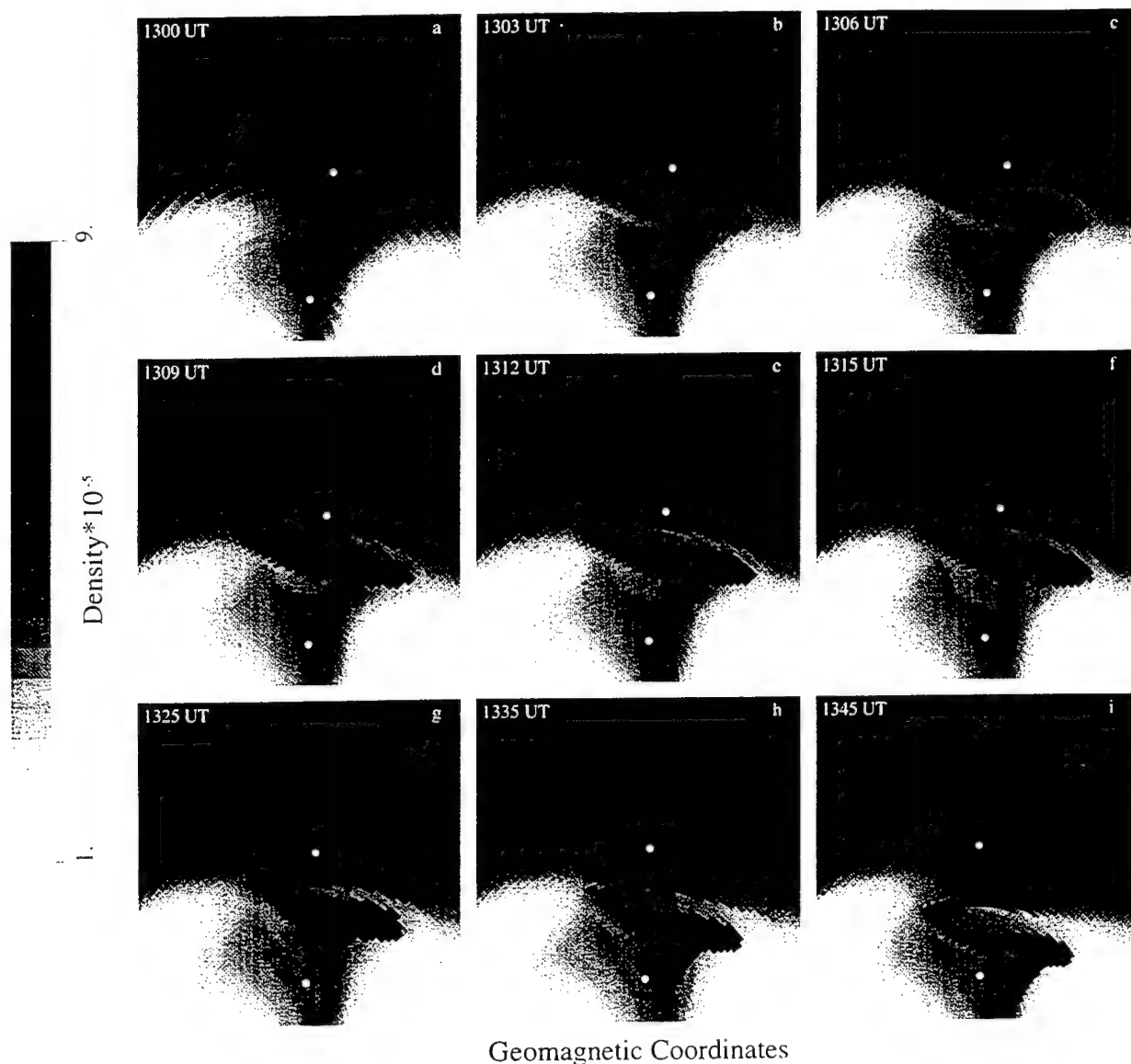


Figure 9. Same as Figure 3 but after eliminating the dependence of the ion temperature on the magnetospheric electric field (section 3.4).

3.4. Assessment of the Temperature Effect on Patch Formation

The fourth case study was performed to quantify the importance of the O^+ recombination rate in producing channels of low density. The results of this study are presented in Figure 9. In this series of simulations, we returned to the Heelis/traveling vortices scenario except we turned off the dependence of T_i on the magnetospheric electric field and hence turned off any enhanced O^+ loss

rates. The goal in this investigation was to determine quantitatively how much plasma depletion is attributed to erosion by enhancements of the O^+ loss rate and what percentage of the plasma depletion is carried from earlier local times by the vortex flow. Evidently, an eastward flow is needed in order to transport the less dense morning side plasma into the afternoon region. A flow of this type exists at the common region between the vortices.

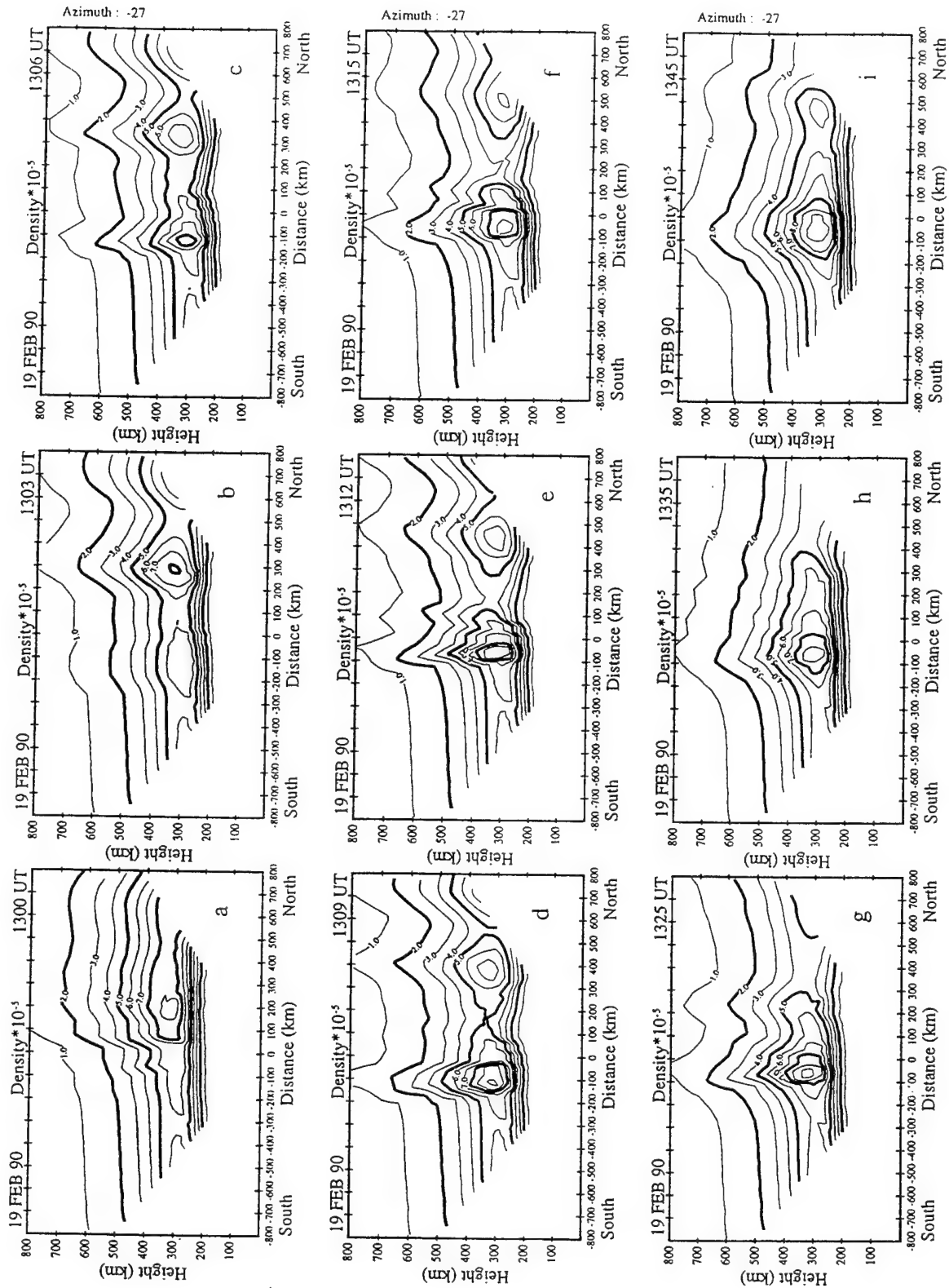


Figure 10. Same as Figure 4 but after eliminating the Ti dependence on the magnetospheric electric field.

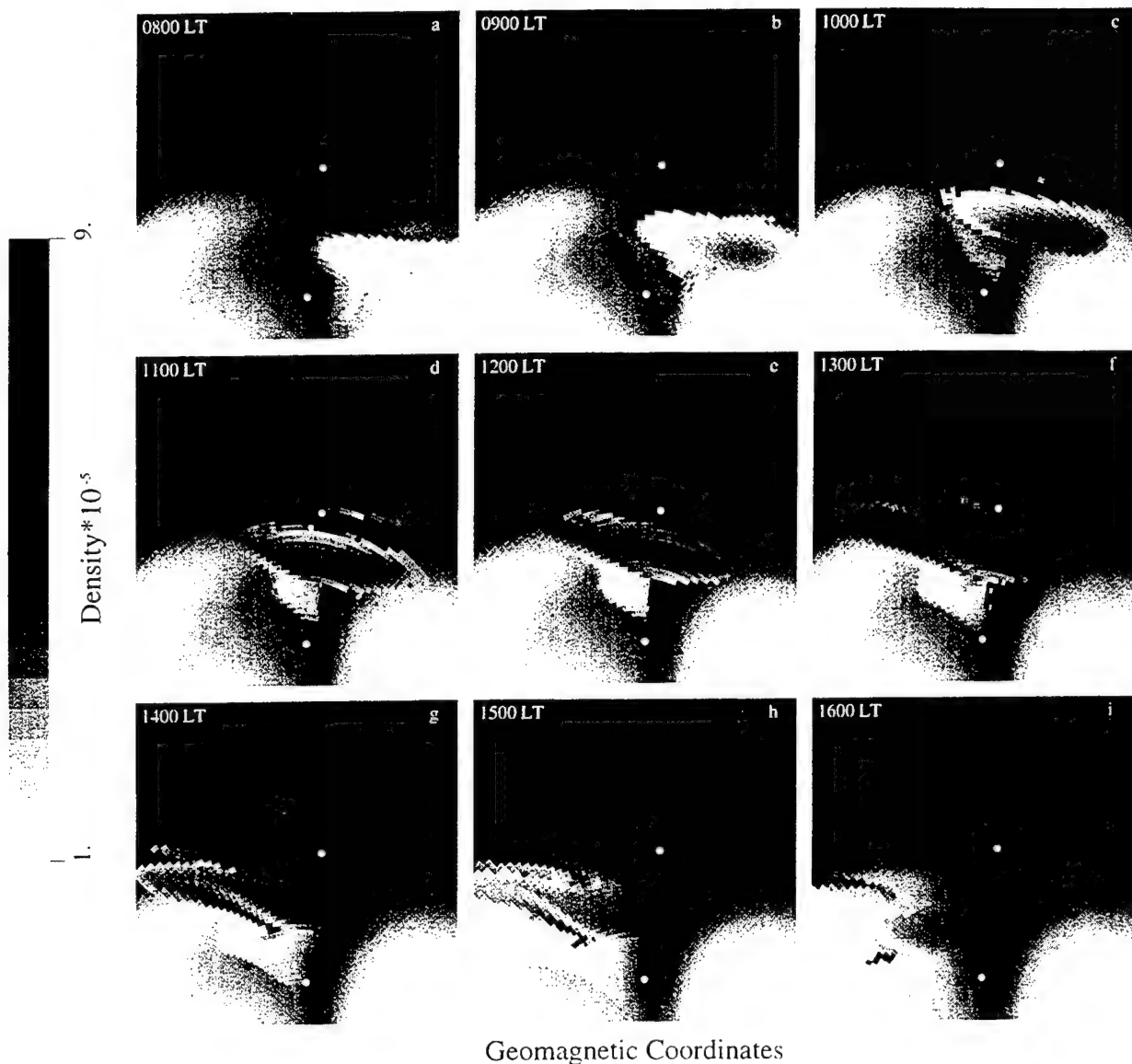


Figure 11. Same as Figure 3, but for nine different initial locations of the traveling vortices.

A comparison of Figures 9 and 5 indicates some resemblance between both figures. The structuring is also initiated with a rotation of the TOI toward a dawn-dusk alignment. Plasma from the early morning side also intrudes equatorward of the northern patch. However, there are also some prominent differences. We did not find a full separation between the N_c structure and the auroral oval, even 15 min into the simulation. There is a channel containing plasma density equal to $4 \times 10^5 \text{ cm}^{-3}$ in the afternoon side of the structure. The southern N_c

structure is absent, because at this latitude the southern vortex can only bring more dense plasma from the afternoon sector. Figure 10f indicates that the deepest depletion achieved in this simulation is $4 \times 10^5 \text{ cm}^{-3}$, while the minimum density value during the full-blown simulation was 10^5 cm^{-3} in Figure 5. Considering that the original density was $9 \times 10^5 \text{ cm}^{-3}$, then 62% of the depletion is due to convection of low-density plasma and 38% is due to erosion by the temperature-dependent loss rate.

4. Traveling Vortices at Different Local Times

In the previous section, we were concerned with the formation of patches under different patterns of global convection. In this section, we search for the preferred local time at which the vortices are more likely to generate polar cap patches.

Traveling vortices have been observed at a large variety of different local times [Friis-Christensen *et al.*, 1988; Heikkila *et al.*, 1989] using radar and magnetometer data. They have also been predicted on theoretical grounds [Newell and Sibeck, 1993]. They postulated an association between the presence of twin vortices and changes in the high-latitude convection patterns due to pressure pulses in the magnetosphere. In order for the vortices to produce patches, evidently, they have to develop near the TOI and have a lifetime long enough to erode a sector of the TOI. We have carried out eight additional simulations placing the vortices at different local times. The local times that were used varied from 0800 to 1600 LT. The results of this study are compiled in Figure 11. This figure compares $N_m F_2$ values obtained 15 min along the simulations (at 1315 UT) for the eight new cases and the simulation described in section 3.2. The number on the upper left corner indicates the local times at which the vortices were located at the beginning of the simulation. Only the vortices located at 1000 LT, 1100 LT and 1200 LT (Figures 11c, 11d and 11e) produce distinct patches. Vortices at 0800 LT and 0900 LT (Figures 11a and 11b) only distort the TOI and create isolated regions of low density ($2 \times 10^5 \text{ cm}^{-3}$) plasma. When these structures circulate within the polar cap, they will consist of plasma equally dense to the polar cap plasma. When the vortices were located at 1300 LT (Figure 11f), we obtained dawn-dusk elongated density traces. No detachment from the auroral oval densities was observed. The last three modeling efforts in this subsection were performed using vortices located at 1400 LT, 1500 LT and 1600 LT (Figures 11g-11i). These figures depict the formation of some kind of structuring in the afternoon cell. These structures are connected to the auroral oval and will not penetrate into the polar cap. In fact, we followed all these case simulations for another 30 min and found the structures continuously elongating in the dawn-dusk direction. These structures could certainly appear as isolated structures to digisondes or to low-orbiting satellites, but an all-sky camera properly located could possibly indicate the connection of these structures to the auroral plasma.

5. Discussion and Conclusions

Several researchers have indicated that the TOI is present at longitudes near Sondrestrom when this high-latitude station is near noon [Foster and Doupnik, 1984; Kelly and Vickrey, 1984]. Our simulation during undisturbed conditions has also demonstrated that the TOI is a prominent feature at Sondrestrom when we select a typical B_z south convection pattern. The mechanism described here requires the existence of an elongated TOI as the basic ingredient to form a patch. It also needs a large plasma jet occurring near and across the TOI. The large plasma velocity will create a region of enhanced T_e , consequently increase the O^+ recombination rate and then erode the local plasma. We found also that low-density plasma can be brought in by the vortex flow from earlier local times. This patch formation mechanism will create, in this way, sections of depleted and enhanced densities across the TOI.

The elevation scans conducted across our simulated volume demonstrated that the TOI or other structures in the polar cap could be wrongly interpreted as isolated entities (say patches). In reality, they may be connected to the auroral/subauroral plasma. We conclude that it is necessary to conduct antenna azimuthal scans or to use an all-sky camera to properly identify a polar cap patch.

Sojka *et al.* [1993, 1994] have used a scheme of continuous changes of the B_y component of the IMF to redirect the TOI toward the dawn or dusk sides of the polar cap. In this study, we have employed the appearance of vortices in the polar cap and their subsequent motion across the polar cap to produce polar cap patches. No repetitive changes in any of the components of the IMF were required. The proposed mechanism only needs the existence of vortices moving with the background plasma. Moreover, it was found that the convecting vortices scenario was the most favorable situation to form disconnected plasma structures inside the polar cap.

The modeled densities of Figures 6 and 8 indicated a good qualitative agreement with the data measured by the Sondrestrom ISR. The discrepancies between measured and modeled densities can be understood in terms of the initial inputs that were used in the simulations and a few of the limitations of the GTIM model. The much smaller density, seen in the depleted density region of Figure 2c, can be attributed to a much smaller density in the morning cell from where the vortices grab the low-density plasma. In fact, the Sondrestrom ISR detected values near $2 \times 10^5 \text{ cm}^{-3}$ at 1100 UT (2 hours before the

measurements reported here) that if unchanged could explain this discrepancy. The radar also measured densities above 10^5 cm^{-3} at 200 km altitude; no similar feature was reported in the simulations because of the lack of molecular ions in our simulations. The GTIM model is at the present time essentially a one-ion (O^+) model. Simulations were performed with and without particle precipitation in the auroral oval, and essentially no differences were seen in the F region. The effects of particle precipitation associated with the vortex located more equatorward where convergent electric fields existed were not included and neither were the effects of soft precipitation that can occur in the cusp/cleft and polar cap. These issues will be topics for future work.

We found that 62% of the density depletion was due to plasma being carried from earlier local times. This fact argues in favor of the ability of smaller potentials associated with the vortices to also create regions of depleted density. However, the vortex potential cannot be too small, otherwise the vortex velocity will also be small, and the time to transport low-density plasma from the morning cell will be considerably longer.

From this study we found the following:

1. Polar cap patches can be generated by traveling vortices independent of the convection pattern being used. We have used a Heelis-type and a Heppner-Maynard-type convection pattern for B_y positive and for B_y negative, respectively. An essential condition for forming well-separated patches was to allow the vortices to travel with the background global convection.
2. Enhanced recombination of O^+ contributes to the creation of a channel of low density. Equally important is the transport of low-density plasma from earlier local times. For the size and potential of the vortices that we used 38% of the depletion was attributed to the O^+ recombination loss and 62% to transport.
3. There is a preferential local time at which the vortices can generate patches. We found that this local time sector is restricted to between 1000 LT and 1200 LT.
4. The simulation presented here qualitatively agrees with the data collected at Sondrestrom on February 19, 1990 [Valladares et al., 1994b]; both exhibit the same salient features.
5. Our modeling described here postulates that the polar cap patches will intrinsically have the shape of the vortices. Circular vortices will reproduce more circular patches. Elliptical vortices, as presented here, will generate the elongated cigar-shaped patches that have been found in the polar cap [Fukui et al., 1994].

Acknowledgments. We would like to thank Ed Weber and Santamay Basu for useful discussions. The work at Boston College was partially supported by Phillips Laboratory contracts F19628-90-K-0007 and F19628-88-K-0008 and by NSF grant ATM-9404088. We thank the Danish Commission for Scientific Research in Greenland for permission to conduct ground experiments at Sondrestrom under continuing project A16-91.

References

- Anderson, D.N., Daily variation of the ionospheric F2 equatorial anomaly in the American and Asian sectors, cooperative thesis, 24 pp. 1-144, Natl. Cent. Atmos. Res., Boulder, Colo., 1971.
- Anderson, D.N., A theoretical study of the ionospheric F region equatorial anomaly, I, theory, *Planet. Space Sci.*, 21, 409, 1973.
- Anderson, D.N., J. Buchau, and R.A. Heelis, Origin of density enhancements in the winter polar cap, *Radio Sci.*, 23, 513, 1988.
- Anderson, D.N., D.T. Decker and C.E. Valladares, Modeling boundary blobs using time varying convection, *Geophys. Res. Lett.*, in press, 1996.
- Basu, Su., S. Basu, E. MacKenzie, and H.E. Whitney, Morphology of phase and intensity scintillations in the auroral oval and polar cap, *Radio Sci.*, 20, 347, 1985.
- Basu, S., Su. Basu, C.E. Valladares, E.J. Weber, J. Buchau, G.J. Bishop, and B.W. Reinisch, Coordinated observations of high latitude ionospheric turbulence, *Physics of Space Plasma (1988)*, SPI Conf. Proc. Reprint Ser., 8, 137, 1989.
- Buchau, J., B.W. Reinisch, E.J. Weber, and J.G. Moore, Structure and dynamics of the winter polar cap F region, *Radio Sci.*, 18, 995, 1983.
- Buchau, J., E.J. Weber, D.N. Anderson, H.C. Carlson Jr., J.G. Moore, B.W. Reinisch, and R.C. Livingston, Ionospheric structures in the polar cap: their origin and relation to 250-Mhz scintillation, *Radio Sci.*, 20, 325, 1985.
- Carlson, H.C., V.B. Wickwar, E.J. Weber, J. Buchau, J.G. Moore, and W. Whiting, Plasma characteristics of polar cap F layer arcs, *Geophys. Res. Lett.*, 11, 895, 1984.
- Cowley, S.W.H., M.P. Freeman, M. Lockwood, and M.F. Smith, The ionospheric signature of flux transfer events, in *CLUSTER - Dayside Polar Cusp*, Eur. Space Agency Spec. Publ. ESA SP-330, 105-112, 1991.
- Crain, D.J., J.J. Sojka, R.W. Schunk, P.H. Doherty and J.A. Klobuchar, A first-principle derivation of the high-latitude total electron content distribution, *Radio Sci.*, 28, 49, 1993.
- Decker, D.T., C.E. Valladares, R. Sheehan, Su. Basu, D.N. Anderson, and R.A. Heelis, Modeling daytime F layer patches over Sondrestrom, *Radio Sci.*, 29, 249, 1994.
- de la Beaujardiere, O., J.D. Craven, V.B. Wickwar, G. Candal, J.M. Holt, L.A. Frank, L.H. Brace, D.S. Evans, and J.D. Winningham, Universal time dependence of nighttime F region densities at high latitudes, *J. Geophys. Res.*, 90, 4319, 1985.

- Foster, J.C., and J.R. Doupnik, Plasma convection in the vicinity of the dayside cleft, *J. Geophys. Res.*, **89**, 9107, 1984.
- Friis-Christensen, E., M.A. McHenry, C.R. Clauer, and S. Vennerstrom, Ionospheric traveling convection vortices observed near the polar cleft: A triggered response to sudden changes in the solar wind, *Geophys. Res. Lett.*, **15**, 253, 1988.
- Fukui, K., J. Buchau, and C.E. Valladares, Convection of polar cap patches observed at Qaanaq, Greenland during the winter of 1989-1990, *Radio Sci.*, **29**, 231, 1994.
- Goertz, C.K., E. Nielsen, A. Korth, K.-H. Glassmeier, C. Haldoupis, P. Hoeg, and D. Hayward, Observations of a possible ground signature of flux transfer events, *J. Geophys. Res.*, **90**, 4069, 1985.
- Hedin, A.E., MSIS-86 thermospheric model, *J. Geophys. Res.*, **92**, 4649, 1987.
- Hedin, A.E., et al., Revised global model of thermosphere winds using satellite and Ground-based observations, *J. Geophys. Res.*, **96**, 7657, 1991.
- Heikkila, W.J., T.S. Jorgensen, L.J. Lanzerotti, and C.G. MacLennan, A transient auroral event on the dayside, *J. Geophys. Res.*, **94**, 15291, 1989.
- Kelly, J.D., and J.F. Vickrey, *F* region ionospheric structure associated with antisunward flow near the dayside cusp, *Geophys. Res. Lett.*, **11**, 907, 1984.
- Lockwood, M., and H.C. Carlson, Production of polar cap density patches by transient magnetopause reconnection, *Geophys. Res. Lett.*, **19**, 1731, 1992.
- Ma, Z.-W., J.G. Hawkins, and L.-C. Lee, A simulation study of impulsive penetration of solar wind irregularities into the magnetosphere at the dayside magnetopause, *J. Geophys. Res.*, **96**, 15751, 1991.
- Newell, P.T., and D.G. Sibeck, *B_y* fluctuations in the magnetosheath and azimuthal flow velocity transients in the dayside ionosphere, *Geophys. Res. Lett.*, **20**, 1719, 1993.
- Rodger, A.S., M. Pinnock, J.R. Dudeney, K.B. Baker, and R.A. Greenwald, A new mechanism for polar patch formation, *J. Geophys. Res.*, **99**, 6425, 1994.
- Schunk, R.W., and J.J. Sojka, A theoretical study of the lifetime and transport of large ionospheric density structures, *J. Geophys. Res.*, **92**, 12343, 1987.
- Schunk, R.W., W.J. Raitt, and P.M. Banks, Effect of electric fields on the daytime high-latitude *E* and *F* regions, *J. Geophys. Res.*, **80**, 3121, 1975.
- Sojka, J.J., and R.W. Schunk, A theoretical study of the production and decay of localized electron density enhancements in the polar ionosphere, *J. Geophys. Res.*, **91**, 3245, 1986.
- Sojka, J.J., and R.W. Schunk, A model study of how electric field structures affect the polar cap *F* region, *J. Geophys. Res.*, **93**, 884, 1988.
- Sojka, J.J., M.D. Bowline, R.W. Schunk, D.T. Decker, C.E. Valladares, R. Sheehan, D.N. Anderson, and R.A. Heelis, Modeling polar cap *F* region patches using time-varying convection, *Geophys. Res. Lett.*, **20**, 1783, 1993.
- Sojka, J.J., M.D. Bowline, and R.W. Schunk, Patches in the polar ionosphere: UT and seasonal dependence, *J. Geophys. Res.*, **99**, 14959, 1994.
- Tsunoda, R.T., High-latitude *F* region irregularities: a review and synthesis, *Rev. Geophys.*, **26**, 719, 1988.
- Valladares, C.E., H.C. Carlson Jr., and K. Fukui, Interplanetary magnetic field dependency of stable sun-aligned polar cap arcs, *J. Geophys. Res.*, **99**, 6247, 1994a.
- Valladares, C.E., Su. Basu, J. Buchau, and E. Friis-Christensen, Experimental evidence for the formation and entry of patches into the polar cap, *Radio Sci.*, **29**, 167, 1994b.
- Weber, E.J., J. Buchau, J.G. Moore, J.R. Sharber, R.C. Livingston, J.D. Winningham, and B.W. Reinisch, *F* layer ionization patches in the polar cap, *J. Geophys. Res.*, **89**, 1683, 1984.
- Weber, E.J., J.A. Klobuchar, J. Buchau, H.C. Carlson, Jr., R.C. Livingston, O. de la Beaujardiere, M. McCready, J.G. Moore, and G.J. Bishop, Polar cap *F* layer patches: structure and dynamics, *J. Geophys. Res.*, **91**, 121, 1986.

D.N. Anderson, Phillips Laboratory, Geophysics Directorate (GPIM), 29 Randolph Rd., Hanscom AFB, MA 01730-3010. (e-mail: danderson@plh.af.mil)

D.T. Decker, R. Sheehan, and C.E. Valladares, Institute for Scientific Research, Boston College, 885 Centre St., Newton, MA 02159. (e-mail: decker@plh.af.mil; sheehan@plh.af.mil; cesar@dlws7.bc.edu)

(Received August 8, 1995; revised February 8, 1996; accepted February 14, 1996.)

Formation of polar cap patches associated with north-to-south transitions of the interplanetary magnetic field

C. E. Valladares, R. Sheehan and D.T. Decker

Institute for Scientific Research, Boston College, Newton Center, Massachusetts

D. N. Anderson and T. Bullett

Phillips Laboratory, Geophysics Directorate, Hanscom Air Force Base, Massachusetts

B. W. Reinisch

Center for Atmospheric Research, University of Massachusetts, Lowell, Massachusetts

short title: VALLADARES ET AL.: PATCH FORMATION DURING IMF B_z REVERSALS

submitted to the Journal of Geophysics Research

December, 1996

Abstract. Based on experimental measurements and computer modeling, we propose that patches can be generated when sun-produced plasma, augmented by particle precipitation, enter the polar cap due to the development of antisunward flows acting in response to a new, even if short lived, B_z south-type global pattern. The data clearly indicates that structured density enhancements can be present near midday during a prolonged period (>1 hour) of steady northward IMF conditions. The nature of the ionospheric flows near the auroral poleward boundary, during B_z northward conditions, prevents the high density plasma from transiting across the polar cap. The experimental evidence is provided by the Sondrestrom incoherent scatter radar, by an all-sky imaging photometer located at Qaanaaq, by two digisondes located at high latitudes and by a magnetometer placed on-board the IMP-8 satellite. In summary, the data reinforce the view that patches can exist inside the polar cap shortly after negative excursions of the IMF B_z occur. Indeed, the Sondrestrom data gives conclusive evidence for the existence of a quasi-stationary structure of high densities detached from a uniform high density plasma. Convergent electric fields and slightly elevated T_e signatures were seen accompanying the F-region N_e feature. This fact supports the conclusion that soft precipitation is probably responsible for slightly augmenting the density and elevating the electron temperature. Several minutes after B_z changes from North to South, a poleward motion of the density structure was detected by the radar, together with the appearance of a large flow jet equatorward of the original location of the N_e structure. Nearly 34 minutes after the N_e structure departs from the Sondrestrom field-of-view, the Qaanaaq digisonde measures a factor of 2 increase in the f_oF_2 values. We have explored the possibility of sudden north-to-south-to-north transitions as a likely generation mechanism of polar cap patches. The results of the modeling work are in quantitative agreement with the time that the patch appears and the density values measured by the Qaanaaq digisonde. The modeling work also predicts the existence of stationary structures residing near the boundary of the auroral oval and the polar cap. The B_z switching mechanism does not dispute the validity of other patch formation mechanisms; it attempts to explain recent observations of patchlike structures inside the polar cap when the hourly value of B_z is positive, but there exists short negative excursion of B_z lasting less than 30 min.

1. Introduction

Polar cap patches consist of density enhancements, with sizes ranging between 100 and 1000 km, that circulate across the polar cap ionosphere. These localized regions of density larger than the background are seen to drift in a generally anti-sunward direction [Weber et al., 1986]. They contain enhancements of plasma density that could be up to one order of magnitude above the surrounding sun-produced background [Buchau et al., 1983; Weber et al., 1984]. They have been predominantly observed under moderate to disturbed magnetic conditions and have been long associated with a B_z south orientation of the IMF. Polar cap patches are also commonly accompanied by intense levels of scintillations which are an indication of the presence of km-scale irregularities [Buchau et al., 1985; Basu et al., 1985, 1989]. Studies of polar cap patches are of great importance due to the association of this type of mesoscale structures with small scale (km to hundreds of m) irregularities which cause severe propagation disturbances even in the GHz frequency window [Basu et al., 1994].

There is a general agreement that the plasma density inside the patches is produced by solar radiation in the sunlit ionosphere, probably at cusp or subcusp latitudes, and then carried into and across the polar cap by the convection pattern. Support for the subcusp as a source of patches was initially given by Buchau et al. [1985]. They found a strong UT control of the diurnal pattern of the occurrence of patches during solar minimum winter conditions. The patches were seen almost exclusively between 12 and 00 UT. The f_oF_2 value observed in the patches during solar minimum conditions was 6 Mhz, in agreement with a source region at 73° CG latitude. In contrast, during solar maximum winter conditions, patches tend to have f_oF_2 values up to 11 Mhz suggesting that the source region could be at latitudes as low as 65° CG latitude [Buchau and Reinisch, 1991]. Clearly, the implication is that the convection pattern expands equatorward and embraces higher density plasma that is located at lower latitudes. Due to the offset of the geographic and magnetic poles, the global convection pattern is able to enclose plasma from lower geographic latitudes only at certain UT periods. During very disturbed, storm geomagnetic conditions, rapid convection carries high density solar produced F-region plasma from a source at middle and low latitudes through the dayside cleft and into the polar cap [Foster, 1993].

It has also been suggested that when the subauroral plasma reaches the cusp/cleft region, enhanced recombination [Valladares et al., 1994a] or merging related phenomena [Lockwood and Carlson, 1992] can favor plasma detachment.

A major step in our understanding of the formation of polar cap patches came with the modeling work of Sojka et al. [1993, 1994]. These researchers demonstrated that continuous changes in the IMF B_y component could lead to large scale plasma structuring [Sojka et al., 1993]. A large plasma flow near midday containing velocities of order 2 km s^{-1} is able to increase the O^+ recombination rate and to yield an east-west aligned region of reduced densities generating a detachment of a plasma patch [Valladares et al., 1994a, 1996; Rodger et al., 1994]. Soft precipitation, as encountered at the cusp, could be also a source of patches [Kelley et al., 1982; Sojka and Schunk, 1986]. Rodger et al. [1994] presented data from the polar anglo-american conjugate experiment (PACE) which the authors claimed supported the view that patches could be originated by the intense cusp precipitation. While it is possible that all of these mechanisms, and others, produce patches, it is also likely that some of them only operate under certain restricted circumstances. Recent measurements at Qaanaaq have shown that the patches can display well elongated shapes with the major axis oriented along the dawn-dusk meridian [Fukui et al., 1994], suggesting a much larger variety of shapes than previously recognized. More recently, Coley and Heelis [1995] developed an adaptive algorithm to conduct an automated identification of patches using the entire DE-2 database. These authors found typical spatial scale size of the patches in the range 300 km to 400 km and the existence of density structures inside the polar cap even when the IMF was positive. However, Coley and Heelis [1995] used hourly values of the IMF and their result may be subject to cases when short negative transitions (20 -30 minutes) of the IMF B_z occurred.

North-to-south reversal of the IMF has not received much attention as a generation mechanism of polar cap patches. Tsunoda [1988] mentioned, in a review paper, that B_z reversals could in fact lead to

patch formation. However, neither experimental nor modeling verification has been forwarded. In this paper, we present experimental data and corresponding computer modeling of a case study event that serves to introduce the B_z reversal mechanism as a possible mechanism of mesoscale plasma structuring at polar cap latitudes.

2. Experimental Observations.

This section presents ionospheric observations conducted with the Sondrestrom incoherent scatter radar, with the Qaanaaq all-sky imaging photometer (ASIP), and with digisondes placed at Sondrestrom and Qaanaaq. It also introduces in-situ measurements of the IMF performed by the IMP-8 satellite. The data sets under discussion were collected on January 15, 1991. The Universal Times of the observations coincide with near midday hours at Sondrestrom. During the observations the magnetic conditions were quiet, $K_p = 2$ and the F10.7 solar flux was 184.6, a typical value of solar max conditions. The K_p value is in agreement with the value of the IMF B_z which remained positive for few hours and only changed for a brief period to a negative configuration. The time interval when the B_z component was oriented southward was 10 minutes, but as the data suggest, it favors an immediate entrance of auroral plasma into the polar cap.

2.1 IMP-8 satellite observations.

During the time of the observations, the IMP-8 satellite was in the solar wind, well upstream from the Earth's bow shock. The X, Y, and Z coordinates, in the GSM system, were 35.0, 2.0, and -12.8 Earth radii, respectively. The IMF observations start at 1210 UT (Figure 1) during a sudden rise of the B_z values. This component remains positive and near 5 nT until 1548 UT, when a sharp decrease and a reversal of B_z occurs. This component of the IMF remains near zero and slightly negative for 10 minutes, until 1610 UT when it starts to climb back to a positive value. During the period of the observations, B_x and B_y are positive and negative respectively. We calculated that the propagation delay for the effect of the B_z IMF negative excursion to reach the Sondrestrom field-of-view (FOV) was ~ 8 min.

2.2 Sondrestrom radar observations.

To conduct the radar observations, we adopted the antenna pattern that was also used on September 14, 1991 [Valladares et al., 1994a]. This antenna scheme consisted of a sequence of a 360° azimuth scan (AZ) at 30° elevation, followed by an elevation scan (EL) in the plane of the magnetic meridian. While the AZ scan gives the largest spatial coverage, the EL scan provides a fine spatial resolution view in a latitudinal sectional cut of any structure within the radar field-of-view (FOV). The two-scan pattern was repeated every 9 min, providing, in this way, a reasonable time resolution. On January 15, 1991 the Sondrestrom radar operated between 1145 and 1700 UT using a transmitter pulse 320 μ sec long which is well suited for F-region measurements. Figure 2 displays the four geophysical parameters as a function of Universal Time and North-South distance along the magnetic meridian. To construct Figure 2 we have included the four geophysical parameters derived from the data that was collected only during the elevation scans. The top panel shows the velocity vectors that have been derived using the line-of-sight ion drifts (V_{los}) from the E and F-layers and the property of the field lines of being equipotential [de la Beaujardiere et al. 1985]. The three lower panels display the ion temperature (T_i), the number density (N_e), and the electron temperature (T_e) at a fixed 320 Km altitude. The resolved flow velocities show that the flow near Sondrestrom is remarkably zonal, directed westward since 1230 UT until the end of the experiment. This measured flow is in agreement with the convection patterns presented by Heppner and Maynard [1987] for B_z positive and B_z negative, and also called DEP and DEPP by these authors. These two statistical patterns show a region between 70° and 76° magnetic latitude and near midday consisting of westward flows and well defined eastward flows poleward of 76° .

The density panel of Figure 2 shows a very sharp decline in its poleward extension. This abrupt latitudinal gradient is located 200 km northward of the station at 1243 UT. The density poleward boundary is seen to be slowly receding southward as time progresses. We propose that the formation of this abrupt N_e boundary is related to the steadiness and the westward nature of the flow that brings less dense plasma from later local times. Within the region of uniform and high densities, the flows are less than 100 m/s (see Figure 3b) which suggests that this region is probably located equatorward of the oval.

A very striking feature in the N_e panel of Figure 2 is also the presence of a density structure that seems to grow and split from the dayside oval at 1300 UT. This density structure slowly moves poleward until 1500 UT, when it becomes quasi-stationary. At 1500 UT, the N_e structure has a density of 10^6 cm^{-3} , is situated 400 km north of the station and seems to be placed very close to the region of the convection reversal as will be seen in the following figures. However, we are not calling this density structure a polar cap patch, at least between 1300 and 1620 UT, because it is not strictly either moving antisunward or transiting across the polar cap. The isolated density region constitutes a prominent feature in the gray scale plot and remains inside the radar field-of-view until 1619 UT, when it finally departs toward the center of the polar cap.

Figures 3-5 show a sequence of the four geophysical parameters derived from 12 consecutive scans recorded between 1549:05 and 1649:26 UT. Each column corresponds to a different scan. The AZ scans are displayed by unfolding the conical surfaces of the antenna sweeps and projecting them onto $1600 \times 1600 \text{ km}$ ground surface with the radar at the center and geographic North directed toward the top of each plot. Due to the nature of the AZ scans, altitude and distance variations are intermixed. Nevertheless, it is possible to identify any localized density structure by examining the variations of the contour lines from an ideal uniform or circular pattern. The EL scans are displayed in the plane of the measurements, with magnetic North always placed in the right side of the plot. The line-of-sight velocities, seen in the second row in figures 3, 4, and 5, are displayed using arrows of different patterns and lengths according to the sign and magnitude of the plasma flow. Velocities directed toward the radar have also been shaded using a light gray tone. In few cases the area probed by the radar has been dark grayed to indicate that V_{los} exceeds 1 km s^{-1} (Figure 4j). The density contours are on a linear scale with the initial values and the interval between levels equal to 10^5 cm^{-3} . The T_i and T_e values (first and fourth rows) are depicted in the form of gray-scaled contours varying in discrete steps of 1000 degrees.

Figures 3a - 3d show the T_i , V_{los} , N_e and T_e values measured during the AZ scan that started at 1549:05 UT. The density contours of Figure 3c show a density structure aligned in the magnetic east-west direction and situated 400 km north of the site. This structure corresponds to the N_e structure seen in Figure 2. This plot shows that at any given instance the density structure extends for hundreds of km and it is well disconnected from a mostly unstructured plasma located in the southern part of Figure 3c. When the N_e structure was closer to the Sondrestrom site (e.g. 1350 UT), the radar was able to scan the E-layer underneath the density enhancement. No appreciable density was observed below 150 km. The magnitude of V_{los} in the region to the south of dense and unstructured plasma is small ($< 100 \text{ m/s}$), this is very suggestive of sub-auroral flows. In the northern part of Figure 3b there is a more complicated pattern of line-of-sight velocity shears and reversals. This can be understood if we consider that the plasma flow is mainly zonal and pointing toward the east poleward of the heavy line, and pointing west equatorward of that line. As the antenna is scanning in azimuth it will point, at one moment, perpendicular to the flows and will measure flows equal to zero, but it will measure V_{los} of different signs at both sides of the point of perpendicularity. The sign of the velocity reversal of Figure 3b indicates that the electric fields near the location marked by a solid line are convergent and are probably associated with an upward field-aligned current. We have also traced this line at the same location in the other panels to indicate that the region containing convergent electric fields is situated near the region of enhanced densities. There is a small difference between the location of the density peak and the location of the velocity reversal, this can be explained by the nature of the AZ scan that intersects the peak value of the N_e structure slightly poleward of the reversal and not at the center of the structure. Enhanced T_e values, above 3000° K , are also observed poleward of the reversal line. Because there is no significant densities below 150 km altitude, we conclude that the precipitating particles, which enhanced T_e are mainly soft ($< 300 \text{ eV}$). During this type of precipitation, the kinetic energy is mainly deposited in the F-region where the heat conductance along the field lines is large, this produces a more pronounced T_e increase appearing at higher altitudes. This effect is displayed in Figure 3d.

The elevation scans during the experiment were performed at -39° azimuth; which is also perpendicular to the ionospheric flows in the northern part of the scan. This fact prevented us from measuring the flow shear during the EL scans. However, the EL scan that started at 1555:09 UT shows the location of the density structure to be 450 km north of the radar site. The T_e is also enhanced at this location, but at altitudes above 450 km. EL scans conducted at earlier times, when the structure was closer to the radar, measured the width of this feature to be 150 km. While the presence of an isolated structure accompanied with elevated T_e and convergent electric fields can lead us to conclude that particle precipitation is the mechanism that created the density structure, we believe that this structure was formed from sun-produced plasma entrapped in the B_z north type global convection. This hypothesis is based on (1) the fact that the density structure was initially part of the uniform auroral-subauroral density which was sliced when B_z became positive, and (2) the modeling work presented in section 3.

The AZ scan that started at 1558:12 UT shows the location of the velocity reversal displaced 50 km poleward with respect to the previous AZ scan. This is the main difference with respect to the previous AZ scan; the magnitudes of the geophysical parameters remain almost unchanged. Data from the following EL scan, gathered between 1604:17 and 1607:19 UT (Figures 3m - 3p), show a more visible reversal than the previous EL scan. The velocity reversal in this scan is located at 500 km north distance.

The AZ scan starting at 1607:20 (Figure 4a - 4d) shows a more structured flow pattern south of the reversal line. This line seems to continue moving poleward, as seen by comparing the location of the heavy trace with its location in the previous two AZ scans. The following EL scan (1613:24 - 1616:26 UT) show a modest increase in the magnitude of V_{los} and a small displacement of the location of the reversal occurring at 550 km distance. The AZ scan that started at 1616:27 UT (Figures 4i - 4l) show a different distribution in all four geophysical parameters. The different pattern of velocities and T_i is probably the response of the high latitude ionosphere to the reversal of the IMF B_z . The T_i panel (Figure 4i) displays two regions of intense Joule heating, one to the east and the other to the west of the station. T_i is above 3000 K in these two regions which are aligned in the east - west direction and almost parallel to the direction of the flows. As expected they are collocated with corresponding large values of V_{los} . The northwestern part of the scan of Figure 4j does not show the complex system of velocity reversal that was present in the previous AZ scans, instead the flow is directed toward the magnetic north direction (-27° from geographic north). Figure 4k reveals that the antenna grazed the density structure for a final time at 1619:29 UT. We have used this time to mark the beginning of the transport of the N_e structure across the polar cap. The new local pattern of large velocities produces also a more abrupt and a wider gap between the structure and the subauroral densities. The EL scan that started at 1628:09 UT confirms the presence of a large plasma jet flowing between 200 and 550 km north distance and endorses the presence of elevated T_i in this same region.

The AZ scan of Figures 5a - 5d started with the radar pointing at -39° (magnetic North) and proceeded counter-clockwise. The large plasma jet and the corresponding enhanced Joule heating is observed only at the beginning of the scan. It has decayed or moved outside the radar FOV when the antenna reached the northeastern quadrant about 5 min later. The density at the north is relatively depleted with peak N_e values here near $3 \times 10^5 \text{ cm}^{-3}$. The following two scans (starting at 1637:16 and 1640:19 UT) show that the large flow event has subsided and that no density structure is within the radar FOV. However, the densities at the northern part of the scan remain almost depleted for few more scans. This quiescent ionosphere is quite typical during IMF B_z northward conditions. The AZ scan of Figures 5m-5p shows the 4 geophysical parameters resembling the scans of Figure 3. A salient feature in Figure 5o is the appearance of a region of enhanced densities containing densities above $5 \times 10^5 \text{ cm}^{-3}$ situated almost at the end of the scan at 400 km north distance and seen at 1655 UT. The modeling work to be described in sections 3 and 4 has helped us to understand that the origin of this structure is closely associated with the general characteristics of the global pattern for B_z north conditions.

2.3 Qaanaaq ASIP observations.

The Qaanaaq (77.5° N, 69.2° W, 86° Invariant Latitude) all-sky imaging photometer (ASIP) has operated at this site since 1983, and it constitutes the most poleward imager currently operated by the Phillips Laboratory. For a complete description of the system hardware, sensitivity, and operational mode, the reader is referred to publications by Weber and Buchau [1981], Weber et al. [1984], and Valladares et al. [1994b].

Figure 6 presents a sequence of six 630.0 nm images collected on January 15, 1991 and during the time when the Sondrestrom radar was operating. This Figure shows the location of the arcs after each pixel in the ASIP images has been transformed to a corrected geomagnetic (CG) coordinate system assuming that the auroral emissions originate at 250 km altitude. In the CG system a sun-aligned arc becomes parallel to the noon-midnight axis and points toward the top of the figure. On the day of the experiment, sun-aligned arcs were first observed at 0930 UT and persisted until 1340 UT. Between this time interval, several arcs brightened, some faded and others quickly moved outside the imager FOV. No arcs were seen after 1340 UT. However, the imager was turned off at 1520 UT, due to the sun rising above 12° below the horizon, and no visual recording of the aurora exists. The image of 1254:54 UT shows an arc intensifying near the center of the Qaanaaq FOV. It also shows a second arc located near the dawn edge of the imager FOV, where its altitude extension produces an apparent much wider arc. During extended periods of IMF B_z positive conditions it is quite typical to observe sun-aligned polar cap arcs drifting in the duskward or dawnward direction [Lassen, 1972; Berkey et al., 1976]. The images presented here show that both arcs drifted duskward and were sometimes located overhead the Qaanaaq station. Sun-aligned arcs are commonly accompanied by enhancements of the F-region density [Carlson et al., 1984]. Close inspection of the ionograms revealed that the arcs detected on this day were in fact associated with small enhancements in the density traces measured between 1200 and 1330 UT. However, this singular type of trace was not seen after 1340 UT when the arcs decayed.

2.4 Qaanaaq and Sondrestrom digisondes.

In Figure 7, we reproduce the f_oF_2 values, and the equivalent peak density (right scale) measured by two digisondes. One located at Qaanaaq (upper panel) and the other at Sondrestrom (66.98° N, 50.95° W, 74° Invariant Latitude) (lower panel). The Sondrestrom digisonde measured peak densities near 10^6 cm^{-3} between 13 and 18 UT. This value is consistent with the density values measured by the Sondrestrom incoherent scatter radar at the same time. The Qaanaaq digisonde detected a much lower density until 1630 UT, when it abruptly increased from $1.3 \times 10^5 \text{ cm}^{-3}$ to $4 \times 10^5 \text{ cm}^{-3}$. Fifteen minutes later, at 1645 UT, the density reaches a value approximately equal to $5 \times 10^5 \text{ cm}^{-3}$. The transit of the patch through Qaanaaq is abruptly terminated at 1715 UT. The f_oF_2 behavior described above is typical for patch observations at Qaanaaq [Buchau et al., 1983; Weber et al., 1984; Buchau and Reinisch, 1991]. We have also included in the upper panel a trace of the peak density that could have been detected at Qaanaaq if the IMF B_z had been southward. This trace was obtained numerically using the GTIM model developed by Anderson et al. [1988] for a B_z south and steady convection pattern. (See also Decker et al. [1994].) As expected the f_oF_2 values measured at Qaanaaq are smaller than the modeled values when B_z is positive, no negative excursions of B_z exist, and no sun-aligned arcs are overhead the Qaanaaq digisonde, say between 1340 and 1800 UT. However, the solid curve is above the dotted line between 1000 and 1340 UT when polar cap arcs populated the polar cap. After 1340 UT, when no polar cap arcs were observed, the Qaanaaq f_oF_2 values are much less than the modeled values until 1630 UT when the N_e structure reached Qaanaaq. It should be noted that the rise of the Qaanaaq f_oF_2 values at 1630 UT occurs more rapid than the increase of the modeled values (dotted line). This plot is consistent with the fact that patches are not seen deep inside the polar cap when the IMF is northward and steady.

3. Numerical Modeling.

We have used the Global Theoretical Ionospheric Model (GTIM) developed by Phillips Lab and Boston College researchers [Anderson et al., 1988; Decker et al., 1994] to simulate the chain of events that led to the initiation of the patch transit across the polar cap. This model can provide a numerical confirmation that the N_e structure measured at Sondrestrom at 1616 UT transited across Qaanaaq producing the plasma enhancements seen by the digisonde at 1650 UT. In general, the GTIM model calculates the O^+ density profile along a single flux tube solving the coupled continuity and momentum equations for ions and electrons. Inputs to the GTIM model are: the neutral density, the neutral wind, the global convection pattern, and the initial plasma density. In the last few years, the GTIM model has been extended to include the effects of large electric fields and particle precipitation [Anderson et al., 1988; Decker et al., 1994]. GTIM has recently proved to be well designed to conduct studies of the formation of polar cap patches, such as using variable convection patterns [Sojka et al., 1993; Decker et al., 1994], or using localized velocity vortices [Decker et al., 1994; Valladares et al., 1996]. The work presented here constitutes an initial examination of the B_z switching mechanism as a potential generator of patches. We are not modeling the formation of the density structure per se, but instead we start with densities measured by the Sondrestrom ISR and model the evolution of the density structure, its reconfiguration into a patch and its transit across the Qaanaaq zenith location.

3.1 Initial conditions.

We used the plasma number density measured by the Sondrestrom ISR between 68° and 80° invariant latitude to define the initial densities in the sub-auroral, auroral and polar cap regions. We also selected the global convection pattern guided by the values of the IMF, but in agreement with the line-of-sight velocities measured at Sondrestrom. Finally, to corroborate the validity of the mechanism under discussion we compare the simulated densities to the f_oF_2 values measured by the Qaanaaq digisonde, and the densities detected at Sondrestrom at the time of the patch crossing at Qaanaaq. We do not intend to model the initial creation of the density structure, but instead we adjust the initial conditions to the densities measured by the Sondrestrom ISR at 1616 UT and examine the journey of the N_e structure from the poleward edge of the Sondrestrom ISR FOV up to the Qaanaaq station.

Figure 8 demonstrates how the initial plasma density was determined. Figure 8a shows the N_mF_2 values as a function of magnetic latitude and local time obtained with the GTIM model after following 12800 flux tubes during 8 hours 16 minutes of simulation time. This initial simulation used solar and magnetic conditions similar to the ones encountered during the experiment. It also employed a steady Heppner and Maynard [1987] DEP ($B_z > 0$; $B_y < 0$) global convection, which resulted in the best fit to the V_{los} measured by the radar AZ scans between 1549:05 and 1613:24 UT (see Figure 9a). Figure 8a shows a plasma intrusion into the polar cap, named a tongue-of-ionization (TOI), with characteristics different than the TOI calculated for B_z negative conditions, (see Plate 1 of Valladares et al. [1996]). In the B_z positive case the TOI is displaced toward the dusk side and does not reach the midnight side of the oval. The plasma simply circulates inside the polar cap and returns back to the afternoon sector. However, this structured plasma enhancement could be mistakenly identified as a polar cap patch by an orbiting satellite like DMSP or DE-2. The TOI produced during B_z north conditions is not an isolated structure, neither is moving antisunward. Figure 8b shows the number densities measured by the Sondrestrom radar during the conical AZ scan that started at 1616:27. The location of Sondrestrom and Qaanaaq are depicted in this figure as black dots. The densities have been projected to the same geomagnetic coordinates used in panels a and c. In this plot, we have included densities measured at all ranges, consequently we are not presenting a display of N_mF_2 , but instead density variations as a function of range from the radar site. The quasi-steady density structure is seen to be located poleward of the radar site and aligned in the magnetic east-west direction.

Figure 8c shows the initial density that was used in the numerical simulations. It basically consists of the densities shown in Figure 8a but multiplied by a factor depending on the solar zenith angle to agree

with the densities measured by the Sondrestrom ISR. The multiplying factor varied from 1.4 for the smallest zenith angles to 1.0 at zenith angles near Sondrestrom and then decreased to 0.7 for solar zenith angles larger than Qaanaaq's. Figure 8c also depicts the peak values of the density structure as it was detected at 1619 UT. To introduce the density structure, the density profiles of all flux tubes located where the structure was detected at 1619 UT, were increased by a factor that made the peak density in this region equal to $9 \times 10^5 \text{ cm}^{-3}$. The final density quantitatively agrees with the density measured at Sondrestrom.

To simulate the negative excursion of the IMF B_z value we changed instantaneously the global convection pattern. Using the AZ scans that started at 1616:27 and at 1631:12 UT, we determined that a Heelis-type pattern [Heelis et al., 1982] would give the best fit to the observed V_{los} . Specifically, we selected a Heelis-type pattern with a cross polar cap potential equal to 90 kV, and a 10° polar cap radius. Twenty minutes later, at 1636 UT, the global pattern was changed again, but in this case we use a Heppner-Maynard DEPP pattern with potentials increased by a factor of 2 which was found to give the best fit to the radar data of 1640 UT. Figure 9b shows the Heelis-type pattern used to implement the negative B_z excursion and Figure 9c the H-M pattern used to simulate B_z northward conditions.

3.2 Modeling of the January 15, 1991 event.

To understand how patches evolve depending on the intensity of the convection pattern and the length of the B_z south excursion, we implemented several simulations changing these two parameters. The first modeling effort used a Heelis pattern lasting 20 min, after this time the global convection was changed to a DEPP pattern with the potential field multiplied by a factor of 2 (Figure 9c). Figure 10 presents the results of this modeling in successive steps 4 min apart. In this format we reproduce the $N_m F_2$ values for a limited region around the northern magnetic pole. The location of Qaanaaq is indicated by a white dot and the coverage of the Sondrestrom ISR during elevation scans by a white line. The magnetic pole is at the center of the bottom edge of each panel.

Figure 10a reproduces a part of the polar cap and auroral ionosphere near midday that was presented in Figure 8c. This corresponds also to the initial peak density that was used in the simulation. No TOI is seen in this panel. Figures 10b and 10c show a gentle poleward displacement of the boundary of the density near midday. The following panels (Figures 10d - 10f) display the formation of the TOI; which is commonly seen in any simulation that uses a velocity pattern typical of a B_z south configuration. This new structure is relatively narrow and does not intrude deep into the polar cap even at 1636 UT. However, a wider or more elongated TOI was obtained when a larger polar cap radius, a more intense cross polar cap potential, or a different day of the year was selected. Evidently, if we had allowed the B_z south Heelis-type pattern to prevail for a longer period, say one hour, then a fully developed TOI would have appeared. During the growth of the TOI, the N_e structure is seen moving poleward (toward the bottom of the figure). The density structure moves antisunward carried by the global convection until 1636 UT when it becomes more dawn-dusk aligned. At this point, the N_e structure has all the characteristics of a polar cap patch, this is, moves antisunwardly and consists of an isolated entity with densities higher than the surroundings. The patch is only subject to a clockwise rotation due to the nature of the flows of being more intense near the center of the polar cap.

At 1636 UT, we changed the global convection pattern into a DEPP ($B_z > 0$; $B_y < 0$) convection pattern [Heppner and Maynard, 1987]. Four minutes later (Figure 10g), the flows associated with the new global convection start to erode and elongate part of the TOI that was formed during the B_z south excursion. This makes the TOI to distort and lose its noon-midnight elongation; instead it becomes extended in the magnetic east west direction. Figure 10h shows that the new B_z positive-type pattern brings low density plasma from the afternoon and morning sides and erodes plasma both equatorward, in the morning side, and poleward in the afternoon section of the TOI. If the B_z north related flow pattern remains unchanged for several minutes, as it occurred before 1616 UT, then an east-west elongated density structure will form near the velocity shear region and remain stationary in a corrected geomagnetic coordinate system.

This new structure, created by the reconfiguration from a B_z south to a B_z north convection pattern, resembles the density structure that was seen to remain stationary in the poleward boundary of the oval before 1616 UT. Thus, we speculate that the N_e structure, that was seen previously by the Sondrestrom ISR until the scan at 1616 UT, could have been formed much earlier by a previous reversal of the IMF B_z component, and was only somewhat enhanced and heated by local soft precipitation.

Figure 11 presents results from the simulation in a format more suitable for comparison with the experimental measurements. The inherent difference in the modeled and the experimental plots is the time resolution of both quantities. The radar AZ scans were gathered every 9 min, with a total sweeping time of 6 min employed to cover 360° of the sky. Conversely, the simulated scans represent instantaneous snapshots of the ionosphere. Figure 11a has many features similar to the density contours of Figure 4k, it illustrates the fact that the initial conditions reflect the experimental data. The peak density at the southern part of the scan is $1.1 \times 10^6 \text{ cm}^{-3}$, equal to the maximum density in the same part of the experimental scan of Figure 4k. Figures 11f and 11g, corresponding to the simulated times of 1636 and 1640 UT show low densities near $3 \times 10^5 \text{ cm}^{-3}$ at the northern end of the scan; this value is in good agreement with the densities detected by the Sondrestrom ISR during the scan between 1640:19 and 1646:23 UT. The densities in the northern part of the simulated scan show the effect of B_z south and the antisunward flow. The last two panels of the simulation, corresponding to values of B_z north simulation, (Figures 11h and 11i) show a new density structure in the poleward part of the scan, this plasma intrusion of the distorted TOI reaches a density near $8 \times 10^5 \text{ cm}^{-3}$ at the scan of 1648 UT. In spite of being 400 km wide and located in the northwestern part of the scan, it resembles the density structure seen at the end of the scan of Figure 5o (1655 UT). The density structure measured by the ISR is much narrower, but this may be caused by the real pattern having very sharp reversal features near the noon sector, at least, sharper than the statistical Heppner and Maynard [1987] pattern that was used in the present simulations.

4. Sensitivity study of B_z south parameters.

Figure 12 shows f_oF_2 values collected by the Qaanaaq digisonde on January 15, 1991 (heavy trace) together with simulated values of f_oF_2 which were obtained by changing the length of the B_z south excursion and the potential across the polar cap during the B_z south interval. The four thin traces of Figure 12a correspond to polar cap potentials of 80, 70, 60 and 50 kV. The size of the polar cap was kept fixed at 10° and the length of the B_z south period remained at 20 min for all 4 cases.

To obtain the trace labeled 80 kV (well separated dots) we used the same input parameters that were used in the simulation discussed in section 3.2, except for the polar cap potential that was changed to 80 kV. In spite that this simulation revealed that the density structure passed overhead the Qaanaaq station, a quantitative comparison shows that the simulated f_oF_2 values are much higher (maximum value is 8.6 Mhz) than the values measured by the digisonde (6.4 Mhz). The 80 kV trace provides only an envelope to both f_oF_2 enhancements, seen between 1600 and 1800 UT. However, the simulated density value is almost a factor of 2 larger than the measured density at Qaanaaq. The other three values of the cross polar cap potential provide smaller density values, but the appearance of the density structure at Qaanaaq is delayed by the smaller velocity inside the polar cap. The 50 kV potential provides f_oF_2 values closer to the measured values, however, the maximum amplitude occurs 5 min after the measured f_oF_2 trace starts to decrease.

A more reasonable agreement between modeled and real f_oF_2 curves can be achieved reducing the time that the Heelis B_z south global pattern is in effect, maintaining the size of the polar cap at 10° , and fixing the polar cap potential at 80 kV. Figure 12b shows the result of varying the length of the negative excursion from 20 min (thin dotted trace) to 12 min (thin continuous trace). This last set of parameters gives a good agreement with the amplitude and the timing of the occurrence of the f_oF_2 maximum, but it does not provide any indication of a second density enhancement as detected by the digisonde at 1735 UT. It should be mentioned that 12 min is in better agreement with the extension of the B_z negative excursion than the 20 min that was used in the modeling event of section 3. We suggest that the second density enhancement may be related to a decrease of the IMF B_z value that is evident in Figure 1 at 1645 UT and it is seen to last for 10 min. Figure 1 shows that at this time B_z did not reverse sign, it only changed from +6 to +1 nT. This variation of the IMF B_z may be strong enough to produce merging of closed field lines at the nose of the magnetopause and generate antisunward plasma flow inside the polar cap. It was also observed at 1645 UT that B_y became more negative and B_x reversed briefly to a negative orientation; both changes favor merging of closed field lines in the northern hemisphere [Reiff and Burch, 1985].

5. Discussion and conclusions.

Figures 2, 3, 4, and 5 demonstrated the presence of an isolated region of enhanced density located slightly poleward of the Sondrestrom site in the post-noon sector. This region was found to coincide with convergent electric fields, implying the existence of upward field aligned currents. Elevated T_e values, at high altitudes, were also measured by the Sondrestrom ISR within the region of high N_e . Based on these key elements several experimenters have concluded in the past that particle precipitation is the generation mechanism of the density structures they have measured. We do not dispute that in some cases, especially when they are located away from the noon sector, this is the correct interpretation. However, the simulations presented here point to solar produced plasma and global velocity reconfiguration as a more likely causative mechanism of the N_e structure observed on January 15, 1991. In this view, an east-west elongated density structure can be formed by zonal flows, that seem to prevail near midday when the IMF B_z is positive and remains stationary for few hours. The zonal flows can also deform any newly formed TOI that can be produced even if the B_z negative excursion lasts for only 12 min. Any soft electron precipitation, accompanying the upward field-aligned currents, will simply augment the number density and increase T_e above 400 km. While soft precipitation, as encountered at the cusp, can enhance the local density, to be effective the particle flux needs to remain stationary for several min in the frame of the moving plasma.

Numerical simulations under steady IMF B_z northward conditions have revealed that a limited TOI can exist at very high latitudes. The TOI was found to be located in the early afternoon local time sector, displaced toward dusk, and extending into the noon-midnight direction barely 10° beyond the center of the polar cap. The TOI did not reach the midnight side of the auroral oval. We have implied that this structured density enhancement, which protrudes well within the polar cap, could be mistakenly identified as a patch by an orbiting satellite. Ground-based measurements or concurrent in-situ velocity measurements are needed to unequivocally identify a polar cap patch [Basu et al., 1990]. It is not clear, at this point, whether the B_z switching mechanism of Sojka et al., [1993] will be able to structure the TOI much further during B_z north conditions, as it normally occurs during B_z south conditions. More extensive modeling work is needed to prove this point.

The IMP-8 satellite measured the three components of the IMF and indicated that between 1200 and 1800 UT the B_z component was predominantly positive. The Qaanaaq all-sky imager observed typical polar cap arcs at 1300 UT (Figure 6), supporting the well-known characteristic of the polar cap of being populated by sun-aligned arcs when the IMF B_z component points northward. However, arcs decayed at 1340 UT, and no arcs were seen at Qaanaaq afterwards. The imager was not in operation between 1520 and 1840 UT to avoid scattered sunlight entering the photometer sensor. Between these times, the Qaanaaq digisonde did not provide any evidence for polar cap arcs transiting throughout the station. It is known that the polar cap arcs can generate enhancements in the F-region density [Carlson et al., 1984], usually peaking at 200 km altitude [Valladares and Carlson, 1991], but rarely at altitudes higher than 300 km. The velocity shears and reversals that commonly accompany polar cap arcs can be also detected by digisondes and can be used to imply the presence of polar cap arcs. Between 1200 and 1330 UT the Qaanaaq digisonde measured density enhancements associated with dawn-dusk moving polar cap arcs peaking at 280 km, and a variable pattern of drift velocities. At 1645 UT, when the density structure reached Qaanaaq, the density peaked at 335 km, the drift was directed antisunwardly and without the variability seen at 1300 UT. Thus, we conclude that the factor of 3 density enhancements detected by the Qaanaaq digisonde can be only explained by a patch transiting the polar cap.

We did not model the formation of a density structure near Sondrestrom, but only its transit across the polar cap and passage through the Qaanaaq FOV. However, the modeling work conducted for steady B_z positive conditions revealed that density structures can be readily created near the noon sector at latitudes near the poleward boundary of the auroral oval. Our first modeling run of this case event, discussed in section 3.2, produced density values at the Qaanaaq station almost a factor of 2 larger than the measured densities. When the time of the B_z negative excursion was changed from 20 to 12 min, we obtained good

quantitative agreement between calculated and measured f_oF_2 values. This latter time interval is in accord with IMP-8 measurements.

This study leads to the following conclusions:

1. The Sondrestrom ISR detected a density structure that remained stationary within the poleward boundary of the auroral oval during a prolonged period of northward IMF B_z condition. This N_e structure was collocated with a region of sheared flows, elevated T_e values, and convergent electric fields.
2. After 1616 UT the Sondrestrom ISR measured a new pattern of velocities consisting of a poleward moving plasma, higher absolute velocity values and the initiation of a poleward motion of the density structure. These changes seem to be the manifestation of the high latitude ionosphere in response to the negative IMF B_z excursion.
3. The modeling work has helped to verify that an elongated density structure residing near the poleward boundary of the oval can be produced during IMF B_z northward conditions and remains stationary in the frame of the global pattern. The role of the precipitating particles is possibly to augment the sun-produced densities and to increase T_e . We have demonstrated that a statistical global pattern corresponding to B_z north, such as Heppner and Maynard [1987] can support the existence of a TOI protruding into the polar cap.
4. Several structures populating the polar cap can be mistakenly catalogued as polar cap patches, but instead may correspond to a duskward shifted TOI or a quasi-stationary density structure. A measurement of the plasma drift inside the structure is needed to discriminate between stationary and antisunward moving structures.
5. The modeling described here postulates that polar cap patches can be created right after B_z becomes negative and the flow inside the polar cap takes an anti-sunward orientation. A good qualitative and quantitative agreement was obtained between the model results and the Qaanaaq digisonde f_oF_2 values when the time extension of the B_z south excursion in the model was adjusted to 12 min.

Acknowledgments.

We would like to thank Jan Sojka for providing numerical values of the density at Qaanaaq under steady conditions, R. Lepping for making the IMF data available for this study, and J. Kelly for providing the Sondrestrom radar data in raw format. The work at Boston College was partially supported by Phillips Laboratory contracts F19628-90-K-0007 and F19628-88-K-0008 and by NSF grants ATM-9404088 and ATM-9613925. We thank the Danish Commission for Scientific Research in Greenland for permission to conduct ground experiments at Sondrestrom under continuing project A16-91.

References.

- Anderson, D.N., Daily variation of the ionospheric F2 equatorial anomaly in the American and Asian sectors, NCAR, Coop. Thesis, 24, 1-144, 1971.
- Anderson, D.N., A theoretical study of the ionospheric F region equatorial anomaly, I, theory, *Planet. Space Sci.*, 21, 409, 1973.
- Anderson, D.N., J. Buchau, and R.A. Heelis, Origin of density enhancements in the winter polar cap, *Radio Sci.*, 23, 513, 1988.
- Basu, Su., S. Basu, E. MacKenzie, and H.E. Whitney, Morphology of phase and intensity scintillations in the auroral oval and polar cap, *Radio Sci.*, 20, 347, 1985.
- Basu, S., Su. Basu, C. E. Valladares, E. J. Weber, J. Buchau, G. J. Bishop, and B. W. Reinisch, Coordinated observations of high latitude ionospheric turbulence, *Physics of Space Plasma* (1988), SPI Conference Proceedings and Reprint Series, 8, 137, 1989.
- Basu, Su., S. Basu, E. MacKenzie, W.R. Coley, J.R. Sharber, W.R. Hoegy, Plasma structuring by the gradient drift instability at high latitudes and comparison with velocity shear driven processes, *J. Geophys. Res.*, 95, 7799, 1990.
- Basu, S., Su. Basu, P.K. Chaturvedi, and C.M. Bryant, Jr. Irregularity structures in the cusp/cleft and polar cap regions, *Radio Sci.*, 29, 195, 1994.
- Berkey, T., L.L. Cogger, S. Ismail, and Y. Kamide, Evidence for a correlation between Sun-aligned arcs and the interplanetary magnetic field direction, *Geophys. Res. Lett.*, 3, 145, 1976.
- Buchau, J., B.W. Reinisch, E.J. Weber, and J.G. Moore, Structure and dynamics of the winter polar cap F region, *Radio Sci.*, 18, 995, 1983.
- Buchau, J., E.J. Weber, D.N. Anderson, H.C. Carlson, Jr., J.G. Moore, B.W. Reinisch, and R.C. Livingston, Ionospheric structures in the polar cap: their origin and relation to 250-Mhz scintillation, *Radio Sci.*, 20, 325, 1985.
- Buchau, J., and B.W. Reinisch, Electron density structures in the polar F region, *Adv. Space Res.*, 11, (10)29, 1991.
- Carlson, H.C., V.B. Wickwar, E.J. Weber, J. Buchau, J.G. Moore, and W. Whiting, Plasma characteristics of polar cap F-layer arcs, *Geophys. Res. Lett.*, 11, 895, 1984.
- Coley, W.R., and R.A. Heelis, Adaptive identification and characterization of polar ionization patches, *J. Geophys. Res.*, 100, 23819, 1995.
- Decker, D.T., C.E. Valladares, R. Sheehan, Su. Basu, D.N. Anderson, and R.A. Heelis, Modeling daytime F layer patches over Sondrestrom, *Radio Sci.*, 29, 249, 1994.
- de la Beaujardiere, O., J.D. Craven, V.B. Wickwar, G. Candal, J.M. Holt, L.A. Frank, L.H. Brace, D.S. Evans, and J.D. Winningham, Universal time dependence of nighttime F region densities at high latitudes, *J. Geophys. Res.*, 90, 4319, 1985.
- Foster, J.C., Storm time plasma transport at middle and high latitudes, *J. Geophys. Res.*, 98, 1675, 1993.
- Fukui, K., J. Buchau, and C.E. Valladares, Convection of polar cap patches observed at Qaanaaq, Greenland during the winter of 1989-1990, *Radio Sci.*, 29, 231, 1994.
- Heelis, R.A., J.K. Lowell, and R.W. Spiro, A model of the high-latitude ionospheric convection pattern, *J. Geophys. Res.*, 87, 6339, 1982.
- Heppner, J.P. and N.C. Maynard, Empirical high latitude electric field models, *J. Geophys. Res.*, 92, 4467, 1987.
- Kelley, M.C., J.F. Vickrey, C.W. Carlson, and R. Torbert, On the origin and spatial extent of high-latitude F region irregularities, *J. Geophys. Res.*, 87, 4469, 1982.
- Lassen, K., On the classification of high-latitude auroras, *Geofys. Publ.*, 29, 87, 1972.
- Lockwood, M., and H.C. Carlson, Production of polar cap density patches by transient magnetopause reconnection, *Geophys. Res. Lett.*, 19, 1731, 1992.

- Reiff, P.H., and J.L. Burch, IMF By-dependent dayside plasma flow and Birkeland currents in the dayside magnetosphere, 2, A global model from northward and southward IMF, *J. Geophys. Res.*, 90, 1595, 1985.
- Rodger, A.S., M. Pinnock, J.R. Dudeney, K.B. Baker, and R.A. Greenwald, A new mechanism for polar patch formation, *J. Geophys. Res.*, 99, 6425, 1994.
- Sojka, J.J. and R.W. Schunk, A theoretical study of the production and decay of localized electron density enhancements in the polar ionosphere, *J. Geophys. Res.*, 91, 3245, 1986.
- Sojka, J.J., M.D. Bowline, R.W. Schunk, D.T. Decker, C.E. Valladares, R. Sheehan, D.N. Anderson, and R.A. Heelis, Modeling polar cap F region patches using time varying convection, *Geophys. Res. Lett.*, 20, 1783, 1993.
- Sojka, J.J., M.D. Bowline, and R.W. Schunk, Patches in the polar ionosphere: UT and seasonal dependence, *J. Geophys. Res.*, 99, 14959, 1994.
- Tsunoda, R.T., High-latitude F region irregularities: a review and synthesis, *Rev. of Geophys.*, 26, 719, 1988.
- Valladares, C.E., Su. Basu, J. Buchau, and E. Friis-Christensen, Experimental evidence for the formation and entry of patches into the polar cap, *Radio Sci.*, 29, 167, 1994a.
- Valladares, C.E., H.C. Carlson, Jr., and K. Fukui, Interplanetary magnetic field dependency of stable sun-aligned polar cap arcs, *J. Geophys. Res.*, 99, 6247, 1994b.
- Valladares, C.E., D.T. Decker, R. Sheehan, and D.N. Anderson, Modeling the formation of polar cap patches using large plasma flows, *Radio Sci.*, 31, 573, 1996.
- Weber, E.J., and J. Buchau, Polar cap F-layer auroras, *Geophys. Res. Lett.*, 8, 125, 1981.
- Weber, E.J., J. Buchau, J.G. Moore, J.R. Sharber, R.C. Livingston, J.D. Winningham, and B.W. Reinisch, F layer ionization patches in the polar cap, *J. Geophys. Res.*, 89, 1683, 1984.
- Weber, E.J., J.A. Klobuchar, J. Buchau, H.C. Carlson, Jr., R.C. Livingston, O. de la Beaujardiere, M. McCready, J.G. Moore, and G.J. Bishop, Polar cap F layer patches: structure and dynamics, *J. Geophys. Res.*, 91, 121, 1986.

Figure Captions.

Figure 1. Interplanetary magnetic field data measured by IMP 8. Shown from the top are the three IMF components in GSM coordinates. Units for all three quantities are nanoteslas.

Figure 2. Low resolution plot of the plasma parameters measured by the Sondrestrom ISR on January 15, 1991 between 1145 and 1655 UT. The T_i , N_e , and T_e values were measured during the antenna EL scans during typical F-region altitude of 320 km. The vector velocities presented in the top panel were derived using the V_{los} values measured in the E- and F-regions during the radar EL scans. The vertical axis of each panel corresponds to North-South horizontal distance from the radar site.

Figure 3. Plasma parameters measured by the Sondrestrom ISR on January 15, 1991 and during 4 consecutive scans. The four geophysical parameters (T_i , V_{los} , N_e , and T_e) presented here were measured during two AZ scans and two EL scans which were interleaved between 1549:05 and 1607:19 UT. The values gathered during the AZ scans at 30° elevation are displayed in a projection to a plane tangent to the earth at the radar site. Data from the EL scans are presented in a vertical plane parallel to the magnetic meridian.

Figure 4. Similar to Figure 3, but for the period extending between 1607:20 and 1631:11 UT.

Figure 5. Same as Figure 3, but for the period extending between 1631:12 and 1655:31 UT.

Figure 6. Images at 630.0 nm from Qaanaaq, corresponding to January 15, 1991, 1250:54 - 1310:24 UT. All 6 images have been transformed to a Corrected Geomagnetic coordinate system in which the direction of the sun is toward the top of the figure and dusk is located to the left side of each frame.

Figure 7. f_oF_2 values as a function of UT on January 15, 1991, recorded at two stations: Qaanaaq and Sondrestrom. The dotted line in the upper panel presents model results of f_oF_2 values under ideal B_z south conditions.

Figure 8. Series of polar plots. (a) N_mF_2 (peak F-region density) values of the high latitude ionosphere at 1616 UT. The values in this plot were obtained by running the GTIM model for 8 h 16 min and using steady B_z north convection pattern. (b) Density values measure by the Sondrestrom ISR during the AZ scan that started at 1616:27 UT. Note the density structure in the poleward part of the scan. (c) N_mF_2 used in the simulation of section 3. The latitudinal circles are in steps of 10°.

Figure 9. Series of polar plots of the global convection patterns used in the simulations described in sections 3 and 4. (a) Heppner and Maynard [1987] DEP pattern corresponding to B_z north conditions. (b) Heelis-type pattern for $B_y=+6$ nT, cross polar cap potential of 90 kV and 10° of polar cap radius. (c) H-M DEPP pattern for B_z north conditions and potential multiplied by a factor of 2.

Figure 10. Each panel presents N_mF_2 values of a section of the high latitude ionosphere at times after the simulation of the patch initiation. The white dot near the bottom of each panel corresponds to the location of the Qaanaaq station. The white line near the left side of the panels indicates the extension of the elevation scans of Figures 3, 4 and 5.

Figure 11. Simulated radar azimuth scans through the volumes displayed in Figure 10. Each panel shows an instantaneous scan of the density around Sondrestrom at the UT indicated in the panels.

Figure 12. The solid line in each panel represents the critical frequency of the F-region peak (f_oF_2) as a function of universal time at Qaanaaq, on January 15, 1991. The dotted lines in both panels correspond to modeled values of the f_oF_2 index for different values of the (a) polar cap potential and (b) time extension of the B_z south excursion.

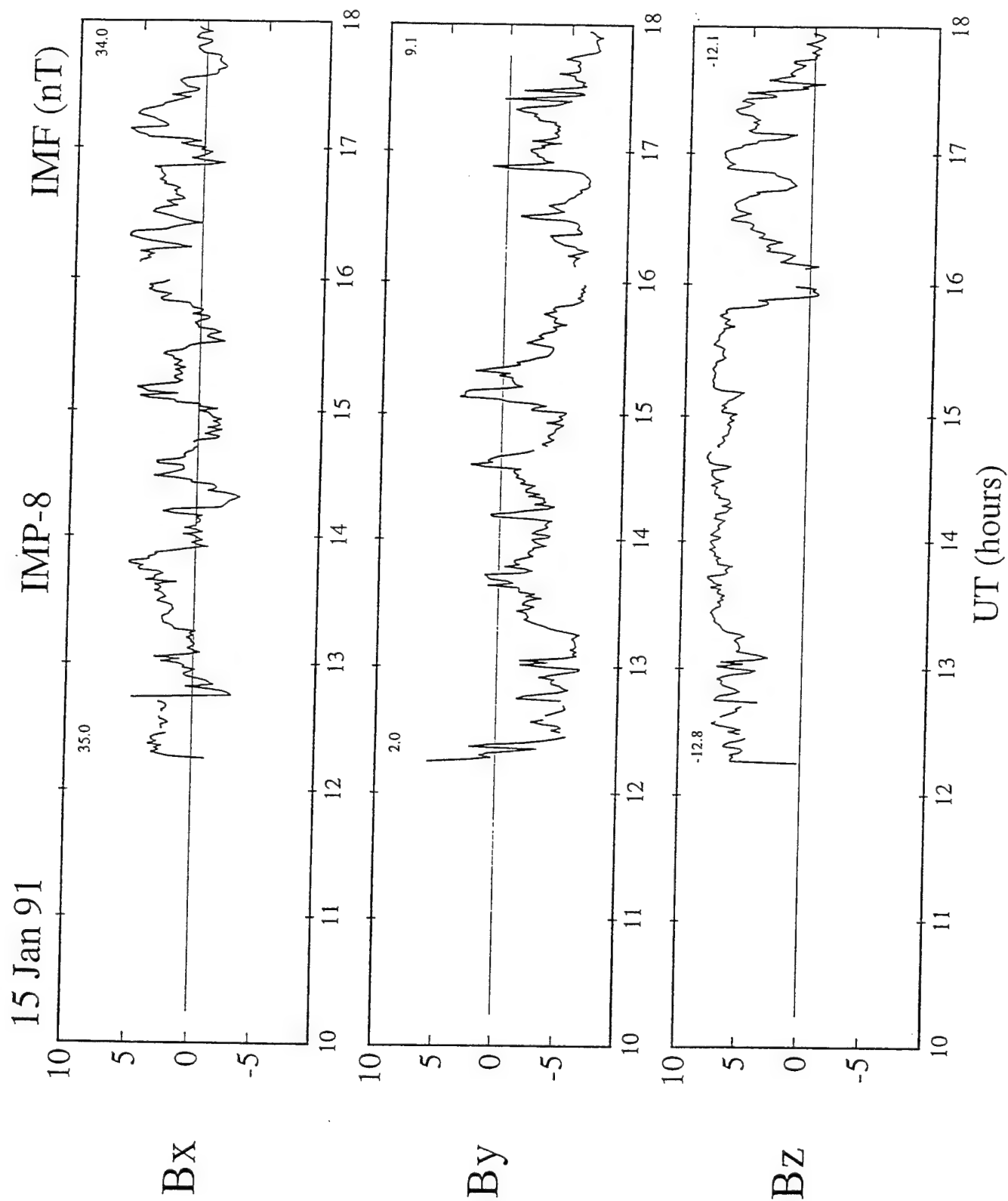


Figure 1

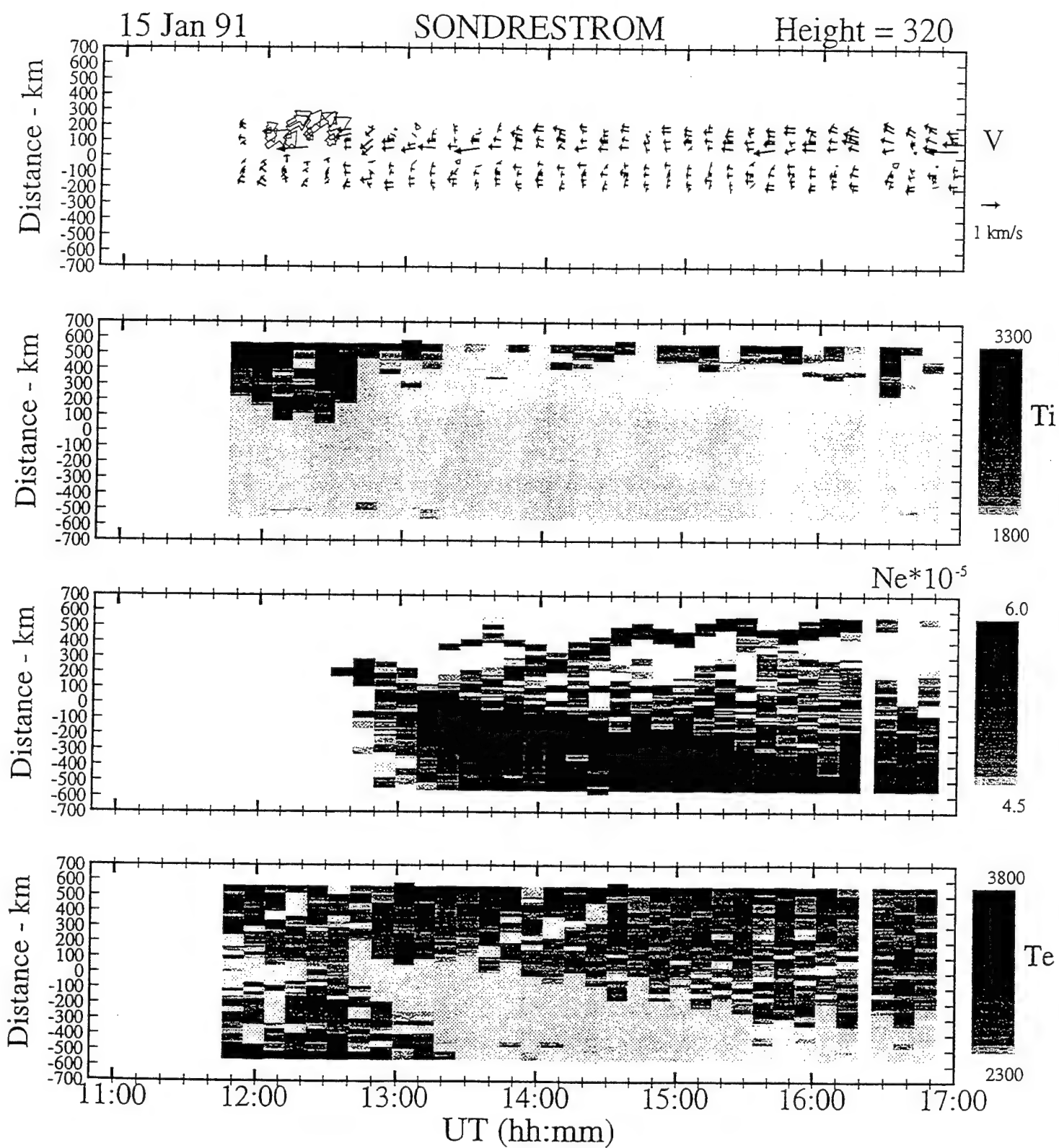


Figure 2

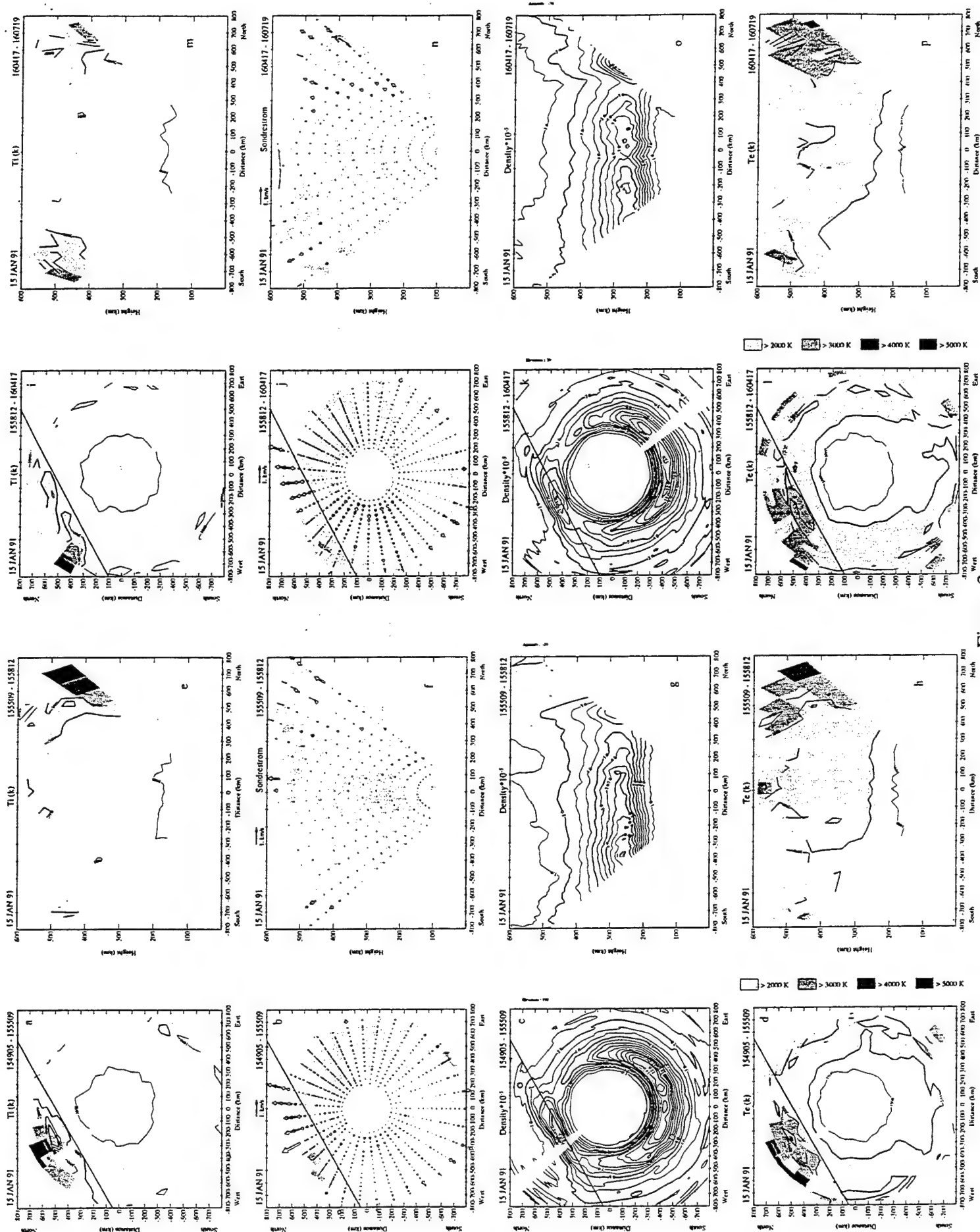


Figure 3.

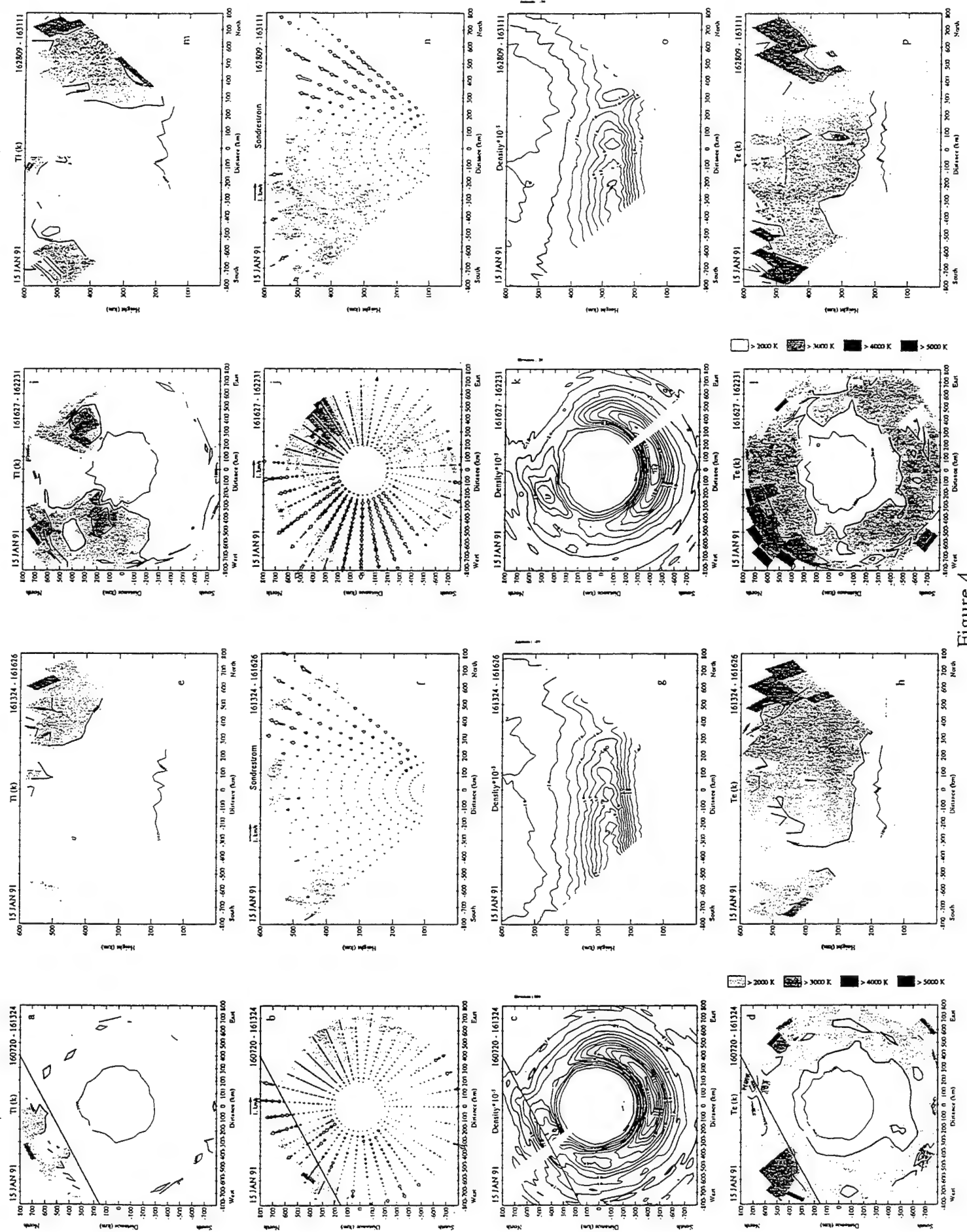


Figure 4.

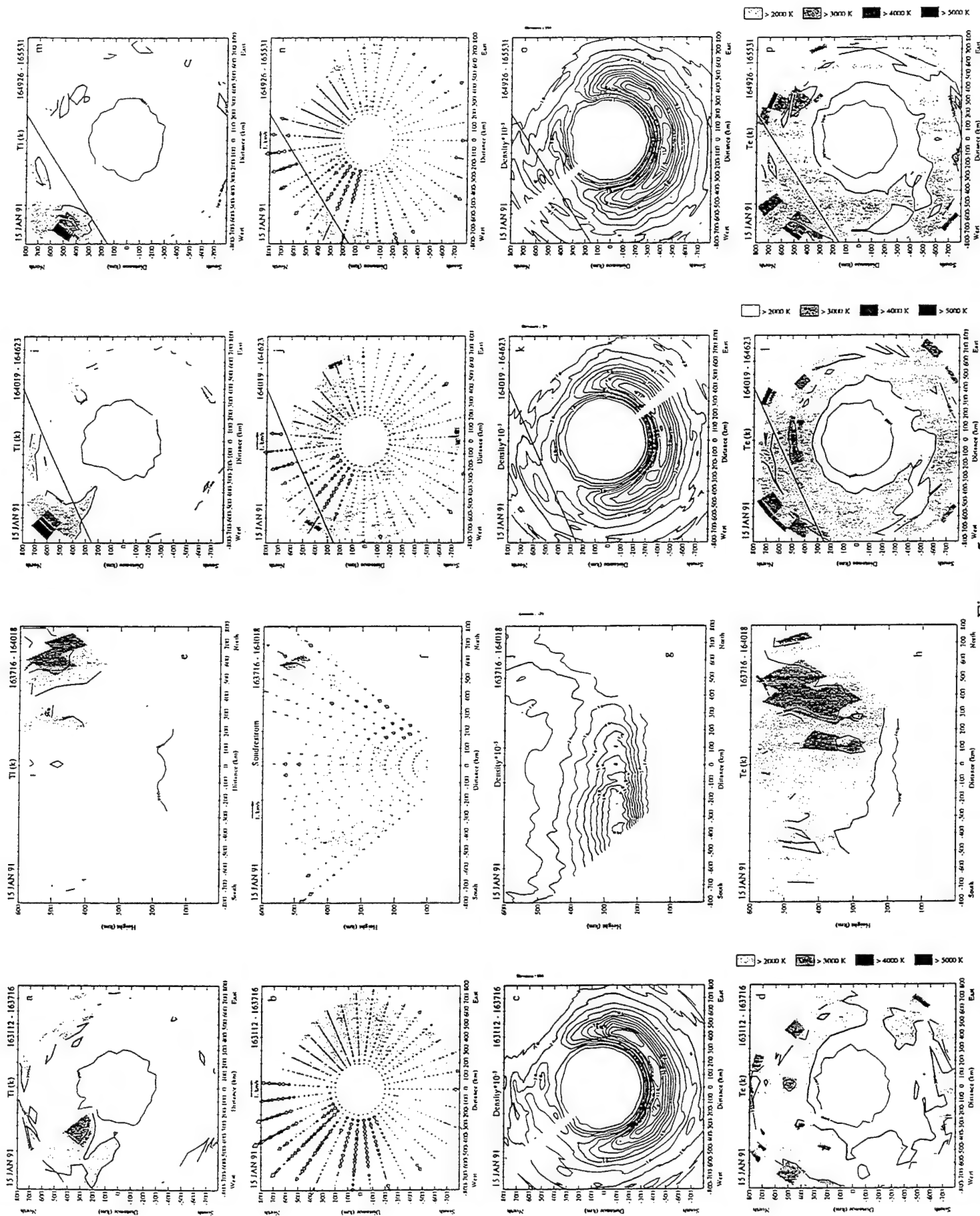


Figure 5.

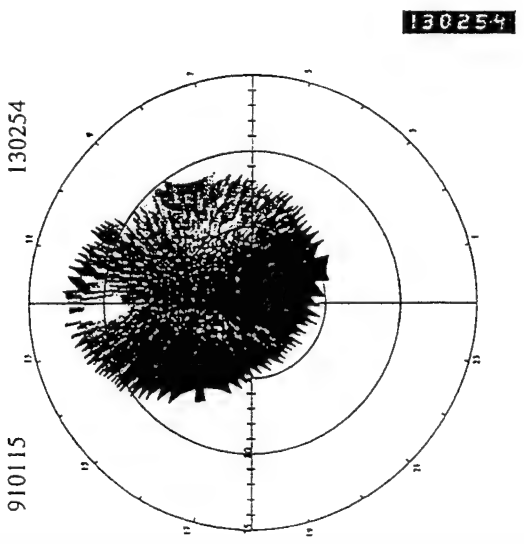
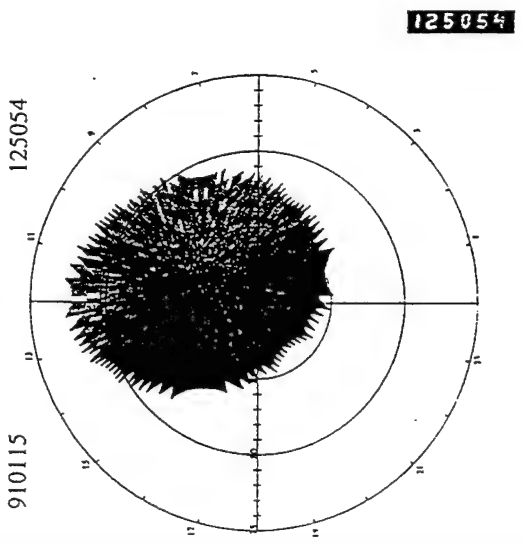
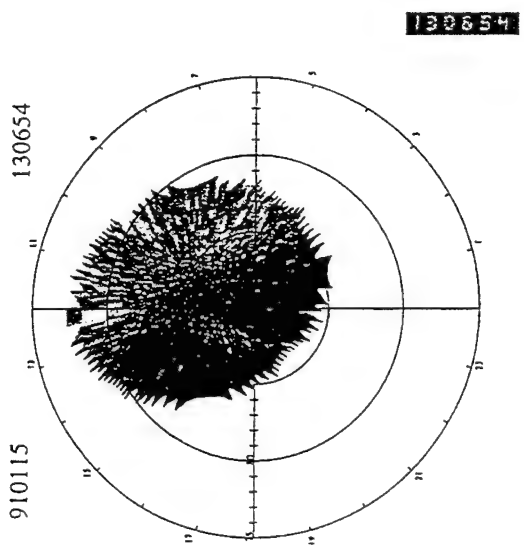
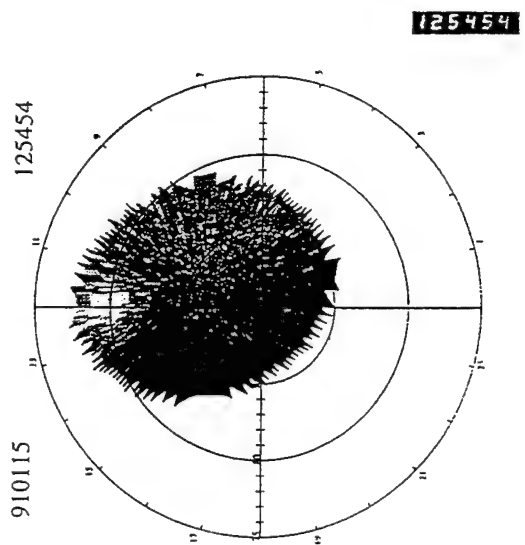
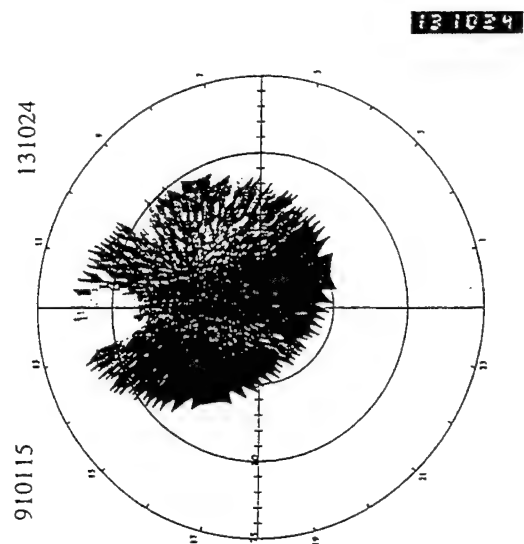
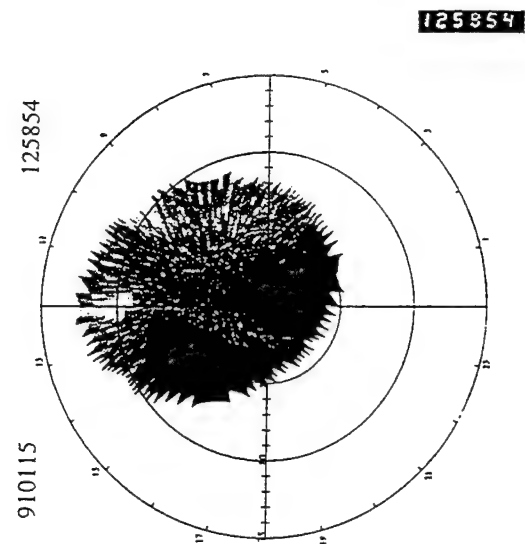


Figure 6.

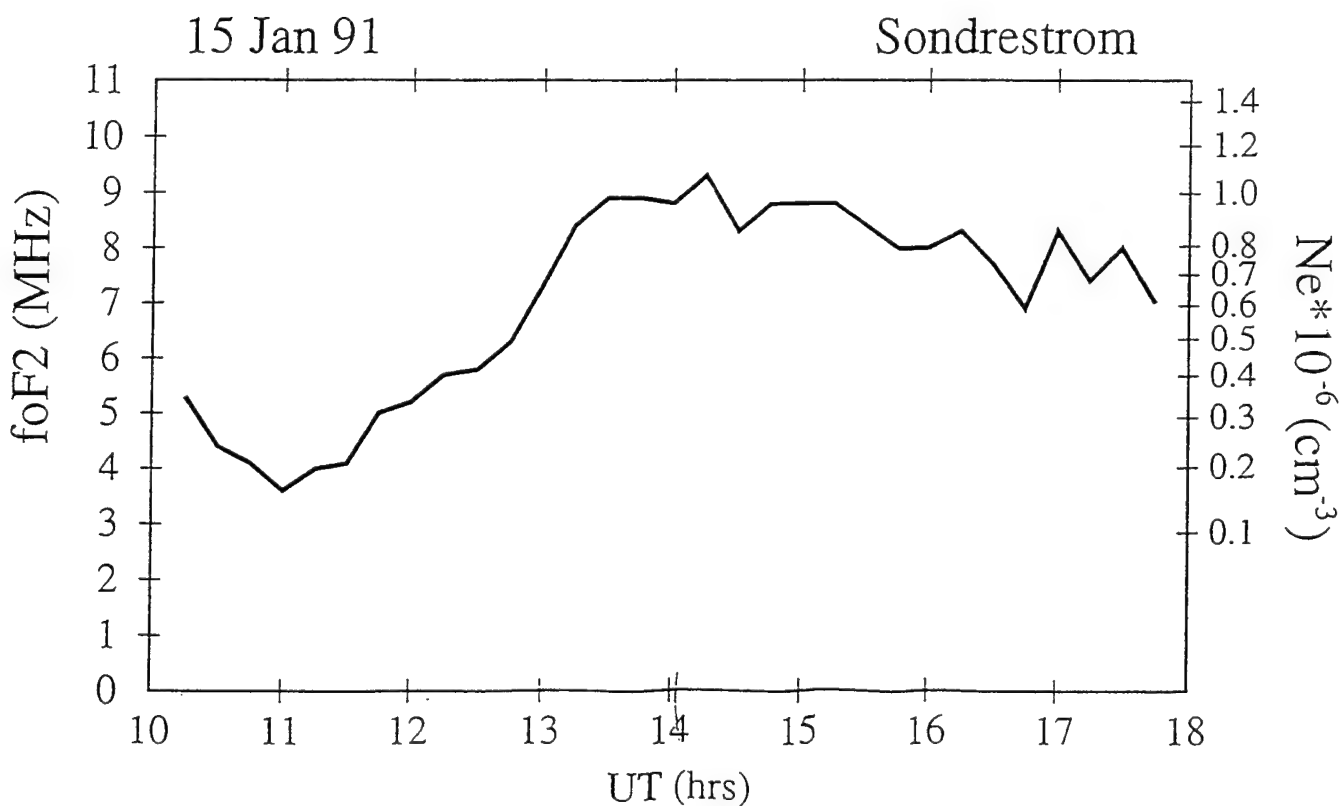
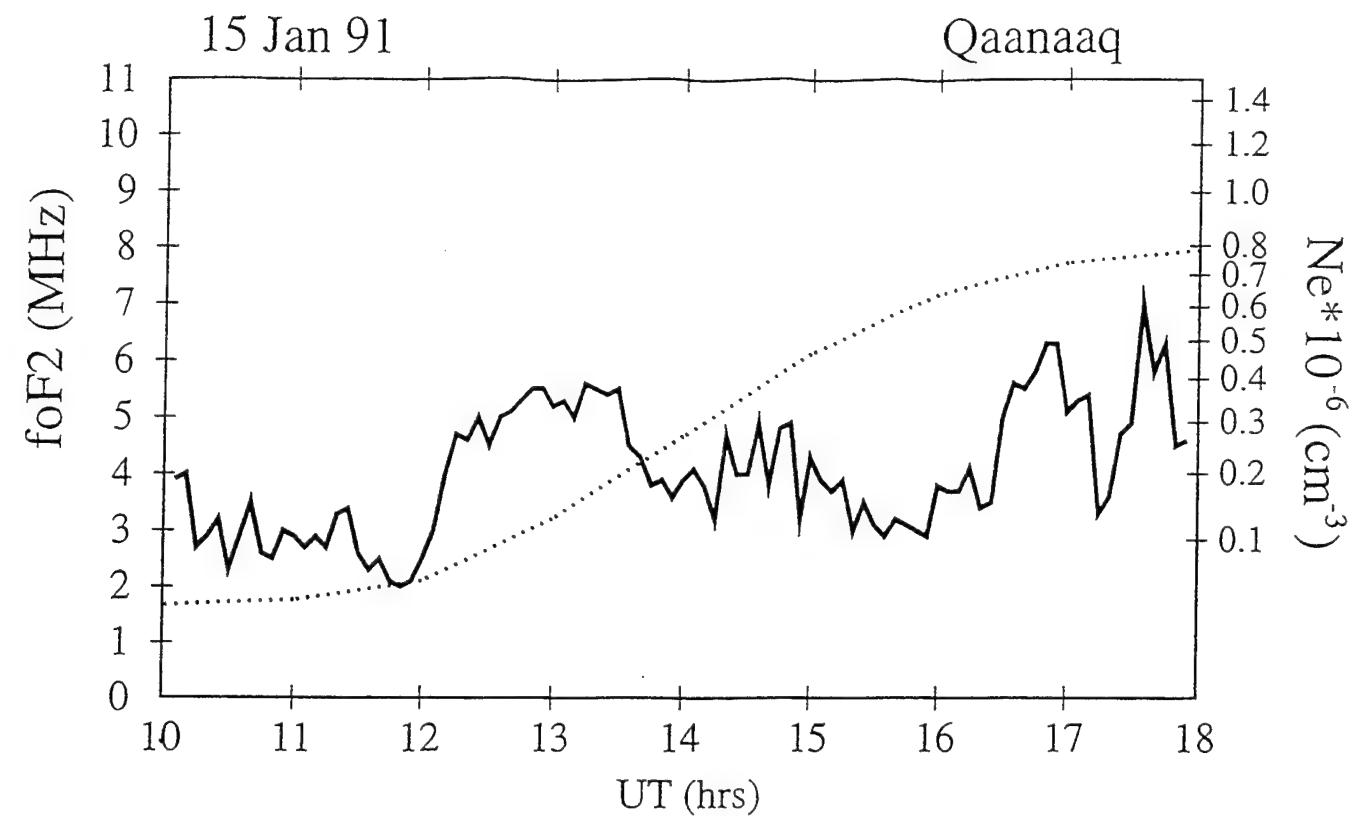


Figure 7.

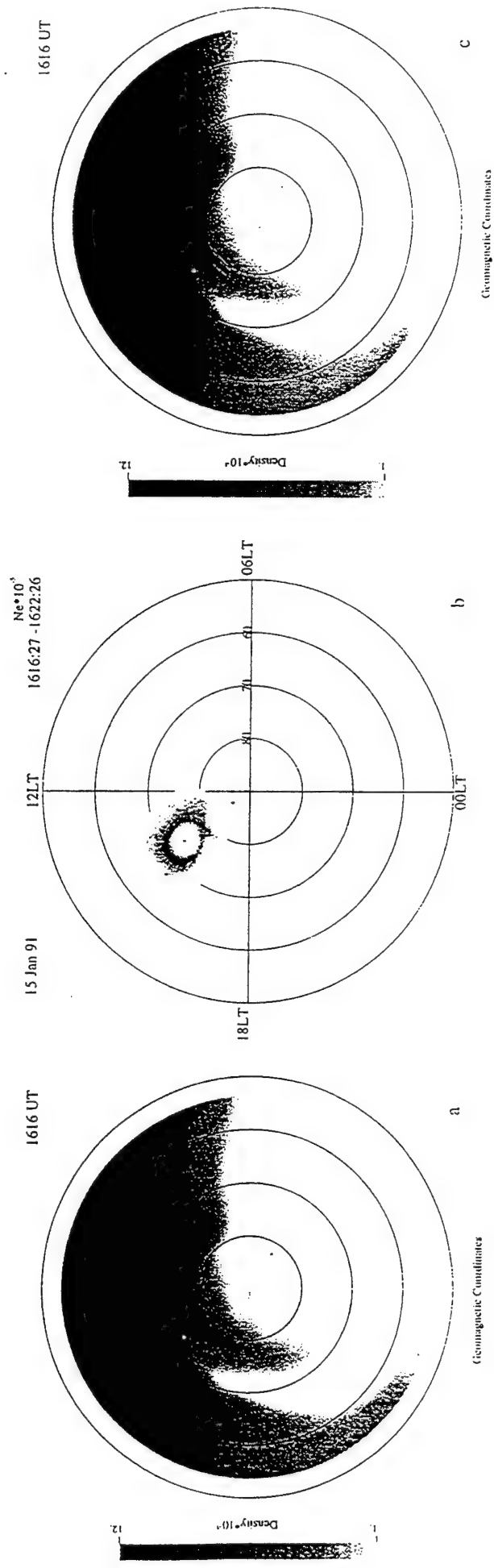


Figure 8.

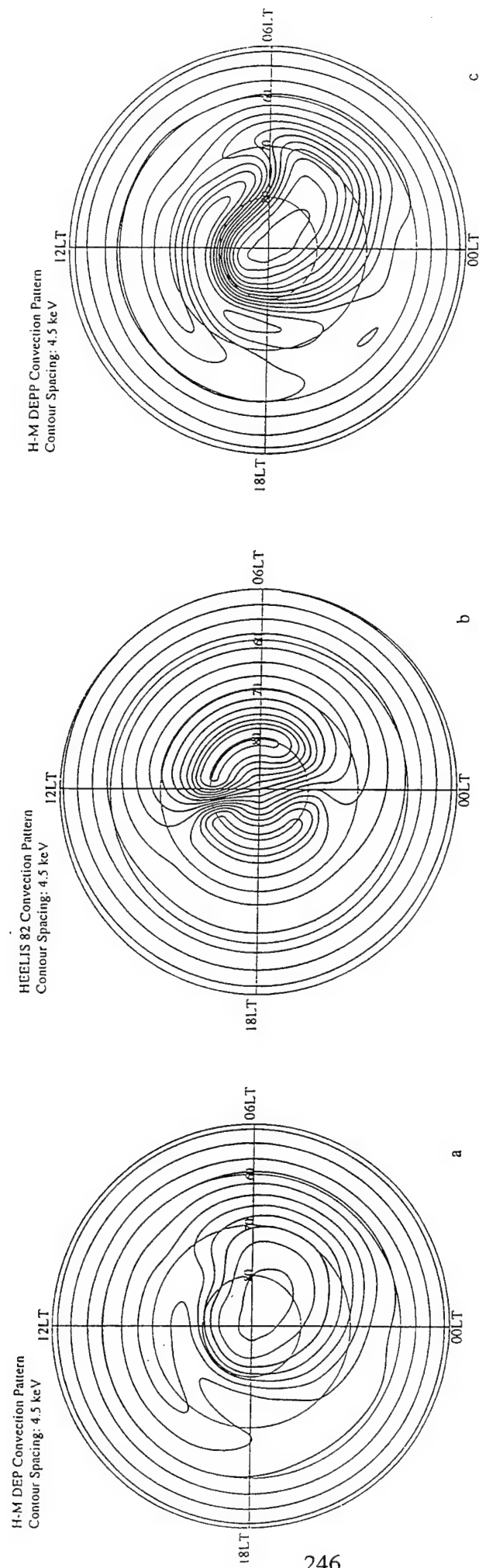


Figure 9.



Geomagnetic Coordinates
Figure 10.

90kV 10d+6B y0.3.7x2

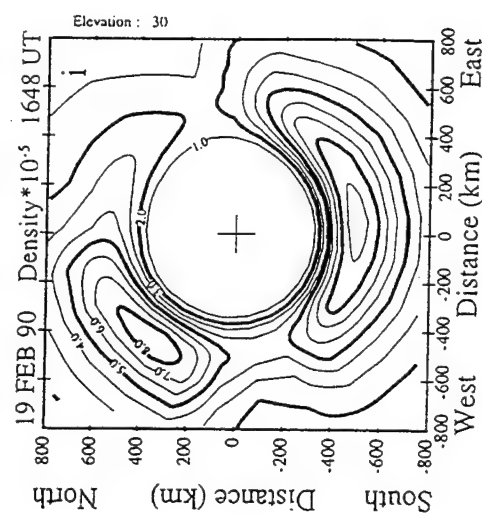
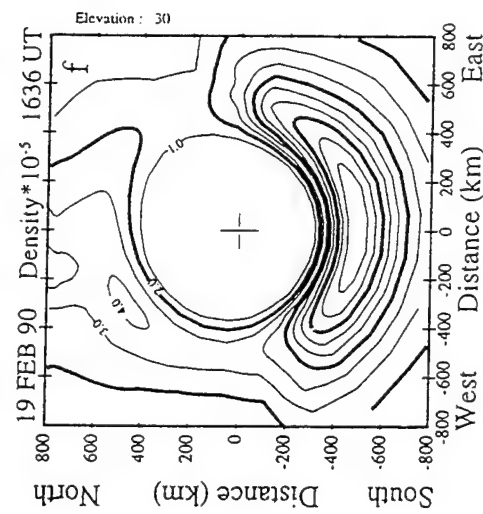
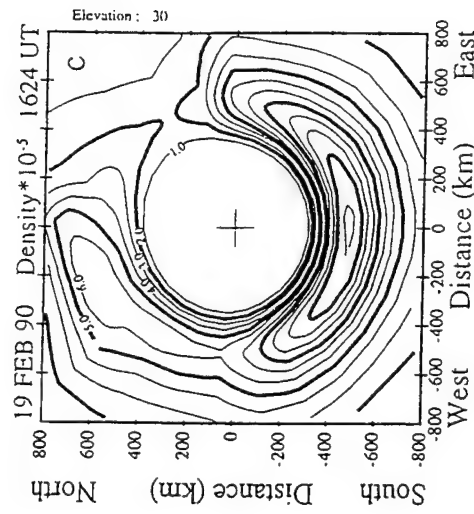
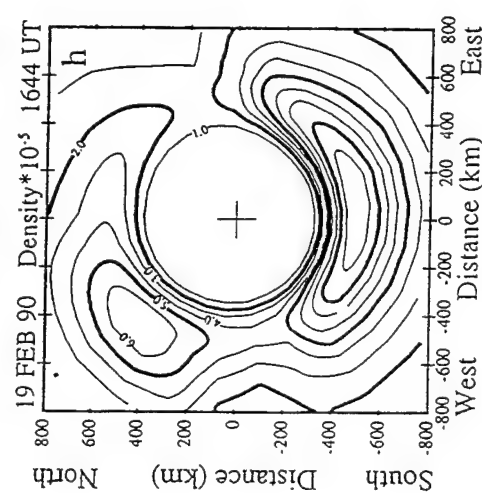
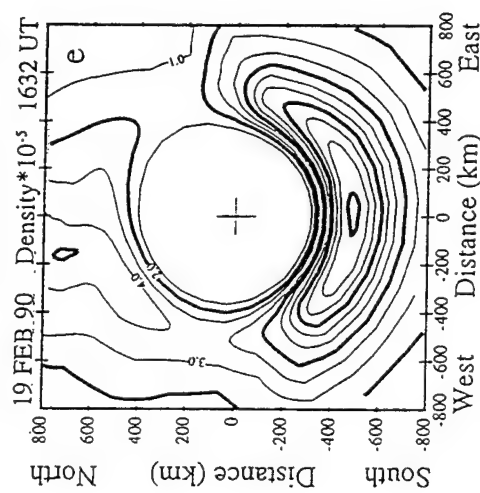
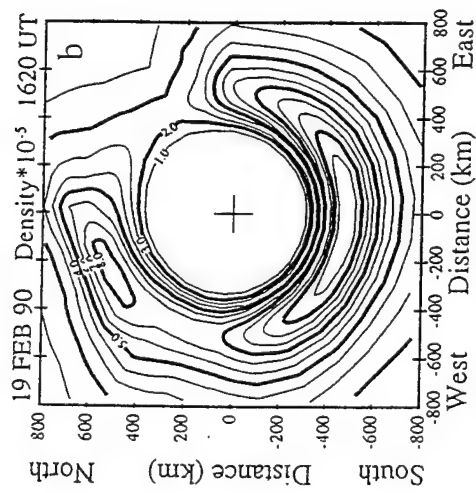
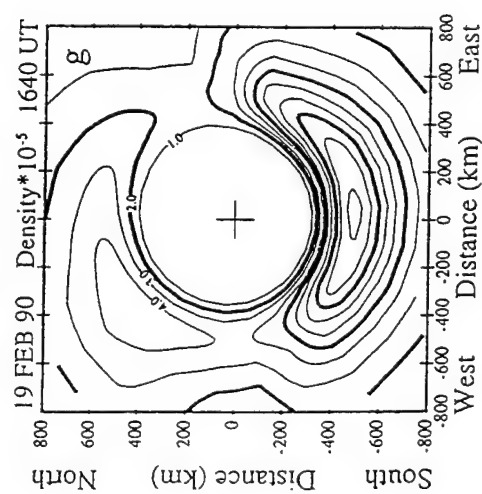
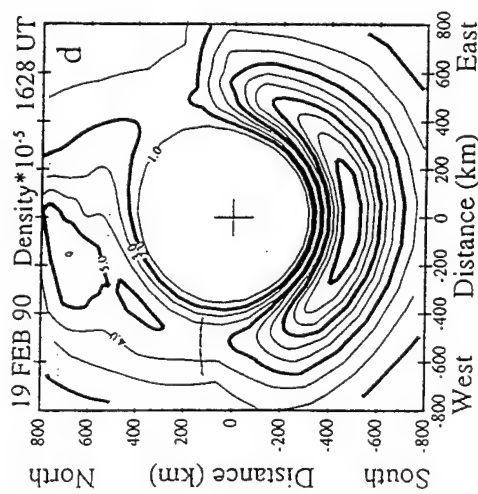
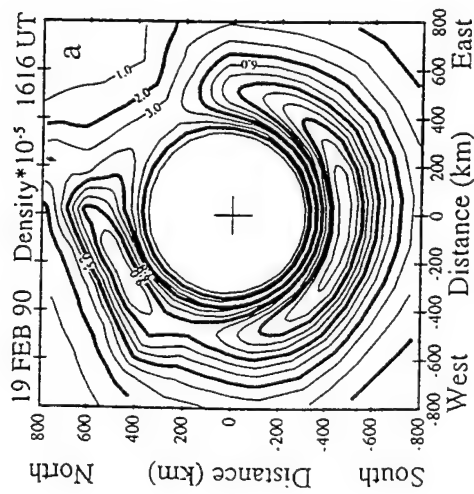


Figure 11.

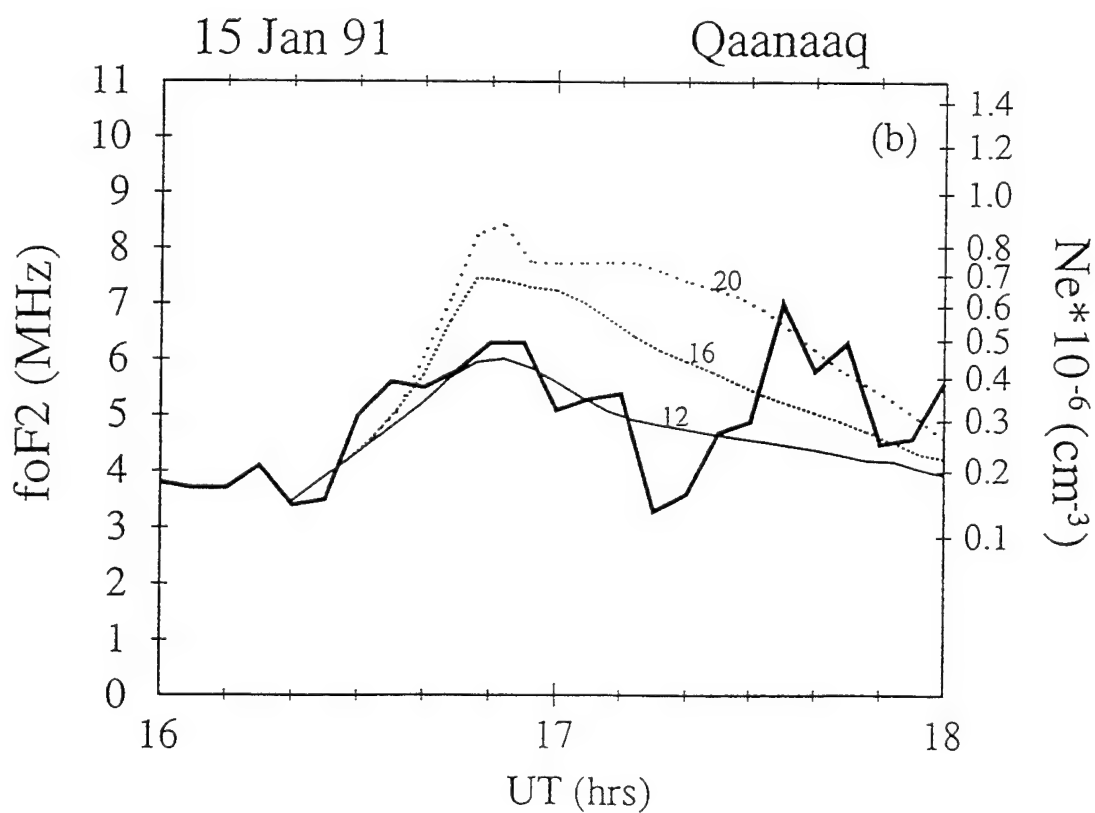
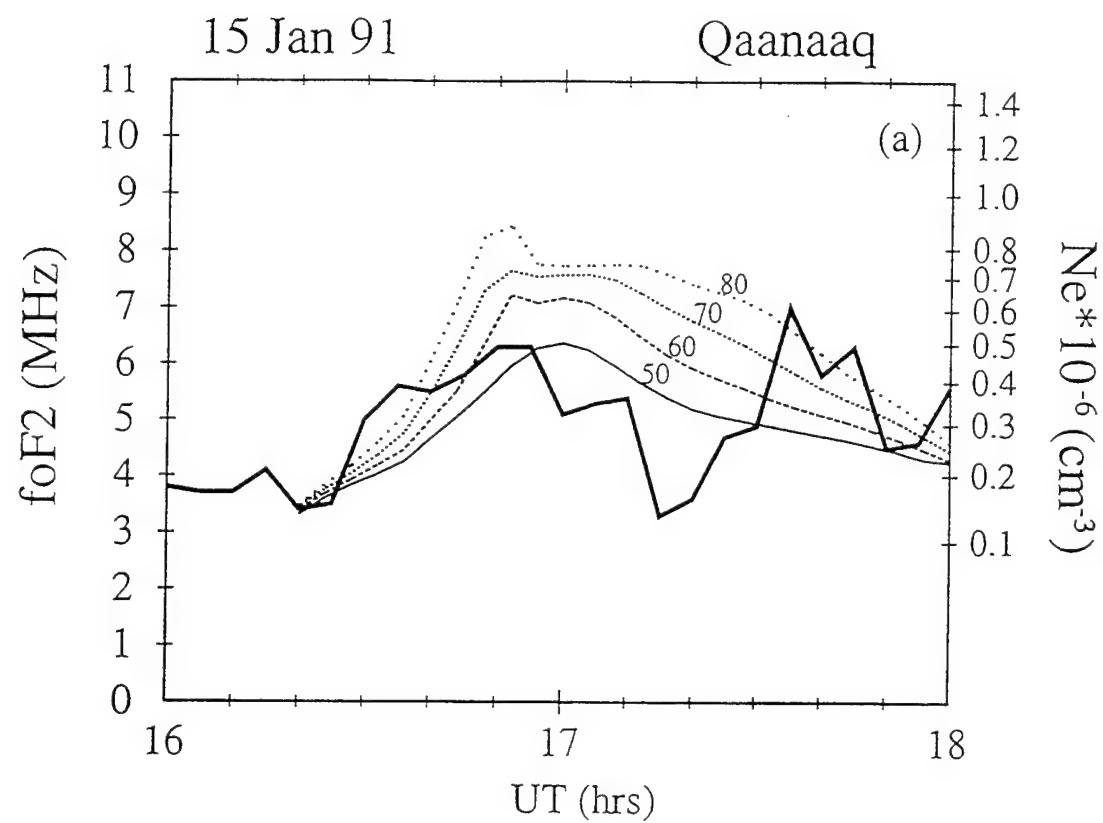


Figure 12

Remote Sensing of Auroral *E* Region Plasma Structures by Radio, Radar, and UV Techniques at Solar Minimum

SUNANDA BASU,^{1,2} S. BASU,³ R. EASTES,³ R. E. HUFFMAN,³ R. E. DANIELL,⁴ P. K. CHATURVEDI,⁵
C. E. VALLADARES,¹ AND R. C. LIVINGSTON⁶

The unique capability of the Polar BEAR satellite to simultaneously image auroral luminosities at multiple ultraviolet (UV) wavelengths and to remote sense large-scale (hundreds to tens of kilometers) and small-scale (kilometers to hundreds of meters) plasma density structures with its multifrequency beacon package is utilized to probe the auroral *E* region in the vicinity of the incoherent scatter radar (ISR) facility near Sondrestrom. In particular, we present coordinated observations on two nights obtained during the sunspot minimum (sunspot number < 10) January–February 1987 period when good spatial and temporal conjunction was obtained between Polar BEAR overflights and Sondrestrom ISR measurements. With careful coordinated observations we were able to confirm that the energetic particle precipitation responsible for the UV emissions causes the electron density increases in the *E* region. These *E* region electron density enhancements were measured by the ISR at Sondrestrom. The integrations up to the topside of these ISR electron density profiles were consistent with the total electron content (TEC) measured by the Polar BEAR satellite. An electron transport model was utilized to determine quantitatively the electron density profiles which could be produced by the particle precipitation, which also produced multiple UV emissions measured by the imager; these profiles were found to be in good agreement with the observed ISR profiles in the *E* region. Surprisingly large magnitudes of phase and amplitude scintillations were measured at 137 and 413 MHz in the regions of TEC enhancements associated with the particle precipitation. Steep phase spectral slopes with spectral index of 4 were found in these regions. Strength-of-turbulence computations utilizing the ISR electron density profiles and observed characteristics of phase and amplitude scintillations are interpreted in terms of an irregularity amplitude varying between 10 and 20% at a several-kilometer outer scale size in the *E* region extending approximately 50 km in altitude. This outer scale size is also consistent with the measured phase to amplitude scintillation ratio. An estimate of the linear growth rate of the gradient-drift instability in the *E* region shows that these plasma density irregularities could have been generated by this process. The mutual consistency of these different sets of measurements provides confidence in the ability of the different techniques to remote sense large- and small-scale plasma density structures in the *E* region at least during sunspot minimum when the convection-dominated high-latitude *F* region is fairly weak.

1. INTRODUCTION

The Polar Beacon Experiment and Auroral Research (Polar BEAR) spacecraft was launched on November 13, 1986, into a 90° inclination, nearly circular orbit of 1000-km altitude. The satellite was sponsored by the Defense Nuclear Agency (DNA) and was the first satellite to have the capability of remote sensing by imaging of auroral luminosities at multiple ultraviolet (UV) and optical wavelengths, as well as by providing multifrequency scintillations and total electron content (TEC) measurements associated with the auroral emission regions. The Polar BEAR UV imager operated until May 1989, and the data base contains about 6000 images [DelGreco *et al.*, 1988, 1989].

Polar BEAR's predecessor, HiLat, had been launched with similar capability, but unfortunately, the imager failed after about 50 images were taken [Huffman *et al.*, 1985] and before any ground stations for beacon measurements be-

came operational. The HiLat satellite was, however, able to provide in situ measurements of the particles, fields, and currents that can lead to high-latitude irregularities, simultaneously with direct radio beacon observations of the scintillations they produce [Fremouw *et al.*, 1985a]. The combined in situ and beacon package on HiLat has produced much new insight into sources of free energy responsible for high-latitude irregularity generation, and their morphology, anisotropy, and dynamics [Basu *et al.*, 1986, 1987, 1988a; Basinska *et al.*, 1987; Bythrow *et al.*, 1984; Fremouw *et al.*, 1985b; Tsunoda *et al.*, 1985, 1989; Vickrey *et al.*, 1986; Valladares *et al.*, 1989; Costa *et al.*, 1988; Keskinen *et al.*, 1988; MacDougall, 1990].

It is the object of this paper to utilize the remote sensing capability of Polar BEAR to diagnose a class of large- and small-scale plasma structures (order of hundreds of kilometers to hundreds of meters) in the auroral *E* region near Sondrestrom. The UV imager on Polar BEAR, known as AIRS, was used to sense the emission regions which are associated with particle precipitation. An electron transport model originally generated for optical emissions [Strickland *et al.*, 1976] and modified to include vacuum ultraviolet (VUV) emissions [Strickland *et al.*, 1983] is used to determine quantitatively the electron density profiles which would be produced by particle precipitation generating such UV emissions. It should be pointed out that the analysis of the AIRS UV data carried out here is similar to that reported by Robinson *et al.* [1992], except that they used intensities at 391.4 nm instead of 159.6 nm. Rees *et al.* [1988] and Steele *et*

¹Institute for Space Research, Boston College, Newton, Massachusetts.

²Now at National Science Foundation, Washington, D. C.

³Phillips Laboratory, Hanscom Air Force Base, Massachusetts.

⁴Computational Physics, Inc., Newton, Massachusetts.

⁵Space Plasma Branch, Plasma Physics Division, Naval Research Laboratory, Washington, D. C.

⁶SRI International, Menlo Park, California.

al. [1992] performed similar analyses of DE 1 and Viking images, although the broad bandwidths of the filters used in those instruments make spectral analysis difficult. The techniques used to deduce electron densities from UV data are fundamentally the same as those used to deduce electron densities from ground-based observations at visible wavelengths. The latter techniques have been described by *Strickland et al.* [1989] and *Rees and Lummerzheim* [1989].

Other objectives of this paper are to utilize the TEC and scintillation measurements from Polar BEAR to determine the integrated effect of the large-scale (tens to hundreds of kilometers) and small-scale (several kilometers to hundreds of meters) irregularities created directly by the particle precipitation or through plasma instabilities. The Sondrestrom incoherent scatter radar (ISR) data of electron densities are used to calibrate the absolute value of the TEC obtained from the beacon measurements. These densities are also compared to the model electron density profiles obtained from the Polar BEAR measured UV emissions to determine how well the modeled values simulate the actual measurements. Finally, the plasma density gradients and convection velocities measured by the ISR at Sondrestrom together with predicted values of the neutral winds obtained from the National Center for Atmospheric Research (NCAR) thermospheric general circulation model (TGCM) are utilized to compute the growth rates of the small-scale *E* region irregularities (several kilometers to hundreds of meters) created by the gradient drift instability in the linear regime [*Fejer and Kelley*, 1980; *Keskinen and Ossakow*, 1983]. Thus with this coordinated set of satellite- and ground-based measurements we hope to establish the capability of Polar BEAR to remote sense a class of large- and small-scale *E* region irregularities which can produce substantial degradation in communications and radar systems. We wish to point out that this type of remote sensing may only be effective during sunspot minimum conditions when the convection-dominated high-latitude *F* region is weak compared to the particle precipitation induced densities in the *E* region. Such conditions are commonly encountered during the low sunspot phase of the solar cycle.

2. INSTRUMENTATION

The Polar BEAR satellite was instrumented with a visible and UV imager known as the auroral ionospheric remote sensor (AIRS) which could measure emissions simultaneously at up to four wavelengths [*Schenkel et al.*, 1986; *Schenkel and Ogorzalek*, 1987]. The AIRS instrument was designed to be operated at two wavelengths in the far-ultraviolet (FUV), such as at 135.6 nm and 159.6 nm, as was the case for the data used in this paper, and also at two wavelengths in the near-UV and visible channels, with most of these images at N_2^+ 391.4 nm. In the imaging mode a spatial resolution of 5.7 km (cross-track) \times 23 km (along track) was achieved, assuming an emission altitude of 120 km, the total cross-track coverage being 5200 km in 3 s. The image is acquired line by line, with one image for each polar orbit. The satellite developed attitude problems when it entered the first period of full sunlight in March 1987 [*Hunt and Williams*, 1987]. Thus, for careful coordinated measurements between space and ground it was important to use data prior to such oscillations.

The Beacon Experiment on Polar BEAR was identical to

that mounted on HiLat [*Cousins et al.*, 1984] and similar to that described in detail by *Fremouw et al.* [1978] for Wideband. The major difference was that an S band signal was used as phase reference in Wideband while an L band signal was used for that purpose in HiLat and Polar BEAR. The phase and amplitude scintillations were obtained in the VHF and UHF bands with respect to the L band signal while the TEC was determined by utilizing a comb of three frequencies in the UHF band. The object of this study was to determine the TEC and scintillation structures along the ray path from Polar BEAR to the ground station at Sondrestrom when the AIRS imager was able to sense UV emissions close to its nadir position. Spectral analysis of the phase scintillation data, in particular, provides information regarding the nature of the hundreds of meter-scale irregularities associated with such auroral emission.

The ISR at Sondrestrom has been described by *Kelly* [1983] and *Wickwar et al.* [1984]. In general, the radar was scheduled to provide coverage to the high-elevation Polar BEAR passes. Usually, the radar made elevation scans close to the foot of the field line of the Polar BEAR overflight. Such measurements provide both electron density and background convection measurements. On some other occasions the radar was held stationary, pointed along the local magnetic field in support of other auroral experiments. In this latter case, only electron density measurements are available.

3. OBSERVATIONS

We present Polar BEAR overflights of the Sondrestrom ISR obtained on two evenings with fairly moderate magnetic activity early in the life of the satellite. The dates when these coordinated measurements were available occurred on January 24, 1987, near 0210 UT when $Kp = 2$ and on February 28, 1987, near 0020 UT when $Kp = 3$. The sunspot number during this period was very low, with the monthly mean being 10 for January 1987 and only 2 for February 1987. In the following subsections we describe the different coordinated data sets and the electron density modeling effort from the VUV emissions. Finally, in section 4 we present evidence for the gradient-drift instability in the *E* region as a plausible mechanism for generating the several kilometer- to hundreds of meter-scale irregularities which cause the phase and amplitude scintillations.

3.1. Event of January 24, 1987

AIRS image. The Polar BEAR AIRS false-color image of O I 135.6 nm for this event is shown in Plate 1. The image is projected on the map of Greenland and surrounding regions by considering that the emission layer height is 110 km. The auroral oval is prominently displayed, with the area near 50°W longitude showing diffuse aurora of intensity approximately 0.5 kR in the equatorward region with discrete arc structures of approximately 1.5 kR intensity at the poleward edge. These arcs were found to be quite stable as their position remained unchanged in an ISR elevation scan taken 5 min prior to the Polar BEAR pass. The solid line is the *E* region (110 km) intercept of the ray path from Polar BEAR to the ground station at Sondrestrom, while the dashed line is the track of the ISR elevation scan in the magnetic meridian plane. It is readily apparent that both the scan and the intercept cut across the stable auroral arc

features at the poleward edge of the oval. Although not shown as a plate, an image at the N₂ Lyman-Birge-Hopfield (LBH) band (159.6 nm) was obtained simultaneously with that shown in Plate 1. We will present in detail the nature of the UV emissions at 135.6 and 159.6 nm associated with these structures as part of the electron density modeling effort based on these emissions later in the paper.

Polar BEAR beacon measurements. The TEC increase and scintillations caused by the ionization due to these precipitation features are presented in Figure 1. The phase and amplitude scintillations at 137 MHz are shown in the top panel with the slant TEC, and its equivalent vertical content is shown in the bottom panel. The background TEC is quite small, about 1 TEC unit ($= 10^{16}$ el m⁻²). Superposed on this is an increase to 3 TEC units in the vertical content centered at approximately 0210 UT, with the increase largely between 0209 and 0211 UT, which covers a distance of 100 km at *E* region altitudes.

A prominent phase scintillation structure is colocated with the TEC enhancement. The phase scintillation is computed over 30 s of data with 15-s overlap between data lengths. Because of the large time window used and the approximately 1 km s⁻¹ velocity of the ray path through the *E* region, it is expected that TEC changes over tens of kilometers would be reflected in the phase scintillations. The other peak at 0211:48 UT at the location where the ray path from the satellites makes the minimum angle with the local *L* shell is due to *L* shell-aligned sheetlike irregularities, first identified from Wideband data [Rino *et al.*, 1978]. The origin of this peak is thus geometrical in nature.

The surprising aspect of the scintillation data is the paucity of amplitude scintillations in both the source enhancement and geometrical enhancement regions. The low level of the amplitude scintillation data seems to indicate that there is little power at scales smaller than the Fresnel dimension, which in this case is 1 km. The dearth of power at the small scales becomes less surprising when one considers the phase spectral slope, which is plotted as a function of time in Figure 2. We note that the spectral slope is very steep in the region of the phase scintillation enhancement, of the order of 4, which would indicate that the three-dimensional spectral slope of the irregularities is 5. The spectra were computed using 15-s samples digitized at 50 Hz and utilizing the maximum entropy (MEM) technique using 40 filter weights. A detailed discussion of the MEM technique and its application to scintillation data have been provided by Fougere [1985]. A particular spectral sample obtained at 0209:18 UT is shown in Figure 3. The slope is fitted between 0.2 and 2.0 Hz, which considering the satellite velocity is equivalent approximately to the scale length range 5 km to 500 m and, given the spectral index, the power at 500 m is 40 dB less than that at 5 km. The moderate level of turbulence at the kilometer scales coupled with the steep spectral slope produces little power at the shorter scales that give rise to amplitude scintillation. Moreover, the maximum elevation for the Polar BEAR pass is 60°, so that the geometrical enhancement is due to sheetlike irregularities which are more effective in giving rise to large phase scintillations [Fremouw *et al.*, 1985b]. We will show with the February 28 case study that when the level of turbulence is much larger at the kilometer scales, it is possible to have amplitude scintillations in spite of a steep spectral index for the irregularities. In an earlier study, Kelley *et al.* [1980] using

the Wideband satellite found phase spectral slopes varying between 2 and 3 in a similar auroral zone study and attributed the scintillations to *F* region irregularities.

ISR measurements. The TEC and scintillation measurements provide an integrated response to the ionization created by the particle precipitation, which also is responsible for the UV emissions. However, in order to determine the exact region within the ionosphere where the ionization is created and to estimate the horizontal electron density gradients and plasma drifts associated with such an ionization region, we used elevation scans made by the Sondrestrom ISR to cover the Polar BEAR overflights. The elevation scan closest in time to the Polar BEAR pass is shown in Figure 4. The elevation scan was made between 0206:56 and 0211:56 UT at an azimuth of 141°. A prominent electron density structure with maximum of approximately 4.5×10^5 cm⁻³ is seen in the *E* region centered at a distance of 100 km south of Sondrestrom, which is colocated with the UV emission feature at the poleward edge of the oval and the TEC enhancement measured by Polar BEAR. Actually, the satellite orbit was such that both the elevation and azimuth of the satellite in the enhancement region matched that of the ISR elevation scan in the density structure. There are no density structures in the *E* region poleward of Sondrestrom, and the *F* region is quite featureless with maximum density of 5×10^4 cm⁻³. Figure 5 represents the reconstructed vertical electron density profile through the center of this enhancement using the elevation scans. While the profile is shown to 300 km, the integration to 450 km yields a TEC of 3 units, which agrees well with the equivalent vertical TEC measured by Polar BEAR up to a height of 1000 km shown in Figure 1. The maximum density in the *E* region is 4.7×10^5 cm⁻³ while that in the *F* region is 10^5 cm⁻³. It is important to note that while the integrated density of the *F* region exceeds that of the *E* region, the effect of the latter is expected to be greater on irregularity generation because of the presence of the sharp horizontal density gradient visible in the radar elevation scan shown in Figure 4. The *F* region, on the other hand, is both low in density and devoid of any correspondingly significant density gradients. An estimation of the growth rate of irregularities in the *E* region based on density gradients and plasma drifts with respect to the neutral medium will be provided in section 4.

Modeling of electron density profiles from AIRS image. The AIRS data are available in the form of smoothed counts at 159.6 nm (designated detector 1), due to N₂ LBH band emission, and 135.6 nm (designated detector 2), due to O I, and unsmoothed counts at 135.6 nm as a function of position of the 110-km intersection of the line of sight between Polar BEAR and the ground station at Sondrestrom. Such a diagram for the image shown in Plate 1 is presented in Figure 6. It is immediately evident from the unsmoothed detector 2 output that the 110-km ray path cuts through two discrete arcs of intensity greater than 1 kR which appear as two blue and yellow features at the poleward edge of the auroral oval in the false-color image of Plate 1. We concentrate on the poleward of the two arcs, as that is the only one which the Sondrestrom ISR could completely probe at a distance 100 km to the south of the station. The equatorward arc was too far south of the radar to be probed fully by the elevation scan at *E* region altitudes, as may be observed from Figure 4. Thus only for the poleward arc is there the possibility of

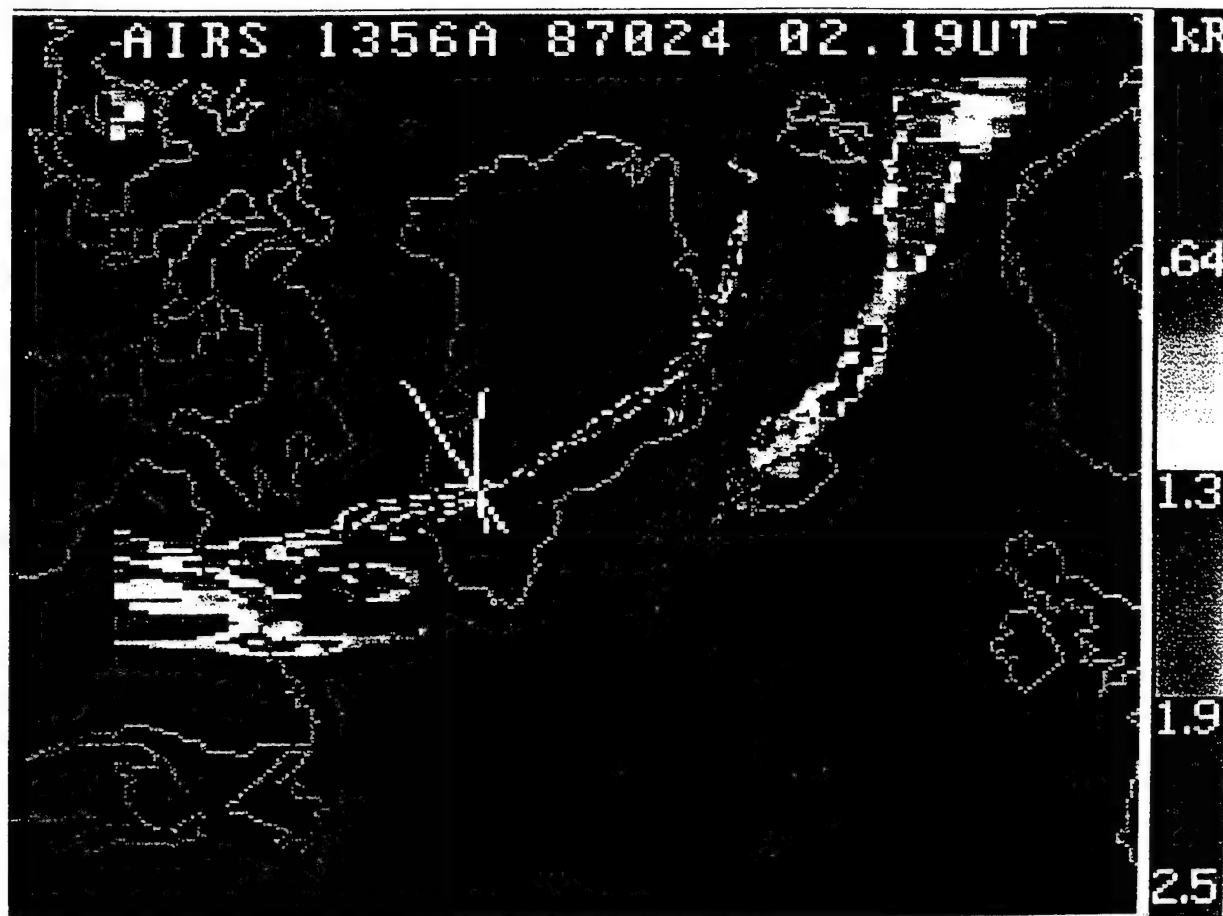
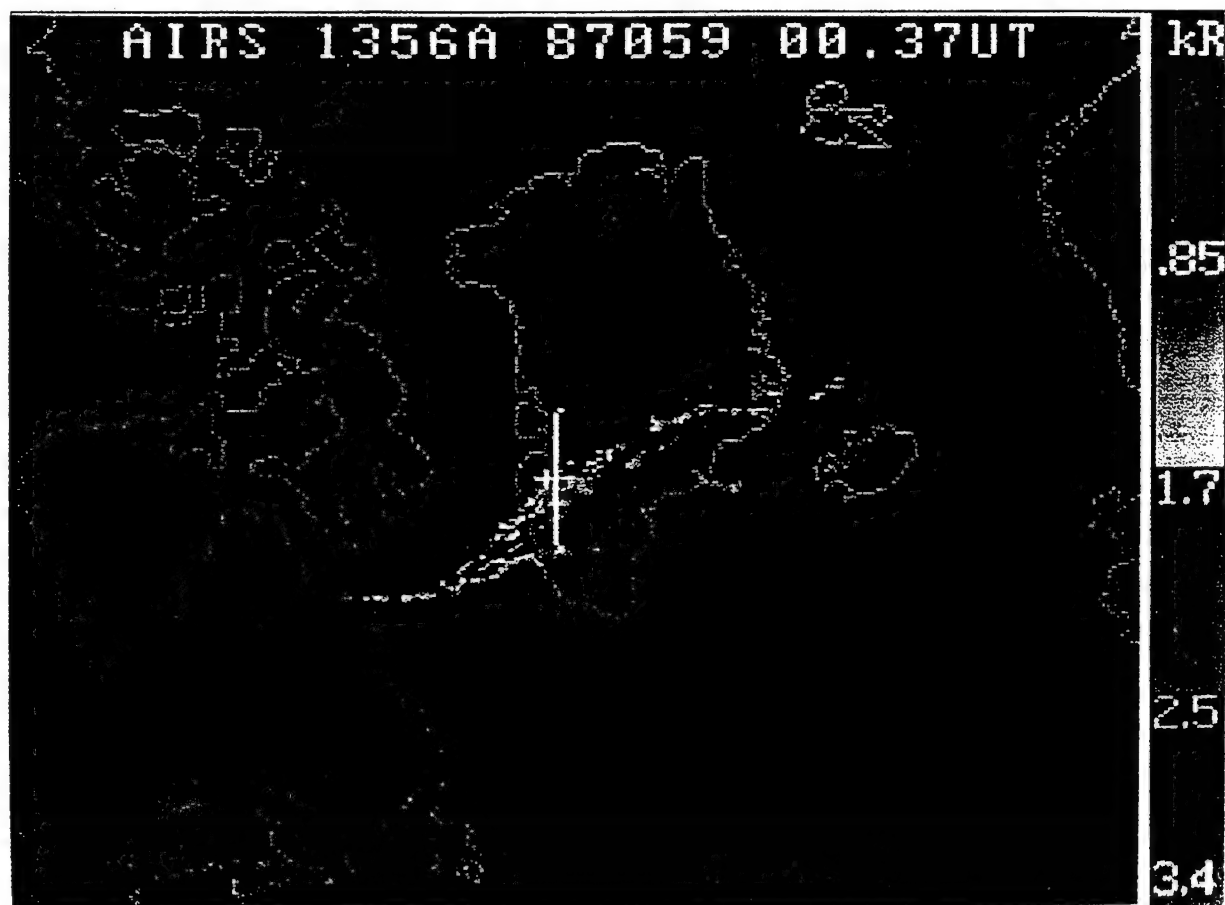


Plate 1. Ultraviolet image at 135.6 nm (O I) obtained by the Polar BEAR satellite on January 24, 1987. The solid line is the 110-km intercept of the ray path from Polar BEAR to the ground station at Sondrestrom, while the dashed line is the track of the ISR elevation scan in the magnetic meridian plane.



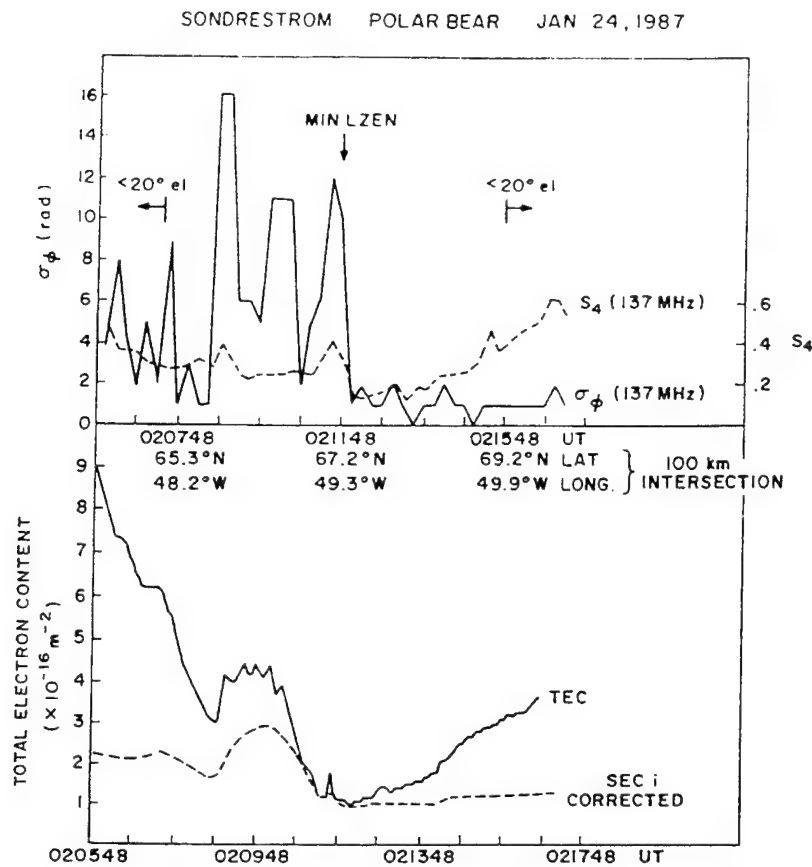


Fig. 1. (Top) The 137-MHz phase (σ_ϕ) and amplitude (S_4) scintillation and (bottom) TEC measured along the 110-km intercept shown in Plate 1. Note the scintillation enhancement associated with the TEC enhancement between 0209 and 0211 UT.

computing electron density profiles from the UV emission features and comparing them against observations.

It is unfortunate that the weak 159.6-nm emission requires averaging over 3 pixels to obtain statistical validity of the counts. Since the mean energy, \bar{E} , of the precipitating flux is obtained from the ratio of the two intensities, the 135.6-nm data were also smoothed in a manner similar to that of the 159.6-nm data. This introduces some uncertainty because \bar{E} is rather sensitive to the precise value of the ratio and smoothing the data smears some of the structure that is clearly present in the unsmoothed data. Since arcs are associated with inverted-V events [Lin and Hoffman, 1982], it is expected that the intensity ratio will vary across the arc. However, smoothing tends to wash out this variation, so the inferred \bar{E} is generally too low at the peak of the inverted-V structure. The energy flux (Q) of the precipitating particles is estimated from the unsmoothed detector 2 output. Since the 135.6-nm column emission rate decreases as \bar{E} increases, an underestimate of \bar{E} produces an overestimate of Q . For modeling electron density profiles, the above method tends to overestimate the peak electron density (related to the high value of Q) and also the altitude of the peak near the centers of discrete arcs (related to the low value of \bar{E}). Further, in

doing the modeling, we assume that the 135.6-nm emission is a combination of O I 135.6 nm and N₂ LBH 135.3 nm as AIRS does not provide sufficient resolution to separate them. In addition, with two auroral UV emission features we had no way of determining the O density independently, an input necessary for the determination of the electron density profile. We therefore used a model for the O density even though this density can be quite variable in aurora, as discussed by Hecht *et al.* [1989].

Having discussed possible sources of errors in the profile modeling effort, we turn to the actual modeling computations. To do this, the first step is to convert the smoothed and unsmoothed counts shown in Figure 6 into intensities by using the respective calibration of the two detectors. We are now in a position to interpret these emission intensities with the aid of the auroral electron transport code (to be referred to as B3C for Boltzmann three constituent) and associated chemistry.

Using B3C and the MSIS-83 (mass spectrometer and incoherent scatter 1983) model atmosphere [Hedin, 1983], intensities of the O I 135.6-nm line and the N₂ Lyman-Birge-Hopfield band system for incident Gaussian electron spectra with mean energies \bar{E} between 1 and 10 keV and an energy flux Q of 1 erg cm⁻² s⁻¹ were calculated. Using the actual instrument response functions for AIRS detectors 1 and 2 (centered at 159.6 nm and 135.6 nm, respectively), the effective intensities that AIRS would observe under those conditions were derived. Since the intensity of each of these

Plate 2. (Opposite) Same as in Plate 1 except that the image was obtained on February 28, 1987. The solid line is the same as in Plate 1 while the plus sign represents the stationary ISR position pointed along the local magnetic field.

emission features is proportional to Q , the ratio of the intensities observed by the two detectors is independent of Q . Therefore, by comparing the actual ratio to the calculated ratios a value for \bar{E} was determined. A value for Q was obtained by comparing the actual detector 2 intensity with that calculated for $Q = 1 \text{ erg cm}^{-2} \text{ s}^{-1}$. Once \bar{E} and Q were determined, then B3C and its related chemistry code were used to calculate the electron density profile.

For the case of January 24, 1987, the 10.7-cm solar flux and A_p were 70.2 and 7, respectively. These parameters were used to run the MSIS-83 model for the neutral atmosphere. The B3C code then provided the inferred \bar{E} and inferred Q as functions of geographic latitude given the ratio of smoothed detectors 1 and 2 as shown in Figure 7.

As mentioned earlier, we concentrate on the poleward arc and find, near the poleward edge of the arc, inferred $\bar{E} = 4.1 \text{ keV}$ and $Q = 7.2 \text{ ergs cm}^{-2} \text{ s}^{-1}$. These parameters were obtained considering a Gaussian spectrum for the electron precipitating flux, as earlier work had shown that this type of spectrum was more appropriate for a discrete arc [Strickland *et al.*, 1983]. The electron density profile obtained from B3C is shown in Figure 8. The maximum density in the E region for this profile is $4.2 \times 10^5 \text{ cm}^{-3}$ at a height of 118 km. The radar scan presented in Figure 5 which represents the actual measurement of the electron density profile in the ionosphere generated in response to the particle precipitation was found to have a maximum density of $4.7 \times 10^5 \text{ cm}^{-3}$ at a height of 112 km. Given all of the approximations involved in determining \bar{E} and Q from the UV emissions at two wavelengths, the comparison is quite good between the

SONDRESTROM PHASE SPECTRUM JAN 24, 1987

137 MHz MEM(40)

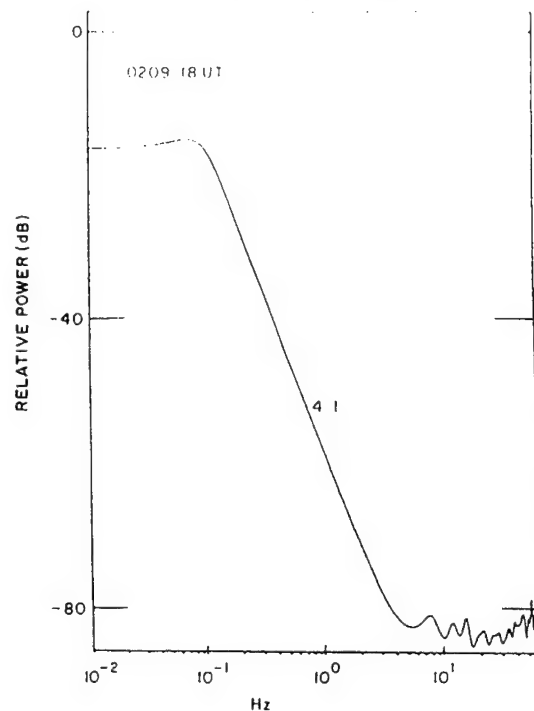


Fig. 3. Sample of phase scintillation spectrum with spectral index of 4 obtained at 0209:18 UT.

SONDRESTROM POLAR BEAR JAN 24, 1987 PHASE SPECTRAL SLOPE, p_ϕ

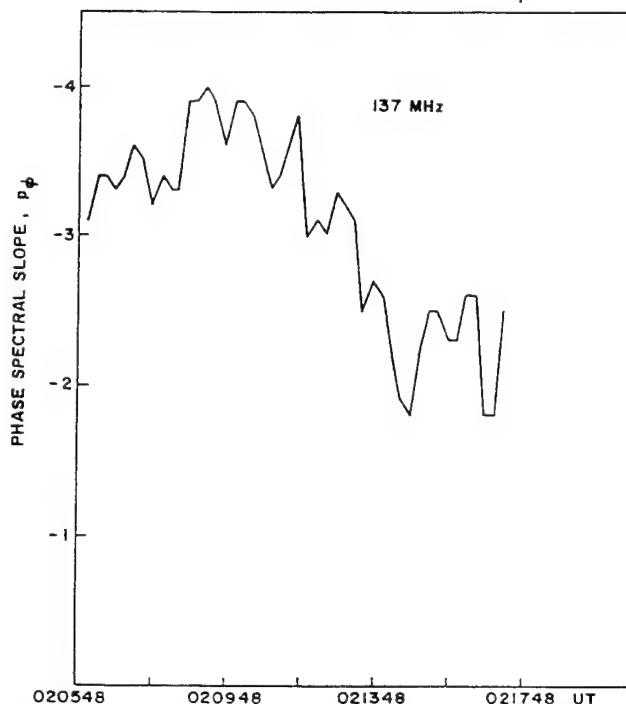


Fig. 2. The phase spectral slope obtained by spectral analysis of phase scintillation data shown in the top panel of Figure 1. Note steep phase spectral indices of 4 in the scintillation enhancement region between 0209 and 0211 UT.

observations and modeled values. We think the goodness of the fit is likely due to the stable nature of the discrete arc.

3.2. Event of February 28, 1987

AIRS image. The Polar BEAR AIRS image of O I 135.6 nm for this event is shown in Plate 2, the straight line through the image representing the 110-km intercept of the ray path from the beacon to the ground station at Sondrestrom. This was a very high elevation pass of the satellite, with the maximum elevation being 80° . By consulting the scale of false-color radiance values (which is different from Plate 1) we note that the discrete auroral features are more intense in this case than those observed on January 24. In particular, we will concentrate on the propagation disturbances created by the intense discrete arc with a maximum intensity of 4.6 kR located at the poleward edge of the auroral oval. On February 28 the Sondrestrom radar was not scanning but was stationed such that the beam was pointed up along the local magnetic field direction (elevation 80° , azimuth 140°). That position is marked by a plus sign in close proximity to the E region intercept in Plate 2. We note that both the stationary radar location and the beacon ray path do intersect the discrete arc at the poleward edge of the oval.

Polar BEAR beacon measurements. The TEC and scintillations obtained along the intercept shown in Plate 2 are presented in Figures 9 and 10. The primary reason for discussing this event is to highlight the magnitude of VHF/UHF radio wave perturbations that can be caused by the E region alone depending on the intensity and width of the

JAN. 24, 1987 020656-021156 SONDRESTROM AZ=141.0

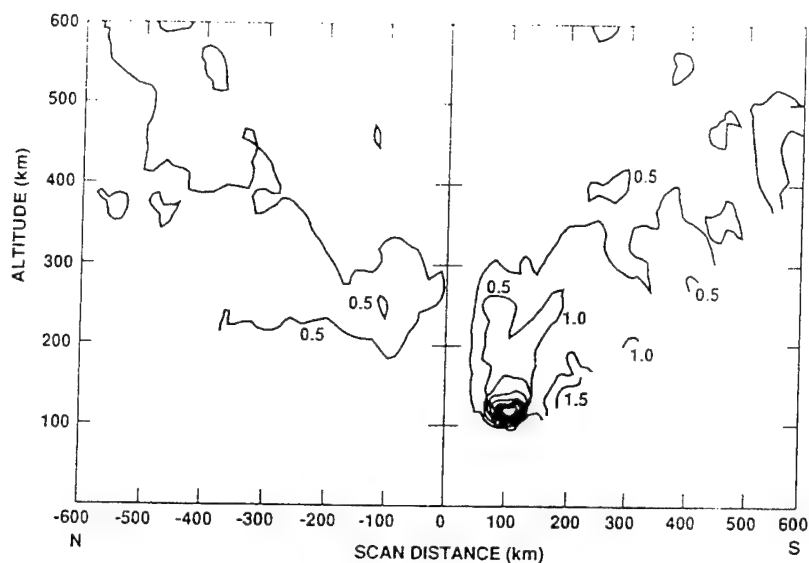


Fig. 4. Electron density contours obtained by the Sondrestrom ISR during the elevation scan of 0206:56-0211:56 UT. The density contours are in units of 10^4 cm^{-3} . Note the prominent electron density structure with maximum of $4.5 \times 10^5 \text{ cm}^{-3}$ to the south of Sondrestrom at a distance of 100 km.

emission region associated with the energetic particle precipitation. The equivalent vertical TEC shows a sharp, narrow, spikelike increase centered at 0023 UT and two broader increases centered at approximately 0017:30 and 0020:30 UT. As in the earlier case study, the background TEC varies between 1 and 2 TEC units. On examining Plate 2 carefully, one finds that the sharp TEC structure around 0023 UT corresponds to the intense narrow arc of approximately 4.5 kR intensity of 135.6-nm emission at the poleward edge of the diffuse aurora mentioned in the last paragraph.

The other two TEC structures presumably are related to the other two structured precipitation regions along the intercept, one immediately equatorward of the very intense arc discussed above and the other near the equatorward edge of the diffuse aurora.

The phase scintillations associated with the TEC structures are very large at 137 MHz, ranging between 40 and 50 rad. This is a factor of 4-5 larger than the phase scintillations observed on January 24. As a result, the phase scintillations at 413 MHz are as large as 20 rad associated with the intense

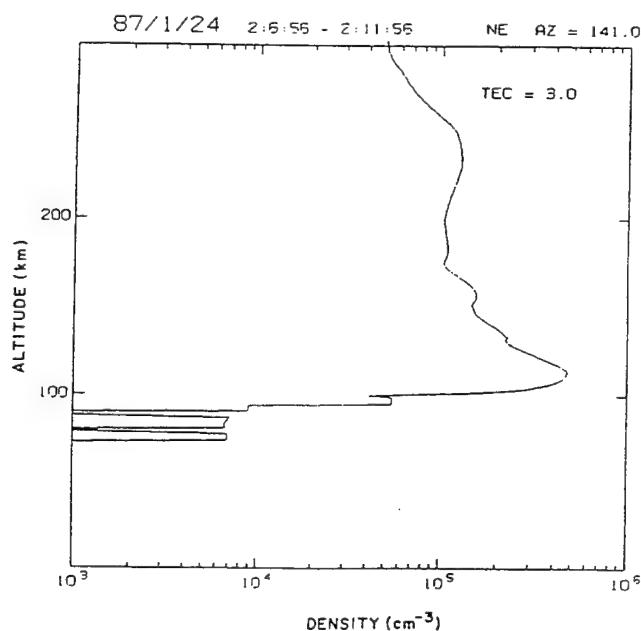


Fig. 5. Reconstructed vertical electron density profile obtained by the Sondrestrom ISR through the center of the density enhancement shown in Figure 4. The maximum density is $4.5 \times 10^5 \text{ cm}^{-3}$ at 114 km.

24 January 1987: AIRS Intensities vs. latitude

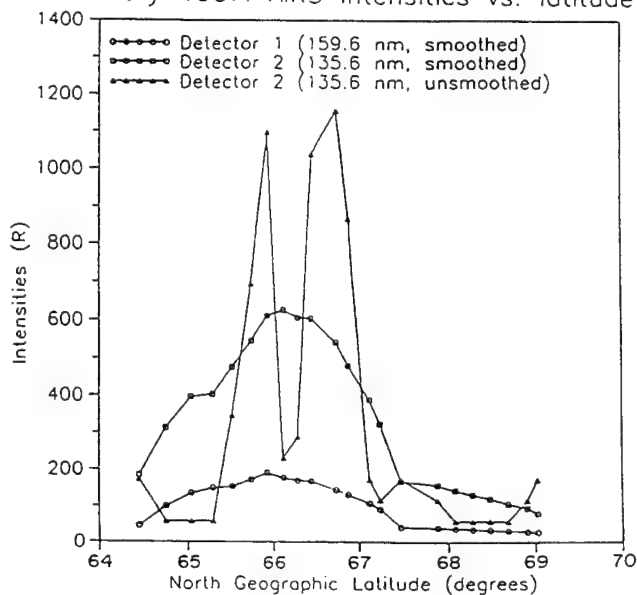


Fig. 6. The smoothed counts at 159.6 nm and the smoothed and unsmoothed counts at 135.6 nm obtained by the UV imager along the 110-km intercept shown in Plate 1.

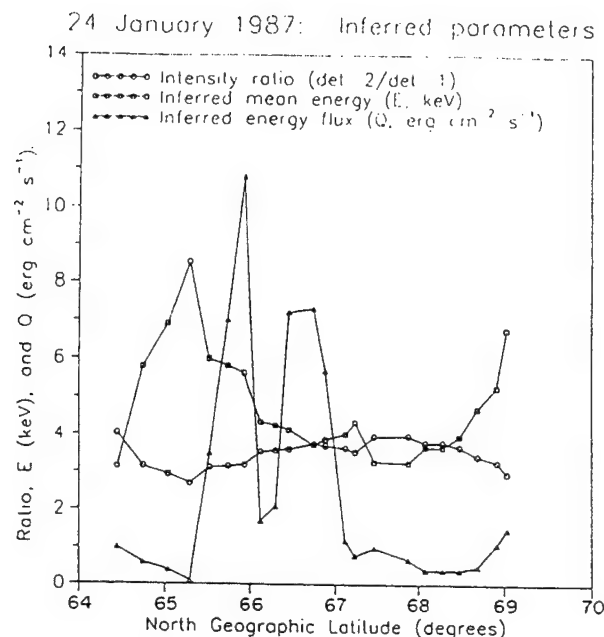


Fig. 7. The ratio of the smoothed 159.6- and 135.6-nm emissions obtained from Figure 6 and the inferred mean energy and energy flux of the precipitating particles obtained from the smoothed and unsmoothed counts as explained in the text.

arc at the poleward edge of the diffuse aurora. The phase scintillations were very small at this frequency on January 24 and hence were not shown in Figure 1.

The amplitude scintillations are also much larger than those observed on January 24. We concentrate on the almost saturated scintillations at 137 MHz and the significant scintillations observed at 413 MHz in association with the discrete arc at the poleward edge of the diffuse aurora. The perturbations on the 137/413-MHz signal amplitudes are as large as those caused by the geometrical enhancement (denoted by MIN LZEN) observed a little to the south of the arc. It should be noted that the geometrical enhancement is not centered on a TEC enhancement. Thus the phase scintillations in this region are relatively modest, ~ 10 rad at VHF. However, the amplitude scintillations are very high for this 80° elevation pass. This may indicate that small-scale (kilometers to hundreds of meters) magnetic field-aligned rods are embedded in larger-scale sheets as postulated by Fremouw *et al.* [1985b]. Another important point to note is that the phase/amplitude scintillation ratio is much larger for the source enhancement region associated with the discrete arc than for the geometrical enhancement region. It is our view (given the ISR data) that the irregularity source is in the E region for the discrete arc and may be in the F region for the geometrical enhancement based on the differences of the spectral character of the irregularities as discussed below.

The spectral slopes of the phase scintillation data at 137 and 413 MHz are shown in Figure 11. If we confine our attention primarily to comparing the spectral slopes in the geometrical enhancement region with those in the poleward discrete arc region, we find the slopes to be much shallower, namely 3, in the geometrical region, particularly at 137 MHz. It should be noted that, in general, phase spectral slopes are steeper in the geometrical enhancement region compared to nearby regions if all irregularities are in the F region [Fre-

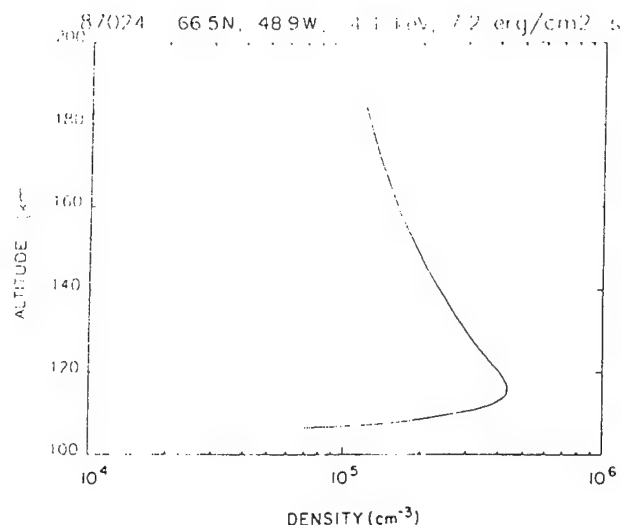


Fig. 8. The modeled electron density profile obtained by using the auroral electron transport code. The maximum density is $4.2 \times 10^5 \text{ cm}^{-3}$ at 118-km altitude in good agreement with the measured ISR profile shown in Figure 5.

mouw *et al.*, 1985b]. In this particular case, they seem shallower in contrast because of the extreme steepness of the E region irregularities characterized by a phase spectral slope of 4. In an earlier study [Basu *et al.*, 1986] where we had invoked velocity shears in the F region as the source of the irregularities, we had found shallow phase spectral slopes in a region contiguous to an auroral arc. The steep spectral slopes associated with the arc irregularities are consistent with the findings of January 24 and indicate that E region spectra have steeper slopes than their F region counterpart. Thus the February 28 observations prove that it is possible to have large-amplitude scintillations even if the phase spectral slope is steep provided the strength of turbulence at the several-kilometer scales is very large. We will provide some order of magnitude estimates of the strength of turbulence in a later subsection.

ISR measurements. As mentioned earlier, the ISR at Sondrestrom was not operating in the scanning mode on February 28, 1987, but was held stationary along the direction of the local magnetic field. Figure 12 shows the contours of electron density as a function of time on February 28 starting at 0018:04 UT. A series of density structures in the E region are observed starting at 0022 UT. The F region in contrast is fairly featureless with maximum density of $4 \times 10^4 \text{ cm}^{-3}$. An electron density profile taken through the center of the first precipitation feature between 0023:06 and 0024:06 UT is shown (Figure 13), as it matches well the time and location of the Polar BEAR crossing of the most poleward discrete arc. The maximum density in the E region is $4.8 \times 10^5 \text{ cm}^{-3}$, an order of magnitude larger than in the F region. The TEC of the integrated profile is 3.4 TEC units, in good agreement with the Polar BEAR TEC. In this case also, it seems evident that the perturbation on the VHF and UHF radio waves is caused by the structure in the E region. In the following subsection we provide order of magnitude estimates of the strength of turbulence in the E region which can give rise to the observed scintillations.

Strength of turbulence in the E region. It is important to establish some limits on the saturation amplitudes and outer

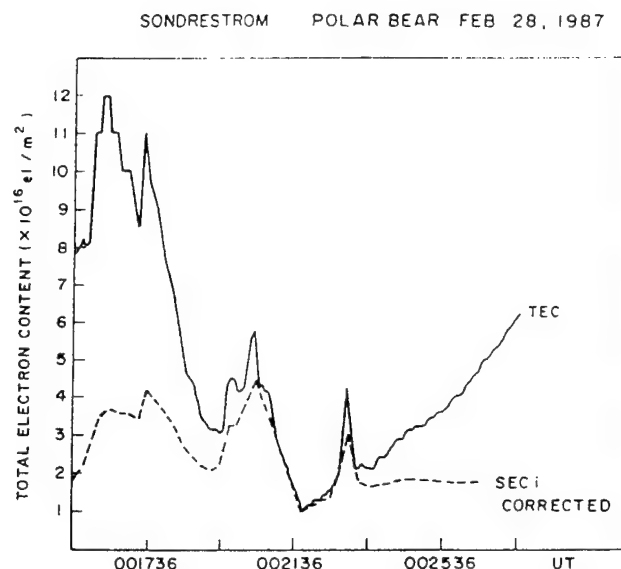


Fig. 9. The TEC measured along the 110-km intercept shown in Plate 2. Note the sharp enhancement at 0023 UT which corresponds to the discrete arc at the poleward edge of the image.

scale characteristics of the *E* region irregularities, which when combined with the measured layer density and thickness yield phase and amplitude scintillations reasonably consistent with the measurements. The UHF measurements at 413 MHz place more severe constraints. Thus the February 28, 1987, event is chosen for illustration.

Figure 14 presents S_4 and σ_ϕ computations for a range of C_s , the strength of turbulence parameter for two values of p , the phase spectral index, using equations valid in the weak scatter regime developed by Rino [1979]. Such diagrams were used by Basu *et al.* [1988b] to estimate the strength of turbulence associated with polar cap patches. For computations of S_4 and σ_ϕ we have assumed the height and thickness of the irregularity layer to be consistent with the ISR measurements, an irregularity anisotropy of 8:4:1 [Fremouw and Secan, 1984], and other geometrical parameters appropriate for the source enhancement region near 0023 UT on February 28, 1987. (We note that there are no systematic modeling efforts of the *E* region irregularity anisotropy, so we made the assumption that the *E* and *F* region anisotropies were similar, at least, in the nightside auroral oval.) It is readily apparent from Figure 14 that the observed large values of σ_ϕ at UHF for a moderate level of S_4 are consistent with the $p = 2\nu = 4$ graphs, a value obtained from the phase spectral analysis. Thus confining our attention to the $p = 4$ case, we find that the observed range of values in the enhancement region of $\sigma_\phi = 10$ –20 rad and $S_4 = 0.1$ –0.2 can be achieved with C_s in the range of 2×10^{18} to 6×10^{18} mks units.

To aid the reader, we wish to point out that this range of C_s values can, in turn, be achieved with irregularity amplitudes in the range 10–20% and outer scale size ranging between 1 and 5 km for an observed peak value of the *E* region density of approximately $5 \times 10^5 \text{ cm}^{-3}$. The irregularity amplitude is consistent with earlier rocket measurements of Kelley and Mozer [1973], who observed broadband integrated density fluctuation levels $\Delta n/n$ of 5–15% in the auroral electrojet with a layer thickness of 30 km. The outer scale can be estimated from the phase spectra, one example

of which was shown in Figure 3 for the January 24 case study. We note that the phase spectral strength increases with decreasing frequency up to 10^{-1} Hz and levels off thereafter. We have to use an effective velocity dependent on irregularity anisotropy, source motion, and ionospheric drift [Rino, 1979] to convert the frequency axis to a scale length axis. An irregularity anisotropy of 8:4:1 is appropriate, as mentioned earlier. Further, in section 4 we shall show that there is an electron drift velocity of 455 m s^{-1} equatorward to the south of Sondrestrom. The satellite was moving poleward in this orbit. Considering all these geometrical and ionospheric parameters, we obtain an effective velocity of approximately 275 m s^{-1} which has to be used to convert the frequency axis to scale size. This translates the outer scale frequency of 10^{-1} Hz to 2.75 km. This value is consistent with the C_s computations presented in Figure 14, albeit for another day. We have mentioned earlier that plasma velocity measurements were only available for January 24 so that such order of magnitude estimates could only be provided for this day. Thus we find that it is possible to model the observed VHF/UHF scintillations on the basis of *E* region parameters which are consistent with the current and earlier measurements.

4. DISCUSSION

By using multitechnique data to diagnose large- and small-scale plasma structures in the *E* region we have been able to show the mutual consistency of the different data sets in resolving the structuring issues. Starting with the UV image of the discrete arcs, we have been able to show that the particle precipitation in the *E* region giving rise to the UV emissions and the electron density increase as measured by the ISR were of the right order of magnitude to cause the TEC increase measured by Polar BEAR. In addition, the ISR measurements were consistent with the electron density profile obtained by utilizing an auroral transport code using the multiple-wavelength UV emissions recorded by AIRS on the satellite. Further, we have shown that it is possible to obtain enough strength of turbulence in the auroral *E* layer to cause the observed magnitude of phase and intensity scintillations. In general, there seemed to be a perception in the propagation community that because of the limited thickness of the *E* region, scintillations caused by this region would be insignificant. However, coordinated case studies of scintillations and ISR measurements at Sondrestrom such as this and others [Basu *et al.*, 1991] are establishing that the structured auroral *E* region because of its high density and considerable vertical extent can, indeed, cause strong phase scintillation and moderate intensity scintillations.

What we have not yet addressed is a viable mechanism that may generate the kilometer to hundreds of meter irregularities in the *E* region that could give rise to the scintillations. We shall show for the data of January 24, 1987, when electron and ion drifts were measured, that the *E* region irregularities could have been caused by the gradient-drift instability. The density structure in the *E* region for this event has been shown in Figure 4. The density gradient scale length at the edges was found to be approximately 15 km. It should be noted that for the mode of observation used here and the integration time of 10 s, the 15-km figure is very close to the measurement limit and the actual gradient scale length could indeed be much smaller. The electron drift in the *E*

SONDRESTROM POLAR BEAR FEB. 28, 1987

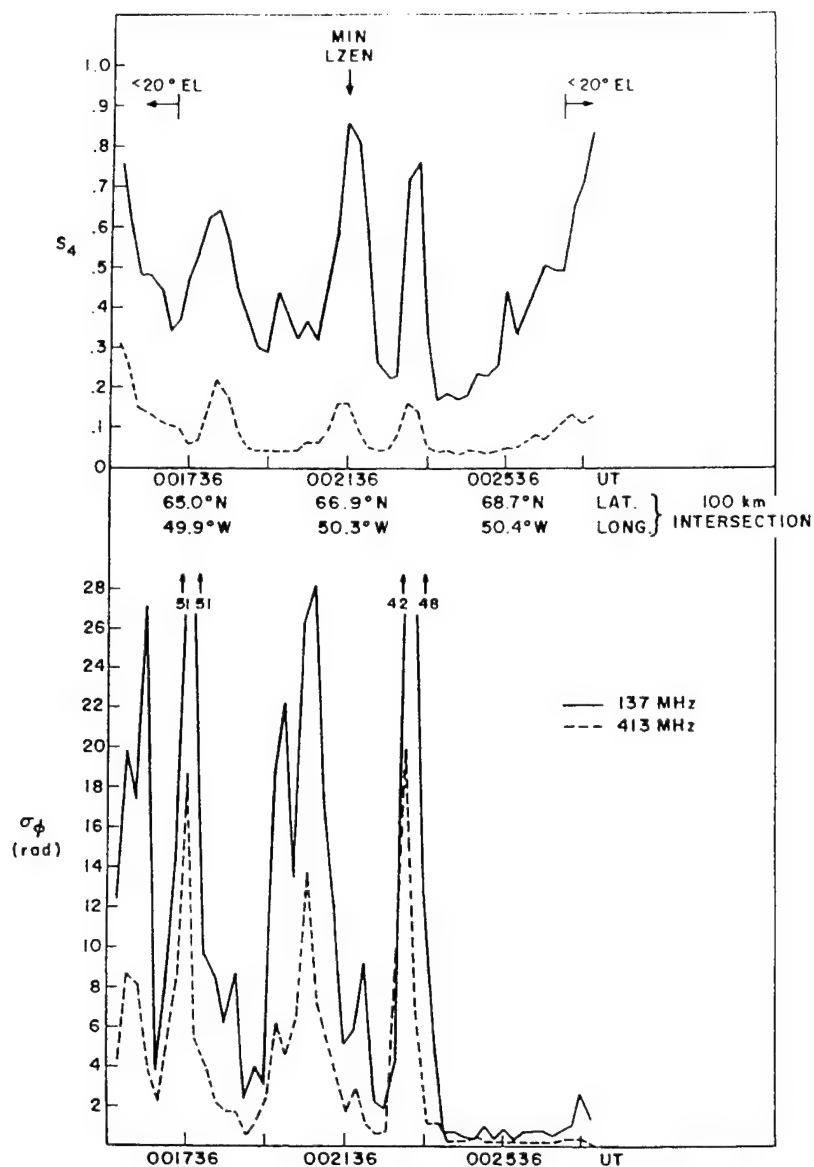


Fig. 10. (Top) Amplitude scintillation at 137 and 413 MHz and (bottom) phase scintillation obtained along the 110-km intercept in Plate 2. Note large phase and amplitude scintillation enhancements associated with the TEC enhancement at 0023 UT.

region or plasma drift in the *F* region simultaneously measured during the same elevation scan is shown in Figure 15. By comparing Figure 15 with Plate 1, we find there are two distinct components of flow for this magnetic midnight event: a large eastward flow poleward of the arc and a steady antisunward, i.e., equatorward, drift of $\sim 455 \text{ m s}^{-1}$ directly across the arc. It is interesting to note that such a flow across a stable arc at magnetic midnight was also noted by Weber *et al.* [1991, and references quoted therein]. They discuss, at length, the electrodynamics associated with such arcs. In the *E* region the ion drift experiences a rotation and attenuation due to collisions with the neutrals. Using the MSIS-86 model of the neutral atmosphere and the ion-neutral collision terms of Schunk and Walker [1970], we have obtained the value of the ion velocity at the peak altitude (114 km) of the *E* region. This value is 40 m s^{-1} poleward, providing a relative electron drift of 495 m s^{-1} equatorward.

The electron and ion drifts in the *F* and *E* regions were calculated using the equations given in Appendix 1 of Valladares and Carlson [1991]. These equations had been developed earlier by Doupnik *et al.* [1977] and de la Beaujardiere *et al.* [1977]. These authors have indicated that the computations of these velocities require a knowledge of the neutral wind.

Unfortunately, no measurements of *E* region neutral winds were available for that day at Sondrestrom. We thus chose to use predicted values of these winds at $\sim 120 \text{ km}$ altitude for the magnetic latitude of Sondrestrom near midnight from the NCAR TGCM developed by Roble *et al.* [1988]. These predictions were obtained from a recent publication by Killeen *et al.* [1992]. The required values were 140 m s^{-1} equatorward for the meridional component and 0 m s^{-1} for the zonal component. The models were run for southern summer, moderate geomagnetic activity, and rela-

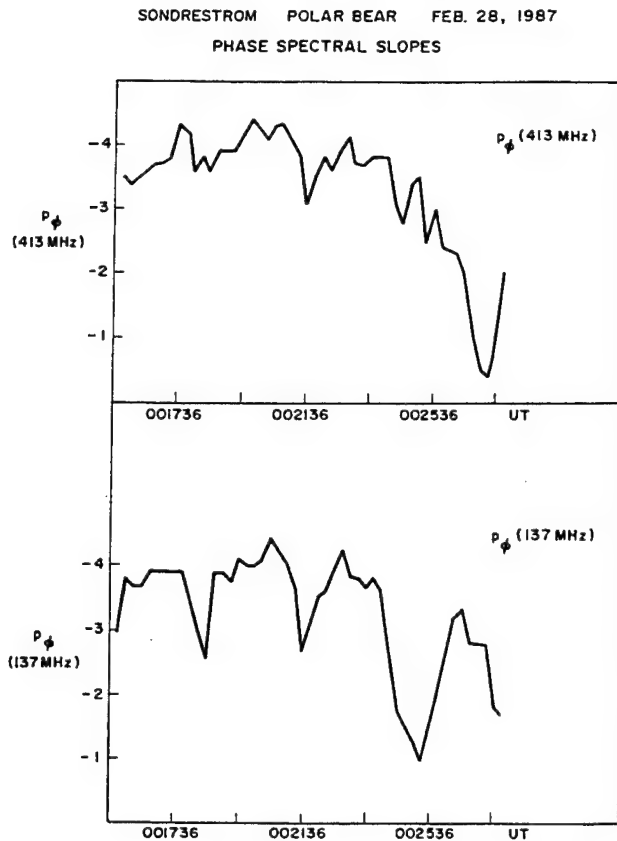


Fig. 11. The phase spectral slopes at (top) 413 MHz and (bottom) 137 MHz obtained by spectral analysis of phase scintillation data shown in the bottom panel of Figure 10.

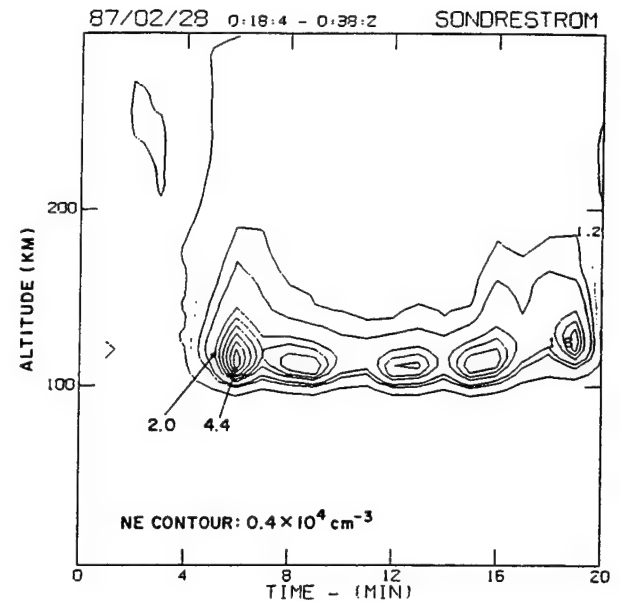


Fig. 12. Contours of electron density obtained as a function of time between 0018:04 and 0038:02 UT at the point marked by the plus sign in Plate 2. The density enhancement at 0023 UT is associated with the poleward discrete arc in Plate 2.

and the linear growth rate, γ , for the gradient-drift instability:

$$\omega_R \equiv \mathbf{k}_\perp \cdot (\mathbf{V}e_0 + \psi \mathbf{V}i_0) / (1 + \psi) \quad (1)$$

and

tively high sunspot numbers. Our measurements were for moderate geomagnetic activity but for winter and low sunspot numbers. It is difficult to find *E* region neutral wind measurements made in winter due to low densities and consequent low signal to noise ratio. Comparison with observations at Sondrestrom made by Johnson [1991] during the Lower Thermospheric Coupling Study (LTCS) for equinox low sunspot conditions shows considerable day-to-day variability of neutral wind speed and variability with altitude. However, the modeled values are fairly consistent with the measurements for moderate geomagnetic activity at an altitude of 120 km. Thus using a value of 120 m s^{-1} in an equatorward direction for the meridional wind in the *E* region with no zonal wind, we obtain an electron drift velocity of 455 m s^{-1} equatorward with an ion drift of 40 m s^{-1} poleward.

Given the above gradient and drift directions in the auroral *E* region, we consider the geometry for the application of the gradient-drift instability in Figure 16. The density gradient ∇n_0 and the relative electron drift \mathbf{V}_d are assumed to be along the *x* direction, which is southward, the equilibrium transverse electric field \mathbf{E}_0 is along the *y* axis, and the *z* axis is aligned with the Earth's magnetic field \mathbf{B}_0 .

Following the work of Fejer *et al.* [1975] and others we obtain the following expressions for the real frequency, ω_R ,

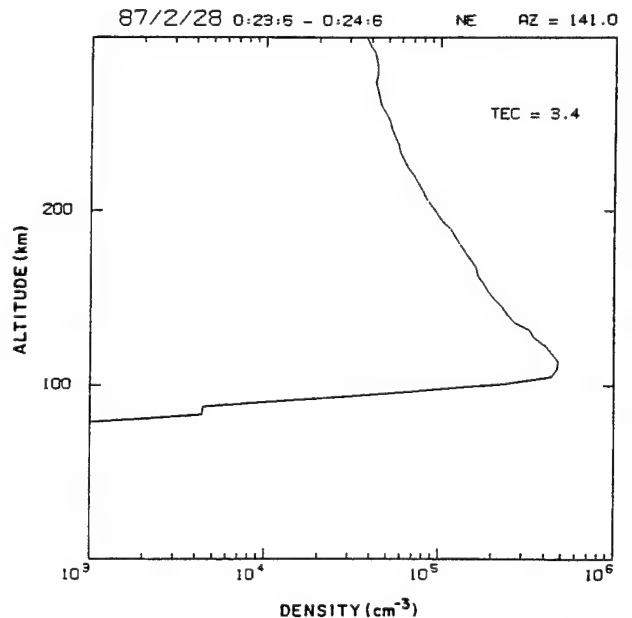


Fig. 13. The electron density profile through the center of the density enhancement between 0023:06 and 0024:06 UT. The maximum density is $4.8 \times 10^5 \text{ cm}^{-3}$ at 110 km.

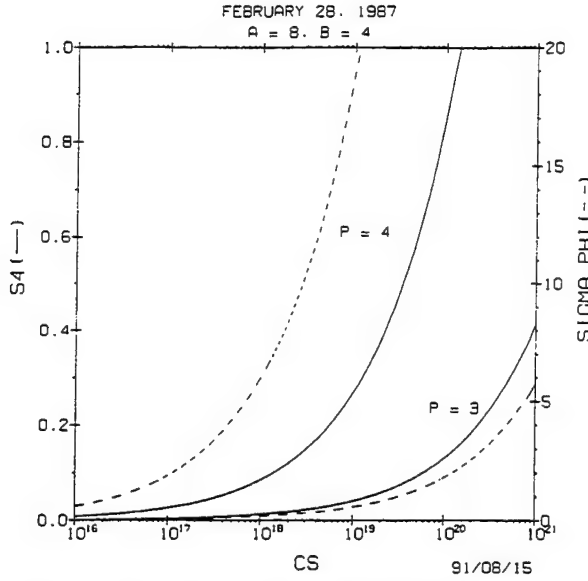


Fig. 14. The phase and amplitude scintillation as a function of the strength of turbulence parameter, C_s , for two values $p = 3$ and 4 of the phase scintillation index.

$$\gamma \cong -\frac{\nu_i}{\Omega_i} \frac{(\mathbf{k}_\perp \times \hat{\mathbf{e}}_z) \cdot \boldsymbol{\epsilon}_n \mathbf{k}_\perp \cdot \mathbf{V}_d}{k_\perp^2 (1 + \psi)^2} - \frac{D_\perp k_\perp^2}{1 + \psi} - 2\alpha n_0 \quad (2)$$

where \mathbf{V}_{e0} and \mathbf{V}_{i0} are the electron and ion drifts, $\mathbf{V}_d = \mathbf{V}_{e0} - \mathbf{V}_{i0}$, and $\psi = \nu_e \nu_i / \Omega_e \Omega_i$ where ν_e , ν_i , Ω_e , and Ω_i are the usual electron and ion collision frequencies and gyrofrequencies; \mathbf{k}_\perp is the wave vector; $\boldsymbol{\epsilon}_n = \nabla n_0 / n_0 = 1/L_N$ where L_N is the horizontal density gradient scale length; $D_\perp = (\nu_e / \Omega_e \Omega_i) C_s^2$ where $C_s^2 = (T_e + T_i)/m_i$, T_e , T_i , and m_i being the electron and ion temperature and ion mass, respectively; $\mathbf{B}_0 = B_0 \hat{\mathbf{e}}_z$ and $\mathbf{V}_{e0} = c \mathbf{E}_{0\perp} \times \hat{\mathbf{e}}_z / B_0$; α is the recombination coefficient, and n_0 is the electron density. For the auroral geometry we have considered above and for long scale lengths ($\lambda_\perp > 100$ m for which the second term due to diffusive damping can be neglected) we get

$$\gamma \cong -\frac{\nu_i}{\Omega_i} \frac{(\mathbf{k}_\perp \times \hat{\mathbf{e}}_z) \cdot \boldsymbol{\epsilon}_n \mathbf{k}_\perp \cdot \mathbf{V}_d}{k_\perp^2 (1 + \psi)^2} - 2\alpha n_0 \quad (3)$$

The instability only occurs for oblique modes such that $[(\mathbf{k}_\perp \times \hat{\mathbf{e}}_z) \cdot \boldsymbol{\epsilon}_n] < 0$. Since $\boldsymbol{\epsilon}_n = \epsilon_n \hat{\mathbf{e}}_x$, the unstable modes are in the $(x)(-y)$ plane as shown in Figure 16. The growth is optimum for modes at $\theta = \pi/4$ where θ is the angle between \mathbf{k} and \mathbf{V}_d (and ∇n_0). Then (3) can be written as

$$\begin{aligned} \gamma &\cong \frac{\nu_i}{\Omega_i} \frac{k_\perp \epsilon_n \sin \theta}{k_\perp^2} \frac{k_\perp V_d \cos \theta}{(1 + \psi)^2} - 2\alpha n_0 \\ &\cong \frac{\nu_i}{\Omega_i} \frac{\epsilon_n V_d \sin 2\theta}{2(1 + \psi)^2} - 2\alpha n_0 \\ &\cong \frac{\nu_i}{\Omega_i} \frac{\epsilon_n V_d}{2(1 + \psi)^2} - 2\alpha n_0 \end{aligned} \quad (4)$$

when $\theta = \pi/4$.

In the auroral E region, $\nu_i / \Omega_i \approx 15$, $\nu_e \nu_i / \Omega_e \Omega_i \ll 1$, and

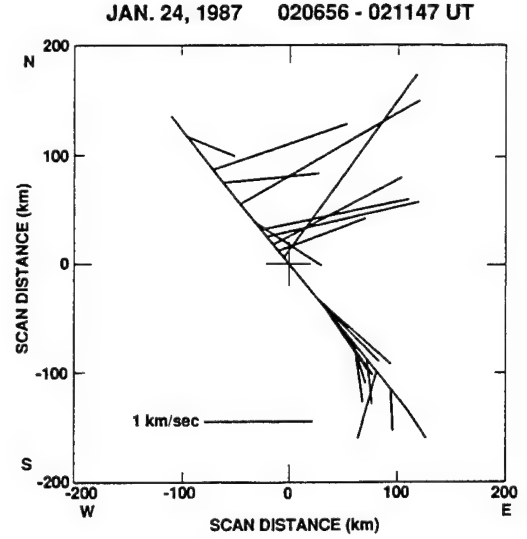


Fig. 15. The plasma drift in the F region, which is equivalent to the electron drift in the E region, measured by the Sondrestrom ISR simultaneously with the density measurements shown in Figure 4.

$\alpha \sim 3 \times 10^{-7}$. With these approximations we obtain the value of the growth rate in (4) to be approximately 0.2 s^{-1} whereas the damping term is 0.3 s^{-1} . However, we note that the growth rate is inversely proportional to the density gradient scale length, which was probably overestimated by the ISR measurement resolution. If the scale length is 5 km, a value widely used in the E region [Fejer and Kelley, 1980], the growth rate is 0.7 s^{-1} and the damping term is 0.3 s^{-1} , providing an effective growth time of the irregularities to be about 2.5 s. Since this is small compared to the lifetime of tens of seconds of the E region irregularities, the gradient drift mechanism is probably a viable one for the generation of these irregularities. Obviously, the foregoing estimates are based on many approximations (such as the neglect of the dispersive nature of the large-wavelength modes discussed by Rogister [1972]), and even the observations are probably made well into the nonlinear regime.

We also note that in developing the gradient-drift instability arguments described above we used a local analysis

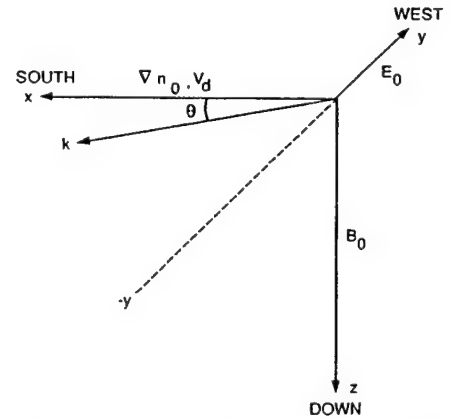


Fig. 16. The coordinate system for the application of the gradient drift instability for the auroral geometry of January 24, 1987.

appropriate for the *E* region alone. It is well known that due to the large conductivity parallel to the magnetic field (σ_{\parallel}) as compared with the transverse conductivity (σ_{\perp}), the potential fields in the ionosphere map to large parallel distances determined by the relationship $\lambda_{\parallel}/\lambda_{\perp} \sim (\sigma_{\parallel}/\sigma_{\perp})^{1/2}$ [Farley, 1959]. Thus the scale sizes considered in this paper (a few kilometers) are likely to map from the *E* region (where Hall conductivity is dominant) to the *F* region (where Pedersen conductivity is important), as $(\sigma_{\parallel}/\sigma_{\perp})^{1/2} \sim 45$ to 100 in the lower ionosphere. In a situation like this, an approach using quantities integrated along the magnetic field is frequently employed [e.g., Perkins, 1973], and the relevant gradient is no longer the local density gradient but is replaced by the gradient in the integrated conductivity, Σ_H^E (integrated Hall conductivity in *E* region), Σ_P^E (integrated Pedersen conductivity in *E* region), or Σ_P^F (integrated Pedersen conductivity in *F* region), as the case may be. However, it is generally recognized that since $\Sigma_H^E \gg \Sigma_P^E \geq \Sigma_P^F$, the effect of coupling to *F* region altitudes is likely to be of relatively lesser importance for the *E* region gradient-drift instability if similar magnitudes of gradients in the *E* and *F* regions prevail. It may be noted that the observed *F* region density gradient, though favorable to instability, was much weaker than the *E* region gradient during these observations, as seen in Figure 4. This would seem to indicate that the *E* region was the more likely driver of the instability. A quantitative analysis of the effects of coupling to other regions on the gradient-drift instability in the *E* region is in progress.

Thus the UV imager provides a method of remote sensing a class of large- and small-scale irregularities which have a deleterious effect on space-based radar and communications systems. It is unfortunate that such coordinated UV and scintillation measurements were not obtained during sunspot maximum conditions when the *F* region is expected to have substantially greater densities. Under such conditions a two-sloped irregularity spectrum has been observed at Sondrestrom [Basu et al., 1991]. It is of interest to determine if the UV/optical imager and modeling studies will be able to provide the relative contributions of perturbations from the *E* and *F* regions. The results of this study also have important ramifications for morphological studies of scintillations in the auroral oval. By establishing the *E* region as the likely seat of VHF/UHF scintillations under fairly average geophysical conditions during sunspot minimum, we have raised several new issues for the consideration of the modeling and user communities.

Acknowledgments. We appreciate the interest of R. A. Skrivanek and H. C. Carlson, Jr., of Phillips Laboratory (PL) and L. A. Wittwer of DNA in this study. We thank E. MacKenzie for help with data analysis and J. Vickrey and J. Kelly for the Sondrestrom radar data. We thank J. MacDougall and two referees for helpful comments. The work at Boston College was partially supported by contract F19628-90-K-0007 with PL. The work at PL was funded by AFOSR task 2310G9 and by DNA. We thank the Danish Commission for Scientific Research in Greenland for permission to conduct ground experiments at Sondrestrom.

The Editor thanks D. J. Strickland and R. T. Tsunoda for their assistance in evaluating this paper.

REFERENCES

- Basinska, E. M., W. J. Burke, Su. Basu, F. J. Rich, and P. F. Fougere, Low-frequency modulation of plasmas and soft electron precipitation near the dayside cusp, *J. Geophys. Res.*, 92, 3304, 1987.
- Basu, S., Su. Basu, E. MacKenzie, and D. Weimer, Ionospheric scintillations and in-situ measurements at an auroral location in the European sector. Scattering and Propagation in Random Media, *AGARD Conf. Proc.*, 419, 50-1, 1987.
- Basu, Su., S. Basu, C. Senior, D. Weimer, E. Nielsen, and P. F. Fougere, Velocity shears and sub-km scale irregularities in the nighttime auroral *F*-region, *Geophys. Res. Lett.*, 13, 101, 1986.
- Basu, Su., et al., Simultaneous density and electric field fluctuation spectra associated with velocity shears in the auroral oval, *J. Geophys. Res.*, 93, 115, 1988a.
- Basu, Su., S. Basu, E. J. Weber, and W. R. Coley, Case study of polar cap scintillation modeling using DE 2 irregularity measurements at 800 km, *Radio Sci.*, 23, 545, 1988b.
- Basu, Su., S. Basu, E. Costa, C. Bryant, C. E. Valladares, and R. C. Livingston, Interplanetary magnetic field control of drifts and anisotropy of high-latitude irregularities, *Radio Sci.*, 26, 1079, 1991.
- Bythrow, P. F., T. A. Potemra, W. B. Hanson, L. J. Zanetti, C.-I. Meng, R. A. Huffman, F. J. Rich, and D. A. Hardy, Earthward directed high density Birkeland currents observed by HiLat, *J. Geophys. Res.*, 89, 9114, 1984.
- Costa, E., P. F. Fougere, and S. Basu, Cross-correlation analysis and interpretation of spaced-receiver measurements, *Radio Sci.*, 23, 141, 1988.
- Cousins, M. D., R. C. Livingston, C. L. Rino, and J. F. Vickrey, The HiLat satellite multifrequency radio beacon, *Johns Hopkins APL Tech. Dig.*, 5, 109, 1984.
- de la Beaujardiere, O., R. R. Vondrak, and M. J. Baron, Radar observations of electric fields and currents associated with auroral arcs, *J. Geophys. Res.*, 82, 5051, 1977.
- DelGreco, F. P., R. E. Huffman, J. C. Larrabee, R. W. Eastes, and C. I. Meng, Organizing and utilizing the imaging and spectral data from Polar BEAR, in *Ultraviolet Technology II*, edited by R. E. Huffman, *Proc. SPIE Int. Soc. Opt. Eng.*, 932, 30, 1988.
- DelGreco, F. P., R. W. Eastes, and R. E. Huffman, UV ionospheric remote sensing with the Polar BEAR satellite, in *Ultraviolet Technology III*, edited by R. E. Huffman, *Proc. SPIE Int. Soc. Opt. Eng.*, 1158, 46, 1989.
- Doupnik, J. R., A. Brekke, and P. M. Banks, Incoherent scatter radar observations during three sudden commencements and a Pc 5 event on August 4, 1972, *J. Geophys. Res.*, 82, 499, 1977.
- Farley, D. T., A theory of electrostatic fields in a horizontally stratified ionosphere subject to a vertical magnetic field, *J. Geophys. Res.*, 64, 1225, 1959.
- Fejer, B. G., and M. C. Kelley, Ionospheric irregularities, *Rev. Geophys.*, 18, 401, 1980.
- Fejer, B. G., D. T. Farley, B. B. Balsley, and R. F. Woodman, Vertical structure of the VHF backscattering region in the equatorial electrojet and the gradient drift instability, *J. Geophys. Res.*, 80, 1313, 1975.
- Fougere, P. F., On the accuracy of spectrum analysis of red noise processes using maximum entropy and periodogram methods: Simulation studies and application to geophysical data, *J. Geophys. Res.*, 90, 4355, 1985.
- Fremouw, E. J., and J. A. Secan, Modeling and scientific application of scintillation results, *Radio Sci.*, 19, 687, 1984.
- Fremouw, E. J., R. L. Leadabrand, R. C. Livingston, M. D. Cousins, C. L. Rino, B. C. Fair, and R. A. Long, Early result from the DNA Wideband satellite experiment: Complex-signal scintillations, *Radio Sci.*, 13, 167, 1978.
- Fremouw, E. J., et al., The HiLat satellite mission, *Radio Sci.*, 20, 416, 1985a.
- Fremouw, E. J., J. A. Secan, and J. M. Lansinger, Spectral behavior of phase scintillation in the nighttime auroral region, *Radio Sci.*, 20, 923, 1985b.
- Hecht, J. H., A. B. Christensen, D. J. Strickland, and R. R. Meier, Deducing composition and incident electron spectra from ground-based auroral optical measurements: Variations in oxygen density, *J. Geophys. Res.*, 94, 13,553, 1989.
- Hedin, A. E., A revised thermospheric model based on mass spectrometer and incoherent scatter data: MSIS-83, *J. Geophys. Res.*, 88, 10,170, 1983.
- Huffman, R. E., J. C. Larrabee, F. J. LeBlanc, and C.-I. Meng,

- Ultraviolet remote sensing of the aurora and ionosphere for C¹I system use, *Radio Sci.*, 20, 425, 1985.
- Hunt, J. W., Jr., and C. E. Williams, Anomalous attitude motion of the Polar Bear satellite, *Johns Hopkins APL Tech. Dig.*, 8, 324, 1987.
- Johnson, R. M., Sondrestrom incoherent scatter radar observations during the lower thermosphere coupling study: September 21–26, 1987, *J. Geophys. Res.*, 96, 1081, 1991.
- Kelley, M. C., and F. S. Mozer, Electric field and plasma density fluctuations due to high-frequency Hall current two-stream instability in the auroral E region, *J. Geophys. Res.*, 78, 2214, 1973.
- Kelley, M. C., K. D. Baker, J. C. Ulwick, C. L. Rino, and M. J. Baron, Simultaneous rocket probe, scintillation, and incoherent scatter radar observations of irregularities in the auroral zone ionosphere, *Radio Sci.*, 15, 491, 1980.
- Kelly, J. D., Sondrestrom radar—Initial results, *Geophys. Res. Lett.*, 10, 1112, 1983.
- Keskinen, M. J., and S. L. Ossakow, Theories of high-latitude ionospheric irregularities: A review, *Radio Sci.*, 18, 1077, 1983.
- Keskinen, M. J., H. G. Mitchell, J. A. Fedder, P. Satyanarayana, S. T. Zalesak, and J. D. Huba, Nonlinear evolution of the Kelvin-Helmholtz instability in the high-latitude ionosphere, *J. Geophys. Res.*, 93, 137, 1988.
- Killeen, T. L., B. Nardi, P. N. Purcell, R. G. Roble, T. J. Fuller-Rowell, and D. Rees, Neutral winds in the lower thermosphere from Dynamics Explorer 2, *Geophys. Res. Lett.*, 19, 1093, 1992.
- Lin, C. A., and R. A. Hoffman, Narrow bursts of intense electron precipitation fluxes within inverted-V events, *Geophys. Res. Lett.*, 9, 211, 1982.
- MacDougall, J., Distribution of irregularities in the northern polar region determined from HiLat observations, *Radio Sci.*, 25, 115, 1990.
- Perkins, F. W., Spread F and ionospheric currents, *J. Geophys. Res.*, 78, 218, 1973.
- Rees, M. H., and D. Lummerzheim, Characteristics of auroral electron precipitation derived from optical spectroscopy, *J. Geophys. Res.*, 94, 6799, 1989.
- Rees, M. H., D. Lummerzheim, R. G. Roble, J. D. Winningham, J. D. Craven, and L. A. Frank, Auroral energy deposition rate, characteristic electron energy, and ionospheric parameters derived from Dynamics Explorer 1 images, *J. Geophys. Res.*, 93, 12,841, 1988.
- Rino, C. L., A power law phase screen model for ionospheric scintillation, 1, Weak scatter, *Radio Sci.*, 14, 1135, 1979.
- Rino, C. L., R. C. Livingston, and S. J. Matthews, Evidence for sheet-like auroral ionospheric irregularities, *Geophys. Res. Lett.*, 5, 1039, 1978.
- Robinson, R., et al., Coordinated measurements made by the Sondrestrom radar and the Polar Bear ultraviolet imager, *J. Geophys. Res.*, 97, 2863, 1992.
- Roble, R. G., E. C. Ridley, A. D. Richmond, and R. E. Dickinson, A coupled thermosphere/ionosphere general circulation model, *Geophys. Res. Lett.*, 15, 1325, 1988.
- Rogister, A., Nonlinear theory of cross-field instability with application to the equatorial electrojet, *J. Geophys. Res.*, 77, 2975, 1972.
- Schenkel, F. W., and B. S. Ogorzalek, Auroral images from space: Imagery, spectroscopy, and photometry, *Johns Hopkins APL Tech. Dig.*, 8, 308, 1987.
- Schenkel, F. W., B. S. Ogorzalek, R. R. Gardner, R. A. Hutchins, R. E. Huffman, and J. C. Larrabee, Simultaneous multispectral narrow band auroral imagery from space (1150 Å to 6300 Å), in *Ultraviolet Technology*, edited by R. E. Huffman, *Proc. SPIE Int. Soc. Opt. Eng.*, 687, 90, 1986.
- Schunk, R. W., and J. C. G. Walker, Thermal diffusion in the F₂ region of the ionosphere, *Planet. Space Sci.*, 18, 535, 1970.
- Steele, D. P., D. J. McEwen, and J. S. Murphree, On the possibility of auroral remote sensing with the Viking ultraviolet imager, *J. Geophys. Res.*, 97, 2845, 1992.
- Strickland, D. J., D. L. Book, T. P. Coffey, and J. A. Fedder, Transport equation techniques for the deposition of auroral electrons, *J. Geophys. Res.*, 81, 2755, 1976.
- Strickland, D. J., J. R. Jasperse, and J. A. Whalen, Dependence of auroral FUV emissions on the incident electron spectrum and neutral atmosphere, *J. Geophys. Res.*, 88, 8051, 1983.
- Strickland, D. J., R. R. Meier, J. H. Hecht, and A. B. Christensen, Deducing composition and incident electron spectra from ground-based auroral optical measurements: Theory and model results, *J. Geophys. Res.*, 94, 13,527, 1989.
- Tsunoda, R. T., I. Häggström, A. Pellinen-Wannberg, Å. Steen, and G. Wannberg, Direct evidence of plasma density structuring in the auroral F region ionosphere, *Radio Sci.*, 20, 762, 1985.
- Tsunoda, R. T., R. C. Livingston, J. F. Vickrey, R. A. Heelis, W. B. Hanson, F. J. Rich, and P. F. Bythrow, Dayside observations of thermal-ion upwellings at 800-km altitude: An ionospheric signature of the cleft ion fountain, *J. Geophys. Res.*, 94, 15,277, 1989.
- Valladares, C. E., and H. C. Carlson, Jr., The electrodynamic, thermal, and energetic character of intense Sun-aligned arcs in the polar cap, *J. Geophys. Res.*, 96, 1379, 1991.
- Valladares, C. E., Su. Basu, R. J. Niciejewski, and R. E. Sheehan, Simultaneous radar and satellite observations of the polar cusp/cleft at Sondre Stromfjord, in *Electromagnetic Coupling in the Polar Clefts and Caps*, edited by P. E. Sandholt and A. Egeland, p. 285, Kluwer Academic, Hingham, Mass., 1989.
- Vickrey, J. F., R. C. Livingston, N. B. Walker, T. A. Potemra, R. A. Heelis, M. C. Kelley, and F. J. Rich, On the current-voltage relationship of the magnetospheric generator at intermediate spatial scales, *Geophys. Res. Lett.*, 13, 495, 1986.
- Weber, E. J., J. F. Vickrey, H. Gallagher, L. Weiss, C. J. Heinselman, R. A. Heelis, and M. C. Kelley, Coordinated radar and optical measurements of stable auroral arcs at the polar cap boundary, *J. Geophys. Res.*, 96, 17,847, 1991.
- Wickwar, V. B., J. D. Kelly, O. de la Beaujardiere, C. A. Leger, F. Steenstrup, and C. H. Dawson, Sondrestrom overview, *Geophys. Res. Lett.*, 11, 883, 1984.
- S. Basu, Phillips Laboratory (GPIS), Hanscom Air Force Base, MA 01731.
- Su. Basu, National Science Foundation, Aeronomy Program, Room 644, 1800 G Street, N.W., Washington, DC 20550.
- P. K. Chaturvedi, Space Plasma Branch, Plasma Physics Division, Naval Research Laboratory, Washington, DC 20375.
- R. E. Daniell, Computational Physics, Inc., Newton, MA 02159.
- R. Eastes and R. E. Huffman, Phillips Laboratory (GPIM), Hanscom Air Force Base, MA 01731.
- R. C. Livingston, SRI International, Menlo Park, CA 94025.
- C. E. Valladares, Institute for Space Research, Boston College, Newton, MA 02159.

(Received October 3, 1991;
revised April 9, 1992;
accepted May 20, 1992.)

Zonal irregularity drifts and neutral winds measured near the magnetic equator in Peru

S. BASU,* SUNANDA BASU,† E. KUDEKI,‡ H. P. ZENGINGONUL,‡ M. A. BIONDI§ and
J. W. MERIWETHER*

* Phillips Laboratory (LIS), Hanscom AFB, MA 01731, U.S.A.; † Institute for Space Research,
Boston College, Newton, MA 02159, U.S.A.; ‡ University of Illinois, Department of Electronics and
Computer Engineering, Urbana, IL 61801, U.S.A.; § University of Pittsburgh, Department of Physics
and Astronomy, Pittsburgh, PA 15260, U.S.A.

(Received in final form 11 February 1991)

Abstract—Measurements of zonal irregularity drifts were made by the spaced receiver scintillation and radar interferometer techniques from Huancayo and Jicamarca, respectively. The Fabry-Perot Interferometer operated at Arequipa provided the zonal neutral winds. These simultaneous measurements were performed during evening hours in the presence of equatorial spread-*F* on three nights in October 1988. The zonal drift of 3-m irregularities obtained with the 50-MHz radar showed considerable variation as a function of altitude. The drift of hundreds of m-scale irregularities obtained by the scintillation technique agreed with the drift of 3-m irregularities when the latter were measured near the *F*-peak. The neutral winds, on the other hand, sometimes exceeded the irregularity drifts by a factor of two. This is a possible result of the partial reduction of the vertical polarization electric field in the *F*-region caused by the effects of integrated Pedersen conductivity of the off-equatorial night-time *E*-region coupled to the *F*-region at high altitudes above the magnetic equator.

1. INTRODUCTION

Measurements of the east-west (zonal) velocities of the *F*-region plasma in the equatorial region are important for an understanding of both the plasma and neutral dynamics. RISHBETH (1971) first showed that the neutral air winds in the equatorial *F*-region blowing across the magnetic field impart a slow transverse drift to the ions perpendicular to both the wind and the magnetic field which results in a polarization electric field directed vertically downwards. During the day, the polarization electric field is neutralized by currents flowing along the magnetic field through the ionized daytime *E*-region. In fact, during the daytime, the electric field in the *E*-region caused by the neutral wind at *E*-region heights is mapped to the *F*-region and influences the *F*-region plasma to move towards the west. During the night, on the other hand, due to the lower conductivity of the *E*-region, the polarization electric field builds up in the *F*-layer and causes the plasma to move towards the east in the direction of the wind. In the case of negligible polarization current, the polarization electric field is fully developed and under such conditions the neutral wind and the plasma move eastward at the same speed. The electrodynamics envisaged above reduces the ion drag and allows the neutral wind to blow from the west to the east at a much faster rate. This reduction of ion

drag due to the development of the polarization electric fields in the night-time equatorial *F*-region causes the 'superrotation' effect which implies that the mean zonal wind in the frame rotating with the Earth is eastward (cf. KELLEY, 1989).

WOODMAN (1972) investigated the 'superrotation' effect using the Jicamarca radar. He measured the *F*-region plasma drift to be 50 m s^{-1} from the east to the west during the daytime at the magnetic equator and as large as 135 m s^{-1} from the west to the east during the night. He thus confirmed RISHBETH's (1971) theory and estimated the 'superrotation' effect to be 50 m s^{-1} to the east.

More recently, the effects of field line integrated Pedersen conductivities of the *E*- and *F*-region on the behavior of the zonal plasma drift and the neutral wind in the night-time equatorial *F*-region have been modeled (ZALESK *et al.*, 1982; ANDERSON and MENDILLO, 1983). In particular, the model of ANDERSON and MENDILLO (1983) providing the altitude profiles of zonal plasma drift at the magnetic equator shows good qualitative agreement with the DE-2 measurements of the latitude variation of zonal plasma velocity in the night-time equatorial region (AGGSON *et al.*, 1987; ANDERSON *et al.*, 1987). It should be noted, however, that the above studies deal with the background ionosphere and do not consider situations related to the presence of equatorial spread-*F*.

In this paper, we shall study the behavior of neutral winds and the drifts of plasma density irregularities under spread- F conditions. We shall use simultaneous measurements of the neutral wind by the Fabry-Perot Interferometer (FPI) and drifts of 3-m and kilometer-scale irregularities in the F -region, respectively, by radar interferometer and spaced receiver scintillation techniques to determine the behavior of drifts of plasma density irregularities and neutral winds near the magnetic equator at night. We will focus attention on the relative magnitudes of neutral winds and plasma density irregularity drifts during the incidence of strong and weak spread- F .

2. RESULTS

Figure 1 shows the geometry of the observations with respect to the coastline of South America and the geographic latitude and longitude grid on which the magnetic equator and the lines of constant magnetic latitudes are superimposed. The location of the Jicamarca radar facility is indicated by J (geographic latitude: 11.95°S ; longitude: 76.86°W ; magnetic dip: 0.3°S). The ground station for scintillation observations at Huancayo is shown as HU (geographic latitude: 12°S ; longitude: 75.3°W ; magnetic dip: 0°) and the 300-km intersection point of the propagation

path from Huancayo to the geostationary satellite Fleetsatcom at 250 MHz is denoted by the point HU/FLT . This intersection point is co-located with the ionospheric volume probed by the radar. From Arequipa (geographic latitude: 16.5°S ; longitude: 71.5°W ; magnetic dip: 3.2°S), the FPI measurements were performed at a zenith angle of 60° to the east and to the west to derive the zonal neutral wind. The Arequipa station is shown by A and the points A_E and A_W indicate the intersections of the eastern and the western measurements with the 275-km level from where 6300 Å emissions originate.

Figure 2 shows the behavior of 50-MHz backscattered power recorded by the Jicamarca radar on 11–12 October 1988 during 1950–2200 LT. This technique, first developed by WOODMAN and LAHOZ (1976), describes the distribution of backscattered power from equatorial spread- F as a function of altitude and time. The grey-scale used in the diagram depicts the strength of the backscattered power, where the darkest shading corresponds to a level of 48 dB above the maximum incoherent scatter power level and the lightest shading corresponds to a level of 6 dB. In view of Bragg's relation, the backscatter at 50 MHz is obtained from spread- F irregularities with 3-m wavelengths that correspond to half the radar wavelength. In view of the extreme aspect sensitivity

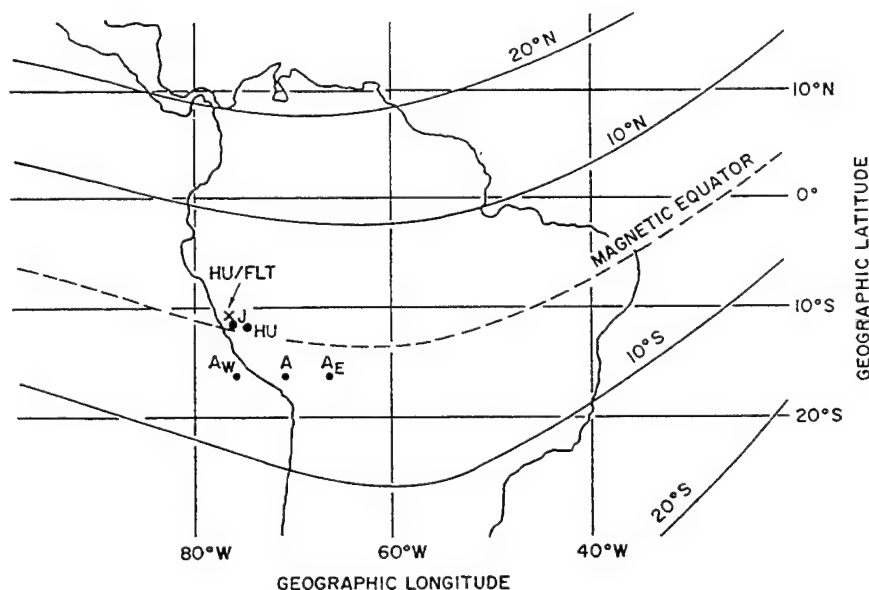


Fig. 1. Locations of 50-MHz backscatter radar at Jicamarca (J), Peru, the scintillation observing station at Huancayo (HU), the 300-km intersection (HU/FLT) of the propagation path from HU to the Fleetsatcom satellite, the optical station at Arequipa (A) performing neutral wind measurements and the ionospheric volumes at 275 km explored by these measurements in the east (A_E) and the west (A_W).

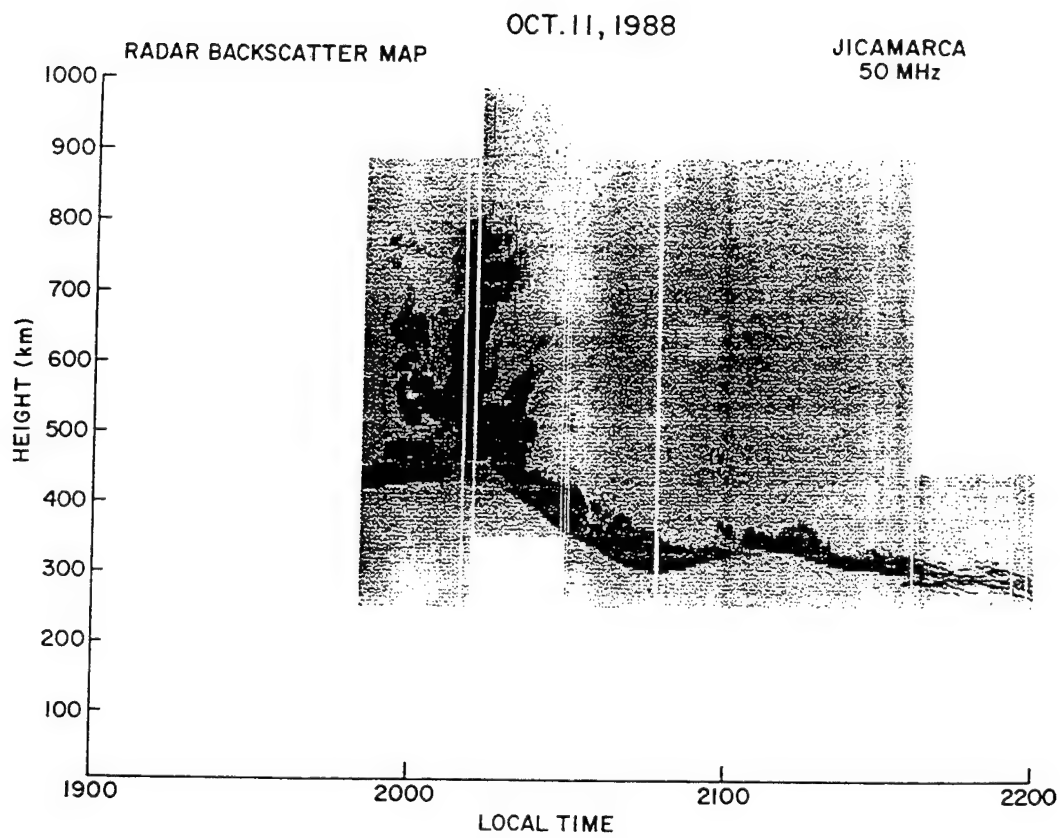


Fig. 2. Radar power map at 50 MHz obtained at Jicamarca on 11–12 October 1988 indicating the temporal variation of range and intensity of backscattered power from 3-m irregularities.

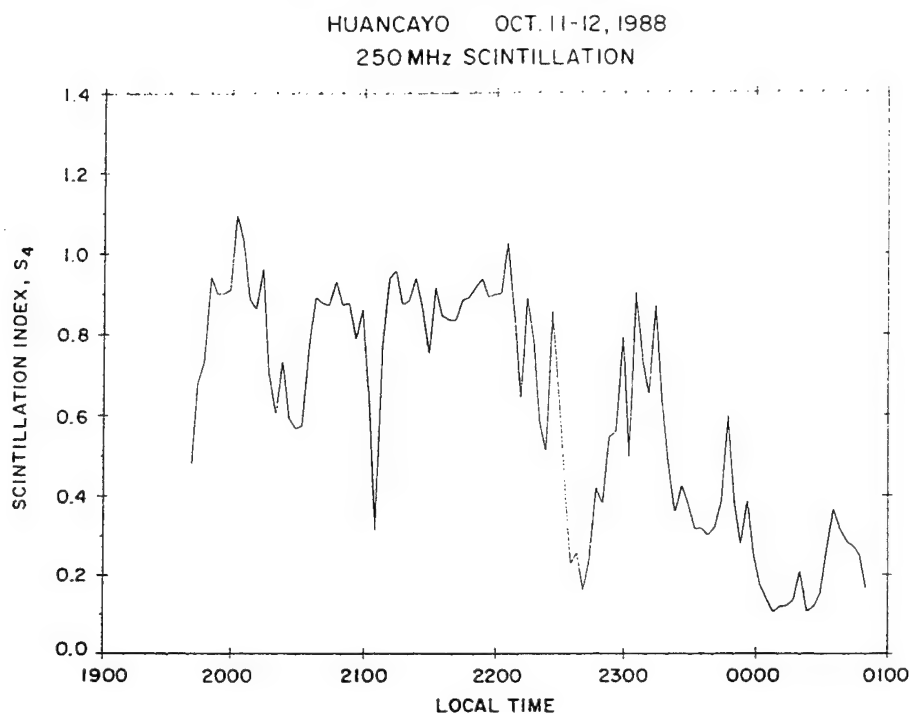


Fig. 3. Temporal variation of the S_4 index of intensity scintillation at 250 MHz on 11-12 October 1988.

of meter-scale irregularities, the radar has to be pointed 3° north of the on-axis position to be perpendicular to the direction of the Earth's magnetic field at the ionospheric height. The backscattered power is proportional to the square of the electron density deviation of 3-m irregularities. Thus the power map shown in Fig. 2 depicts the distribution of the strength of 3-m irregularities as a function of altitude and time. The time-scale on the abscissa can be translated to the east-west distance from a knowledge of the drift velocity of the irregularities in the east-west direction. The diagram shows that in the initial phase the irregularities are extended in altitude in the form of three plumes, the central one penetrating to altitudes as high as 800 km. After about 2020 LT, a steep descent of the F -layer takes place and the irregularities become much more confined in altitude not exceeding 100 km in thickness. After 2040 LT, a gradual and small increase of F -layer altitude followed by a descent is observed. The thickness of the irregularity layer during this period becomes much reduced.

In Fig. 3, the time variation of the strength of intensity scintillations, observed on the 250-MHz transmissions of the Fleetsatcom satellite, is shown. As mentioned in conjunction with Fig. 1 the satellite signals were received at Huancayo, Peru, and the sub-

ionospheric point was co-located with the ionospheric volume probed by the Jicamarca radar. As a result, the radar explored the plasma density structures nearly simultaneously with the scintillation experiment. It should be noted that scintillations at 250 MHz are caused by the drifting irregularities in the scale length range of about 1 km to 100 m which forward scatter the radio signals. Comparing Figs 2 and 3, we note that the plume structure in Fig. 2 ending at 2020 LT corresponds to the first scintillation structure recorded between 1940 and 2020 LT. The second scintillation structure (2020-2105 LT) possibly corresponds to the portion of the radar backscatter map between 2020 and 2055 LT. During this period, when the radar power map indicates the descent of the F -layer and the presence of a relatively thin layer of 3-m irregularities, the scintillations remain high. During the next scintillation event, we again observe very strong scintillation activity to co-exist with relatively thin layer of 3-m irregularities. The observed persistence of strong scintillations even though the 3-m irregularities are decaying signifies that the lifetime of kilometer-scale irregularities responsible for scintillations is longer than the 3-m irregularities (BASU *et al.*, 1978).

Figure 4 compares the results of irregularity drift

OCTOBER 11-12, 1988

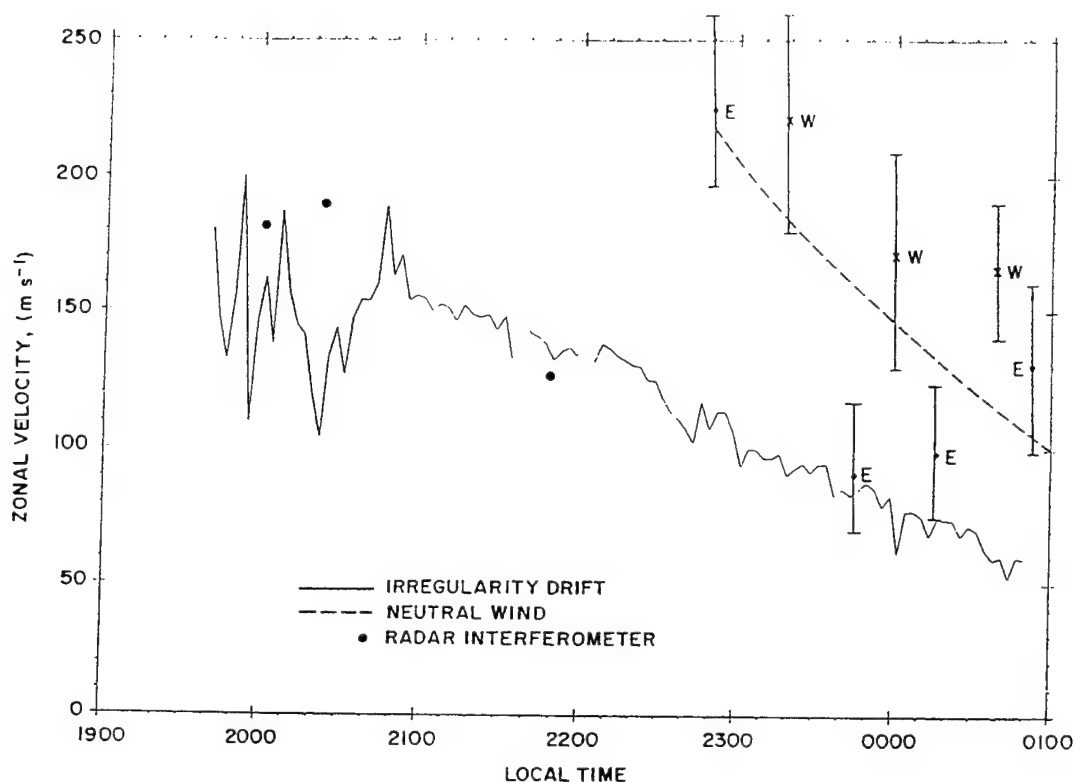


Fig. 4. Comparison of the eastward drift of 3-m irregularities obtained by the 50-MHz radar interferometer (indicated by dots), the drift of kilometer-scale irregularities obtained by the scintillation technique (solid line), the neutral wind flow in the east and the west indicated by *E* and *W* and the best fit quadratic curve to the neutral wind data during the entire night on 11-12 October 1988.

velocity measurements in the east-west direction by scintillation and radar interferometer techniques with the neutral wind speed measurements in the east-west direction being provided by the FPI at Arequipa. From auto- and cross-correlation analysis of scintillations recorded by three antennae separated in the magnetic east-west direction over baselines of 366 and 244 m, the drift velocity of kilometer-scale irregularities causing scintillations are determined by using the peak value method (VACCHIONE *et al.*, 1987). These results are shown by the solid-line curve in Fig. 4. The drift of kilometer-scale irregularities as measured by the spaced-receiver scintillation technique is observed to be as high as 150 m s^{-1} during the onset of spread-*F*, commences to decrease from about 2100 LT and decreases to a value of 50 m s^{-1} at 0100 LT.

The east-west drift of 3-m wavelength spread-*F* irregularities was determined by the radar inter-

ferometer technique (KUDEKI *et al.*, 1981). In this technique, the full Jicamarca radar antenna system is used to transmit the 50 MHz radar pulse and the backscattered echo is received by the east and west quarters separately. When discrete scattering centers are present, an analysis of the normalized cross-spectrum of the Fourier transforms of the digitized signals from the east and west antennae can be performed to obtain the east-west drift velocity of the scattering centers. With these measurements, the altitude profile of the eastward drift of these scattering centers containing 3-m irregularities are obtained. The maximum values of the zonal irregularity drift obtained from the velocity profiles during three time intervals between 20 and 21 LT are plotted as three dots in Fig. 4. We consider that the altitude of maximum velocity corresponds to the level of maximum ionization density, h_{max} . This follows the findings of ANDERSON *et al.* (1987), who have shown that when the zonal neutral

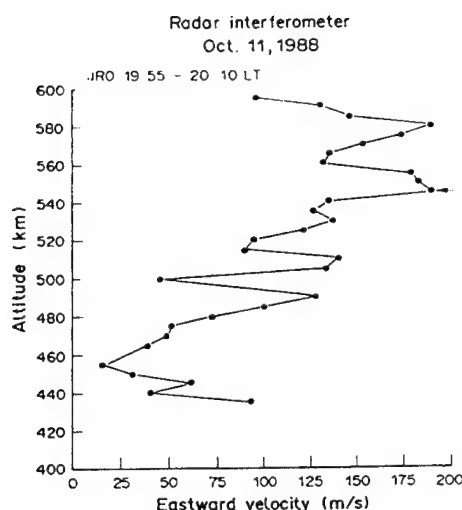


Fig. 5. The altitude profile of the zonal component of the 3-m irregularity drift between 1955 and 2010 LT on 11 October 1988.

wind is maximum at the magnetic equator and decreases with latitude, the zonal plasma drift attains its maximum value at the magnetic equator near h_{max} . Such an altitude selection is appropriate for a comparison of drift results from the radar interferometer and the spaced-receiver scintillation measurements since the scintillation technique reflects the drift of irregularities at heights where the ionization is most concentrated. This is because the magnitude of scintillation is controlled by the product of relative irregularity amplitude ($\Delta N/N$) and the background ionization density (N_i) integrated over the irregularity layer thickness. Since satellite *in-situ* observations indicate that, in equatorial spread- F , the irregularity amplitude is nearly constant with altitude around the level of maximum ionization density, the integrated value of ΔN is determined by the weighting of the ionization distribution. Figure 5 shows the altitude profile of the zonal drift of 3-m irregularities. It shows the general trend of increasing drift with altitude up to about 580 km and a decrease at higher altitudes. The figure also shows thin layers with velocity shear in this early phase of plume generation. In Fig. 5, the arrow indicates the selection of an appropriate data point for drift comparison which was replotted in Fig. 4 at 1953 LT.

Referring to Fig. 4, we find that, in the initial phase, the zonal drift of 3-m irregularities measured by the interferometer agrees quite well with the drift of kilometer-scale irregularities obtained from the spaced-receiver scintillation measurements. Such agreement

was also observed earlier when similar measurements were performed during the Project Condor equatorial F -region rocket campaign (BASU *et al.*, 1986).

Figure 4 also shows the zonal neutral wind drift measured by the FPI at Arequipa, Peru. High resolution determinations of the center frequency of the forbidden oxygen line emission at 630.0 nm with respect to the center frequency in zenith observations give a direct indication of the thermospheric flow in the observing direction (MERIWETHER *et al.*, 1986). The results of these measurements performed in the east and the west directions at a zenith angle of 60° are indicated by E and W along with the error of measurement. The difference between the E and W results as indicated by some of the points may arise due to the local time difference of about 40 min between these two sets of observing locations. A quadratic best fit to the observational results obtained during the entire night is indicated by the dotted line. These measurements could not be performed at local times earlier than those shown because at such times the pronounced height increase of the F -layer leaves little ionization at 250–300 km for the dissociative recombination of the molecular oxygen ions and electrons to occur for the emission of 630.0 nm. The decrease of the eastward neutral wind flow with increasing local time may be noted as reported earlier by MERIWETHER *et al.* (1986). The most interesting finding is related to the fact that the zonal neutral wind is at least a factor of 2 higher than the drift of the scintillation causing kilometer-scale irregularities at ~ 2300 LT and remains 50 m s^{-1} higher even at 0100 LT. It is quite likely that the neutral wind drifts refer to altitudes of about 250 km and kilometer-scale irregularity drifts correspond to higher altitudes. However, as one expects smaller plasma drifts at lower altitudes as indicated by the radar interferometer results in Fig. 5, this difference will be more than that shown. Thus we conclude that the flow of neutral wind towards the east in the night-time equatorial F -region remains considerably faster than that of either the kilometer- or the meter-scale irregularities. It is interesting to note that the average zonal plasma drift obtained by the incoherent scatter radar measurements on non spread- F nights indicate values that are less than the zonal winds by 40% during the equinoxes and 100% during the winter (FEJER *et al.*, 1991, this issue).

In order to discuss the observed differences in zonal drift, detailed above, we should consider three components, namely the drift of the neutrals, the drift of the plasma and the drift of the irregularities. The observations lead us to consider that the neutral wind moves eastward faster than the $\mathbf{E} \times \mathbf{B}$ drift of the back-

ground plasma. As mentioned in the Introduction, the eastward neutral wind develops in the background *F*-region ionosphere, near the equator, a vertical polarization electric field pointing towards the ground. If the *F*-region were totally isolated from the off-equatorial *E*-region during the night-time, the $\mathbf{E} \times \mathbf{B}$ drift would have been just sufficient to have the ions and electrons travel at the same speed as the neutral wind and reduce the ion drag to zero. The fact that the eastward $\mathbf{E} \times \mathbf{B}$ plasma drift is less than the neutral wind flow signifies that the integrated field-aligned Pedersen conductivity of the *E*-region contributes significantly to the total integrated Pedersen conductivity of the *E*- and the *F*-region (ANDERSON *et al.*, 1987). The polarization current will also develop polarization electric field on the irregularities and force the irregularities to travel slower than the $\mathbf{E} \times \mathbf{B}$ drift. Since the polarization electric field varies inversely as the irregularity scale length L , the meter-scale irregularities will travel faster than the kilometer-scale irregularities. Yet, this polarization electric field on the irregularities will be several orders of magnitude smaller than the background polarization electric field (HAERENDEL *et al.*, 1967), leading to imperceptible differences between the zonal drift of the irregularities and the background plasma drift. However, the equatorial spread-*F* irregularities evolve in a large-scale bubble which will polarize with a substantial amount of polarization electric field and the velocity of the bubble will be much less than the $\mathbf{E} \times \mathbf{B}$ drift. Thus, the $\mathbf{E} \times \mathbf{B}$ plasma drift will be slower than the neutral wind velocity and the bubble containing all irregularity scales will travel more slowly than the $\mathbf{E} \times \mathbf{B}$ drift. In fact, in the frame of reference of the $\mathbf{E} \times \mathbf{B}$ drift, the neutral wind will flow eastward and the bubble with its irregularities will travel westward. This accounts for the westward tilt in some of the plumes in Fig. 2 as pointed out by WOODMAN and LAHOZ (1976).

Figures 6–8 refer to observations on the next night, 12–13 October 1988, and illustrate the parameters similar to those illustrated in Figs 2–4. The weak scintillation activity recorded on this night indicates that the spread-*F* developed very marginally. The very limited period of weak irregularity activity accounts for so few observational results of spaced receiver and radar interferometer drifts shown in Fig. 8. The sparse observational results indicate, however, rather low zonal drift of both the 3-m and kilometer-scale irregularities. In addition, the velocity profiles obtained by the radar interferometer indicate that h_{\max} did not exceed 350 km. The zonal neutral wind results indicate considerable dispersion between the east and west measurements. In view of this, a best fit quadratic was

not attempted as done on 11–12 October. Two neutral wind data points at 2130 and 2310 LT are not shown because of low *S/N* ratio in these westward measurements and particularly for the overhead calibration fringes. Although there is a difference of 30 min in local time, the scatter between the *E* (east) and *W* (west) measurements indicate considerable inhomogeneity in the flow pattern. Overall, a non-plume evening in the equatorial region seems to provide a not too dramatic post-sunset increase of *F*-layer altitude, with low values of irregularity drift and considerable spatial variation of neutral winds. It appears that on such nights the equatorial *F*-region remains strongly coupled with the *E*-region which precludes the turn-on of the enhanced zonal electric field that causes the *F*-layer to rise and also inhibits the development of the polarization electric field in the *F*-region.

Figure 9 shows the example of fully developed night-time spread-*F* observed on 14–15 October which is similar to that of 11–12 October. The bottomside of the *F*-layer attained a height of 400 km at 2000 LT when 50 MHz backscatter power returns were recorded from altitudes as high as 900 km. The scintillation behavior on this night is also very similar to that observed on 11–12 October. Figure 10 shows that, in the initial phase (1930 LT), the spaced-receiver scintillation technique recorded 250 m s⁻¹ eastward drift of kilometer-scale irregularities. This drift decreased to a value of about 100 m s⁻¹ at about 2300 LT. The radar interferometer measured zonal drifts approaching 200 m s⁻¹ at 2000 LT (at 700-km altitude) and detected at high altitudes relatively thin regions with pronounced shear in the zonal irregularity drift. As explained earlier, the drifts of 3-m and kilometer-scale irregularities were compared by reading off the maximum radar interferometer drift values. The two sets are in close correspondence with one another. Owing to the marked altitude increase of the *F*-layer in the early phase, 630.0 nm emission could not be detected prior to 2300 LT. At 2300 LT, the neutral wind was about a factor of two higher than the drifts of kilometer-scale irregularities. Thus, we note that similar to the event noted on 11–12 October, the fully developed spread-*F* nights yield marked increase in *F*-layer altitude, high zonal drifts of plasma density irregularities with the neutral wind flow much faster than the irregularity drifts.

3. SUMMARY

The observations presented in this paper indicate that, on nights when equatorial spread-*F* is fully developed, the zonal neutral wind flow is more uniform and the eastward neutral wind, in the pre-mid-

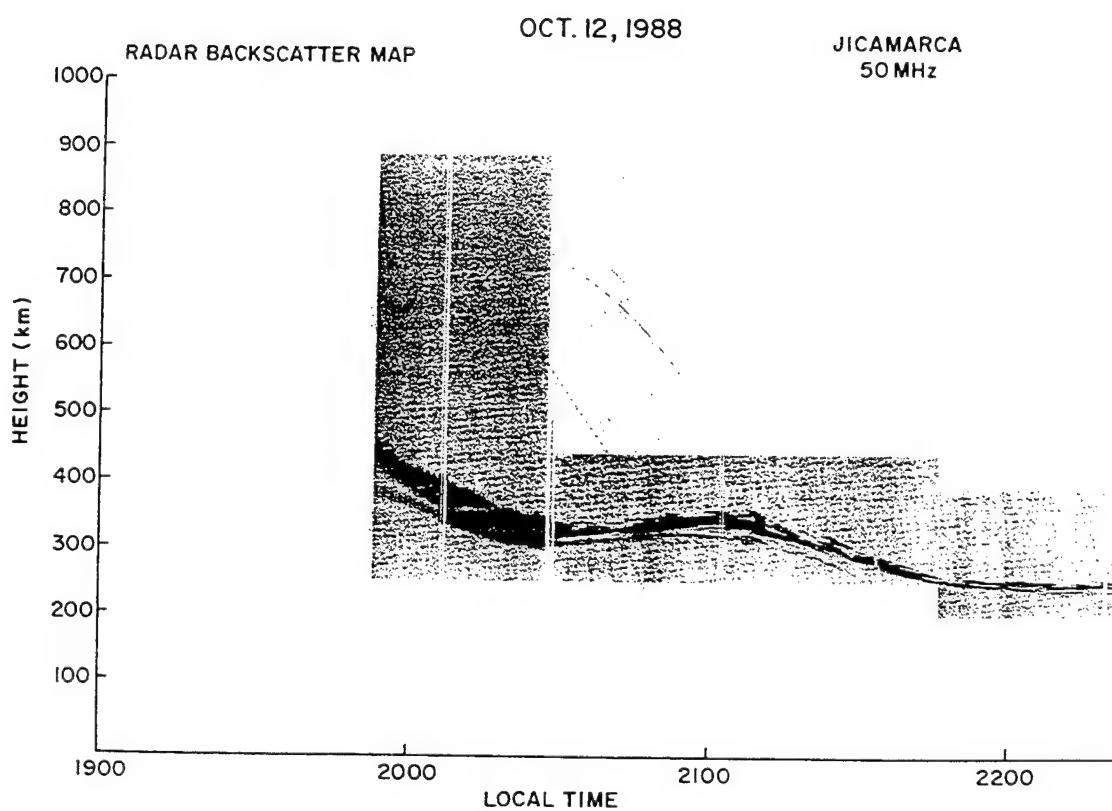


Fig. 6. Same as Fig. 2, except the date is 12-13 October 1988.

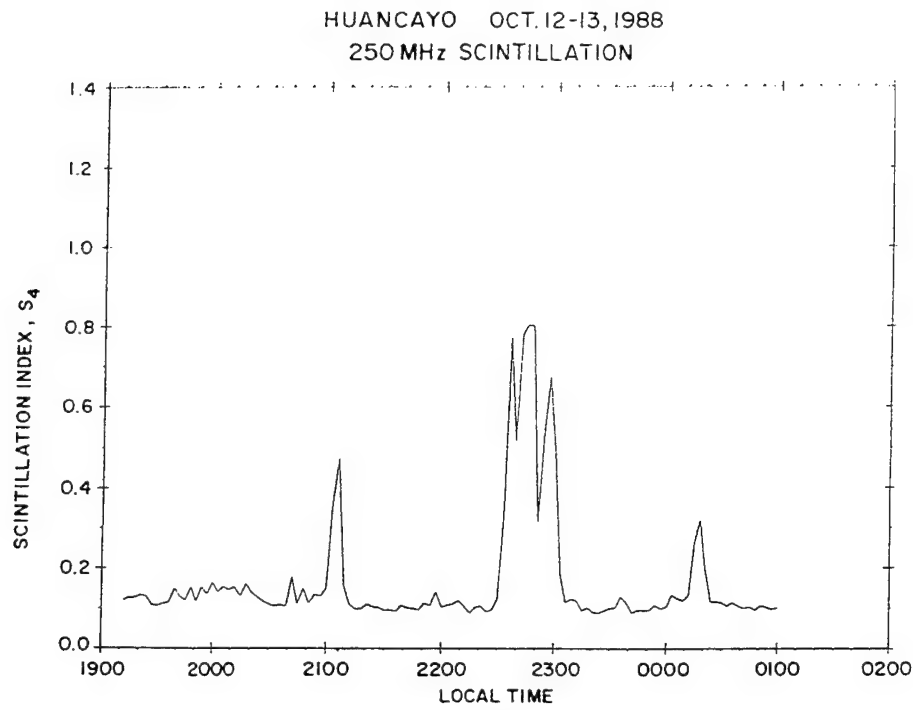


Fig. 7. Same as Fig. 3, except the date is 12-13 October 1988.

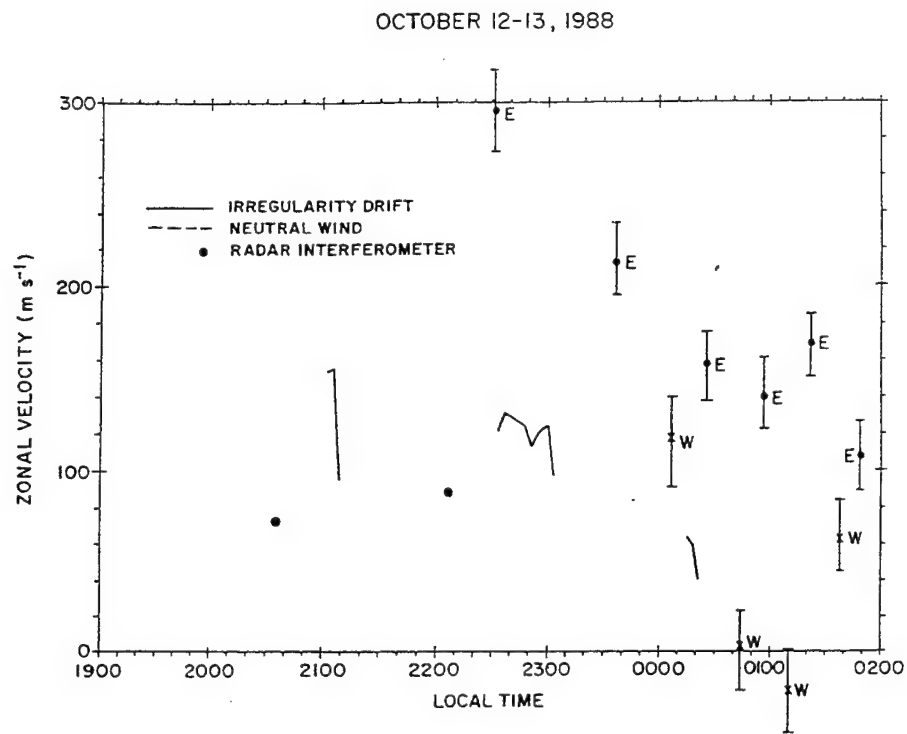


Fig. 8. Same as Fig. 4, except the date is 12-13 October 1988.

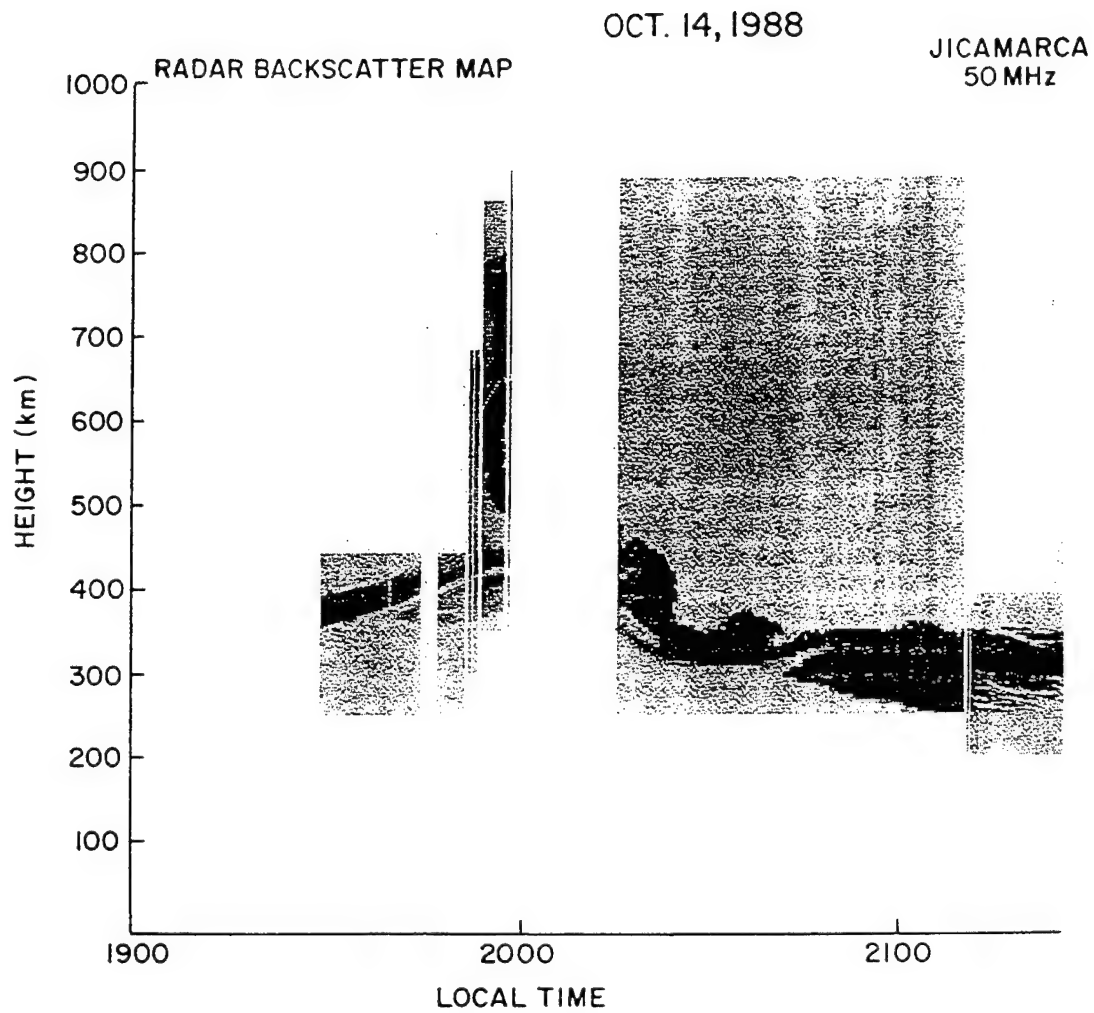


Fig. 9. Same as Fig. 2, except the date is 14–15 October 1988.

OCTOBER 14-15, 1988

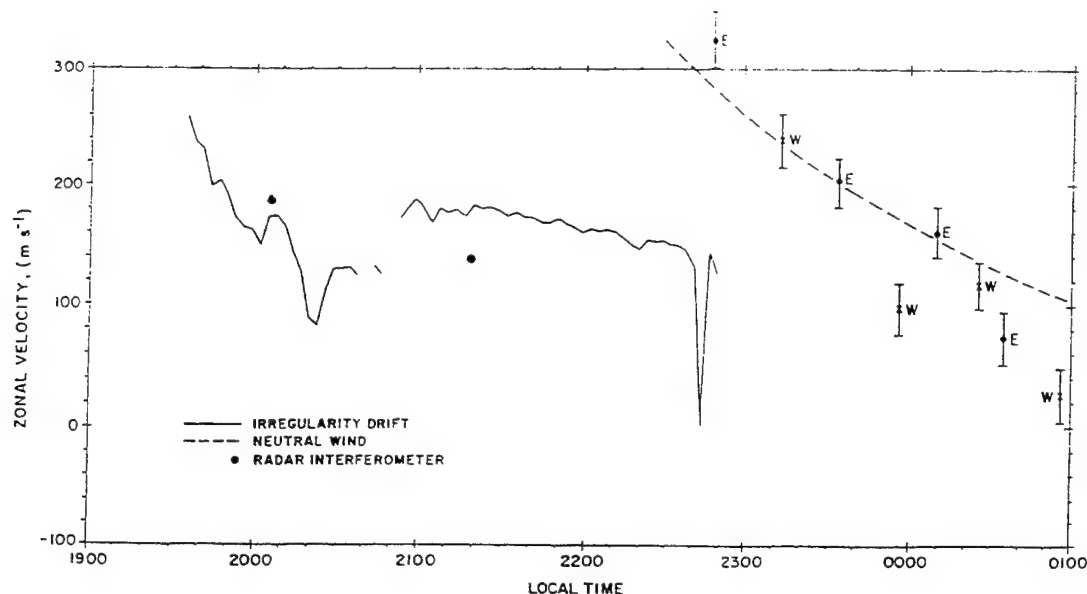


Fig. 10. Same as Fig. 4, except the date is 14-15 October 1988.

night period, is at least twice as large as the eastward drift of either the kilometer or the meter-scale irregularities when the latter are measured at the F -peak or higher. This difference is expected to be enhanced when the irregularity drifts are referred to the lower altitude of airglow emission, since the irregularity drift profiles obtained by the radar interferometer indicate the irregularity drifts to be smaller at lower altitudes. It should be noted that the irregularities embedded within large-scale plasma bubbles owing to the polarization of the bubble will travel more slowly than the $E \times B$ plasma drift. Even under this constraint, the observations performed on spread- F nights with marked increase in F -layer altitude indicate the difference between the plasma drift and neutral wind to be significantly larger than that predicted by the current models (ANDERSON and MENDILLO, 1983; ANDERSON *et al.*, 1987). The models do reproduce qualitatively the altitude profiles of irregularity drifts but cannot provide quantitative agreement. It is necessary to establish whether this difference between the plasma drift and the neutral wind flow arises from a not too realistic representation of integrated E -region Pedersen conductivity on field tubes that are

transported to high altitudes at the magnetic equator on strong spread- F nights.

On weak spread- F nights, the marked increase of h_{\max} is not observed and the irregularity drifts remain considerably slower. The zonal neutral winds show spatial gradients. It is not clear if such gradients in the neutral wind flow are responsible for the inhibition of the F -region dynamo. More co-ordinated observations of neutral winds and irregularity drifts are necessary under varying levels of spread- F activity to determine if such measurements can provide a better understanding of F -region electrodynamics and their relationship to spread- F occurrence.

Acknowledgment—The authors wish to thank Cesar E. Valadares and D. C. Hallenbeck for help with the observations, D. N. Anderson for useful discussions, and C. Bryant for computational assistance. The co-operation of the personnel of the Instituto Geofisico del Peru is gratefully acknowledged. The work at Boston College was partially supported by Phillips Laboratory Contract F19628-90-K-0007 and National Science Foundation grant ATM-8715445. The work at the University of Pittsburgh was supported by NSF grants ATM-8740490 and ATM-8800464 and that at the University of Illinois by ATM-8814629.

REFERENCES

- AGGSON T. L., MAYNARD N. C., HERRERO F. A., 1987 *J. geophys. Res.* **92**, 311.
MAYR H. G., BRACE L. H. and LIEBRECHT M. C.

- ANDERSON D. N., HEELIS R. A. and McCURE J. P. 1987 *Ann. Geophys.* **5A**, 435.
 ANDERSON D. N. and MENDILLO M. 1983 *Geophys. Res. Lett.* **10**, 541.
 BASU S., BASU S. U., AARONS J., McCURE J. P. and COUSINS M. D. 1978 *J. geophys. Res.* **83**, 4219.
 BASU S., BASU S. U., LABELLE J., KUDEKI E., FEJER B. G., KELLEY M. C., WHITNEY H. E. and BUSHBY A. 1986 *J. geophys. Res.* **91**, 5526.
 FEJER B. G. 1991 *J. atmos. terr. Phys.* **53**, 677.
 HAERENDEL G., LÜST R. and RIEGER E. 1967 *Planet. Space Sci.* **15**, 1.
 KELLEY M. C. 1989 *The Earth's Ionosphere* (p. 104). Academic Press, San Diego.
 KUDEKI E., FEJER B. G., FARLEY D. T. and IERKIC H. M. 1981 *Geophys. Res. Lett.* **8**, 377.
 MERIWETHER J. W. JR., MOODY J. W., BIONDI M. A. and ROBLE R. G. 1986 *J. geophys. Res.* **91**, 5557.
 RISHBETH H. 1971 *Planet. Space Sci.* **19**, 357.
 VACCHIONE J. D., FRANKE S. J. and YEH K. C. 1987 *Radio Sci.* **22**, 745.
 WOODMAN R. F. 1972 *Space Res.* **12**, 969.
 WOODMAN R. F. and LAHOZ C. 1976 *J. geophys. Res.* **81**, 5447.
 ZALESAK S. T., OSSAKOW S. L. and CHATURVEDI P. K. 1982 *J. geophys. Res.* **87**, 151.

The U.S. Government is authorized to reproduce and sell this report.
Permission for further reproduction by others must be obtained from
the copyright owner.

The multi-instrumented studies of equatorial thermosphere aeronomy scintillation system: Climatology of zonal drifts

C. E. Valladares and R. Sheehan

Institute for Scientific Research, Boston College, Newton Center, Massachusetts

S. Basu and H. Kuenzler

Phillips Laboratory, Geophysics Directorate, Hanscom Air Force Base, Massachusetts

J. Espinoza

Observatorio de Ancon. Instituto Geofisico del Peru, Lima

Abstract. A spaced-antenna scintillation system was installed at Ancon, Peru, in May 1994 to measure scintillation of 250-MHz signals from a geostationary satellite by three antennas spaced in the magnetic east-west direction. These measurements were used to establish the climatology of the zonal drift of the irregularities which cause equatorial scintillations. The major objective of this study is to compare this drift climatology to the climatology of zonal neutral wind which is the driver of the equatorial electrodynamics. A comparison of these two climatologies in conjunction with scintillation statistics may provide some clues regarding factors which help or hinder the formation of equatorial spread-F (ESF). With these objectives in mind, the first year's drift and scintillation statistics have been presented as a function of local time, season and magnetic activity and compared with the statistics of ion drift published earlier from incoherent scatter radar observations. The scintillation drift is in good agreement with the Jicamarca radar observations except for the fact that the local time dependence of our drift observations exhibit a broader maximum. The broad maximum may be attributed to lower ion drag experienced in the presence of ESF due to sustained uplifting of the ionosphere. During magnetically active periods, the scintillation drift often exhibits east to west reversals presumably because of the disturbance dynamo effects. The westward drifts during such reversals may be as large as 100 m/s. We have also modeled the zonal drifts as a seasonal basis by using Hedin's neutral wind model and Anderson's fully analytical ionospheric model. The modeled zonal drifts present good quantitative agreement with the drifts obtained with the scintillation technique.

1. Introduction

Comprehensive reviews of the electrodynamical processes that control the plasma motion of the equatorial ionosphere have been presented in recent years by Kelley [1989] and Fejer [1991]. These authors have pointed out that during quiet conditions the ionospheric plasma drifts are driven by the neutral wind through a dynamo action at both *E* and *F* layers [Rishbeth, 1971; Heelis *et al.*, 1974; Farley *et al.*, 1986; Crain *et al.*, 1993]. During nighttime a special situation occurs in the equatorial ionosphere. Due to the absence of a conductive *E* region, large polarization electric fields can develop in the *F* region. This *E* field is the result of an interaction of the neutral wind and the *F* region plasma and drives the ionized gas in the same direction and with near the same magnitude of the zonal neutral wind. During disturbed conditions the equatorial plasma drift is also affected, sometimes quite strongly, by

prompt penetration of high-latitude electric fields or by ionospheric disturbance dynamo generated electric fields [Gonzales *et al.*, 1979; Blanc and Richmond, 1980; Fejer *et al.*, 1983; Senior and Blanc, 1984; Spiro *et al.*, 1988; Sastri, 1988; Fejer *et al.*, 1990]. While the zonal component of the electric field may respond very rapidly to penetrating fields, the vertical electric field does not show a similar response [Fejer *et al.*, 1990].

The seasonal, solar, and magnetic dependence of the equatorial *F* region vertical and zonal plasma drifts have been presented by Fejer *et al.* [1991]. These authors used an extensive data set that was accumulated during 20 years of measurements at Jicamarca. The *F*-region drifts show largest variations in the nighttime periods. Daytime drifts are nearly independent of solar activity. In addition, the daytime zonal drift are also independent of season and magnetic activity. The prereversal enhancement of the vertical drift show the largest excursions during the equinox. Fejer *et al.* [1991] also reported that the afternoon reversal time of the zonal drifts was season independent, but the morning reversal time occurred earliest during summer and latest during winter.

A spaced-antenna scintillation system was installed in Ancon, Peru, as part of the multi-instrumented studies of equatorial thermosphere aeronomy (MISETA) initiative. The main goal of the MISETA initiative is to study the onset, development and decay of the spread F phenomenon and the general electrodynamics of the equatorial ionosphere. The spaced-antenna scintillation system together with a Fabry-Perot interferometer and an all-sky imager at Arequipa and the digisonde deployed at Jicamarca constitutes the core of the MISETA measurements. Other studies committed to relating data from all the MISETA instruments during specific campaigns are under way and will be reported elsewhere. This paper is more limited in scope and presents synoptic data from only one instrument, namely, the spaced-antenna scintillation system.

In this paper, we present the results of the zonal drift of equatorial F region irregularities obtained by the spaced-antenna measurements of scintillation of 250 MHz signals from a geostationary satellite. These measurements were performed at Ancon, Peru (11.79°S, 77.18°W, dip latitude 0.9°N) with a fully automated scintillation system. Since the post-sunset enhancement of vertical ion drift is a necessary condition for the generation of irregularities, the zonal drift measurements made using the scintillation technique pertain to those periods when the postsunset enhancement of vertical ion drift also occurred. We present a detailed study of the scintillation and the variation of the zonal drift of the irregularities on a monthly and seasonal basis during both magnetically quiet and disturbed periods. Our results should provide an accurate description of zonal drifts in the presence of irregularities for comparison with predictions from low latitude thermospheric and ionospheric models. We have also used the fully analytic ionospheric model (FAIM) of Anderson *et al.* [1989] to establish the time-varying electron distribution as a function of latitude and used the neutral wind model of Hedin *et al.* [1988] to model the zonal ion drift. These modeled results are compared with the observed zonal drifts.

2. System Description

The MISETA spaced antenna scintillation system collects and processes UHF (~250 MHz) scintillation amplitude data from a geostationary satellite located at 100° W geographic longitude and L band scintillation signals from the GOES-8 satellite. The subionospheric intersection of the UHF ray path is at 11.09° S, 78.74° W, dip latitude 1.4°N. The system consists of three UHF antennas aligned in the magnetic east-west direction, with baselines of 122 and 366 m, and a 10-m dish that is used for L band scintillations. UHF and L band signals are down converted at the antenna sites to minimize cable losses to centrally located RACAL receivers. After amplification and anti-alias (low-pass) filtering of the receiver automatic gain control (AGC) response, a voltage proportional to the logarithm of the signal strength is digitized at 50-Hz, processed, and then stored in a 486-50 MHz PC. The on-line processing includes calculations of several scintillation parameters (S_4 , power spectrum, decorrelation time) and the zonal ionospheric drift. Other special features that have been implemented are an option to record raw data

and an automatic restart sequence after power is temporarily interrupted.

Drift velocities are calculated every 82 sec using the peak value and the intersection methods described by Vacchione *et al.* [1987] and Spatz *et al.* [1988]. These authors reported that both methods provide similar results for the irregularity drift velocity V_o , while there is typically wider disagreement between estimates for the random velocity, denoted V_c . Both methods are quite simple and well suited for on-line calculations. However, each assumes a quadratic dependence of the correlation about the lag time at maximum correlation. Since the peak value method is based on times closer to the correlation maxima, it is more robust and less likely to fail because of the breakdown on the quadratic dependence of the correlation assumption. The V_c parameter has been variously interpreted as a measure of the velocity distribution about the frozen-in drift velocity of irregularities.

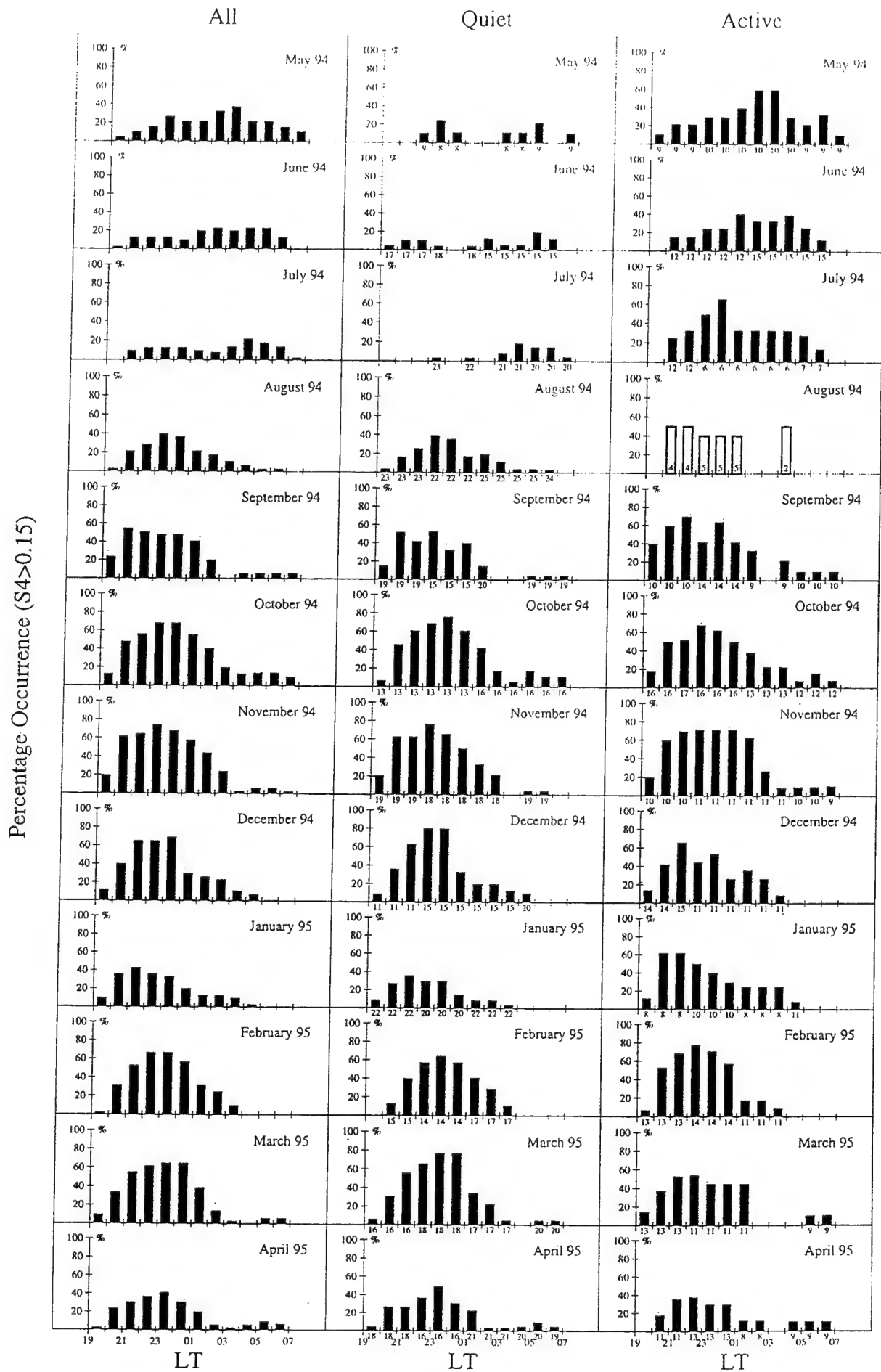
It can arise from a combination of true velocity dispersion within a relatively thin slab of drifting plasma and an altitude shear in V_o [Wernik *et al.*, 1983]. In this paper, we discuss the drift velocity V_o of the irregularities of electron concentration with scale sizes of the order of 1 km which corresponds to the Fresnel dimension of 250-MHz scintillation observations.

3. S_4 Index Statistics

This section presents monthly distributions of the percentage occurrence of scintillations corresponding to the first 12 months of operation between May 1994 and April 1995. Figure 1 shows the monthly distributions of scintillation occurrence for all, quiet, and active conditions. The quiet conditions refers to K_p between 0 and 3, whereas the active conditions refers to $K_p \geq 3^+$. For each evening hour (1900 to 0700 LT), we counted the number of days when the system was operating and whether scintillations were observed in that hour. If scintillations persisted for at least 10 continuous minutes in a given hour, then the whole hour was considered as having scintillations. We also indicate at the bottom of the vertical bars the total number of days on which each monthly statistics is based. The number of days that were used to generate Figure 1 provides a good statistical significance for the majority of the histograms. It is only during the month of August that a small number of days (<6) were magnetically disturbed. The histogram for this month contains larger uncertainties and is indicated using open bars.

In general, all the distributions of Figure 1 show a strong local time variation. The equinoctial and December solsticial histograms (August through April) show a maximum in the pre-midnight hours. In contrast, during the June solstice the scintillation occurrence presents a small peak in the postmidnight hours. In conformity with the well-established statistics of scintillations in the Peruvian sector [Aarons, 1977; Basu and Basu, 1985] the percentage occurrence shows the expected variation from month to month. It is ~40% in May, decreases to 20% in June and July, then steadily increases up to 70% in December, and finally decreases to 40% in April. According to previous reports of scintillation occurrence

Figure 1. Percentage occurrence of UHF scintillations for the first year of operation of the MISETA scintillation system. A K_p index less than or equal to 3 was used to represent a quiet level of magnetic activity. A K_p index larger than 3 indicated active magnetic conditions.



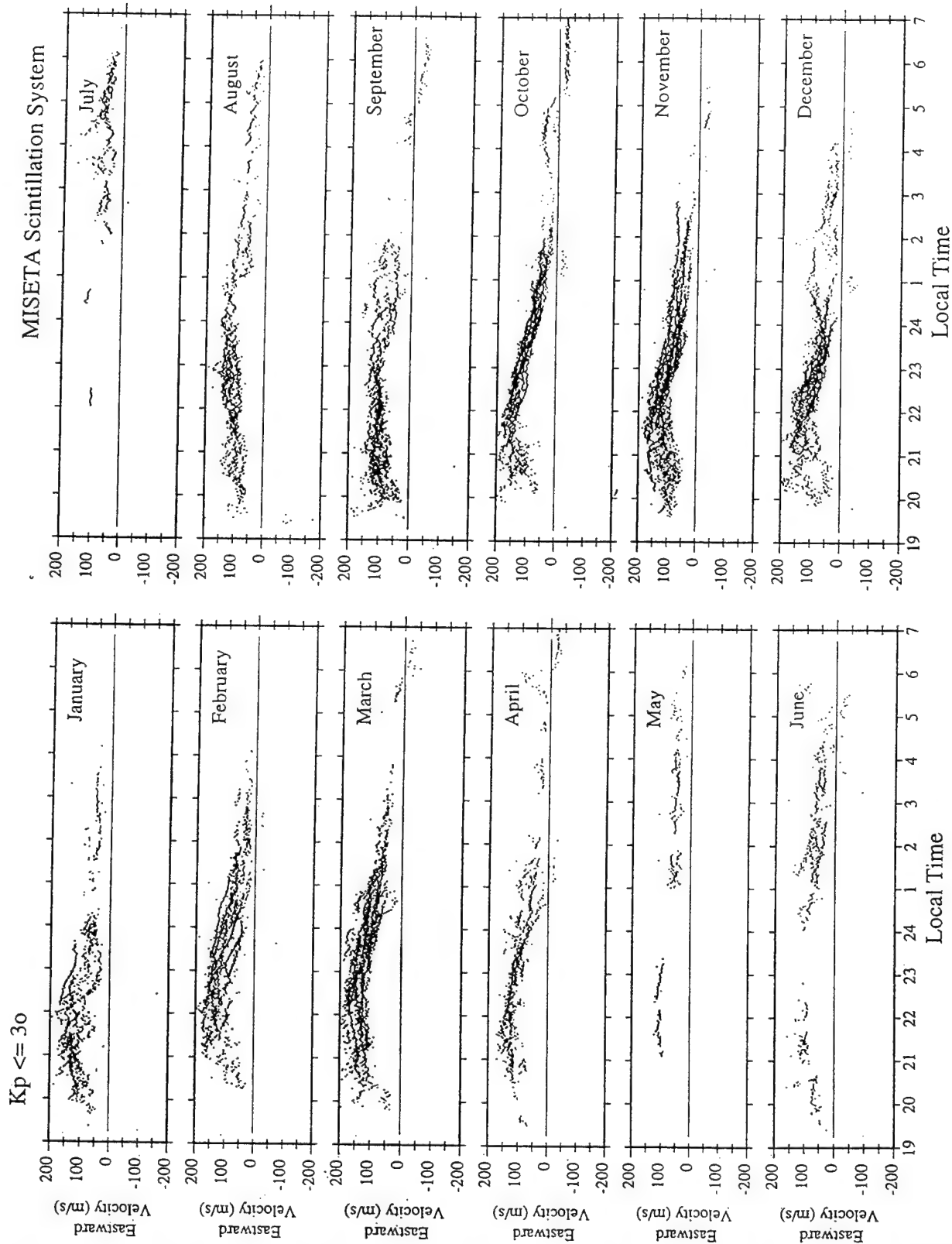


Figure 2. Scatter plot of the eastward irregularity velocity versus local time for each month of the first year of operations. Each dot in this plot corresponds to an independent measurement. During the observations the magnetic conditions were quiet.

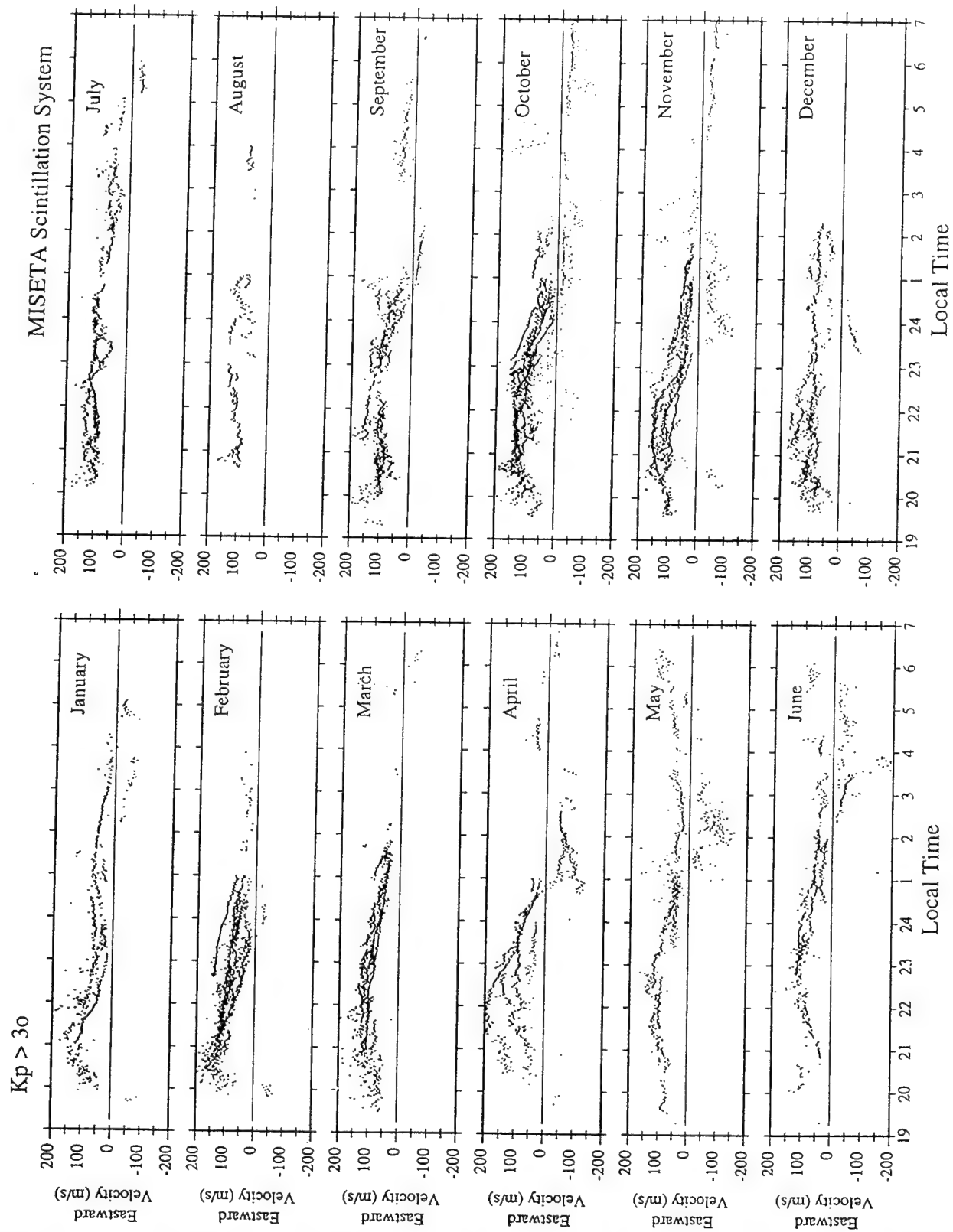


Figure 3. Same as Figure 2 but for active magnetic conditions.

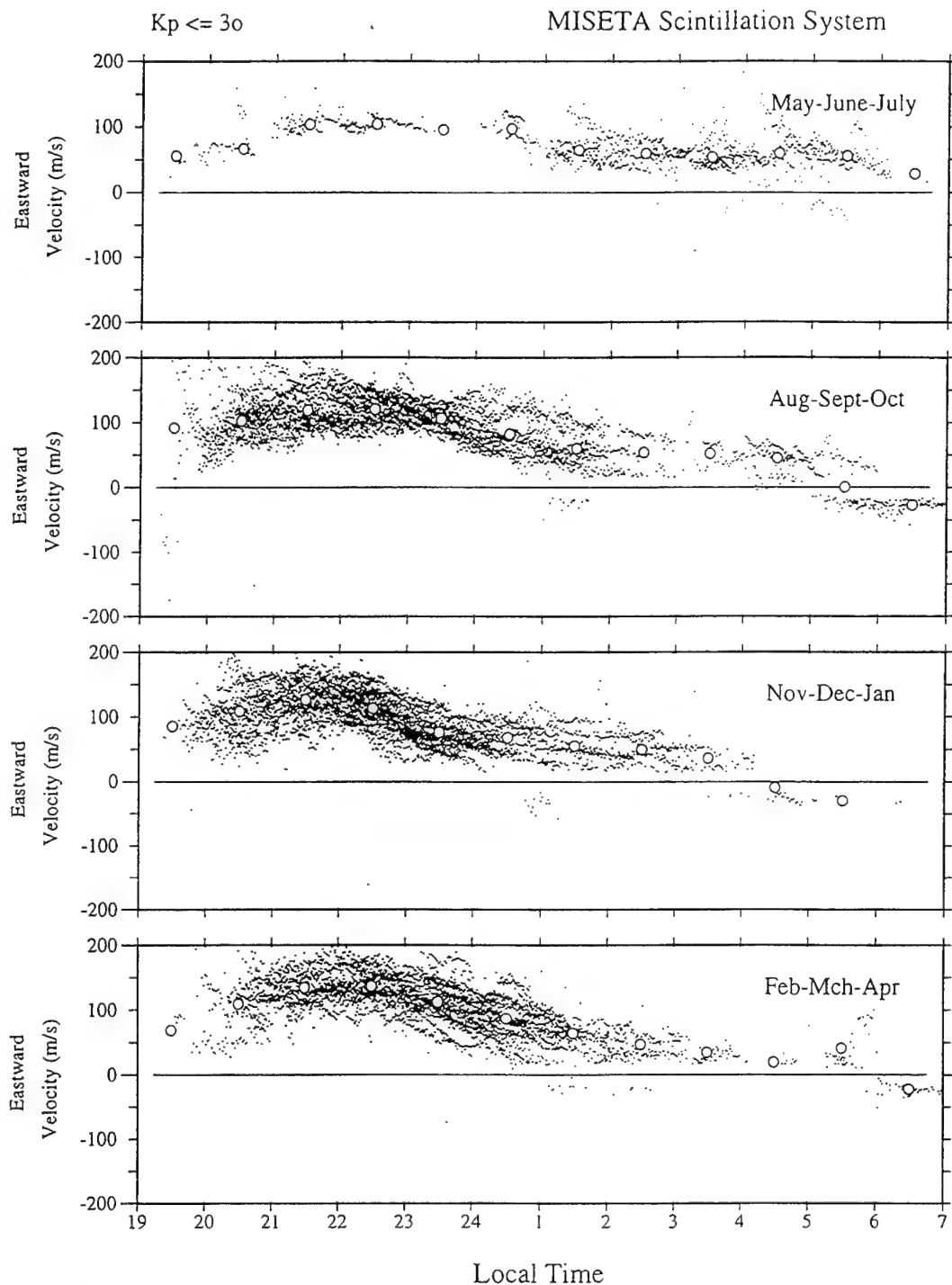


Figure 4. Same as Figure 2 but binned according to season. The circles in the each of the four frames correspond to hourly average drifts.

[Aarons *et al.*, 1980], active magnetic conditions increase the occurrence of scintillations at any hour of the evening during the months of May, June and July. For the other months of the year (August through April) the magnetic dependence of scintillation occurrence is more variable and changes as a function of the local time. Magnetic activity favors an increase of scintillations in the postmidnight hours [Aarons *et al.*, 1980], but does not favor it in the premidnight hours. Thus the Ancon scintillation statistics follows the well known pattern of magnetic control of scintillation occurrence during the June solstice months and also during the postmidnight hours the rest

of the year. However, in the premidnight hours (August through April months), we sometimes see an increase in scintillation activity when the magnetic conditions are active. This is observed in the histograms corresponding to the months of August, September, January, and February.

4. Zonal Irregularity Drift

Every 82-s record of scintillations has served to provide an independent measurement of the zonal drift of ~1-km scale irregularities. These values have been binned according to the

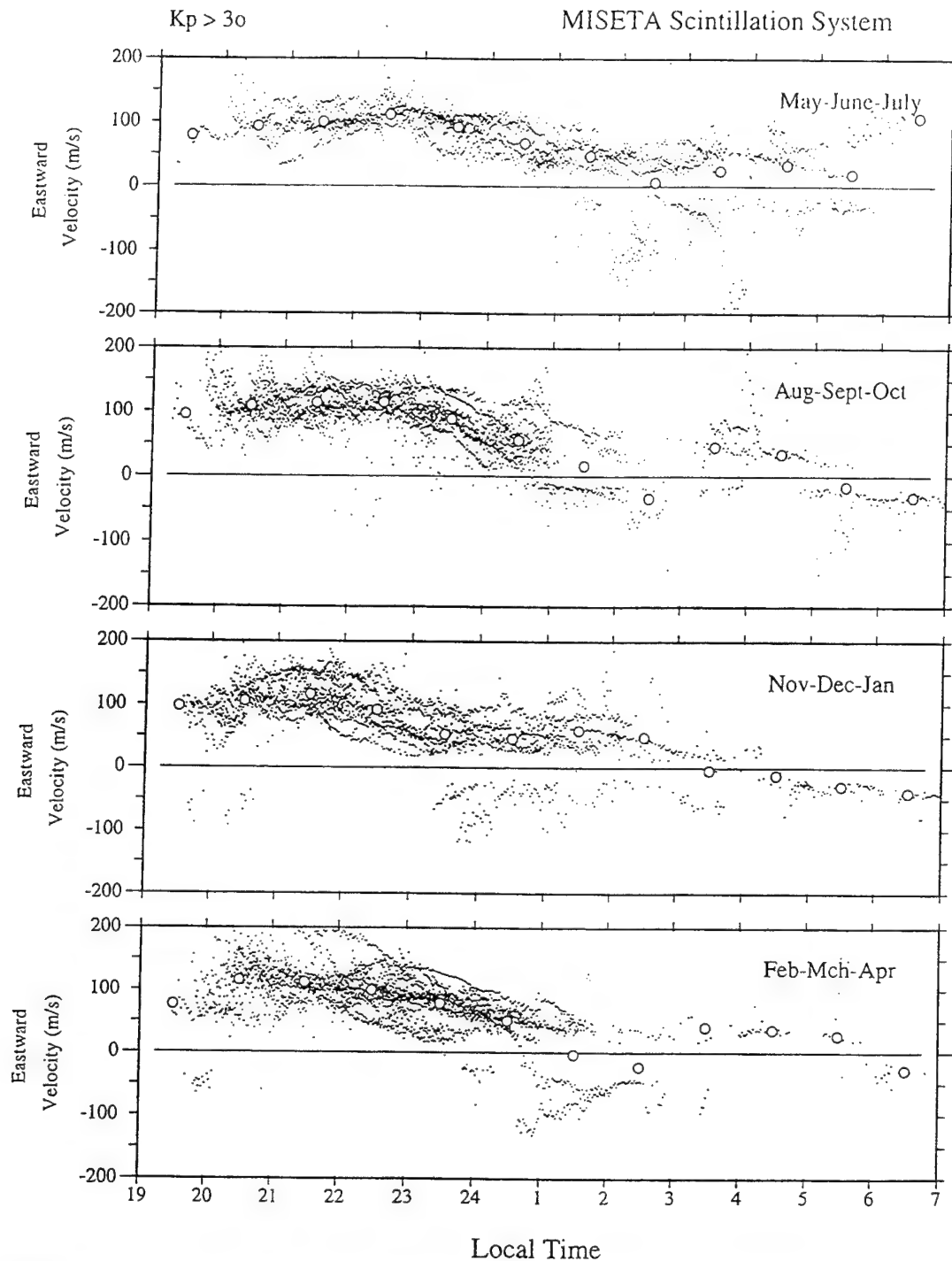


Figure 5. Same as Figure 4 but for active conditions. Notice the large number of westward velocities near and after local midnight.

magnetic activity and the month of the year. Figure 2 shows the irregularity drifts measured during quiet magnetic conditions and Figure 3 displays the drifts for disturbed periods. It is evident in Figure 2 that during quiet times, the irregularity drift is predominantly eastward. As expected, the irregularity drift reverses to westward near sunrise. This feature occurs near 0700 LT in May and consistently appears at earlier hours as the year progresses. In December, during the local summer, the reversal is seen as early as 0400 LT. Each panel of Figure 2 shows a large scatter in the velocity values. The maximum velocity in each panel is about 150 m/s and occurs between

2100 and 2400 LT. The December distribution presents a double-peaked pattern; other months show an increase in the early evening, then a decrease followed by a reversal. Figure 3 shows that the general trend of the monthly velocity distributions for magnetically active periods is quite similar to the quiet day distributions. That is to say, the velocity increases in the early evening and then slowly decreases during the rest of the night. However, there is a much larger velocity spread in the data points, especially in the postmidnight hours. Occasionally, the velocity reverses, sometimes abruptly, toward an unexpected westward direction. These anomalous reversals

occur during the postmidnight hours and can reach a magnitude of 150 m/s.

Figures 4 and 5 display the zonal drifts presented in Figures 2 and 3, but here they are grouped by season. Hourly averages of the zonal drift are indicated using large circles. The zonal drift in Figure 4 under quiet magnetic conditions is basically eastward, with most of the points bunched near the average values. The velocity reversal seems to occur after 07 LT during the June solstice. The other three seasons display a reversal time at 0530, 0400 and 0600 LT. The maximum average zonal drift is seen between 2200 and 2400 LT and has a magnitude of ~ 130 m/s for all four seasons. Figure 5 shows the zonal drifts corresponding to disturbed conditions. Figure 5 shows that the postmidnight anomalous reversals occur during all seasons. In some seasons the anomalous reversals occur so frequently that even the average drift shows a reversal at 0200 LT (more prominent during the equinoxes). This type of event seems to be restricted to the post-midnight hours. Occasionally, the anomalous reversal occurs before local midnight. It was seen at 2200 LT during the month of October and at 2330 LT during the month of December. In the following two sections we compare the scintillation drifts with values originated from an F region dynamo model and with previously reported experimental drifts from Jicamarca.

5. Model Calculations

It is almost universally accepted that during nighttime the equatorial F region ionosphere is driven by a polarization electric field set up by a dynamo effect operating entirely in the F region [Rishbeth, 1971, 1981]. We can also consider that any leakage of the F region polarization field would be small since during nighttime the E region conductivity is small and consequently no currents should be flowing in or out of the E region. As a result the equations of the equatorial electric field are greatly simplified because neither E region coupling nor E region dynamo effects need to be included. Thus the equatorial zonal F region plasma drift can be calculated if we know the values of the Pedersen conductivity and the zonal neutral wind along the F region portion of magnetic field lines. Several theoretical studies have successfully reproduced some of the prominent characteristics of the equatorial drifts that have been measured by incoherent scatter radars or by orbiting satellites [Heelis *et al.*, 1974; Bonelli, 1985; Farley *et al.*, 1986; Crain *et al.*, 1993]. The works of Anderson *et al.* [1987], Carter *et al.* [1994] and Coley *et al.* [1994] have added a higher degree of refinement to the theoretical computations of the nighttime zonal drift. Anderson and Mendillo [1983] showed that the equatorial zonal plasma drift velocity (V_i) is given by

$$V_i = \frac{\int_{S_1}^{S_2} \sigma_p B U ds}{B \int_{S_1}^{S_2} \sigma_p ds} \quad (1)$$

where σ_p is the Pedersen conductivity, B the magnetic field strength, and U the zonal wind. The integration is conducted along the field line. Points S_1 and S_2 are at the bottom of the E region at opposite ends of the field line.

Coley *et al.* [1994] have also modeled the nighttime equatorial zonal plasma drift. They retained the height derivative term ($\partial/\partial n$) in the current continuity equation and included effects of the vertical gradients of the Pedersen conductivity and the zonal neutral wind. These authors concluded that vertical shears in the zonal neutral wind could

explain why, at least partially, the ion drift observed by the DE-2 satellite were higher than the local wind values.

In this section, we will try to determine if the seasonal patterns of the irregularity drift measured by the Ancon scintillation system can be reproduced using empirical models of the F region ionosphere and the thermosphere. This is justified because we are trying to study seasonally averaged quantities and not specific measurements that will clearly require knowledge of the plasma density and the neutral wind along the field lines during a particular time and day. To represent the equatorial ionosphere, we have used the fully analytical ionospheric model (FAIM) of Anderson *et al.* [1989].

To delineate the zonal wind we use the Hedin neutral wind model of 1987 [Hedin *et al.*, 1988]. To calculate the Pedersen conductivity we employed the MSIS86 model of the neutral densities. We decided to use the Hedin 87 model of the neutral wind in view of the recent note by Biondi *et al.* [1995] regarding the Arequipa values which were used in the more recent Hedin 90 wind model. We will not consider the effect of vertical gradients or Hall currents, because their effects are small and our modelling results were not affected substantially when they were incorporated in equation (1).

Figure 6 displays the result of the numerical solution of equation (1) for the four seasons and for 12 hours through the night. The averaged scintillation drifts are shown as lines with small crosses. The modeled drifts are displayed as lines and small circles. During all four seasons the modeled drifts reproduce the general trend or local time dependence of the experimental values. This is to say, the modeled drift is about 60 m/s at the beginning of the evening, increases and reaches a maximum of ~ 100 m/s at 2300 LT, and then slowly decreases and reverses to westward direction at a time near 0400 LT. The agreement is the best for the equinoxes and the December solstice after 2200 LT. During these seasons the maximum difference between the modeled and experimental curves is observed in the early morning hours when the E region dynamo may play a more significant role. The early morning east-to-west reversal of the drifts is also present in the modeled drifts; however, they appear 30 to 60 min before the time indicated by the experimental drifts. The largest disagreement between the modeled and experimental values occurs in the June solstice. This season contains also the least number of scintillation events; thus the average drift pattern is the least representative, because it is based on a small number of measurements.

6. Discussion

It is evident from the results presented that the zonal drift of plasma density irregularities exhibits significant seasonal, local time and magnetic activity variations. We found that the climatology of the scintillation drifts changes considerably depending upon the magnetic condition. During quiet magnetic conditions, we found the zonal drift to be mainly eastward throughout most of the evening. During magnetically active days, the zonal drift presented anomalous westward reversals occurring preferentially in the postmidnight hours. This result is somewhat different from the conclusion drawn by Fejer *et al.* [1991] based on zonal drift measurements at Jicamarca employing the incoherent scatter technique. Fejer *et al.* [1991], based on Jicamarca measurements that spanned 20 years, reported an almost constant difference, less than 20 m/s, between the zonal plasma drifts corresponding to quiet and active magnetic conditions. Our 1-hour average scintillation

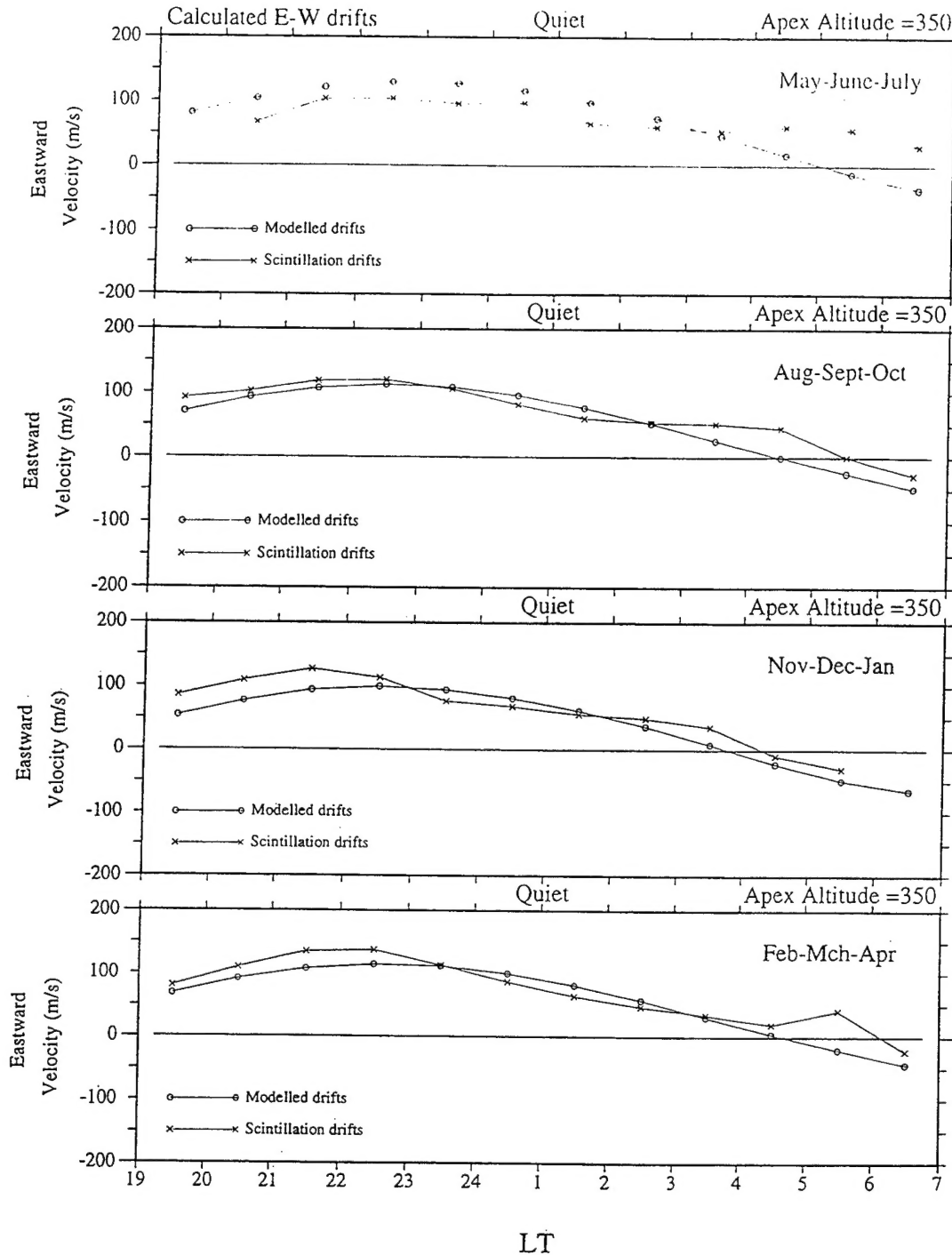


Figure 6. Comparison of the hourly averaged scintillation drifts and a model of the nighttime F region dynamo that uses the Hedin 87 model of the neutral wind and the FAIM and MSIS models to calculate the conductivity. The magnetic conditions are quiet.

drifts for quiet and active conditions present differences of 70 m/s occurring at times near and after local midnight. We will address this apparent discrepancy later in this discussion section when we superimpose the average drift values measured at Jicamarca on the irregularity drifts measured at Ancon.

The F region dynamo model calculations conducted in this study predict zonal drifts in reasonable agreement with the km-scale irregularity drifts measured at Ancon. The modeled and experimental drifts for the equinoxes and the December solstice show an excellent quantitative agreement for most hours of the

night. The drifts for the other season, June solstice, are in a good qualitative agreement. This fact confirms the ability of the spaced-antenna scintillation system to measure plasma drifts. It also endorses the current view that km-scale irregularities move with the local plasma, specially at times when equatorial spread F (ESF) plumes are fully formed, and it lends credence to the F -region dynamo as the driving mechanism of the equatorial plasma during quiet magnetic conditions.

To perform the F region dynamo calculations we used wind

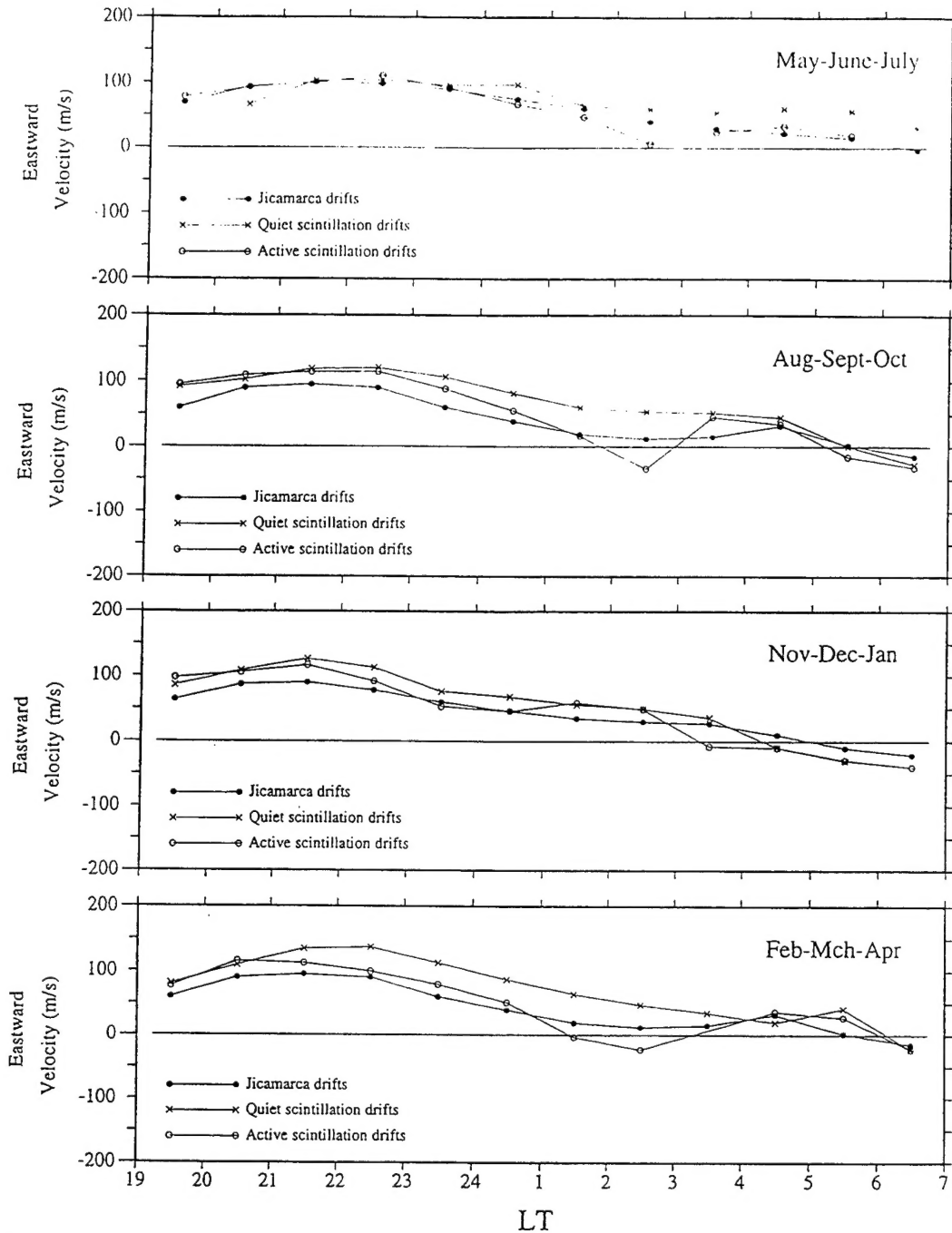


Figure 7. Comparison of experimental drifts gathered by the scintillation and incoherent scatter radar techniques. The scintillation drifts have been separated according to the prevailing magnetic conditions.

values generated by the Hedin 87 wind model [Hedin *et al.*, 1988]. Here we compare these wind values provided by Hedin's model to ground-based observations of the neutral wind conducted at Arequipa in the years of 1983 and 1988 [Biondi *et al.*, 1990, 1995]. Wind data from Arequipa is nonexistent between the months of November and February, a period of cloudy sky at this ground station. For the rest of the year the general nighttime trend of Hedin's wind model and the wind measured by the FPI at Arequipa are very similar. Close comparison indicates that the experimental values are 10% higher than the values provided by the Hedin's model. If this difference is introduced in our calculations, then the

discrepancy between the Ancon drifts and the calculated plasma velocities will certainly decrease for most of the nighttime hours. To improve the agreement of the modeled and experimental values, it would be necessary to increase Hedin's wind values by 15%, for the equinoxes, for the December solstice and for early evening hours and after 0300 LT hours. It is also possible that increasing the nominal altitude of the subionospheric intersection point, set at 350 km altitude, for certain local time hours could bring a better agreement between calculated and measured drifts.

Figure 7 presents the zonal plasma drifts measured at Jicamarca (solid circles) for solar minimum conditions and for

all 4 seasons [Fejer *et al.*, 1991]. Notice that we have repeated the same drift values in the panels for the September and March equinoxes, because Fejer *et al.* [1991] lumped together the Jicamarca drifts for both equinoxes. Figure 7 also displays the average zonal drifts measured at Ancon for quiet (crosses) and for active (open circles) magnetic conditions. In summary all three curves show reasonable agreement in the early part of the evening and in the early morning period. During hours close to midnight (between 2300 and 0400 LT) all three curves show the largest differences. The separation is less than 20 m/s in the December solstice and not larger than 30 m/s in the June solstice. However, during both equinoxes the separations between the quiet and active scintillation drifts become as large as 70 m/s.

Close comparison of the quiet drifts obtained by both techniques indicates that the Jicamarca values are most of the time much smaller than the scintillation drifts. It is only during the early evening hours in the June solstice and the morning hours of the other seasons that the Jicamarca velocities are slightly higher than the scintillation drifts. We have also examined individual (82-s) records of scintillation drift and concluded that most of them are larger than the Jicamarca average values. It is only between 1900 and 2100 LT that some of the scintillation drifts fall below the Jicamarca averages. We suggest that this discrepancy is due to the intrinsic conditions prevailing when the measurements are conducted. Jicamarca radar observations pertain to periods of no ESF. Spaced antenna drifts measurements pertain to ESF.

A qualitative explanation of this finding is advanced in terms of a variation of the F region altitude. During ESF the postsunset enhancement causes an uplift of the F region and a consequent reduction of the ion drag. This smaller ion drag facilitates a larger zonal wind, resulting in a larger zonal plasma drift. A slow lowering of the F layer through the night during ESF events as compared to a much rapid lowering for no ESF nights will also help to maintain larger drifts for several hours during the nighttime.

The markedly different average scintillation drifts seen during the postmidnight hours of both equinoxes were due to the occurrence of anomalous westward reversals of the zonal drift. Two salient features of these anomalous reversals are worth mentioning: (1) they occur predominantly in the postmidnight, early morning hours, and (2) average Jicamarca drifts (mainly no ESF) do not seem affected by them. The latter statement is based on the Jicamarca drifts presented by Fejer *et al.* [1991] where no significant variation occurred in the postmidnight hours of magnetically active days. Blanc and Richmond [1980] suggested that auroral heating during magnetic storms is able to disturb the quiet pattern of winds, electric fields and currents at mid latitudes and low latitudes. The numerical model of these authors indicated the development of a low latitude westward plasma drift (~ 100 m/s) well restricted to the postmidnight and early morning hours of the day. This is in excellent agreement with the anomalous drifts measured with the scintillation technique. We conclude that the equatorial disturbance dynamo is responsible for the westward reversals of the normally eastward zonal drifts. We also suggest that low-latitude electric fields setup by the disturbance dynamo or winds associated with this dynamo can help to seed and trigger the ESF phenomena. The numerical work of Blanc and Richmond [1980] suggested a maximum eastward electric field of about 1.5 mV/m in the premidnight sector. This disturbed electric field is able to lift the ionosphere and favor the initiation of the Rayleigh-Taylor instability.

7. Conclusions

Analysis of the scintillation drift data and comparison with Jicamarca drifts and model results show the following:

1. We have demonstrated that the scintillation technique is able to provide an accurate estimate of the zonal drift of the plasma irregularities and to establish the climatology of the zonal drifts. In spite of the requirements for the existence in the ionosphere of kilometer-scale irregularities, its fairly inexpensive cost makes the use of this technique very attractive for aeronomical studies.
2. F region dynamo calculations of the zonal drift reproduced quite well the average drift obtained with the scintillation technique during quiet magnetic conditions.
3. The average scintillation drifts were larger than the incoherent scatter drifts. We have attributed this discrepancy to the predominant ionospheric conditions when the measurements are performed. Scintillation drifts are associated with times of ESF, IS drifts are related to no ESF.
4. We have observed occasional sudden westward reversals of the zonal drift. These events occurred solely during active magnetic conditions and at times near or after local midnight. We suggest that electric fields of disturbance dynamo origin or winds associated with this dynamo act in some way to trigger the ESF phenomenon. This may explain the well-known enhancement of ESF activity during active magnetic conditions and in the postmidnight sector.

Acknowledgments. We would like to extend our appreciation to Ruben Villafani, Jesus Caballero and Abelardo Chiroque whose dedication and hardware ingenuity under the leadership of Jorge Espinoza has made possible to operate continuously the spaced receiver scintillation system at Ancon, Peru. The work at Boston College was partially supported by Phillips Laboratory contract F19628-90-K-0007, AFOSR task 2310G9 and by NSF grant ATM-9202350. The Observatory of Ancon is operated by the Geophysical Institute of Peru, Ministry of Education.

The Editor thanks J.C. Foster and B.A. Tinsley for their assistance in evaluating this paper.

References

- Aarons, J., Equatorial scintillations: A review, *IEEE Trans. Antennas Propag.*, AP-25(5), 729, 1977.
- Aarons, J., J.P. Mullen, J.P. Koster, R.F. DaSilva, J.R. Medeiros, R.T. Medeiros, A. Bushby, J. Pantoja, J. Lanat, and M.R. Paulson, Seasonal and geomagnetic control of equatorial scintillations in two longitudinal sectors, *J. Atmos. Terr. Phys.*, 42, 861, 1980.
- Anderson, D.N., and M. Mendillo, Ionospheric conditions affecting the evolution of equatorial plasma depletions, *Geophys. Res. Lett.*, 10, 541, 1983.
- Anderson, D.N., R.A. Heelis, and J.P. McClure, calculated nighttime eastward plasma drift velocities at low latitudes and their solar cycle dependence, *Ann. Geophys.*, Ser. A, 5, 435, 1987.
- Anderson, D.N., J.M. Forbes, and M. Codrescu, A fully analytical, low and middle latitude ionospheric model, *J. Geophys. Res.*, 94, 1520, 1989.
- Basu, Su., and S. Basu, Equatorial scintillations: advances since ISEA-6, *J. Atmos. Terr. Phys.*, 47, 753, 1985.
- Basu, S., Su. Basu, E. Kudeki, H.P. Zenggonul, M. A. Biondi and J.W. Meriwether, Zonal irregularity drifts and neutral winds measured near the magnetic equator in Peru, *J. Atmos. Terr. Phys.*, 53, 743, 1991.
- Biondi, M.A., J.W. Meriwether, B.G. Fejer, and S.A. Gonzalez, Seasonal variations in the equatorial thermospheric wind measured at Arequipa, Peru, *J. Geophys. Res.*, 95, 12243, 1990.
- Biondi, M.A., et al., Correction to "Seasonal variations in the equatorial thermospheric wind measured at Arequipa, Peru" and "Equatorial thermospheric wind changes during the solar cycle: Measurements at Arequipa, Peru from 1983 to 1990" *J. Geophys. Res.*, 100, 7863, 1995.

- Blanc, M., and A.D. Richmond, The ionospheric disturbance dynamo, *J. Geophys. Res.*, **85**, 1669, 1980.
- Bonelli, E., Equatorial electric fields: A numerical model, Ph.D. thesis, Cornell Univ., Ithaca, N. Y., 1985.
- Carter, L.N., and D.N. Anderson, Comparison of plasma drift modeling to DE 2 data, *Radio Sci.*, **29**, 769, 1994.
- Coley, W.R., R.A. Heelis, and N.W. Spencer, Comparison of low-latitude ion and neutral zonal drifts using DE 2 data, *J. Geophys. Res.*, **99**, 341, 1994.
- Crain, D.J., R.A. Heelis, G.J. Bailey, and A.D. Richmond, Low-latitude plasma drifts from a simulation of the global atmospheric dynamo, *J. Geophys. Res.*, **98**, 6039, 1993.
- Farley, D.T., E. Bonelli, B.G. Fejer, and M.F. Larsen, The prereversal enhancement of the zonal electric field in the equatorial ionosphere, *J. Geophys. Res.*, **91**, 13723, 1986.
- Fejer, B.G., Low latitude electrodynamic plasma drifts: A review, *J. Atmos. Terr. Phys.*, **53**, 677, 1991.
- Fejer, B.G., M.F. Larsen, and D.T. Farley, Equatorial disturbance dynamo electric fields, *Geophys. Res. Lett.*, **10**, 537, 1983.
- Fejer, B.G., R.W. Spiro, R.A. Wolf, and J.C. Foster, Latitudinal variation of perturbation electric fields during magnetically disturbed periods: 1986 SUNDIAL observations and model results, *Ann. Geophys.*, **8**, 441, 1990.
- Fejer, B.G., E.R. de Paula, S.A. Gonzalez, and R.F. Woodman, Average vertical and zonal F region plasma drifts over Jicamarca, *J. Geophys. Res.*, **96**, 13901, 1991.
- Gonzales, C.A., M.C. Kelley, B.G. Fejer, J.F. Vickrey, and R.F. Woodman, Equatorial electric fields during magnetically disturbed conditions, 2, Implications of simultaneous auroral and equatorial measurements, *J. Geophys. Res.*, **84**, 5803, 1979.
- Hedin, A.E., N.W. Spencer, and T.L. Killeen, Empirical global model of upper thermospheric winds based on Atmospheric and Dynamics explorer satellite data, *J. Geophys. Res.*, **93**, 9959, 1988.
- Heelis, R.A., P.C. Kendall, R.J. Moffett, D.W. Windle, and H. Rishbeth, Electrical coupling of the E- and F-regions and its effect on F-region drifts and winds, *Planet. Space Sci.*, **22**, 743, 1974.
- Kelley, M.C., *The Earth's Ionosphere*, Int. Geophys. Ser., vol. 43, p. 71, Academic, San Diego, Calif., 1989.
- Rishbeth, H., Polarization fields produced by winds in the equatorial F region, *Planet. Space Sci.*, **19**, 357, 1971.
- Rishbeth, H., The F-region dynamo, *J. Atmos. Terr. Phys.*, **43**, 387, 1981.
- Sastri, J.H., Equatorial electric fields of ionospheric disturbance dynamo origin, *Ann. Geophys.*, **6**, 635, 1988.
- Senior, C., and M. Blanc, On the control of magnetospheric convection by the spatial distribution of ionospheric conductivities, *J. Geophys. Res.*, **89**, 261, 1984.
- Spatz, D.E., S.J. Franke, and K.C. Yeh, Analysis and interpretation of spaced receiver scintillation data recorded at an equatorial station, *Radio Sci.*, **23**, 347, 1988.
- Spiro, R.W., R.A. Wolf, and B.G. Fejer, Penetration of high-latitude electric-field effects to low latitudes during SUNDIAL 1984, *Ann. Geophys.*, **6**, 39, 1988.
- Vacchione, J.D., S.J. Franke, and K.C. Yeh, A new analysis technique for estimating zonal irregularity drifts and variability in the equatorial F-region using spaced receiver scintillation data, *Radio Sci.*, **22**, 745, 1987.
- Wernik, A.W., C.H. Liu, and K.C. Yeh, Modeling of spaced receiver scintillation measurements, *Radio Sci.*, **18**, 743, 1983.

S. Basu and H. Kuenzler, Phillips Laboratory, Geophysics Directorate, Hanscom Air Base, MA 01731. (e-mail: santimay@aol.com; Kuenzler@plh.af.mil)

J. Espinoza, Calle Calatrava 216, Urb. Camino Real, La Molina, Instituto Geofísico del Perú, Lima. (e-mail: jespino@geo.igp.gob.pe)

R. Sheehan and C. E. Valladares, Institute for Space Research, Boston College, 885 Centre Street, Newton, MA 02159. (e-mail: sheehan@plh.af.mil; cesar@dlws7.bc.edu)

(Received November 1, 1995; revised January 8, 1996; accepted January 15, 1996.)